CFD APPLICATIONS IN NUCLEAR ENGINEERING, 2nd Edition

EDITED BY: Wenxi Tian, Victor Petrov, Nejdet Erkan, Yixiang Liao and Mingjun Wang

PUBLISHED IN: Frontiers in Energy Research

frontiers Research Topics

frontiers

ISSN 1664-8714
ISBN 978-2-8325-3326-0
DOI 10.3389/978-2-8325-3326-0

About Frontiers

Frontiers is more than just an open-access publisher of scholarly articles: it is a pioneering approach to the world of academia, radically improving the way scholarly research is managed. The grand vision of Frontiers is a world where all people have an equal opportunity to seek, share and generate knowledge. Frontiers provides immediate and permanent online open access to all its publications, but this alone is not enough to realize our grand goals.

Frontiers Journal Series

The Frontiers Journal Series is a multi-tier and interdisciplinary set of open-access, online journals, promising a paradigm shift from the current review, selection and dissemination processes in academic publishing. All Frontiers journals are driven by researchers for researchers; therefore, they constitute a service to the scholarly community. At the same time, the Frontiers Journal Series operates on a revolutionary invention, the tiered publishing system, initially addressing specific communities of scholars, and gradually climbing up to broader public understanding, thus serving the interests of the lay society, too.

Dedication to Quality

Each Frontiers article is a landmark of the highest quality, thanks to genuinely collaborative interactions between authors and review editors, who include some of the world's best academicians. Research must be certified by peers before entering a stream of knowledge that may eventually reach the public - and shape society; therefore, Frontiers only applies the most rigorous and unbiased reviews.
Frontiers revolutionizes research publishing by freely delivering the most outstanding research, evaluated with no bias from both the academic and social point of view. By applying the most advanced information technologies, Frontiers is catapulting scholarly publishing into a new generation.

What are Frontiers Research Topics?

Frontiers Research Topics are very popular trademarks of the Frontiers Journals Series: they are collections of at least ten articles, all centered on a particular subject. With their unique mix of varied contributions from Original Research to Review Articles, Frontiers Research Topics unify the most influential researchers, the latest key findings and historical advances in a hot research area! Find out more on how to host your own Frontiers Research Topic or contribute to one as an author by contacting the Frontiers Editorial Office: frontiersin.org/about/contact

CFD APPLICATIONS IN NUCLEAR ENGINEERING, 2nd Edition

Topic Editors:
Wenxi Tian, Xi'an Jiaotong University, China
Victor Petrov, University of Michigan, United States
Nejdet Erkan, The University of Tokyo, Japan
Yixiang Liao, Helmholtz-Gemeinschaft Deutscher Forschungszentren (HZ), Germany
Mingjun Wang, Xi'an Jiaotong University, China

Publisher's note: In this 2nd edition, the following articles have been added: Yan H, Zhang H, Höhne T, Liao Y, Lucas D and Liu L (2022) Numerical modeling of horizontal stratified two-phase flows using the AIAD model. *Front. Energy Res*. 10:939499. doi: 10.3389/fenrg.2022.939499 ; Choi C-J and Cho HK (2022) Numerical Investigations of Liquid Film Offtake by Transverse Gas Flow in a Downcomer Annulus Geometry. *Front. Energy Res*. 10:847458. doi: 10.3389/fenrg.2022.847458 ; Xiao Y, Duan TC, Ren Q-Y, Zheng X-Y, Zheng M and He R (2022) Modeling and Simulation Analysis on Mixing Characteristics of Two-Phase Flow Around Spacer Grid. *Front. Energy Res*. 10:891074. doi: 10.3389/fenrg.2022.891074

Citation: Tian, W., Petrov, V., Erkan, N., Liao, Y., Wang, M., eds. (2023). CFD Applications in Nuclear Engineering, 2nd Edition. Lausanne: Frontiers Media SA. doi: 10.3389/978-2-8325-3326-0

Table of Contents

frontiers in Energy Research

EDITORIAL
published: 09 February 2021
doi: 10.3389/fenrg.2021.630305

Editorial: CFD Applications in Nuclear Engineering

Wenxi Tian[1]*, *Mingjun Wang*[1], *Victor Petrov*[2], *Nejdet Erkan*[3] and *Yixiang Liao*[4]

[1]Xi'an Jiaotong University, Xi'an, China, [2]University of Michigan, Ann Arbor, MI, United States, [3]The University of Tokyo, Bunkyō, Japan, [4]Helmholtz-Zentrum Dresden-Rossendorf, Helmholtz-Gemeinschaft Deutscher Forschungszentren (HZ), Dresden, Germany

Keywords: CFD, nuclear reactor, two-phase flow, thermal-hydraulics and safety analyses, Best practice guidline

Editorial on the Research Topic

CFD Applications in Nuclear Engineering

Computational fluid dynamics (CFD) and computational multiphase fluid dynamics (CMFD) methods have attracted great attentions in predicting single-phase and multiphase flows under steady-state or transient conditions in the field of nuclear reactor engineering. The CFD research circle is rapidly expanding, and the CFD topic has been covered in many international conferences on nuclear engineering, such as ICONE, NURETH, NUTHOS, and CFD4NRS, which greatly extends the forum to exchange information in the application of CFD codes to nuclear reactor safety issues.

Currently, more and more scholars are devoting their efforts to CFD study in the nuclear engineering community, and a series of valuable research results have emerged in recent years. Therefore, this research topic was proposed, and the issue was organized by Tian from Xi'an Jiaotong University, Petrov from University of Michigan, Erkan from the University of Tokyo, Liao from Helmholtz-Zentrum Dresden-Rossendorf, and Wang from Xi'an Jiaotong University, aiming to share the most advanced progress and innovations related to CFD study in nuclear engineering around the world.

In this topic, the CFD simulation in rod bundles is carried out, and the simulation results are validated based on the LDA measurement in a 5 × 5 rod bundle installed with two split-mixing-vane grids (Xiong et al.). The models of internal heating and natural convention buoyancy, as well as the models of WMLES turbulence and phase changing, were applied in the open-source CFD software OpenFOAM to perform numerical simulations of the COPRA single-layer molten pool experiment (Xi et al.). Three-dimensional computational fluid dynamic (CFD) simulations were performed to study the long-term heat removal mechanisms in the General Atomics' Modular High Temperature Gas-cooled Reactor (MHTGR) design during a P-LOFC accident (Wang et al.). The transient hydraulic characteristics of multistage centrifugal pump during start-up process were also studied using the CFD method (Long et al.).

In terms of two-phase flow simulation using the CFD method, the capabilities and advantages provided by a model that includes an elliptic-blending Reynolds stress turbulence closure (EB-RSM), allowing fine resolution of the velocity field in the near-wall region, are tested over a large database (Colombo and Fairweather). Ling et al. (2020) present a numerical simulation of subcooled flow boiling at a high-pressure condition. An interface tracking method, VOSET, was used to handle the moving interface, and conjugate heat transfer between the wall and the fluid was included in the numerical model. A comparison of the CFD simulation results with the high-resolution experimental data from a helical coil experimental setup operated with a mixture of water and air is discussed, with special emphasis on two-phase pressure drops and void fraction distributions (Che et al.). Zeng et al.

OPEN ACCESS

Edited by:
Muhammad Zubair, University of Sharjah, United Arab Emirates

Reviewed by:
Ivo Kljenak, Institut Jožef Stefan (IJS), Slovenia

***Correspondence:**
Wenxi Tian
wxtian@mail.xjtu.edu.cn

Specialty section:
This article was submitted to Nuclear Energy, a section of the journal Frontiers in Energy Research

Received: *17 November 2020*
Accepted: *04 January 2021*
Published: *09 February 2021*

Citation:
Tian W, Wang M, Petrov V, Erkan N and Liao Y (2021) Editorial: CFD Applications in Nuclear Engineering. Front. Energy Res. 9:630305. doi: 10.3389/fenrg.2021.630305

studied the detailed helium bubble rising behavior in the cross-type channel using CFD software ANSYS Fluent.

With the rapid development of the GEN-IV reactors, the application of CFD in liquid metal flow and heat transfer is also widely accepted. Chai et al. performed the wall-resolved large-eddy simulation (LES) to study the flow and heat transfer properties in a turbulent channel at low Prandtl number. The numerical study on the 19-pin wire-wrapped assembly cooled by lead–bismuth eutectic in liquid metal cooled reactor was also carried out using the CFD method (Li et al.).

Park et al. summarizes the recent activities in the development of SOPHIA code using smoothed particle hydrodynamics (SPH), which is effective to solve the nuclear safety issues encountered in natural disasters and severe accidents accompanied by highly nonlinear deformations. Numerical simulation and validation of aerosol particle removal by water spray droplets with OpenFOAM during the Fukushima daiichi fuel debris retrieval was performed by considering the collection mechanisms of inertial impaction, interception, and Brownian diffusion (Liang et al.).

Finally, 12 articles in total from the United States, Europe, Japan, Korea, and China were collected, to show the recent progress of CFD study in nuclear engineering around the world. This research topic covers across both light water reactors and liquid metal cooled reactors and is definitely a pioneer in this field. It provides valuable references, guidelines, and is leading a fast-forwarding progress for the application of CFD in the nuclear reactor thermal hydraulic analysis. Anyway, we have to confess that the CFD is still developing, and more efforts are required to make it play a more significant role in the nuclear reactor design and safety analysis. We are planning to initiate a new special issue on the "CFD in Numerical Nuclear Reactor" in future. Please feel free to contact us if you have any questions or suggestions.

AUTHOR CONTRIBUTIONS

WT, leading guest editor; MW, guest editor; VP, guest editor; NE, guest editor; and YL, guest editor

Conflict of Interest: The authors declare that the research was conducted in the absence of any commercial or financial relationships that could be construed as a potential conflict of interest.

frontiers in Energy Research

ORIGINAL RESEARCH
published: 20 March 2020
doi: 10.3389/fenrg.2020.00044

Multi-Fluid Computational Fluid Dynamic Predictions of Turbulent Bubbly Flows Using an Elliptic-Blending Reynolds Stress Turbulence Closure

Marco Colombo and Michael Fairweather*

School of Chemical and Process Engineering, University of Leeds, Leeds, United Kingdom

OPEN ACCESS

Edited by:
Yixiang Liao,
Helmholtz-Gemeinschaft Deutscher Forschungszentren (HZ), Germany

Reviewed by:
Mingjun Wang,
Xi'an Jiaotong University, China
Liu Liu,
Central South University, China
Jinbiao Xiong,
Shanghai Jiao Tong University, China

****Correspondence:***
Marco Colombo
m.colombo@leeds.ac.uk

Specialty section:
This article was submitted to Nuclear Energy, a section of the journal Frontiers in Energy Research

Received: *10 January 2020*
Accepted: *03 March 2020*
Published: *20 March 2020*

Citation:
Colombo M and Fairweather M (2020) Multi-Fluid Computational Fluid Dynamic Predictions of Turbulent Bubbly Flows Using an Elliptic-Blending Reynolds Stress Turbulence Closure. Front. Energy Res. 8:44. doi: 10.3389/fenrg.2020.00044

The accurate prediction of bubbly flows is critical to many areas of nuclear reactor thermal hydraulics, mainly, but not only, in relation to the key role bubble behavior plays in boiling flows. Large scale computations of flows with hundreds of thousands of bubbles are possible at a reasonable computational cost using computational fluid dynamic, multi-fluid Eulerian-Eulerian models. The main limitation of these models is the need to entirely model interfacial transfer processes with proper closure relations. Here, the capabilities and advantages provided by a model that includes an elliptic-blending Reynolds stress turbulence closure (EB-RSM), allowing fine resolution of the velocity field in the near-wall region, are tested over a large database. This database includes mostly monodispersed bubbly flows over a wide range of operating conditions and geometrical parameters, including upward and downward pipe flows, large diameter pipes and a square duct. The model shows encouraging accuracy and robustness, with good agreement over most void fraction distributions and accurate prediction of the magnitude and position of the near-wall void fraction peak. The model does not include any wall force, avoiding all the related uncertainties, and the prediction of the void fraction peak relies on the fine resolution of the near-wall pressure gradient induced by the turbulence field. Overall, the EB-RSM allows accurate resolution of the velocity and turbulence field near the wall, and the transition to this and similar turbulence closures is of value in assisting the ongoing quest for thermal hydraulic models that are accurate and of general applicability. Additional modifications to the near-wall modeling approach, which is still based on its single-phase counterpart, may be required to deal with high void fraction conditions and, in the overall model, additional improvements to momentum and, most importantly, bubble-induced turbulence closures are desirable.

Keywords: bubbly flows, nuclear thermal hydraulics, computational fluid dynamics, multi-fluid model, Reynolds stress model

INTRODUCTION

Bubbly flows are frequent in nature and in numerous industrial and engineering applications. Bubbles dispersed in a continuous liquid promote mixing in the liquid phase and large interfacial areas in industrial processes that cause high rates of heat and mass transfer between the phases or the different fluids/components (Lehr et al., 2002; Risso, 2018). In nuclear thermal hydraulics, bubbly flows have a critical role in boiling, and therefore impact the operation, safety limits and accident response of water-cooled reactors. Detailed knowledge of the behavior and size distribution of bubbles is essential for the accurate prediction of boiling, three dimensional void fraction distribution and evolution of the flow regime in boiling flows. Given its impact on nuclear reactor thermal hydraulics, a significant amount of recent research has been focused on improving our understanding of, and predictive capability for, gas-liquid bubbly flows (Mimouni et al., 2010, 2015; Hosokawa et al., 2014; Colombo and Fairweather, 2015; Hazuku et al., 2016; Lucas et al., 2016; Sugrue et al., 2017; Liao et al., 2018; Lubchenko et al., 2018).

The presence of two or more phases complicates the physics of the flow and their multiple interactions make modeling particularly challenging. The liquid phase alters the motion and distribution of bubbles, which mutually impact the continuous phase flow in multiple ways (Liu and Bankoff, 1993a,b; Feng and Bolotnov, 2017). Bubble size distribution continuously evolves, driven by collision and coalescence between bubbles, which can also breakup following interactions with the continuous fluid phase (Liao et al., 2015; Colombo and Fairweather, 2016; Liu and Hibiki, 2018). Most of the time, these processes that impact the large scale fluid behavior are governed by phenomena at much smaller scales (Prince and Blanch, 1990; Legendre and Magnaudet, 1997; Martinez-Bazan et al., 1999; Liao and Lucas, 2009, 2010; Feng and Bolotnov, 2017, 2018). This multiscale complexity has limited the accuracy achievable with empirical or one-dimensional modeling approaches, and is driving the development of computational fluid dynamic (CFD) models given their increased ability to account for small scale physical effects on the three-dimensional fluid motion (Bestion, 2014; Liao et al., 2018; Podowski, 2018).

Recently, a significant research effort has been dedicated to the development of more advanced CFD models for bubbly flows. Significant improvements have been made in interface tracking/resolving methods which are able to resolve all the interfacial details of each individual bubble and that are helping to improve understanding of many still poorly known physical details (Santarelli and Fröhlich, 2016; Feng and Bolotnov, 2017; Magolan et al., 2017; Mehrabani et al., 2017; Chen et al., 2019; du Cluzeau et al., 2019). However, these methods are computationally expensive and remain prohibitive when more than a few hundred bubbles are present. Therefore, for industrial flows and applications where hundreds of thousands of bubbles may be present, Eulerian-Eulerian multi-fluid models remain the preferred choice (Hosokawa and Tomiyama, 2009; Rzehak and Krepper, 2013; Colombo and Fairweather, 2015; Mimouni et al., 2017; Liao et al., 2018). In these approaches, field equations are averaged and interfacial transfer processes entirely modeled by means of often empirically-based closure relations that clearly impact the overall accuracy and applicability of the models. At present, no general agreement has been found on the best closure models available, and the use in these of multiple adjustable constants, eventually optimized on a case-by-case basis over limited experimental databases, remains a major constraint (Lucas et al., 2016; Podowski, 2018).

Momentum transfer governs the dynamic interaction between bubbles and the liquid phase and is modeled by introducing interfacial force terms. In bubbly flows, the lift force has received special attention, with it being the major driver of the bubbles' transverse motion and the accumulation of near spherical bubbles near the wall, and large cap bubbles in the center, of closed ducts. Near the wall, the addition of a wall force has been used to prevent bubbles moving below a certain distance from the wall. In the literature, general agreement on a unified formulation has not been reached and numerous lift-wall formulations exist that often differ only in the value of some model coefficients (Colombo and Fairweather, 2019). In addition to this uncertainty, not only the validity of some of the modeling assumptions, but the entire existence of the wall lubrication force, essentially introduced to predict the correct wall-peaked near-wall void fraction profiles in closed ducts, has been recently questioned. Rzehak et al. (2012) have questioned the linear decrease of the wall force with the distance from the wall, and the accuracy of the widely used model of Antal et al. (1991). More recently, Lubchenko et al. (2018), have predicted the wall-peaked void profile in bubbly flows with a modified expression for the turbulence dispersion force, but without the direct action of any wall lubrication force. The authors' work started from the observation, supported by measurements (Hassan, 2014) and interface tracking results (Lu and Tryggvason, 2013), that the liquid film that, in wall lubrication theory, remains between the bubble and the wall, is either negligibly small or absent.

Another open area in multi-fluid modeling is the development of multiphase turbulence closures. At the present time, the most often adopted strategy consists in adding specific source terms to the turbulence model equations to account for bubble-induced turbulence. Although significant advances have been made in recent years, particularly in modeling based on the conversion of energy from drag to turbulence kinetic energy in bubble wakes (Troshko and Hassan, 2001; Rzehak and Krepper, 2013; Ma et al., 2017; Magolan et al., 2017), turbulence modeling still often relies on the eddy viscosity assumption (Yao and Morel, 2004; Rzehak and Krepper, 2013; Sugrue et al., 2017; Liao et al., 2018). In contrast, second moment closures have only been applied in a few studies (Lopez de Bertodano et al., 1990; Lahey et al., 1993). The necessity for moving beyond the limiting assumptions of eddy viscosity based approaches is well-documented in single-phase flows (Benhamadouche, 2018), and similar arguments can be made for multiphase flows. Using Reynolds stress based closures, it has been demonstrated that turbulence and its modeling can have an additional impact on the distribution of the dispersed phase (Ullrich et al., 2014; Santarelli and Frohlich, 2015) and, as an example in nuclear thermal hydraulics, in the prediction of flow rotation effects induced by mixing blades in pressurized water reactor coolant channels

(Mimouni et al., 2017). Advances in bubble-induced turbulence modeling for implementation in Reynolds stress closures have also recently been achieved (Colombo and Fairweather, 2015; Parekh and Rzehak, 2018).

In a recent paper, we made a preliminary assessment of the additional impact that flow turbulence has on the bubble distribution through the pressure gradient in the fluid phase generated by the anisotropic turbulence field (Colombo and Fairweather, 2019). This was captured using an elliptic-blending Reynolds stress model (EB-RSM) implemented in the STAR-CCM+ CFD code that, to the best of the authors' knowledge, represented the first application of near-wall modeling to bubbly flows. Improved near-wall predictions of multiple quantities were achieved and, through the action of the pressure gradient induced by the turbulence field, accurate prediction of the usual near-wall peak in the void fraction distribution was found without the need for any additional wall force. In the present work, the accuracy of the same multi-fluid model coupled with the EB-RSM is tested against a large database of air-water bubbly flows and its assessment extended over a significantly wider range of conditions. The EB-RSM is coupled with a set of momentum transfer interfacial closures previously assessed with other turbulence models and a specific source for bubble-induced turbulence modeling and, initially, this model is compared against a high-Reynolds number RSM that was previously tested against a similarly large database (Colombo and Fairweather, 2015). Given the already mentioned abundant availability of slightly different and not extensively validated models (Lucas et al., 2016), assessment against a large database including a wide range of conditions is particularly important. The databases used in this paper therefore include, in addition to commonly used upward flows in pipes, other flows less frequently or never tested such as downward flows, large pipes and a square duct. To focus on momentum transfer and turbulence closure effects without adding the additional complication of a population balance model, some effort is taken to limit as much as possible the database to monodispersed bubble diameter distributions that can be characterized reasonably well by a single value of the average bubble diameter. The advantages of RSM closures and near-wall modeling in comparison to more standard methodologies in the critical area of reactor thermal hydraulics are highlighted, and areas for further improvements identified and discussed.

COMPUTATIONAL FLUID DYNAMIC MODEL

The CFD model employed is a two-fluid Eulerian-Eulerian model, where a set of averaged conservation equations is solved for each phase. Given the focus on air-water bubbly flows, only continuity and momentum balances are solved, with the phases treated as incompressible with constant properties:

$$\frac{\partial}{\partial t}\left(\alpha_k \rho_k\right) + \frac{\partial}{\partial x_i}\left(\alpha_k \rho_k U_{i,k}\right) = 0 \tag{1}$$

$$\frac{\partial}{\partial t}\left(\alpha_k \rho_k U_{i,k}\right) + \frac{\partial}{\partial x_j}\left(\alpha_k \rho_k U_{i,k} U_{j,k}\right) = -\alpha_k \frac{\partial}{\partial x_i} p_k + \frac{\partial}{\partial x_j}\left[\alpha_k \left(\tau_{ij,k} + \tau_{ij,k}^{Re}\right)\right] + \alpha_k \rho_k g_i + M_{i,k} \tag{2}$$

In the above equations, U is the velocity and p the pressure. τ and τ^{Re} are the laminar and turbulent stress tensors, respectively, and g is the gravitational acceleration. ρ_k and α_k are the density and the volume fraction of phase k although, for simplicity, in the following we will refer to α only to identify the void fraction of the gas phase. The last term on the right hand side of Equation (2) is the interfacial momentum transfer source M_k and includes drag, lift and the turbulent dispersion force. Wall lubrication, following wall-peaked void fraction profiles obtained even in the absence of any wall force when a Reynolds stress turbulence model is used (Ullrich et al., 2014; Colombo and Fairweather, 2019), and the reported uncertainties in its theoretical foundation (Lubchenko et al., 2018), is neglected. Also, the virtual mass force is neglected in view to its negligible effect in the considered multiphase flow conditions (Politano et al., 2003; Rzehak and Krepper, 2013; Colombo and Fairweather, 2015).

The drag force expresses the resistance opposed to bubble motion by the surrounding liquid and is modeled using the correlation of Tomiyama et al. (2002a):

$$C_D = \frac{8}{3}\frac{Eo}{E^{\frac{2}{3}}\left(1-E^2\right)^{-1} Eo + 16E^{\frac{4}{3}}} F^{-2} \tag{3}$$

The model is a function of the Eötvös number ($Eo = \Delta\rho g d_B / \sigma$, where σ is the surface tension and d_B the diameter of the bubbles) and accounts for the effect of the bubble aspect ratio E on the drag coefficient C_D:

$$E = \max\left[1.0 - 0.35\frac{y_w}{d_B}, E_0\right] \tag{4}$$

Experimental evidence shows that the bubble aspect ratio and drag coefficient increases near the wall, causing a reduction in the relative velocity between the bubbles and the fluid (Hosokawa and Tomiyama, 2009). Consistently with this, in Equation (4) the aspect ratio tends to a value of 1 (spherical bubble) at the wall and reduces with distance from the wall, y_w, to approach a reference value E_0 calculated from the correlation of Welleck et al. (1966). In Equation (3), F is also a function of the bubble aspect ratio (Tomiyama et al., 2002a).

In a shear flow, each bubble experiences a lift force perpendicular to its direction of motion that impact the lateral movement of the bubble and the void fraction distribution. Overall, the lift coefficient is positive for spherical bubbles and pushes them in the direction of lower liquid, and higher relative, velocity, i.e., toward the wall in upflow, resulting in typical wall-peaked void fraction profiles, and toward the center of the duct in downflow. For larger and more deformed non-spherical bubbles, the lift force reverses its direction, producing a shift in void fraction profiles from wall-peaked to core peaked. as observed in numerous upflow experiments (Tomiyama et al., 2002b; Lucas et al., 2005, 2010). Over the years, agreement with experiments has been reported using values of the lift coefficient ranging from 0.1 (Wang et al., 1987; Yeoh and Tu,

2006) to 0.5 (Mimouni et al., 2010), and there remains a lot of uncertainty on the best possible model available. Numerous authors have used the correlation of Tomiyama et al. (2002b) that also predicts the change in sign of the lift coefficient. In this work, a constant value $C_L = 0.1$ is adopted, following good agreement over a wide range of experimental conditions found by Colombo and Fairweather (2015) and in the work of other authors (Lopez de Bertodano et al., 1994; Lahey and Drew, 2001). Overall, the choice of a constant positive value of the lift coefficient will limit the applicability of the model to polydispersed bubbly flows, but is acceptable in the present work where only experimental conditions exhibiting a positive lift force coefficient were selected. In addition, as a consequence of the much more refined resolution near the wall required by the EB-RSM, very high lift values would be predicted in the small cells adjacent to the wall and at a distance much smaller than the bubble diameter. Therefore, and in the absence of a physically based approach, the lift force is decreased at a distance from the wall lower than the bubble diameter, to approach zero at the wall (Shaver and Podowski, 2015):

$$C_L = \begin{cases} 0 & y_w/d_B < 0.5 \\ C_{L0}\left[3\left(2\frac{y_w}{d_B}-1\right)^2 - 2\left(2\frac{y_w}{d_B}-1\right)^3\right] & 0.5 \le y_w/d_B \le 1 \\ C_{L0} & y_w/d_B > 1 \end{cases} \quad (5)$$

The model of Burns et al. (2004) is used to model the turbulent dispersion force:

$$F_{td} = \frac{3}{4}\frac{C_D \alpha \rho_c |U_r|}{d_B}\frac{\nu_{t,c}}{\sigma_\alpha}\left(\frac{1}{\alpha}+\frac{1}{(1-\alpha)}\right)\nabla\alpha \quad (6)$$

In Equation (6), $\boldsymbol{U}_r$ is the relative velocity between the phases, $\nu_{t,c}$ the turbulent kinematic viscosity of the continuous phase and σ_α the turbulent Prandtl number for the volume fraction, assumed equal to 1.0.

Multiphase Turbulence Modeling

Turbulence is resolved in the continuous phase only using the EB-RSM (Manceau and Hanjalic, 2002; Manceau, 2015), based on an extension of the single-phase transport equations for the Reynolds stresses $R_{ij} = \tau_{i,j}^{Re}/\rho_c$ (CD-adapco, 2016):

$$\frac{\partial}{\partial t}\left((1-\alpha)\rho_c R_{ij}\right) + \frac{\partial}{\partial x_j}\left((1-\alpha)\rho_c U_{j,c} R_{ij}\right) = \frac{\partial}{\partial x_j}\left[(1-\alpha) D_{ij}\right] + (1-\alpha)\left(P_{ij}+\Phi_{ij}-\varepsilon_{ij}\right) + (1-\alpha) S_{ij}^{BI} \quad (7)$$

Here, P_{ij} is the turbulence production due to shear and D_{ij} the diffusion of the turbulent stresses, modeled following Daly and Harlow (1970). The turbulence energy dissipation rate ε_{ij} is modeled following the isotropic hypothesis. Φ_{ij} is the pressure-strain correlation and accounts for the redistribution of the turbulence kinetic energy between the stress components. Away from the wall, the pressure-strain is modeled using the "SSG model" model (Speziale et al., 1991), which is quadratically non-linear in the turbulence anisotropy tensor a_{ij}:

$$\Phi_{ij}^h = -\left[C_{1a}\varepsilon + C_{1b} tr(P)\right] a_{ij} + C_2\varepsilon\left(a_{ik}a_{kj} - \frac{1}{3}a_{mn}a_{mn}\delta_{ij}\right) + \left[C_{3a} - C_{3b}\left(a_{ij}a_{ij}\right)^{0.5}\right] k S_{ij} + C_4 k\left(a_{ik}S_{jk} + a_{jk}S_{ik} - \frac{2}{3}a_{mn}S_{mn}\delta_{ij}\right) + C_5 k\left(a_{ik}W_{jk} + a_{jk}W_{ik}\right) \quad (8)$$

In Equation (8), S_{ij} and W_{ij} are the strain and the rotation rate tensors. In the elliptic-blending formulation (Manceau and Hanjalic, 2002; Manceau, 2015), the SSG model is blended with a near-wall model that predicts the correct asymptotic behavior of the turbulent stresses near the wall. In this way, the flow can be entirely resolved in the near-wall region, without the need of imposing the velocity via a wall function. The near-wall model for the pressure-strain reads:

$$\Phi_{ij}^w = -5\frac{\varepsilon}{k}\left[\overline{u_i u_k} n_j n_k + \overline{u_j u_k} n_i n_k - \frac{1}{2}\overline{u_k u_l} n_k n_l \left(n_i n_j + \delta_{ij}\right)\right] \quad (9)$$

In Equation (9), n are the components of the wall-normal vector. Blending between the near-wall and the SSG model is achieved using the elliptic relaxation function α_{EB}, calculated by solving an elliptic relaxation equation with the $\alpha_{EB} = 0$ wall boundary condition:

$$\alpha_{EB} - L\nabla^2\alpha_{EB} = 1 \quad (10)$$

Here, L is the turbulence length scale given by $L = C_l \max\left(C\eta\nu^{3/4}\varepsilon^{-1/4}, k^{3/2}\varepsilon^{-1}\right)$. Near-wall blending, in addition to the pressure-strain, is also enforced for the turbulence energy dissipation rate:

$$\Phi_{ij} = \left(1-\alpha_{EB}^3\right)\Phi_{ij}^w + \alpha_{EB}^3\Phi_{ij}^h \quad (11)$$

$$\varepsilon_{ij} = \left(1-\alpha_{EB}^3\right)\frac{\overline{u_i u_j}}{k}\varepsilon + \frac{2}{3}\alpha_{EB}^3\varepsilon\delta_{ij} \quad (12)$$

The bubble-induced turbulence contribution to the continuous phase turbulence field is included by assuming that the energy lost by the bubbles to drag is converted into turbulence kinetic energy in the bubble wakes (Troshko and Hassan, 2001; Rzehak and Krepper, 2013). Source terms can accordingly defined for the turbulence kinetic energy and dissipation rate transport equations:

$$S_k^{BI} = K_{BI} F_d U_r \quad (13)$$

$$S_\varepsilon^{BI} = \frac{C_{\varepsilon,BI}}{\tau_{BI}} S_k^{BI} \quad (14)$$

Here, F_d is the drag force and τ_{BI} the timescale of the bubble-induced turbulence. This is modeled, following Rzehak and Krepper (2013), from the turbulence velocity scale and the bubble length scale. The constant $K_{BI}$is introduced to account for the modulation of the turbulence source, with its value optimized to 0.25 following comparison with a large database of bubbly flows (Colombo and Fairweather, 2015). The bubble-induced turbulence source in Equation (13) needs to be partitioned amongst the normal Reynolds stress components for use with the EB-RSM approach. In a previous work, we have obtained good agreement with experimental data by apportioning a higher fraction of the bubble-induced contribution to the streamwise

TABLE 1 | Coefficients used in the turbulence model.

C_{1a}	C_{1b}	C_2	C_{3a}	C_{3b}
1.7	0.9	1.05	0.8	0.65
C_4	C_5	C_l	C_η	$C_{\varepsilon,BI}$
0.625	0.2	0.133	80	1.0

direction, and the same assumption is used here (Colombo and Fairweather, 2015):

$$S_{ij}^{BI} = \begin{bmatrix} 1.0 & 0.0 & 0.0 \\ 0.0 & 0.5 & 0.0 \\ 0.0 & 0.0 & 0.5 \end{bmatrix} S_k^{BI} \tag{15}$$

In view of the low value of the density ratio in air-water bubbly flows, and the consequent much smaller values of the Reynolds stresses in the gas-phase, turbulence is resolved only in the continuous phase, while it is derived from this in the dispersed gas phase (Gosman et al., 1992; Behzadi et al., 2004). Values of the model coefficients used can be found in **Table 1**.

Numerical Settings

Numerical simulations were performed using the STAR-CCM+ code (CD-adapco, 2016). For pipe flows, a radial slice of the geometry was considered, whereas a quarter section of the domain was employed for the square duct. At the inlet, constant phase velocities and void fractions were imposed. An isotropic inlet turbulence profile with 2% turbulence intensity was also imposed at the inlet, to facilitate the development toward fully-developed conditions. At the outlet, a fixed pressure boundary condition, and zero gradient conditions on all the other variables, were employed. At the wall, no-slip boundary conditions were enforced on the velocity, with a zero value imposed for the turbulence stresses and the asymptotic limit $\varepsilon = 2\nu\ (k\ /\ y_w)_{\mathrm{yw}\to 0}$ used for the turbulence energy dissipation rate. At the wall, the elliptic relaxation function α_{EB} was set to zero, while a constant value equal to one was imposed at the inlet. On the lateral surfaces of the section, symmetry boundary conditions were imposed on all variables. Convective terms were discretized using second order upwind schemes and the pressure-velocity coupling was solved using a multiphase extension of the SIMPLE algorithm. Simulations were advanced implicitly in time using a second order scheme and, after an inlet development region, fully developed steady-state conditions were reached before recording the results. Strict convergence of residuals as ensured and the mass balance was checked to ensure an error always <0.1 % for both phases.

Grid sensitivity studies ensured that solutions independent of the mesh resolution were reached. Given that significant resolution is needed to properly resolve the near-wall region, the first near-wall cell in the mesh employed was always located at a non-dimensional distance from the wall of $y^+ \sim 1$. A sensitivity study is reported in **Figure 1** for one of the experiments from Hosokawa and Tomiyama (2009) (experiment H22 in **Table 2**). Specifically, the figure shows the radial profiles of the water mean velocity, the air void fraction, the radial turbulent stress (responsible for the radial pressure gradient and its impact on the bubble distribution) and the turbulent shear stress. Values are plotted as a function of the non-dimensional radial co-ordinate, which equals 0 in the center of the pipe and 1 at the pipe wall. Three different meshes were tested, having a number of mesh elements equal to 256 × 250 (on the surface perpendicular to the main flow motion and the axial direction, respectively), 420 × 400 and 975 × 750. Both velocity (**Figure 1A**) and void fraction (**Figure 1B**) do not show any appreciable difference even from the low to the medium refinement. For the radial normal stress and the turbulent shear stress in **Figures 1C,D**, some changes are visible from the low to the medium refinement, while no additional differences are found from the medium to the high refinement. Therefore, the mesh with medium refinement (168,000 elements) was used in the simulations. Comparable refinements were used for the other experiments. Given the fact that Hosokawa and Tomiyama (2009) employed a pipe of small diameter, a significantly higher number of elements was necessary for the larger diameter pipes, and 1,280,000 elements were employed for the square duct of Sun et al. (2014) (more details on the specific experiments are provided in the following section).

RESULTS AND DISCUSSION

Experimental Database

The CFD model will be assessed against a database built using measurements from a number of literature datasets. These includes measurements in vertical upward pipe flows from the works of Liu (1998), Hosokawa and Tomiyama (2009), and Liu and Bankoff (1993a,b) in downward pipe flows from Kashinsky and Randin (1999), in large vertical pipes using the TOPFLOW facility (Shawkat et al., 2008; Lucas et al., 2010), and in a vertical square duct flows (Sun et al., 2014).

The data include a large variety of liquid and gas flow rates, void fractions, bubble diameters and geometries. Since the work described focused on the modeling of multiphase turbulence and interfacial momentum transfer, experiments having as much as possible a monodispersed bubble size distribution were selected as these can be effectively simulated using a constant value of the bubble diameter. Since the present database extends to cases at a high void fraction (for a bubbly flow), it is difficult to assume a monodispersed bubble size distribution in some instances. However, data that showed a marked wall-peaked (in upflow) and core-peaked (in downflow) void fraction profile were selected, allowing the use of a constant lift coefficient. Liquid and gas superficial velocities, and averaged values of the void fraction and the bubble diameter, were used to obtain the correct inlet conditions in the experiments. For the experiments of Liu (1998) and Shawkat et al. (2008), corrections to the nominal gas velocity and averaged void fractions were made from integration of measured radial profiles.

Hosokawa and Tomiyama (2009) measured liquid and gas velocities, void fraction, turbulence in the liquid phase, and bubble number and shape in a vertical upward pipe flow of

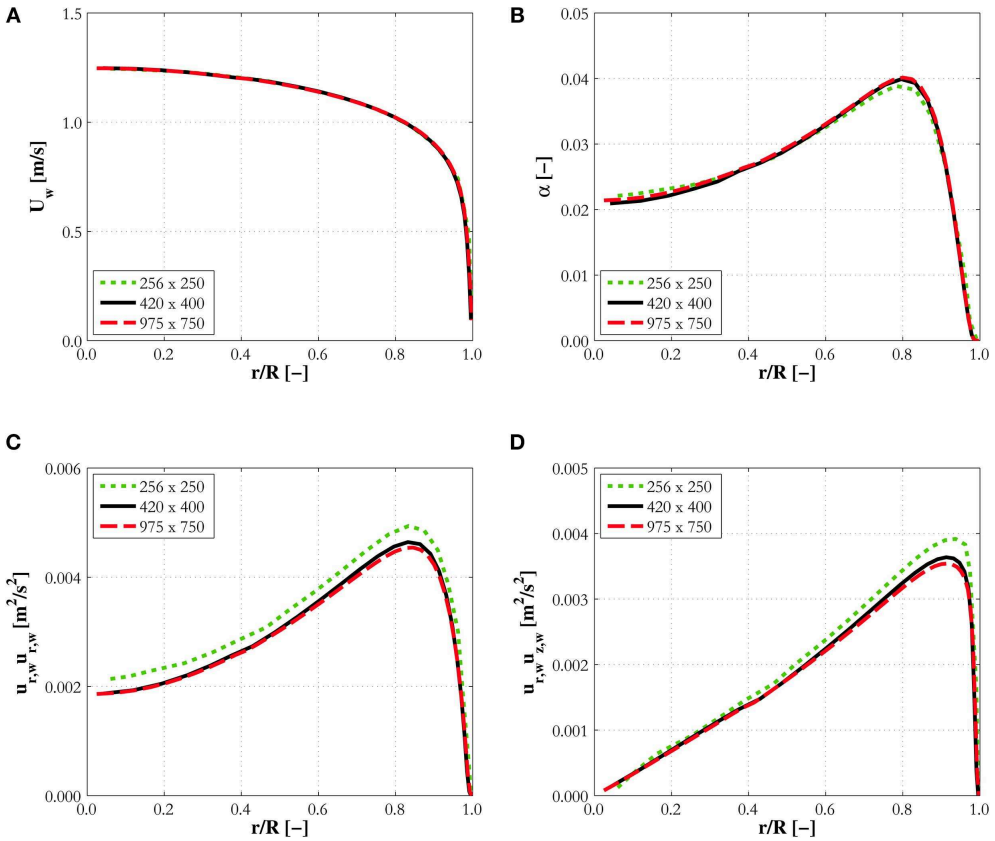

FIGURE 1 | Mesh sensitivity study for experiment H22 from Hosokawa and Tomiyama (2009): **(A)** water mean velocity; **(B)** air void fraction; **(C)** radial turbulent stress; **(D)** Reynolds shear stress.

TABLE 2 | Experimental database.

Case	Source	j_w [m s^{-1}]	j_a [m s^{-1}]	$< \alpha_g >$ [-]	$<d_B>$ [mm]	D_h [m]
H12	Hosokawa and Tomiyama (2009)	0.5	0.025	0.0399	4.25	0.025
H22	Hosokawa and Tomiyama (2009)	1.0	0.036	0.033	3.66	0.025
L11A	Liu (1998)	0.5	0.12	0.152	2.94	0.0572
L22A	Liu (1998)	1.0	0.22	0.157	3.89	0.0572
LB3	Liu and Bankoff (1993a)	0.347	0.112	0.184	3.36	0.038
LB18	Liu and Bankoff (1993a)	0.753	0.180	0.16	3.15	0.038
LB21	Liu and Bankoff (1993a)	0.753	0.347	0.269	3.92	0.038
LB33	Liu and Bankoff (1993a)	1.087	0.230	0.150	3.10	0.038
K1	Kashinsky and Randin (1999)	0.5	0.0194	0.0383	0.8	0.0423
K4	Kashinsky and Randin (1999)	1.0	0.0917	0.108	1.5	0.0423
TL12-041	Lucas et al. (2010)	1.017	0.0096	0.009	4.99	0.195
S1	Shawkat et al. (2008)	0.6	0.016	0.017	3.46	0.200
SN1	Sun et al. (2014)	0.75	0.067	0.075	4.11	0.136
SN2	Sun et al. (2014)	1.0	0.09	0.075	4.05	0.136

inside diameter 25 mm. Liu (1998) studied vertical upward flows of air bubbles in water in a pipe of inside diameter 57.2 mm, measuring the liquid velocity, turbulence and the void fraction. In the present simulations, the liquid superficial velocity and the averaged void fraction were imposed, and the latter was used to adjust the gas velocity to achieve the correct flux of air at the measurement position. Liu and Bankoff (1993a) measured liquid and gas velocities, turbulence levels, void fraction and bubble diameter in an upward air-water bubbly flow in a pipe of inside diameter 38 mm. Kashinsky and Randin

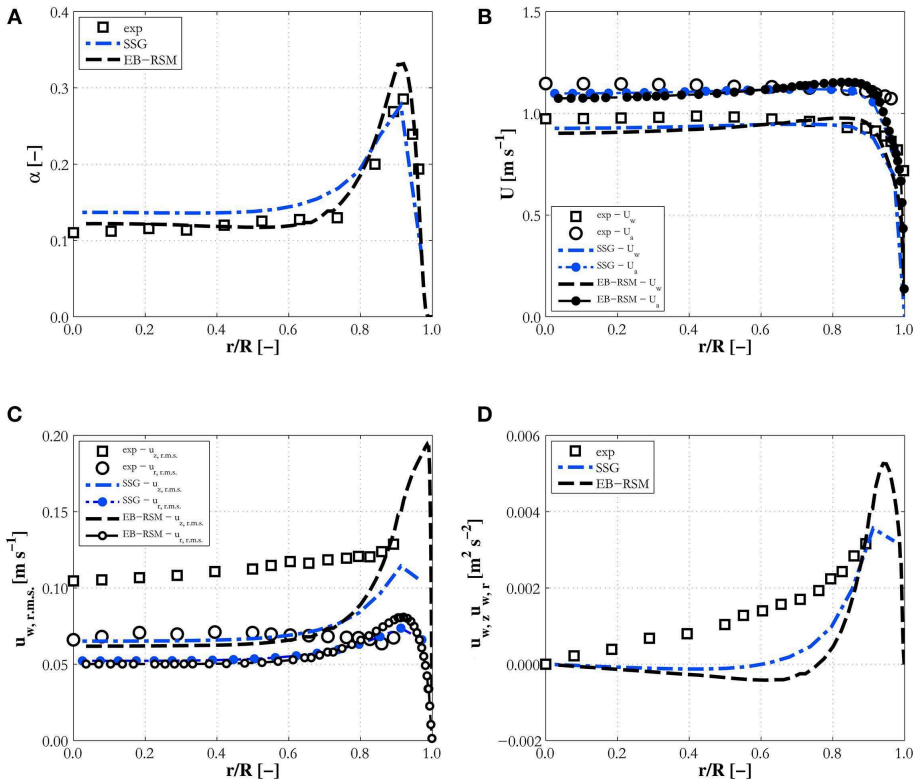

FIGURE 2 | Comparison of EB-RSM simulation results against the SSG model with high-Reynolds number wall treatment for experiment LB18. Radial profiles of: **(A)** void fraction; **(B)** water and air mean velocities; **(C)** axial and radial normal stresses; **(D)** Reynolds shear stress.

(1999) measured liquid velocity, turbulence and void fraction in downflow conditions inside a pipe of diameter 42.3 mm. Shawkat et al. (2008) measured upward air-water bubbly flows in a much larger vertical pipe, having a diameter of 200 mm. Liquid and gas velocities and turbulence, void fraction and bubble diameter were measured. A large pipe, having diameter of 195.3 mm, was also used in the TOPFLOW facility (Lucas et al., 2010) to measure bubble size distribution and evolution using the wire-mesh sensor technique. Gas velocity profiles were also measured. Finally, Sun et al. (2014) measured void fraction, bubble diameter and frequency, water velocity and turbulence kinetic energy in a vertical upward bubbly air-water flow in a square duct of side length 136 mm. Details of the experiments are summarized in **Table 2**. Given that some of the experiments have been used multiple times in previous works [see, for example, Rzehak and Krepper (2015), Rzehak et al. (2017), Parekh and Rzehak (2018), and Magolan and Baglietto (2019)], to reduce confusion and favor consistency we have tried as much as possible to maintain the same naming convention.

Comparison With High-Reynolds Number RSM

In this section, using a first set of simulation results, the EB-RSM predictions are compared with existing results from a previously assessed high-Reynolds number model based on the SSG Reynolds stress model. Details of the model can be found in one of our previous publications (Colombo and Fairweather, 2015). Results are compared against experiments LB18 from Liu and Bankoff (1993a) (**Figure 2**), H22 from Hosokawa and Tomiyama (2009) (**Figure 3**) and L22A from Liu (1998) (**Figure 4**). On the ordinate, the plots show the void fraction, mean liquid (and gas where available) velocity and radial profiles of the turbulence kinetic energy, and the r.m.s. of the velocity fluctuations for Liu and Bankoff (1993a) and Hosokawa and Tomiyama (2009).

This first comparison serves as an assessment of the capabilities of the EB-RSM compared with a more tested model. The models show similar capabilities and good accuracy. Void fraction profiles (**Figures 2A**, **3A**, **4A**) have the typical and expected wall-peaked features and are in very good agreement with the experiments. Most importantly, the magnitude and location of the wall peak are well-predicted by the EB-RSM without the addition of any wall force, and the relative uncertainties connected to a formulation that is, unavoidably, at least partially empirical. This is achieved because, as a consequence of the radial turbulent stress, a radial pressure gradient is generated in the liquid phase and bubbles are pushed toward the pressure minimum in the near-wall region. The radial behavior of the pressure for the three experiments considered is shown in **Figure 5**. Although the variation in pressure is only a few Pascal, it acts over a few millimeters and is sufficient to affect the bubble distribution and, in the near-wall region,

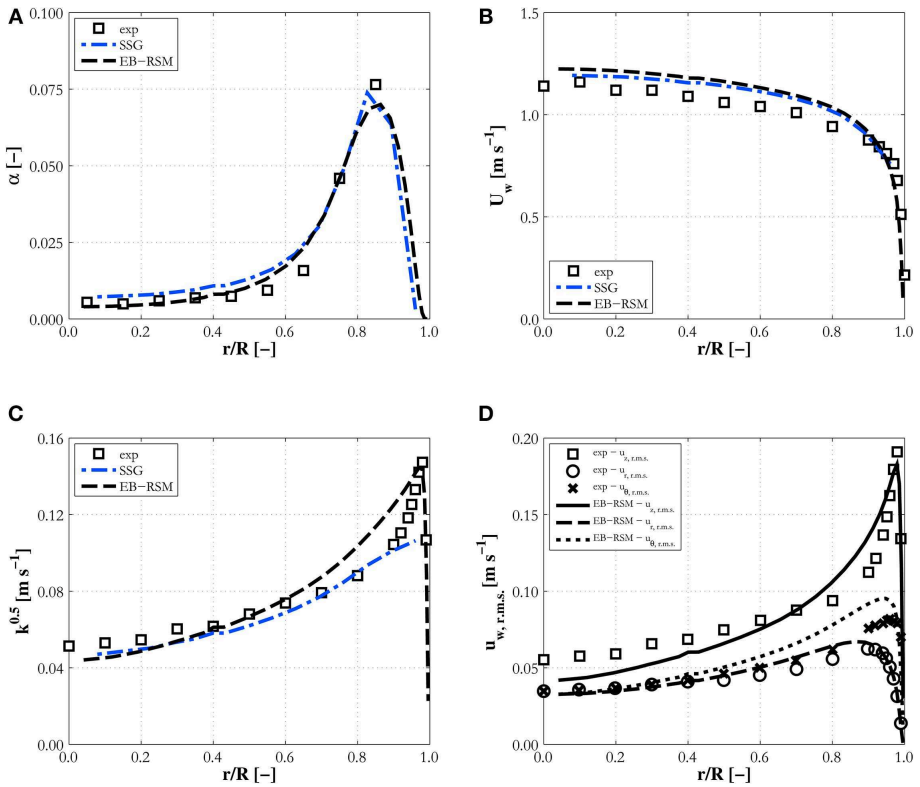

FIGURE 3 | Comparison of EB-RSM simulation results against the SSG model with high-Reynolds number wall treatment for experiment H22. Radial profiles of: **(A)** void fraction; **(B)** water mean velocity; **(C)** turbulence kinetic energy; **(D)** r.m.s. of water velocity fluctuations (for the EB-RSM only).

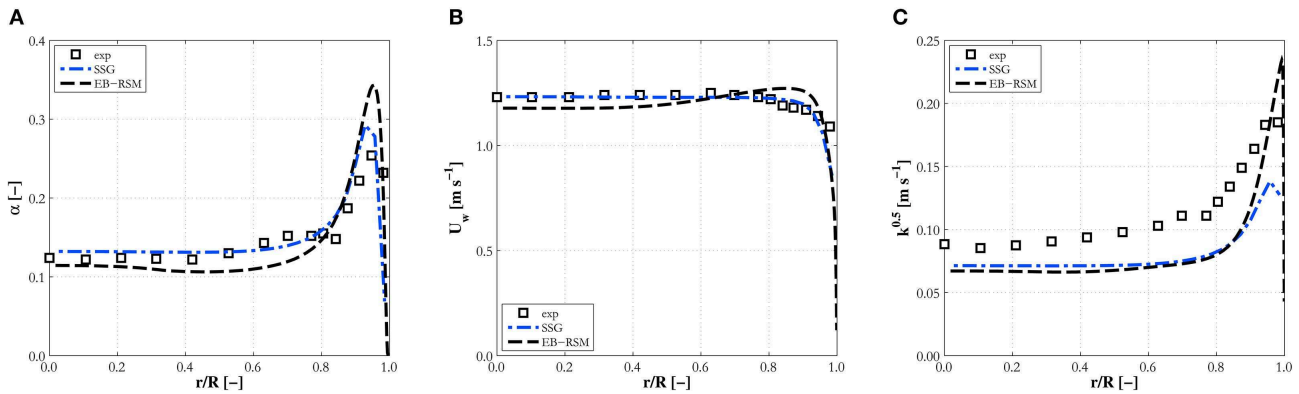

FIGURE 4 | Comparison of EB-RSM simulation results against the SSG model with high-Reynolds number wall treatment for experiment L22A. Radial profiles of: **(A)** void fraction; **(B)** water mean velocity; **(C)** turbulence kinetic energy.

to produce the wall-peaked void fraction profile. Clearly, this pressure gradient, being related to the radial turbulent stress, can only be predicted with accuracy if the anisotropic structure of the turbulence field is accounted for through a Reynolds stress turbulence model, and the near-wall region properly resolved without resorting to wall functions.

Velocity profiles are also in good agreement with experiments and very similar predictions are found between the two models (**Figures 2B**, **3B**, **4B**), although the EB-RSM provides a much more refined resolution in the near-wall region. Turbulence predictions are in agreement with data for Hosokawa and Tomiyama (2009) (**Figure 3C**) and Liu (1998) (**Figure 4C**), although both models show discrepancies for Liu and Bankoff (1993a) (**Figures 2C,D**), for which turbulence levels and the Reynolds shear stress are underpredicted. Additional discussion of these discrepancies will be provided later when predictions

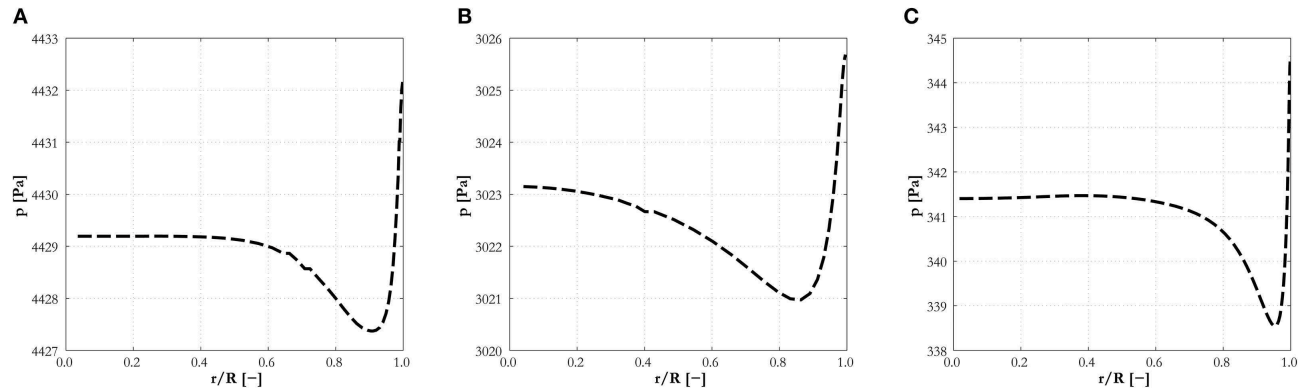

FIGURE 5 | Radial pressure gradient predicted by the EB-RSM for experiments: **(A)** L18; **(B)** H22; **(C)** L22A.

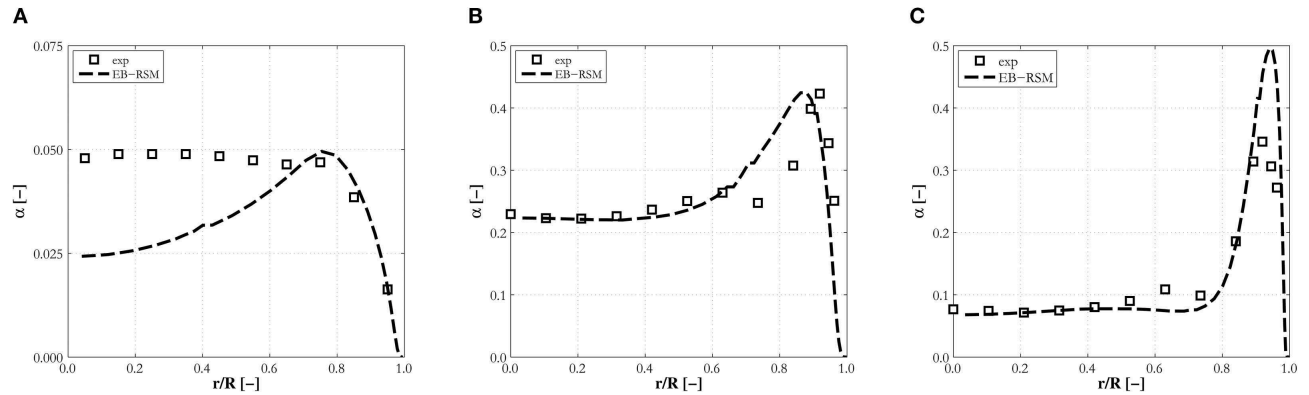

FIGURE 6 | Radial void fraction profiles predicted by the EB-RSM compared against experiments in upward pipe flows: **(A)** H12; **(B)** LB21; **(C)** LB33.

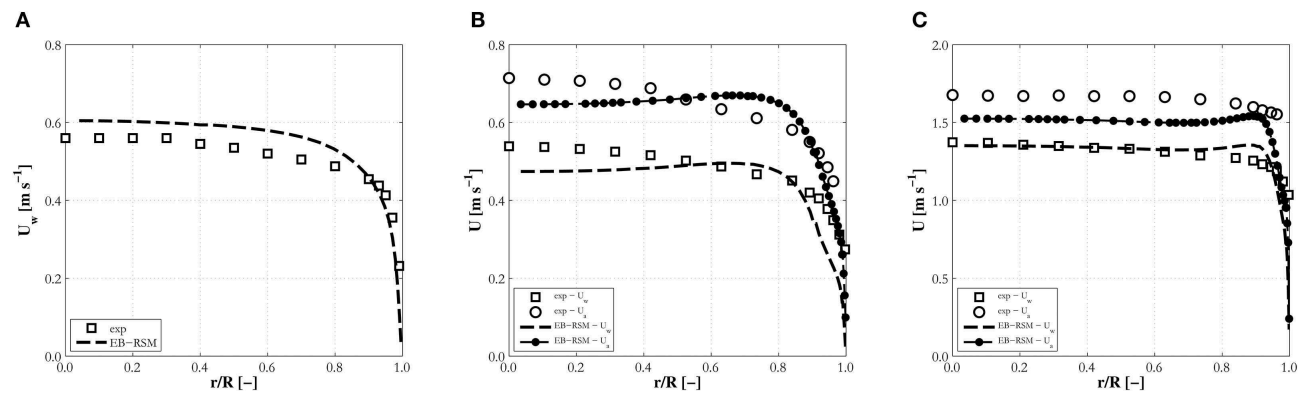

FIGURE 7 | Radial water and air (where available) mean velocity profiles predicted by the EB-RSM compared against experiments in upward pipe flows: **(A)** H12; **(B)** LB3; **(C)** LB33.

with additional data from the same database are presented. It is worth noting here that, while specifically the streamwise, but also the radial, r.m.s. velocities are underpredicted in experiment LB18, much better agreement is found in all three co-ordinate directions for experiment H22 (**Figure 3D**) from Hosokawa and Tomiyama (2009), proving the models' ability to predict the anisotropic turbulence structure. Away from the wall, predictions from the two models are similar. Near the wall, in contrast, the EB-RSM's higher resolution provides a much improved prediction of the turbulence kinetic energy peak, at least for

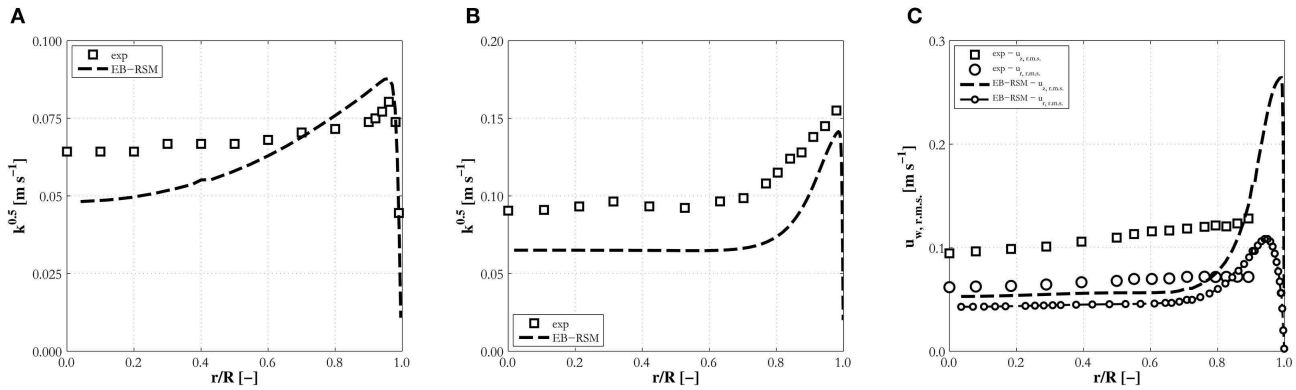

FIGURE 8 | Radial profiles of turbulence kinetic energy, **(A,B)**, and r.m.s. of water velocity fluctuations **(C)** predicted by the EB-RSM compared against experiments in upward pipe flows: **(A)** H12; **(B)** L11A; **(C)** LB33.

the cases where turbulence measurements near the wall are available (**Figures 3C,D**, **4C**). In contrast, the SSG model employs a high-Reynolds formulation and wall functions near the wall. For this reason, the first near-wall cell is located at a non-dimensional distance from the wall of $y^+ \sim 30$, necessary for the wall function to be valid, and the formulation is not able, as expected, to predict the near-wall peak. Overall, the superior capabilities of the EB-RSM in the near-wall region, and their impact on model predictions, in particular, for the void fraction and turbulence in the fluid phase, suggests that models with near-wall modeling capabilities should be adopted wherever possible. For this reason, only predictions from the EB-RSM will be addressed in the following.

Upward Pipe Flows

In this section, results from the comparisons against the remaining upward pipe flows (excluding large diameter pipes that will be addressed separately) in the database are discussed, and these include the cases from Hosokawa and Tomiyama (2009), Liu and Bankoff (1993a) and Liu (1998). Void fraction profiles were almost always found to be in good agreement with experiments, and **Figure 6** provides some examples. Discrepancies are only found in experiment H12 (**Figure 6A**) in the center of the pipe, and these can be attributed to the presence of some larger bubbles that cannot be predicted using a constant positive value of the lift coefficient. From Hosokawa and Tomiyama (2009), measurements show how a tail of bubbles in the range 6–8 mm is present in the bubble size distribution of this experiment only. The predictions remain accurate at large void fractions, approaching or even exceeding 0.4, such as in experiments LB3 and LB21 (**Figure 6B**), although for larger liquid velocities (LB33, **Figure 6C**), the model has a tendency to overpredict the void fraction peak. Overall, the accuracy of the model, even without the addition of any wall force contribution, is encouraging. Clearly, improvements to the lift model, allowing it to predict the change in sign of the lift coefficient, are necessary to extend the overall model's applicability to polydispersed bubbly flows.

Velocity profiles are in general in good agreement with data, and well-predicted in the very near-wall region (**Figure 7A**), for cases where the void fraction is not excessively high. At high void fraction, the velocity, driven by bubble buoyancy, tends to peak at the wall (**Figures 7B,C**), and specific modifications to the drag and near-wall turbulence models might be necessary. Overall, the velocity profiles are almost flat and the slight decrease toward the center of the pipe causes the discrepancies in the prediction of the turbulent shear stress mentioned previously (**Figure 2D**). It is worth noting that in Liu and Bankoff (1993a) measurements were taken at the shortest distance from the inlet and the turbulent shear stress behavior is not entirely consistent with the close-to-flat velocity profile also observed in the experiments (**Figures 2C,D**). Additional model testing is therefore desirable, although detailed experimental characterization of the turbulence structure in pipe flows is not frequently found in the literature. The relative velocity, mainly governed by the drag model, tends to be underpredicted on occasion (**Figure 7C**), contributing to the peak in the liquid velocity profile.

Overall, the area in need of most improvement is multiphase turbulence modeling, and the model for bubble-induced turbulence specifically. Although accurate in many cases (**Figures 8A**, **3C**, **4C**) discrepancies are found, with the data from Liu and Bankoff (1993a) generally underpredicted (**Figure 8C**). It is therefore necessary to progress beyond the simple constant values used in the bubble-induced source and the partitioning of this between the different stresses [Equations (13,15)]. Nevertheless, available measurements confirm how the near-wall resolution allows accurate prediction of the peak in the turbulence kinetic energy at the wall (**Figures 8A,B**).

Downward Pipe Flows

This section extends the previous comparisons, limited to upflow cases, to downward flow conditions. In these flows, the bubbles travel at a lower velocity with respect to the liquid phase, and the same lift force pushes them toward the higher relative velocity region that is now in the center of the pipe. This produces core-peaked void fraction profiles, such as those shown

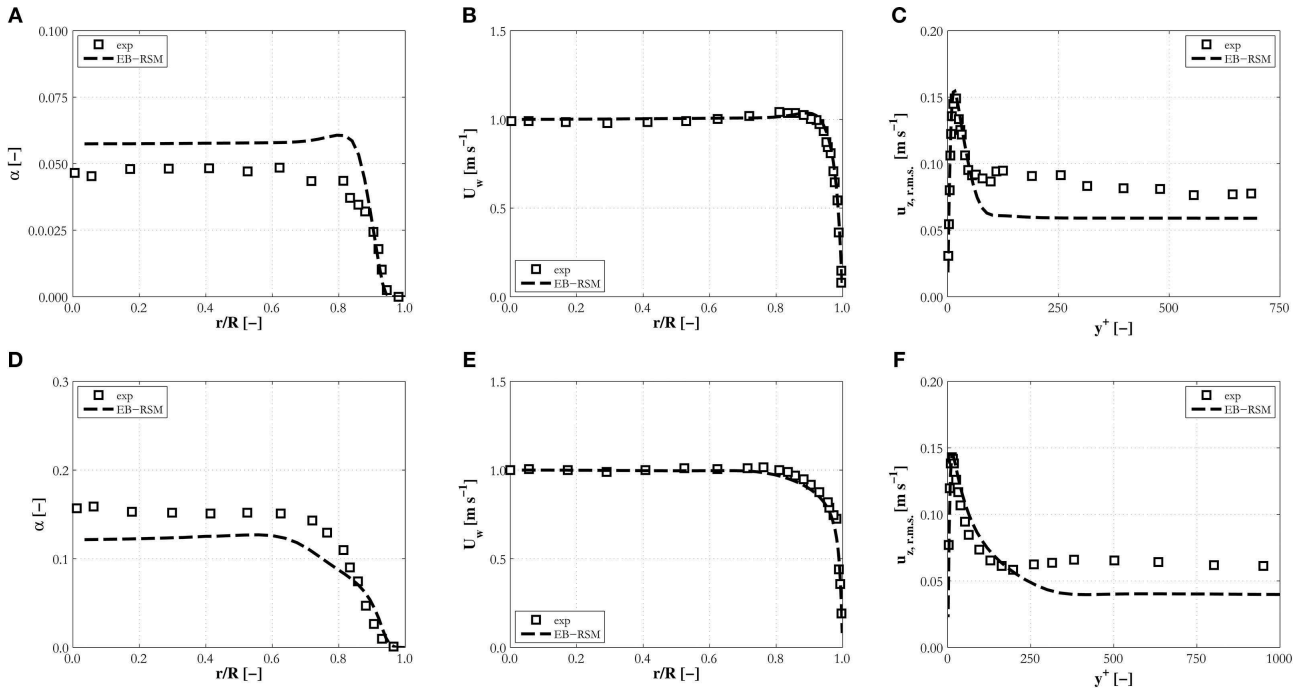

FIGURE 9 | Radial profiles of the void fraction, **(A,D)**, water mean velocity, **(B,E)**, and r.m.s. of axial velocity fluctuations (as a function of the non-dimensional wall distance y^+), **(C,F)**, predicted by the EB-RSM compared against experiments in downward pipe flows: **(A–C)** K1; **(D–F)** K4.

in **Figures 9A,D** for the experiments of Kashinsky and Randin (1999). This behavior is predicted by the model which maintains consistent predictions of the void fraction and shows very good agreement in the near-wall region.

Velocity profiles are in very good agreement (**Figures 9B,E**), and predictions of the mean velocity and turbulence (**Figures 9C,F**) are remarkably good in the near-wall region. For these experiments only, the r.m.s. of the streamwise velocity fluctuations is shown as a function of the non-dimensional distance from the wall, in agreement with the way they were originally provided by Kashinsky and Randin (1999). The turbulence intensity is underpredicted by 20–30 % in the center of the pipe. However, in these experiments an additional complication is included since the bubbles have a much smaller diameter than in previous cases, for which the contribution to turbulence from their wakes may become negligible with respect to that due to their random motion. The latter is not properly captured by the type of model used for bubble-induced turbulence in the present work, it being based on the conversion of energy from drag to turbulence kinetic energy in the bubble wakes.

Vertical Pipes of Large Diameter

In previous comparisons, measurements were taken in pipes with diameters of a few centimeters. In the database, two cases with much larger diameter pipes are also included; TL12-041 from the TOPFLOW facility (Lucas et al., 2010) and S1 from Shawkat et al. (2008). These are included to extend the model assessment as much as possible. The pipes considered have diameters of tens of centimeters and their hydrodynamics can be considered to have features similar to those of bubble columns. Wall effects are still present, but their impact extends into the body of the flow much less than in smaller diameter pipes, with uniform velocity and void fraction distributions dominated by mixing found in the bulk of the pipe cross-section. This is clearly evident in the results of **Figure 10**, where wall effects are confined to the very near-wall region. The model maintains satisfactory agreement with data in these conditions, with the overprediction of the void fraction peak at the wall being the major discrepancy. The air velocity, which has shown some discrepancies in a few previous cases, is instead well-predicted in TL12-041 (**Figure 10B**). It must also be pointed out that measurements of air velocity and turbulence levels are also available for case S1. However, large and not entirely explicable discrepancies with model predictions have been observed in other studies, for example Parekh and Rzehak (2018), and, for this reason, these data are not included here.

Square Duct

Finally, predictions are compared against data in a square channel having a relatively large cross sectional area (Sun et al., 2014). In **Figures 11**, **12**, results are shown for three distinct locations, along the diagonal D of the duct, with the abscissa showing the non-dimensional distance from the duct center d / D, and along two lines parallel to the duct wall, one passing through the center of the duct and the other in the near-wall region. For the latter two locations, the abscissa identifies the non-dimensional distance along the line from the center of the duct, x / L. Void fraction behavior has similarities with pipe flows,

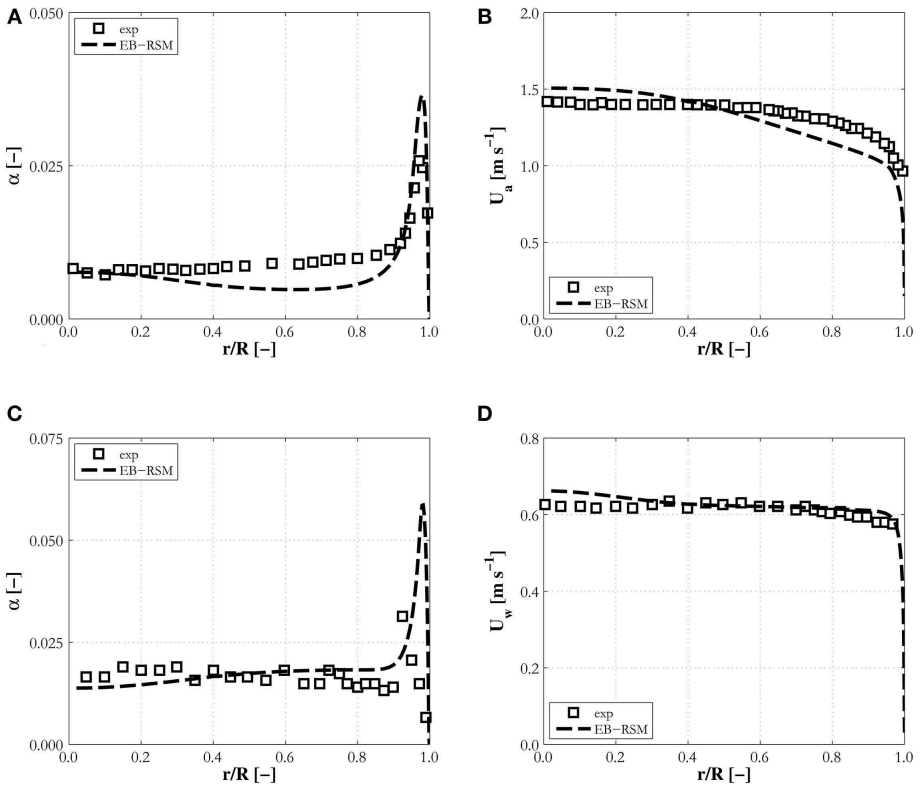

FIGURE 10 | Radial profiles of the void fraction, **(A,C)**, and air **(B)** and water **(D)** mean velocities predicted by the EB-RSM compared against experiments in large diameter pipes: **(A,B)** TL12-041; **(C,D)** S1.

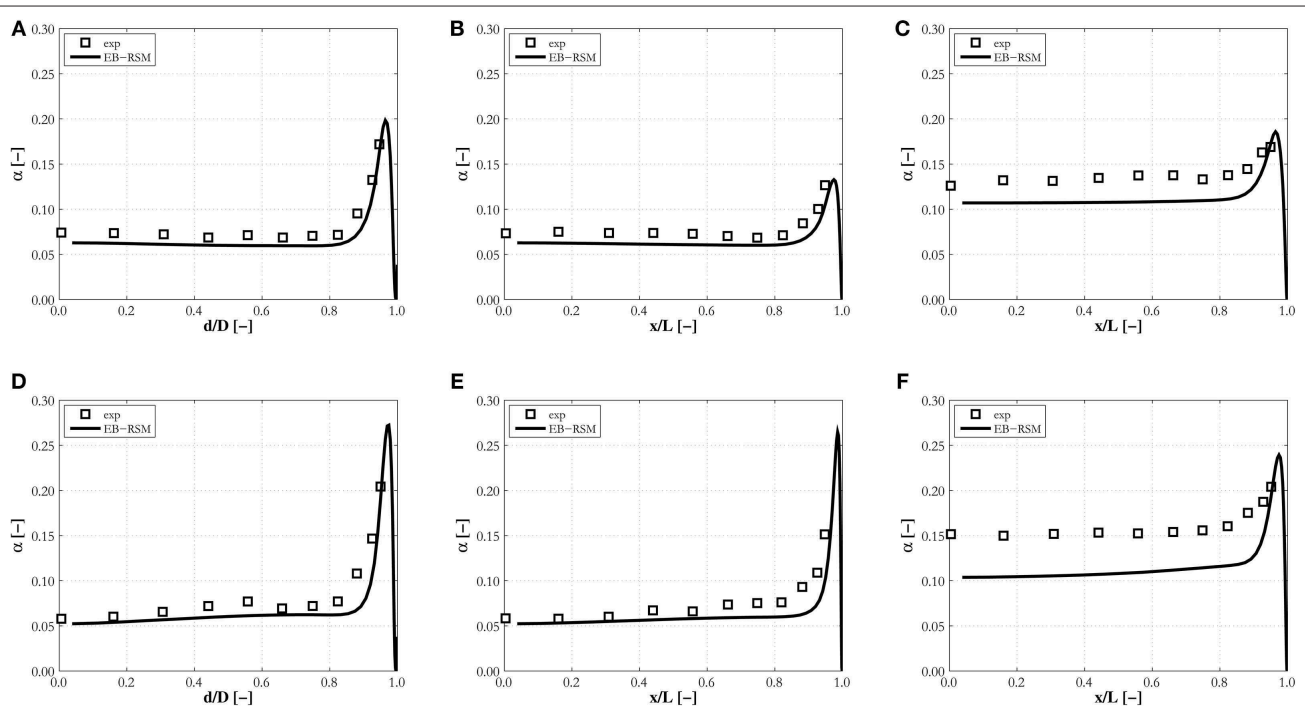

FIGURE 11 | Profiles of the void fraction on the diagonal, **(A,D)**, and a line parallel to the wall passing through the duct center, **(B,E)**, and close to the wall, **(C,F)**, predicted by the EB-RSM compared against Sun et al. (2014) experiments in a square duct: **(A–C)** SN1; **(D–F)** SN2.

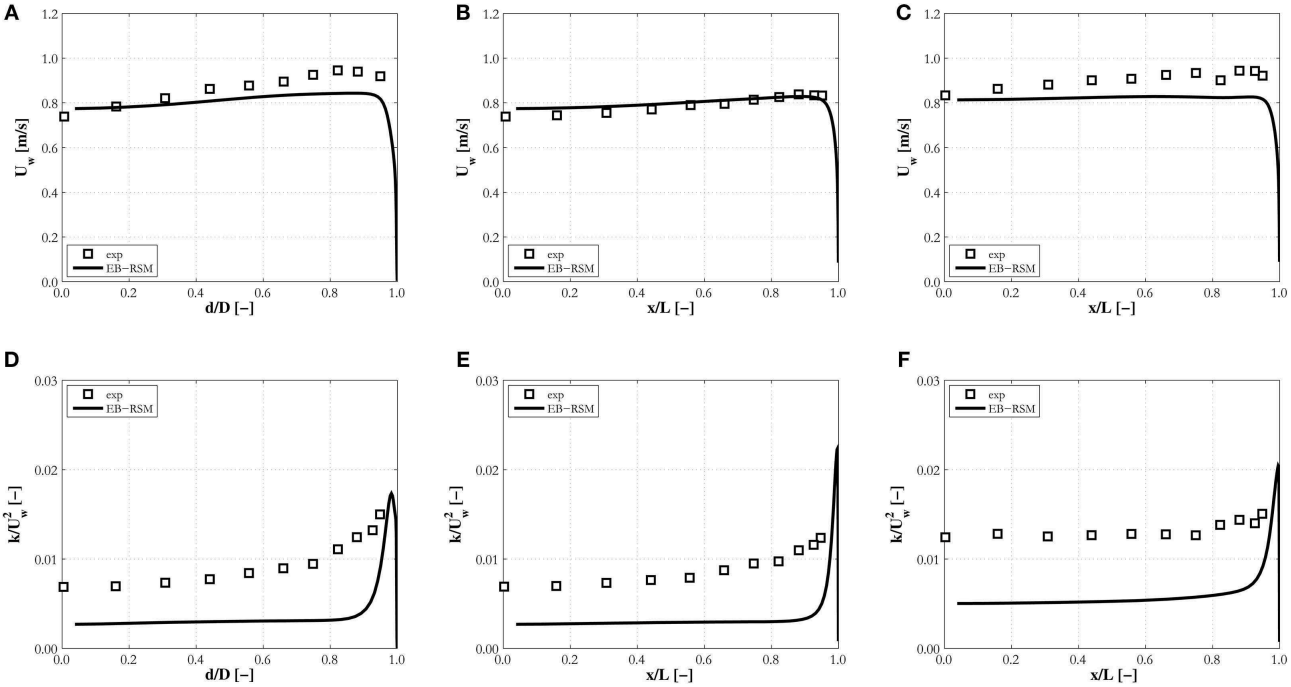

FIGURE 12 | Profiles of the mean liquid velocity and turbulence kinetic energy on the diagonal, **(A,D)**, and a line parallel to the wall passing through the duct center, **(B,E)**, and close to the wall, **(C,F)**, predicted by the EB-RSM compared against Sun et al. (2014) experiments in a square duct: **(A–C)** SN1; **(D–F)** SN2.

with the lift force again pushing the bubbles toward the walls of the duct, where the void fraction peaks. Comparing profiles through the duct center from **Figures 11B,E** with profiles along the wall in **Figures 11C,F**, it may be noted that the latter are higher, given that they essentially detect the near-wall peak along the wall. The highest values are found in the duct corners, as shown by the peaks along the diagonal in **Figures 11A,D**, and the line parallel to the near-wall region in **Figures 11C,F**. The void fraction is well-reproduced by the model for both experiments considered in **Figure 11**, particularly along the diagonal and the line through the duct center. Some underestimation is found on the line in the near-wall region, although the peak in the duct corner remains well-predicted.

Lastly, **Figure 12** shows mean velocity profiles for experiment SN1 and turbulence kinetic energy, normalized with the square of the mean velocity, for experiment SN2. The qualitative behavior of the velocity, peaking at the walls and corners and slightly decreasing toward the duct center, are well-captured, although the wall-peak is underpredicted. Turbulence levels, in line with previous results, are underestimated in the center of the duct, again confirming remaining challenges in obtaining accurate predictions. In this case, the cross-sectional area is large and the void fraction relatively high, and additional effects promoted by the interaction between bubbles may add to the contribution from their wakes, explaining the underestimation. Peaks in the turbulence kinetic energy are visible at the walls, although the absence of measurements taken in the very near-wall region prevents any comprehensive assessment. Overall, additional model improvements are necessary, but the model performance remains robust even in the square duct geometry.

CONCLUSIONS

The performance of an Eulerian-Eulerian multi-fluid CFD model coupled with the EB-RSM turbulence closure, allowing fine resolution of the near-wall region, has been assessed against a large database of air-water bubbly flows. The overall model has demonstrated robust applicability and encouraging accuracy over a wide range of operating conditions and geometrical parameters, with the experimental database including upward and downward pipe flows, large diameter pipe and square duct flows, some of which have rarely, if ever, been tested against.

Good agreement with data for the void fraction distribution was obtained for all experimental cases, with accurate predictions of the magnitude and positon of the near-wall peak found in most experiments. The model does not account for any wall lubrication force, and all the associated uncertainties in modeling this force, and the wall peak is obtained from the action of the radial pressure gradient induced by the turbulence field and its accurate prediction near the wall. In this regard, these results confirm and support recent findings where wall peaked void fraction distributions were also obtained without any wall lubrication effect, as a consequence of which the theoretical basis of the wall lubrication force was questioned. Further evidence will be required, as well as extension to the modeling to handle laminar conditions where turbulent effects are not present, such as with the addition of the turbulent dispersion regularization model of Lubchenko et al. (2018). Overall, and although the lift force remains dominant, these mentioned additional turbulent effects should be taken into account as accurately as possible in any model that aims to be general applicability. For this reason,

the transition to models based on Reynolds stress turbulence model formulations, able to capture the anisotropy of the turbulence field, with near-wall resolution capabilities is to be preferred when possible. Such approaches allow fine resolution of the velocity and turbulence field near the wall, although modifications seem necessary at high void fraction given that the elliptic-blending model is still based on its single-phase counterpart. For this to be achieved, the availability of detailed measurements of the turbulent stresses in the near-wall region for further model validation is desirable.

Overall, multiphase turbulence models and the modeling of bubble-induced turbulence are areas in need of major improvement. Over the wide range of conditions tested, multiple physical processes coexist which all contribute in determining a flows' characteristics, which makes predictions particularly challenging. In the short term, more physically based modeling improvements of the bubble-induced source and the attribution of a larger portion of that source to the streamwise direction are necessary. In this regard, some advances have started to appear in the very recent literature (du Cluzeau et al., 2019; Liao et al., 2019).

Finally, it is worth stressing the role of assessments of the kind described for the future development of computational models of bubbly flows. When focusing on only a few experiments for model validation purposes, these can show trends not observable in other cases (see, for example, the differences between **Figures 7C**, **10B** for the air velocity, and **Figures 2C**, **3D** for the turbulence field), and results and modeling improvements should be accepted only when consistent over multiple datasets.

DATA AVAILABILITY STATEMENT

Datasets obtained from the CFD simulations with the EB-RSM for the experiments included in this paper are available at https://doi.org/10.5518/800.

AUTHOR CONTRIBUTIONS

MC and MF conceived and planned the research, wrote and finalized the manuscript. MC developed the model and performed the simulations.

ACKNOWLEDGMENTS

The authors gratefully acknowledge the financial support of the EPSRC under grants EP/R021805/1, Can modern CFD models reliably predict DNB for nuclear power applications?, EP/R045194, Computational Modeling for Nuclear Reactor Thermal Hydraulics, and EP/S019871/1, Toward comprehensive multiphase flow modeling for nuclear reactor thermal hydraulics.

REFERENCES

Antal, S. P., Lahey, R. T., and Flaherty, J. E. (1991). Analysis of phase distribution in fully developed laminar bubbly two-phase flow. *Int. J. Multiphase Flow* 17, 635–652. doi: 10.1016/0301-9322(91)90029-3

Behzadi, A., Issa, R. I., and Rusche, H. (2004). Modelling of dispersed bubble and droplet flow at high phase fractions. *Chem. Eng. Sci.* 59, 759–770. doi: 10.1016/j.ces.2003.11.018

Benhamadouche, S. (2018). On the use of (U)RANS and LES approaches for turbulent incompressible single phase flows in nuclear engineering applications. *Nucl. Eng. Des.* 312, 2–11. doi: 10.1016/j.nucengdes.2016.11.002

Bestion, D. (2014). The difficult challenge of a two-phase CFD modelling for all flow regimes. *Nucl. Eng. Des.* 279, 116–125. doi: 10.1016/j.nucengdes.2014.04.006

Burns, A. D., Frank, T., Hamill, I., and Shi, J. M. (2004). "The Favre averaged drag model for turbulent dispersion in Eulerian multi-phase flows," in *5th International Conference on Multiphase Flows* (Yokohama).

CD-adapco (2016). *STAR-CCM+® Version 10.04 User Guide*.

Chen, C., Wang, M., Zhao, X., Ju, H., Wang, X., Tian, W., et al. (2019). Numerical study on the single bubble rising behaviors under rolling conditions. *Nucl. Eng. Des.* 349, 183–192. doi: 10.1016/j.nucengdes.2019.04.039

Colombo, M., and Fairweather, M. (2015). Multiphase turbulence in bubbly flows: RANS simulations. *Int. J. Multiphase Flow* 77, 222–243. doi: 10.1016/j.ijmultiphaseflow.2015.09.003

Colombo, M., and Fairweather, M. (2016). RANS simulation of bubble coalescence and break-up in bubbly two-phase flows. *Chem. Eng. Sci.* 146, 207–225. doi: 10.1016/j.ces.2016.02.034

Colombo, M., and Fairweather, M. (2019). Influence of multiphase turbulence modelling on interfacial momentum transfer in two-fluid Eulerian-Eulerian CFD models of bubbly flows. *Chem. Eng. Sci.* 195, 968–984. doi: 10.1016/j.ces.2018.10.043

Daly, B. J., and Harlow, F. H. (1970). Transport equations of turbulence. *Phys. Fluids* 13, 2634–2649. doi: 10.1063/1.1692845

du Cluzeau, A., Bois, G., and Toutant, A. (2019). Analysis and modelling of reynolds stresses in turbuent bubbly up-flows from direct numerical simulations. *J. Fluid Mech.* 866, 132–168. doi: 10.1017/jfm.2019.100

Feng, J., and Bolotnov, I. A. (2017). Evaluation of bubble-induced turbulence using direct numerical simulation. *Int. J. Multiphase Flow* 93, 92–107. doi: 10.1016/j.ijmultiphaseflow.2017.04.003

Feng, J., and Bolotnov, I. A. (2018). Effect of the wall presence on the bubble interfacial forces in a shear flow field. *Int. J. Multiphase Flow* 99, 73–85. doi: 10.1016/j.ijmultiphaseflow.2017.10.004

Gosman, A. D., Lekakou, C., Politis, S., Issa, R. I., and Looney, M. K. (1992). Multidimensional modeling of turbulent two-phase flows in stirred vessels. *AIChE J* 38, 1946–1956. doi: 10.1002/aic.690381210

Hassan, Y. A. (2014). *Full-field Measurements of Turbulent Bubbly Flow Using Innovative Experimental Techniques*. Technical Report CASL-U-2014-0209-000.

Hazuku, T., Hibiki, T., and Takamasa, T. (2016). Interfacial area transport due to shear collision of bubbly flow in small-diameter pipes. *Nucl. Eng. Des.* 310, 592–603. doi: 10.1016/j.nucengdes.2016.10.041

Hosokawa, S., Hayashi, K., and Tomiyama, A. (2014). Void distribution and bubble motion in bubbly flows in a 4×4 rod bundle. *part I: experiments. J. Nucl. Sci. Technol.* 51, 220–230. doi: 10.1080/00223131.2013.862189

Hosokawa, S., and Tomiyama, A. (2009). Multi-fluid simulation of turbulent bubbly pipe flow. *Chem. Eng. Sci.* 64, 5308–5318. doi: 10.1016/j.ces.2009.09.017

Kashinsky, O. N., and Randin, V. V. (1999). Downward bubbly gas-liquid flow in a vertical pipe. *Int. J. Multiphase Flow* 25, 109–138. doi: 10.1016/S0301-9322(98)00040-8

Lahey, R. T., and Drew, D. A. (2001). The analysis of two-phase flow and heat transfer using a multidimensional, four field, two-fluid model. *Nucl. Eng. Des.* 204, 29–44. doi: 10.1016/S0029-5493(00)00337-X

Lahey, R. T., Jr, Lopez de Bertodano, M., and Jones, O.C., Jr. (1993). Phase distribution in complex geometry conduits. *Nucl. Eng. Des.* 141, 177–201. doi: 10.1016/0029-5493(93)90101-E

Legendre, D., and Magnaudet, J. (1997). A note on the lift force on a spherical bubble or drop in a low-Reynolds-number shear flow. *Phys. Fluids* 9, 3572–3574. doi: 10.1063/1.869466

Lehr, F., Millies, M., and Mewes, D. (2002). Bubble-size distributions and flow fields in bubble columns. *AIChE J.* 48, 2426–2443. doi: 10.1002/aic.690481103

Liao, Y., and Lucas, D. (2009). A literature review of theoretical models for drop and bubble breakup in turbulent dispersions. *Chem. Eng. Sci.* 64, 3389–3406. doi: 10.1016/j.ces.2009.04.026

Liao, Y., and Lucas, D. (2010). A literature review on mechanisms and models for the coalescence process of fluid particles. *Chem. Eng. Sci.* 65, 2851–2864. doi: 10.1016/j.ces.2010.02.020

Liao, Y., Ma, T., Krepper, E., Lucas, D., and Frohlich, J. (2019). Application of a novel model for bubble-induced turbulence to bubbly flows in containers and vertical pipes. *Chem. Eng. Sci.* 202, 55–69. doi: 10.1016/j.ces.2019.03.007

Liao, Y., Ma, T., Liu, L., Ziegenhein, T., Krepper, E., and Lucas, D. (2018). Eulerian modelling of turbulent bubbly flow based on a baseline closure concept. *Nucl. Eng. Des.* 337, 450–459. doi: 10.1016/j.nucengdes.2018.07.021

Liao, Y., Rzehak, R., Lucas, D., and Krepper, E. (2015). Baseline closure model for dispersed bubbly flow: bubble coalescence and breakup. *Chem. Eng. Sci.* 122, 336–349. doi: 10.1016/j.ces.2014.09.042

Liu, H., and Hibiki, T. (2018). Bubble breakup and coalescence models for bubbly flow simulation using interfacial area transport equation. *Int. J. Heat Mass Tran.* 126, 128–146. doi: 10.1016/j.ijheatmasstransfer.2018.05.054

Liu, T. J. (1998). "The role of bubble size on liquid phase turbulent structure in two-phase bubbly flow," in *3rd International Conference on Multiphase Flow (ICMF1998)* (Lyon).

Liu, T. J., and Bankoff, S. G. (1993a). Structure of air-water bubbly flow in a vertical pipe—I. *liquid mean velocity and turbulence measurements. Int. J. Heat Mass Tran.* 36, 1049–1060. doi: 10.1016/S0017-9310(05)80289-3

Liu, T. J., and Bankoff, S. G. (1993b). Structure of air-water bubbly flow in a vertical pipe—II. *void fraction, bubble velocity and bubble size distribution. Int. J. Heat Mass Tran.* 36, 1061–1072. doi: 10.1016/S0017-9310(05)80290-X

Lopez de Bertodano, M., Lahey, R. T., and Jones, O. C. (1994). Phase distribution in bubbly two-phase flow in vertical ducts. *Int. J. Multiphase Flow* 20, 805–818. doi: 10.1016/0301-9322(94)90095-7

Lopez de Bertodano, M., Lee, S. J., and Lahey, R. T. Jr., Drew, D.A. (1990). The prediction of two-phase turbulence and phase distribution phenomena using a reynolds stress model. *J. Fluid Eng.* 112, 107–113. doi: 10.1115/1.2909357

Lu, J., and Tryggvason, G. (2013). Dynamics of nearly spherical bubbles in a turbulent channel upflow. *J. Fluid Mech.* 732, 166–189. doi: 10.1017/jfm.2013.397

Lubchenko, N., Magolan, B., Sugrue, R., and Baglietto, E. (2018). A more fundamental wall lubrication force from turbulent dispersion regularization for multiphase CFD applications. *Int. J. Multiphase Flow* 98, 36–44. doi: 10.1016/j.ijmultiphaseflow.2017.09.003

Lucas, D., Beyer, M., Szalinski, L., and Schutz, P. (2010). A new databse on the evolution of air-water flows along a large vertical pipe. *Int. J. Therm. Sci.* 49, 664–674. doi: 10.1016/j.ijthermalsci.2009.11.008

Lucas, D., Krepper, E., and Prasser, H. M. (2005). Development of co-current air-water flow in a vertical pipe. *Int. J. Multiphase Flow* 31, 1304–1328. doi: 10.1016/j.ijmultiphaseflow.2005.07.004

Lucas, D., Rzehak, R., Krepper, E., Ziegenhein, T., Liao, Y., Kriebitzsch, P., et al. (2016). A strategy for the qualification of multi-fluid approaches for nuclear reactor safety. *Nucl. Eng. Des.* 299, 2–11. doi: 10.1016/j.nucengdes.2015.07.007

Ma, T., Santarelli, C., Ziegenhein, T., Lucas, D., and Frohlich, J. (2017). Direct numerical simulation-based reynolds-averaged closure for bubble-induced turbulence. *Phys. Rev. Fluids* 2:034301. doi: 10.1103/PhysRevFluids.2.034301

Magolan, B., and Baglietto, E. (2019). Assembling a bubble-induced turbulence model incorporating physcial understanding from DNS. *Int. J. Multiphase Flow* 116, 185–202. doi: 10.1016/j.ijmultiphaseflow.2019.04.009

Magolan, B., Baglietto, E., Brown, C., Bolotnov, I. A., Tryggvason, G., and Lu, J. (2017). Multiphase turbulence mechanisms identification from consistent analysis of direct numerical simulation data. *Nucl. Eng. Technol.* 49, 1318–1325. doi: 10.1016/j.net.2017.08.001

Manceau, R. (2015). Recent progress in the development of the elliptic blending reynolds-stress model. *Int. J. Heat Fluid Flow* 51, 195–220. doi: 10.1016/j.ijheatfluidflow.2014.09.002

Manceau, R., and Hanjalic, K. (2002). Elliptic blending model: a new near-wall reynolds-stress turbulence closure. *Phys. Fluids* 14, 744–754. doi: 10.1063/1.1432693

Martinez-Bazan, C., Montanes, J. L., and Lasheras, J. C. (1999). On the breakup of an air bubble injected into a fully developed turbulent flow. part 1. breakup frequency. *J. Fluid Mech.* 401, 157–182. doi: 10.1017/S0022112099006680

Mehrabani, M. T., Nobari, M. R. H., and Tryggvason, G. (2017). An efficient front-tracking method for simulation of multi-density bubbles. *Int. J. Numer. Methods Flow* 84, 445–465. doi: 10.1002/fld.4355

Mimouni, S., Archambeau, F., Boucker, M., Lavieville, J., and Morel, C. (2010). A second order turbulence model based on a reynolds stress approach for two-phase boiling flows. part 1: application to the ASU-annular channel case. *Nucl. Eng. Des.* 240, 2233–2243. doi: 10.1016/j.nucengdes.2009.11.019

Mimouni, S., Baudry, C., Guingo, M., Hassanaly, M., Lavieville, J., Mechitoua, N., et al. (2015). "Combined evaluation of bubble dynamics, polydispersion model and turbulence modelling for adiabatic two-phase flow," in *16th International Topical Meeting on Nucelar Reactor Thermal-Hydraulics (NURETH-16)* (Chicago, IL).

Mimouni, S., Guingo, M., Lavieville, J., and Merigoux, N. (2017). Combined evaluation of bubble dynamics, polydispersion model and turbulence modeling for adiabatic two-phase flow. *Nucl. Eng. Des.* 321, 57–68. doi: 10.1016/j.nucengdes.2017.03.041

Parekh, J., and Rzehak, R. (2018). Euler-Euler multiphase CFD-simulation with full Reynolds stress model and anisotropic bubble-induced turbulence. *Int. J. Multiphase Flow* 99, 231–245. doi: 10.1016/j.ijmultiphaseflow.2017.10.012

Podowski, M. Z. (2018). Is reactor multiphase thermal-hydraulics a mature field of engineering science? *Nucl. Eng. Des.* 345, 196–208. doi: 10.1016/j.nucengdes.2019.01.022

Politano, M. S., Carrica, P. M., and Converti, J. (2003). A model for turbulent polydisperse two-phase flow in vertical channels. *Int. J. Multiphase Flow* 29, 1153–1182. doi: 10.1016/S0301-9322(03)00065-X

Prince, M. J., and Blanch, H. W. (1990). Bubble coalescence and breakup in air-sparged bubble columns. *AIChE J.* 36, 1485–1499. doi: 10.1002/aic.690361004

Risso, F. (2018). Agitation, mixing and transfers induced by bubbles. *Annu. Rev. Fluid Mech.* 50, 25–48. doi: 10.1146/annurev-fluid-122316-045003

Rzehak, R., and Krepper, E. (2013). CFD modeling of bubble-induced turbulence. *Int. J. Multiphase Flow* 55, 138–155. doi: 10.1016/j.ijmultiphaseflow.2013.04.007

Rzehak, R., and Krepper, E. (2015). Bubbly flows with fixed polydispersity: validation of a baseline closure model. *Nucl. Eng. Des.* 287, 108–118. doi: 10.1016/j.nucengdes.2015.03.005

Rzehak, R., Krepper, E., and Lifante, C. (2012). Comparative study of of wall-force models for the simulation of bubbly flows. *Nucl. Eng. Des.* 253, 41–49. doi: 10.1016/j.nucengdes.2012.07.009

Rzehak, R., Ziegenhein, T., Kriebitzsch, P., Krepper, E., and Lucas, D. (2017). Unified modelling of bubbly flows in pipes, bubble columns, and airlift columns. *Chem. Eng. Sci.* 157, 147–158. doi: 10.1016/j.ces.2016.04.056

Santarelli, C., and Frohlich, J. (2015). Direct numerical simulations of spherical bubbles in vertical turbulent channel flow. *Int. J. Multiphase Flow* 75, 174–193. doi: 10.1016/j.ijmultiphaseflow.2015.05.007

Santarelli, C., and Fröhlich, J. (2016). Direct numerical simulations of spherical bubbles in vertical turbulent channel flow. *Influence of bubble size and bidispersity. Int. J. Multiphase Flow* 81, 27–45. doi: 10.1016/j.ijmultiphaseflow.2016.01.004

Shaver, D. R., and Podowski, M. Z. (2015). Modeling of interfacial forces for bubbly flows in subcooled boiling conditions. *Trans. Am. Nucl. Soc.* 113, 1368–1371.

Shawkat, M., Ching, C., and Shoukri, M. (2008). Bubble and liquid turbulence characteristics of bubbly flow in a large diameter vertical pipe. *Int. J. Multiphase Flow* 34, 767–785. doi: 10.1016/j.ijmultiphaseflow.2008.01.007

Speziale, C. G., Sarkar, S., and Gatski, T. B. (1991). Modelling the pressure-strain correlation of turbulence: an invariant dynamical system approach. *J. Fluid Mech.* 227, 245–272. doi: 10.1017/S0022112091000101

Sugrue, R., Magolan, B., Lubchenko, N., and Baglietto, E. (2017). Assessment of a simplified set of momentum closure relations for low volume fraction regimes in STAR-CCM+ and OpenFOAM. *Ann. Nucl. Energy* 110, 79–87. doi: 10.1016/j.anucene.2017.05.059

Sun, H., Kunugi, T., Shen, X., Wu, D., and Nakamura, H. (2014). Upward air-water bubbly flow characteristics in a vertical square duct. *J. Nucl. Sci. Technol.* 51, 267–281. doi: 10.1080/00223131.2014.863718

Tomiyama, A., Celata, G. P., Hosokawa, S., and Yoshida, S. (2002a). Terminal velocity of single bubbles in surface tension dominant regime. *Int. J. Multiphase Flow* 28, 1497–1519. doi: 10.1016/S0301-9322(02)00032-0

Tomiyama, A., Tamai, H., Zun, I., and Hosokawa, S. (2002b). Transverse migration of single bubbles in simple shear flows. *Chem. Eng. Sci.* 57, 1849–1858. doi: 10.1016/S0009-2509(02)00085-4

Troshko, A. A., and Hassan, Y. A. (2001). A two-equation turbulence model of turbulent bubbly flows. *Int. J. Multiphase Flow* 27, 1965–2000. doi: 10.1016/S0301-9322(01)00043-X

Ullrich, M., Maduta, R., and Jakirlic, S. (2014). "Turbulent bubbly flow in a vertical pipe computed by an eddy-resolving reynolds stress model," *10th International ERCOFTAC Symposium on Engineering Turbulence Modelling and Measurements (ETMM 10)* (Marbella).

Wang, S. K., Lee, S. J., Jones, O. C., and Lahey, R. T. (1987). 3-D turbulence structure and phase distribution measurements in bubbly two-phase flows. *Int. J. Multiphase Flow* 13, 327–343. doi: 10.1016/0301-9322(87)90052-8

Welleck, R. M., Agrawal, A. K., and Skelland, A. H. P. (1966). Shape of liquid drops moving in liquid media. *AIChE J.* 12, 854–862. doi: 10.1002/aic.690120506

Yao, W., and Morel, C. (2004). Volumetric interfacial area prediction in upward bubbly two-phase flow. *Int. J. Heat Mass Tran.* 47, 307–328. doi: 10.1016/j.ijheatmasstransfer.2003.06.004

Yeoh, G. H., and Tu, J. Y. (2006). Two-fluid and population balance models for subcooled boiling flow. *Appl. Math. Model.* 30, 1370–1391. doi: 10.1016/j.apm.2006.03.010

Conflict of Interest: The authors declare that the research was conducted in the absence of any commercial or financial relationships that could be construed as a potential conflict of interest.

The handling editor declared a past co-authorship with one of the authors MC.

frontiers in Energy Research

ORIGINAL RESEARCH
published: 24 March 2020
doi: 10.3389/fenrg.2020.00043

Validation for CFD Simulation in Rod Bundles With Split-Vane Spacer Grids Based on LDA Measurement

Jinbiao Xiong[1]*, *Chuan Lu*[2] and *Wenhai Qu*[1]

[1] School of Nuclear Science and Engineering, Shanghai Jiao Tong University, Shanghai, China, [2] State Key Laboratory of Reactor System Design Technology, Nuclear Power Institute of China, Chengdu, China

Laser Doppler anemometry (LDA) measurement of axial flow velocity and pressure drop measurement has been carried out in a 5 × 5 rod bundle installed with two split-mixing-vane grids. The measured results are utilized to validate the CFD simulation. The realizable and non-linear k-ε turbulence model is utilized in the CFD computation, while the two-layer wall treatment is employed with both models. Mesh sensitivity investigation shows that the pressure drop is weakly affected by local mesh refinement in the spacer grid, while its effect on the velocity in the near wake of spacer grid is apparent. The validation shows that prediction on the mean axial velocity is relatively poor in the near wake of the spacer grid where the measured result shows relatively smooth distribution of axial velocity. Refinement of mesh in the spacer grid eliminates some peaks for the non-linear model. Comparing with the effect of mesh refinement, the difference caused by the turbulence models is relatively weak in the near wake region. In the far-wake region it is still difficult to judge which model shows definite superiority to the other. For pressure drop, prediction of non-linear k-ε is closer to the experiment.

Keywords: rod bundle, split-type mixing vane, Laser Doppler anemometer (LDA), CFD validation, two-equation turbulence model

OPEN ACCESS

Edited by:
Mingjun Wang,
Xi'an Jiaotong University, China

Reviewed by:
Xiaochang Li,
Harbin Engineering University, China
Muhammad Saeed,
East China University of Technology, China

***Correspondence:**
Jinbiao Xiong
xiongjinbiao@sjtu.edu.cn

Specialty section:
This article was submitted to Nuclear Energy, a section of the journal Frontiers in Energy Research

Received: *10 January 2020*
Accepted: *03 March 2020*
Published: *24 March 2020*

Citation:
Xiong J, Lu C and Qu W (2020) Validation for CFD Simulation in Rod Bundles With Split-Vane Spacer Grids Based on LDA Measurement. Front. Energy Res. 8:43. doi: 10.3389/fenrg.2020.00043

INTRODUCTION

Turbulent flow in the fuel assemblies of nuclear reactors significantly affects heat transfer and pressure drop performances which are the essential factors in the research and design (R&D) of advanced fuel assembly. Computation fluid dynamics (CFD) analysis has been extensively applied in screening and optimizing the design of spacer grid of rod-bundle fuel assembly in pressurized water reactors (PWRs). For example, Ikeda (Ikeda, 2014) utilized CFD analysis in the design of high-efficiency spacer grid to increase the critical heat flux (CHF) performance. It has also been well-recognized that the best practices should be complied with in the CFD analysis to obtain the high-fidelity results (Mahaffy et al., 2014).

In order to understand the flow structure in rod-bundle geometry and to obtain CFD-grade data to validate CFD methodology, numerous experiments on flow measurement in rod bundles have been carried out. Krauss et al. investigated large-scale quasi-periodic fluctuations in the enlarged tight-lattice bundles based on the three dimensional (3D) flow measurement utilizing the hot-wire probe with x-wire (Krauss and Meyer, 1998; McClusky, 2004) employed the particle image

velocimetry (PIV) to measure the cross flow induced by split mixing vane in one of the subchannels in the 5 × 5 rod bundle. With their experimental data, Smith III et al. validated their CFD methodology (Smith et al., 2002). Dominguez-Ontiveros et al. (2012) utilized the two-dimensional time-resolved PIV (2D TR-PIV) to measure the flow field in a 5 × 5 rod bundle with spacer grid. With the laser Doppler anemometry (LDA) Conner et al. (2013a) obtained the cross flow in rod bundle with the same configuration as Dominguez-Ontiveros et al.'s. Dominguez-Ontiveros et al.'s and Conner et al.'s experimental data has been included in the CFD benchmark database (Conner et al., 2013b). With the aid of telecentric optic Xiong et al. (2018a) measured the 2D cross flow in a 5 × 5 rod bundle with 2D PIV. More recently, Qu et al. (2019a,b,c) carried out the high-fidelity PIV measurement in rod bundle with split mixing vanes.

For the sake of establishing the best practices for CFD analysis on flow in rod-bundle fuel assembly, two international collaborative CFD benchmark activities, i.e., OECD/NEA KAERI MATiS-H benchmark (Lee et al., 2012), EPRI-NESTOR benchmark (Wells et al., 2015) and IAEA benchmark (Xiong et al., 2018b), have been carried out. Step-by-step experimental activities are on-going in Shanghai Jiao Tong University to provide the high-quality CFD validation data. Experimental measurement of turbulent flow in a 3 × 3 rod bundle is first carried out for CFD validation (Xiong et al., 2014a). Following the 3 × 3 rod bundle experiment, the flow field in the 6 × 6 rod bundle installed with simple ring-type grids is measured with the LDA and utilized for CFD validation (Xiong et al., 2014b). In this paper, the turbulent flow in the 5 × 5 rod bundle is measured in the downstream of spacer grid with split-type mixing vanes using the LDA. The CFD methodology is validated based on the experiment result.

EXPERIMENT

Hydraulic Facility and Test Section

The flow measurement experiments have been carried out on the MEdium-Scale Hydraulic (MESH) facility in Shanghai Jiao Tong University which is shown in **Figure 1**. In the test facility two parallel pumps supply the water flow rate as high as 225 m^3/h. The bypass line is utilized to adjust the flow rate through the test section line. The flow meter with measurement error <1% is installed on the test section line to measure the flow rate. A heat exchanger is installed to remove the pump heat from the main loop.

Figure 2 shows the vertical cross-sectional and three-dimensional (3D) view of 5 × 5 rod bundle test section in which the 9.5 mm-in-diameter rods are squarely arrayed with the pitch of 12.6 mm. The rod bundle, 1,156 mm in length, is vertically installed in the housing channel which has the inner dimension of 65 × 65 mm. A honeycomb flow straightener, 50 mm in height, is installed upstream of the rod bundle, in order to remove the upstream effect of elbow and adapter and to achieve relatively uniform flow distribution in the cross section. On the bottom support plat of rod bundle the circular and oval holes are drilled to distribute the flow more uniformly across the rod bundle. The cone-shaped bottom end is manufactured on each rod to facilitate assembling. In the rod bundle two spacer grids with split mixing vanes, 33 mm in height, are installed. $Z = 0$ is defined on the top surface of bottom support plate. The first spacer grid locates 410 mm above the bottom support plate, i.e., $Z =$ 410 mm. The distance between the first and second spacer grid is 300 mm. Upstream and downstream of the first spacer grid one measurement window is fabricated, respectively. Both windows are 65 × 120 mm in size. Downstream of the second spacer grid

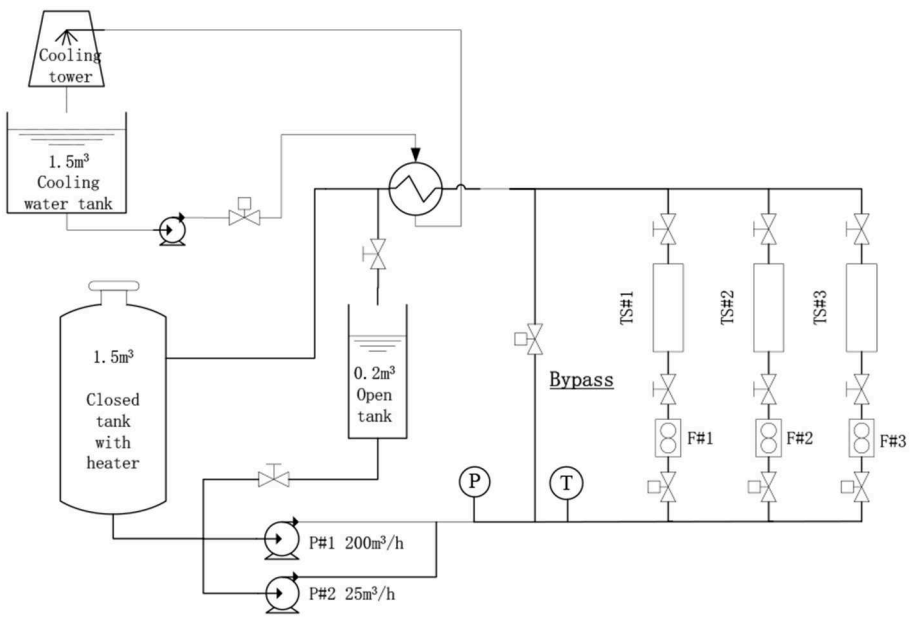

FIGURE 1 | Schematic of test facility utilized in the experiment (Xiong et al., 2014b).

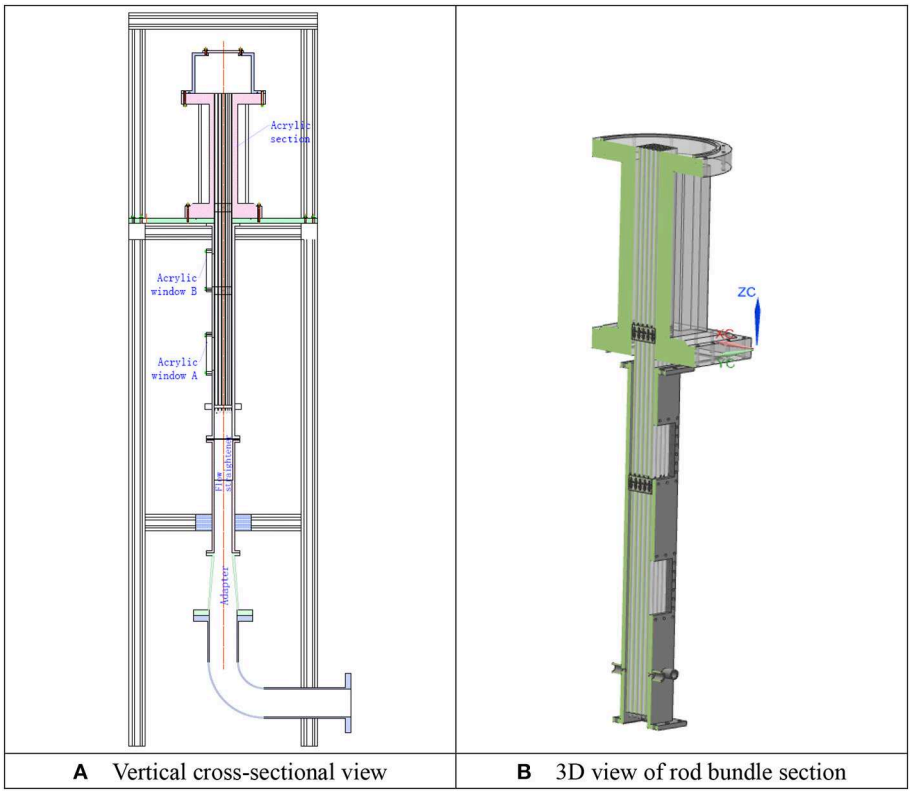

FIGURE 2 | Geometry of the rod-bundle test section. **(A)** Vertical cross-sectional view. **(B)** 3D view of rod bundle section.

the acrylic channel is utilized. On the top of the test section a water tank is installed where water flows away from the three circumferential outlets.

Velocity and Pressure Measurement

The pressure drop over the span of the first spacer grid is measured between $Z = 344$ and 677mm with the differential pressure transducer YOKOKAWA EJA110A. The five-beam Dantec FiberFlow Laser Doppler Anemometry (LDA) is employed for flow measurement. However, due to the blockage of rods, only the axial velocity component is measured with the green laser ($\lambda = 514.5$ nm). The 5 μm Dantec polyamide particle, 1.03 g/cm^3 in density, is utilized as the seeding particle. At each sample point the measurement is stopped when either of the two conditions is satisfied, i.e., the maximum number of samples reaches 5,000 or the sampling time is 60 s. Axial velocity is measured over two cross sections upstream of the first spacer grid, i.e., $Z = 165$ and 205 mm and over three cross sections downstream of the first spacer grid, i.e., $Z = 460$, 490, and 520 mm. The downstream cross sections are, respectively 2.54D_h, 5.08D_h, and 7.62D_h downstream of the spacer grid. The measured points on each cross section are shown as black dots in **Figure 3**. There are nine measuring lines and 45 measuring points on each line.

Figure 4 presents an example of measured instantaneous velocity samples at one of the measuring positions. Based on the instantaneous velocity, the mean velocity is derived via

$$W = \sum_{i=1}^{N} w_i \Delta t_i / \sum_{i=1}^{n} \Delta t_i$$

where the transit time weighting is utilized. N is the number of valid samples; w_i is the ith instantaneous axial velocity; Δt_i is the transit time through the measurement volume of the ith sampled particle. The transit time weighting is also used while deriving the root mean square of fluctuating velocity, i.e.,

$$W_{rms} = \sqrt{\sum_{i=1}^{N} \Delta t_i w_i'^2 / \sum_{i=1}^{n} \Delta t_i}$$

where $w_i' = w_i - W$.

Error Estimation

Several sources of error have been recognized in LDA measurement.

Type 1: Velocity bias, i.e., more high velocity particles are sampled than the low velocity ones. This type of error is minimized by introducing transit time weighting method, which has been introduced above.

Type 2: Misalignment of the laser beams can lead to non-uniform spacing of fringe model. This error is mitigated by alignment with a pin-hole which is 50 μm in diameter.

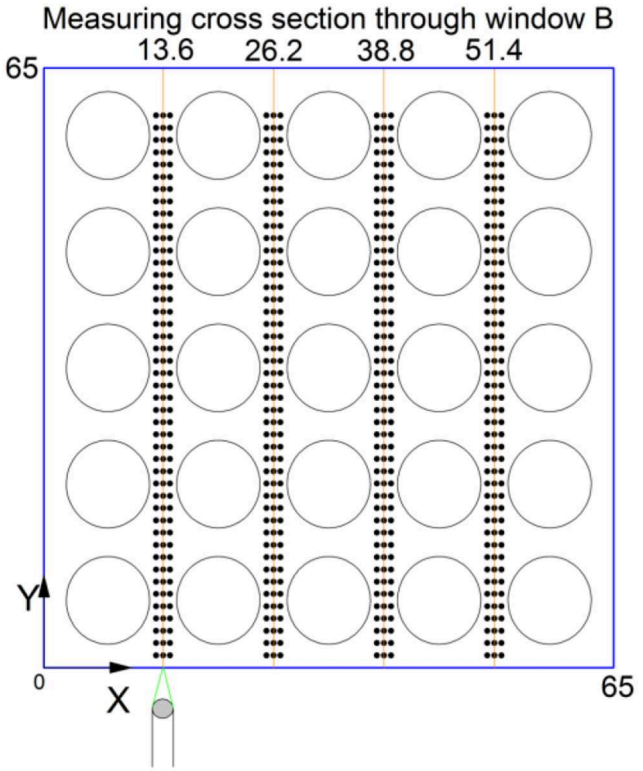

FIGURE 3 | Measuring position in the cross section downstream of the first spacer grid.

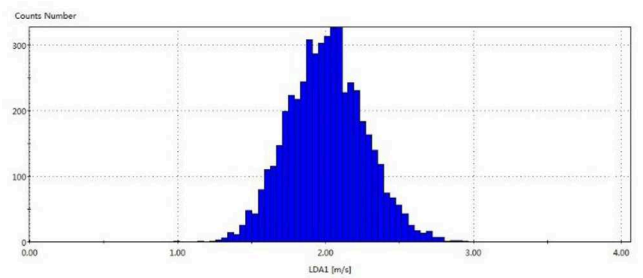

FIGURE 4 | Example of sampled velocity distribution.

Type 3: Velocity gradient bias resulted from velocity gradient in the measurement volume. While using the lens with focal length of 310 mm, the measurement volume of LDA is an ellipsoid whose axis lengths are 50, 800, and 50 μm, respectively. For two-dimensional flows the error of mean velocity caused by velocity gradient bias can then be quantified as follows

$$U_{real} - U_{meas} = -\frac{{d_x}^2}{32}\frac{\partial^2 U_{real}}{\partial x^2} - \frac{{d_y}^2}{32}\frac{\partial^2 U_{real}}{\partial y^2} + H(d^3)$$

Type 4: Uncertainty due to limited sampling number. The 95% confidence bound of mean velocity can be estimated with

$$\varepsilon_{mean} = \frac{\sigma_u}{U_{mean}\sqrt{N}}$$

while the 95% confidence bound of RMS velocity can be calculated with

$$\varepsilon_{rms} = \frac{1}{\sqrt{2N}}$$

The velocity gradient bias is proportional to the measurement volume size and the second derivatives of velocity. However, quantification of the bias is difficult since lack of data on the second derivatives. Here, we take the 95%-confidence-bound uncertainty as the error bound.

Experiment Results

The experiment is carried out at the bulk velocity of 3 m/s. The temperature in the test section is 21°C. The Reynolds number is 3.6×10^4. The axial velocity is measured from both windows. **Figure 5** compares the measured axial velocity at two cross sections upstream of the first spacer grid, i.e., $Z = 165$ mm (14 D_h) and 205 mm (17.4 D_h), with the data obtain by Chang et al. (2012) who measured the flow in the cross section 90 D_h downstream of the spacer where the flow can be regarded as fully developed. The comparison shows that our measured data on the plane $Z = 205$ mm matches with Chang et al.'s fully developed data. In the fully developed condition the velocity distribution become even more non-uniform. There is an apparent peak of axial velocity in the center of wall subchannel when the flow is fully developed. Due to the higher velocity, the turbulence intensity in the wall subchannel becomes stronger due to turbulence production in the vicinity of wall. In the contrast the turbulence intensity in the inner subchannel is weaker in the full developed condition. The estimated error is also shown in **Figure 5**. We can see that the mean velocity has been well-measured while the uncertainty of the RMS velocity is relatively large.

Through the upper window which is downstream of the first spacer grid axial velocity is measured on the three horizontal planes. The measured mean and RMS velocity are shown in **Figures 6**, **7**. Apparent similarity has been observed between the first and third measured zones and between the second and fourth measured zones. The disturbance by the spacer grids decays in the plane further from the spacer grid. However, its effect is still remarkable on the plane $Z = 515$ mm. The uncertainty of mean velocity is large at the positions where y is large. It is resulted from the low sampling data rate when the measured position is far away from the visualization window. However, the largest relative error is estimated to be within 2%.

CFD VALIDATION

Based on the continuous validation efforts, Westinghouse and AREVA developed their best practice guidelines (BPGs) for

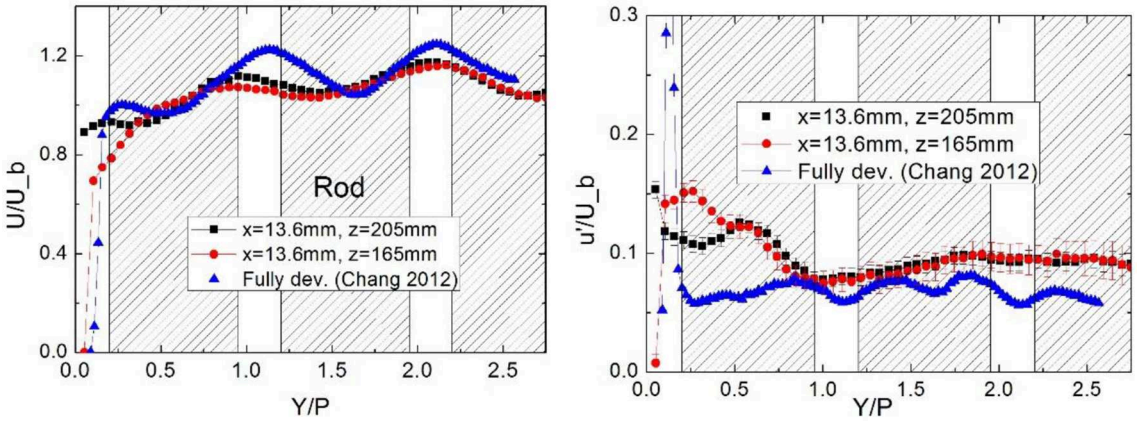

FIGURE 5 | Comparing the present result with Chang et al.'s data (Chang et al., 2012).

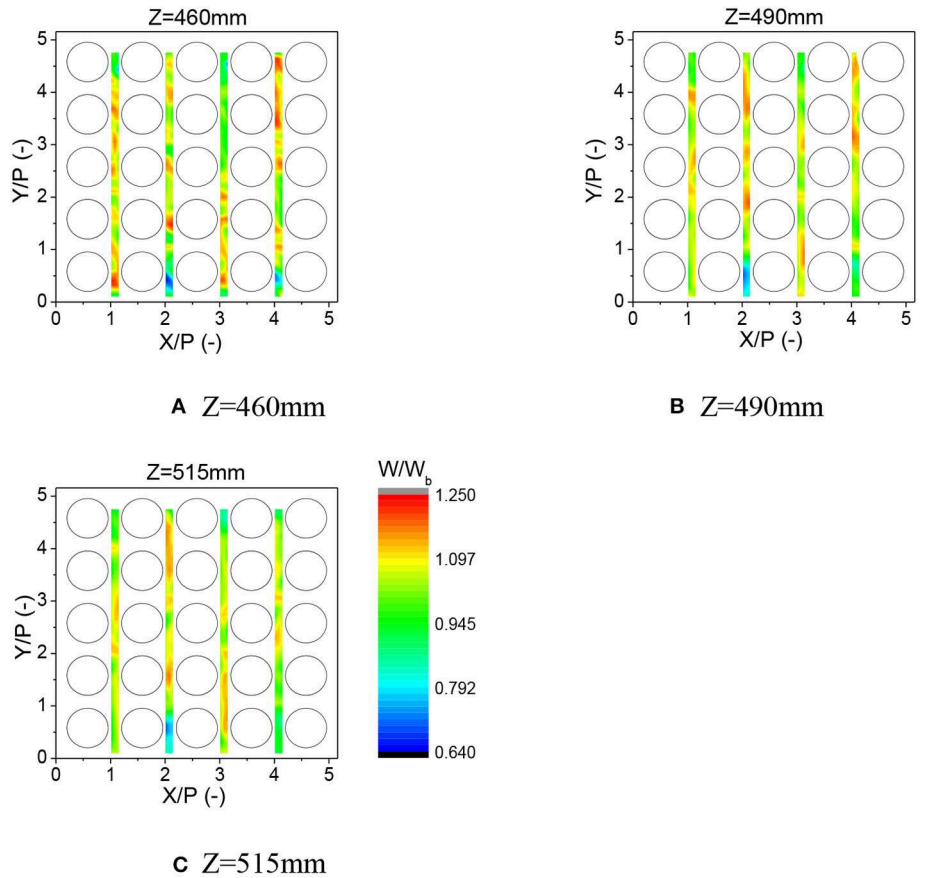

FIGURE 6 | Evolution of axial mean velocity distribution downstream of the mixing-vane spacer grid ($Re = 3.6 \times 104$). **(A)** $Z = 460$ mm. **(B)** $Z = 490$ mm. **(C)** $Z = 515$ mm.

CFD simulation of flow in rod-bundle fuel assembly. Conner et al. summarized the Westinghouse best practices in reference (Conner et al., 2015), including the recommendation for mesh size and model selection. Martin et al. (2015) presented AREVA's best practices in the EPRI-NESTOR benchmark, which includes utilization of a modified quadratic k-ε model, trimmed mesh with the base size of 0.3 mm and two prism layers which guarantee the y+ is around 65 in the majority of the domain.

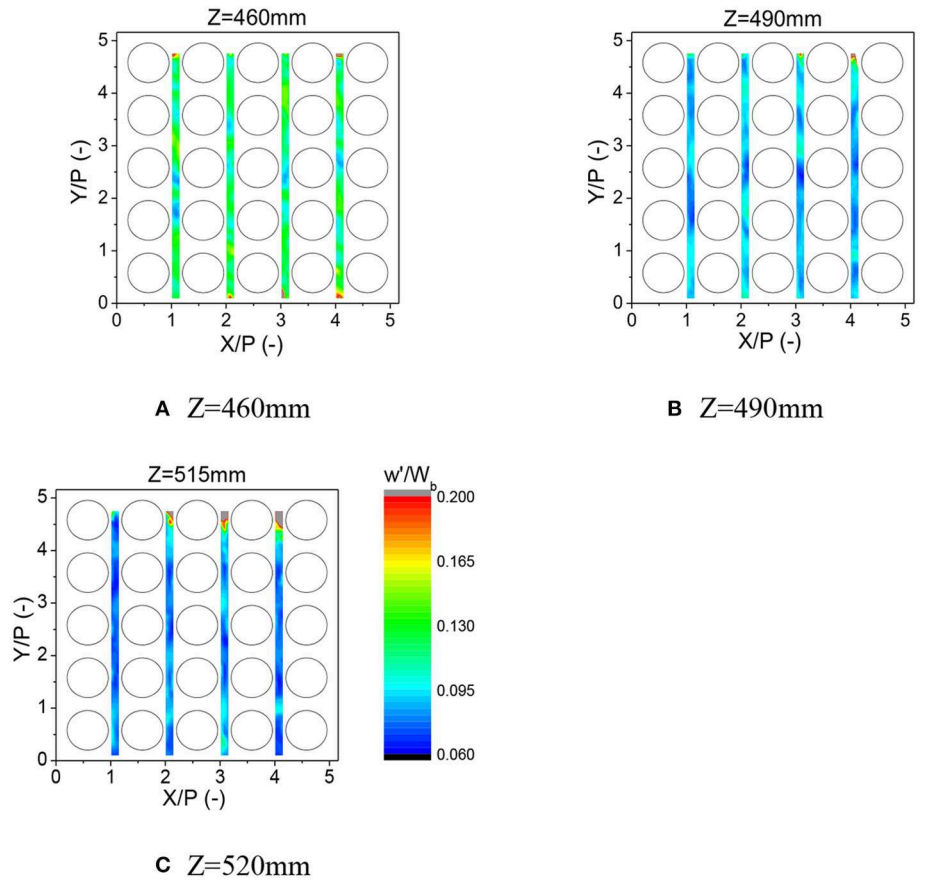

FIGURE 7 | Evolution of axial root mean square velocity distribution downstream of the mixing-vane spacer grid ($Re = 3.6 \times 104$). **(A)** $Z = 460$ mm. **(B)** $Z = 490$ mm. **(C)** $Z = 520$ mm.

CD-adapco validated their best practices for rod-bundle flow simulation in the EPRI-NESTOR benchmark in which Brewster et al. (2015) used a hex-dominated trimmed cell mesh with the base size of 0.3 mm and the constraints of 0.075 mm minimum mesh dimension. Brewster et al. (2015) selected a high y+ implementation of non-linear quadratic k-ε turbulence model with standard wall function.

In this study the CFD computation is carried out with STAR CCM+. As shown in **Figure 8A**, the computation domain is 996 mm in height and includes two spans of spacer grid. The inlet boundary of domain locates 315 mm upstream of the first spacer grid, while the outlet boundary is 315 mm downstream of the second spacer grid. The realizable k-ε model and the non-linear (quadratic) k-ε model are validated. At the inlet boundary the uniform velocity distribution is assumed, while the outlet boundary is pressure-outlet type. On the wall boundary the two-layer wall treatment is utilized which blends a one-equation model with the two-equation k-ε model. The one-equation model is activated in the vicinity of the wall and solves for k, while ε is algebraically calculated according to the distance from the wall. The second-order upwind scheme is utilized for the convection term of all the equations.

Mesh Sensitivity

The meshing strategy of trimmed mesh with prism layer is employed for the region of spacer grid, while the extruder is utilized to generated the mesh in the bare rod parts. In order to improve mesh quality, the dimples and springs on the spacer grid have been extruded out to avoid the unacceptable narrow gaps where the spacer grid contacts the rods. Exactly the same meshing parameters have been configured for the two spacer grids. In order to generate conformal mesh at the interface while extruding the mesh, the periodic interface is utilized for the mesh solver. The cross-sectional view of mesh in the spacer grid and rod bundle section are shown in **Figures 8B,C**. Two meshes are utilized to show the mesh sensitivity. The major difference between the two meshes in the spacer grid part.

The overall configuration of two meshes are collectively given in **Table 1**. According to the recommendation by AREVA and CD-adapco, the base size which controls the bulk flow mesh size is set as 0.3 mm. The prism layer on the wall surface affects y^+ value which can affect the applicability of wall treatment or function. Since the two-layer wall treatment is utilized in the computation, the value of y^+ at first wall cell should avoid the transition of the two layer ($y^+ \approx 11.3$) because the accuracy of two-layer model is relatively poor there. Here one prism layer

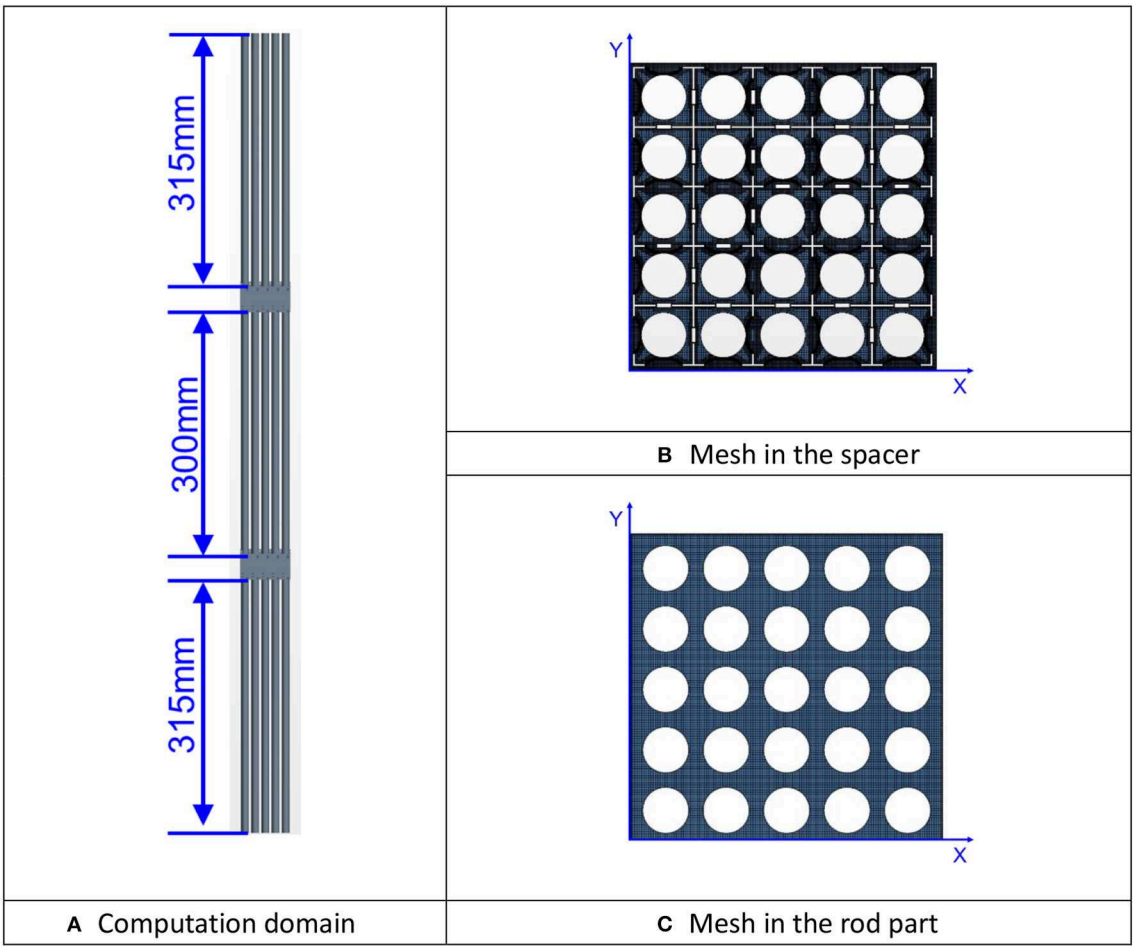

FIGURE 8 | The computation domain and the cross section of mesh. **(A)** Computation domain. **(B)** Mesh in the spacer. **(C)** Mesh in the rod part.

TABLE 1 | Configuration of mesh for sensitivity analysis.

	Mesh #1	Mesh #2
No. of prism layers	1	1
Base size	0.3	0.3
Cell number	96 million	36 million
Surface mesh size on spacer	0.18 mm (target)	0.2 mm (target)
	0.045 mm (minimum)	0.06 mm (minimum)
Prism layer height on spacer surface	0.045 mm	0.075 mm

is utilized. The thickness of prism layer is 0.045 and 0.075 mm, respectively for two meshes. Comparing with the mesh #2, the mesh #1 also significantly refined the surface mesh size on the spacer grid which will leads to much finer mesh near the spacer grid surface. The cell number in mesh #1 is 96 million, and 36 million in mesh #2.

Figure 9 presents the sensitivity of pressure drop on mesh refinement in the section of spacer grid. We can see that the influence of mesh refinement on the pressure drop is generally negligible and mainly observed in the bare rod part near the inlet. The effect of mesh refinement on the velocity is much more pronounced, as shown in **Figure 10**. However, such effect decays in the far downstream. It is also observed that the non-linear k-ε model shows stronger sensitivity on mesh refinement than the realizable k-ε model.

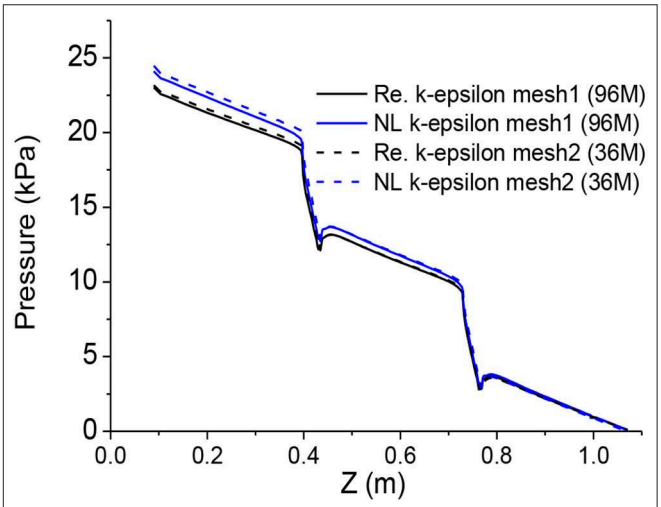

FIGURE 9 | Mesh sensitivity on pressure drop along the line (X, Y) = (0,0).

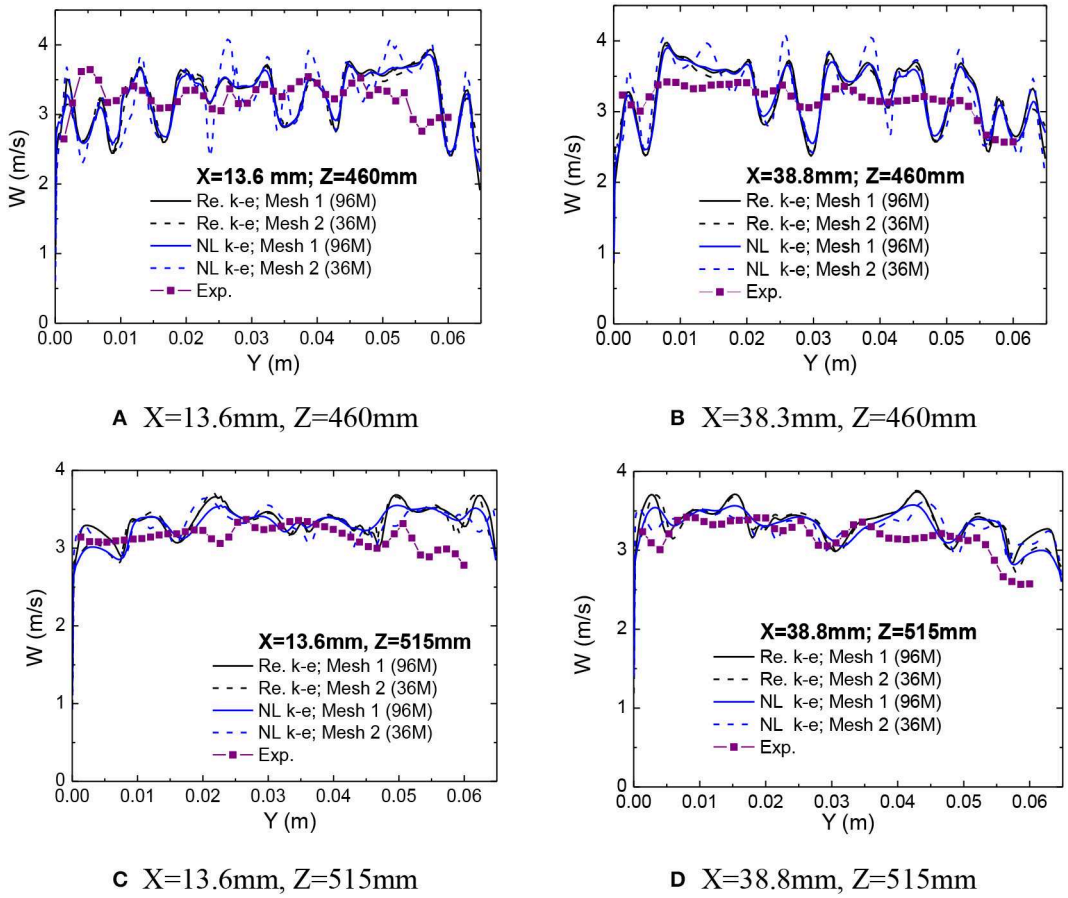

FIGURE 10 | Validation of the computed axial velocity. **(A)** $X = 13.6$ mm, $Z = 460$ mm. **(B)** $X = 38.3$ mm, $Z = 460$ mm. **(C)** $X = 13.6$ mm, $Z = 515$ mm. **(D)** $X = 38.8$ mm, $Z = 515$ mm.

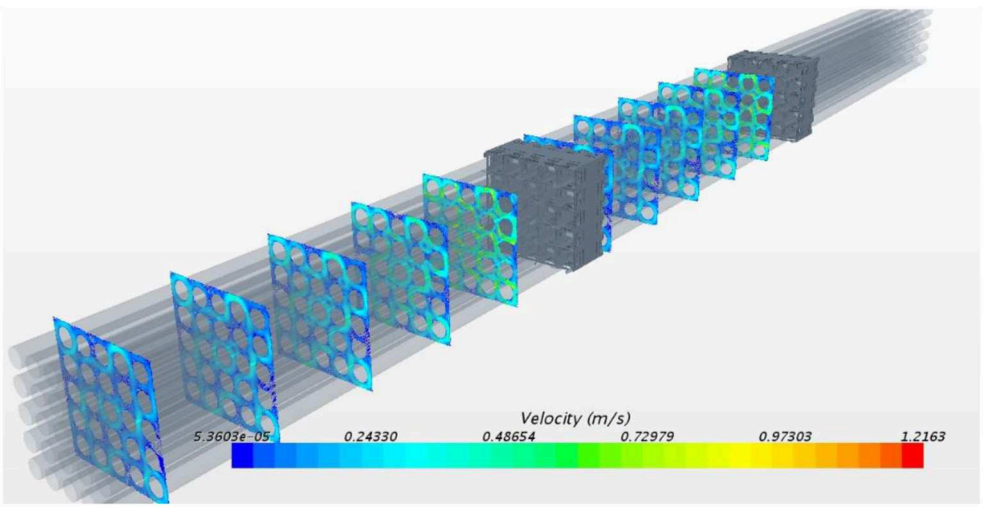

FIGURE 11 | Predicted cross flow with non-linear k-ε model at $5D_h$, $10D_h$, $15D_h$, $20D_h$, $25D_h$ downstream of spacer grid.

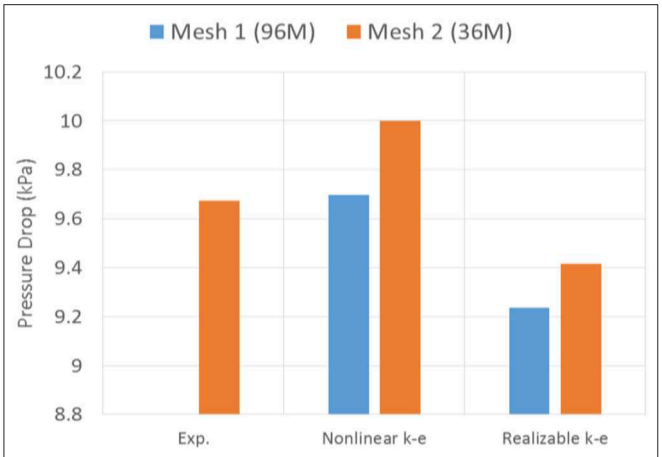

FIGURE 12 | Comparison on pressure drop prediction.

Velocity

Since only the axial flow velocity component is measured, direct comparison on the turbulence intensity is not possible here. Hence, the measured axial velocity is compared in **Figure 10**. The comparison is carried out along the line $x = 13.6$ and 38.3 mm on the two measuring planes, i.e., $Z = 460$ and 515 mm. From **Figure 10**, we can see that the prediction on the mean axial velocity is relatively poor in the cross section closer to the spacer grid, i.e., $Z = 460$ mm. In **Figure 10B** the computations show more small-scale flow structures while the measured result shows relatively smooth distribution of axial velocity. It should be noted that the refinement of mesh in the spacer grid eliminates some peaks for the non-linear model, which emphasize the importance of mesh quality in the complex geometry. Fortunately, such effect only signifies in the near wake of spacer grid. It should also be noted that the measurement volume of LDA is an ellipsoid in which the long axis is about 1 mm and the short axis is about 0.05 mm. Hence, the obtained velocity is average value in the measurement volume. Hence, the local variation can be smeared in the LDA measurement. Comparing with the effect of mesh refinement, the difference caused by the turbulence models is relatively weak in the near wake region. In the far-wake region it is still difficult to judge which model shows definite superiority to the other.

The cross flow is of great interest for inter-subchannel mixing analysis. The predicted cross flow downstream of the two spacer grids is shown in **Figure 11**. We can see that the vortices can be predicted with the non-linear k-ε model. A pair of small vortices appear in the diagonal of the subchannel which merges into a big one in the downstream. And the intensity of cross flow decays from $5D_h$ to $25D_h$ downstream of a spacer grid. Comparing the cross flow downstream of 1st and 2nd spacer grids, we can observe negligible difference, which implies little effect of upstream flow condition on the flow downstream of spacer grid.

Pressure Drop

Pressure drop is an important factor to consider when evaluating design of spacer grid, and hence an important parameter to predict with the CFD simulation. The calculated pressure drop with different models and different meshes are compared with the experiment measurement in **Figure 12**. The mesh refinement in the spacer grid region shows weak effect on pressure drop (2% to 4%). However, refinement of mesh reduces the pressure drop for both models. We can see that the non-linear k-ε predicts the pressure drop close to the experiment, when the mesh is refined.

CONCLUSION

The flow field is measured in a 5 × 5 rod bundle installed with split-type mixing vane grids with laser Doppler anemometry (LDA) downstream of the spacer grid. The measured results are utilized to validate the CFD simulation based on the commercial CFD code, Star-CCM+. The realizable and non-linear k-ε turbulence model is utilized in the CFD computation, while the two-layer wall treatment is employed with both models. The mesh sensitivity investigation shows that the pressure drop is weakly affected by the mesh refinement, while its effect on the velocity is apparent. The validation shows that prediction on the mean axial velocity is relatively poor in the near wake of the spacer grid where the measured result shows relatively smooth distribution of axial velocity. Refinement of mesh in the spacer grid eliminates some peaks for the non-linear model. Comparing with the effect of mesh refinement, the difference caused by the turbulence models is relatively weak in the near wake region. In the far-wake region it is still difficult to judge which model shows definite superiority to the other. For pressure drop, prediction of non-linear k-ε is closer to the experiment.

DATA AVAILABILITY STATEMENT

The datasets generated for this study are available on request to the corresponding author.

AUTHOR CONTRIBUTIONS

JX carried out the CFD simulation and prepared the manuscript. CL and WQ provided their suggestion on the contents of the manuscript.

FUNDING

The authors would like to express their gratitude to the fund of National Natural Science Foundation of China (No. 51676120).

REFERENCES

Brewster, R., Carpenter, C., Volpenhein, E., Baglietto, E., Smith, J. (2015). "Application of CD-adapco best practices to NESTOR OMEGA MVG benchmark exercises using STAR-CCM+," in *The 16th International Topical Meeting on Nuclear Reactor Thermal Hydraulics (NURETH-16)* (Chicago, IL). p. 13164.

Chang, S., k., Kim, S., and Song, C. H. (2012). "OECD/NEA—KAERI rod bundle CFD benchmark exercise test," in *4th OECD/NEA-IAEA Workshop Experimental Validation and Application of CFD and CMFD Codes in Nuclear Reactor Technology (CFD4NRS-4)* (Daejon).

Conner, M. E., Dominguez-Ontiveros, E. E., and Hassan, Y. A. (2013a). "Advanced hydraulic benchmark data for PWR mixing vane grid," in *The 15th International Topical Meeting on Nuclear Reactor Thermal-Hydraulics* (Pisa). p. NURETH15–039.

Conner, M. E., Hassan, Y. A., and Dominguez-Ontiveros, E. E. (2013b). Hydraulic benchmark data for PWR mixing vane grid. *Nucl. Eng. Des.* 264, 97–102. doi: 10.1016/j.nucengdes.2012.12.001

Conner, M. E., Karoutas, Z. E., and Xu, Y. (2015). "Westinghouse CFD modeling and results for EPRI NESTOR CFD round robin exercise of PWR rod bundle testing," in *The 16th International Topical Meeting on Nuclear Reactor Thermal Hydraulics (NURETH-16)*. (Chicago, IL). p. 13601.

Dominguez-Ontiveros, E. E., Hassan, Y. A., Conner, M. E., Karoutas, Z. (2012). Experimental benchmark data for PWR rod bundle with spacer-grids. *Nucl. Eng. Des.* 253, 396–405. doi: 10.1016/j.nucengdes.2012.09.003

Ikeda, K. (2014). CFD application to advanced design for high efficiency spacer grid. *Nucl. Eng. Des.* 279, 73–82. doi: 10.1016/j.nucengdes.2014.02.013

Krauss, T., and Meyer, L. (1998). Experimental investigation of turbulent transport of momentum and energy in a heated rod bundle. *Nucl. Eng. Des.* 180, 185–206. doi: 10.1016/S0029-5493(98)00158-7

Lee, J. R., Kim, J., and Song, C. H. (2012). "Synthesis of OECD/NEA-KAERI rod bundle benchmark exercise," in *4th OECD/NEA-IAEA Workshop Experimental Validation and Application of CFD and CMFD Codes in Nuclear Reactor Technology (CFD4NRS-4)* (Daejon). p. KN-02.

Mahaffy, J., Chung, B., Dubois, F., Ducros, F., Graffard, E., Heitsch, M., et al. (2014). *Best Practice Guidelines for the use of CFD in Nuclear Reactor Safety Applications-Revision*. NEA/CSNI/R(2014)11. Organisation for Economic Co-operation and Development.

Martin, M., Keheley, T., Goodheart, K., Hatman, A., Chatelain, A. (2015). "Validation of AREVA's best practices in the round robin CFD benchmark," in *The 16th International Topical Meeting on Nuclear Reactor Thermal Hydraulics (NURETH-16)* (Chicago, IL). p. 13220.

McClusky, H. L., et al. (2004). Mapping of the lateral flow field in typical subchannels of a support grid with vanes. *J. Fluid. Eng.* 125, 987–996. doi: 10.1115/1.1625688

Qu, W., Wang, Z., Xiong, J., Cheng, X. (2019a). Experimental study of cross flow and lateral pressure drop in a 5 × 5 rod bundle with mixing vane spacer grid. *Nucl. Eng. Des.* 353:110209. doi: 10.1016/j.nucengdes.2019.110209

Qu, W., Xiong, J., Chen, S., Cheng, X. (2019b). High-fidelity PIV measurement of cross flow in 5 × 5 rod bundle with mixing vane grids. *Nucl. Eng. Des.* 344, 131–143. doi: 10.1016/j.nucengdes.2019.01.021

Qu, W., Xiong, J., Chen, S., Qiu, Z., Deng, J., Cheng, X. (2019c). PIV measurement of turbulent flow downstream of mixing vane spacer grid in 5×5 rod bundle. *Ann. Nucl. Energy* 132, 277–287. doi: 10.1016/j.anucene.2019.04.016

Smith, L. D., Conner, M. E., Liu, B., Dzodzo, B., Paramonov, D. V., Beasley, D. E., et al. (2002). "Benchmarking computational fluid dynamics for applicatoin to PWR fuel," in *10th International Conference on Nuclear Engineering* (Arlington, VA). p. ICONE10–22475.

Wells, D. M., Peturaud, P., and Yagnik, S. K. (2015). "Overview of CFD round robin benchmark of the high fidelity fuel rod bundle NESTOR experimental data," in *The 16th International Topical Meeting on Nuclear Reactor Thermal Hydraulics (NURETH-16)* (Chicago, IL). p. 13173.

Xiong, J., Cheng, R., Lu, C., Chai, X., Liu, X., Cheng, X. (2018b). CFD simulation of swirling flow induced by twist vanes in a rod bundle. *Nucl. Eng. Des.* 338, 52–62. doi: 10.1016/j.nucengdes.2018.08.003

Xiong, J., Qu, W., Wu, Z., Cheng, X. (2018a). PIV measurement of cross flow in a rod bundle assisted by telecentric optics and matched index of refraction. *Ann. Nucl. Energy* 120, 540–545. doi: 10.1016/j.anucene.2018.06.024

Xiong, J., Yu, Y., Yu, N., Fu, X., Cheng, X., Yang, Y. (2014b). Experimental investigation on anisotropic turbulent flow in a 6×6 rod bundle with LDV. *Nucl. Eng. Des.* 278, 333–343. doi: 10.1016/j.nucengdes.2014.08.004

Xiong, J., Yu, Y., Yu, N., Fu, X., Wang, H., Yang, Y., et al. (2014a). Laser Doppler measurement and CFD validation in 3x3 bundle flow. *Nucl. Eng. Des.* 270, 396–403. doi: 10.1016/j.nucengdes.2014.02.009

Conflict of Interest: The authors declare that the research was conducted in the absence of any commercial or financial relationships that could be construed as a potential conflict of interest.

frontiers in Energy Research

ORIGINAL RESEARCH
published: 07 May 2020
doi: 10.3389/fenrg.2020.00065

CFD Simulation of Two-Phase Flows in Helical Coils

*Shuai Che[1], David Breitenmoser[1,2], Yuriy Yu Infimovskiy[3], Annalisa Manera[1] and Victor Petrov[1]**

[1] Experimental and Computational Multiphase Flow Laboratory, Department of Nuclear Engineering and Radiological Sciences, University of Michigan, Ann Arbor, MI, United States, [2] Laboratory of Nuclear Energy Systems, Department of Mechanical and Process Engineering, Institute of Energy Technology, Swiss Federal Institute of Technology, Zurich, Switzerland, [3] Department of Physics and Mathematics, Faculty of Fundamental Sciences, Bauman Moscow State Technical University, Moscow, Russia

The behavior of two-phase flow and corresponding flow regimes in helical tubes significantly differ when compared to two-phase flows in straight tubes due to centrifugal and torsion effects. In order to gain physical insight and gather data for validating computational models, a large number of experiments were performed on a helical coil experimental setup operated with a mixture of water and air. The experimental data were used to assess the predictive capabilities of current two-phase Computational Fluid Dynamics (CFD) models based on the Volume of Fluid (VOF) approach. In the present paper, a comparison of the CFD simulation results with the high-resolution experimental data is discussed, with special emphasis on two-phase pressure drops and void fraction distributions. It is shown that the CFD VOF model is able to correctly capture the occurrence of five flow regimes observed in the experiments, namely bubbly flow, plug flow, slug flow, slug-annular flow, and annular flow. However, a good quantitative agreement for pressure drops and void fraction distributions is found in slug flow and slug-annular flow regimes only. The good agreement found only in a limited range of flow regimes demonstrates that there is not a single set of best-practice guidelines for CFD VOF models that can be applied across a wide range of two-phase flow regimes. Also, there is not a single mesh that can be used to simulate all of the flow regimes and a case-specific mesh and time-step convergence study is needed for each individual flow regime. In the current study, optimal mesh size and time step were obtained for a slug flow test case. Hence, good agreement was obtained only for similar flow regimes, leading to significant disagreement with experimental data for test cases with substantially different flow patterns.

Keywords: CFD, VOF, helical coil, void fraction, two-phase pressure drop

OPEN ACCESS

Edited by:
Jun Wang,
University of Wisconsin-Madison, United States

Reviewed by:
Xiao-Yu Wu,
Massachusetts Institute of Technology, United States
Norbert Kockmann,
Technical University Dortmund, Germany

***Correspondence:**
Victor Petrov
petrov@umich.edu

Specialty section:
This article was submitted to Nuclear Energy, a section of the journal Frontiers in Energy Research

Received: *13 January 2020*
Accepted: *03 April 2020*
Published: *07 May 2020*

Citation:
Che S, Breitenmoser D, Infimovskiy YY, Manera A and Petrov V (2020) CFD Simulation of Two-Phase Flows in Helical Coils. Front. Energy Res. 8:65. doi: 10.3389/fenrg.2020.00065

INTRODUCTION

Because of their superior heat transfer performance when compared to straight pipes and the compactness of the cylindrical geometry, helical coils are widely used in the food industry, steam generators, chemical processing, and medical equipment (Fsadni et al., 2016). In the field of nuclear engineering, helical coil designs have also been widely used for steam generators in several types of nuclear power plants such as the Otto Hahn nuclear ship reactor, the Thorium High Temperature

Reactor (THTR-300), the Super Phoenix fast reactor, the Advanced Gas-cooled Reactor (AGR), the Fort St. Vrain High Temperature Gas Reactor (HTGR) and the Monju reactor (Matsuura et al., 2007; Santini et al., 2008). In addition, helical coil steam generators are considered for future reactor designs such as International Reactor Innovative and Secure (IRIS), BREST-OD-300, System-integrated Modular Advanced ReacTor (SMART), CAREM-25 and NuScale (Carelli et al., 2004; Dragunov et al., 2012; Kim et al., 2013; Marcel et al., 2013; Ingersoll et al., 2014).

El-Genk and Schriener (2017) published a literature review on convection heat transfer and pressure losses for single-phase flows in toroidal and helically coiled tubes. They collected 2,410 pressure losses data and 193 Nusselt number data and summarized the effect of the dimensions, geometric parameters, flowrates, and the fluids' properties on the critical Reynolds number, friction factor, and Nusselt number. However, in many helical coil steam generator designs, the two-phase flow appears within the coils instead of the shell side. Therefore, detailed information on pressure drops, void fraction distributions and flow regime in helical coil geometries are relevant as well. Experiments on two-phase flow in vertical helical coils have been performed in the past (Kasturi and Stepanek, 1972; Xin et al., 1996; Mandal and Das, 2003; Zhu et al., 2017) to investigate pressure losses, void fraction and flow regimes and corresponding empirical correlations have been proposed.

In the past decades, more advanced measurement techniques have been introduced that are able to provide higher resolution experimental data on void fraction distributions (Rahman et al., 2009). Experimental data from high-speed cameras, high-speed X-ray radiography, and wire-mesh sensor can provide the additional resolution for a more extensive validation of CFD models. Because of the wide range of void fraction, an interface-capturing method is the most suitable for the corresponding CFD simulations. Hirt and Nichols (1981) proposed the Volume of Fluid (VOF) approach to track and locate the free surface of immiscible phases. Previous studies have shown that this model has the capability to correctly capture void fraction distributions (Hernandez Perez, 2008; Fernandes et al., 2009; Abdulkadir, 2011; Akhlaghi et al., 2019; Kiran et al., 2020). All of them performed mesh independence studies based on a reference case, but not all showed a good agreement with the experimental data in terms of the two-phase pressure drops when the optimal mesh was extrapolated to other cases. Alizadehdakhel et al. (2009) showed that their mesh is suitable for several flow regimes with the relative error below 10 percent when compared with experimental data. In two other studies instead a large discrepancy was found when simulating flow regimes different from the reference case used to perform the mesh convergence study (Akhlaghi et al., 2019; Kiran et al., 2020). Therefore, a point of interest for the current paper is to investigate how far the extrapolation can be applied when simulating two phase flows in helical coils.

However, most of the past studies mentioned above focused on straight pipes or curved pipes and very few studies were dedicated to the simulation of two-phase flow in helical coils using VOF. In the present study, CFD simulations have been carried out using the commercial code STAR-CCM+ v13.06 and 14.04 to model air-water flows in the helical coil geometry. The simulation results are compared with the experimental data obtained by Breitenmoser et al. (2019).

EXPERIMENTAL SETUP

The scheme of the Michigan Adiabatic Helical Coil (MAHICan) facility is reported in **Figure 1**. The geometrical details of the test section are summarized in **Table 1**. Two pressure drop transducers are used to measure the pressure drop across the entire coil and across the last half turn of the coil, upstream of the test section outlet (indicated as DP1 and DP2 in **Figure 1**, respectively). In addition, a high-speed X-ray radiography system was used to measure the void fraction. The X-ray measurements were performed 4.86 m, i.e., 1.5 turns downstream of the helical coil pipe entrance to avoid entrance effects. In total 136 measurements were performed for an adiabatic air-water two-phase flow in the MAHICan facility. The superficial air and water velocities for the data points range from 0.18 to 35.32 m/s and from 0.05 to 1.83 m/s, respectively. The experimental flow regime identification was based solely on the X-ray radiography measurements and the resulting postprocessed quantitative void fraction data. According to the methodology introduced by Zhu et al. (2017), the 136 measurements were classified into six different flow regimes, namely bubbly, plug, slug, wavy, slug-annular, and annular flow. More detailed information of the facility and experimental procedures are reported by Zhuang et al. (2018) and Breitenmoser et al. (2019). In the present study, 12 experimental measurements were selected as references for the CFD simulations.

CFD MODELING

This section introduces all of the physical models used in the simulations presented below, including the multiphase flow model, multiphase interaction model, turbulence model, and transient model. Moreover, boundary and initial conditions are discussed as well.

Multiphase Flow Model

Based on the Eulerian framework, the VOF methodology was developed as an interface capturing model to predict the distribution and the movement of the interface of immiscible phases. The volume fraction of each phase in the computation domain is used to describe the distribution of phases and the position of the interface. The volume fraction of phase q is defined as:

$$\alpha_q = \frac{V_q}{V} \tag{1}$$

where V_q is the volume of phase q in the cell and V is the volume of the cell.

The VOF model uses a single set of equations to model the multiphase flow and treats the immiscible phases as a mixture. Accordingly, the density and dynamic viscosity of the mixture

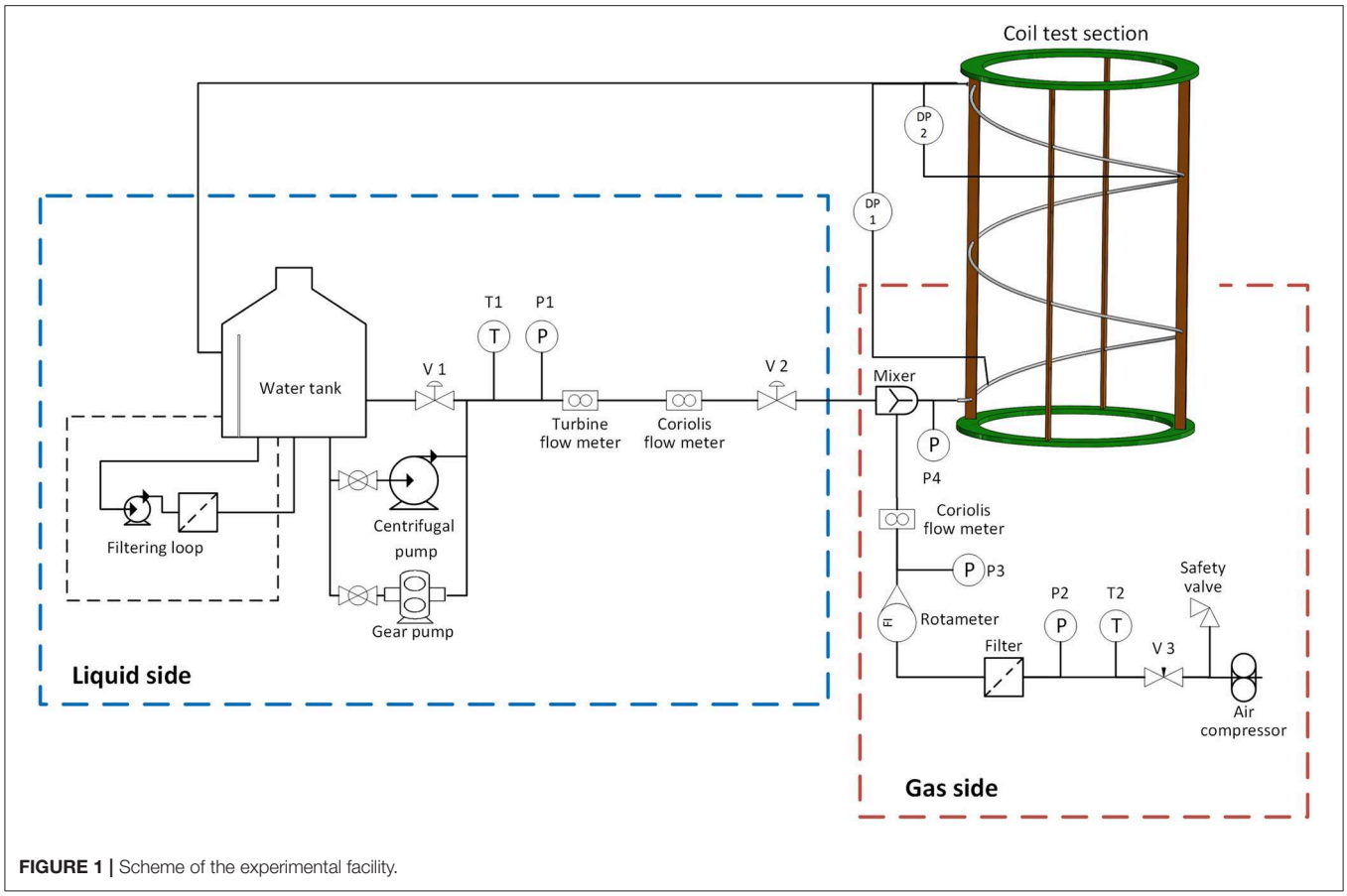

FIGURE 1 | Scheme of the experimental facility.

are defined as the sum of volume fraction weighted properties of each phase:

$$\rho_m = \sum_q \rho_q \alpha_q \tag{2}$$

$$\mu_m = \sum_q \mu_q \alpha_q \tag{3}$$

The volume fraction transport equation is used to resolve the movement of the interface:

$$\frac{\partial \alpha_q}{\partial t} + \frac{\partial (\alpha_q u_j)}{\partial x_j} + \frac{\partial}{\partial x_j}\left[C_\alpha |\mathbf{u}| \frac{1}{|\nabla \alpha_q|} \frac{\partial \alpha_q}{\partial x_j} \alpha_q \left(1 - \alpha_q\right)\right] = 0 \tag{4}$$

where C_α is a sharpening factor and $\mathbf{u}$ is the mixture velocity vector. The u_j and x_j denote, respectively, the mixture velocity component and the coordinate in the j direction, and t represents the time. The first and second term on the left hand side denote the change rate of volume fractions and convective term respectively. The third term on the left hand side is caused by the non-zero sharpening factor. The sharpening factor is used to reduce numerical diffusion in the simulation. In the present study, the sharpening factor was assigned as 1 to avoid smearing of the interface due to numerical diffusion.

The conservation equations of mixture mass and momentum are defined as follow:

TABLE 1 | Geometric parameters of the helical coil.

Parameter	Tube inner diameter [mm]	Length [m]	Coil diameter [m]	Pitch [m]	Turns [–]
Value	12.57	6.48	1	0.8	2

$$\frac{\partial \rho_m}{\partial t} + \frac{\partial \left(\rho_m u_j\right)}{\partial x_j} = 0 \tag{5}$$

$$\frac{\partial (\rho_m u_i)}{\partial t} + \frac{\partial \left(\rho_m u_i u_j\right)}{\partial x_j} = -\frac{\partial p}{\partial x_i} + \frac{\partial}{\partial x_j}\left[\mu_m \left(\frac{\partial u_i}{\partial x_j} + \frac{\partial u_j}{\partial x_i}\right)\right] + \rho_m g_i \tag{6}$$

where p and g are the mixture pressure and the gravitational acceleration respectively. The energy equation is omitted in the simulations since the experiments were carried out in adiabatic conditions.

The accuracy of the VOF model depends on the mesh grid or cell size. At least three cells across each bubble are required to fully capture the interface between two phases (Siemens, 2018). As a result, this model is computationally suitable for simulating flows in which large two-phase structures are present.

Moreover, the multiphase interaction model is crucial for the interface reconstruction that directly determines the accuracy of

the void fraction distribution. Taha and Cui (2006) performed numerical simulations to study the motion of single Taylor bubbles in vertical tubes. They concluded that the terminal rising velocity and shape of slug in air-water flows are significantly affected by surface tension and buoyancy force. Surface tension is particularly important for multiphase flows in the presence of strongly curved surfaces. In the VOF model, the surface tension is introduced as a body force by adding a momentum term to the momentum equation. In STAR CCM+, the interfacial surface force is modeled as a volumetric force using the Continuum Surface Force (CSF) approach proposed by Brackbill et al. (1992). Therefore, this model was selected and a constant surface tension of 0.072 N/m was specified in the present study, corresponding to the surface tension of water-air at the operating temperature of 20°C. In addition, for the VOF-VOF phase interaction model, the water was selected as the primary phase.

Turbulence Model

To model the turbulence in multiphase flows, the k-ϵ model is recommended for internal flows and the k-ω model for external flows (Siemens, 2018). The standard k-ϵ model requires the solution of two transport equations for the turbulence kinetic energy (k) and the turbulence dissipation rate (ϵ) respectively:

$$\frac{\partial k}{\partial t} + u_j \frac{\partial k}{\partial x_j} = \tau_{Rij} \frac{\partial u_i}{\partial x_j} - \epsilon + \frac{\partial}{\partial x_j}\left[\left(\nu + \frac{\nu_t}{\sigma_k}\right)\frac{\partial k}{\partial x_j}\right] \quad (7)$$

$$\frac{\partial \epsilon}{\partial t} + u_j \frac{\partial \epsilon}{\partial x_j} = C_{\epsilon 1}\frac{\epsilon}{k}\tau_{Rij}\frac{\partial u_i}{\partial x_j} - C_{\epsilon 2}\frac{\epsilon^2}{k} + \frac{\partial}{\partial x_j}\left[(\nu + \frac{\nu_t}{\sigma_\epsilon})\frac{\partial \epsilon}{\partial x_j}\right] \quad (8)$$

TABLE 2 | Comparison between experimental and CFD-predicted pressure drops.

Test no.	j_f [m/s]	j_g [m/s]	Re_f	Re_g	Flow regime	Two-phase pressure drop [Pa]		Relative error [%]
						Simulation data	Experimental data	
1	1.83	0.18	25,420	212	Bubble	9916.70	5409.26	83.33
2	1.83	0.19	25,556	217	Bubble	9941.65	5419.53	83.44
3	1.77	0.34	24,551	414	Plug	9835.93	5573.64	76.47
4	1.72	0.77	23,482	993	Plug	10343.32	6549.67	57.92
5	1.64	1.53	22,319	2,142	Slug	11099.26	8527.41	30.16
6	1.55	2.46	20,893	3,757	Slug	11711.03	11414.40	2.60
7	1.50	2.85	20,228	4,488	Slug	12208.87	12575.36	2.91
8	1.20	6.56	16,016	12,498	Slug	15439.02	21046.27	26.64
9	0.85	12.18	11,330	26,646	Slug-annular	25904.52	27333.95	5.23
10	0.71	15.16	9,361	34,601	Slug-annular	44685.33	28607.92	56.20
11	0.60	17.50	7,934	40,919	Annular	97504.33	30873.34	215.82
12	0.55	18.39	7,325	43,436	Annular	155137.61	32111.35	383.12

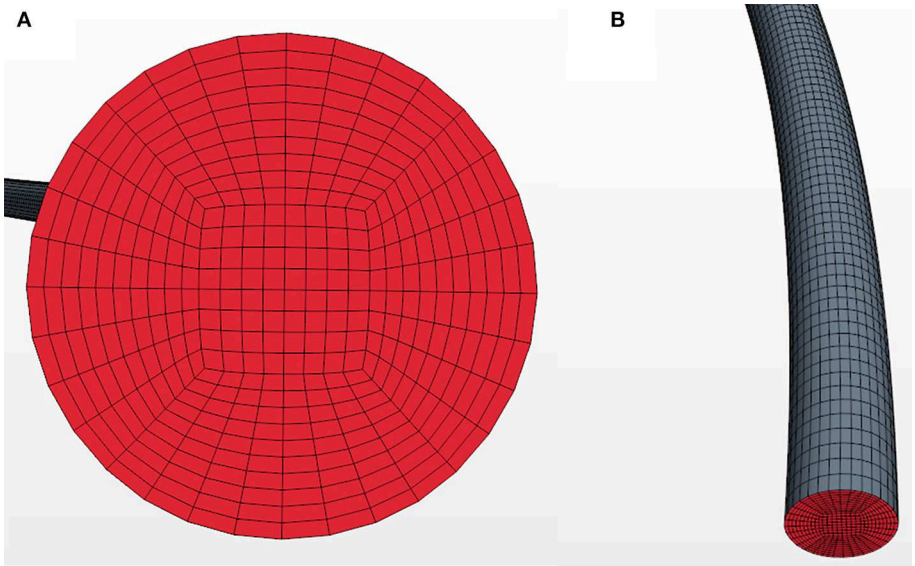

FIGURE 2 | O-grid mesh **(A)** on the initial cross section and **(B)** in axial direction.

where the τ_{Rij} is the Reynolds stress tensor, ν is the kinematic viscosity, ν_t is the turbulence eddy viscosity, and $C_{\epsilon 1}$, $C_{\epsilon 2}$, $\sigma_\epsilon, \sigma_k$ are model coefficients. This model is based on the eddy viscosity approximation to relate the Reynolds stress tensor to the local mean flow strain rate tensor $\overline{S_{ij}}$:

$$\tau_{Rij} = -\overline{u_i' u_j'} = 2\nu_t \overline{S}_{ij} - \frac{2}{3} k \delta_{ij} \tag{9}$$

$$\nu_t = C_\mu \frac{k^2}{\epsilon} \tag{10}$$

where u_i' and u_j' is the velocity fluctuation component in i and j direction, δ_{ij} is the delta function, and C_μ is a model coefficient.

For the realizable k-ϵ model, the equation for the turbulent dissipation rate is modified, and the model coefficient C_μ is expressed as a function of mean flow and turbulence properties instead of a constant. These two modifications to the formulation of the standard k-ϵ model guarantees that mathematical requirements (positive normal Reynold stresses and Schwartz inequality) based on the physics of turbulence are always satisfied. Hence, the realizable k-ϵ model was selected for the simulation of internal flows in the helical coil.

Owing to the unsteady nature of the two-phase flow, the simulations were performed in transient mode and the implicit unsteady numerical scheme was selected. The integration time-step convergence study is discussed in section mesh generation and convergence study. All simulations were run for 4 s of transient time.

Boundary and Initial Conditions

In the present study, only the coil test section shown in **Figure 1** was simulated. The dimensions of the helical coil are reported in **Table 1**. A mixer installed upstream of the test section inlet provides a uniform two-phase mixture at the inlet of the test section. Detailed information on the mixer geometry was reported by Zhuang et al. (2018). A pressure transducer was installed to measure the mixture pressure, together with two pressure drop sensors, as discussed in section experimental setup. The properties of air and water were specified based on the measured mixture pressure and temperature. The results of the simulations in the present study show that the air density, as well as the water density, plays a minor role, therefore, the constant density model was applied for both air and water in the finalized CFD simulations.

The inlet and outlet boundaries of the helical coil were defined as a "velocity inlet" and "outlet" boundary conditions respectively. The mixture velocity and void fraction were specified at the inlet, based on the measured experimental data. For the coil pipe walls, a no-slip wall condition was imposed. Due to the large range of wall y^+ value induced by different properties of air and water, the two-layer all y^+ wall treatment was used. The surface average wall y^+ values obtained in the simulations range from 23.6 to 106.2, indicating that the mesh wall discretization is appropriate for the turbulence model. For the simulations initial condition, the computational domain was specified as stagnant water to ease the convergence process.

MESH GENERATION AND CONVERGENCE STUDY

Before performing the CFD simulations, a convergence study was carried out to guarantee the computational solution is not affected by the selected mesh size and integration time step. The reference case selected for the convergence study corresponds to inlet gas and liquid superficial velocities of 2.85 and 1.5 m/s respectively (cf. **Table 2**), i.e., the test No. 7.

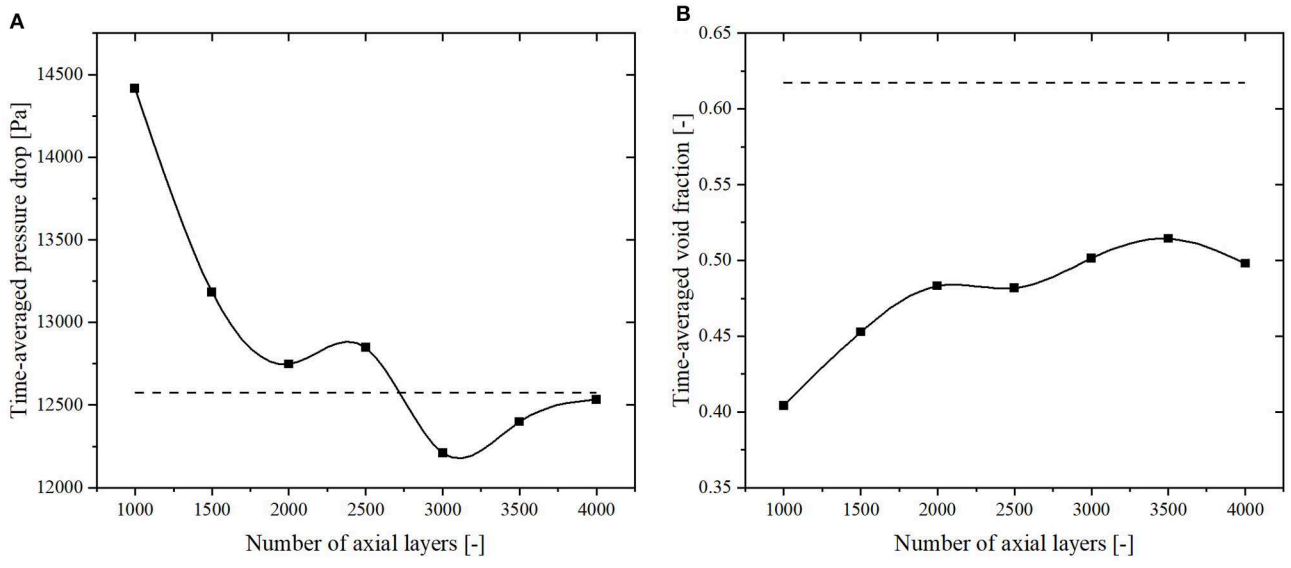

FIGURE 3 | Results of the mesh convergence study. **(A)** Two-phase pressure drop. **(B)** Void fraction.

Mesh Convergence Study

The most suitable mesh type for two-phase flows in the pipe geometry is given by the O-grid mesh (Hernandez-Perez et al., 2011), so this type of mesh was selected for the present study. Firstly a surface O-grid mesh is generated on the inlet surface and then it is extruded equally along the axis of the helical coil as shown in **Figure 2**.

The prism layer is uniformly generated from the wall, and defined by 10 equal spacing nodes. The growth factor of the prism layer is 1 and the thickness of each cell is around 0.35 mm. In the center of the cross section, the side length of one square shape cell is about 0.5 mm, which is small enough to capture the large structure of free surface like Taylor bubbles in the helical coil when compared with the diameter of the coil, 12.57 mm. Therefore, seven simulations were performed to investigate the effect of the number of axial layers. The nodalization along the axis of the helical coil was changed from 1.62 mm (corresponding to 4,000 axial layers) to 6.48 mm (corresponding to 1,000 axial layers).

The results of the two-phase pressure drop for the last half turn upstream of the helical coil outlet and the void fraction at 1.5 turns downstream of the coil inlet are shown in **Figure 3**. The two-phase pressure drop is averaged from the time that the first bubble goes through the outlet to the end of simulation, and the time-averaged void fraction is evaluated from 2 to 4 s. The dashed lines in **Figure 3** represent the experimental data. It is clear that increasing the number of axial layer makes the results close to the experimental data. A large variation occurs refining the mesh from 1,000 to 2,000 axial layers. The relative differences between the intermediate mesh (3,000 layers) and the finest mesh (4,000 layers) are <3 and 0.7% for pressure drop and void fraction, respectively. Therefore, an axial mesh consisting of 3,000 axial

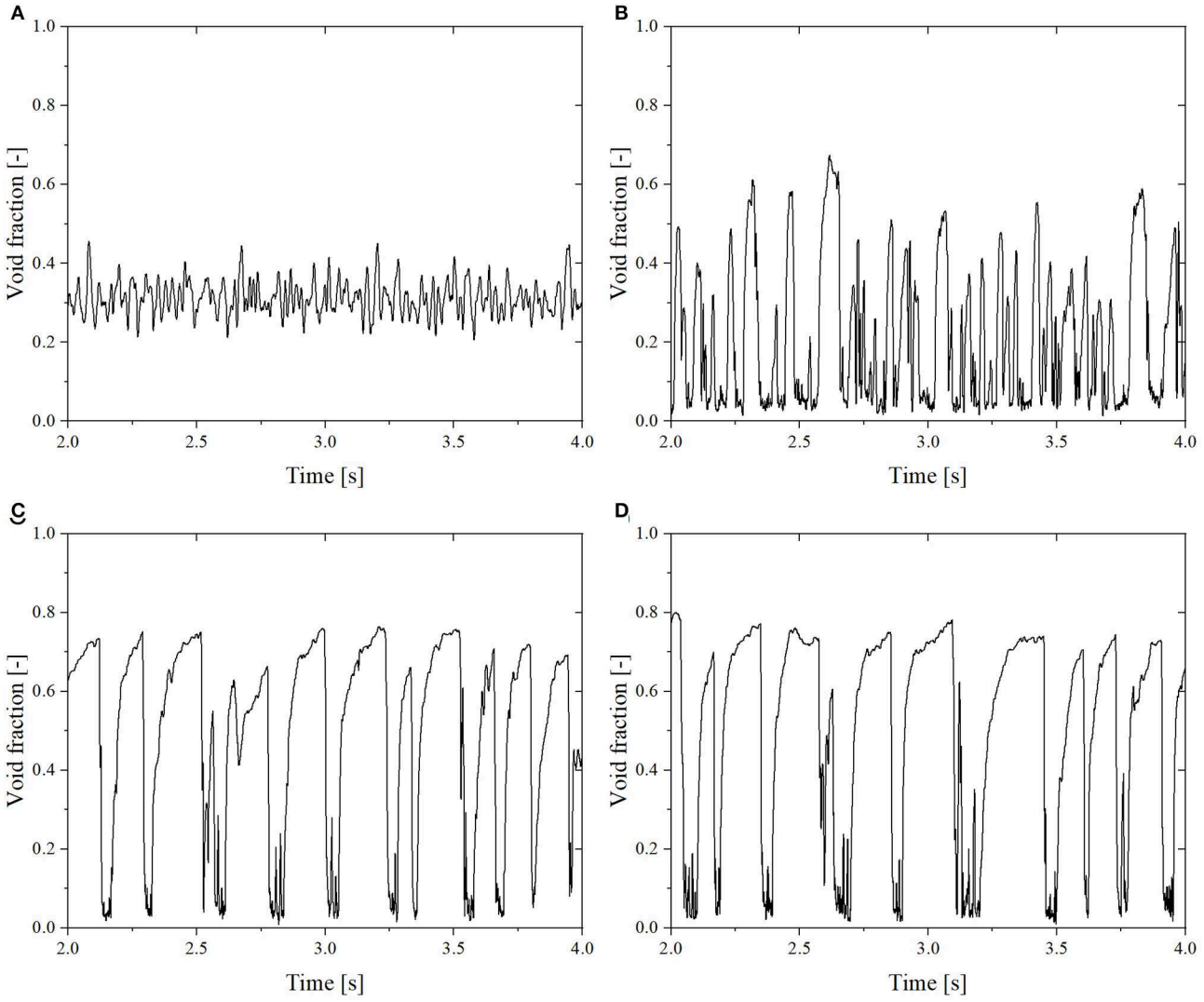

FIGURE 4 | Simulation data of void fraction for different integration time steps. **(A)** Time-step = 0.5 ms. **(B)** Time-step = 0.2 ms. **(C)** Time-step = 0.1 ms. **(D)** Time-step = 0.05 ms.

layers was selected for the simulations reported in section results and discussion.

Time Step Convergence Study

Four simulations were performed using different integration time steps ranging from 0.05 ms up to 0.5 ms, and the results of the time dependent void fraction averaged over a selected volume of the helical coil are shown in **Figure 5**. The dimensions and location of the volume on which the void fraction has been averaged is the same used by Breitenmoser et al. (2019) to postprocess the experimental data.

In the test No. 7, the slug flow regime occurs as indicated by the experimental data. The time step convergence study shows that if the integration time step is larger than 0.1 ms, the simulation is not able to capture the characteristic of slug flow, as demonstrated in **Figures 4A,B**. In contrast, simulations with a smaller time step show a good agreement with the experimental data as indicated in **Figure 9A**. In **Figures 4C,D**, the repeating high peaks represent the large slug bubbles passing through the volume selected for the void fraction spatial averaging, and the fluctuations after the peaks correspond to the wake behind a large slug bubble.

In addition, the time-averaged data was also investigated as shown in **Figure 5**, and the same time-averaged range as mentioned in previous subsection was used. There is a clear convergence trend from 0.5 to 0.1 ms and the experimental data is indicated by the dashed lines. The relative differences between the smallest time step (0.05 ms) and the intermediate time step (0.1 ms) are $<1.5\%$ for both parameters. To reduce the computational time associated to the simulations, a time step of 0.1 ms was selected for the results discussed in section results and discussion.

RESULTS AND DISCUSSION

In this section, the simulation results for two-phase pressure drops and time-dependent volume averaged void fractions are presented and compared with the experimental data. All of the following figures are obtained using Origin Pro 2019.

Two-Phase Pressure Drop

As mentioned earlier, the two-phase pressure drop is an important parameter for designing a new helical coil heat exchanger. In the experiments, the two-phase pressure drops for the last half turn upstream of the helical coil outlet were measured, so in the simulations, the pressure drop across the same section was monitored for comparison with the experimental data. The comparison obtained for the time-averaged pressure drop is reported in **Table 2**.

The results show that for the slug and slug-annular flow regimes (tests No. 5 to No. 9), the two-phase pressure drops can be predicted reasonably well with relative errors ranging from $<3\%$ to up to about 30%. This also supports the conclusion that the VOF model is suitable for modeling immiscible two-phase flows in which large structures are present. However, for all other flow regimes, the two-phase pressures drops are all significantly overestimated with relative errors up to more than 300%.

The possible reason for the poor agreement between the simulation and experiment could be explained by the fact that the superficial velocities and flow patterns of the other cases are far from the reference case No. 7 for which the mesh and time-step convergence study were performed. There are few other cases (test No. 5, No. 6, No. 8, and No. 9) which shows reasonable agreement with experimental data and also has reasonably similar close superficial velocities and belongs to the same flow regime. However, the large discrepancy in results between simulations and experimental data suggests that mesh and time-step should

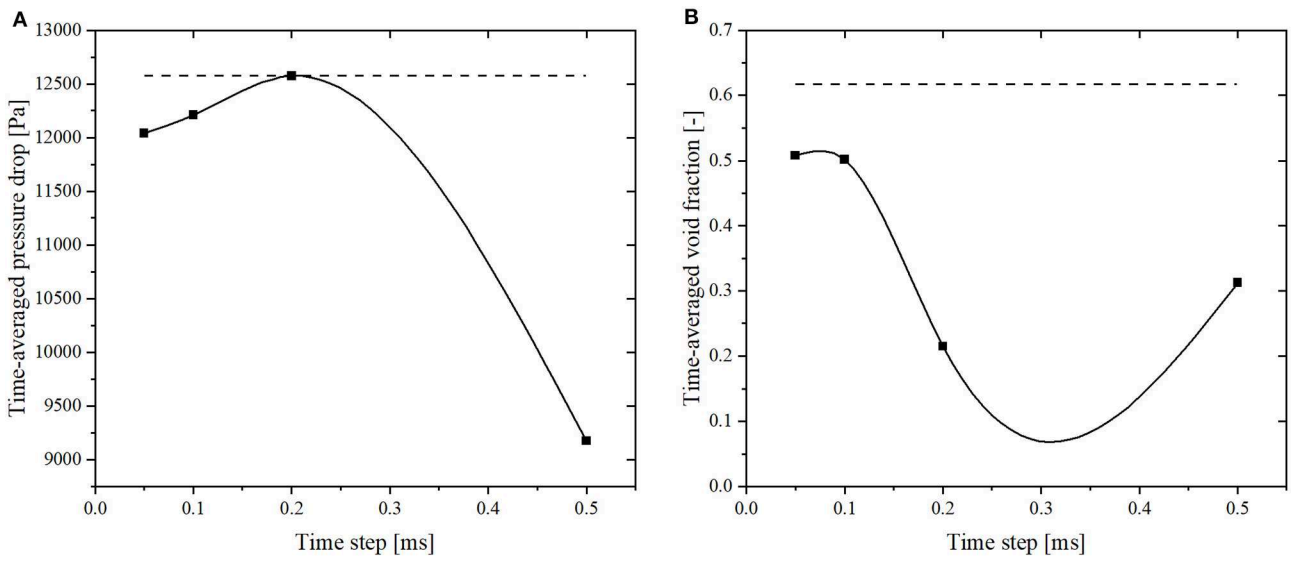

FIGURE 5 | Results of the time step convergence study. **(A)** Two-phase pressure drop. **(B)** Void fraction.

be verified on a case-specific basis and cannot be extrapolated too far from the reference case. With this, we can conclude that universal mesh and time-step for this modeling approach does not exist due to significant variation in boundary conditions imposed for different cases. The possible reasons for the poor agreement for each flow regime are presented in the next subsection with the analysis of the void fraction distribution.

Void Fraction

In this subsection, the results of the void fraction are compared between the experimental and CFD-predicted data. All of 12 tests are separated into five different flow regimes, and six representative results for the different identified flow regimes are presented and discussed.

Bubbly Flow

The test No. 1 and No. 2 correspond to the bubbly flow regime. The time evolution of the void fraction and the corresponding void fraction histogram of test No. 2 for both experimental and simulation data are shown in **Figure 6**. The void fraction time evolution in **Figure 6A** shows small oscillations around 0.02 and the maximum void fraction is <0.1. However, the simulation

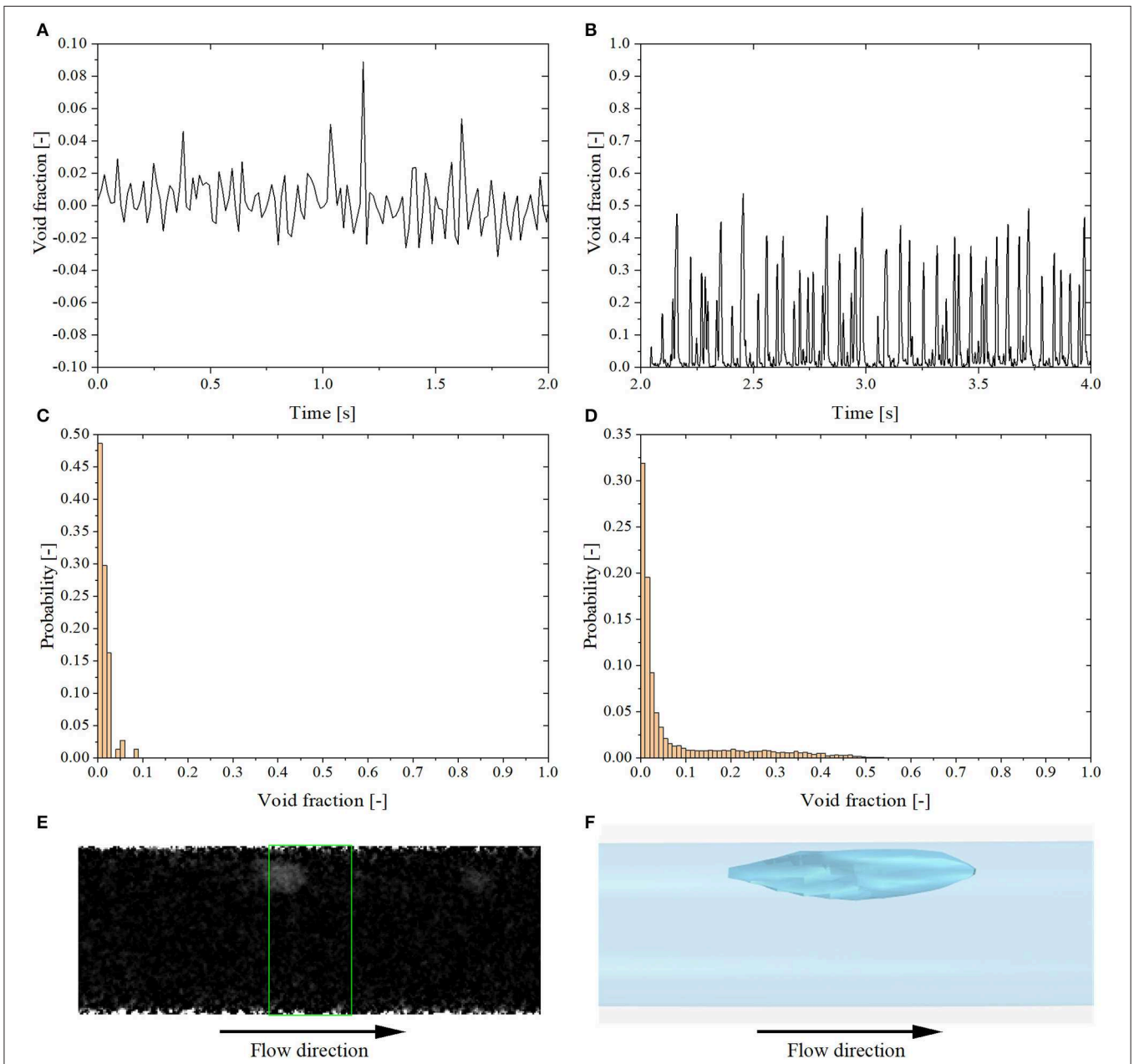

FIGURE 6 | Results of test No. 2. **(A)** Experimental void fraction time evolution. **(B)** Simulation void fraction time evolution. **(C)** Experimental void fraction histogram. **(D)** Simulation void fraction histogram. **(E)** X-ray void fraction contrast image. **(F)** Void fraction isosurface image.

results in **Figure 6B** show much larger peaks and more frequent oscillations, which means that the simulation produces larger bubbles which move faster than in the experiment. **Figures 6E,F** confirm that the computational model results in larger bubbles than what found in the experiments. This might be due to the mesh not being fine enough to capture the small bubbles, which leads to small bubbles merged into a large bubble. As mentioned above, in subsection multiphase flow model, at least three cells across a small bubble are required to capture the interface between two immiscible phases fully. It is evident that the finer mesh helps simulate smaller bubbles better, but the simulations will become too expensive to afford. Nevertheless, both the two histograms reported in **Figures 6C,D** demonstrate a unimodal void fraction distribution peaked at low void fraction values, caused by the dominant continuous liquid phase present in bubbly flow. Due to the low void fraction, i.e., high X-ray attenuation, the noise level in the experimental data is relatively high compared to other flow regimes. This noise causes some

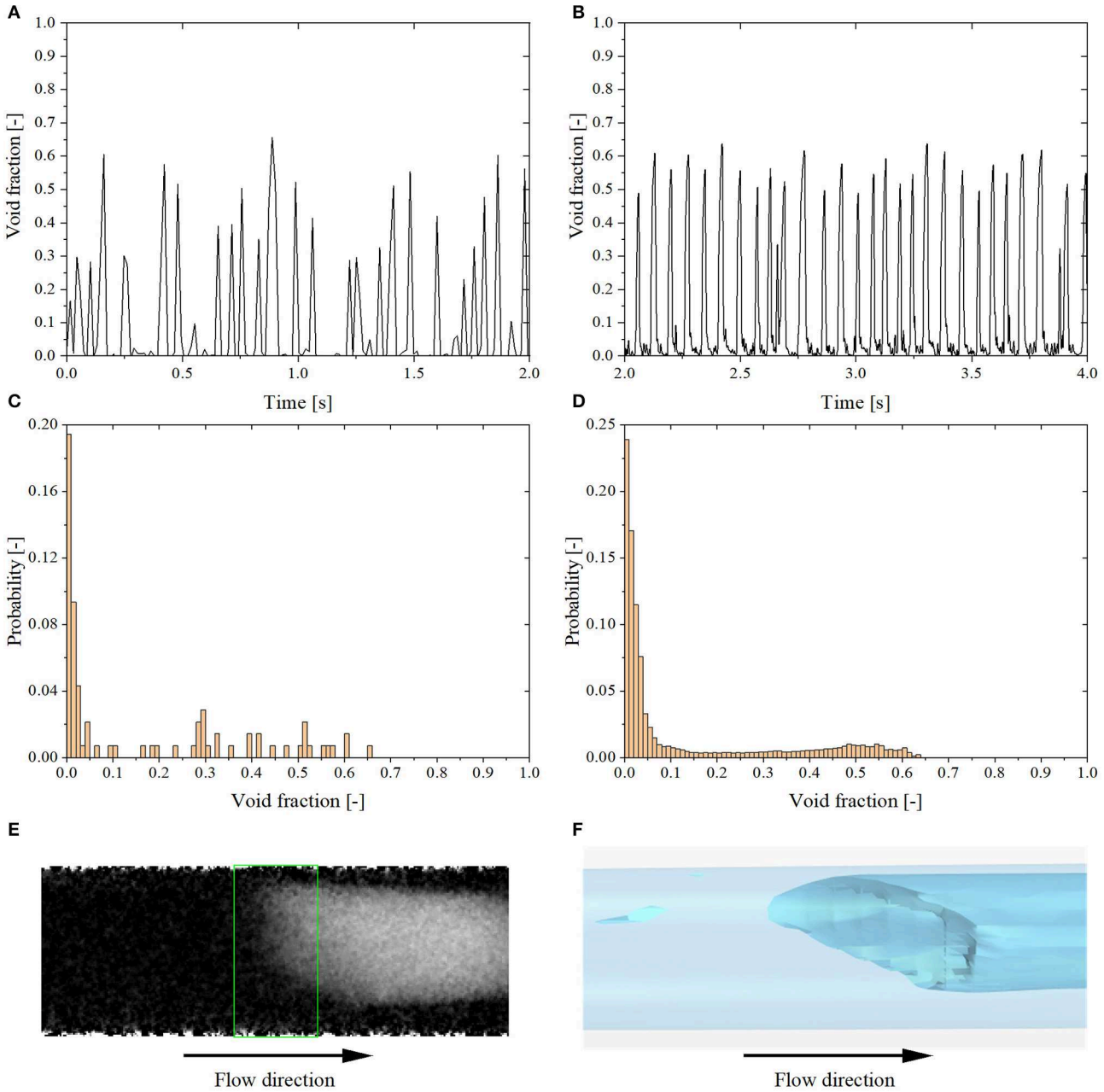

FIGURE 7 | Results of test No. 3. **(A)** Experimental void fraction time evolution. **(B)** Simulation void fraction time evolution. **(C)** Experimental void fraction histogram. **(D)** Simulation void fraction histogram. **(E)** X-ray void fraction contrast image. **(F)** Void fraction isosurface image.

values of the measured void fraction to be <0, as demonstrated in **Figure 6A**.

Plug Flow

By increasing the air flow rate, the small bubbles tend to agglomerate together and the bubble clusters develop into elongated Taylor bubbles or plugs. According to the definition of Zhu et al. (2017), tests No. 3 and No. 4 are identified as plug flow regime. As shown in **Figures 7A,B**, the peaks values are similar for the simulation and experiments, but still the simulation shows the occurrence of peaks at higher frequency than the experimental data. In terms of the histograms, the void fraction histogram presents a bimodal distribution with the appearance of a second peak in the high void fraction range, around 0.5 (cf. **Figures 7C,D**). Since the plug flow is characterized by large structures, the simulation is able to correctly capture the phenomenology observed in the experiments (cf. **Figures 7E,F**). In addition, the staircase shaped tail of a plug proposed by Conte et al. (2017) can be seen both in **Figures 7E,F**. However, the mesh used in these two simulations is still not fine enough to track

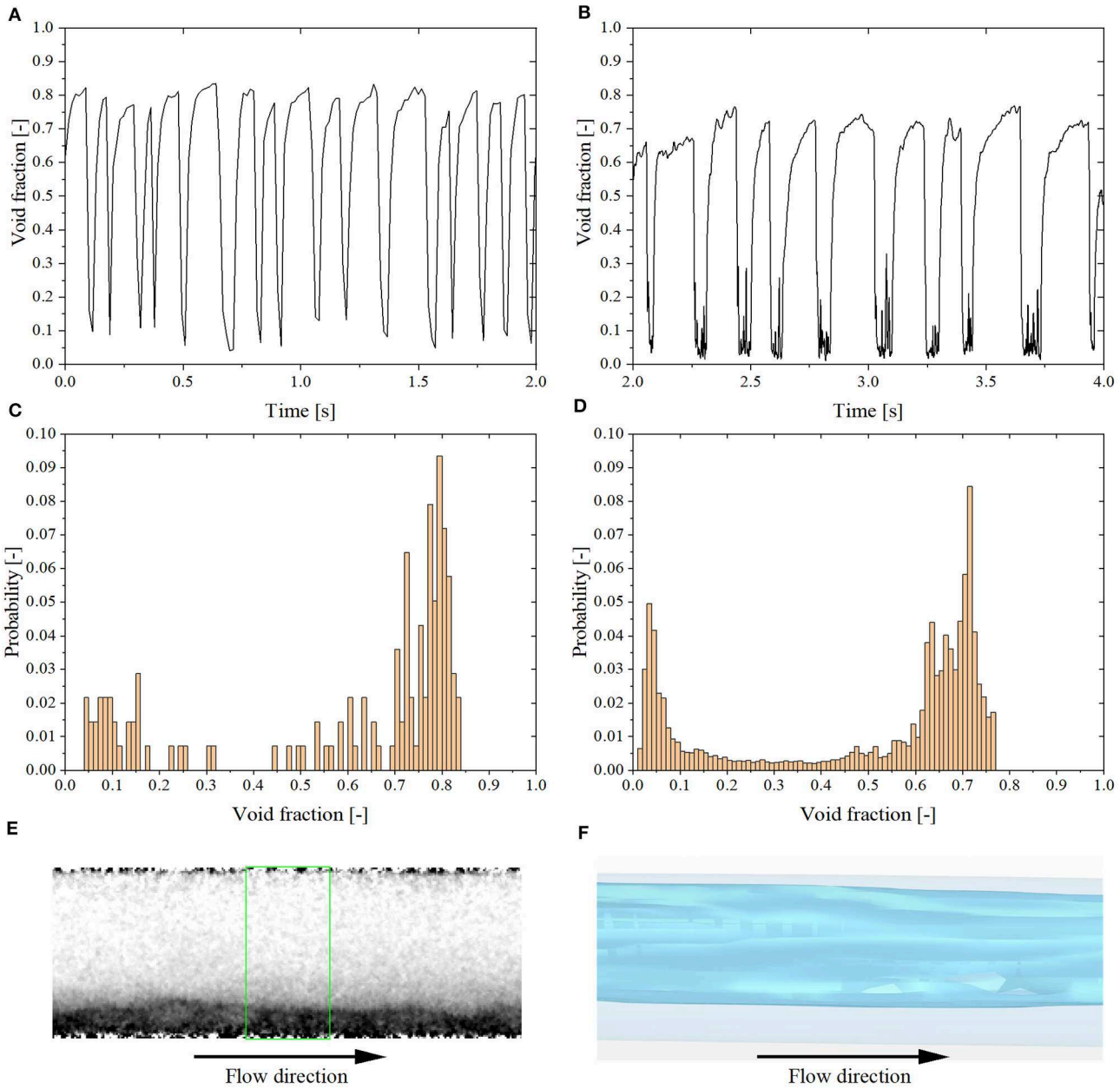

FIGURE 8 | Results of test No. 6. **(A)** Experimental void fraction time evolution. **(B)** Simulation void fraction time evolution. **(C)** Experimental void fraction histogram. **(D)** Simulation void fraction histogram. **(E)** X-ray void fraction contrast image. **(F)** Void fraction isosurface image.

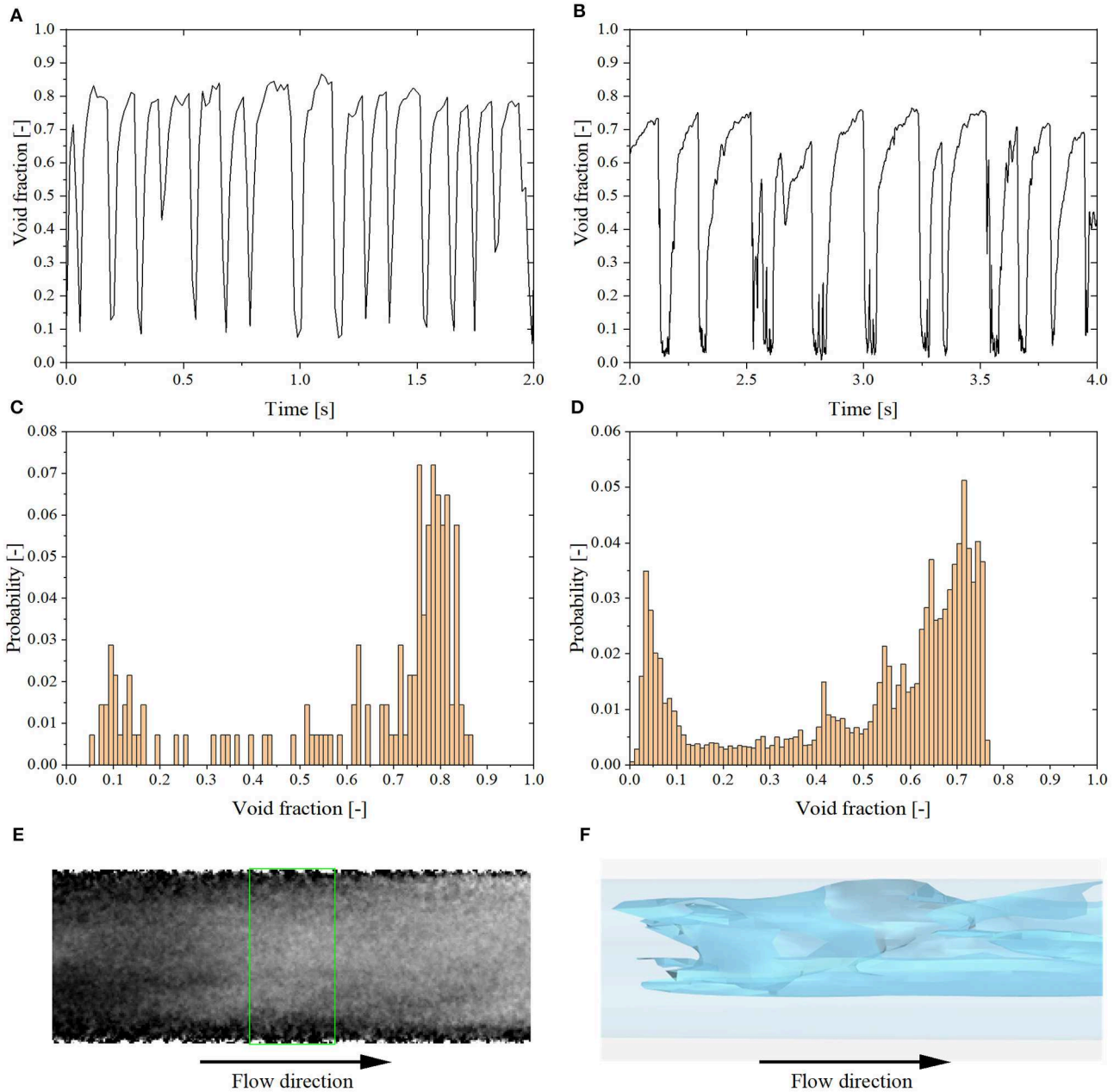

FIGURE 9 | Results of test No. 7. **(A)** Experimental void fraction time evolution. **(B)** Simulation void fraction time evolution. **(C)** Experimental void fraction histogram. **(D)** Simulation void fraction histogram. **(E)** X-ray void fraction contrast image. **(F)** Void fraction isosurface image.

the interfaces of small bubbles, which might lead to the large discrepancy for the two-phase pressure drop.

Slug Flow

With higher air superficial velocity, the flow regime transits from plug to slug flow. This flow regime is characterized by higher and wider void fraction peaks, as illustrated in **Figures 8**, **9**. However, in the simulation, the Taylor bubbles are longer than in experiments and have lower peak values of void fraction compared with the experimental data (cf. **Figures 8A,B**, **9A,B**). The slug flow regime is identified for tests No. 5 to No. 8 (cf. **Table 2**). In addition, the second void fraction peak in the histogram becomes higher than the first peak as shown in **Figures 8C,D**, **9C,D**. Besides, as shown in **Figures 9E,F**, a slug tail similar to what observed in the experiments is predicted in the simulation.

Slug-Annular Flow

Based on the definition proposed by Zhu et al. (2017), tests No. 9 and No. 10 are identified as slug-annular flow regime. Due

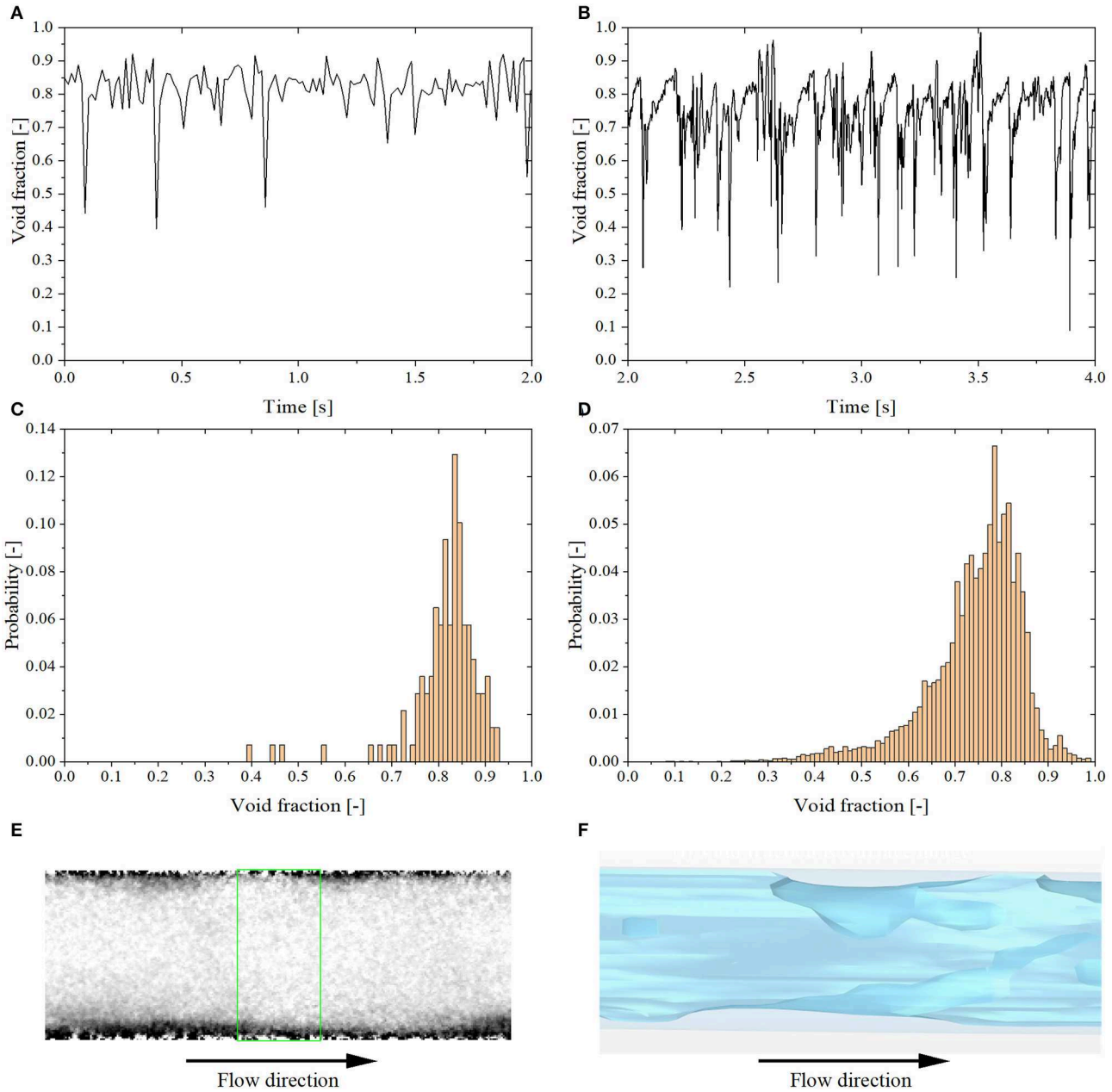

FIGURE 10 | Results of test No. 9. **(A)** Experimental void fraction time evolution. **(B)** Simulation void fraction time evolution. **(C)** Experimental void fraction histogram. **(D)** Simulation void fraction histogram. **(E)** X-ray void fraction contrast image. **(F)** Void fraction isosurface image.

to the higher air superficial velocity, some of the long Taylor bubbles coalesce together, showing typical features of annular flow. In **Figure 10F**, cavities on the slug bubble surface induced by the high air superficial velocity are clearly visible, while they are hard to notice from a 2d projection in **Figure 10E**. As a result, the number of large oscillations decreases and the void fraction fluctuates around 0.8 (cf. **Figures 10A,B**). The void fraction histogram return to a unimodal distribution, but with the peak located at higher void fraction values (cf. **Figures 10C,D**). As shown in **Table 2**, the air superficial velocity of test No. 10 is five-time larger than the reference case (test No. 7), so the large discrepancy between experiments and simulations is probably due to a not sufficiently small integration time step.

Annular Flow

Tests No. 11 and No. 12 correspond to the annular flow regime. The main characteristic of the transition from slug-annular flow to annular flow is the disappearance of the slugs. The smooth annular region appears both in the experiment and simulation

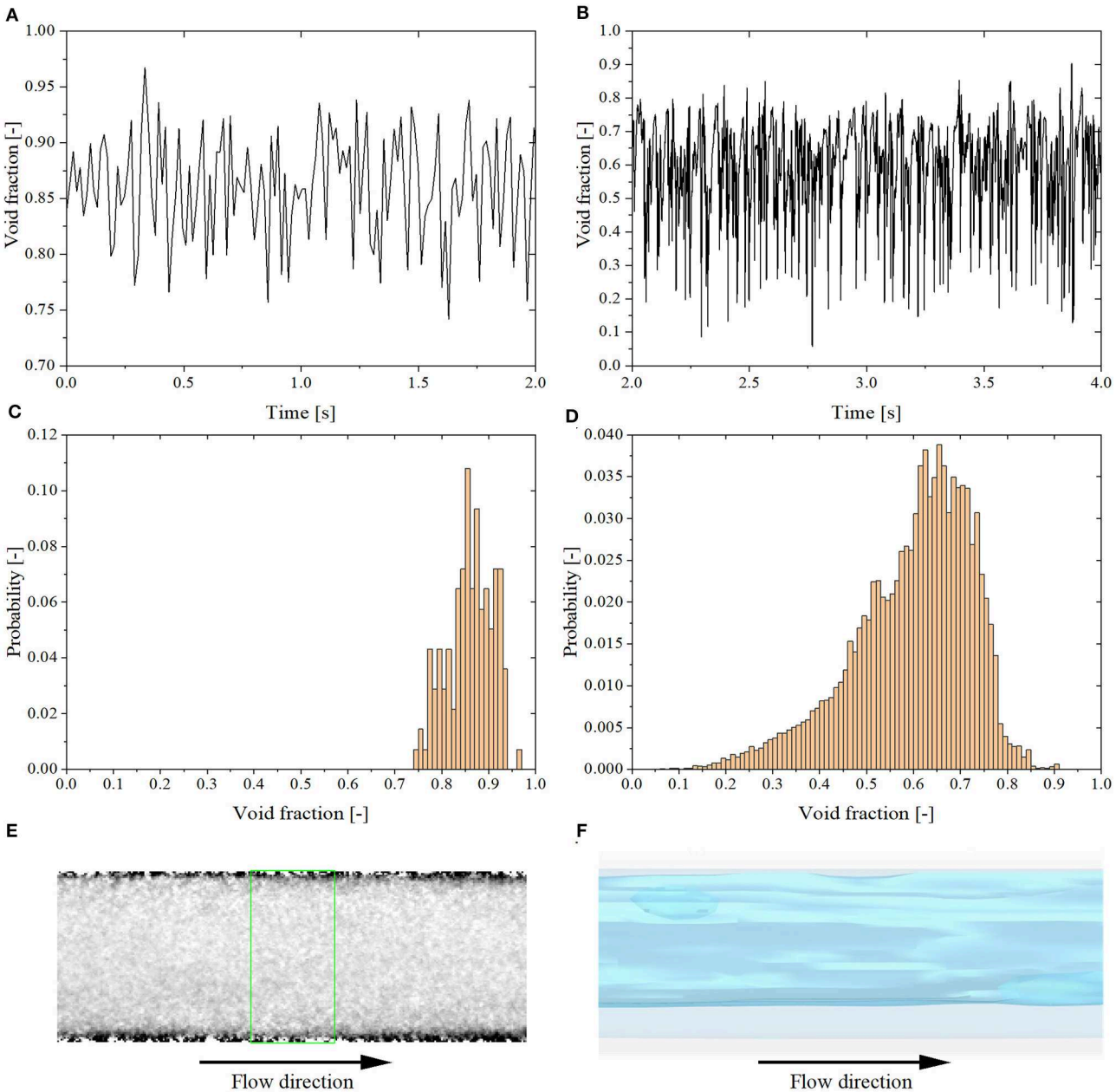

FIGURE 11 | Results of test No. 11. **(A)** Experimental void fraction time evolution. **(B)** Simulation void fraction time evolution. **(C)** Experimental void fraction histogram. **(D)** Simulation void fraction histogram. **(E)** X-ray void fraction contrast image. **(F)** Void fraction isosurface image.

(cf. **Figures 11E,F**). Therefore, there is a unimodal void fraction distribution present in the histogram with a single peak in the high void fraction regime (cf. **Figures 11C,D**). Comparing with the experimental data, the simulation results still show some slugs, not found in the experimental data (cf. **Figures 11A,B**). This might explain why the computed two-phase pressure drops are much larger than the experimental data (cf. **Table 2**). Another possible reason of the large difference is that the annular flow simulation requires smaller time step owing to the highest air superficial velocity. The time step convergence used test No. 7 as a reference and it was extrapolated into other 11 simulations, so the time step may not be accurate enough. The smaller time step might give better results, but it absolutely makes the computation much more expensive.

CONCLUSION

The behavior of air-water two-phase adiabatic flows in helical coils was investigated using CFD simulations. The VOF model was applied to track and locate the free surface of two immiscible

phases, namely water and air. The realizable k-ϵ model was employed to simulate the turbulence of the two-phase flow. Following a convergence study, the optimal parameters for mesh generation and integration time steps were determined based on the reference case, test No. 7. The simulation results show that by employing proper boundary conditions, initial conditions, mesh and time step, the air-water flow regime as well as the pressure drop can be predicted by CFD models reasonably well. The bubbly, plug, slug, slug-annular and annular flow regimes were observed in the simulations, but a good quantitative agreement with the experimental data for two-phase pressure drops and void fractions was found only for slug and slug-annular flow regimes. This good quantitative agreement proves that the VOF model can predict and capture the two-phase flow very well with the case-specific mesh and time-step convergence study. However, for other cases, the two-phase pressure drops were considerably overestimated in the simulations, and phenomenological differences for the void fraction time evolutions were also observed. The large discrepancy of pressure drops and time-dependent void fraction shown in these cases confirms that the optimal mesh and time-step obtained for the reference case cannot be used for different flow regimes cases, especially for those whose superficial velocities differ a lot from the reference case. Also, there is not a single mesh that can be used to simulate all the flow regimes due to the significant flow topology variation. Hence, a case-specific mesh and time-step convergency are indispensable for each flow regime.

DATA AVAILABILITY STATEMENT

The datasets generated for this study are available on request to the corresponding author.

AUTHOR CONTRIBUTIONS

SC is the main author of the paper and was responsible for drafting the paper and performing the numerical simulations. DB carried out the experiments, the associated experimental data post-processing and provided the experimental data. YI, AM, and VP are the group supervisors and have provided SC and DB with technical guidance on the execution of the computational and experimental work and on the drafting of this manuscript.

FUNDING

This work was partially funded by a DOE NEAMS HIP grant and by the China Scholarship Council.

ACKNOWLEDGMENTS

The work presented herein was supported by the US Department of Energy's Nuclear Energy Advanced Modeling and Simulation (NEAMS) program as part of the Steam Generator Flow Induced Vibration High Impact Problem, by the China Scholarship Council, and by the Advanced Research Computing at the University of Michigan, Ann Arbor.

REFERENCES

Abdulkadir, M. (2011). *Experimental and Computational Fluid Dynamics (CFD) studies of gas-liquid flow in bends*. (Ph.D. thesis). Nottingham, UK: University of Nottingham.

Akhlaghi, M., Mohammadi, V., Nouri, N. M., Taherkhani, M., and Karimi, M. (2019). Multi-fluid VoF model assessment to simulate the horizontal air–water intermittent flow. *Chem. Eng. Res. Des.* 152, 48–59. doi: 10.1016/j.cherd.2019.09.031

Alizadehdakhel, A., Rahimi, M., Sanjari, J., and Alsairafi, A. A. (2009). CFD and artificial neural network modeling of two-phase flow pressure drop. *Int. Commun. Heat Mass Transf.* 36, 850–856. doi: 10.1016/j.icheatmasstransfer.2009.05.005

Brackbill, J. U., Kothe, D. B., and Zemach, C. (1992). A continuum method for modeling surface tension. *J. Comput. Phys.* 100, 335–354. doi: 10.1016/0021-9991(92)90240-Y

Breitenmoser, D., Manera, A., Prasser, H. M., and Petrov, V. (2019). "High-resolution high-speed void fraction measurements in helical tubes using X-ray radiography," in *18th International Topical Meeting on Nuclear Reactor Thermal Hydraulics (NURETH 2019)* (Portland), 3554–3567.

Carelli, M. D., Conway, L. E., Oriani, L., Petrovic, B., Lombardi, C., Ricotti, M. E., et al. (2004). The design and safety features of the IRIS reactor. *Nuclear Eng. Des.* 230, 151–167. doi: 10.1016/j.nucengdes.2003.11.022

Conte, M. G., Hegde, G. A., da Silva, M. J., Sum, A. K., and Morales, R. E. M. (2017). Characterization of slug initiation for horizontal air-water two-phase flow. *Exp. Therm. Fluid Sci.* 87, 80–92. doi: 10.1016/j.expthermflusci.2017.04.023

Dragunov, Y. G., Lemekhov, V. V., Smirnov, V. S., and Chernetsov, N. G. (2012). Technical solutions and development stages for the BREST-OD-300 reactor unit. *Atomic Energy* 113, 70–77. doi: 10.1007/s10512-012-9597-3

El-Genk, M. S., and Schriener, T. M. (2017). A review and correlations for convection heat transfer and pressure losses in toroidal and helically coiled tubes. *Heat Transf. Eng.* 38, 447–474. doi: 10.1080/01457632.2016.1194693

Fernandes, J., Lisboa, P. F., Simoes, P. C., Mota, J. P. B., and Saatdjian, E. (2009). Application of CFD in the study of supercritical fluid extraction with structured packing: wet pressure drop calculations. *J. Supercrit. Fluids* 50, 61–68. doi: 10.1016/j.supflu.2009.04.009

Fsadni, A. M., Whitty, J. P., and Stables, M. A. (2016). A brief review on frictional pressure drop reduction studies for laminar and turbulent flow in helically coiled tubes. *Appl. Therm. Eng.* 109, 334–343. doi: 10.1016/j.applthermaleng.2016.08.068

Hernandez Perez, V. (2008). *Gas-liquid two-phase flow in inclined pipes.* (Ph.D. thesis). Nottingham, UK: University of Nottingham.

Hernandez-Perez, V., Abdulkadir, M., and Azzopardi, B. (2011). Grid generation issues in the CFD modelling of two-phase flow in a pipe. *J. Comput. Multiphase Flows* 3, 13–26. doi: 10.1260/1757-482X.3.1.13

Hirt, C. W., and Nichols, B. D. (1981). Volume of Fluid (Vof) method for the dynamics of free boundaries. *J. Comput. Phys.* 39, 201–225. doi: 10.1016/0021-9991(81)90145-5

Ingersoll, D. T., Houghton, Z. J., Bromm, R., and Desportes, C. (2014). NuScale small modular reactor for Co-generation of electricity and water. *Desalination* 340, 84–93. doi: 10.1016/j.desal.2014.02.023

Kasturi, G., and Stepanek, J. (1972). Two phase flow—I. pressure drop and void fraction measurements in concurrent gas-liquid flow in a coil. *Chem. Eng. Sci.* 27, 1871–1880. doi: 10.1016/0009-2509(72)85049-8

Kim, H. K., Kim, S. H., Chung, Y. J., and Kim, H. S. (2013). Thermal-hydraulic analysis of SMART steam generator tube rupture using TASS/SMR-S code. *Ann. Nuclear Energy* 55, 331–340. doi: 10.1016/j.anucene.2013.01.007

Kiran, R., Ahmed, R., and Salehi, S. (2020). Experiments and CFD modelling for two phase flow in a vertical annulus. *Chem. Eng. Res. Des.* 153, 201–211. doi: 10.1016/j.cherd.2019.10.012

Mandal, S. N., and Das, S. K. (2003). Gas–liquid flow through helical coils in vertical orientation. *Ind. Eng. Chem. Res.* 42, 3487–3494. doi: 10.1021/ie0200656

Marcel, C. P., Acuna, F. M., Zanocco, P. G., and Delmastro, D. F. (2013). Stability of self-pressurized, natural circulation, low thermo-dynamic quality, nuclear reactors: the stability performance of the CAREM-25 reactor. *Nuclear Eng. Des.* 265, 232–243. doi: 10.1016/j.nucengdes.2013.08.057

Matsuura, M., Hatori, M., and Ikeda, M. (2007). Design and modification of steam generator safety system of FBR MONJU. *Nuclear Eng. Des.* 237, 1419–1428. doi: 10.1016/j.nucengdes.2006.09.046

Rahman, M., Heidrick, T., and Fleck, B. (2009). A critical review of advanced experimental techniques to measure two-phase gas/liquid flow. *Open Fuels Energy Sci. J.* 2, 54–70. doi: 10.2174/1876973X00902010054

Santini, L., Cioncolini, A., Lombardi, C., and Ricotti, M. (2008). Two-phase pressure drops in a helically coiled steam generator. *Int. J. Heat Mass Transf.* 51, 4926–4939. doi: 10.1016/j.ijheatmasstransfer.2008.02.034

Siemens, P. (2018). *Simcenter STAR-CCM+ User Guide V13. 06.* Plano: Siemens PLM.

Taha, T., and Cui, Z. F. (2006). CFD modelling of slug flow in vertical tubes. *Chem. Eng. Sci.* 61, 676–687. doi: 10.1016/j.ces.2005.07.022

Xin, R. C., Awwad, A., Dong, Z. F., Ebadian, M. A., and Soliman, H. M. (1996). An investigation and comparative study of the pressure drop in air-water two-phase flow in vertical helicoidal pipes. *Int. J. Heat Mass Transf.* 39, 735–743. doi: 10.1016/0017-9310(95)00164-6

Zhu, H. Y., Li, Z. X., Yang, X. T., Zhu, G. Y., Tu, J. Y., and Jiang, S. Y. (2017). Flow regime identification for upward two-phase flow in helically coiled tubes. *Chem. Eng. J.* 308, 606–618. doi: 10.1016/j.cej.2016.09.100

Zhuang, N., Zhang, K., Manera, A., and Petrov, V. (2018). X-ray radiography and high-speed videography measurement on void fraction in helical coil. *Adv. Thermal Hydraul.* 2018, 250−262.

Conflict of Interest: The authors declare that the research was conducted in the absence of any commercial or financial relationships that could be construed as a potential conflict of interest.

frontiers in Energy Research

ORIGINAL RESEARCH
published: 19 May 2020
doi: 10.3389/fenrg.2020.00076

Research on the Transient Hydraulic Characteristics of Multistage Centrifugal Pump During Start-Up Process

Long Yun, Lin Bin, Fang Jie, Zhu Rongsheng and Fu Qiang*

China National Research Center of Pumps, Jiangsu University, Zhenjiang, China

Compared with the periodic unsteady flow induced by single-stage centrifugal pump, the internal flow state of multistage centrifugal pump is more complicated and the flow is more disordered. In this paper, the start-up process is divided into two stages: the closed-valve transition and the open-valve transition. The transient operation process is simulated numerically, and the pump characteristics and the evolution characteristics of the internal flow field are analyzed. It is found that multistage centrifugal pump start-up process of the closed-valve transition, when the impeller does the same work, compared with the steady state at the same speed, the mechanical energy in the internal flow field is converted into more kinetic energy and less pressure. Compared with the steady state at the same flow rate, in the initial stage of the open-valve start-up process, the stall group in the impeller flow channel is larger and the number of stall groups is more during the transient process, which exacerbates the rotational stall of the internal flow of the impeller, and the flow is more disordered. As a result, the amplitude of the hump fluctuation is greater than that under the same flow steady state. The research on the transient characteristics of the low specific speed multi-stage centrifugal pump during startup conditions is of great significance to the safety and reliability of nuclear power equipment and systems.

Keywords: multistage centrifugal pump, start-up process, numerical simulation, internal flow, transient characteristics

OPEN ACCESS

Edited by:
Yixiang Liao,
Helmholtz-Zentrum Dresden-Rossendorf (HZ), Germany

Reviewed by:
Jian Zhang,
Harbin Institute of Technology, China
Yu-Liang Zhang,
Quzhou University, China

****Correspondence:***
Zhu Rongsheng
zrs@ujs.edu.cn

Specialty section:
This article was submitted to Nuclear Energy, a section of the journal Frontiers in Energy Research

Received: *10 February 2020*
Accepted: *14 April 2020*
Published: *19 May 2020*

Citation:
Yun L, Bin L, Jie F, Rongsheng Z and Qiang F (2020) Research on the Transient Hydraulic Characteristics of Multistage Centrifugal Pump During Start-Up Process. Front. Energy Res. 8:76. doi: 10.3389/fenrg.2020.00076

INTRODUCTION

Multi-stage centrifugal pumps need to be started frequently due to changes in operating conditions. During start-up, the speed of the pump increases rapidly from zero to thousands. The internal flow state of the pump changes from laminar to strong turbulent, and it also includes periodic unsteady flow induced by the dynamic and static interference of the impeller and the pressure water chamber. The internal flow of the pump exhibits unconventional transient characteristics. This article takes the CAP1400 Capacitive Water Pump (CVS) as the research object. The pump is a 13-stage low specific speed centrifugal pump. Capacitive make-up water pump is an extremely important class D pump in nuclear power plants, and it is a key device to ensure the safe and reliable operation of nuclear power plants.

In the running process of the multistage centrifugal pump, due to the change of operating conditions, it is necessary to start frequently, and the rapid increase of speed and flow during the start-up process will cause the pressure, velocity, radial force, and other parameters of the flow

field to change strongly in a short time. At present, the research on the start-up process of the centrifugal pump generally uses the quasi-steady-state hypothesis method instead of the start-up transient process (Wu et al., 2009). However, due to the obvious transient effects of the start-up process, the numerical simulation is inaccurate. With the expansion of the centrifugal pump start-up process in various application fields and the increase of system complexity, it has been paid more and more attention by scholars in recent years.

Tsukamoto and Ohashi (1982) and Tsukamoto et al. (1995) considered that the pulse pressure and the hysteresis of the flow around the blade during the start-up process of the small low specific speed centrifugal pump were the main reasons for the dimensionless head curve to be lower than the quasi-steady head curve. And the fluctuation frequency of impeller speed was directly related to the transient effect of the head curve. Thanapandi and Prasad (1995) established a numerical model for a screw pump with different opening degrees by using the future analysis method. The transient dynamic characteristics of the pump were analyzed and verified by experiments. It was found that the dynamic characteristics of the pump deviated greatly from its steady-state characteristics. Xu et al. (2010), Li et al. (2010), and Li (2009) created a complete system model including circulating pipes and pumps. In the numerical simulation of rapid start-up process of centrifugal pumps, the sliding grid method was used to analyze the evolution process of unsteady flow in centrifugal pumps under transient conditions. Ping et al. (2007) established the basic equation describing the rapid start-up of centrifugal pumps. Taking a fast-start mixed-flow pump as an example, the transient effect of the flow field under the transient operation of fast start-up was theoretically analyzed and numerically calculated. It was found that the pump characteristics in the initial start-up stage were obviously different from those of the quasi-steady-state process. Wang et al. (2017) studied the transient characteristics of an ultra-low specific speed centrifugal pump under the start-up process of the closed-valve condition by compared the quasi-steady-state process. It was found that the magnitude of the start-up acceleration has an important influence on the transient impact head at the end of the closed-valve process. At the beginning of the start-up process, the static pressure distribution of them has the largest difference. With the rotational speed increases, the difference between them decreases gradually.

Up to now, scholars at home and abroad have a deep understanding of the transient characteristics of centrifugal pumps in the start-up process, but most of the research objects of the transient characteristics of the start-up process are limited to single-stage centrifugal pumps. Compared with single-stage centrifugal pump, the complex series structure of multistage centrifugal pump makes its internal flow more complex (Zhang et al., 2012; Liu et al., 2014; Wang et al., 2017), and because of the transfer of the flow states between stages, the transient internal flow characteristics will be more disordered during the start-up process.

CAP1400 is this new type of third-generation reactor. The performance of many equipment needs to be studied, especially the pumps that are very important to safety. The research focus and innovation of this paper is to reveal the transient characteristics of a new type of nuclear power pump through existing methods, together to provide a reference for the safety design of nuclear power plants. Therefore, based on the predecessors, this paper further studies the transient state of multistage centrifugal pumps by numerical simulation. Carrying out the research on the transient characteristics of the low specific speed multi-stage centrifugal pump during startup conditions is of great significance to the safety and reliability of nuclear power equipment and systems.

THEORETICAL ANALYSIS OF START-UP TRANSIENT PROCESS OF CENTRIFUGAL PUMP

Zhang (2013) according to the momentum moment theorem and the energy conservation principle, deduced the generalized Euler equation suitable for the start-up transient process of the centrifugal pumps, which is shown in Equation (1).

$$H_{th} = \frac{u_2 V_{u2} - u_1 V_{u1}}{g} + \frac{\omega D^5}{gQ}\Omega_J \frac{\partial \omega}{\partial t} - \frac{\omega D^2}{gQ}\Omega_M \frac{\partial Q}{\partial t} \quad (1)$$

In Equation, V_{u1} and V_{u2} are the circumferential component of the absolute velocity of the liquid particle in the impeller at leading edge and trailing edge, u_1 and u_2 are the circumferential velocity of the liquid particle in the impeller at leading edge and trailing edge, ω is the instantaneous rotational angular velocity of the impeller, Q is the instantaneous volume flow, D is the nominal diameter of the impeller. For radial centrifugal impellers, $D = D_2$. Ω_J and Ω_M are two different blade influence coefficients, and the size is related to the impeller geometry parameters such as blade shape and blade thickness,

$$\begin{cases} \Omega_J = \frac{\pi}{32}\left(\bar{D}_2^4 \bar{b}_2 - \bar{D}_1^4 \bar{b}_1\right) \\ \Omega_M = \frac{1}{8}\left(\frac{\bar{D}_2^2}{\psi_2 \tan\beta_2} - \frac{\bar{D}_1^2}{\psi_1 \tan\beta_1}\right) \end{cases} \quad (2)$$

Where, $\bar{D}_1 = D_1/D, \quad \bar{D}_2 = D_2/D, \quad \bar{b}_1 = b_1/D, \quad \bar{b}_2 = b_2/D.$

According to Equation, the head of the centrifugal pump during the start-up transient process is mainly composed of two parts. One is the steady head of the centrifugal pump at the corresponding speed during the start-up process, as shown in the first item on the right side of the equation. Another is rotational acceleration and additional head of flow inertia during the start-up process, as shown in the second and third terms on the right side of the equation. The latter is the main reason for the transient effect in the start-up process of centrifugal pump.

SUMMARY OF START-UP PROCESS OF MULTISTAGE CENTRIFUGAL PUMP

The start-up process of centrifugal pump is a necessary process for the normal operation of pump system. This process usually refers to the stage in which the flow rate increases gradually from zero to the rated flow rate (Li, 2012). In order to prevent start-up power overload of multistage centrifugal pump, the start-up

process usually includes two processes: closed-valve start and open-valve control. This paper uses full pressure start and the motor speed changes linearly. As shown in **Figure 1**, the closed-valve transition stages are divided into two sections, the first stage is impeller acceleration stage, the second stage is shut-off point operation stage. Under the condition of closing dead-point flow rate, the impeller speed increases rapidly from zero to rated speed, and then the multistage centrifugal pump operates at the critical dead-point condition of stable speed. When the start-up process of the closed-valve, full pressure start-up is preferred when the minimum torque and maximum flow rate are satisfied. The third and fourth stages are the open-valve transition stage. In the third stage, after the impeller reaches the rated speed, the valve is opened according to the predetermined law, and the flow rate gradually increases from zero to the rated flow rate. The fourth stage indicates stable operation stage. In the open-valve transition stage, because the boundary conditions change with time during the start-up process is not clear, this paper will use Flowmaster software and CFX software to simulate. Firstly, Flowmaster software is used to build the operation model of multistage centrifugal pump to obtain the parameters of the relevant boundary conditions, and then the boundary conditions are input into CFX. The transient numerical simulation of the start-up stage of the open-valve is carried out in the software.

COMPUTING MODEL AND MESH GENERATION

The main design parameters of the multistage centrifugal pump selected in this paper are as follows: flow rate $Q_d = 34.1\ m^3/h$, head $H = 1{,}800$ m, speed $n = 2{,}985$ r/min, $n_s = 26.3$. The main geometric parameters of the flow passage parts of the model pump are shown in **Table 1**.

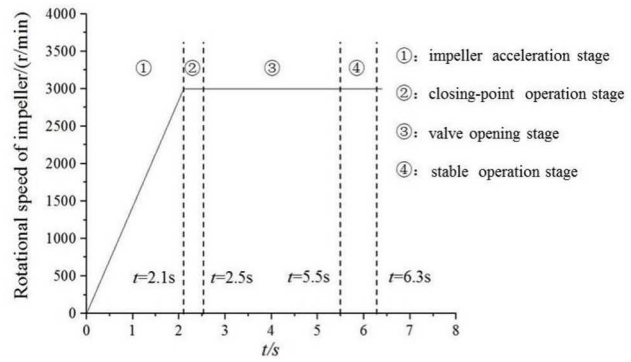

FIGURE 1 | Different stages of the start-up process.

Commercial software Cero is used to build the three-dimensional model of the flow passage area of the multistage centrifugal pump, including the suction chamber, impellers at all levels, radial guide vanes, and pump casing. Compared with the other guide vanes at all levels, there is no anti-guide vane in the final guide vanes and the outlet of the last guide vanes directly contacts with the fluid field of the pump casing. The fluid field model of the multistage centrifugal pump is shown in **Figure 2**. Considering that the internal fluid flow state varies greatly during the start-up process, the impeller is divided into structured hexahedron mesh, which is shown in **Figure 3**.

Radial guide vane, suction chamber and pump casing adopt unstructured tetrahedral mesh with strong self-adaptability to realize complex structure mesh generation, which guarantees mesh quality above 3.0. At the beginning of the study, we conducted a grid-independent verification of a single-stage pump, as shown in **Figure 3A**. When the total number of grid cells is 1584810, the head change is <0.5%. Finally, the mesh number of suction chamber, pump casing, and impeller are 570325, 107906, and 326751, respectively. The number of radial guide vanes at the last stage is 144854, and the total number of grids is 13763729.

TURBULENCE MODEL AND BOUNDARY CONDITION SETTING

This paper based on ANSYS CFX 18.1 to complete the start-up transient simulation numerical calculation. The Shear Stress Transport (SST) model is used in the turbulence model. The results of steady flow field with zero rotational speed and flow rate are taken as initial documents. The interface between impeller and radial guide vane is set to Frozen rotor mode with fixed rotor, the wall roughness is set to 0.125 mm, and the wall boundary condition is set to non-slip wall. The import boundary condition is set to the full pressure inlet, and the reference pressure is set to 1 atm. The outlet boundary condition is set to the mass flow outlet. The turbulence intensity is moderate [Medium (Intensity = 5%)]. When the closed-valve starts at the closing dead-point, the flow rate can be regarded as 0. But in fact, the internal flow of multistage centrifugal pump is still circulating under small flow rate, and the flow rate can be regarded as a constant value during the whole shut-off start-up process (Shao, 2016). The flow rate is about 1 5% of the design flow rate of the pump, and the mass flow rate is 0.01 kg/s in this chapter. When it is in the open-valve

TABLE 1 | Dimensional parameters of impeller and radial guide vane.

Main dimensional parameters of impeller	Value	Main dimensional parameters of radial guide vanes	Value
Impeller outlet diameter D_2/mm	315	Radial guide vane base circle diameter D_3/mm	320
Number of impeller blades Z	6	Radial guide vane throat axial width b_3/mm	12
Blade outlet placement angle β_2/°	30	Radial guide vane throat plane width a_3/mm	12
Blade outlet width b_2/mm	10	Number of radial guide vanes Z	8

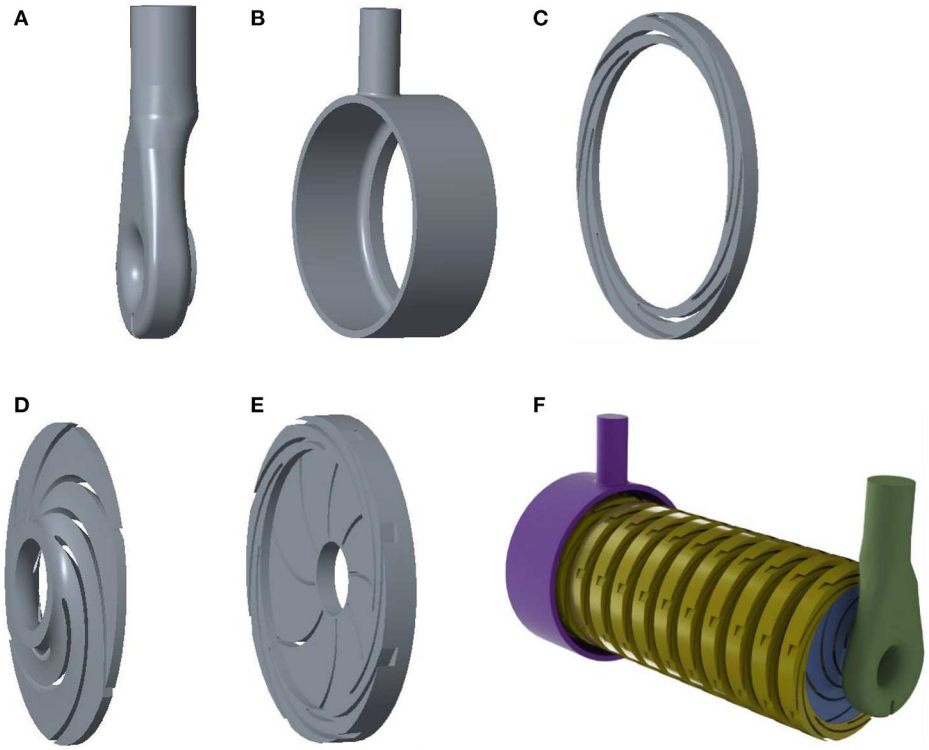

FIGURE 2 | Fluid domain of multistage centrifugal pump. **(A)** Suction chamber, **(B)** pump casing, **(C)** final guide vane, **(D)** impeller, **(F)** radial guide vane, and **(G)** multistage centrifugal pump integral flow domain.

transition stage, the boundary condition of flow is the change value of flow parameters obtained by Flowmaster simulation.

In this paper, the total calculation time of closed-valve transition stage is set to 2.5 s, and the total time of open-valve transition stage is 3.8 s, and the time step is 0.002 s. In order to ensure absolute convergence within each time step, the maximum number of iterations within a time step is set to 50, and the residual value of convergence is set to 0.0001.

The rated speed is 2,985 r/min, the total calculating time is 2.5 s. Within $0 \leq t \leq 2.1$ s, the rotational speed is uniformly accelerated to the rated speed of 2,985 r/min, and within 2.1 s $\leq t \leq$ 2.5 s, the rotational speed is stable at 2,985 r/min.

The equation for calculating speed in expression function of closed-valve transition stage is shown in Equation (3).

$$\begin{aligned} n_t = &-2985[\text{rev min}\hat{}-1]/(\text{Ttol}/1[\text{s}]) * (t/1[\text{s}]) \\ &* \text{step}((\text{Ttol}-t)/1[\text{s}]) - 2985[\text{rev min}\hat{}-1] \\ &* (1 - \text{step}((\text{Ttol}-t)/1[\text{s}])) \end{aligned} \tag{3}$$

The rotational speed n_t remains constant during the open-valve transition stag, i.e., $n_t = -2{,}985\ [rev\ min^{-}1]$.

In Equation (3), Ttol = 2.1 [s], which means the start-up time is 2.1 s, among them function step () is the function of CFX itself, and its expression value is shown in Equation (4).

$$\text{step}(x) = \begin{cases} 0, & x < 0 \\ 0.5 & x = 0 \\ 1 & x > 0 \end{cases} \tag{4}$$

In Equation (4), x is dimensionless.

The equation for calculating head H in expression function is shown in Equation (5).

$$H = (\text{Ptout-Ptin})\ /998\left[\text{kg m}\hat{}-3\right]/9.81\left[\text{m s}\hat{}-2\right] \tag{5}$$

$$\begin{aligned} \text{Ptout} = &\text{ mass Flow AveAbs(Total Pressure in St n Frame)} \\ &\text{@OUTLET} \end{aligned} \tag{6}$$

$$\begin{aligned} \text{Ptin} = &\text{ mass Flow AveAbs(Total Pressure in Stn Frame)} \\ &\text{@INLET} \end{aligned} \tag{7}$$

The equation for calculating power P written in the expression function is shown in Equation

$$P = torqu * n_t/1[\text{rad}] \tag{8}$$

Where:

torqu represents the all impellers torque consumed.

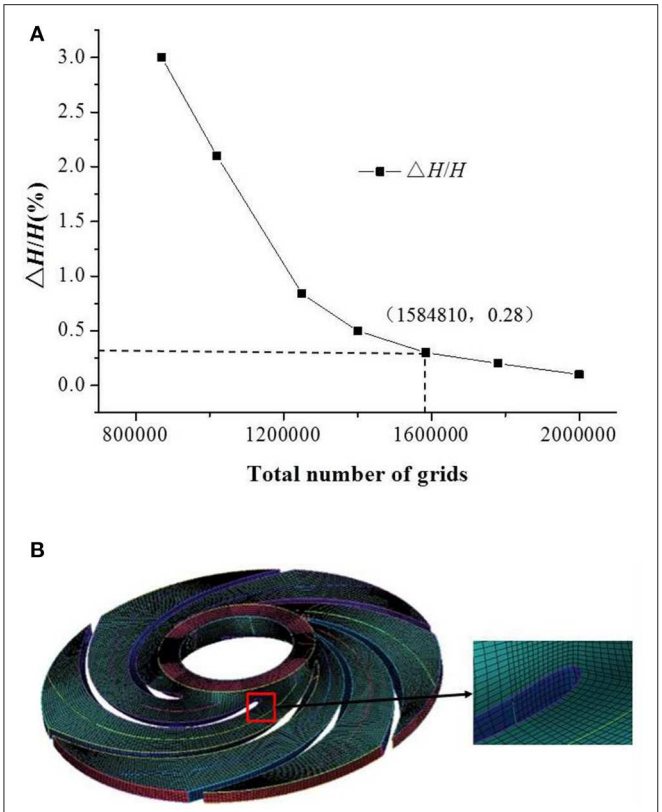

FIGURE 3 | Meshing. **(A)** Grid independence verification and **(B)** structured grid of impeller.

The calculation equation written in the expression function of efficiency η is as shown in Equation (9).

$$\eta = \text{massFlow()@INLET(ptout–ptin)/(998[kg m\^{}]* torqu* } \eta_t) * 1[\text{rad}] \quad (9)$$

ANALYSIS OF CALCULATION RESULTS OF THE START-UP PROCESS OF THE CLOSED-VALVE TRANSITION

Contrastive Analysis of Pump Characteristics of the Start-Up Process of the Closed-Valve Transition

During the start-up process of the closed-valve transient, the speed increases linearly with the start-up time. In order to explore the relationship between the pump characteristics and the change of the speed during the start-up process of the multistage centrifugal pump. In this paper, the rotation period f of the custom function rotor is used to describe the variation law of the pump characteristics during the start-up process of the closed-valve transition. The rotor rotation period f represents the time taken for each revolution of the impeller. The calculation equation is shown in Equation (10).

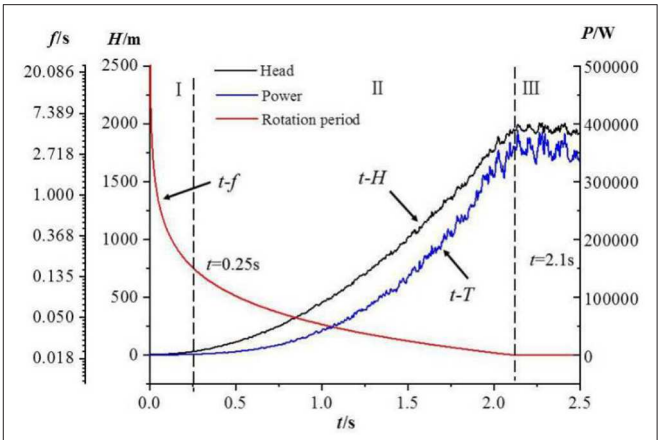

FIGURE 4 | Pump characteristic change during the start-up process of the closed-valve transitional.

$$f = \begin{cases} \frac{42}{995t} \; 0 \le t \le 2.1\text{s} \\ 0.02012.1 \le t \le 2.5\text{s} \end{cases} \quad (10)$$

Figure 4 shows the variation of characteristics of multistage centrifugal pump with start-up time in the process of the closed-valve transition. In order to make the change law of f function clear, the interval of ordinate values in the t-f function in **Figure 4** is interpolated by natural logarithm.

As can be seen from **Figure 4**, when the initial stage of the I-stage closed-valve is $0 \le t \le 0.25$ s, the rotor rotation period is rapidly reduced from 25.2 to 0.169 s, and the head and power are almost unchanged. In this time range, the multistage centrifugal pump has just started, and the fluid is in a static state before starting. Although the impeller starts to rotate to work on the flow, the fluid still maintains its original state characteristics under the action of fluid inertia force. In the II-stage, when the start-up process develops to $0.25 \le t \le 2.1$ s at the end of start-up, the rotor rotation cycle decreases slowly until it tends to decrease linearly, while the head and power increase slowly at the beginning of the closed-valve. With the increase of start-up time, the rotor rotation cycle increases gradually until it tends to increase linearly (Zhang et al., 2019a). Obviously, the change of head and power is closely related to the change of rotor rotation period. Within this time range, with the development of the start-up process of the closed-valve transition, the rotating speed increases, the working force of the fluid increases, the rotating centrifugal force of the fluid increases, the ability to overcome the inertia force of the fluid increases, and the head and power begin to increase linearly. At the $2.1 \le t \le 2.5$ s end of the start-up process of the closed-valve transition, the rotating period of the rotor remains unchanged at 0.0201 s. At the end of the start-up process, the fluid still maintains the state of rotational acceleration, and the head and power will continue to increase in a short time. With the increase of time, the head and power gradually show periodic fluctuations. During the whole start-up process of the closed-valve transition, the fluid has obvious transient flow characteristics.

In order to explore the transient effect of multistage centrifugal pump in the start-up process of the closed-valve transition, the flow field under the steady state of the same speed at the corresponding time is simulated and calculated, and compared with the transient calculation results of the start-up process of the closed-valve transition. Five rotational speeds, 600, 1,200, 1,800, 2,400, and 2,985 r/min are taken here. The corresponding start-up process of the closed-valve transition is 0.42, 0.84, 1.27, 1.69, and 2.1 s, respectively. **Figure 5** is a comparison diagram of the pump characteristics between the start-up process of the closed-valve transition and the steady state of the same speed.

Figure 5 shows that the head and power curves of steady state at the same speed basically coincide with the change trend of head and power curves of the start-up process of the closed-valve transition. It can be shows that the numerical simulation results of the start-up process of the closed-valve transition in this chapter are correct. Within the starting transition time of $0 \leq t \leq 2.1$ s, the corresponding values of power and head in steady state are higher than those in transient state. At the end of the start-up process, the power and head states are basically the same, indicating that the fluid state during the closed-valve process has a certain hysteresis compared to the fluid state at the steady speed. In the start-up process of the closed-valve transition, on the one hand, the acceleration of liquid rotation and water flow leads to the instability of flow state. On the other hand, the flow field is extremely uneven due to the inertia of liquid flow in the start-up process of the closed-valve transition, which all aggravates the hydraulic loss in the passage. As a result, the head and power in the start-up process of the closed-valve transient state are lower than in the steady-state steady state.

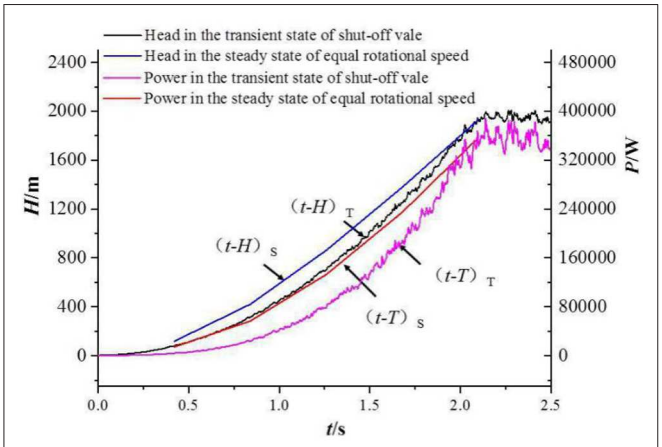

FIGURE 5 | Comparison of the pump characteristics between the start-up process of the closed-valve transition and the steady state of the same speed. Subscript S indicates steady state and subscript T represents transient state.

Contrastive Analysis of Internal Flow Field During the Start-Up Process of the Closed-Valve Transition

This section compares and analyzes the differences in the distribution of the velocity field and pressure field during the closed-valve transitional start-up process by combining the flow at the same speed and steady state at the corresponding moment. The effects of transient effects on internal flow distribution are analyzed. It is used to explore the influence of transient effect on internal flow distribution during the start-up process of the closed-valve transition (Zhang et al., 2019b). Among them, **Figures 6–8** are the velocity distribution diagrams of the first stage impeller during the start-up process of the closed-valve transition and the constant speed steady state of $n = 600$, 1,800, and 2,985 r/min. **Figures 9–11** are the static pressure distribution diagrams of the first stage impeller during the start-up process of the closed-valve transition and the constant speed steady state of $n = 600$, 1,800, and 2,985 r/min.

Comparing the static pressure distribution and speed distribution in the two states, it can be seen that with the increase of the impeller speed, the inlet speed of the first stage impeller gradually increases, and the static pressure in the flow channel also gradually increases. This is because with

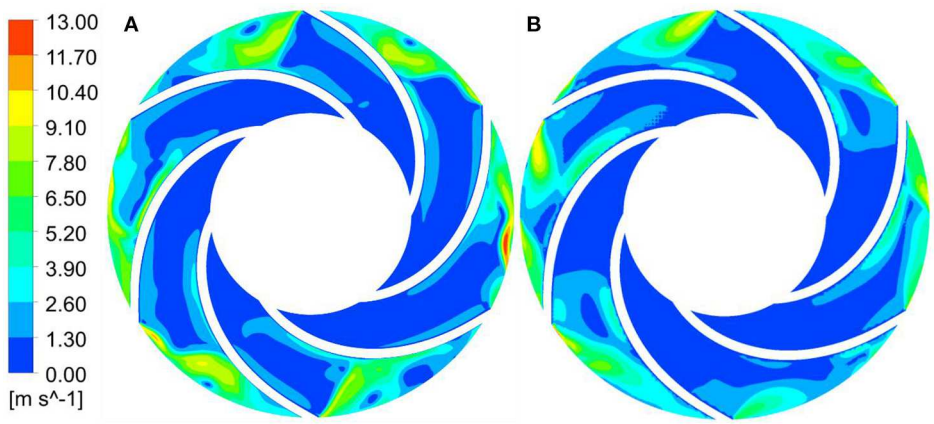

FIGURE 6 | Velocity distribution of the first stage impeller with $n = 600$ r/min. **(A)** Start-up transient of closed-valve and **(B)** steady state at the same speed.

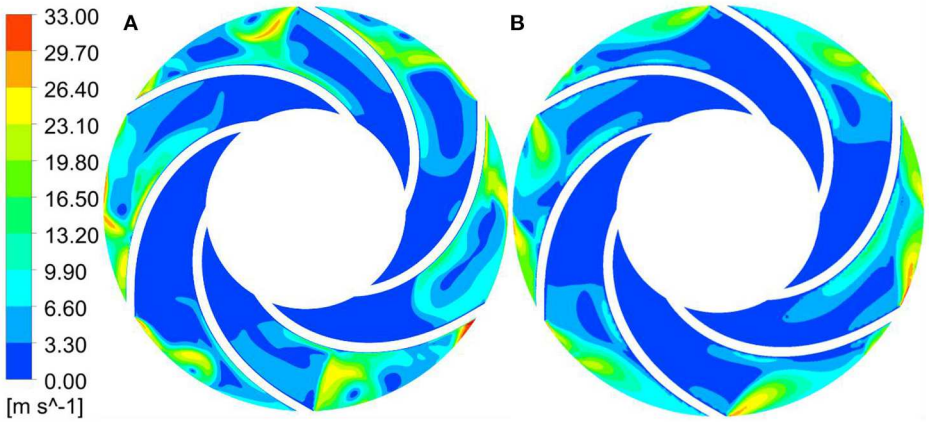

FIGURE 7 | Velocity distribution of the first stage impeller with $n = 1{,}800$ r/min. **(A)** Start-up transient of closed-valve, **(B)** steady state at the same speed.

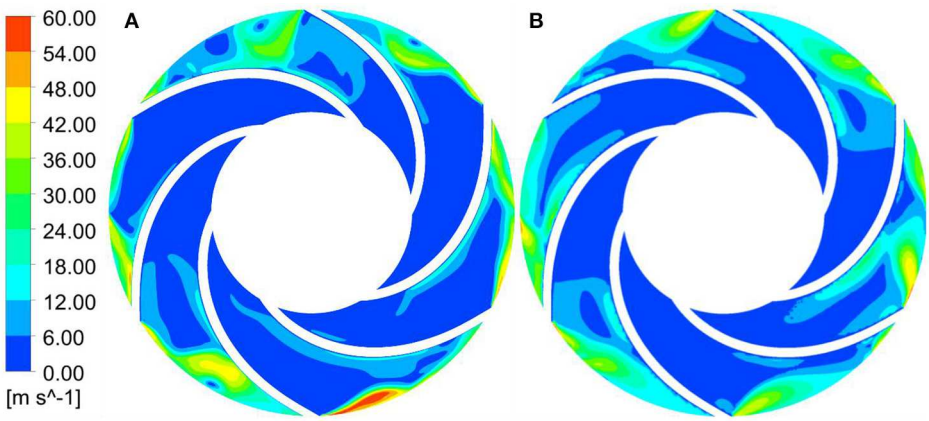

FIGURE 8 | Velocity distribution of the first stage impeller with $n = 2985$ r/min. **(A)** Start-up transient of closed-valve and **(B)** steady state at the same speed.

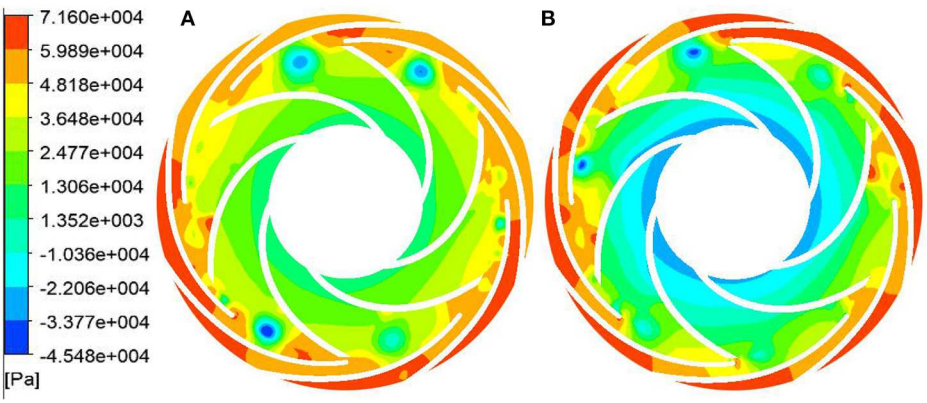

FIGURE 9 | Static pressure distribution of the first stage impeller with $n = 600$ r/min. **(A)** Start-up transient of closed-valve and **(B)** steady state at the same speed.

the increase of time, the speed of the impeller continuously increases, and the functional force for liquids also increases. The total mechanical energy converted into liquid also increases, that is, the dynamic pressure head and the static pressure head are increasing. However, compared with the stable speed starting process at the corresponding moment, the internal

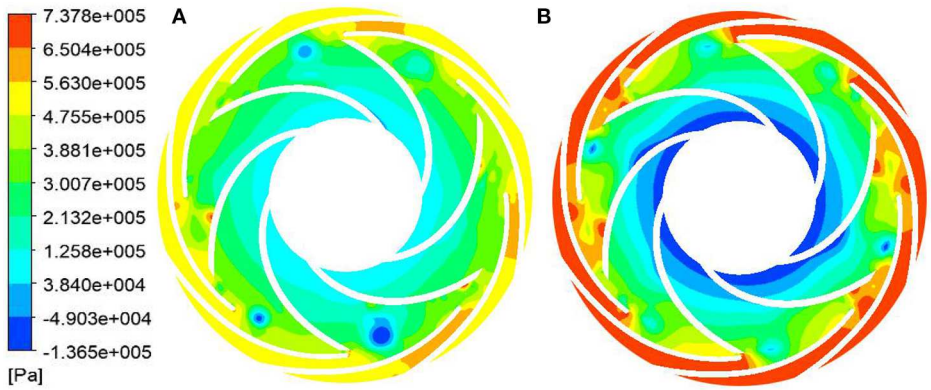

FIGURE 10 | Static pressure distribution of the first stage impeller with $n = 1{,}800$ r/min. **(A)** Start-up transient of closed-valve and **(B)** steady state at the same speed.

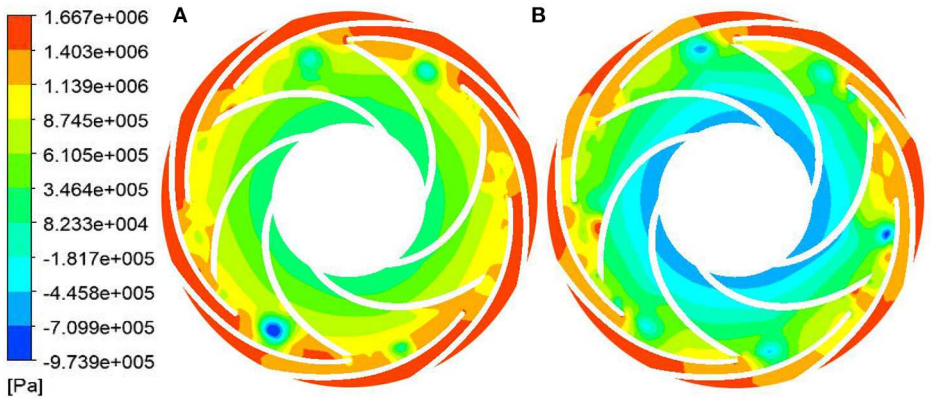

FIGURE 11 | Static pressure distribution of the first stage impeller with $n = 2{,}985$ r/min. **(A)** Start-up transient of closed-valve and **(B)** steady state at the same speed.

speed of the impeller during the transient variable speed starting process is relatively large, and the static pressure of the static pressure in the flow channel is relatively small. This shows that under the condition that the impeller does the same work, the mechanical energy is converted into kinetic energy and the pressure energy is less during the transient variable speed startup process. This is a typical manifestation of transient effects in the transient operation of closed-valve transient starting. This is also consistent with the phenomenon that the transient flow head curve is lower than the flow head curve under the same speed and steady state at the corresponding moment.

During the start-up process of the closed-valve transition, there are a lot of zero velocity regions from the impeller inlet to the middle passage area. The velocity regions with magnitude are mainly accumulated near the back outlet area of the blade, while the distribution at the outlet area of the blade working face is relatively small. The maximum velocity region mainly exists in the middle passage near the impeller outlet. A small amount of liquid is distributed at the outlet of the blade back under the centrifugal force of the impeller. In the start-up process of the closed-valve transition, the zero-speed zone is the dead water zone, which means that there is no flow through the region. If a long time to maintain this state, it will consume a large number of impeller work energy, and make the pump body and fluid in the process of starting heat (Li et al., 2019). Compared with the transient variable speed start-up process of the closed-valve transition, the velocity gradient in the impeller passage during the steady speed start-up process at the corresponding moment is more uniform. And there is no zero velocity zone at the impeller outlet, while there is a scattered zero velocity zone at the impeller outlet during the transient variable speed start-up process. In the static pressure cloud diagram of the start-up process of the closed-valve transition, the static pressure distribution at different moments is similar. And the four main low-pressure vortex zones are at the impeller exit and exhibit a central symmetric distribution. Compared with the stable speed start-up process at corresponding time, the area of low-pressure vortices is larger, the central pressure is lower, the pressure gradient is larger and the number is larger. It shows that the internal flow condition of the start-up process of the closed-valve transient is more turbulent and more complicated than the steady-state steady state at the corresponding moment.

CALCULATION SETTING AND RESULT ANALYSIS OF THE START-UP PROCESS OF THE OPEN-VALVE TRANSITION

Setting Up of Simulating and Calculating Settings for the Start-Up Process of the Open-Valve Transition

The start-up process of the open-valve transition studied is the next stage of the start-up process of the closed-valve transition. During the start-up process of the open-valve transition, the flow rate increases rapidly from zero to the rated flow rate while the impeller maintains the rated speed. Because it is difficult to simulate the transient process of multistage centrifugal pump of the start-up process of the open-valve transition in the laboratory, and the boundary conditions of numerical simulation calculation of the start-up process of the open-valve transition cannot be obtained, Flowmaster and CFX software will be used to simulate the start-up process of the open-valve transitions of multistage centrifugal pump. Firstly, Flowmaster software is used to build the operation model of multistage centrifugal pump, and the outlet flow rate and inlet pressure can be obtained. Secondly, the boundary condition is input through the UDF function in CFX, which can simulate the internal flow condition of multistage centrifugal pump during the open-valve transition. The simulation process steps are: (1) collecting and sorting out component parameters; (2) importing parameters and testing the operation status of components; (3) using Flowmaster for modeling and simulation; (4) importing the boundary condition parameters into CFD simulation software for numerical calculation.

In this paper, Flowmaster software is used to build centrifugal pump operation model. The operation model of centrifugal pump is shown in **Figure 12**. The operation model is mainly composed of circulating pipeline, elbow, centrifugal pump, torque controller, ball valve and water tank. In order to make the simulation process close to the actual situation, the setting parameters of the centrifugal pump come from the actual test measurement of the centrifugal pump. According to the start-up test report of the multistage centrifugal pump, this chapter determines that the time required for the flow rate to change from zero to rated flow rate in the start-up stage of the valve is 3 s, and the total calculation time for the numerical simulation of the whole start-up process of the open-valve transition is 3.8 s.

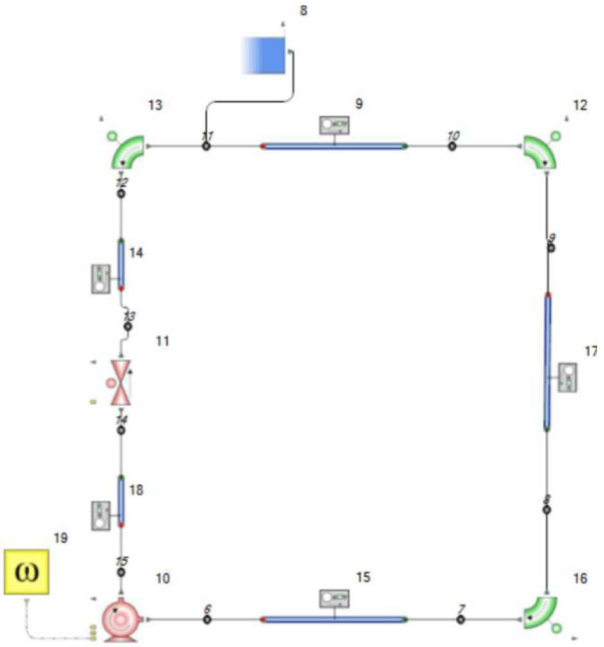

FIGURE 12 | Operation model of multistage centrifugal pump. 8: water tank; 10: centrifugal pump; 11: ball valve; 15, 17, 9, 14, 18: pipeline; 12, 13, 16: elbow; 19: torque controller; others: monitoring nodes.

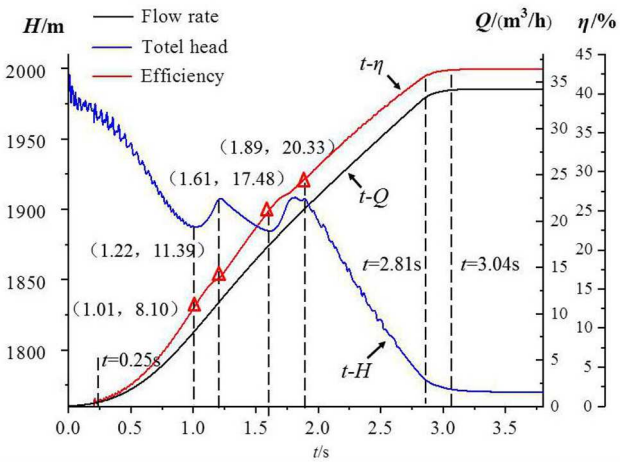

FIGURE 13 | Pump characteristic change of start-up transient state in open-valve stage.

Contrastive Analysis of Pump Characteristics of the Start-Up Process of the Open-Valve Transition

The flow rate of multistage centrifugal pump varies with the start-up time during the start-up process of the open-valve transition. The change trend of pump characteristics with time under the transient start-up state is shown in **Figures 13**. **Figure 14** shows the head changes of different series in the transient state of the start-up process of the open-valve transition. The single-stage head is obtained by calculating the pressure difference corresponding to the inlet of the impeller and the outlet of the guide vane. Due to the excessive number of stages, only the typical levels 1, 2, 3, 7, 8, and 13 are selected for analysis.

As can be seen from **Figure 13**, in the start-up process of the open-valve transition, the flow rate and efficiency changes with the start-up time is similar. In the initial stage of start-up, $0 \leq t \leq 0.25$ s and the final stage of start-up 2.75 s $\leq t \leq$ 3.04 s, the flow rate and efficiency increase smoothly. While in the start-up stage, the flow rate and efficiency increase linearly, and at the beginning of the start-up, the head decreases with the start-up time. When $t = 1.01$ s, the head begins to rise. At $t = 1.22$ s, the first local

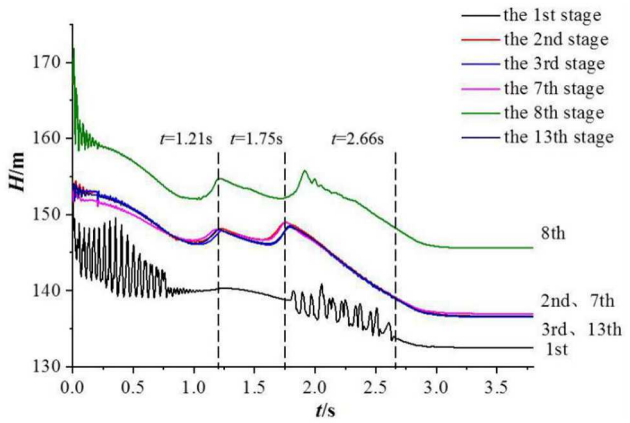

FIGURE 14 | Head change of different stages in transient start-up state during open-valve stage.

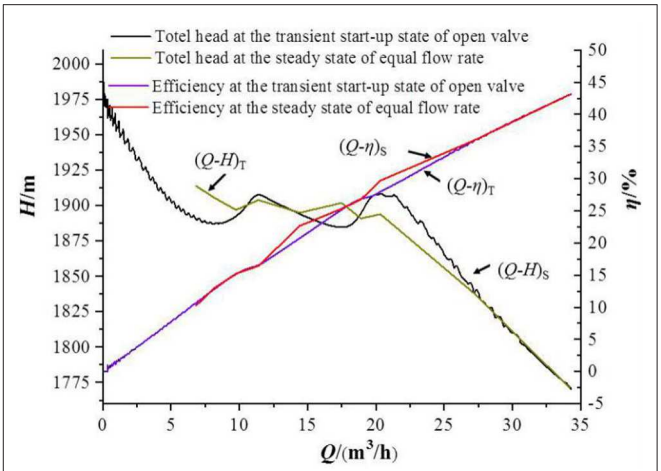

FIGURE 15 | Comparison of outer characteristics of start-up transient state and steady state of equal flow rate in open-valve stage.

maximum value appears, and then the head decreases again. At $t = 1.61$ s, the local minimum value appears, and then the head starts to rise again. Near $t = 1.89$ s, the second local maximum value appears, and the two maximum values are almost equal. Then, as the start-up time increases, the head continues to drop.

As can be seen from **Figure 14**, the difference between the first stage and the other stage is larger than that of other stages. Especially in the two periods of $t \leq 1$ s and $1.75\,\text{s} \leq t \leq 2.66$ s, the fluctuation is intense, and there are fluctuations in different degrees at the beginning of the start-up of other stages. The boundary condition at the inlet is total pressure in the transient numerical simulation of the start-up process of the open-valve transition. This is not fully in line with the actual situation of the start-up process of the open-valve transition, which leads to drastic changes in the static pressure of the inlet, and the difference between the first head and other stages is significant. Except for the first stage, the change trend of the other single-stage head is the same as that of the total head, and there are different degrees of double humps. The time of the first hump appearing in the flow head curve at all levels is about $t = 1.21$ s, but the time of the second hump appearing is different. The second hump time at the 8th level head curve is the latest, and the 8th level single stage head is also the highest.

In order to further analyze the influence of the transient effect on the pump characteristics of the open-state transient state, especially the effect on flow head hump. The pump characteristics under steady state and transient start-up state under the same flow rate are compared. The flow rate here is 6.84, 8.10, 9.75, 11.39, 14.44, 17.48, 18.91, 20.33, 27.20, and 34.20 m^3/h, the corresponding start-up transition time is 0.93, 1.01, 1.11, 1.22, 1.41, 1.61, 1.71, 1.89, 2.35, and 3.10 s. **Figure 15** is a comparison of the pump characteristics of the start-up process of the open-valve transition and the steady state of the same flow rate. In the graph, subscript S denotes steady state, subscript T denotes transient state.

As can be seen from **Figure 15** that in the steady state of the same flow rate and the start-up process of the open-valve transition, when the open-valve transition starts in the middle and late development period $27.20\ m^3/h \leq Q \leq 34.20\ m^3/h$, the flow efficiency curve and the flow head curve are basically the same. When $Q \leq 20.33\ m^3/h$, there are three hump peaks in the flow head curve under the same flow steady state, and the hump fluctuation amplitude is smaller than the hump fluctuation amplitude of the flow head curve under the start-up process of the open-valve transition.

Comparative Analysis of Streamlines Between Blades

In order to explore the influence of transient effect of the start-up process of the open-valve transition on hump, this paper chooses four flow points: maximum and minimum position of hump $Q = 8.10\ m^3/h$, $Q = 11.39\ m^3/h$, $Q = 17.48\ m^3/h$, $Q = 20.33\ m^3/h$. The streamline distribution between the blades of the second stage impeller at different flow points in the same steady flow state and the transient effect of the start-up process of the open-valve transition is compared and analyzed. **Figure 15** shows the streamline distribution between blades with different flow rates in the start-up process of the open-valve transition. **Figure 16** shows the streamline distribution between blades with different flow rates under the steady state of the same flow rate.

Compared with **Figures 16**, **17**, the flow disorder in the impeller passage and stall groups of varying degrees are the main reasons for the hump of the flow head curve, whether in the start-up process of the open-valve transition or in the steady state of the same flow condition. However, the range of stall groups is larger and the number of stall groups is larger in the start-up process of the open-valve transition. For example, stall groups exists not only at the inlet and outlet of impeller, but also in the middle passage at the flow rate of $Q = 17.48\ m^3/h$ and $Q = 20.33\ m^3/h$. In the start-up process of the open-valve transition, the flow inertia of liquid will make the flow rate change out of step with the head change. And the increase of flow velocity will aggravate the rotational stall of impeller internal flow. Therefore, the hump fluctuation amplitude in the start-up process of the

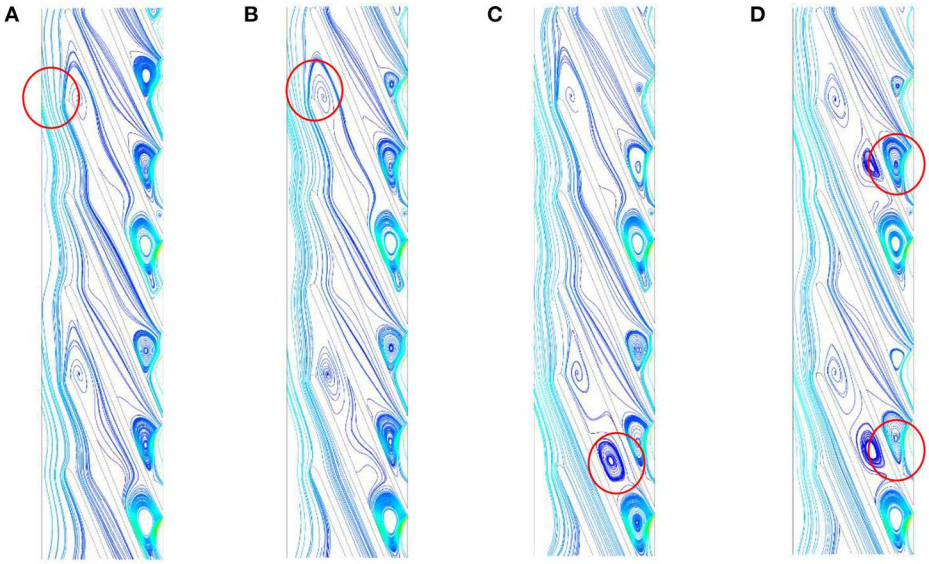

FIGURE 16 | Streamline distribution among blades with different flow rates in the start-up process of the open-valve transient. **(A)** $Q = 8.01$ m^3/h, **(B)** $Q = 11.39$ m^3/h, **(C)** $Q = 17.48$ m^3/h, and **(D)** $Q = 20.33$ m^3/h.

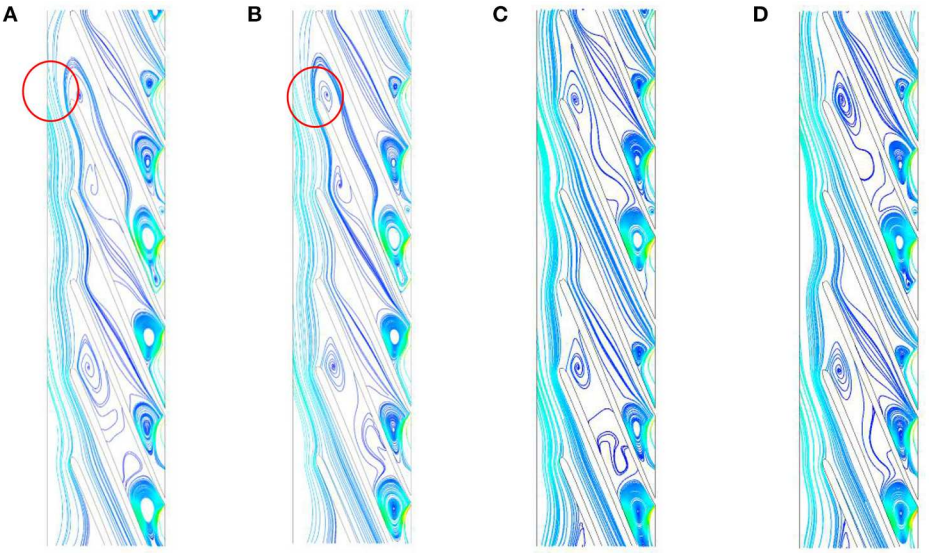

FIGURE 17 | Streamline distribution among blades with different flow rates under steady state of equal flow rate. **(A)** $Q = 8.01$ m^3/h, **(B)** $Q = 11.39$ m^3/h, **(C)** $Q = 17.48$ m^3/h, and **(D)** $Q = 20.33$ m^3/h.

open-valve transition is higher than that in the steady state of the same flow rate.

Analysis of Internal Flow Field in the Start-Up Process of the Open-Valve Transition

In this paper, the secondary (stage 2) impeller is used to analyze the internal flow field changes during the start-up process of the open-valve transition. The static pressure distribution of the impeller of stage 2 under the start-up process of the open-valve transition is shown in **Figure 18**.

As can be seen from **Figure 18**, under the start-up process of the open-valve transition, the average static pressure in the secondary impeller decreases with the increase of start-up time, increasing gradually along the radial direction from the impeller inlet, and the gradient of change becomes more uniform. This is because the impeller does have a certain functional force when the rotational speed is kept constant. With the increase of flow rate, the flow velocity in the impeller passage will also increase.

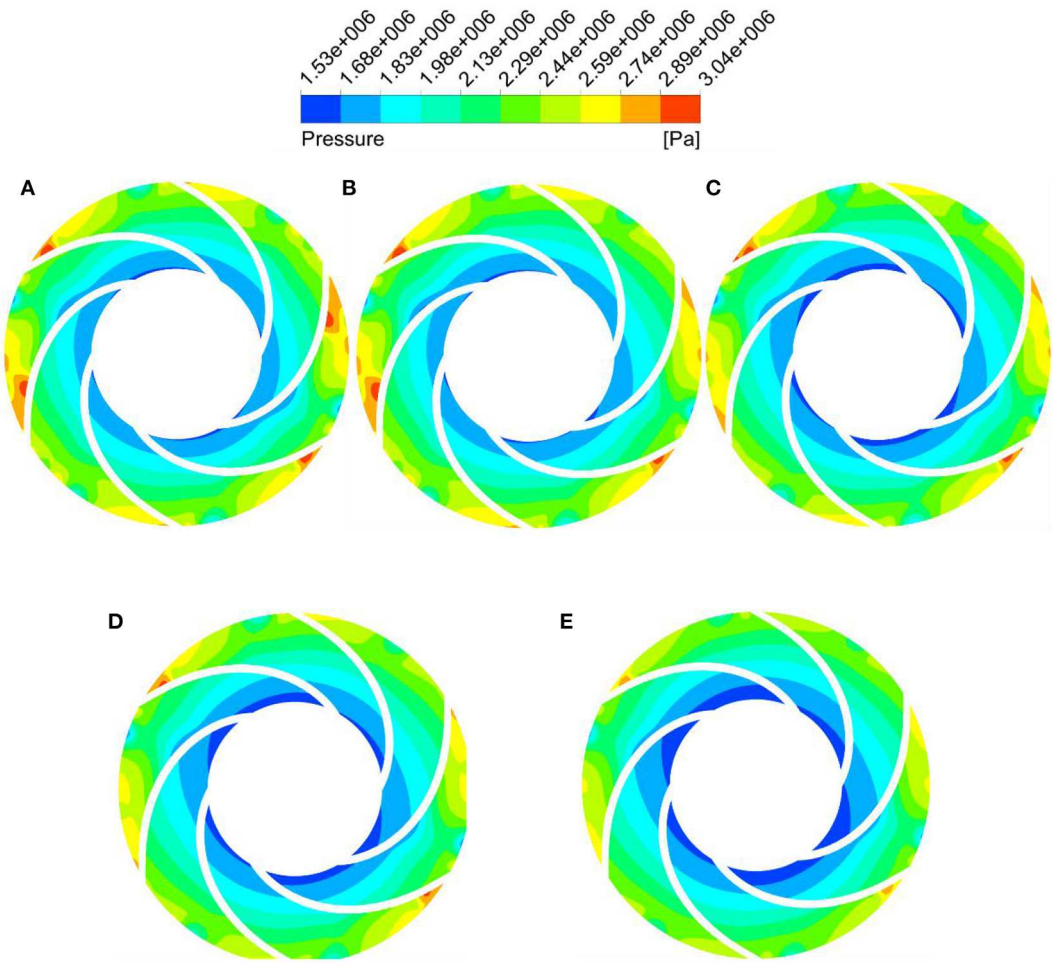

FIGURE 18 | Static state distribution of the second stage impeller in the start-up process of the open-valve transition. **(A)** $t = 0.93$ s, **(B)** $t = 1.36$ s, **(C)** $t = 1.83$ s, **(D)** $t = 2.35$ s, and **(F)** $t = 3.10$ s.

According to the Bernoulli energy conservation equation, the dynamic pressure increases and the static pressure gradually decreases. However, with the liquid flows in the radial direction, the cross-section area of the channel increases gradually, and the static pressure value increases gradually. In the initial stage of the start-up process of the open-valve transition, there are many high-pressure vortices on the back of secondary impeller blade outlet. With the increase of start-up time, the number and scope of high-pressure vortices are gradually decreasing, which indicates that the internal flow tends to be stable with the development of start-up process. This is more evident from the turbulent kinetic energy distribution in the secondary impeller.

Turbulence kinetic energy is a measure of turbulence intensity. Its size and spatial distribution can reflect the scope and magnitude of fluctuating diffusion and viscous dissipation loss in the channel to a certain extent. And it is also an intuitive expression of the stability of internal flow. In this paper, the turbulent kinetic energy during the start-up process of the open-valve transition is analyzed, and the influence of transient flow rate on the stability of the internal flow field is studied.

Figure 19 shows the turbulent kinetic energy distribution of the secondary impeller during the start-up process of the open-valve transition.

It can be seen from **Figure 19** that there is a certain similarity between the magnitude and distribution of the turbulent kinetic energy of the secondary impeller in the start-up process of the open-valve transition. The turbulent energy is the largest at the exit of each flow channel near the impeller, and there is a large pulsation diffusion and viscous dissipation loss, which is symmetrically distributed in the center. As shown in (a), the turbulent energy distribution is shown in the red circle, and a similar turbulent energy distribution appears again after three flow paths. The number of the impeller blades is 6, and the number of radial vane blades is 8, which are not mutually prime. The radial vanes and impellers have periodic dynamic and static interference. The internal flow field at each outlet of the impeller changes drastically, so the turbulent energy is the largest, and the distribution presents a central symmetric distribution. In the early start $0 \leq t \leq 1.83$ s turbulent kinetic energy distribution is small change. In the middle and late stages of start-up 1.83 s

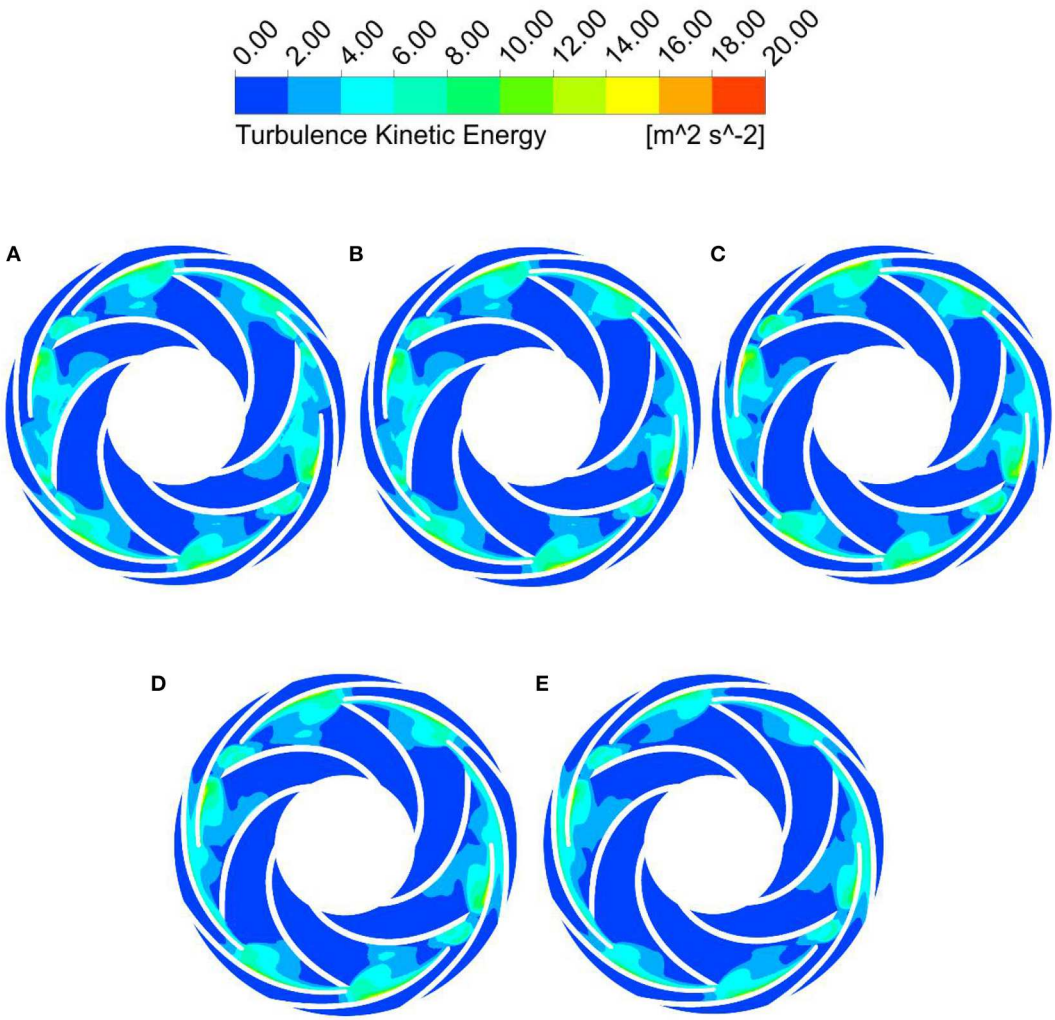

FIGURE 19 | Turbulent energy distribution of the second stage impeller in the start-up process of the open-valve transition. **(A)** $t = 0.93$ s, **(B)** $t = 1.36$ s, **(C)** $t = 1.83$ s, **(D)** $t = 2.35$ s, and **(E)** $t = 3.10$ s.

$\leq t \leq 3.1$ s, the distribution range of turbulent kinetic energy gradually decreases with the development of the start-up process of the open-valve transition. The kinetic energy value is also gradually decreasing, indicating that its internal flow gradually begins to stabilize.

DISCUSSIONS

The two transient processes of the closed-valve transition and the open-valve transition are numerically simulated, and the pump characteristics and the evolution characteristics of the internal flow field are analyzed. During the start-up process of the closed-valve transition, the head, and power curves of the same steady-state are slightly higher than the head and power curves of the start-up process of the closed-valve transition, but the trends in the two states are basically consistent. At the end of the start-up process of the closed-valve transition, the power and head are basically the same in both states, but the transient head will still increase in a short time under the influence of fluid inertia. When the impeller does the same work energy, compared with the steady state of the same speed, in the transient internal flow field of the closed-valve transient start process, the mechanical energy is converted into kinetic energy and the pressure energy is less. The mechanical energy in the internal flow field is converted into more kinetic energy and less pressure energy. This is a typical manifestation of transient effects during the closed-valve transitional start-up process.

Compared with the steady flow state of the same flow rate, in the initial stage of the open-valve transition process, the range of stall groups in the impeller flow channel is larger during the transient process, the number of stall groups is more, During the start-up process of the open-valve transient, there is a certain similarity between the size and distribution of turbulent energy in the flow field inside the impeller. With the development of

the open-valve process, the flow rate gradually increases, internal flows have gradually stabilized.

CONCLUSIONS

In this paper, the start-up process of low specific speed multistage centrifugal pump is divided into two stages: variable speed closed-valve transition and variable flow open-valve transition. The difference of flow characteristics between the variable speed closed-valve transient start-up processes and the steady state of the same speed at the corresponding moment, and difference of flow characteristics between variable flow open-valve transient start-up processes and the steady state of the same flow rate at the corresponding moment are analyzed. The main conclusions are as follows.

(1) According to the theoretical analysis, the centrifugal pump impeller has transient effects caused by two kinds of additional heads, a rotational acceleration head and a flow inertia head during the pump-start transient operation.
(2) During the start-up process of the closed-valve transition, the variation trend of the pump characteristic with time is highly correlated with the variation trend of the rotor rotation period f with time. During the development period of the start-up process of the closed-valve transition, the head and power curves of the same steady state are slightly higher than the head and power curves of the start-up process of the closed-valve transition. But the variation trend in the two states are basically consistent, and the start-up process of the closed-valve transition is instantaneous. And the state of fluid flow during the start-up process has a certain hysteresis. At the end of the start-up process of the closed-valve transition, the power and head are basically the same in both states, but the transient head will still increase in a short time under the influence of flow inertia, and there is an impact head.
(3) It is found that when the impeller does the same work, compared with the steady state at the same speed, the mechanical energy in the internal flow field is converted into more kinetic energy and less pressure, which is a typical performance of the transient effect during the start-up process of the closed-valve transition.
(4) Compared with the steady state of the same flow rate, in the initial stage of the start-up process of the open-valve transition, the range of stall group in the impeller flow channel is larger. During the transient process, the number of stall groups is more, which exacerbates the rotational stall of the internal flow of the impeller and the flow is more disordered. This results in a hump fluctuation amplitude is greater than it in the steady state of the same flow rate. During the middle and later process of the open-valve transition, the changes of the flow efficiency curve and the flow head curve are basically consistent. There is a maximum value of the radial force in the time range of the hump in the initial stage of the start-up stage.
(5) During the start-up process of the open-valve transient, there is a certain similarity between the size and distribution of turbulent energy in the flow field inside the impeller. The turbulent energy has a central symmetric distribution in each flow channel, and the turbulent energy is the largest near the impeller exit, and there is a large pulsation diffusion and viscous dissipation loss. With the development of the open-valve process, the flow rate gradually increases, the distribution range of turbulent energy is gradually reduced and the internal flow tends to become stable.

DATA AVAILABILITY STATEMENT

The raw data supporting the conclusions of this article will be made available by the authors, without undue reservation, to any qualified researcher.

AUTHOR CONTRIBUTIONS

LY: investigation, visualization, conceptualization, methodology, and software. LB: writing—reviewing and editing. FJ: data curation and writing—original draft preparation. ZR: supervision, methodology, and investigation. FQ: software and validation.

FUNDING

This work was funded by the China Postdoctoral Science Foundation Funded Project (Grant No. 2019M651734), National Youth Natural Science Foundation of China (Grant No. 51906085), Jiangsu Province Innovation and Entrepreneurship Doctor Project (2019), Zhejiang Postdoctoral Project (2019). This work was also supported by Key R&D programs of Jiangsu Province of China (BE2018112) and National Key R&D Program of China (2018YFB0606105).

REFERENCES

Li, D., Qin, Y., Zuo, Z., Wang, H., Liu, S., and Wei, X. (2019). Numerical simulation on pump transient characteristic in a model pump turbine. *J. Fluids Eng. Trans. ASME* 141:111101. doi: 10.1115/1.4043496

Li, W. (2012). Experimental Study and Numerical Simulation on Transient Characteristics of Mixed-Flow Pump during Starting Period. Zhenjiang: Jiangsu University.

Li, Z. (2009). *Numerical Simulation and Experimental Study on the Transient Flow in Centrifugal Pump during Starting Period.* Hangzhou: Zhejiang University. doi: 10.1115/1.4002056

Li, Z., Wu, D., Wang, L., Dai, W., Chen, F. (2010). Experiment on instantaneous characteristics in centrifugal pump during startup period. *J. Drain. Irrig. Machin. Eng.* 28, 389–393.

Liu, H., Zhou, X., Wang, K., Mao, L.. (2014). Analysis on pressure fluctuation of radial diffusers in a multistage centrifugal pump. *J. Central South Univ.* 45, 3295–3300.

Ping, S., Wu, D., Wang, L. (2007). Transient effect analysis of centrifugal pump during rapid starting period. *J. Zhejiang Univ.* 814–817.

Shao, C. (2016). *Research on Characteristics of Super-Low Specific Speed Centrifugal Pumps during Transient Period*. Zhenjiang: Jiangsu University.

Thanapandi, P., and Prasad, R. (1995). Centrifugal pump transient characteristics and analysis using the method of characteristics. *Int. J. Mechan. Sci.* 37, 77–89. doi: 10.1016/0020-7403(95)93054-A

Tsukamoto, H., and Ohashi, H. (1982). Transient characteristics of a centrifugal pump during starting stage. *ASME J. Fluids Eng.* 104, 6–13. doi: 10.1115/1.3240859

Tsukamoto, H., Yoneda, H., and Sagara, K. (1995). The response of a centrifugal pump to fluctuating rotational speed. *ASME J. Fluids Eng.* 117, 479–484. doi: 10.1115/1.2817287

Wang, Y., Chen, J., Liu, H., Shao, C., Zhang, X. (2017). Transient characteristics analysis of ultra-low specific-speed centrifugal pumps during start-up period under shut-off condition. *Trans. Chin. Soc. Agric. Eng.* 33, 76–82. doi: 10.11975/j.issn.1002-6819.2017.11.009

Wu, D., Xu, B., Li, Z., Wang, L.-Q. (2009). Numerical simulation on internal flow of centrifugal pump during transient operation. *J. Eng. Thermophys.* 30, 781–783.

Xu, B., Li, Z., Wu, D., et al. (2010). Numerical simulation on transient turbulent flow in centrifugal pump during starting period. *Chin. Sci. Technol.* 5, 683–687.

Zhang, D., Pei, Y., Wang, J., et al. (2012). Numerical simulation of the impeller-guide vane interaction flow field in multistage centrifugal pump. *Petrol. Mach.* 93–97.

Zhang, N., Liu, X., Gao, B., Wang, X., and Xia, B. (2019b). Effects of modifying the blade trailing edge profile on unsteady pressure pulsations and flow structures in a centrifugal pump. *Int. J. Heat Fluid Flow* 75, 227–238. doi: 10.1016/j.ijheatfluidflow.2019.01.009

Zhang, N., Liu, X., Gao, B., and Xia, B. (2019a). DDES analysis of the unsteady wake flow and its evolution of a centrifugal pump. *Renew. Energy* 141, 570–582. doi: 10.1016/j.renene.2019.04.023

Zhang, Y. (2013). *Transient Internal Flow and Performance of Centrifugal Pumps during Startup Period*. Hangzhou: Zhejiang University.

Conflict of Interest: The authors declare that the research was conducted in the absence of any commercial or financial relationships that could be construed as a potential conflict of interest.

frontiers in Energy Research

ORIGINAL RESEARCH
published: 28 May 2020
doi: 10.3389/fenrg.2020.00080

Numerical Study on the Corium Pool Heat Transfer With OpenFOAM

Zhiguo Xi[1], Yuwen Hu[2], Houjun Gong[2], Luteng Zhang[1,3]*, Zaiyong Ma[1], Wan Sun[1], Shanshan Bu[1,3] and Liangming Pan[1]*

[1] Key Laboratory of Low-Grade Energy Utilization Technologies and Systems (Chongqing University), Ministry of Education, Chongqing, China, [2] CNNC Key Laboratory on Nuclear Reactor Thermal Hydraulics Technology, Nuclear Power Institute of China, Chengdu, China, [3] Postdoctoral Station of Power Engineering and Engineering Thermophysics, Chongqing University, Chongqing, China

In order to ensure the successful implementation of in-vessel retention strategy to terminate molten corium pool evolution, it is necessary to evaluate the heat flux distribution on the lower head wall of reactor pressure vessel. In the present study, the models of internal heating and natural convention buoyancy, as well as the models of WMLES turbulence and phase changing, were applied in the open source CFD software OpenFOAM to perform numerical simulations for the COPRA single-layer molten pool experiment. The distributions of temperature, heat flux, and crust thickness were obtained. The simulation results were in good comparison with COPRA experimental data, proving the validity of the developed model for corium pool heat transfer characteristics. The simulation method and results could be applied to further in-depth study of thermal behavior in the corium pool.

Keywords: in-vessel retention, heat transfer, large-eddy simulation, solidification, OpenFOAM

OPEN ACCESS

Edited by:
Wenxi TIAN,
Xi'an Jiaotong University, China

Reviewed by:
Xiaoyang Gaus-liu,
Karlsruhe Institute of Technology (KIT), Germany
Yapei Zhang,
Xi'an Jiaotong University, China

***Correspondence:**
Houjun Gong
ghjtsing@126.com
Luteng Zhang
ltzhang@cqu.edu.cn

Specialty section:
This article was submitted to Nuclear Energy, a section of the journal Frontiers in Energy Research

Received: *07 February 2020*
Accepted: *17 April 2020*
Published: *28 May 2020*

Citation:
Xi Z, Hu Y, Gong H, Zhang L, Ma Z, Sun W, Bu S and Pan L (2020) Numerical Study on the Corium Pool Heat Transfer With OpenFOAM. Front. Energy Res. 8:80. doi: 10.3389/fenrg.2020.00080

INTRODUCTION

The nuclear reactor core may melt into high-temperature corium and then relocate into the reactor pressure vessel's lower plenum, where the molten material may form a corium pool after a severe reactor accident occurred. In-Vessel Retention (IVR) has been proposed to prevent the deterioration of the severe nuclear accident. The decay heat generated in the corium pool in the lower plenum can be removed by cooling water outside the reactor vessel. The thermal load distributions along the lower head wall were determined by the natural convection heat transfer characteristics inside the corium melt pool, which imposed great significance for ensuring the successful implementation of IVR strategy (Heofanous et al., 1996).

The main components of the relocated corium were non-eutectic mixtures in compositions of metal and metal oxides from fuel rods and brackets. In the early stages of corium pool formation, the lower oxidation fraction may lead to the stratification of melt layers. However, in the late stages, with increasing dissolved oxygen in the corium, the melt pool was in a homogeneous configuration of ceramic mixture according to the Zr-U phase diagram (Asmolov et al., 2004). Therefore, the simulation of homogenous pool remained an important issue with the solidification character of non-eutectic melt (Gaus-Liu and Miassoedov, 2014).

Heat transfer characteristics of melt in the reactor's lower head were studied experimentally and numerically in past years. The main purpose of these studies was to understand the fundamental behavior of the melt pool inside the reactor vessel (Zhang Y. et al., 2015). These experiments have been simplified due to the complexity of the actual molten pool and the experimental cost. The facilities can be divided into three categories based on the geometry: quarter-circular slice,

semi-circular slice, and hemispherical pool (Zhang L. et al., 2015). Famous experiments such as BALI (Bonnet and Seiler, 1999), COPO (Kymäläinen et al., 1992), SIMECO (Sehgal et al., 1999), and COPRA (Zhang Y. et al., 2016) have provided important data of heat transfer characteristics based on different boundary conditions.

The key points of experiment simulation were the modeling of appropriate turbulence models and solidification models. Horvat and Mavko (2004) performed the simulation of UCLA's experiment (Asfia and Dhir, 1996) using the SST turbulence model and good comparisons were obtained. Dinh and Nourgaliev (1997) pointed out that the k-ε turbulence model could not represent the thermal distributions accurately in the cases with high Rayleigh number turbulence. Fukasawa et al. (2008) compared the turbulence models of the k-ε and large eddy simulation based on the BALI experiment (Bonnet and Seiler, 1999). The results showed that the LES method was capable of describing flow physics and heat transfer characteristics. Tran et al. (Tran et al., 2010) indicated that the implicit LES worked quite well in predicting natural convection heat transfer for strong turbulent pools. Tran and Dinh (2009) developed a phase-change effective convection model (PECM) to simulate the heat transfer characteristics inside molten pool. However, this method failed to analyze the inner temperature and flow field. Zhang et al. (2014) developed the 2D numerical model based on the SIMPLE algorithm and modified k-ε model for the simulation of the partial solidification process with diffusive convection.

In this paper, the simulation work based on LES turbulence model and solidification model was performed for the COPRA experiments in the platform of OpenFOAM. The distributions of thermal parameters were obtained and compared to validate the simulation model.

SOLIDIFICATION MODEL

There were two numerical methods for dealing with phase-change problems. The dynamic mesh technique was able to track the evolution of interfaces but was also computation consuming. Therefore, a traditional grid technology was chosen with theoretical and empirical formula to analyze the process of phase changing. For the melt pool with natural convection and solidification, the governing equations can be established based on the assumption of incompressible fluid.

Mass equation:

$$\frac{\partial \rho}{\partial t} + \nabla \cdot (\rho u) = 0 \tag{1}$$

Momentum equation:

$$\frac{\partial \rho u}{\partial t} + \nabla \cdot (\rho u u) = \nabla^2 \left(\mu_{eff} u\right) - \nabla p + S_b + S_m \tag{2}$$

$$S_b = \rho g \left\{1 - \max\left[\beta \left(T - T_s\right), 0\right]\right\} \tag{3}$$

Abbreviations: CFD, Computational Fluid Dynamics; LES, Large Eddy Simulation; IVR, In-Vessel Retention; OpenFOAM, Open Field Operation and Manipulation; WMLES, Wall-Modeled LES model.

where μ_{eff} is the effective dynamic viscosity; S_b is the buoyancy force related to density ρ; β is the thermal expansion coefficient; T_s is the solidus temperature; S_m is the Darcy source term in the mushy region with similar flow resistance of porous medium.

Enthalpy energy equation:

$$\frac{\partial \left(\rho h\right)}{\partial t} + \cdot\left(\rho u h\right) = \nabla \cdot \left(\lambda_{eff} \nabla T\right) + Q \tag{4}$$

where λ_{eff} is the effective thermal conductivity and Q is the inner heating density.

The solidification will occur if the temperature is lower than the solidus temperature. The enthalpy-porosity model proposed by Voller and Prakash (1987) was used to describe the solidification process inside the molten pool. The Darcy term of the momentum equation was derived from Darcy's law (Darcy, 1856) in equation as follows:

$$u = -\frac{K}{\mu} \nabla p \tag{5}$$

where K is the permeability and μ is the fluid viscosity.

Due to the non-eutectic characteristics for corium simulant, there existed a mushy zone in front of the curst interface with both solid and liquid phases. It was assumed that the mushy zone was generally characterized with dendrites, which can be treated as porous medium (Flemings, 1974). Then the Darcy equation was obtained as:

$$K = \frac{\phi^3}{C\left(1 - \phi^2\right)} \tag{6}$$

$$\nabla p = -C \frac{\mu \left(1 - \phi\right)^2}{\phi^3} u \tag{7}$$

The Darcy source term in momentum equation was formulated as:

$$S_m = -C \frac{(1 - \phi)^2}{\phi^3 + \varepsilon} u \tag{8}$$

where Φ is the liquid fraction; C is the mushy zone constant depending on the morphology of the porous media and recommended here as 1.6×10^3 kg/(s·m^{-3}) (Voller and Prakash, 1987); ε is a minimum value of 0.001 to prevent the error of division by zero. The porosity in mushy zone was considered as a function of temperature and was expressed in form of error function as (Rösler and Brüggemann, 2011):

$$\phi = 0.5 erf \left[\frac{4\left(T - T_m\right)}{T_l - T_s}\right] + 0.5 \tag{9}$$

where T_l and T_m are the liquidus temperature and average temperature of the mushy zone respectively.

Both sensible heat and latent heat of fusion were included in the enthalpy energy equation:

$$h = c_p T + \Delta h \tag{10}$$

$$\Delta h = \begin{cases} L_h & T \geq T_l \\ \phi \cdot L_h & T_l \geq T \geq T_s \\ 0 & T < T_s \end{cases} \tag{11}$$

where L_h is the latent heat of fusion. Then the enthalpy energy equation was rewritten into:

$$\frac{\partial\left(\rho c_p T\right)}{\partial t}+\nabla\cdot\left(\rho c_p u T\right)=\nabla\cdot\left(\lambda_{eff}\nabla T\right)+S_h+Q \quad (12)$$

$$S_h=-L_h\left[\frac{\partial\left(\rho\phi\right)}{\partial t}+div\left(\rho u\phi\right)\right] \quad (13)$$

$$S_h=-\rho L_h\frac{4\exp\left[\frac{4(T-T_m)}{T_l-T_s}\right]}{\left(T_l-T_s\right)\sqrt{\pi}}\left(\frac{\partial T}{\partial t}+u\nabla t\right) \quad (14)$$

Incorporating the models of internal heating and natural convention buoyancy, as well as the models of WMLES turbulence and phase changing into solvers in the open source platform of OpenFOAM, the numerical work was performed for the COPRA single-layer corium pool experiments with strong turbulence.

SIMULATION METHOD

The COPRA single-layer corium pool facility was a two-dimensional 1/4 circular slice vessel to simulate the Chinese advanced PWR reactor lower head at full scale. The inner radius of the vessel was 2.2 m and the height was 1.9 m. The curved vessel (30 mm thickness) was enclosed from outside with the cooling path and the vessel's top surface was adiabatic. The molten salt of $NaNO_3$-KNO_3 (in mole fraction) compositions was applied as test material. The selected mixture of 20% to 80% has the maximum temperature difference of 60 K between solidus and liquidus line. Dinh et al. (2000) pointed out that the binary mixture of $NaNO_3$-KNO_3 has similar characteristics in phase diagrams compared to the real melt. The internal Rayleigh number could reach up to 10^{14}-10^{16} in COPRA melt pool (Zhang Y. et al., 2016).

Before performing the numerical simulation, some basic assumptions need to be done. The melt was an incompressible Newtonian fluid and the volumetric heat source in the pool was homogenously distributed. The Boussinesq hypothesis was employed, except for the density in the buoyancy term in momentum equation. Other properties are all treated as constants. The geometry of the mesh was the same as the COPRA melt pool with pool height of 1.9 m. The mesh setup was shown in **Figure 1**. The grid independence was verified by comparisons with 1.2, 1.35, and 1.4 million mesh. The simulation results from 1.35 million were selected with good enough results considering calculation effectiveness. The mesh encryption was performed in the regions near the inner wall with a minimum of 0.6 mm to better interpret the solidification process.

The internal heating density was set to be 10,500 W/m^3 estimated from test data. The initial temperature of the molten pool was set as 600 K and the isothermal boundary of 303.15 K was adopted on the outside curved wall surface. The upper surface of the molten pool was set as radiative with emissivity of 0.44. The other vertical boundary conditions were all set as adiabatic. The transient simulation was required for the large eddy simulation method but only steady results were compared with experimental data.

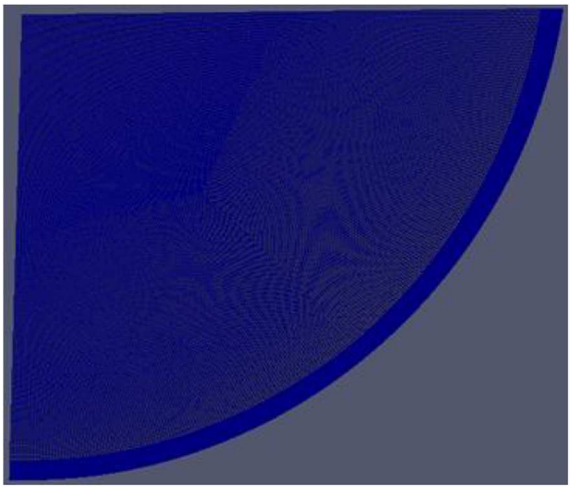

FIGURE 1 | Mesh setup of the COPRA.

TABLE 1 | Main properties of COPRA experiment.

Property	Value
Q_v/W·m^{-3}	10,500
T_{liq}/K	557
T_{sol}/K	497
ρ/kg·m^{-3}	1,914
c_p/J·kg^{-1}·K^{-1}	1,328
λ_l/W·m^{-1}·K^{-1}	0.44
λ_s/W·m^{-1}·K^{-1}	1.575
λ_{wall}/W·m^{-1}·K^{-1}	2.304
ν/m^2·s^{-1}	1.73×10^{-6}
β/K^{-1}	3.81×10^{-4}
h_s/kJ·kg^{-1}	161.96

Some physical property parameters for the COPRA salt simulant were listed in **Table 1** (Zhang L. T. et al., 2016). It should be noted that the thermal conductivity of the curved wall was modified to consider the additional thermal resistance introduced by the 0.3 mm air gap between the crust and the curved wall.

RESULTS AND DISCUSSION

The temperatures along pool height in steady state were extracted to compare with experimental data in **Figure 2**. It can be seen that the temperature increasing rate was relatively rapid within a distance of 200 mm above the pool bottom. The weak turbulence flow and thick crust formation was predicted in the bottom region, leading to larger temperature gradient. With pool height increasing, the rate of temperature increase slowed down and temperature distribution tended to be flat. Overall, the trend

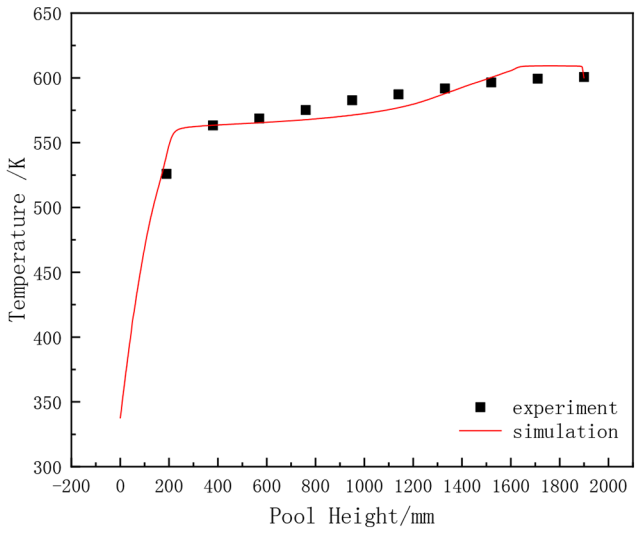

FIGURE 2 | Comparison of experimental and simulated temperature distribution.

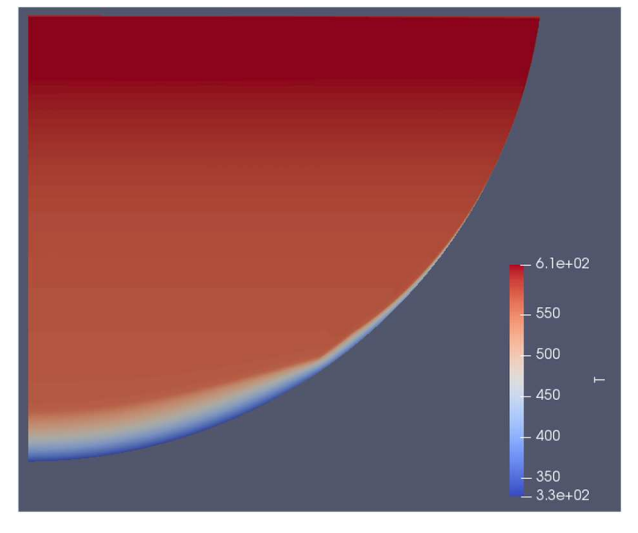

FIGURE 3 | Temperature distribution in the corium pool.

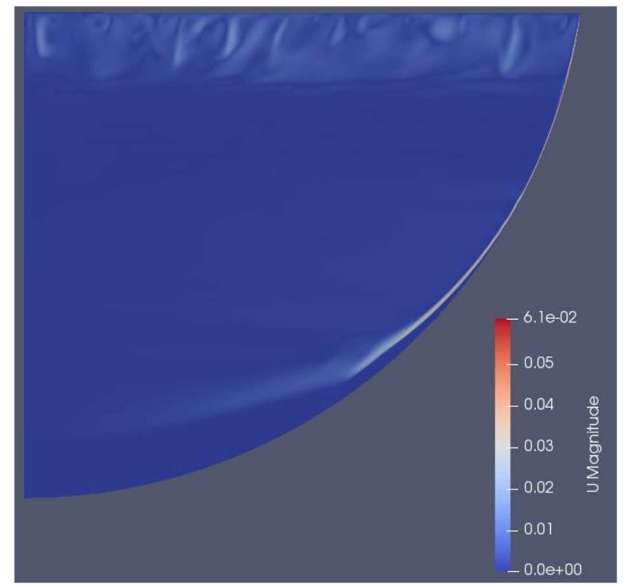

FIGURE 4 | Velocity distribution in the corium pool.

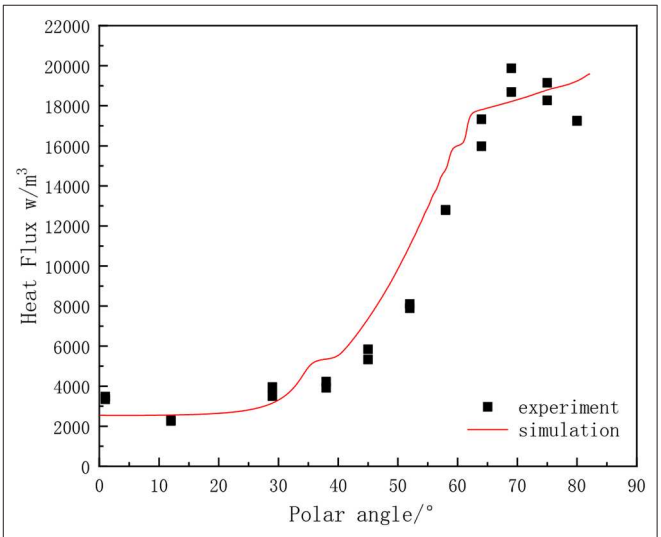

FIGURE 5 | Comparison of experimental and simulated heat flux distribution.

of temperature distribution agreed well with the experimental results in the full height regions.

The temperature and velocity distribution in the corium pool from the simulation were presented in **Figures 3**, **4** respectively. The results clearly illustrated the temperature stratification across the pool region with increasing temperature in the top region. The lower temperatures at the bottom represented the solidified crust along the curved wall. Similarly, the velocity reflecting the turbulence intensity was also higher near the top and side boundaries due to radiation loss and direct cooling. The natural convection inside the corium pool driven by the internal heating gradually transferred heat and energy toward the top region and cooling boundary to achieve its final thermal balance.

The heat flux distribution of the curved wall with the polar angle was compared in **Figure 5**. The results showed that the heat fluxes from the simulation and experiments were in good comparison at all regions except for the top part. The heat flux decreased near the top surface from experiment because of obvious thermal loss. The calculated heat flux didn't represent this thermal reduction.

When the molten pool solidifies, the crust was formed on the inner wall surface to effectively reduce the heat flux, which was beneficial to the realization of IVR. The calculated crust thickness and experimental data were compared in **Figure 6** below 60°. It was shown that the crust thickness was decreasing

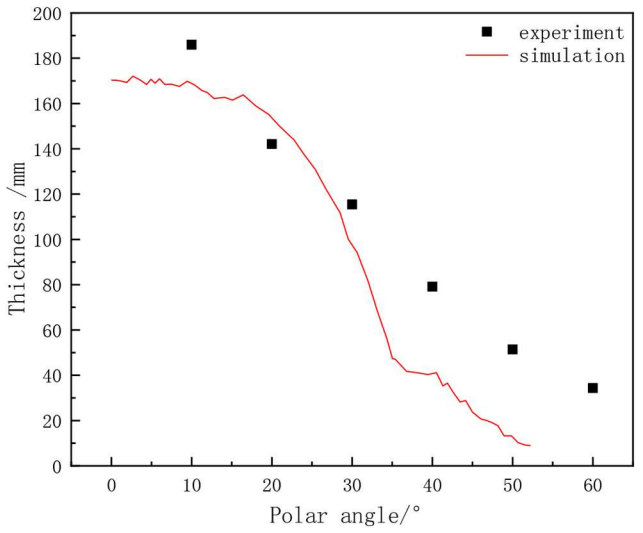

FIGURE 6 | Comparison of experimental and simulated thickness.

with increasing angle, which was in opposite trend of heat flux. It indicated that the simulated crust thickness was obviously lower than the experimental results at polar angles greater than 40°. In addition, the crust thickness from simulation nearly disappeared over 60°, resulting in the heat flux continuously increasing. This phenomenon may result from the arrangement of bottom heating rods without enough heating generated near the curved wall in COPRA experiment. The completely homogenous heating from the simulation resulted in little existing crust in the upper region with strong turbulence and higher heat fluxes.

CONCLUSIONS

In order to understand the natural convection heat transfer characteristics of the molten pool under the high Rayleigh number, the models of internal heating and natural convention buoyancy, as well as the models of WMLES turbulence and solidification, were applied in the open source CFD software OpenFOAM to perform numerical simulations for the COPRA single-layer molten pool experiment.

The temperature distributions along pool height and the heat flux distributions along curved wall were all in good comparisons with experimental results. The temperature and velocity distributions across the pool region were obtained to clearly demonstrate the thermal stratification due to natural convection. The calculated thickness distribution of the crust differs over polar angle of 60° because the internal heating in experiment was not homogenous near wall. Different from the previous simple model of solidification, the present solidification model is specially treated with Darcy source term in this paper. The overall simulation results reasonably reflected the heat transfer characteristics of the molten pool, proving the validity of the developed model for corium pool thermal behavior. The simulation method and results could be applied to further in-depth study of thermal behavior in the corium pool.

DATA AVAILABILITY STATEMENT

The raw data supporting the conclusions of this article will be made available by the authors, without undue reservation, to any qualified researcher.

AUTHOR CONTRIBUTIONS

For the enclosed manuscript entitled Numerical study on the corium pool heat transfer with OpenFOAM. The author contributions are listed as follows: ZX contributed the simulation work and also contributed the original writing and revision. HG and YH contributed conceptions. LZ provided experimental data and contributed constructive discussions. ZM, WS, and SB contributed review and suggestions. LP contributed the supervision of the study.

FUNDING

This work is financially supported by the National Natural Science Foundation of China (Grant Nos. 11705188 and 11805026) and the China Postdoctoral Science Foundation funded project (Grant No. 2019T120811).

REFERENCES

Asfia, F. J., and Dhir, V. K. (1996). An experimental study of natural convection in a volumetrically heated spherical pool bounded on top with a rigid wall. *Nucl. Eng. Des.* 163, 333–348. doi: 10.1016/0029-5493(96)01215-0

Asmolov, V. G., Bechta, S. V., Khabensky, V. B., Gusarov, V. V., Vishnevsky, V. Y., Kotova, S. Y., et al. (2004). "Partitioning of U, Zr and Fe between molten oxidic and metallic corium," in *Proceeding of MASCA Seminar* (Aix-en-Provence), 1–13.

Bonnet, J. M., and Seiler, J. M. (1999). "Thermal hydraulic phenomena in corium pools: the bali experiment," *in the 7th International Conference on Nuclear Engineering (ICONE-7)* (Tokyo: ASME).

Darcy, H. (1856). *Les Fontaines Publiques De la ville De Dijon* (Paris: Victor Dalmont).

Dinh, T. N., Konovalikhin, M. J., and Sehgal, B. R. (2000). Core melt spreading on a reactor containment floor. *Prog. Nucl. Energy* 36, 405–468. doi: 10.1016/S0149-1970(00)00088-3

Dinh, T. N., and Nourgaliev, R. R. (1997). Turbulence modelling for large volumetrically heated liquid pools. *Nucl. Eng. Des.* 169, 131–150 doi: 10.1016/S0029-5493(96)01281-2

Flemings, M. C. (1974). Solidification Processing. *Metall. Trans.* 5, 2121–2134. doi: 10.1007/BF02643923

Fukasawa, M., Hayakawa, S., and Saito, M. (2008). Thermal-hydraulic analysis for inversely stratified molten corium in lower vessel. *J. Nucl. Sci. Technol.* 45, 873–888. doi: 10.1080/18811248.2008.9711489

Gaus-Liu, X., and Miassoedov, A. (2014). "Live experimental results of melt pool behaviour in the pwr lower head with insulated upper lid and external cooling," in *Proceedings of the 21st International Conference on Nuclear Engineering 2013* (Chengdu: ASME). doi: 10.1115/ICONE21-15204

Heofanous, T. G., Liu, C., Additon, S., Angelini, S., Kymäläinen, O., and Salmassi, T. (1996). *In-vessel Coolability and Retention of Core Melt*. 1:DOE/ID-10460. doi: 10.2172/491623

Horvat, A., and Mavko, B. (2004). "Numerical investigation of natural convection heat transfer in volumetrically heated spherical segments," in *Conference of Nuclear Energy for New Europe* (Portorož).

Kymäläinen, O., Tuomisto, H., and Theofanous, T. G. (1992). "Critical heat flux on thick walls of large, naturally convecting loops," in *ANS Proc 1992 National Heat Transfer Conference* (San Diego, CA: HTD) 6, 44–50.

Rösler, F., and Brüggemann, D. (2011). Shell- and- tube type latent heat thermal energy storage: Numerical analysis and comparison with experiments. *Heat Mass Transfer* 47, 1 027–1 033. doi: 10.1007/s00231-011-0866-9

Sehgal, B. R., Nourgaliev, R. R., Dinh, T. N., Karbojian, A., Green, J. A., and Bui, V. A. (1999). "FOREVER experiments on thermal and mechanical behavior of a reactor pressure vessel during a severe accident," in *Conference: Workshop on In-Vessel Core Debris Retention and Coolability* (Garching).

Tran, C. T., and Dinh, T.-N. (2009). The effective convectivity model for simulation of melt pool heat transfer in a light water reactor pressure vessel lower head. Part II: model assessment and application. *Prog. Nucl. Energy* 51, 860–871. doi: 10.1016/j.pnucene.2009.06.001

Tran, C. T., Kudinov, P., and Dinh, T. N. (2010). An approach to numerical simulation and analysis of molten corium coolability in a boiling water reactor lower head. *Nucl. Eng. Des.* 240, 2148–2159. doi: 10.1016/j.nucengdes.2009.11.029

Voller, V. R., and Prakash, C. (1987). A fixed-grid numerical modeling methodology for convection-diffusion mushy region phase- change problems. *Heat Mass Transfer* 30, l 709–1 720. doi: 10.1016/0017-9310(87)90317-6

Zhang, L., Zhou, Y., Zhang, Y., Tian, W., Qiu, S., and Su, G. (2015). Natural convection heat transfer in corium pools: a review work of experimental studies. *Prog. Nucl. Energy* 79, 167–181. doi: 10.1016/j.pnucene.2014.11.021

Zhang, L. T., Zhang, Y. P., Zhou, Y. K., Su, G. H., Tian, W. X., and Qiu, S. Z. (2016). COPRA experiments on natural convection heat transfer in a volumetrically heated slice pool with high rayleigh numbers. *Ann. of Nucl. Energy* 87, 81–88. doi: 10.1016/j.anucene.2015.08.021

Zhang, Y., Niu, S., Zhang, L., Qiu, S., Su, G., and Tian, W. (2015). A review on analysis of LWR severe accident. *J. Nucl. Eng. Radiat. Sci.* 1:041018. doi: 10.1115/1.4030364

Zhang, Y., Zhang, L., Zhou, Y., Tian, W., Qiu, S., Su, G., Zhao, B., Yuan, Y., and Ma, R. (2016). The COPRA experiments on the in-vessel melt pool behavior in the RPV lower head. *Ann. Nucl. Energy* 89, 19–27. doi: 10.1016/j.anucene.2015.11.013

Zhang, Y. P., Su, G. H., Qiu, S. Z., Tian, W. X., Gaus-Liu, X., Kretzschmar, F., and Miassoedov, A. (2014). Numerical study on the heat transfer characteristics of LIVE-L4 melt pool with a partial solidification process. *Prog. Nucl. Energy* 74, 213–221. doi: 10.1016/j.pnucene.2014.03.011

Conflict of Interest: The authors declare that the research was conducted in the absence of any commercial or financial relationships that could be construed as a potential conflict of interest.

NOMENCLATURE

c_p	specific heat at constant pressure ($J \cdot kg^{-1} \cdot K^{-1}$)
g	gravitational acceleration ($m \cdot s^{-2}$)
h	enthalpy ($J \cdot kg^{-1}$)
K	permeability (m^2)
L_h	latent heat of fusion ($J \cdot kg^{-1}$)
Q	heating power density ($W \cdot m^{-3}$)
S_b	buoyancy force term ($kg \cdot m^{-2} \cdot s^{-2}$)
S_m	Darcy source term ($kg \cdot m^{-2} \cdot s^{-2}$)
T	temperature (K)
T_l	liquidus temperature (K)
T_m	average temperature of the mushy zone (K)
T_s	solidus temperature(K)

Greek symbols

β	thermal expansion coefficient (K^{-1})
ε	a minimum value
λ_{eff}	effective thermal conductivity ($W \cdot m^{-1} \cdot K^{-1}$)
λ_l	thermal conductivity of the liquid phase ($W \cdot m^{-1} \cdot K^{-1}$)
λ_s	thermal conductivity of the solid phase ($W \cdot m^{-1} \cdot K^{-1}$)
λ_{wall}	thermal conductivity of the curve ($W \cdot m^{-1} \cdot K^{-1}$)
ν	kinematic viscosity ($m^2 \cdot s^{-1}$)
μ_{eff}	effective dynamic viscosity (Pa·s)
ρ	density ($kg \cdot m^{-3}$)
ϕ	liquid fraction

frontiers in Energy Research

ORIGINAL RESEARCH
published: 03 June 2020
doi: 10.3389/fenrg.2020.00102

Numerical Simulation and Validation of Aerosol Particle Removal by Water Spray Droplets With OpenFOAM During the Fukushima Daiichi Fuel Debris Retrieval

Hui Liang[1]*, *Nejdet Erkan*[2], *Virginie Solans*[3] and *Shunichi Suzuki*[1]

[1] Department of Nuclear Engineering and Management, The University of Tokyo, Tokyo, Japan, [2] Nuclear Professional School, The University of Tokyo, Ibaraki, Japan, [3] Section of Physics, École Polytechnique Fédérale de Lausanne (EPFL), Lausanne, Switzerland

OPEN ACCESS

Edited by:
Jun Wang,
University of Wisconsin-Madison,
United States

Reviewed by:
Xianping Zhong,
University of Pittsburgh, United States
Muhammad Saeed,
East China University of
Technology, China

***Correspondence:**
Hui Liang
h_liang@vis.t.u-tokyo.ac.jp

Specialty section:
This article was submitted to
Nuclear Energy,
a section of the journal
Frontiers in Energy Research

Received: 01 April 2020
Accepted: 07 May 2020
Published: 03 June 2020

Citation:
Liang H, Erkan N, Solans V and
Suzuki S (2020) Numerical Simulation
and Validation of Aerosol Particle
Removal by Water Spray Droplets
With OpenFOAM During the
Fukushima Daiichi Fuel Debris
Retrieval. Front. Energy Res. 8:102.
doi: 10.3389/fenrg.2020.00102

In the decommissioning of damaged Fukushima Daiichi reactors, the melted and re-solidified fuel debris in the bottom of the reactor pressure vessel and primary containment vessel need to be cut into small pieces before removing them from reactor buildings. During the cutting operations, submicron radioactive aerosol particles are expected to be generated and dispersed into the atmosphere of the primary containment vessel. Those suspended particles must be removed from the air atmosphere inside the containment before escaping to the environment. The water spray system in the upper part of the primary containment vessel is an effective and applicable method to remove airborne radioactive aerosol particles. Computational Fluid Dynamics simulation of aerosol scavenging by spray droplets is complicated but necessary to investigate the aerosol removal process inside the vessel. In this paper, a numerical model was developed and implemented into an open-source computational fluid dynamic code OpenFOAM to simulate the aerosol removal by water spray droplets with considering the collection mechanisms of inertial impaction, interception, and Brownian diffusion. In this model, the dispersed spray droplets were described using the Lagrangian particle tracking method, the continuous particle-laden gas was described using the Eulerian method, and a two-way interaction between dispersed and continuous phases was considered. The polydisperse aerosol particles at different diameters from 0.2 to 1 μm were treated as different gas species of the continuous phase. Continuity equations of each gas specie were solved using a passive scalar transport equation. The numerical model was validated by comparing the simulation results with the experimental data obtained from UTARTS facility. Simulation results agreed well with the experimental results. The simulation results provided more insights to better understand the aerosol removal process, including the time evolution of aerosol mass fraction and flow field of the gas phase.

Keywords: CFD, aerosol removal, spray droplets, Euler-Lagrange approach, OpenFOAM, UTARTS

INTRODUCTION

In the decommissioning of Fukushima Daiichi reactors, the re-solidified fuel debris in the bottom of the reactor pressure vessel (RPV) and primary containment vessel (PCV) need to be cut into small pieces before removing them from reactor buildings (Porcheron et al., 2018). The aerosol clouds will be generated in the cutting process and the small particles attached on the surface of internal structures may also resuspend. These aerosol particles will disperse in the air atmosphere of PCV and must be suppressed inside the reactor buildings. Otherwise, they may escape to the outside environment and impose unpredictable health effects on the decommissioning workers and also on the public with intensified inhaled radiation doses.

The water spray system in the upper part of PCV is originally designed to depressurize the containment vessel and mix the stratified atmosphere during a hypothetical severe accident. However, it is also an effective and applicable mitigation method to remove the suspended aerosol particles in the PCV atmosphere. The aerosol particles can be removed by water spray droplets under different collection mechanisms, including mechanical effects (inertial impaction, interception, and Brownian diffusion) and phoretic effects (diffusiophoresis and thermophoresis) (Williams et al., 1997). Though these mechanisms work simultaneously, different mechanism dominates in different size range: Brownian diffusion predominates for the scavenging of particles with diameter $d_P < 0.1\,\mu m$; while inertial impaction and interception are predominant for particles with $d_P > 1\,\mu m$; the phoretic effects are negligible when the temperature difference between droplets and particle-laden gas is small (Ardon-Dryer et al., 2015). Within the size range of 0.1–1 μm (also called Greenfield gap), neither mechanism works efficiently, and the total collection efficiency is much lower than that of other size ranges (Greenfield, 1957).

It is important to clarify the size distribution of generated aerosol particles for the Fukushima case since aerosol particles with different diameters will be removed by spray droplets under different mechanisms. The laser cutting experiments were conducted on in- and ex-vessel fuel debris simulants in IRSN, France (Journeau et al., 2017; Porcheron et al., 2018). The experiments yielded aerosol particles with the diameter sizes of 0.01–10 μm, and its mass mean diameter D_{50} was 0.16 μm for the ex-vessel cutting and 0.27 μm for the in-vessel cutting, which indicated that a large proportion of generated aerosol particles had sizes within the Greenfield gap. So, the collection mechanisms of inertial impaction, interception, and Brownian diffusion will work simultaneously but not that efficiently when these aerosol particles are removed by spray droplets.

Previous researchers had conducted aerosol removal experiments by water sprays. The French research institute IRSN performed aerosol removal tests in the TOSQAN facility, which was initially pressurized with steam to simulate the primary circuit breach and seeded with silicon carbide (SiC) particles with arithmetic mean diameter D_{10}= 1.11 μm to simulate the released fission products (Porcheron et al., 2010). Their results showed that water spray can significantly remove aerosol particles under the mechanical effects and also diffusiophoresis caused by the steam concentration gradient around spray droplets. Based on the aerosol removal experiments in the TOSQAN facility, an aerosol removal model with considering mechanical and phoretic collection mechanisms was developed and implemented in the Lumped-parameter Accident Source Term Evaluation Code (ASTEC; Marchand et al., 2006). The aerosol washout experiments were also conducted in the THAI experimental facility, in which the soluble Cesium Iodine (CsI) particles with a mean diameter of 1.76 and 1.19 μm were used as fission product simulants and the containment was pressurized up to 1.5 bar (Kaltenbach and Laurien, 2018). The corresponding numerical simulation was conducted in commercial CFD software ANSYS CFX with employing Euler-Euler two-fluid and Euler-Euler three-fluid approaches. In their numerical model, the water spray droplets were treated as a component in the continuous phase and conservation equations were solved by using the Eulerian method. Different mechanisms including settling, inertial impaction, interception, and Brownian diffusion were implemented to ANSYS CFX via user-defined functions. However, the priority of the Lagrangian method over the Eulerian method in modeling the dispersed spray droplets was proved by previous research (Ding et al., 2017). Goniva et al. (2009) simulated the capturing of dust particles by droplets in a Venturi scrubber using a Euler–Lagrange approach with CFD code OpenFOAM (Open-source Field Operation And Manipulation). The droplets were modeled in a Lagrangian frame of reference and the gas phase was solved using the Eulerian approach, while the fine dust particles were treated as additional passive Eulerian phases. The dust particles were represented by 6 diameter fractions ranging from 0.1 to 1 μm and the collection mechanisms of inertial impaction, interception and Brownian diffusion were considered. The advantage of the Lagrangian method in modeling dispersed droplets was taken in their simulation. Nevertheless, the simulated capturing efficiency did not agree well with experimental data for smaller particles with diameter $d_P < 0.4\,\mu m$ in low gas velocity case. What's worse, in high gas velocity case the accuracy of the capturing prediction for all diameters within 0.1–1 μm was not yet satisfying. This might be caused by an unsuitable choice of empirical correlations in defining the collection efficiency of different mechanisms, especially Brownian diffusion which works more effectively for removing smaller particles in a moderate or low inertia dominated flow fields. Moreover, the flow physics in a Venturi scrubber were different from that in the spray systems. In a Venturi scrubber, droplets were formed by atomization of the liquid when high-velocity gas flowed through and came into contact with the liquid at the Venturi throat. For spray systems, high-velocity spray droplets were injected into gas phase using spray nozzles and large velocity gradients existed between the areas with and without spray droplets.

Fukushima problem exclusively differs from the aforementioned studies, particularly, in terms of the thermal-hydraulic conditions, such as pressure and temperature, and spatial dimensions i.e., a large enclosure with coexisting multi variable flow fields. In addition, many empirical correlations in literature are available for describing the collection efficiency of different mechanisms. Proper correlations should be selected to

predict the capture of particles accurately, especially for smaller particles with $d_P < 0.4\,\mu m$. Considering these factors, a new numerical model of aerosol scavenging by water spray droplets for Fukushima case is needed. The aim of this paper is to develop the aerosol removal model which can predict the capturing of smaller particles more accurately comparing with previous researches. Still, the Lagrangian particle tracking method was used to model dispersed spray droplets and the collection mechanisms of inertial impaction, interception, and Brownian diffusion were considered to remove aerosol particles as Goniva et al. (2009) did. However, more case-specific empirical correlations, especially the collection efficiency of inertial impaction for particles with smaller Stokes number and the collection efficiency of Brownian diffusion which predominates for the scavenging of smaller particles in a moderate or low inertia dominated flow fields, were chosen and implemented into OpenFOAM source code. The numerical model was validated by comparing the simulated time evolution of total aerosol mass and the aerosol mass at different diameters ranging from 0.2 to 1 μm with experimental data. The simulation results were expected to provide more detailed information for a better understanding of the aerosol scavenging process.

NUMERICAL SIMULATION MODEL IN OPENFOAM

Euler-Lagrange Approach

In this study, numerical simulations of aerosol removal by water spray droplets were carried out using the Euler-Lagrange approach. The Euler method was used to describe the continuous phase (particle-laden gas) and the Lagrange method was used to describe the dispersed phase (spray droplets). The continuous phase was consistent with air and small Zirconium dioxide (ZrO_2) particles. The ZrO_2 particles at different diameters were viewed as different gas species in the continuous phase and were transported by diffusion and convection. The particles were small enough (0.2–1 μm in the current study) to ensure the Stokes number *St* was below 1. Thus, the suspended particles can follow the flow of the gas phase very well and had the same velocity as the gas phase. Continuous phase and dispersed droplet phase influenced each other by means of drag force. Aerosol removal was considered as source and sink terms in mass equations. Such kind of simulations can be realized using the sprayFoam solver in OpenFOAM together with our developed aerosol removal model.

Originally, the sprayFoam solver inside OpenFOAM was used to simulate high-pressure diesel injection in the form of droplet parcels using the Lagrangian particle tracking method. In this study, the sprayFoam solver was used to simulate the dispersed spray droplets. Also, the existed phase change model in OpenFOAM was used to simulate the steam condensation on cold water spray droplets (Erkan and Okamoto, 2015). Similar to the process of steam condensation on the spray droplet surface, the aerosol particles were also captured on the droplet surface due to different collection mechanisms. In this study, an aerosol removal model considering the mechanical collection mechanisms was developed based on the steam condensation model and was implemented into the OpenFOAM source code to simulate the aerosol scavenging by water spray droplets.

Governing Equations

The control equations for different phases and the empirical formula for calculating the collection efficiency of different collection mechanisms are presented below. The energy conservation equation is not considered because the temperatures of spray droplets and particle-laden gas are both at room temperature.

Particle-Laden Gas Using Eulerian Method

The total mass transfer equation for the particle-laden gas phase can be written as:

$$\frac{\partial \rho}{\partial t} + \nabla \cdot (\rho \boldsymbol{U}_G) = \dot{\rho}_s \tag{1}$$

where, ρ is gas density, t is time, $\boldsymbol{U}_G$ is gas velocity, $\dot{\rho}_s$ is the sink term to model aerosol removal by spray droplets.

All species in the gas phase are solved by the passive scalar transport equation and only aerosol particles are consumed due to the capturing by spray droplets. The mass equation for individual specie in the gas phase can be described as:

$$\frac{\partial \rho Y_i}{\partial t} = \nabla \cdot (\rho \boldsymbol{U}_G Y_i) - \nabla \cdot \left(\mu_{eff} \nabla Y_i\right) = \dot{\rho}_s^i \tag{2}$$

$$\dot{\rho}_s = \sum_i \dot{\rho}_s^i \tag{3}$$

where, Y_i is the mass fraction of aerosol with a diameter of $d_{P,i}$ for i^{th} gas specie ($i = 1, 2, 3, \cdots$). μ_{eff} is the total viscosity and is defined as the sum of laminar and turbulent viscosities, i.e., $\mu_{eff} = \mu_L + \mu_T$. The source term $\dot{\rho}_s^i$ is non-zero only for aerosol particle species.

The momentum transport equation is:

$$\frac{\partial \rho \boldsymbol{U}_G}{\partial t} + \nabla \cdot (\rho \boldsymbol{U}_G \boldsymbol{U}_G) = -\nabla p + \nabla \cdot \left(\mu_{eff} \nabla \boldsymbol{U}_G\right) + \nabla \cdot \left[dev(\mu_{eff} (\nabla \boldsymbol{U}_G)^T)\right] + \rho \boldsymbol{g} + \boldsymbol{F}_S \tag{4}$$

where, p is the pressure, g is the gravitational acceleration, F_S is the momentum source term induced by the spray droplets. *dev* returns the deviatoric part of a symmetric tensor defined as $dev\,(A) = A - \frac{2}{3} Itr(A)$.

Spray Droplets Using Lagrangian Method

The dispersed spray droplets are described using the Lagrangian particle tracking method. The method assumes that spray injection consists of different droplet parcels and each parcel consists of many spray droplets sharing the same location, diameter, velocity, and temperature. In current simulations, droplets are assumed to be spherical and droplet fragmentation and coalescence are neglected because of their limited effect on aerosol removal. The motions of droplets are affected by the drag force F_D from continuous phase and gravity force G_D. And the motion equation for one droplet can be described as:

$$m_D \frac{\boldsymbol{U}_D}{t} = \boldsymbol{F}_D + \boldsymbol{G}_D \tag{5}$$

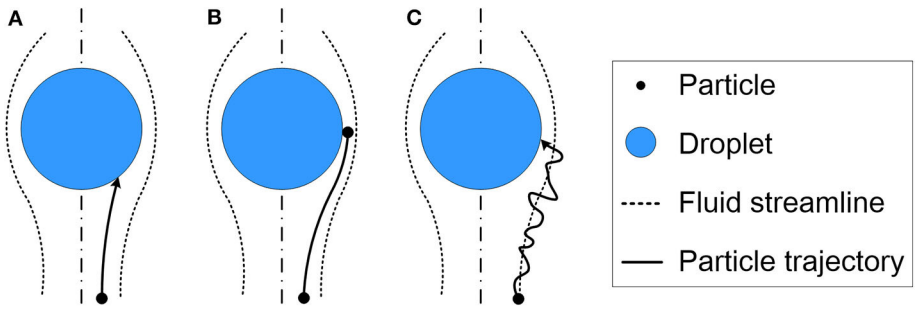

FIGURE 1 | Aerosol collection mechanisms of **(A)** inertial impaction; **(B)** interception; and **(C)** Brownian diffusion (Hähner et al., 1994, with permission from the copyright holder John Wiley and Sons).

where, m_D is droplet mass and U_D is droplet velocity. The drag force F_D and gravity force G_D are written as:

$$\boldsymbol{F}_D = \rho \frac{\pi}{8} d_D^2 C_D \left|\boldsymbol{U}_G - \boldsymbol{U}_D\right| \left(\boldsymbol{U}_G - \boldsymbol{U}_D\right) \tag{6}$$

$$\boldsymbol{G}_D = \rho_D \boldsymbol{g} \frac{\pi}{6} d_D^3 \tag{7}$$

where, d_D is droplet diameter, C_D is the drag coefficient, and ρ_D is droplet density.

Modeling of Aerosol Removal by Water Spray Droplets

Among all the aerosol collection mechanisms, the inertial impaction, interception, and Brownian diffusion play more important roles for removing aerosol particles than diffusiophoresis and thermophoresis (Hähner et al., 1994; Williams et al., 1997). So only the first three mechanisms are considered in our aerosol removal model as depicted in **Figure 1**.

To model the inertial impaction accurately, the single droplet collection efficiency of inertial impaction η_{imp} is defined according to different Stokes number St ranges (Powers and Burson, 1993):

$$\eta_{imp} = \begin{cases} 0, \& for\ St \le 0.0833 \\ 8.57^* \left(\frac{St}{St+0.5}\right)^2 * (St - 0.08336), \& for\ 0.0833 < St < 0.2 \\ \left(\frac{St}{St+0.5}\right)^2, \& for\ St \ge 0.2 \end{cases} \tag{8}$$

The modified Stokes number St is used for characterizing inertial collection (Goniva et al., 2009):

$$St = \frac{\rho_P d_P^2 \left|\boldsymbol{U}_G - \boldsymbol{U}_D\right|}{9 \mu_G d_D} \tag{9}$$

where, ρ_P is particle density, μ_G is the dynamic viscosity of air.

The single droplet collection efficiency for interception η_{int} is given by Park et al. (2005):

$$\eta_{int} = \frac{1 - \alpha_L}{J + \sigma \cdot K} \left\{ \left(\frac{R}{1+R}\right) + \frac{1}{2}\left(\frac{R}{1+R}\right)^2 \cdot (3\sigma + 4) \right\} \tag{10}$$

$$with J = 1 - \frac{6}{5} \cdot \alpha_L^{\frac{1}{3}} + \frac{1}{5} \cdot \alpha_L^2,$$

$$K = 1 - \frac{9}{5} \cdot \alpha_L^{\frac{1}{3}} + \frac{1}{5} \cdot \alpha_L^2,$$

$$\sigma = \frac{\mu_D}{\mu_G}, R = \frac{d_P}{d_D}.$$

where, α_L is the volume fraction of liquid phase, J and K are empirical factors, σ is the ratio of dynamic viscosities between droplets and gas phase $\frac{\mu_D}{\mu_G}$, R is a ratio of diameters between aerosol particle and spray droplet $\frac{d_P}{d_D}$.

The single droplet collection efficiency for Brownian diffusion η_{diff} is given by Powers and Burson (1993):

$$\eta_{diff} = \left(2^* Pe^* d_D\right)^{-\frac{1}{2}} \tag{11}$$

with $Pe = \frac{d_D \left|\mathbf{U}_G - \mathbf{U}_D\right|}{D_{diff}}$, $D_{diff} = \frac{k_B T C}{3\pi\ \nu_G \rho_G d_P}$

where, P_e is the Peclet number, D_{diff} is the diffusion coefficient, k_B is Boltzmann constant, ν_G is the kinematic viscosity of air, C is the Cunningham correction factor and is defined as:

$$C = \frac{2.609\sqrt{2l}}{\sqrt{d_P}}, for 0.05\,\mu m < d_P < 1.0 \mu m \tag{12}$$

here, l is mean free path length of air.

The total collection efficiency for a single droplet η_{total} can then be calculated as:

$$\eta_{total} = 1 - (1 - \eta_{imp})(1 - \eta_{int})(1 - \eta_{diff}) \tag{13}$$

To calculate the removed aerosol mass $dm_{D,i}$ by a single droplet during time dt, the volume V that one droplet passes through during time dt and the aerosol molar concentration $C_{APs,i}$ need to be considered. And they have the following relationship:

$$dm_{D,i} = \eta_{total,i} \cdot V \cdot C_{APs,i} \cdot M_{APs,i} \tag{14}$$

$$V = \frac{\pi}{4} d_D^2 \boldsymbol{U}_D \cdot dt \tag{15}$$

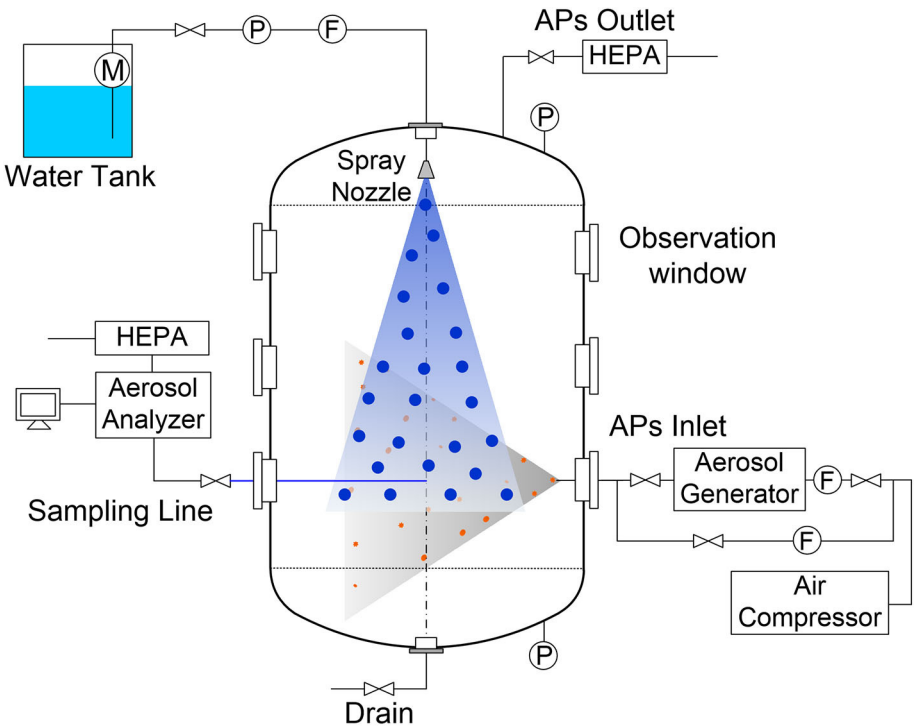

FIGURE 2 | UTARTS facility (Aerosol Removal Tests using Water Spray in the University of Tokyo).

where, $m_{D,i}$ is the droplet mass increase due to capturing of i^{th} gas specie, $C_{APs,i}$ is the molar concentration of i^{th} gas specie around the droplet, and $M_{APs,i}$ is the molecular weight of i^{th} gas specie.

Thus, the mass variation rate of a single droplet caused by capturing i^{th} gas specie is calculated as:

$$\frac{dm_{D,i}}{\mathrm{dt}} = \eta_{total,i} \cdot \frac{\pi}{4} d_D^2 \boldsymbol{U}_D \cdot C_{APs,i} \cdot M_{APs,i} \tag{16}$$

And the total mass variation rate of a single droplet is:

$$\frac{dm_D}{\mathrm{dt}} = \sum_i \frac{dm_{D,i}}{dt} \tag{17}$$

VALIDATION EXPERIMENT

Experiment Setup

Figure 2 depicts the schematic layout of the vessel and instrumentation, as well as other equipment in our experimental setup of UTARTS facility (Aerosol Removal Tests using Water Spray in the University of Tokyo). Aerosol scavenging experiments were conducted inside a cylindrical vessel with two hemispherical heads made of stainless steel (with a height of 2.5 m, internal diameter of 1.5 m, and total volume of 3.92 m^3). Thirteen optical windows were designed on the lateral side of the vessel for observing the experimental phenomena and measuring the spray droplet size and velocity. Several small holes were designed in the walls of the vessel for the insertion of instrumentation. The ZrO_2 particles with mass mean diameter D_{50} of 0.15 μm was put inside the aerosol generator and then dispersed inside the vessel. The ZrO_2 particles were chosen as aerosol particle simulants because there was a large proportion of ZrO_2 according to chemical compositions of in-vessel fuel debris simulants (Journeau et al., 2017). The full-cone spray nozzle was used to inject spray droplets at 300 mm below the top of the vessel. Water for the spray was pumped from a water tank at the flow rate of 2 L/min. During the experiment, the sampling gas flow was pulled from the measurement point on the half radius of the vessel and 1,400 mm below the nozzle outlet and then transferred to the aerosol analyzer Welas2000 to measure the aerosol number concentration. The Welas2000 is a light-scattering spectrometer system which determines particle concentration in the range from <1 particle/cm^3 up to 10^6 particles/cm^3 and size between 0.2 and 10 μm. An aerosol particle outlet pipe with a High-efficiency Particulate Air (HEPA) filter near the spray nozzle entrance flange was used to exhaust the aerosol-containing gas to the outside. The water accumulated at the lower plenum of the vessel was discharged outside with a water drain pipe at the bottom of the vessel.

Experiment Procedure

The experiment procedure is as below. The experiment began with the injection of aerosol particles. After the aerosol concentration reached the targeted value, the aerosol injection was stopped. Then we waited for 10 min so that large particles can deposit and other aerosol particles can disperse inside the vessel uniformly. Then the spray injection

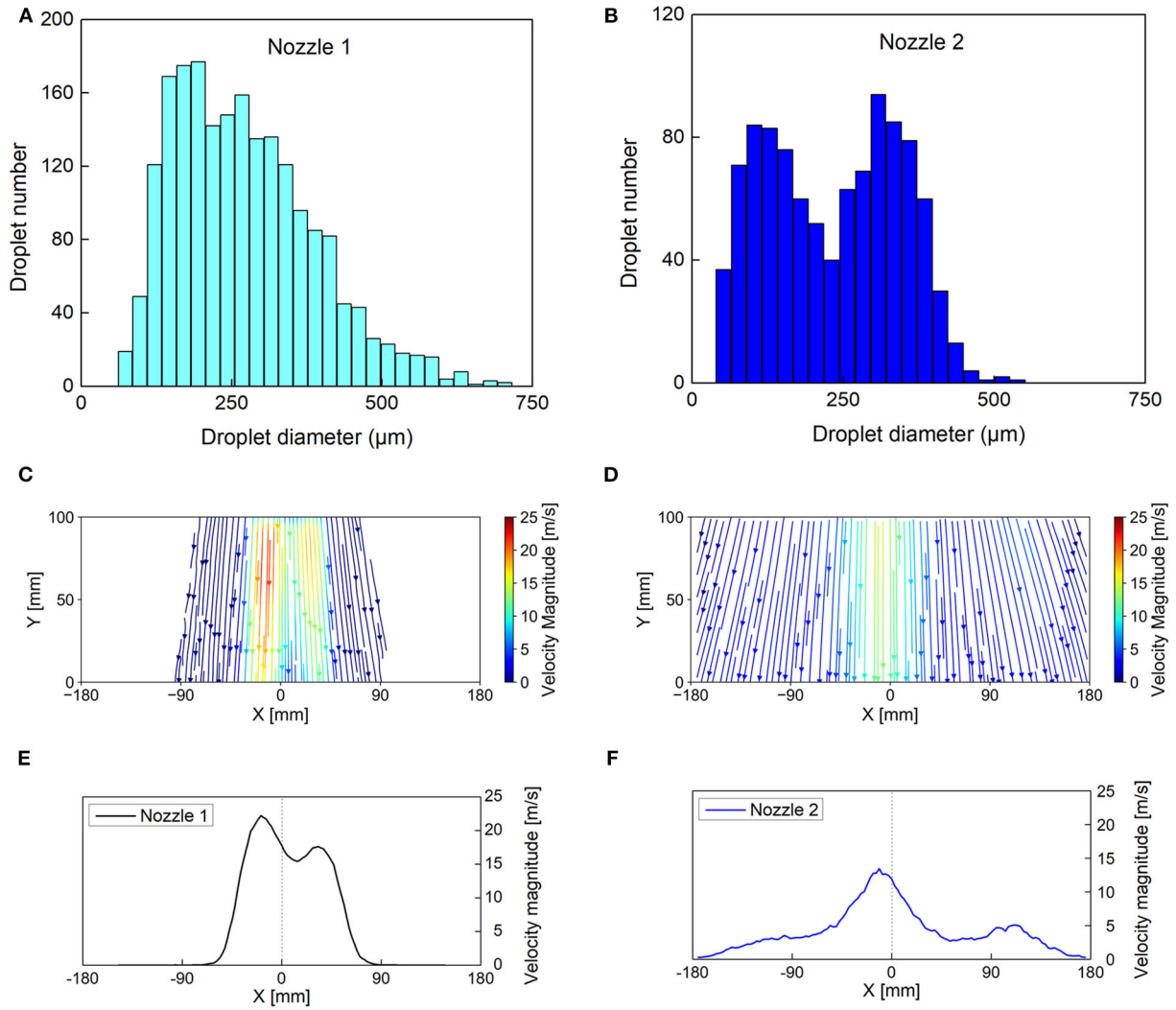

FIGURE 3 | Spray characterization: **(A)** spray droplet size distribution of nozzle 1; **(B)** spray droplet size distribution of nozzle 2; **(C)** spray droplet streamlines of nozzle 1; **(D)** spray droplet streamlines of nozzle 2; **(E)** droplet velocity magnitude at 250 mm below the outlet of nozzle 1; and **(F)** droplet velocity magnitude at 250 mm below the outlet of nozzle 2.

was activated and spray droplets were continuously injected inside the vessel to remove the aerosol particles. Each experiment case was repeated for three times to check the experiment repeatability.

Validation Experiment Cases

Two experiment cases using two different full-cone spray nozzles were used to validate our numerical simulation model. The two spray nozzles are spray nozzle 1 (model: 1/8GG-SS3004, from the Spraying System Company) and spray nozzle 2 (model: TG2, also from the Spraying System Company), respectively. The spray injection flow rate in both cases was kept at 2 L/min during the experiments. The spray droplet size distribution of two nozzles was measured using a non-intrusive technique of Interferometric Laser Imaging for Droplet Sizing method (Lemaitre et al., 2006) and results are shown in **Figures 3A,B**, respectively. For spray nozzle 1, most droplets have a size between 121 and 340 μm, with a peak around 195 μm. While for spray nozzle 2, there exist two size groups of droplets, the smaller ones have a peak of around 103 μm, and the larger ones have a peak of around 308 μm. Also, the velocity fields of spray droplets were measured using a non-intrusive technique of Particle Image Velocimetry (Raffel et al., 2018) as shown in **Figures 3C–F**. For nozzle 1, the measurement area was 207.5 mm below the spray nozzle exit. Based on the PIV measurement results, the spray nozzle 1 has a narrow spray angle of 27° and its maximum droplet velocity magnitude was 22.22 m/s. For nozzle 2, its measurement area was 250 mm below the nozzle outlet. The corresponding spray angle was 66° and the maximum droplet velocity magnitude was 15.05 m/s.

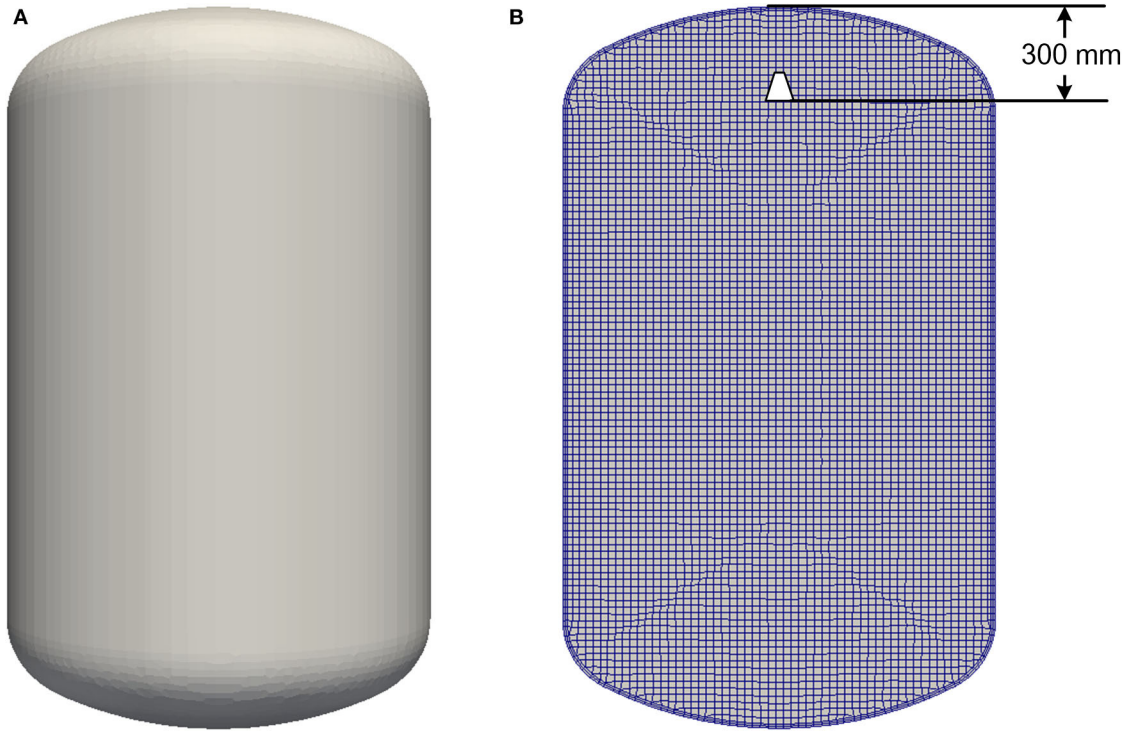

FIGURE 4 | (A) Geometry of the vessel and **(B)** mesh details on a vertical slice.

SIMULATION OF AEROSOL SCAVENGING BY SPRAY DROPLETS

Boundary Conditions

The numerical simulation was conducted using the three-dimensional geometry of the vessel (2.5 m height, 1.5 m diameter, and 3.92 m^3 volume) as shown in **Figure 4A**. The spray nozzle was installed 300 mm below the top of the vessel. Three different mesh schemes were used in the simulation to conduct the mesh independence check and the mesh details were listed in **Table 1**. The total number of cells for coarse, medium and fine mesh was 141335, 268252, and 555653, respectively. The mesh details on a vertical slice of medium mesh are shown in **Figure 4B**. Since the interaction between aerosol particles and spray droplets were focused while the flow in the wall-adjacent area was not that important for the interaction, only two layers were added in the boundary layer near the vessel's internal wall. The maximum skewness for all three meshes was smaller than 0.54. The simulated physical time for both cases was the first 1,200 s from the spray activation.

Two numerical simulation cases were conducted corresponding to the two validation experiment cases as shown in **Table 2**. The simulation case 1 was conducted at 291 K and atmospheric pressure, while case 2 was conducted at 288 K and atmospheric pressure. The orifice diameter for both nozzles was 1.2 mm. The spray injection flow rate was set as 2 L/min for both simulation cases. The measured droplet size and spray angle of nozzle 1 and nozzle 2 were used in simulation case 1 and case 2, respectively. The accumulation of spray water at the bottom of the vessel was neglected by setting those spray droplets would disappear once they hit the internal wall of the vessel. The adjustable time step was chosen for all simulation cases under the condition that Courant number $Co < 1$. The convergence criteria were set as 10^{-6} for all transient terms.

TABLE 1 | Mesh schemes for the mesh independence check.

Mesh	Cells in horizontal direction	Cells in vertical direction	Total number of cells
Coarse	60	100	141,335
Medium	75	125	268,252
Fine	100	150	555,653

Nine size groups of aerosol particles with diameters from 0.2 to 1 μm were treated as nine gas species named from AP2 to AP10, as shown in **Table 3**. And the initial aerosol mass at different diameters for simulation was obtained from the measured experimental data. It was assumed that aerosol particles were uniformly dispersed inside the vessel at the beginning of two simulation cases.

Simulation Results

Mesh Independence Check

Mesh independence check was conducted by comparing the simulated time evolution of total aerosol mass using three mesh

schemes. Take simulation case 1 as an example, the comparison of simulation results using three meshes is shown in **Figure 5**. According to **Figure 5A**, the simulation result using coarse mesh was smaller than the results using the other two meshes. If we focus on the details between the spraying time of 1,100–1,200 s as shown **Figure 5B**, it was found that the maximum difference ratio of simulation results between coarse and medium meshes was 3.82%, while it was only 0.54% between medium and fine meshes. So, the medium mesh was chosen for the following simulation.

TABLE 2 | Boundary conditions.

	Case 1	Case 2
Temperature	291 K	288 K
Pressure	1 atm	1 atm
Nozzle model	Nozzle 1	Nozzle 2
Nozzle orifice diameter	1.2 mm	1.2 mm
Spray injection flow rate	2 L/min	2 L/min
Droplet size	Peak at 195 μm	Peaks at 103 and 308 μm
Spray angle	27°	66°
Droplet-wall interaction	Disappear	Disappear
Courant number	<1	<1
Convergence criteria	10^{-6}	10^{-6}

TABLE 3 | Size class of polydisperse aerosol particles.

Case 1			Case 2		
	d_P [μm]	Initial mass [mg]		d_P [μm]	Initial mass [mg]
AP2	0.198	0.42	AP2	0.198	0.65
AP3	0.305	2.24	AP3	0.305	3.20
AP4	0.407	7.32	AP4	0.407	9.38
AP5	0.505	18.94	AP5	0.505	20.43
AP6	0.583	31.07	AP6	0.583	27.66
AP7	0.724	38.14	AP7	0.724	24.31
AP8	0.778	38.66	AP8	0.778	22.43
AP9	0.899	35.50	AP9	0.899	17.82
AP10	1.038	33.12	AP10	1.038	15.52

Validation of Aerosol Removal Model

Comparison of the time evolution of aerosol mass at different diameters between experimental and simulation results was used to validate our numerical model. Take case 1 as an example as depicted in **Figures 6A,B**, the simulation results were in good agreement with experimental data at particle diameters ranging from 0.2 to 1 μm. Therefore, the aerosol removal model can predict the time evolution of aerosol mass at different diameters very well, even for small aerosol particles of $d_P < 0.4$ μm. For aerosol particles with a diameter of 1 μm, the measured aerosol mass was a little smaller than that of the simulation results. This was likely to be caused by the deposition of large particles. Moreover, the comparison of the time evolution of total aerosol mass between experiment and simulation results was also used to validate our numerical model. **Figure 6C** is for case 1 and **Figure 6D** is for case 2. For both cases, a good agreement can be found between the simulation results and experimental data.

Based on the above comparisons, our aerosol removal model with considering collection mechanisms of inertial impaction, interception, and Brownian diffusion was capable of simulating aerosol removal by water spray droplets for particles with diameters from 0.2 to 1 μm.

Spray Droplets

Figure 7 shows the simulated spray droplets and velocity magnitude of gas-phase for two simulation cases. The spheres stand for spray droplets and the spheres' color refers to the spray droplet diameters as shown in the color bar. The spray droplets would disappear once they hit the vessel's internal wall. The background of the slice refers to the velocity magnitude of the gas-phase. Since two-way coupling was considered in our simulation, the velocity magnitude of the gas-phase was

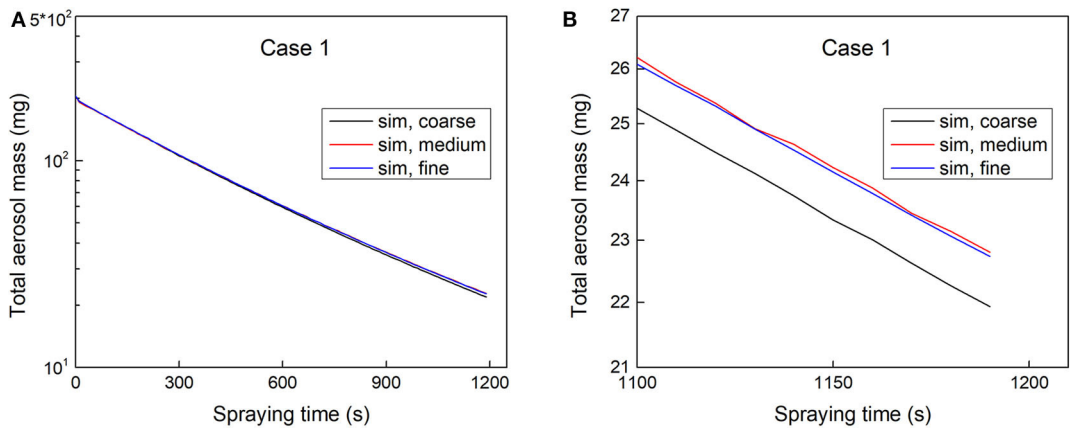

FIGURE 5 | Mesh independence check based on simulation case 1: **(A)** comparison of total aerosol mass during 0–1,200 s and **(B)** comparison of total aerosol mass during 1,100–1,200 s.

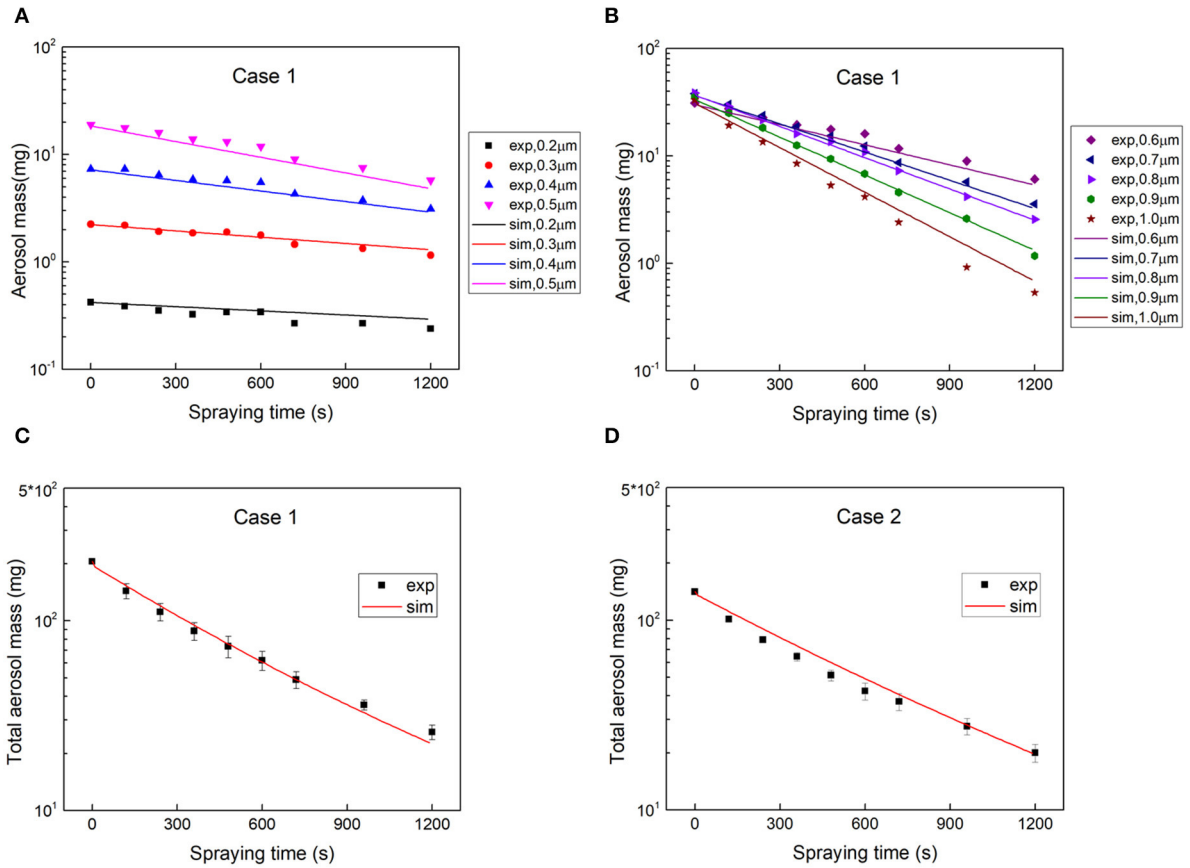

FIGURE 6 | Validation of aerosol removal model: **(A)** comparison of the time evolution of aerosol mass at d_P of 0.2–0.5 μm based on case 1; **(B)** comparison of the time evolution of aerosol mass at d_P of 0.6–1 μm based on case 1; **(C)** comparison of the time evolution of total aerosol mass based on case 1; and **(D)** comparison of the time evolution of total aerosol mass based on case 2.

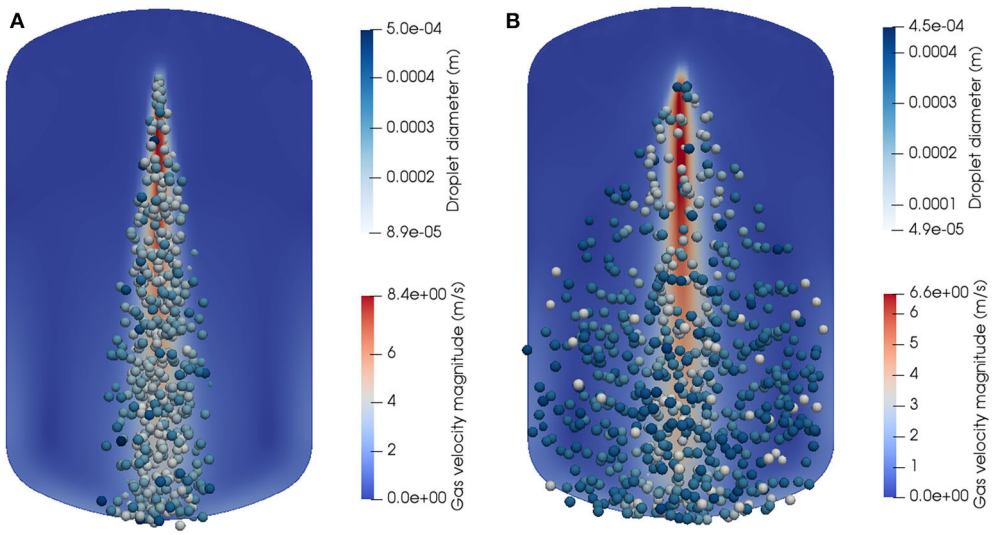

FIGURE 7 | Spray droplets modeling using the Lagrangian particle tracking method: **(A)** nozzle 1 with a narrow spray angle of 27° and **(B)** nozzle 2 with a wide spray angle of 66°.

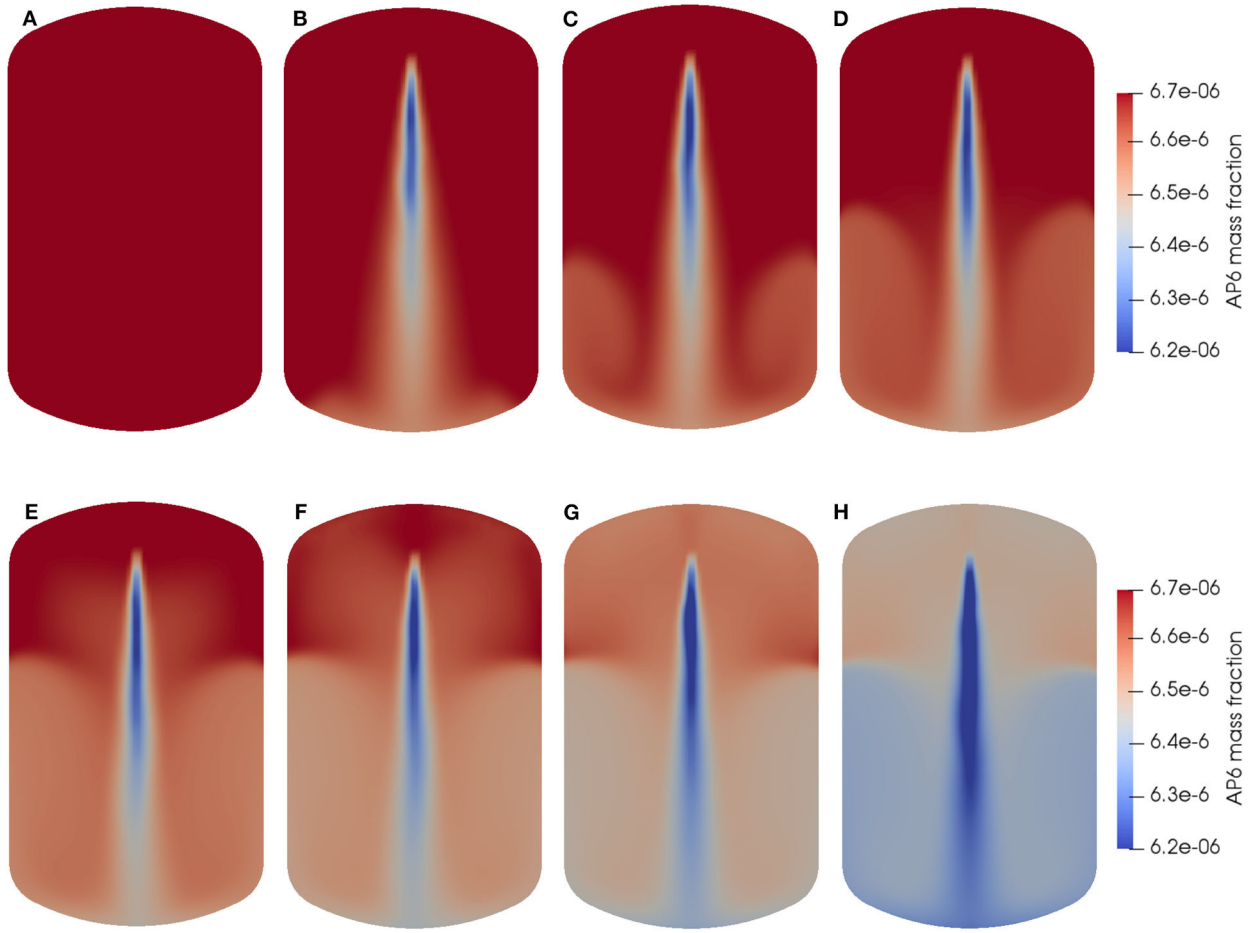

FIGURE 8 | Time evolution of AP6 mass fraction during spraying of simulation case 1: **(A)** $t = 0$ s; **(B)** $t = 1$ s; **(C)** $t = 3$ s; **(D)** $t = 5$ s; **(E)** $t = 10$ s; **(F)** $t = 15$ s; **(G)** $t = 20$ s; and **(H)** $t = 30$ s.

higher inside the spray region than that in other areas, which was caused by the drag between the continuous phase and dispersed phase.

Time Evolution of Aerosol Mass Fraction During Spraying

Figure 8 shows the time evolution of aerosol mass fraction for aerosol particles having a diameter of 0.6 μm (AP6) in case 1. At the beginning $t = 0$ s as shown in **Figure 8A**, the aerosol particles were uniformly dispersed inside the vessel. Once the spray injection was activated, the aerosol particles near spray droplets were removed firstly as shown in **Figure 8B**. From **Figures 8B–E**, the aerosol particles near the bottom left and right sides started to be removed and the regions expanded along with the spraying time. In **Figure 8E** at the spraying time of $t = 10$ s, the washout region in two bottom sides did not expand any more, while the aerosol particles in the upper space of the vessel started to be removed. From $t = 10$ s, there existed clear boundaries among different regions as shown in **Figures 8E–H**, which can be explained with the velocity vectors of gas-phase as shown in **Figure 9**.

Figure 9 shows both velocity vectors of gas-phase and AP6 mass fraction for case 1 during the spraying time of the first 20 s. The vectors refer to velocity vectors of the gas-phase and the background of slice refers to AP6 mass fraction. In **Figure 9A** at $t = 1$ s, two vortex structures started to form at two lateral sides near the bottom of the vessel. Then the vortex structures developed and shifted upwards until they became dynamically stable at $t = 10$ s as depicted in **Figure 9C**. The aerosol particles circulated along with the vortex structures in the lower space of the vessel then were entrained inside the spray region, and finally were removed by spray droplets. From **Figures 9C,D**, the aerosol particles in the upper part of the vessel were also entrained inside the spray region.

Figure 10 shows the time evolution of AP6 mass fraction for case 2 and **Figure 11** shows the velocity vectors of gas-phase and AP6 mass fraction for case 2. The results also exhibited vortex structures and clear boundaries among

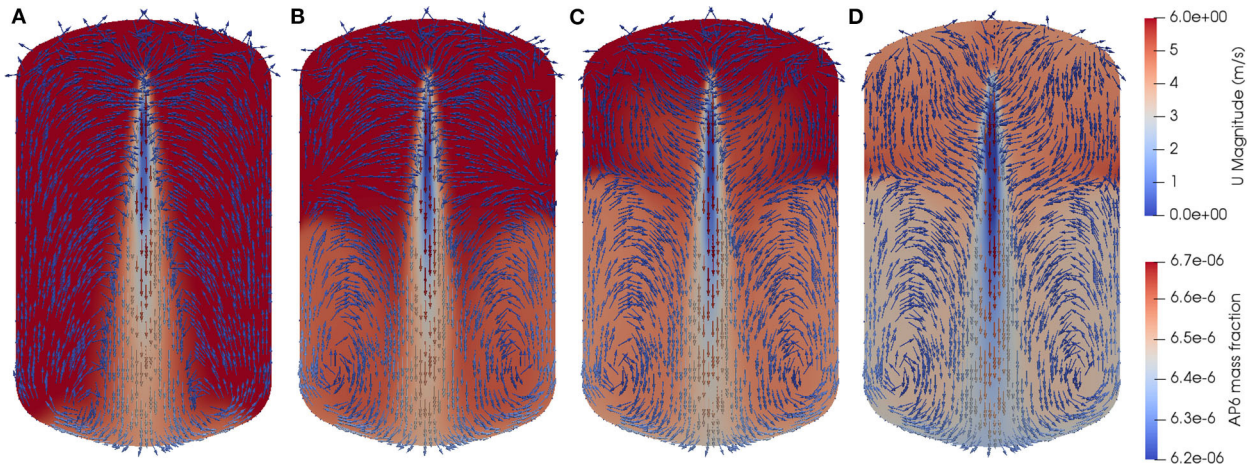

FIGURE 9 | Gas velocity vectors together with AP6 mass fraction of simulation case 1: **(A)** $t = 1$ s; **(B)** $t = 5$ s; **(C)** $t = 10$ s; and **(D)** $t = 20$ s.

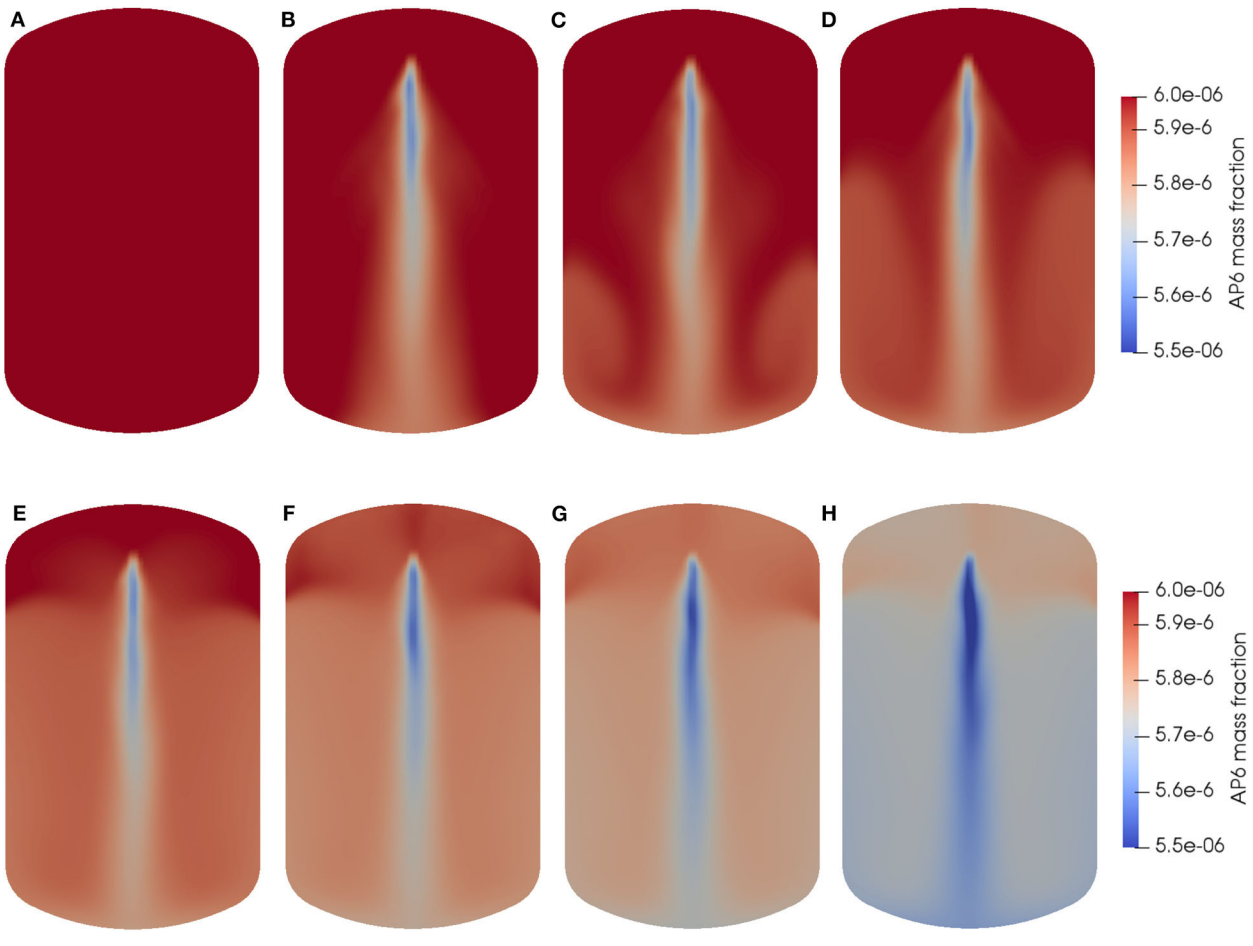

FIGURE 10 | Time evolution of AP6 mass fraction during spraying of simulation case 2: **(A)** $t = 0$ s; **(B)** $t = 1$ s; **(C)** $t = 3$ s; **(D)** $t = 5$ s; **(E)** $t = 10$ s; **(F)** $t = 15$ s; **(G)** $t = 20$ s; and **(H)** $t = 30$ s.

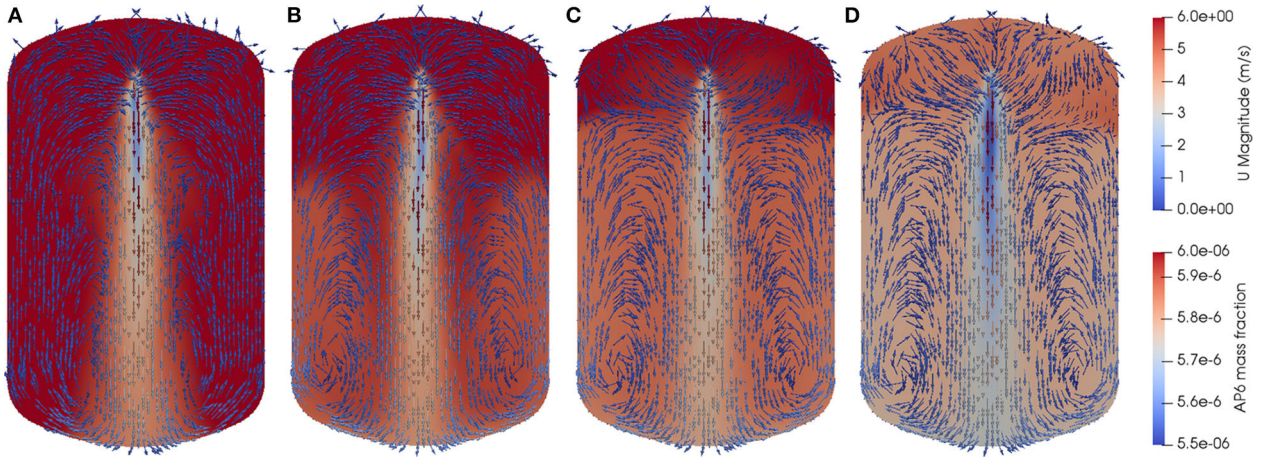

FIGURE 11 | Gas velocity vectors together with AP6 mass fraction of simulation case 2: **(A)** $t = 1$ s; **(B)** $t = 5$ s; **(C)** $t = 10$ s; and **(D)** $t = 20$ s.

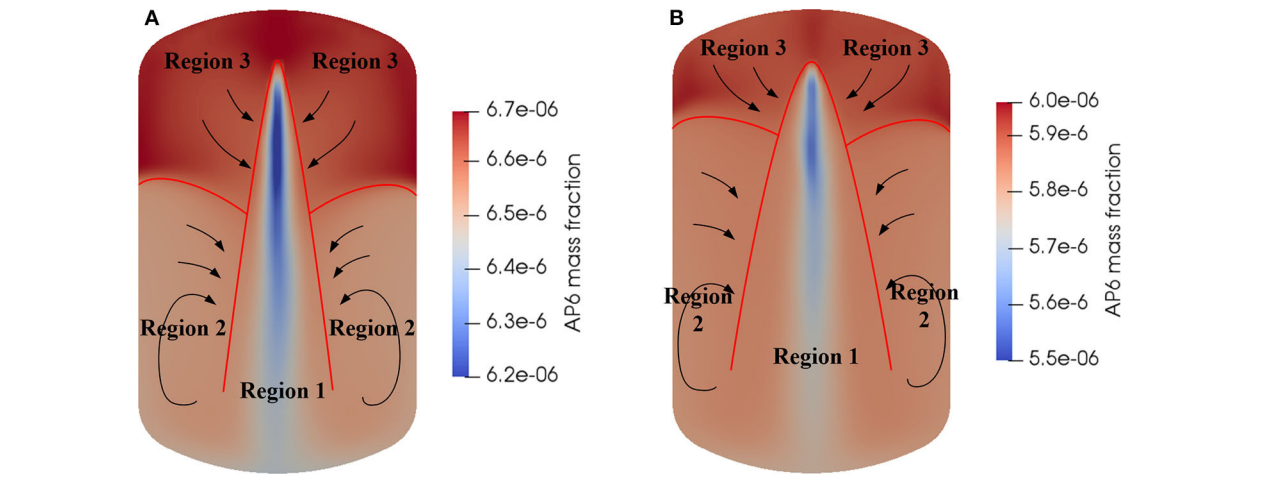

FIGURE 12 | Flow regions inside the vessel during spraying: **(A)** case 1 with a narrow spray angle and **(B)** case 2 with a wide spray angle.

different flow regions as that in case 1. However, spray nozzle 2 can cover a wider area due to its wider spray angle. And the vortex structures were larger in case 2 than that in case 1.

According to the time evolution of aerosol mass fraction and velocity fields of the gas-phase in two simulation cases, the flow area inside the vessel can be divided into three regions after it became dynamically stable as shown in **Figure 12**. Region 1 is the spray region (or aerosol washout region), the aerosol particles are mainly removed in this region by interacting with spray droplets directly. Region 2 is the circulation region, aerosol particles in this region circulate along with the vortex structures first, then are entrained inside the spray region, and finally are removed by spray droplets. Region 3 is the entrainment region, the aerosol particles in this region are also entrained inside the spray region first and then removed by spray droplets. Meanwhile, the differences between the two cases are also obvious. The region 1 and region 2 of case 2 are larger than that of case 1 due to different spray angles.

CONCLUSIONS

In this paper, a numerical model of aerosol scavenging by water spray droplets with considering collection mechanisms of inertial impaction, interception, and Brownian diffusion was developed and implemented into OpenFOAM. Empirical formula from published papers was selected to calculate the collection efficiency of these three aerosol collection mechanisms. The dispersed spray droplets were solved using the Lagrangian particle tracking method and the continuous phase of particle-laden gas was described using the Eulerian method. Nine size groups of aerosol particles with diameters varying from 0.2 to 1 μm were treated as nine gas species in the continuous phase and their movements were solved using passive scalar

transport equations. The aerosol removal model was validated by comparing the simulation results about the time evolution of aerosol mass with experimental data and it was proven that the numerical model can predict the removal of aerosol particles accurately, even for smaller particles with $d_P < 0.4\ \mu m$.

The details of the aerosol removal process, including the time evolution of aerosol mass fraction and flow field of gas-phase, were provided by numerical simulation. According to the simulation results, the flow field inside the vessel can be divided into three regions, they are spray region (or aerosol washout region), circulation region and entrainment region. The aerosol particles were mainly removed in the spray region by interacting with spray droplets directly, while the aerosol particles in the circulation region and entrainment region were entrained inside the spray region first and then removed by spray droplets.

When the nozzle 1 with a narrow spray angle was used, the maximum droplet velocity was larger, causing a larger relative velocity between droplets and particle-laden gas and also stronger mixing and turbulence inside the vessel, which was further aiding in removing aerosol particles. When the nozzle 2 with a wide spray angle was used, the spray can cover a wider area, causing a larger spray region and circulation region, which can also increase the interaction between spray droplets and aerosol particles. In the real utilization of the spray system in Fukushima decommissioning, multiple spray nozzles can be used simultaneously. With understanding the aerosol removal process by different spray nozzles, the combination of different spray nozzles can be used to improve the aerosol spray scavenging efficiency. The related experiments and simulations using multiple spray nozzles will be conducted in the future.

Still, there are some improvements can be done about the numerical simulation model for future study. The collection mechanism of thermophoresis was not considered in our aerosol removal model because the temperature difference between spray droplets and particle-laden gas was negligible. However, the humidity inside the vessel may increase after spray activation, thus the diffusiophoresis would start to perform and should be considered in the aerosol removal model.

DATA AVAILABILITY STATEMENT

The raw data supporting the conclusions of this article will be made available by the authors, without undue reservation.

AUTHOR CONTRIBUTIONS

NE, SS, and HL contributed conception and design of the study. HL and NE carried out the validation experiments. HL, VS, and NE developed the source code of aerosol removal model under supervision of NE. HL conducted the numerical simulation and the results analysis, and wrote the first draft of the manuscript. NE contributed to manuscript revision. All authors contributed to discussion of simulation results.

FUNDING

This work was financially supported by the Nuclear Energy Science & Technology and Human Resource Development Project from the Japan Atomic Energy Agency/Collaborative Laboratories for Advanced Decommissioning Science.

REFERENCES

Ardon-Dryer, K., Huang, Y. W., and Cziczo, D. J. (2015). Laboratory studies of collection efficiency of sub-micrometer aerosol particles by cloud droplets on a single-droplet basis. *Atmos. Chem. Phys.* 15, 9159–9171. doi: 10.5194/acp-15-9159-2015

Ding, P., Liu, Y., Wang, B., Li, W., and Wang, J. (2017). The Homogeneous and lagrangian tracking approaches of the spray simulation in the containment. *Ann. Nucl. Energy* 101, 203–214. doi: 10.1016/j.anucene.2016.09.038

Erkan, N., and Okamoto, K. (2015). "Analysis of PANDA spray experiments performed in two interconnected vessel with openFOAM," in *Proceedings of NURETH-16* (Chicago, IL).

Goniva, C., Tukovic, Z., Feilmayr, C., Burgler, T., and Pirker, S. (2009). "Simulation of offgas scrubbing by a combined eulerian-lagrangian model," in *Proceedings of Seventh International Conference on CFD in the Minerals and Process Industries* (Melbourne, VIC). doi: 10.1504/PCFD.2010.035359

Greenfield, S. M. (1957). Rain scavenging of radioactive particulate matter from the atmosphere. *J. Meteorol.* 14, 115–125. doi: 10.1175/1520-0469(1957)014<0115:RSORPM>2.0.CO;2

Hähner, F., Dau, G., and Ebert, F. (1994). Inertial impaction of aerosol particles on single and multiple spherical targets. *Chem. Eng. Technol.* 17, 88–94. doi: 10.1002/ceat.270170204

Journeau, C., Monneris, J., Tormos, B., Brissonneau, L., Excoiffier, E., Testud, V., et al. (2017). "Fabricating Fukushima Daiichi in-vessel and ex-vessel fuel debris simulants for the development and qualification of laser cutting technique," in *Proceedings of ERMSAR-2017 European Review Meeting on Severe Accident Research* (Warsaw).

Kaltenbach, C., and Laurien, E. (2018). CFD Simulation of aerosol particle removal by water spray in the model containment thai. *J. Aerosol Sci.* 120, 62–81. doi: 10.1016/j.jaerosci.2018.03.005

Lemaitre, P., Porcheron, E., Nuboer, A., and Grehan, G. (2006). "Interferometric Laser Imaging development for Droplets Sizing (ILIDS) in hostile environment," in *Proceedings of ICLASS* (Kyoto).

Marchand, D., Porcheron, E., Lemaitre, P., and Grehan, G. (2006). "Characterization of the washout of aerosol by spraying water for thermal hydraulic conditions representative of a severe accident in a nuclear reactor containment," in *Proceedings of 10th International Conference on Liquid Atomization and Spray Systems* (Kyoto).

Park, S. H., Jung, C. H., Jung, K. R., Lee, B. K., and Lee, K. W. (2005). Wet scrubbing of polydisperse aerosols by freely falling droplets. *J. Aerosol Sci.* 36, 1444–1458. doi: 10.1016/j.jaerosci.2005.03.012

Porcheron, E., Lemaitre, P., Marchand, D., Plumecocq, W., Nuboer, A., and Vendel, J. (2010). Experimental and numerical approaches of aerosol removal in spray conditions for containment application. *Nucl. Eng. Des.* 240, 336–343. doi: 10.1016/j.nucengdes.2008.08.023

Porcheron, E., Peillon, S., Gelain, T., Chagnot, C., Journeau, C., and Roulet, D. (2018). "Analysis of aerosol emission and dispersion during the laser cutting of Fukushima fuel debris simulants," in *Proceedings of 2018 26th International Conference on Nuclear Engineering* (London). doi: 10.1115/ICONE26-81531

Powers, D. A., and Burson, S. B. (1993). *A Simplified Model of Aerosol Removal by Containment Sprays (No. NUREG/CR-5966; SAND-92-2689).*

Washington, DC; Albuquerque, NM: Nuclear Regulatory Commission, Division of Safety Issue Resolution; Sandia National Labs. doi: 10.2172/6503368

Raffel, M., Willert, C. E., Scarano, F., Kähler, C. J., Wereley, S. T., and Kompenhans, J. (2018). *Particle Image Velocimetry: A Practical Guide*. Cham: Springer doi: 10.1007/978-3-319-68852-7

Williams, K. M. D., Tills, J., Griffith, R. O., Gido, R. G., Tadios, E. L., Davis, F. J., et al. (1997). *Code Manual for CONTAIN 2.0: A Computer Code for Nuclear Reactor Containment Analysis.* Albuquerque, NM; Sandia National Laboratories, Prepared for the US Nuclear Regulatory Commission, NUREG/CR-6533, SAND97-1735.

Conflict of Interest: The authors declare that the research was conducted in the absence of any commercial or financial relationships that could be construed as a potential conflict of interest.

NOMENCLATURE

C	Cunningham correction factor
C_{APs}	Molar concentration of aerosol particles, mol/L
C_D	Drag coefficient
Co	Courant number
d_D	Spray droplet diameter, μm
d_P	Aerosol particle diameter, μm
D_{10}	Aerosol arithmetic median diameter, μm
D_{50}	Aerosol mass median diameter, μm
D_{Diff}	Diffusion coefficient
F_D	Drag force, kg·m/s^2
F_S	Momentum source term induced by the spray droplets
G_D	Gravity force, kg·m/s^2
g	Gravitational acceleration, m/s^2
J	Empirical factors
K	Empirical factors
k_B	Boltzmann constant
l	Mean free path length of air, m
m_D	Droplet mass, kg
M_{APs}	Molecular weight of aerosol particles, kg/mol
p	Pressure of gas phase, Pa
Pe	Peclet number
R	Ratio of aerosol diameter and spray droplet diameter, $\frac{d_P}{d_D}$
St	Stokes number
t	Water spraying time, s
T	Temperature of gas, K
U_G	Gas velocity, m/s
U_D	Droplet velocity, m/s
Y_i	Mass fraction of *ith* species
α_L	Volume fraction of liquid phase
σ	Ratio of droplet dynamic viscosity and gas dynamic viscosity, $\frac{\mu_D}{\mu_G}$
ρ	Gas density, kg/m^3
ρ_D	Droplet density, kg/m^3
ρ_P	Particle density, kg/m^3
$\dot{\rho}_S$	Sink term calculated from the aerosol scavenging by spray droplets, kg/(m^3·s)
μ_{eff}	Sum of laminar and turbulent viscosities, kg/(m·s)
μ_D	Dynamic viscosity of spray droplets, kg/(m·s)
μ_G	Dynamic viscosity of gas, kg/(m·s)
μ_L	Laminar viscosity, kg/(m·s)
μ_T	Turbulent viscosity, kg/(m·s)
ν_G	Kinematic viscosity of air, m^2/s
η_{imp}	Collection efficiency of inertial impaction
η_{int}	Collection efficiency of interception
η_{diff}	Collection efficiency of Brownian diffusion
η_{total}	Total collection efficiency

frontiers in Energy Research

ORIGINAL RESEARCH
published: 05 June 2020
doi: 10.3389/fenrg.2020.00086

Development of Multi-GPU–Based Smoothed Particle Hydrodynamics Code for Nuclear Thermal Hydraulics and Safety: Potential and Challenges

*So-Hyun Park, Young Beom Jo, Yelyn Ahn, Hae Yoon Choi, Tae Soo Choi, Su-San Park, Hee Sang Yoo, Jin Woo Kim and Eung Soo Kim**

Department of Nuclear Engineering, Seoul National University, Seoul, South Korea

Advanced modeling and analysis are always essential for the development of safe and reliable nuclear systems. Traditionally, the numerical analysis codes used for nuclear thermal hydraulics and safety are mostly based on mesh-based (or grid-based) methods, which are very mature for well-defined and fixed domains, both mathematically and numerically. In support of their robustness and efficiency, they have been well-fit into many nuclear applications for the last several decades. However, the recent nuclear safety issues encountered in natural disasters and severe accidents are associated with much more complex physical/chemical phenomena, and they are frequently accompanied by highly non-linear deformations. Sometimes, this means that the conventional methods encounter many difficult technical challenges. In this sense, the recent advancement in the Lagrangian-based CFD method shows great potential as a good alternative. This paper summarizes recent activities in the development of the SOPHIA code using Smoothed Particle Hydrodynamics (SPH), a well-known Lagrangian numerical method. This code incorporates the basic conservation equations (mass, momentum, and energy) and various physical models, including heat transfer, turbulence, multi-phase flow, surface tension, diffusion, etc. Additionally, the code newly formulates density and continuity equations in terms of a normalized density in order to handle multi-phase, multi-component, and multi-resolution problems. The code is parallelized using multiple graphical process units (GPUs) through multi-threading and multi-streaming in order to reduce the high computational cost. In the course of the optimization of the algorithm, the computational performance is improved drastically, allowing large-scale simulations. For demonstration of its applicability, this study performs three benchmark simulations related to nuclear safety: (1) water jet breakup of FCI, (2) LMR core melt sloshing, and (3) bubble lift force. The simulation results are compared with the experimental data, both qualitatively and quantitatively, and they show good agreement. Besides its potential, some technical challenges of the method are also summarized for further improvement.

Keywords: Lagrangian CFD, Smoothed Particle Hydrodynamics, multi-GPU parallelization, severe accident, Fuel Coolant Interaction, LMR core sloshing

OPEN ACCESS

Edited by:
Victor Petrov,
University of Michigan, United States

Reviewed by:
Xianping Zhong,
University of Pittsburgh, United States
Jiankai Yu,
Massachusetts Institute of Technology, United States
Rahim Shamsoddini,
Sirjan University of Technology, Iran

****Correspondence:***
Eung Soo Kim
kes7741@snu.ac.kr

Specialty section:
This article was submitted to Nuclear Energy, a section of the journal Frontiers in Energy Research

Received: *12 January 2020*
Accepted: *24 April 2020*
Published: *05 June 2020*

Citation:
Park S-H, Jo YB, Ahn Y, Choi HY, Choi TS, Park S-S, Yoo HS, Kim JW and Kim ES (2020) Development of Multi-GPU–Based Smoothed Particle Hydrodynamics Code for Nuclear Thermal Hydraulics and Safety: Potential and Challenges. Front. Energy Res. 8:86. doi: 10.3389/fenrg.2020.00086

INTRODUCTION

Since the Fukushima accident, nuclear safety issues related to severe accidents [i.e., Fuel–Coolant Interaction (FCI), In-Vessel Melt Retention (IVMR), and Molten Corium Concrete Interaction (MCCI)] (Bauer et al., 1990; Sehgal et al., 1999; Ma et al., 2016; Bonnet et al., 2017) and natural disasters (i.e., tsunami, earthquake, etc.; Zhao et al., 1996; Barto, 2014) are gaining more attention than ever. These issues generally involve various physically/chemically complicated phenomena such as fluid dynamics, heat transfer, multiple phases, multiple components, diffusion, fluid–solid interaction, chemical reaction, phase change, etc., successively interacting each other. For example, when the molten core relocates to the lower head of the vessel, the hot fuel melt contacts with water coolant followed by FCI. This phenomenon includes hydraulic fragmentation, heat transfer, phase change, multi-phase flow, etc., which have the potential to trigger a steam explosion or porous debris bed formation (Allelein et al., 1999; Sehgal et al., 1999). This accident progression adds complexities to the phenomenon, such as solidification and vapor bubble dynamics. In the IVMR situation, a huge corium pool is formed at the lower head of the vessel, and it is continuously cooled by external vessel coolant. In this case, the corium pool experiences numerous observed phenomena, such as natural convection with strong turbulence, crust formation, stratification, ablation, and eutectic and focusing effects (Ma et al., 2016). In the MCCI, more complicated phenomena occur through intricate interactions between the molten fuel, concrete, and water (Bonnet et al., 2017). In such scenarios, the reactor vessel and/or containment integrity is threatened in various ways, such as by steam explosion, thermal/chemical ablation, direct impinging, and so on. In addition to the above examples, the large complexity of the physics/chemistry involved in these phenomena still leaves us with significant uncertainty in understanding and predicting reactor safety.

In recent years, advances in Computational Fluid Dynamics (CFD) have provided an opportunity to explore the nuclear thermal hydraulics and safety in more a realistic and mechanistic manner. The mesh-based numerical methods [i.e., Finite Difference Method (FDM), Finite Element Method (FEM), and Finite Volume Method (FVM)] have a long development history in many engineering fields, including nuclear engineering, and they are highly matured both mathematically and numerically. Based on their robustness and efficiency, they have dominated the CFD field for decades, and they are successfully applied in various applications. Generally, the mesh-based methods are known to be suitable for handling a pre-defined computational domain where the boundaries and interfaces are not moving. However, they suffer from difficulties in handling complex phenomena accompanied by highly non-linear deformations, which are frequently encountered in recent nuclear safety-related problems such as multi-phase flow, a free surface, and large deformation.

In order to address and handle the weaknesses of the mesh-based methods, several new methods have been proposed and developed based on a Lagrangian meshless framework (Liu and Liu, 2003; i.e., SPH, MPS, MPM, DEM, etc.). Those methods are advantageous in handling free surface flow, interfacial flow, and large deformation because the mesh or mass points are carried with the flow, possessing the properties of the material. Additionally, the interfaces or boundaries are traced naturally in the process of simulation. In this study, Smoothed Particle Hydrodynamics (SPH), which is the most widely used meshless CFD method, has been selected and used for various applications (Wang et al., 2016). The SPH method discretizes the fluid system into a set of particles (or parcels) that contain the material properties, and these particles move according to the governing equations. The most widely used SPH method is the Weakly Compressible SPH (WCSPH) method, which allows slight compressibility, even for liquid fluids, using an equation of state (EOS). In this method, the basic conservation equations such as for mass, momentum, and energy conservation are solved with various physical models of heat transfer, turbulence, multi-phase flow, phase change, diffusion, etc. (Jo et al., 2019). Many recent studies showed that the SPH methodology has very good potential for handling complicated phenomena in nuclear engineering and other engineering fields (Wang et al., 2016; Park et al., 2018; Jo et al., 2019).

Although many successful studies on the SPH have been reported, the SPH methodology has high computational cost, like other particle-based methods, for many reasons. In this regard, the SPH method suffers from the limitation of the simulation time and size (Valdez-Balderas et al., 2013; Nishiura et al., 2015; Guo et al., 2018). Therefore, enhancing its computational performance efficiently and effectively is essential to make this method more practical and useful. Recently, massive parallel-computer-system-based techniques have been actively employed to address this issue, such as the multi-core Central Processing Unit (CPU), Graphics Processing Unit (GPU), and Many Integrated Core (MIC) processor (Nishiura et al., 2015). Such techniques demonstrate high computational performance by executing computations in parallel. In particular, the GPU, which was originally designed for graphical data processing, is increasingly being used in parallel computing in general engineering and science because of the efficiency arising by having thousands of computing cores. These general-purpose GPUs (GPGPU) are generally suitable for high-throughput computations featuring data-parallelism. Therefore, GPU-based parallelization is strongly advocated for and preferred in the SPH method, which consists of highly linear numerical expressions

Abbreviations: AOS, Array of Structure; CFD, Computational Fluid Dynamics; CPU, Central Processing Unit; CSF, Continuum Surface Force; CSPM, Corrective Smoothed Particle Method; δ-SPH, Delta-Smoothed Particle Hydrodynamics; EOS, Equation of State; FCI, Fuel–Coolant Interaction; FDM, Finite Difference Method; FEM, Finite Element Method; FPM, Finite Particle Method; FVM, Finite Volume Method; GPGPU, General Purpose Graphics Processing Unit; GPU, Graphics Processing Unit; IPF, Inter-molecular Potential Force; IS, Interface Sharpness; ISPH, Incompressible Smoothed Particle Hydrodynamics; IVMR, In-Vessel Melt Retention; KGC, Kernel Gradient Correction; KGF, Kernel Gradient Free; LES, Large Eddy Simulation; LMR, Liquid Metal Reactor; LWR, Light Water Reactor; MCCI, Molten Corium Concrete Interaction; MIC, Many Integrated Core; NNPS, Nearest Neighbor Particle Search; P2P, Peer-to-Peer (GPU-to-GPU); RANS, Reynolds Average Navier-Stokes; RHS, Right-Hand Side; SPH, Smoothed Particle Hydrodynamics; SPS, Sub-Particle Scale; WCSPH, Weakly Compressible Smoothed Particle Hydrodynamics.

that can be computed independently one by one (Valdez-Balderas et al., 2013).

The SOPHIA code is an SPH-based numerical code developed by Seoul National University (SNU) for conducting simulations of nuclear thermal hydraulics and safety (Jo et al., 2019). The original SOPHIA code was written in C++ and parallelized using a single GPU. The main physics behind this code includes (1) liquid flow, (2) heat transfer, (3) melting/solidification, (4) natural convection, (5) multi-phase flow, etc. In this study, the physical models and numerical methods of the SOPHIA code have been highly improved in order to simulate the phenomena accurately. Moreover, the code has been parallelized using multiple GPUs to obtain high-resolution and large-scale simulations for more practical applications. This parallelization has been implemented through multi-threading and multi-streaming. The multi-threading technique divides the computational domain into GPUs and then executes the GPUs concurrently. The multi-streaming technique effectively schedules computing tasks within each GPU. Based on these techniques, the SOPHIA code has achieved a drastic improvement in computational performance. To demonstrate its capability and applicability, this study performs simulations on three different benchmark experiments related to nuclear safety: (1) water jet breakup of FCI, (2) Liquid Metal Reactor (LMR) core sloshing, and (3) bubble lift force. The simulation results are then compared with experimental data, both qualitatively and quantitatively.

This paper summarizes the overall features of the newly developed SOPHIA code, including its governing equations, algorithms, and parallelization methods, along with benchmark simulations. Section Smoothed Particle Hydrodynamics (SPH) describes the basic SPH concepts and the physical models implemented in the code. Section Code Implementation explains the parallelization techniques used for multiple GPU computation. Section Benchmark Analysis presents three benchmark simulations with some validations. Section Summary and Conclusion summarizes and concludes this study.

SMOOTHED PARTICLE HYDRODYNAMICS (SPH)

Smoothed Particle Hydrodynamics (SPH) is a computational method used for simulating the mechanics of continuum media based on a Lagrangian meshless framework. It was first developed by Gingold and Monaghan (1977) and Lucy (1977) for astrophysics. In recent years, it has been extended to many other research fields such as mechanical engineering, ocean engineering, chemical engineering, and nuclear engineering. Since SPH is a mesh-free method, it is ideal for simulating phenomena dominated by complicated boundary dynamics like free surface flows or with large boundary deformations. In addition, this method simplifies the model implementation and parallelization. This section briefly summarizes the basic concepts of SPH and how the basic conservation laws and physical models are constructed for nuclear thermal-hydraulics and safety applications.

Fundamentals of SPH

Mathematically, SPH approximation is based on the theory of integral interpolants using a delta function.

$$f(\boldsymbol{r}) = \int_{\Omega} f(\boldsymbol{r}')\,\delta(\boldsymbol{r}-\boldsymbol{r}')\,d\boldsymbol{r}' \tag{1}$$

where the variable r denotes the point vector in infinite volume domain Ω, and δ denotes the Dirac delta function, which has a value of zero everywhere except for at a certain point, and whose integral over the entire region is equal to one. Although Equation (1) is mathematically valid, it is numerically difficult to handle due to the discontinuity of the delta function. Therefore, the basic idea of SPH is to approximate the Dirac delta function using a continuous kernel function and discretize the integral by summation (Monaghan, 1992).

$$f(\boldsymbol{r}_i) = \sum\nolimits_j \frac{m_j}{\rho_j} f(\boldsymbol{r}_j)\, W(\boldsymbol{r}_i - \boldsymbol{r}_j, h) \tag{2}$$

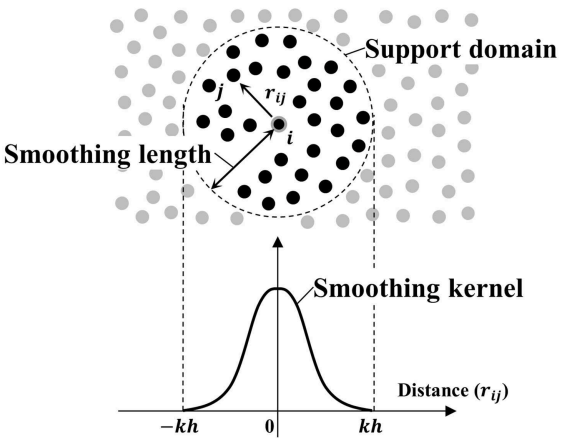

Conditions for Kernel Function

Unity	$\int_{-\infty}^{\infty} W(\boldsymbol{r}_{ij}, h)dr = 1$
Symmetry	$W(\boldsymbol{r}_{ij}, h) = W(-\boldsymbol{r}_{ij}, h)$
Delta function Property	$\lim_{h\to 0} W(\boldsymbol{r}_{ij}, h) = \delta(\boldsymbol{r}_{ij})$
Compact	$W(\boldsymbol{r}_{ij}, h) = 0, \quad for\ \lvert\boldsymbol{r}_{ij}\rvert > kh$
Monotonic Decrease	$\frac{\partial}{\partial \boldsymbol{r}} W(\boldsymbol{r}, h) < 0$
Positive	$W(r_{ij}, h) \geq 0$
Sufficiently Smooth	

FIGURE 1 | Schematic diagram of SPH kernel approximation.

TABLE 1 | Commonly used SPH kernel functions $\left(R = \frac{|\boldsymbol{r}-\boldsymbol{r}'|}{h}, \quad R^* = \frac{|\boldsymbol{r}-\boldsymbol{r}'|}{2h}\right)$.

Kernel function	Formulation
Gaussian (Gingold and Monaghan, 1977)	$W(R,h) = \begin{cases} \frac{1}{(\pi^{0.5}h)} e^{-R^2} & \text{for 1D} \\ \frac{1}{(\pi^{0.5}h)^2} e^{-R^2} & \text{for 2D} \\ \frac{1}{(\pi^{0.5}h)^3} e^{-R^2} & \text{for 3D} \end{cases}$
Quartic (Liu et al., 2003)	$W(R,h) = \begin{cases} \frac{1}{h}\left(\frac{2}{3} - \frac{9}{8}R^2 + \frac{19}{24}R^3 - \frac{5}{32}R^4\right) & \text{for 1D} \\ \frac{15}{7\pi h^2}\left(\frac{2}{3} - \frac{9}{8}R^2 + \frac{19}{24}R^3 - \frac{5}{32}R^4\right) & \text{for 2D} \\ \frac{315}{208\pi h^3}\left(\frac{2}{3} - \frac{9}{8}R^2 + \frac{19}{24}R^3 - \frac{5}{32}R^4\right) & \text{for 3D} \end{cases}$
Wendland C2 (Dehnen and Aly, 2012)	$W(R^*,h) = \begin{cases} \frac{5}{4(2h)}\left(1-R^*\right)^3\left(1+3R^*\right) & \text{for 1D} \\ \frac{7}{\pi\,(2h)^2}\left(1-R^*\right)^4\left(1+4R^*\right) & \text{for 2D} \\ \frac{21}{2\pi\,(2h)^3}\left(1-R^*\right)^4\left(1+4R^*\right) & \text{for 3D} \end{cases}$

where m and ρ denote the particle mass and particle density. The subscripts i and j denote center particle and neighboring particle, respectively. $W\left(\boldsymbol{r}_i - \boldsymbol{r}_j,\ h\right)$ stands for the kernel function, where h denotes the influencing area of the kernel weighting function. The kernel function is a symmetric weighting function of particle distance that should be normalized over its support domain. The particle system and conditions for kernel function are described in **Figure 1**. This kernel determines the weight of a certain particle at r_j with regard to the distance from the center (r_i) (Liu and Liu, 2003). **Table 1** summarizes the kernel functions that are commonly used. This study applied the Wendland C2 kernel (Dehnen and Aly, 2012), which helps to maintain low numerical instability.

Spatial derivatives of a function can also be simply approximated in a similar way by taking derivatives of a kernel function as follows (Monaghan, 1992).

$$\nabla f\left(\boldsymbol{r}_i\right) = \sum\nolimits_j V_j f\left(\boldsymbol{r}_j\right) \nabla W\left(\boldsymbol{r}_i - \boldsymbol{r}_j, h\right) \tag{3}$$

$$\nabla \cdot f\left(\boldsymbol{r}_i\right) = \sum\nolimits_j V_j f\left(\boldsymbol{r}_j\right) \nabla \cdot W\left(\boldsymbol{r}_i - \boldsymbol{r}_j, h\right) \tag{4}$$

$$\nabla^2 f\left(\boldsymbol{r}_i\right) = \sum\nolimits_j V_j f\left(\boldsymbol{r}_j\right) \nabla^2 W\left(\boldsymbol{r}_i - \boldsymbol{r}_j, h\right) \tag{5}$$

where $V_j = \frac{m_j}{\rho_j}$ denotes the particle volume. When the particles are distributed uniformly in space, the SPH approximations of scalar function and its derivatives ensure the second-order accuracy (Liu and Liu, 2003). However, an irregular particle distribution or truncation near the free surface causes numerical errors (Belytschko et al., 1996). Such particle-domain-induced problems, referred to as particle inconsistency, influence the accuracy of the simulation profoundly. In order to restore the particle inconsistency and improve the accuracy, various methods have been proposed. For the scalar approximation, applying a Shepard filter is the most well-known method to restore the particle inconsistency (Randles and Libersky, 1996).

$$f\left(\boldsymbol{r}_i\right) = \frac{\sum_j f\left(\boldsymbol{r}_j\right) W\left(\boldsymbol{r}_i - \boldsymbol{r}_j, h\right) V_j}{\sum_j W\left(\boldsymbol{r}_i - \boldsymbol{r}_j, h\right) V_j} \tag{6}$$

This Shepard filter normalizes the kernel to correct the underestimated contributions of particle deficiency. For the derivative approximation, the following Kernel Gradient Correction (KGC) is commonly applied (Bonet and Lok, 1999).

$$\nabla f\left(\boldsymbol{r}_i\right) = \sum\nolimits_j f\left(\boldsymbol{r}_j\right) L_i \nabla W\left(\boldsymbol{r}_i - \boldsymbol{r}_j, h\right) V_j \tag{7}$$

$$L_i = \begin{bmatrix} \sum_j \left(x_j - x_i\right) W_x V_j & \sum_j \left(y_j - y_i\right) W_x V_j & \sum_j \left(z_j - z_i\right) W_x V_j \\ \sum_j \left(x_j - x_i\right) W_y V_j & \sum_j \left(y_j - y_i\right) W_y V_j & \sum_j \left(z_j - z_i\right) W_y V_j \\ \sum_j \left(x_j - x_i\right) W_z V_j & \sum_j \left(y_j - y_i\right) W_z V_j & \sum_j \left(z_j - z_i\right) W_z V_j \end{bmatrix}^{-1} \tag{8}$$

where $\left[W_x, W_y, W_z\right] = \nabla W$. This KGC filter is incorporated into the original kernel derivative to re-evaluate the contributions of irregularly distributed particles. Other than the above correction methods, more sophisticated kernel approximation schemes for SPH have been proposed by several researchers. They include the Corrective Smoothed Particle Method (CSPM), Finite Particle Method (FPM), and Kernel Gradient Free (KGF). They all aim to resolve the particle inconsistency caused by particle truncation at the boundaries as well as irregular particle distribution. The details can be found in the Bonet and Lok (1999), Chen and Beraun (2000), Liu and Liu (2006), and Huang et al. (2016).

Governing Equations of the SOPHIA Code

The SOPHIA code consists of three basic conservation laws (mass, momentum, and energy conservations), which are

expressed as follows in a Lagrangian manner.

$$\text{Continuity Equation}: \frac{d\rho}{dt} = -\rho\nabla\cdot\boldsymbol{u} \tag{9}$$

$$\text{Navier}-\text{Stokes Equation}: \frac{d\boldsymbol{u}}{dt} = -\frac{\nabla p}{\rho} + \nu\nabla^2\boldsymbol{u} + \boldsymbol{g} + \boldsymbol{f}_{ext} \tag{10}$$

$$\text{1st Law of Thermodynamics}: \frac{dh}{dt} = -\frac{\lambda}{\rho}\nabla^2 T + \dot{q} \tag{11}$$

where $\boldsymbol{u}, p, \nu, \boldsymbol{g}$, f_{ext}, h, λ, T, and $\dot{q}$ denote the velocity vector, pressure, kinematic viscosity, gravitational acceleration, external body force, specific enthalpy, thermal conductivity, temperature, and heat generation rate, respectively. In the SOPHIA code, these equations are formulated in SPH as described in section Fundamentals of SPH.

Continuity Equation (Mass Conservation)

The SOPHIA code is based on the conventional weakly compressible SPH (WCSPH) (Gingold and Monaghan, 1977; Lucy, 1977; Monaghan, 1992), which allows slight compressibility for liquid according to the given equation of state (EOS). Therefore, the density estimation is very important for predicting pressure in the fluid flow. The SOPHIA code estimates the density by either direct mass summation or a continuity equation (Monaghan, 1992). In the direct mass summation, the density is estimated by the following SPH kernel approximation.

$$\rho_i = \sum\nolimits_j m_j W\left(\boldsymbol{r}_i - \boldsymbol{r}_j,\ h\right) \tag{12}$$

Although Equation (12) is the most commonly used formulation in the WCSPH, it frequently suffers from an over-smoothing problem for the density near an interface or a large-density-gradient field, which is easily encountered in multi-component/multi-fluid/multi-phase flows. In this case, the over-smoothed density becomes the main source of numerical error/instability by generating unphysical pressure force near the interface (Hu and Adams, 2006). To avoid this issue, the SOPHIA code adapts the newly proposed formulation, which is derived based on the normalized density as follows (Park et al., 2019).

$$\frac{\rho_i}{\rho_{ref,i}} = \sum\nolimits_j \frac{m_j}{\rho_j}\left(\frac{\rho_j}{\rho_{ref,j}}\right) W_{ij} \tag{13}$$

where ρ_{ref} denotes the reference density of the particle and $W_{ij} = W\left(\mathbf{r}_i - \mathbf{r}_j,\ h\right)$. Numerically, this new equation can eliminate the density smoothing problem without any numerical treatments or additional issues. As mentioned above, the density of the fluid can also be evaluated by solving a continuity equation. The continuity equation in the SOPHIA code is expressed as follows.

$$\left(\frac{d\rho}{dt}\right)_i = -\rho_i \sum\nolimits_j \frac{m_j}{\rho_j}\left(u_i - u_j\right)\cdot\nabla_i W_{ij} + \xi h c_0 \sum\nolimits_j \frac{m_j}{\rho_j}\psi_{ij}\cdot\nabla_i W_{ij} \tag{14}$$

where ξ, c_0 denote the diffusion intensity coefficient, speed of sound and $\nabla_i W_{ij} = \frac{\partial W(\boldsymbol{r}_i - \boldsymbol{r}_j, h)}{\partial r_i}$. In this formulation, an artificial density diffusion term (the last term on the RHS), which is called δ-SPH, is added to remove high-frequency numerical pressure noise (Molteni and Colagrossi, 2009). The diffusion coefficient in Equation (14) is recommended to be set as $(0 < \xi \leq 0.2)$. Determination of the variable ψ_{ij} is proposed by several studies. In the SOPHIA code, the method proposed by Antuono et al. (2010) is used, as follows.

$$\psi_{ij} = 2\left(\rho_i - \rho_j\right)\frac{\boldsymbol{r}_{ij}}{|\boldsymbol{r}_{ij}|} - \left[\sum\nolimits_j V_j\left(\rho_j - \rho_i\right) L_i\nabla_i W_{ij} + \sum\nolimits_k V_k\left(\rho_k - \rho_j\right) L_j\nabla_j W_{jk}\right] \tag{15}$$

where L denotes KGC kernel correction as mentioned in section Fundamentals of SPH. The subscripts j and k denote the neighboring particle of particle i (main particle) and the neighboring particle of particle j (neighbor of the main particle), respectively. The continuity equation can also be re-formulated in terms of the normalized density as in the direct mass summation (Park et al., 2019).

$$\left(\frac{d\rho}{dt}\right)_i = -\rho_i \sum\nolimits_j \frac{m_j}{\rho_j}\boldsymbol{u}_{ij}\cdot\nabla_i W_{ij} + \left(\frac{\rho}{\rho_{ref}}\right)_i\left(\frac{d\rho_{ref}}{dt}\right)_i + \xi h c_0 \sum\nolimits_j \frac{m_j}{\rho_j}\psi_{nd,ij}\cdot\nabla_i W_{ij} \tag{16}$$

$$\psi_{nd,ij} = 2\rho_{ref,\,i}\left(\frac{\rho_i}{\rho_{ref,i}} - \frac{\rho_j}{\rho_{ref,j}}\right)\frac{\boldsymbol{r}_{ij}}{|\boldsymbol{r}_{ij}|} - \left[\rho_{ref,i}\nabla\left(\frac{\rho}{\rho_{ref}}\right)_i^L + \rho_{ref,j}\nabla\left(\frac{\rho}{\rho_{ref}}\right)_j^L\right] \tag{17}$$

$$\rho_{ref,i}\nabla\left(\frac{\rho}{\rho_{ref}}\right)_i^L = \rho_{ref,i}\sum\nolimits_j V_j\left(\frac{\rho_j}{\rho_{ref,j}} - \frac{\rho_i}{\rho_{ref,i}}\right) L_i\nabla_i W_{ij} \tag{18}$$

where $\boldsymbol{u}_{ij} = \boldsymbol{u}_i - \boldsymbol{u}_j$ and the variable $\psi_{nd,ij}$ denotes a normalized-density formulated diffusion term. Equation (16) consists of a mass transport term, a reference density time derivative term (derived only from mass variation), and a density diffusive term. The mass transport term is equivalent to the original continuity equation. The time derivative term can be explicitly calculated by the chain rule. The normalized δ-SPH term diffuses out the numerical noise of the normalized density $\left(\frac{\rho}{\rho_{ref}}\right)$, while the original model diffuses out the density itself. This normalized continuity equation can achieve the same improvement as the new mass summation (Equation 13). These newly devised equations (Equations 13, 16) estimate the density ratio that would be applied in EOS, thus addressing the density-smoothing problem. In the case of a uniform density field, these formulations exactly converge to the conventional SPH density equations.

TABLE 2 | Pressure and viscous force models.

Physical model	Formulation	
Pressure force (Monaghan, 1992; Liu and Liu, 2003; Sun et al., 2017)	$\left(\frac{d\boldsymbol{u}}{dt}\right)_i = -\sum_j m_j \left(\frac{p_i}{\rho_i^2} + \frac{p_j}{\rho_j^2}\right) \nabla_i W_{ij}$	(20)
	$\left(\frac{d\boldsymbol{u}}{dt}\right)_i = -\sum_j m_j \frac{(p_i+p_j)}{\rho_i \rho_j} \nabla_i W_{ij}$	(21)
	$\left(\frac{d\boldsymbol{u}}{dt}\right)_i = -\sum_j m_j \frac{(p_j-p_i)}{\rho_i \rho_j} \nabla_i W_{ij}$	(22)
Viscous force (Morris et al., 1997; Cleary, 1998; Hu and Adams, 2006)	$\left(\frac{du}{dt}\right)_i = \frac{1}{m_i} \sum_j \frac{2\mu_i \mu_j}{(\mu_i+\mu_j)} \left(\frac{m_i^2}{\rho_i^2} + \frac{m_j^2}{\rho_j^2}\right) \boldsymbol{u}_{ij} \frac{\boldsymbol{r}_{ij}}{\lvert\boldsymbol{r}_{ij}\rvert^2} \cdot \nabla W_{ij}$	(23)
	$\left(\frac{du}{dt}\right)_i = \sum_j \frac{m_j(\mu_i+\mu_j)}{\rho_i \rho_j} \boldsymbol{u}_{ij} \frac{\boldsymbol{r}_{ij}}{\lvert\boldsymbol{r}_{ij}\rvert^2} \cdot \nabla W_{ij}$	(24)
	$\left(\frac{du}{dt}\right)_i = \sum_j \frac{4m_j}{\rho_i \rho_j} \frac{\mu_i \mu_j}{(\mu_i+\mu_j)} \boldsymbol{u}_{ij} \frac{\boldsymbol{r}_{ij}}{\lvert\boldsymbol{r}_{ij}\rvert^2} \cdot \nabla W_{ij}$	(25)

Navier-Stokes Equation (Momentum Conservation)

The momentum conservation (Equation 10) can be decomposed into several individual terms: pressure force, viscous force, gravitational force, and external force. The following is the basic SPH form of the momentum equation used in the SOPHIA code.

$$\left(\frac{du}{dt}\right)_i = -\sum_j m_j \frac{(p_i + p_i)}{\rho_i \rho_j} \nabla_i W_{ij} + \sum_j \frac{4m_j}{\rho_i \rho_j} \frac{\mu_i \mu_j}{(\mu_i + \mu_j)} \boldsymbol{u}_{ij} \frac{r_{ij}}{\left|r_{ij}\right|^2} \cdot \nabla W_{ij} + \mathbf{g} + \mathbf{f}_{ext} \quad (19)$$

where μ denotes the viscosity involving laminar and turbulence effects, and $\boldsymbol{u}_{ij} = \boldsymbol{u}_i - \boldsymbol{u}_j$. As mentioned in many SPH studies (Monaghan, 1992, 1994; Liu and Liu, 2003; Wang et al., 2016), there are various different ways to convert mathematical equations into SPH formulations.

Table 2 summarizes the SPH-formulated models for pressure force and laminar viscous force. The pressure force model (Equation 20), first proposed by Monaghan (1992), was derived from the Euler-Lagrangian equations. This pairwise symmetric model ensures the linear momentum conservation inherently, but it calculates an unphysical pressure gradient at the interfaces of different fluids (density) like multi-phase flow. To handle the discontinuity of multi-phase flow, a new pressure force model (Equation 21) was suggested by Liu and Liu (2003). This equation not only satisfies pairwise symmetricity but also estimates the pressure gradient based on the particle volume so that physically valid pressure forces are obtained for the discontinuous density field. However, near the free surface, where the particle pressure generally oscillates around zero, the negative pressure causes this model to calculate an unphysical repulsive force, which leads to numerical instability. To address this issue, the minus-signed model (Equation 22) was proposed by Sun et al. (2017). This pressure force model eliminates the unphysical force near the free surface, but it should only be applied to the particles close to the free surface. Laminar viscous force models have also been developed in a similar manner to pressure force models. Particularly, the viscous force models vary in their way of treating viscosity. At the interfaces where the particle viscosities are different such as in multi-phase or multi-fluids, both Equations (23) and (25) employ a harmonic mean, while Equation (24) employs an arithmetic mean value. On the other hand, all the viscous models are valid for a discontinuous density field, because they calculate the force based on the particle volume. Finally, Equation (19) is selected to be well-suited for multi-phase/multi-fluid flow simulations.

1st Law of Thermodynamics (Energy Conservation)

For non-radiative, homogeneous, and isotropic energy conservation, heat transfer is mainly subject to conduction and convection. In a Lagrangian framework, the convective heat transfer can be resolved inherently, and therefore energy conservation is simply expressed by the following (Monaghan, 2005).

$$\left(\frac{dh}{dt}\right)_i = \sum_j \frac{4m_j}{\rho_i \rho_j} \left(\frac{\lambda_i \lambda_j}{\lambda_i + \lambda_j}\right) \left(T_i - T_j\right) \frac{\boldsymbol{r}_{ij}}{\left|\boldsymbol{r}_{ij}\right|^2} \cdot \nabla W_{ij} + \dot{q}_i \quad (26)$$

where h, λ, T, and $\dot{q}$ denote the specific enthalpy, thermal conductivity, temperature, and heat source, respectively. The heat source or heat flux of boundary conditions is represented as the source term of energy conservation. In the SPH method, these source terms are modeled as a specific heat rate, and they are exerted on the particles that are involved.

Equation of State

In the WCSPH, the pressure of the fluid is evaluated by an equation of state (EOS). The most commonly used EOS is Tait's equation (Monaghan, 1994). In the SOPHIA code, the modified form is implemented in terms of reference density as follows.

$$p_i = \frac{{c_0}^2 \rho_{ref,i}}{\gamma} \left[\left(\frac{\rho_i}{\rho_{ref,i}}\right)^{\gamma} - 1\right] \quad (27)$$

where c_0, ρ_{ref}, and γ denote the speed of sound, reference density, and EOS stiffness parameter, respectively; γ is recommended to be set as $(1 \leq \gamma \leq 7)$. This equation calculates the pressure based on the density ratio between the particle density and the reference density, which allows a slight volume compression for liquid fluids.

Turbulence

As in the conventional CFD methods, the turbulence models in the SPH are divided into two groups: (1) Reynolds Average Navier-Stokes (RANS)-based models and (2) Large Eddy Simulation (LES)-based models. In the SOPHIA code, both models are implemented. In the case of a RANS-based k-ϵ model (Violeau and Issa, 2007), the viscous force of the fluid flow is calculated by considering both laminar and turbulence viscous effects as follows.

$$\left(\frac{d\boldsymbol{u}}{dt}\right)_i^{turb} = \sum_j \frac{m_j}{\rho_i \rho_j} \frac{4\mu_{e,i}\,\mu_{e,j}}{\left(\mu_{e,i}+\mu_{e,j}\right)} \boldsymbol{u}_{ij} \frac{\boldsymbol{r}_{ij}\cdot\nabla W_{ij}}{\left|\boldsymbol{r}_{ij}\right|^2} \tag{28}$$

$$\mu_e = \mu_\nu + \mu_T, \qquad \mu_T = \frac{\rho C_\mu k^2}{\epsilon} \tag{29}$$

where μ_ν, μ_T, C_μ, k, and ϵ denote laminar viscosity (material property), turbulent viscosity, turbulent viscous coefficient, turbulence kinetic energy, and turbulent dissipation rate, respectively. The turbulence kinetic energy and the dissipation rate are estimated by solving transport equations. The transport equation for the turbulence kinetic energy is expressed by

$$\left(\frac{dk}{dt}\right)_i = P_i - \epsilon_i + \sum_j \frac{m_j}{\rho_i \rho_j}\left(\mu_{k,i}+\mu_{k,j}\right) k_{ij} \frac{\boldsymbol{r}_{ij}\cdot\nabla W_{ij}}{\left|\boldsymbol{r}_{ij}\right|^2} \tag{30}$$

$$\mu_k = \mu_\nu + \frac{\mu_T}{\sigma_k} \tag{31}$$

where $k_{ij} = k_i - k_j$ and $\sigma_k = 1.0$. The RHS of the above equation consists of turbulence production (P), turbulence dissipation (ϵ), and turbulence diffusion terms. The production of turbulence kinetic energy is calculated by the strain tensor of the time-averaged velocity, and the dissipation rate is calculated by solving the transport equation as follows.

$$\left(\frac{d\epsilon}{dt}\right)_i = \frac{\epsilon_i}{k_i}\left(C_{\epsilon,1}P_i - C_{\epsilon,2}\epsilon_i\right) + \sum_j \frac{m_j}{\rho_i \rho_j}\left(\mu_{\epsilon,i}+\mu_{\epsilon,j}\right)\epsilon_{ij}\frac{\boldsymbol{r}_{ij}\cdot\nabla W_{ij}}{\left|\boldsymbol{r}_{ij}\right|^2} \tag{32}$$

$$\mu_\epsilon = \mu_\nu + \frac{\mu_T}{\sigma_\epsilon} \tag{33}$$

where $C_{\epsilon,1}$ and $C_{\epsilon,2}$ denote the constant coefficients and $\sigma_\epsilon = 1.3$. The Sub-Particle Scale (SPS) turbulence model, based on LES, is commonly employed in the SPH simulations (Rogers and Dalrymple, 2008). The Smagorinsky model, the basis of the SPS model, formulates the eddy viscosity as the product of the characteristic length scale and the strain rate tensor, which is defined by time-averaged velocity. In the SPH formulation, the SPS model is expressed as follows (Rogers and Dalrymple, 2008; Zhang et al., 2017).

$$\nu_{SPS} = \left(C_s l\right)^2 \left|\boldsymbol{S}^{\alpha\beta}\right| \tag{34}$$

$$\boldsymbol{S}^{\alpha\beta} = \frac{1}{2}\left[\sum_j \frac{m_j}{\rho_j}\left(u_j^\alpha - u_i^\alpha\right)\frac{\partial W_{ij}}{\partial r_i^\beta} + \sum_j \frac{m_j}{\rho_j}\left(u_j^\beta - u_i^\beta\right)\frac{\partial W_{ij}}{\partial r_i^\alpha}\right] \tag{35}$$

where l and C_s denote the particle spacing and the pre-defined coefficient. $\mathbf{S}^{\alpha\beta}$ denotes the strain rate tensor in the Einstein notation ($\alpha,\ \beta = 1,2,3$) and $\left|\mathbf{S}^{\alpha\beta}\right| = \sqrt{2S:S}$. In this model, the smallest turbulence scale is modeled as a sub-particle-scale stress tensor that includes the interactions at all scales (resolved scale, unresolved scale, and cross-scale). The turbulence viscous force of the SPS model is added to the momentum equation.

$$\left(\frac{d\boldsymbol{u}}{dt}\right)_i^{turb} = \sum_j m_j\left(\frac{\tau_i^{\alpha\beta}}{\rho_i^2} + \frac{\tau_j^{\alpha\beta}}{\rho_j^2}\right)\cdot\nabla W_{ij} \tag{36}$$

$$\boldsymbol{\tau}^{\alpha\beta} = \rho\left(2\nu_T \boldsymbol{S}^{\alpha\beta} - \frac{2}{3}\boldsymbol{S}^{rr}\delta^{\alpha\beta}\right) - \frac{2}{3}\rho C_I \Delta l^2 \delta^{\alpha\beta} \tag{37}$$

where $\boldsymbol{\tau}^{\alpha\beta}$ and $\boldsymbol{\delta}^{\alpha\beta}$ denote the sub-particle scale stress tensor and the Kronecker delta in the Einstein notation, respectively ($\alpha,\ \beta,\gamma = 1,2,3$).

Molecular Diffusion

In the SOPHIA code, the molecular diffusion of the chemical components is formulated similarly to the heat transfer model (Monaghan, 2005).

$$\left(\frac{dS}{dt}\right)_i = \sum_j \frac{4m_j}{\rho_i \rho_j}\left(\frac{D_i D_j}{D_i + D_j}\right)\left(S_i - S_j\right)\frac{\boldsymbol{r}_{ij}\cdot\nabla W_{ij}}{\left|\boldsymbol{r}_{ij}\right|^2} \tag{38}$$

where D and S denote the molecular diffusivity and molecular concentration, respectively. It is noted that the above equation is based on the molecular concentration, and if the other definition for concentration is used, the diffusivity should be incorporated within it. When binary diffusion (material A and B) is involved, the reference density time derivative term $\left(\frac{d\rho_{ref}}{dt}\right)_i$ in the continuity equation (Equation 16) can be expressed as follows using molar fraction (Park et al., 2019).

$$\left(\frac{d\rho_{ref}}{dt}\right)_i = \chi_i \sum_j \frac{m_j}{\rho_i \rho_j}\left[\frac{4D_i D_j}{D_i + D_j}\right] x_{ij}\nabla_i W_{ij} \tag{39}$$

$$\chi_i = \rho_{ref,i}^2\left(\frac{1}{\rho_A} - \frac{1}{\rho_B}\right)\left(\frac{M_A M_B}{\left(xM_A + (1-x)M_B\right)^2}\right) \tag{40}$$

where M and x denote the molar mass and molar fraction. The coefficient χ describes the conversion from a molar fraction (Δx) to a mass fraction.

Buoyancy Force

Buoyancy force is considered in the SOPHIA code in two ways: (1) a Boussinesq model, and (2) a Non-Boussinesq model. The Boussinesq model is the most commonly used in the conventional SPH simulations. It assumes a slight density variation ($\Delta\rho \ll \rho$) of the fluid, which ensures that the density has a negligible effect on the main flow (Boussinesq approximation). Therefore, it is straightforward to apply the model by adding the following buoyancy force term to the momentum equation (Equation 19).

$$\left(\frac{d\boldsymbol{u}}{dt}\right)_i^{fb} = \left(1 - \alpha_T\left(T - T_0\right)\right)\boldsymbol{g} \tag{41}$$

where fb, α_T, and T_0 denote the buoyancy force, thermal expansion coefficient, and reference temperature, respectively. This Boussinesq model is simple to apply, and the results are relatively good. However, the model reliability is significantly reduced when the density variation is spatially large. For a large density gradient, a non-Boussinesq model, which is applicable for SPH, has been developed and adopted for the SOPHIA code (Park et al., 2019). In this model, the density change is directly estimated by mass and volume changes of particles, which are determined by temperature and concentration as follows.

$$m_i = m_{0,i}\left(1+\alpha_S\left(S-S_0\right)\right) \tag{42}$$

$$V_i = V_{0,i}\left(1-\alpha_T\left(T_i-T_0\right)\right)^{-1} \tag{43}$$

$$\rho_{ref,i} = \frac{m_i}{V_i} \tag{44}$$

where α_T, α_S, T_0, and S_0 denote thermal expansion coefficient, saline contraction coefficient, initial temperature, and initial concentration, respectively. m_0 and V_0 denote the initial particle mass and initial particle volume, respectively. In this model, the mass, volume, and reference density of the particles are updated in every time step. The resultant reference density is used in the pressure calculation of the EOS (Equation 27). This approach not only allows large density-gradient-driven flow beyond the Boussinesq approximation but also represents the real physics more properly.

Surface Tension

In the SOPHIA code, two types of surface tension models are employed: (1) a Continuum Surface Force (CSF) model, and (2) an Intermolecular Potential Force (IPF) model. The CSF model estimates the surface tension force at the macroscopic scale. In this model, the surface tension force is expressed as the product of the surface curvature and the surface normal (Brackbill et al., 1992). According the previous studies (Morris, 2000; Hu and Adams, 2006), there are several ways to determine the curvature and surface normal, and the SOPHIA code adopted the following forms.

$$\left(\frac{du}{dt}\right)_i^{CSF} = -\frac{\sigma_i}{\rho_i}\kappa_i \boldsymbol{n}_i \tag{45}$$

$$\boldsymbol{n}_i = \sum_j \frac{1}{V_i}\left(V_i^2+V_j^2\right)c_{ij}\nabla W_{ij} \tag{46}$$

$$\kappa_i = -d\frac{\sum_j V_j\left(\hat{\boldsymbol{n}}_i-\varphi_{ij}\hat{\boldsymbol{n}}_j\right)\cdot\nabla W_{ij}}{\sum_j V_j\left|r_{ij}\right|\left|\nabla W_{ij}\right|} \tag{47}$$

$$c_{ij} = \begin{cases} 0 & for\ f_i = f_j \\ \frac{\rho_i}{\rho_i+\rho_j} & for\ f_i \neq f_j \end{cases}, \quad \varphi_{ij} = \begin{cases} 1 & for\ f_i = f_j \\ -1 & for\ f_i \neq f_j \end{cases} \tag{48}$$

where σ, κ, $\boldsymbol{n}$, and d denote a surface tension coefficient, the curvature, surface-normal vector, and dimension, respectively $\left(d=1,2,3\right)$. $\hat{\boldsymbol{n}}_i$ denotes the unit surface-normal vector. The notation $f_i = f_j$ means that the phase of the fluid particle "i" is the same as that of particle "j," and $f_i \neq f_j$ means the opposite case.

In the IPF model (Tartakovsky and Meakin, 2005), the interaction between particle i and neighboring j is considered in terms of molecular dynamics, such as repulsive force for short range and attractive force for long range. The combination of these forces naturally determines the interfacial particle distance. Therefore, calculations of curvature and surface normal are not required. In addition, the wettability effect can be estimated straightforwardly. This model is applied to the momentum equation (Equation 19) as an additional particle interaction force.

$$\left(\frac{d\boldsymbol{u}}{dt}\right)_i^{IPF} = -\frac{1}{m_i}\sum_j f_{ij} \tag{49}$$

where f_{ij} denotes inter-particle force between particle i and its neighbor j. Many previous studies have developed various different forms of the inter-particle force. **Table 3** summarizes some of them.

Multi-Phase Flow

Multi-phase phenomena are frequently encountered in nuclear thermal-hydraulics and safety issues. Since the SPH method is based on the Lagrangian framework, no surface detection or tracking method is necessary, which is essential for Eulerian-based CFD methods. Therefore, handling multi-phase flow with SPH is relatively simple and easy compared to the conventional Eulerian-based methods. The SOPHIA code has carefully adopted and organized the governing equations based on first principle in order to capture the multi-phase physics. Nevertheless, an additional term is introduced to stabilize the interface between the phases (Grenier et al., 2009). The interface sharpness force used in the SOPHIA code is formulated as follows.

$$\left(\frac{d\boldsymbol{u}}{dt}\right)_i^{IS} = -\frac{\varepsilon}{m_i}\sum_j\left(\left|p_i\right|V_i^2+\left|p_j\right|V_j^2\right)\nabla W_{ij},\ \ for\ f_i \neq f_j \tag{50}$$

where ε is a tuning parameter that ranges between 0.01 and 0.1 (Grenier et al., 2009). The notation $f_i \neq f_j$ means that the phase of the fluid particle "i" is dissimilar to that of particle "j." The kernel summation of the RHS only includes a neighboring particle 'j' that belongs to a different phase to particle "i." This force should be large enough to stabilize the interface between the phases, but it should be small enough not to cause any unphysical effects.

Particle Shifting

As mentioned in section Fundamentals of SPH, particle deficiency and irregular distribution are the main sources of numerical errors in the SPH interpolations. Particle shifting is one of the methods to address this issue. It adjusts the particle position to enhance the uniformity of the distribution. The SOPHIA code adopted the shifting method proposed by Lind et al. (2012). This adjusts the particle spacing in proportion to the particle number density, which is an indicator of particle uniformity. In this method, the particle adjustment vector ($\delta\boldsymbol{r}$) is evaluated by the following equation.

$$\delta\boldsymbol{r}_i = -0.5h^2\sum_j V_j\left(1+R\left(\frac{W\left(r_{ij},\ h\right)}{W\left(\Delta r,\ h\right)}\right)^n\right)\nabla W_{ij} \tag{51}$$

TABLE 3 | Inter-particle force terms for the IPF surface tension model.

Model	Formulation
Cosine (Tartakovsky and Meakin, 2005)	$f_{ij} = s_{ij} \cos\left(\frac{1.5\pi}{\kappa h} \left\|\boldsymbol{r}_{ij}\right\|\right) \frac{\boldsymbol{r}_{ij}}{\left\|\boldsymbol{r}_{ij}\right\|}$
Cohesive (Shigorina et al., 2017)	$f_{ij} = s_{ij} \left[A_{ij} W\left(\boldsymbol{r}_{ij}, \frac{h}{2}\right) \frac{\boldsymbol{r}_{ij}}{\left\|\boldsymbol{r}_{ij}\right\|} - W\left(\boldsymbol{r}_{ij}, h\right) \frac{\boldsymbol{r}_{ij}}{\left\|\boldsymbol{r}_{ij}\right\|}\right]$
Lennard-Jones (Zhang et al., 2008)	$f_{ij} = -4\varepsilon \frac{m_j}{\rho_j} \left[\left(\frac{\boldsymbol{r_0}}{\left\|\boldsymbol{r}_{ij}\right\|}\right)^{12} - \left(\frac{\boldsymbol{r}_0}{\left\|\boldsymbol{r}_{ij}\right\|}\right)^{6}\right] \nabla W_{ij}$

where R and n denote the constant parameters, set as to be 0.2 and 4, respectively. $\delta \boldsymbol{r}$ denotes the initial particle spacing. In every time step, the particle positions are updated by adding adjustment vector $\left(\boldsymbol{r}_i^* = \boldsymbol{r}_i + \delta \boldsymbol{r}_i\right)$. The particle properties on the new positions can be updated through SPH interpolation depending on the proposed numerical scheme.

Time Integration

In the SOPHIA code, a modified predictor-corrector scheme is applied (Gomez-Gesteira et al., 2012). The predictor-corrector scheme divides the time integration into two steps and determines the physical variables (position, velocity, density, and energy) and their time derivatives in turn. First, the prediction step extrapolates the physical variables as follows.

$$\begin{cases} \boldsymbol{u}^p_{\Delta t+\frac{\Delta t}{2}} = \boldsymbol{u}_t + \frac{\Delta t}{2}\left(\frac{du}{dt}\right)_{t-\frac{\Delta t}{2}} \\ \boldsymbol{r}^p_{\Delta t+\frac{\Delta t}{2}} = \boldsymbol{r}_t + \frac{\Delta t}{2}\left(\frac{dr}{dt}\right)_{t-\frac{\Delta t}{2}} \\ \rho^p_{\Delta t+\frac{\Delta t}{2}} = \rho_t + \frac{\Delta t}{2}\left(\frac{d\rho}{dt}\right)_{t-\frac{\Delta t}{2}} \end{cases} \tag{52}$$

where t and Δt denote time and time step, respectively. Superscript p denotes "predictor." The time derivatives of position, velocity, density, and energy are newly evaluated by solving the discretized SPH governing equations based on the predicted values. After that, the field variables are re-integrated over the full time step using the updated time derivatives in the correction step.

$$\begin{cases} \boldsymbol{u}^c_{\Delta t+t} = \boldsymbol{u}_t + \Delta t\left(\frac{du}{dt}\right)_{t+\frac{\Delta t}{2}} \\ \boldsymbol{r}^c_{\Delta t+t} = \boldsymbol{r}_t + \Delta t\left(\frac{dr}{dt}\right)_{t+\frac{\Delta t}{2}} \\ \rho^c_{\Delta t+t} = \rho_t + \Delta t\left(\frac{d\rho}{dt}\right)_{t+\frac{\Delta t}{2}} \end{cases} \tag{53}$$

where the superscript c denotes "corrector." These corrected values become initial values for the next time step.

CODE IMPLEMENTATION

The SPH generally has very high computational cost compared to conventional CFD methods. To address this issue, massive parallel-computer-system-based techniques have been actively employed in the SPH field, and the general-purpose GPU (GPGPU) is one of the most commonly favored. The GPU was originally developed for effective graphic rendering using thousands of parallel cores, but currently, its usage has been extended widely into general science and engineering applications due to the high-throughput computations and data-parallelism. Since the SPH formulations have no non-linear equations and every particle is calculated independently, the SPH code implementation is suitable for GPU parallelization.

In previous research by Jo et al. (2019), the SOPHIA code was fully parallelized using a single GPU, and it was demonstrated that the computational cost can be significantly reduced by GPU parallelization when compared to serial CPU computing. However, due to the limitation of the internal memory size of a single GPU, the allowable number of particles was highly restricted, being about 15 million particles for the original code. Therefore, it became essential to distribute computational load using multiple GPUs, which is critical for many practical large-scale applications. For this reason, the code has been restructured and fully parallelized using multiple GPUs along with domain decomposition. The technical details are summarized in the following sections.

GPU Implementation

Basic Algorithm

Figure 2 shows the basic algorithm of the code. The algorithm consists of several main steps and the sub-steps in the gray box in **Figure 2**. The gray box indicates that they are parallelized using multiple GPUs. The bold characters (Multi-GPU Allocation, Sub-domain Division, and Inter-GPU Communication) indicates the added steps for domain decomposition and data exchange between GPUs for distributing the computational load to multiple GPUs. The other steps are quite similar to the original SOPHIA code based on a single GPU (Jo et al., 2019). The first step of the code is Initialization. In this step, the input parameters and the initial particle information (position, velocity, temperature, pressure, property, etc.) are read from external input files and stored in the computer memory. This process is conducted by a single host CPU. After this process, the computational domain is divided into multiple sub-domains to distribute computational load and memory, and each GPU is assigned to each sub-domain, respectively. This allows the GPU to solve the governing equations and the physical models for only assigned/allocated sub-domain. Then, the particle data of the CPU host are copied to GPUs to have only their own sub-domains separately (Multi-GPU Allocation). The details are explained in section Multi-GPU Allocation. Once this process is completed, each GPU has the initial particle input data along with additional buffer data of the nearby domain for data exchange. The main loop is started from the Prediction step, which is conducted for predictor-corrector time integration,

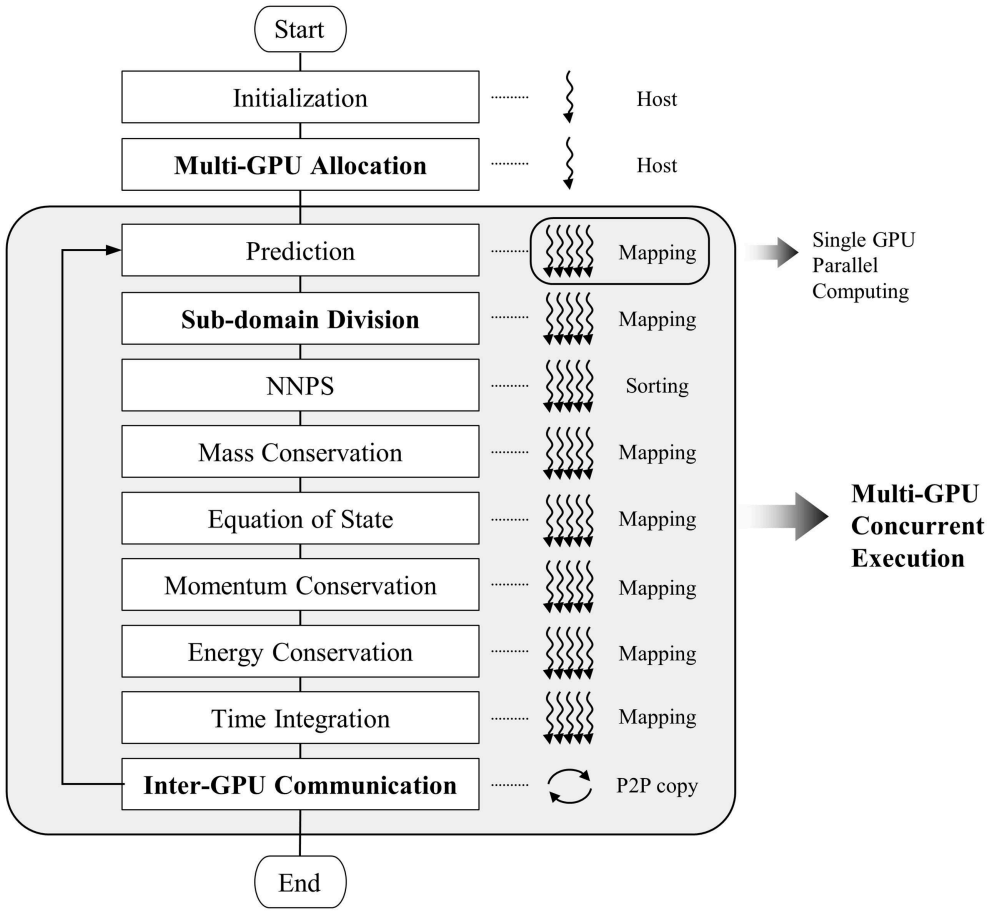

FIGURE 2 | Algorithm of the SOPHIA code.

as explained in section Time Integration. After the Prediction step, the particle positions are updated, and the sub-domain is partitioned into four groups according to Sub-domain Division. This step is applied for optimizing the computational load and data transfer of the GPUs. According to the particle groups, calculation and data transfer are differently scheduled. The details are explained in section Sub-domain Division. Once this step is completed, neighboring particles are searched for every particle (NNPS). NNPS is the key step in the particle simulation since it usually entails the largest computational load. In this code, the uniform grid and sorting-based algorithm are implemented with full GPU adaptation. Once this process is done, each particle has its neighboring particle information, which is necessary for the following particle interaction steps. The NNPS algorithm implemented here is briefly explained in section Concurrent Execution. After the NNPS step, the particle interactions are calculated according to the SPH equations and physical models (density, momentum, energy, etc.) explained in section Smoothed Particle Hydrodynamics (SPH). For the SPH interpolations, massive parallel GPU mapping is applied extensively. The details can be found by reference to Jo et al. (2019). After the particle interactions, the corrector step in the time integration is followed, with major updates. Once all these main calculation steps are completed, it is checked whether the updated particles escape from the original subdomain. If so, their information is transferred to the new subdomain by memory copying to adjacent GPUs (Inter-GPU Communication). After this step is finished, all the GPUs have the newly updated particle data with a fully preserved computational domain. The simulation then proceeds to the next time step in a loop. This multi-GPU parallel algorithm consists of two-level parallelization. At the higher level, multiple GPUs concurrently execute the main loops within the decomposed sub-domains (Multi-GPU Concurrent Execution), and at the lower level, each GPU carries out parallel computation (mapping or sorting) and data transmission for each sub-domain using thousands of computing cores simultaneously.

Multi-GPU Allocation

The multi-GPU allocation divides a whole computational domain into small sub-domains, as shown in **Figure 3**. First, as many threads are created as there are GPUs. The generated threads control the GPUs which are assigned the same index number, repectively. Then, the computational domain is divided

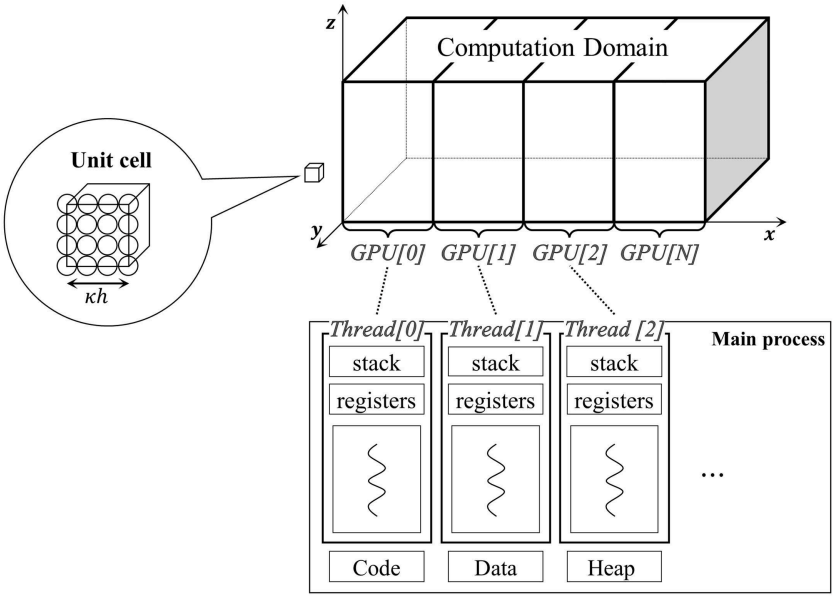

FIGURE 3 | Schematic process of the multi-GPU allocation step.

in a specific direction (x, y, or z) to have a similar number of particles, and then the threads allocate these sub-domains to their own GPUs. Currently, the code allows the domain decomposition in only one direction, because it minimizes the memory usage for data exchange in the inter-GPU communication.

Sub-domain Division

After the domain is decomposed and each sub-domain data is allocated to each GPU, the sub-domain is partitioned into four small sections for more efficient computation and data exchange. **Figure 4** shows the concept of the sub-domain division. R0 is the inner particle region. The particles located in R0 have little chance to escape the sub-domain in a single time step. Therefore, the particle in this region is not involved in the data exchange. R1 is the outer particle region. The particles in R1 have some chance to escape the sub-domain boundary during time integration. Therefore, the particles in this region must be traced to determine whether they still exist in the sub-domain after position update. R2 is the outer buffer region. The particles in R2 are located on the right outside of the sub-domain boundary. Since this region is overlapped with the R1 of adjacent GPUs, the particles in this region are only involved in the calculation of the R1 particles. R3 is the dummy region. The particles in R3 are not involved in any computation and data exchange processes.

Concurrent Execution

After subdomains are partitioned, each GPU individually calculates the particle behaviors. As shown in **Figure 2**, the Nearest Neighbor Particle Search (NNPS) is proceeded with prior to the SPH interpolation steps. In the SPH, the NNPS step is the most time-consuming part; hence, the performance of the whole algorithm depends heavily on the efficiency of the NNPS. In the SOPHIA code, the NNPS is optimized using an algorithm

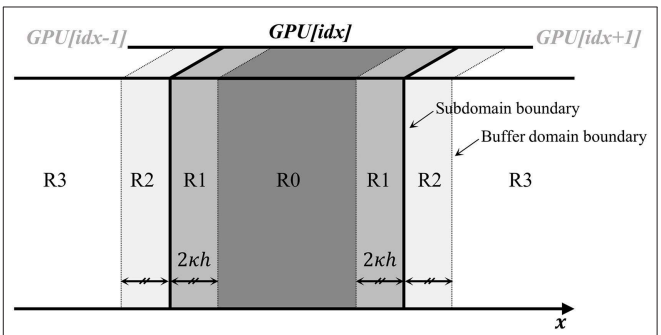

FIGURE 4 | Concept of sub-domain division.

based on a uniform grid and parallel sorting (Harada and Howes, 2011) that re-arranges the array of particles according to the order of each cell index. **Figure 5** shows the concept of the NNPS algorithm with a uniform grid and sorting.

1. The computational domain is divided into the grid cells.
2. The cell index (CI) is calculated and assigned to every particle.
3. The particle array is sorted (PI*) and ordered by cell index (CI*).
4. The starting (Cstr) and ending (Cend) particle index arrays are constructed.

The subsequent processes are performed during the SPH interpolation using these starting particle indices and ending particle indices. In the SPH interpolation, the particles in the adjacent cells are scanned and it is checked whether the distance from the center particle "*i*" is within the search range.

Once the NNPS step is complete, the density of each particle is calculated by solving either the mass summation or continuity

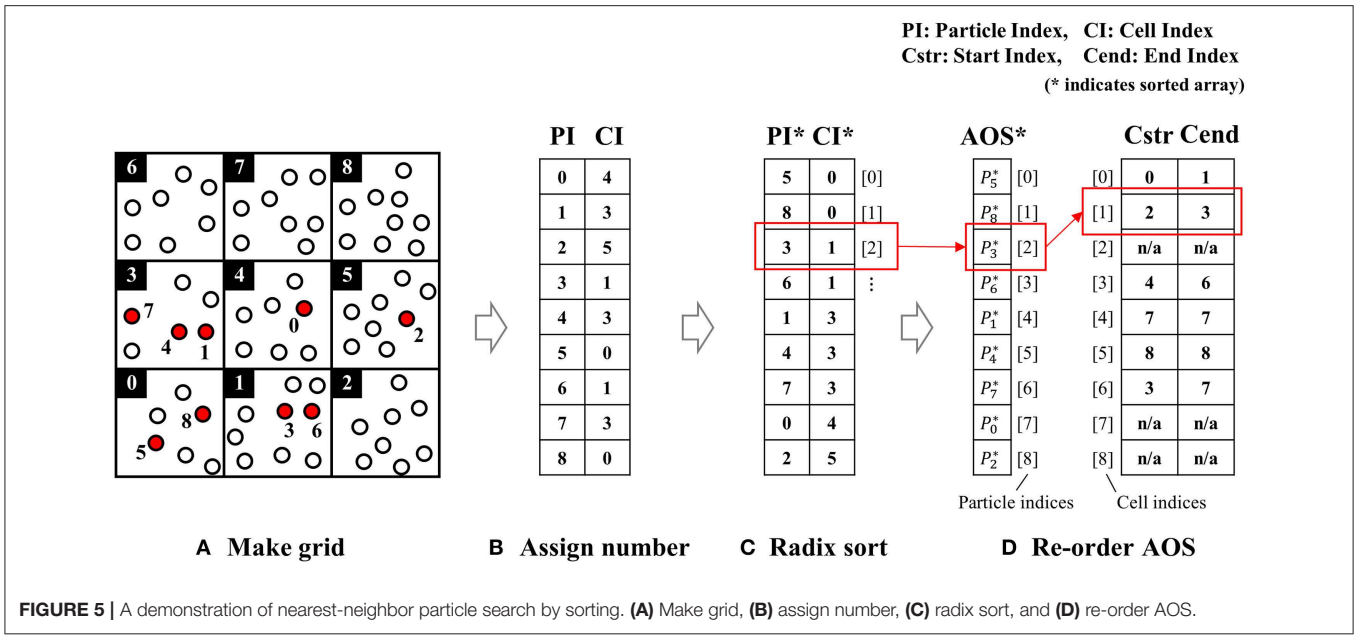

FIGURE 5 | A demonstration of nearest-neighbor particle search by sorting. **(A)** Make grid, **(B)** assign number, **(C)** radix sort, and **(D)** re-order AOS.

equation. The particle pressure is then calculated according to the EOS. Afterward, all the particle interactions, including momentum conservation, energy conservation, molecular diffusion, etc., are computed with the physical models described in section Smoothed Particle Hydrodynamics (SPH). For all these calculations, parallel mapping is used. This method calls the same number of computing cores as there are particles, and each core computes the equations of each particle in parallel.

Inter-GPU Communication

After time integration and position update are conducted, the particles across the boundaries are checked, and information is exchanged between the adjacent GPUs through peer-to-peer (P2P) memory copy. **Figure 6** shows the schematic process of the inter-GPU communication. First, the particles in R1 are labeled as "left" or "right" depending on their position, as shown in **Figure 6A**. The GPU[idx] sends the "left" particle data to the "idx-1"th GPU and the "right" data to the "idx+1"th GPU. Conversely, the "left" data of GPU[idx+1] and the "right" data of GPU[idx-1] are transferred to GPU[idx] and stored in memory. Among the received data, some particles may cross the boundaries and enter into the "idx"th subdomain. These particles remain as R1, and the rest are re-assigned as R2 to serve as neighbors of R1 particles. The unnecessary data will be dumped as dummy particles (R3) at the Sub-domain Division step of the next loop. This repetitive sub-domain division and inter-GPU communication ensures that each GPU occupies the subdomain that overlaps some buffer regions with the neighbor GPUs.

In order to increase the efficiency of the inter-GPU communication, multi-streaming is applied in the code. The basic concept is shown in **Figure 6B**. In this algorithm, the calculations are split into two parallel streams. In one stream, the particle interactions of the physical models are solved. At the same time, Peer-to-Peer (P2P) memory transfer is conducted in the other stream in parallel. A combination of two streams reduces latency time effectively since data copying (referring to P2P copy) and kernel execution (referring to particle calculation) do not share computing resources. In addition, the data transaction is reliably completed during the calculation because the number of inner particles is much larger than that of outer particles.

Evaluation of Multi-GPU Parallel Performance

In the previous research, it was found that a single GPU parallelization reduced the computational cost compared to the serial CPU computation by a factor of 100 for a million particles. The details can be found in Jo et al. (2019). In this section, the performance of the domain decomposition and the multi-GPU parallelization is examined to evaluate its large-scale computing capability. The evaluation is performed by two types of scaling tests: (1) strong scaling and (2) weak scaling. The strong scaling measures the execution time for a fixed-size problem (the number of particles) with an increase in the number of GPUs. In the strong scaling, the speed-up factor is defined as

$$S_s\,(N,P) = \frac{T\,(N,1)}{T(N,P)} \tag{54}$$

where T, N, P, and S_s denote an execution time, a problem size, the number of GPUs, and a speed-up factor, respectively. On the other hand, the weak scaling measures the execution time by increasing the problem size (the number of particles) and the number of GPUs simultaneously. In this case, the ratio of the number of particles to the number of GPUs is maintained constant. In the weak scaling, the efficiency is defined as

$$E_W\,(N,P) = \frac{T\,(N_1,1)}{T(N_1 \times P,P)} \tag{55}$$

where N_1 and E_w denote the problem size of a single GPU and an efficiency factor, respectively. In this study, a well-known

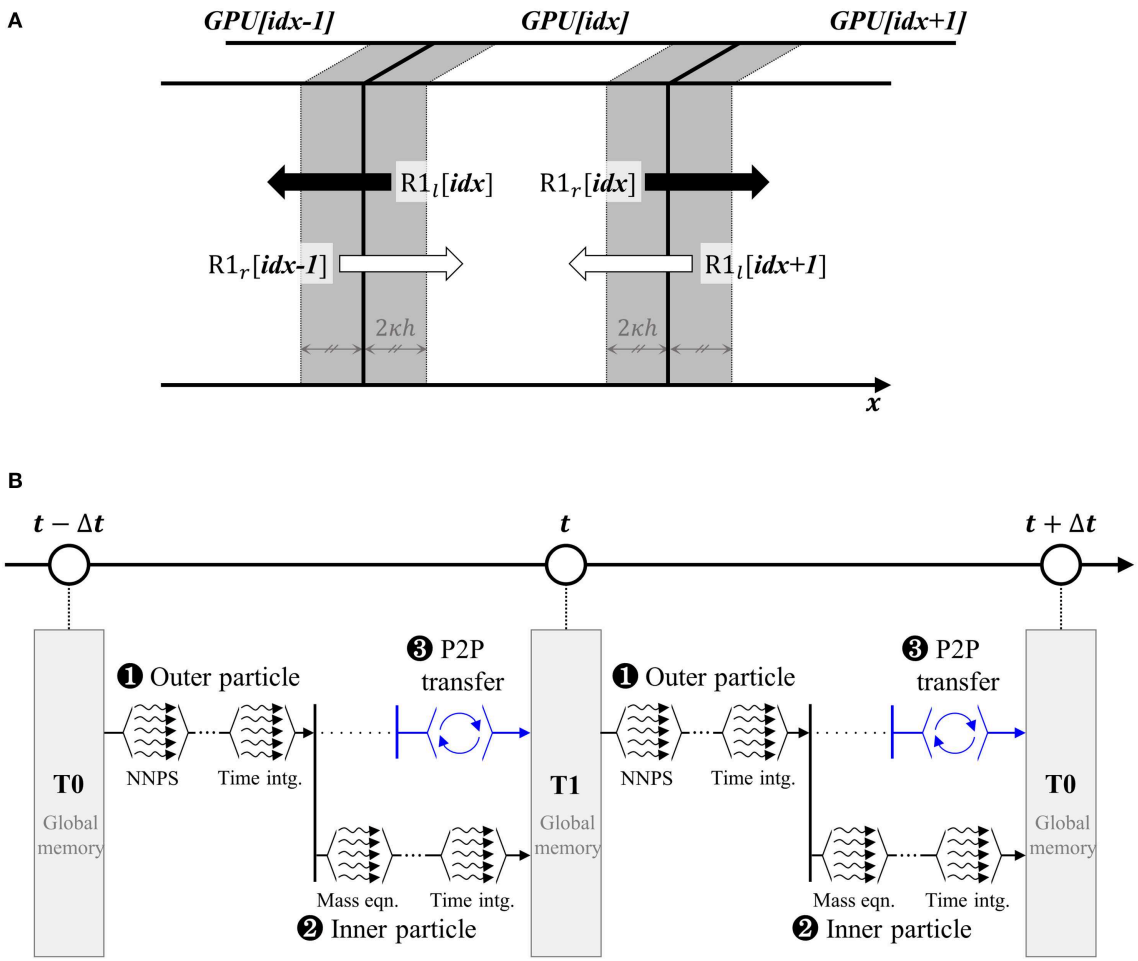

FIGURE 6 | Schematic process of the inter-GPU communication step: **(A)** concept of inter-GPU communication and **(B)** multi-stream scheme with time marching.

benchmark problem (3-D dam-break) by Arnason et al. (2009) and Cummins et al. (2012) was used.

In the strong scaling test, the total number of particles was fixed to be 16,784,004, which occupies the maximum memory allowable for a single GPU (NVIDIA P100). Accordingly, in the weak scaling test, the total number of particles was increased from 16,784,004 to 101,362,964, in proportion to the number of GPUs. In this case, the model size was substantially increased by maintaining constant memory usage for each GPU. **Figure 7** shows the performance evaluation results. This study measures the time taken to calculate the main loop 1,000 times using the clocking method. This process was repeated four times, then averaging these measured times determines the performance time. For a single GPU simulation with 16,784,004 particles, the computation takes about 11 min for 1,000 time steps ($\Delta t = 10^{-6}$ s). **Figure 7A** shows the speed-up factor for the strong scaling test. As shown in this figure, the speed-up factor increases with the number of GPUs, but the efficiency tends to decrease slightly. This is because the number of outer particles within the sub-domain is not sufficiently small to hide the latency of data exchange. **Figure 7B** shows the parallel efficiency of the weak scaling test. As the number of GPUs increases, the efficiency decreases, and it reaches about 78% for six-GPU parallelization (101 million particles). Although the size of the problem increases by six times, the computation time is only increased by 20% using six GPUs, which allows us to handle large-sized simulations efficiently. Overall, multi-GPU-based parallelized algorithm shows good performance.

BENCHMARK ANALYSIS

As described in section Smoothed Particle Hydrodynamics (SPH), SOPHIA consists of various models such as hydrodynamics, heat transfer, turbulence, multi-phase flow, etc. Although all the details are not described in this paper, the code has conducted various basic V&V simulations including hydrostatic pressure, Poiseuille & Couette flow, lid-driven flow, 2D/3D dam break, 3D wave generation, hydrostatic pressure in immiscible fluids, the lock exchange problem, Rayleigh-Tayler instability, multi-dimensional heat conduction, and natural circulation. Some of the results are

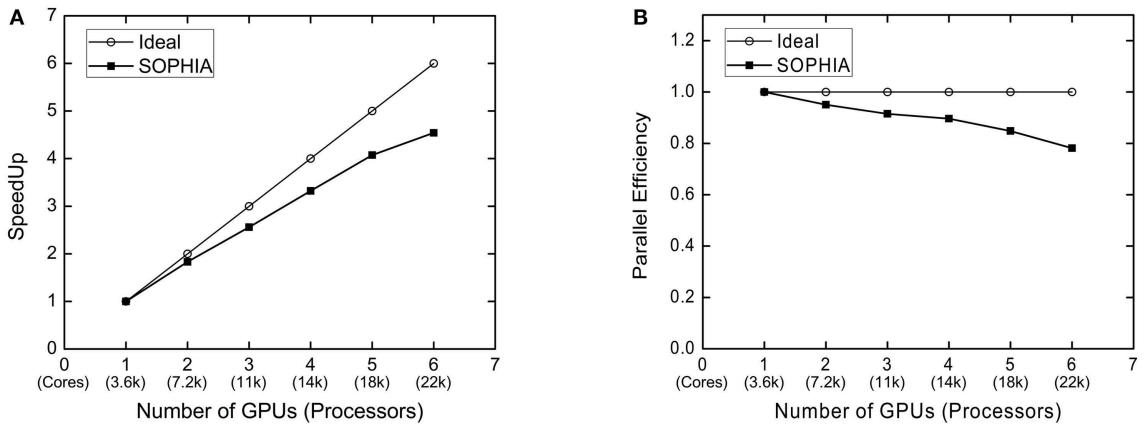

FIGURE 7 | Performance scalability test of multi-GPU code. **(A)** Speedup factor of strong scaling and **(B)** efficiency of weak scaling.

summarized in Jo et al. (2019) and Park et al. (2019). For the newly implemented physical models such as turbulence, chemical reaction, etc., the verification and validation processes are currently underway. In this section, the simulations are conducted on three benchmark experiments related to nuclear safety. The selected benchmark experiments are (1) water jet breakup of Fuel–Coolant Interaction (FCI), (2) Liquid Metal Reactor (LMR) centralized sloshing, and (3) bubble lift force.

Jet Breakup of Fuel–Coolant Interaction

Fuel–Coolant Interaction (FCI) is one of major phenomena of severe accidents and occurs when molten fuel falls into the coolant or vice versa. The interaction between coolant and the molten fuel involves many complicated physical phenomena, which may lead to a catastrophic event such as a steam explosion. Especially, jet breakup, where the bulk of molten fuel breaks into droplets, is the most important pre-mixing phase for a steam explosion or re-melting of fuel fragments, which threatens the reactor vessel/containment integrity (Allelein et al., 1999; Sehgal et al., 1999). In this study, an isothermal benchmark experiment on jet breakup conducted by Park et al. (2016) is simulated using the SOPHIA code and the results are discussed.

The impinging jet simulation model consists of a jet column and a tank filled with Fluorinert. The tank is a rectangular column of 0.1 m width, 0.02 m depth, and 0.4 m height, and the pool is filled up to a height of 0.2 m. As in the experiment, the rest of the tank is filled with the air in the simulation. The jet diameter is 10 mm. The water jet has a density of 1,000 kg/m^3, a viscosity of 1.0 $mPa \cdot s$, and a surface tension of 0.072 N/m and the Fluorinert pool has a density of 1,880 kg/m^3, a viscosity of 4.7 $mPa \cdot s$, and a surface tension of 0.043 N/m. The inlet jet velocity was set as 3.8 m/s. The total number of particles was 57,430,016. The simulation was conducted using six GPUs.

Figure 8 shows snapshots of the simulation. The jet, injected at a high velocity, penetrates into the pool. This penetration causes a U-shaped air pocket just behind the jet front. The interaction with the pool dissipates the initial momentum of the jet front, suspending further penetration. At the same time, the air pocket collapses due to the compression of the pool. The jet continuously drags the air into the pool and breaks up through the interaction with the pool. Mixing of jet droplets and air bubbles enhances the buoyant effect of the jet. As a result, the jet fails to penetrate below a certain depth, and the jet disperses out radially. According to previous studies (Ikeda et al., 2001; Park et al., 2016), it is noted that this jet breakup and fragmentation can only be modeled physically by three-dimensional two-phase flow simulation. This is because ignoring the air cavity may distort the consequent phenomena. As shown in **Figure 8**, such jet behavior is well-reproduced through the three-dimensional two-phase flow simulation with high resolution. Especially, in the simulation, the droplets are generated at the pool–jet–air interfaces by velocity differences (referred to as Kelvin-Helmholtz instability) or surface tension effects (referred to as critical Weber number theory).

For rigorous analysis, the simulation results are compared with experimental data in two ways: (1) jet penetration depth and (2) overall pool surface shape/level. **Figure 9A** compares the jet front penetration depth in the simulation with the experimental data. The jet front in the simulation shows very good agreement with the experimental data over time. **Figure 9B** compares the pool surface shape in the simulation and in the experiment (the red lines represent the surface of the experimental visual images at the same time). As shown in the figure, the simulation agrees very well with the experimental results, not only for the surface level but also in terms of the overall features.

Liquid Metal Reactor Centralized Sloshing

In the transient phase of a core-disruptive Liquid Metal Reactor (LMR) accident, a neutronically active multi-phase pool can be formed, which is composed of solid fuel, molten fuel, re-frozen fuel, fission gas, fuel vapor, steel particles, etc. In this configuration, abrupt pressure build-up due to local vapor

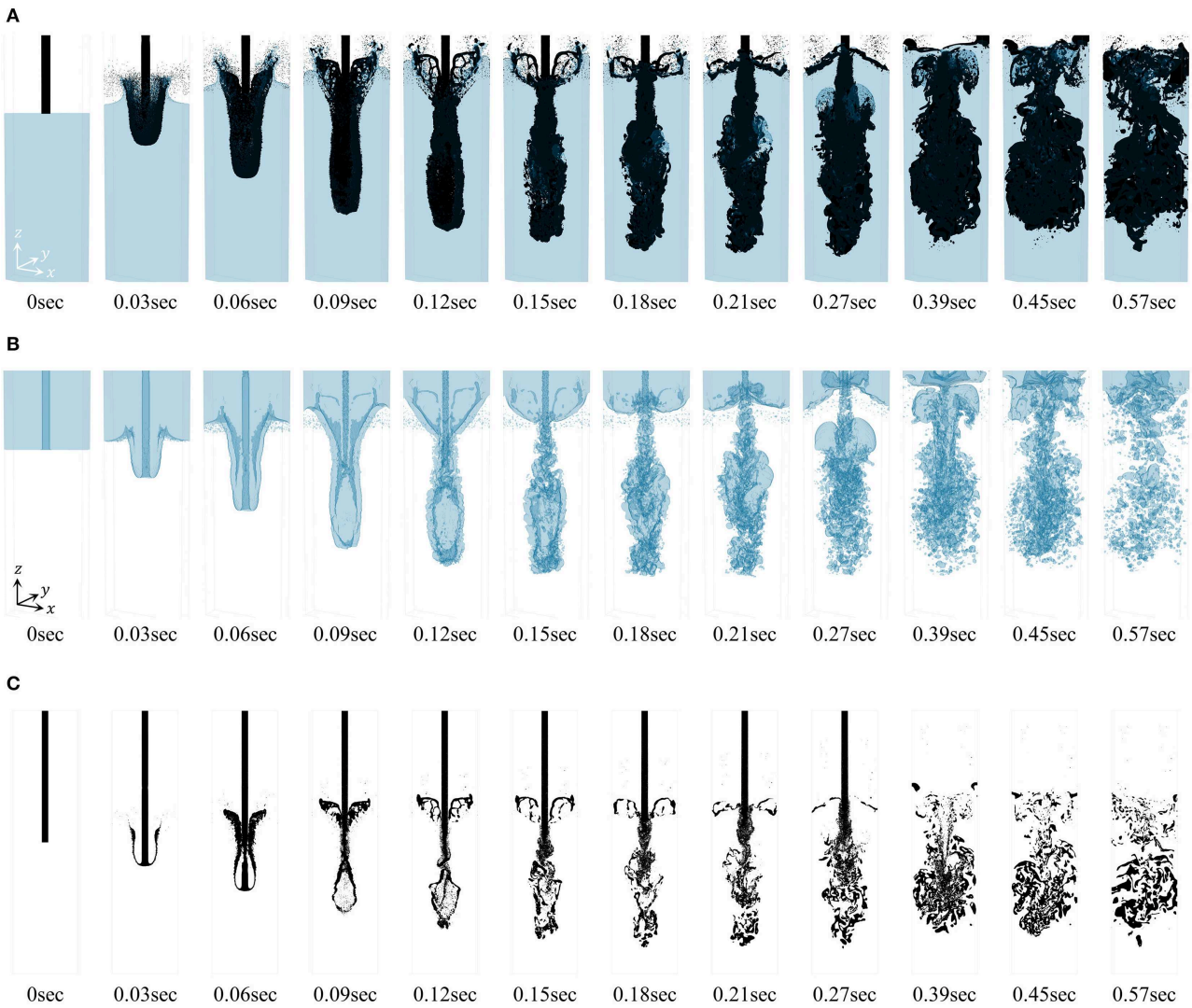

FIGURE 8 | Snapshots of two-phase simulation of jet breakup: **(A)** two fluids with rendering (blue for the Fluorinert pool, and black for the water jet), **(B)** air with rendering, and **(C)** jet breakup behavior at the x–z plane.

generation can initiate so-called centralized sloshing motion, which has the potential for energetic fuel re-criticalities (Suzuki et al., 2014). In this study, three-dimensional sloshing simulations are conducted using the SOPHIA code on the benchmark experiment by Maschek et al. (1992a).

The simulation model consists of a water column, a container, and 12 vertical rods. The container is an open cylinder with a 44-cm diameter. The water column, with 11 cm diameter and 20 cm height, is located in the center of the container. Regarding the vertical rods, which all have the same diameter of 2 cm, the three simulation cases were considered.

- Case 1 has no vertical rods but only the water column.
- Case 2 has inner vertical rods that surround the water column in a ring with a diameter of 19.8 cm.
- Case 3 has outer vertical rods that surround the water column in a ring with a diameter of 35.2 cm diameter.

Figure 10 shows the simulation results for Case 1, Case 2, and Case 3, respectively. In Case 1, the water column collapses due to gravity, and it makes a circular wave moving toward the container wall. After collision with the wall, the water converges toward the center area, and it forms a high central water peak. In Case 2 and Case 3, 12 vertical inner/outer rods are placed around the central water column. The simulations reproduce the damping and interference motion of water waves induced by rod disturbances well.

In this study, the maximum sloshing height and arrival time in the simulations are compared with the experimental data, as shown in **Table 4**. The (1) arrival time, (2) time of maximum height, and (3) maximum height at the outer container wall and the pool center are taken into account. In general, the SOPHIA simulation results show very good agreement with the benchmark experimental data, both qualitatively and quantitatively.

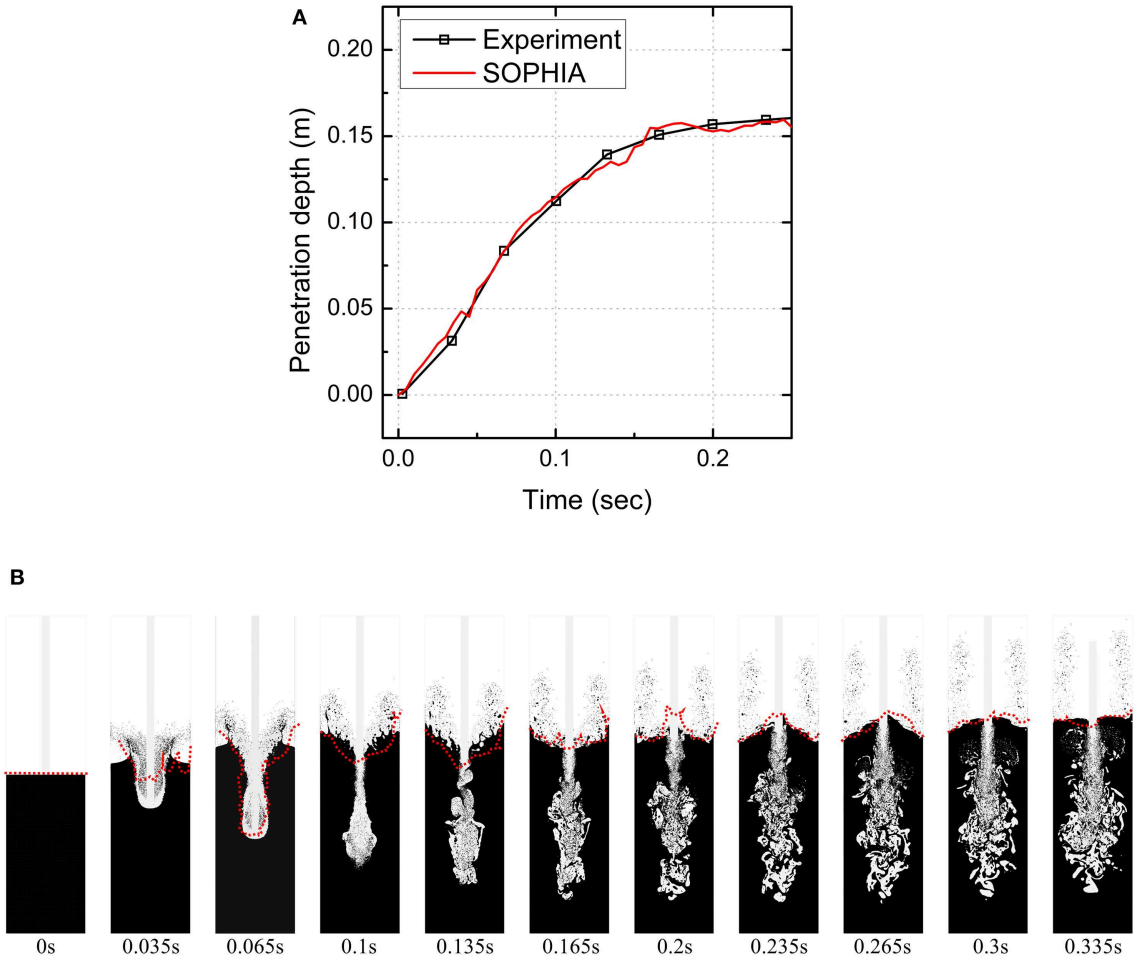

FIGURE 9 | Comparison of the simulation results with the experimental results: **(A)** comparison of the jet penetration depth and **(B)** comparison of the pool surface level with the experimental visualization (red lines for experimental results; Park et al., 2016).

Bubble Lift Force

Bubbly flow plays an important role not only in Light Water Reactors (LWRs) but also in many industries because it involves large interfacial areas for heat and mass transfer. In recent multi-phase CFD analysis, the lift force is one of the important forces for tracing bubble dynamics because it greatly affects the spatial distribution of bubbles and void fractions. In nuclear safety analysis, the effect of lift force was noticed early on by observing an accumulation of gas near the wall in the pipe flow (Tomiyama et al., 2002; Ziegenhein et al., 2018). In conventional CFD analysis, the lift force is commonly considered by empirical correlations based on experimental data. In this study, the bubble lift force in laminar shear flow is simulated, referring to the benchmark experiment by Tomiyama et al. (2002), and the bubble trajectories are compared with the experimental data.

In the benchmark experiment, a tank was filled with a glycerol-water solution, and a belt was continuously rotated at a constant speed to induce simple shear flow. At the steady state, a single air bubble was released on the linear velocity gradient field through a nozzle tip. For the simulation, a stationary vertical wall is placed in the middle of the tank, and both sidewalls are set to have a constant velocity to generate simple shear flow as in the experiment. The tank is a rectangular cavity with 60-mm width and 0.5-m height, and it is divided into two channels with 30-mm width by the stationary wall. As in the experiment, the tank is filled with a glycerol-water solution, and the fluid flows rotating clockwise. After achieving steady-state shear flow, a single air bubble is injected at the left channel of the model. The glycerol-water solution has a density of 1,154 kg/m^3 and a viscosity of 0.091 $Pa \cdot s$. This study performed two-dimensional simulation with 518,259 particles. Regarding the velocity gradient (ω) and bubble diameter (d), four experimental cases were considered.

- Case 1 has a small velocity gradient ($\omega = 5.7\ s^{-1}$) and large bubble diameter ($d = 5.54$ mm).
- Case 2 has a large velocity gradient ($\omega = 6.2\ s^{-1}$) and large bubble diameter ($d = 5.54$ mm).
- Case 3 has a small velocity gradient ($\omega = 5.7\ s^{-1}$) and small bubble diameter (d =3.52 mm).

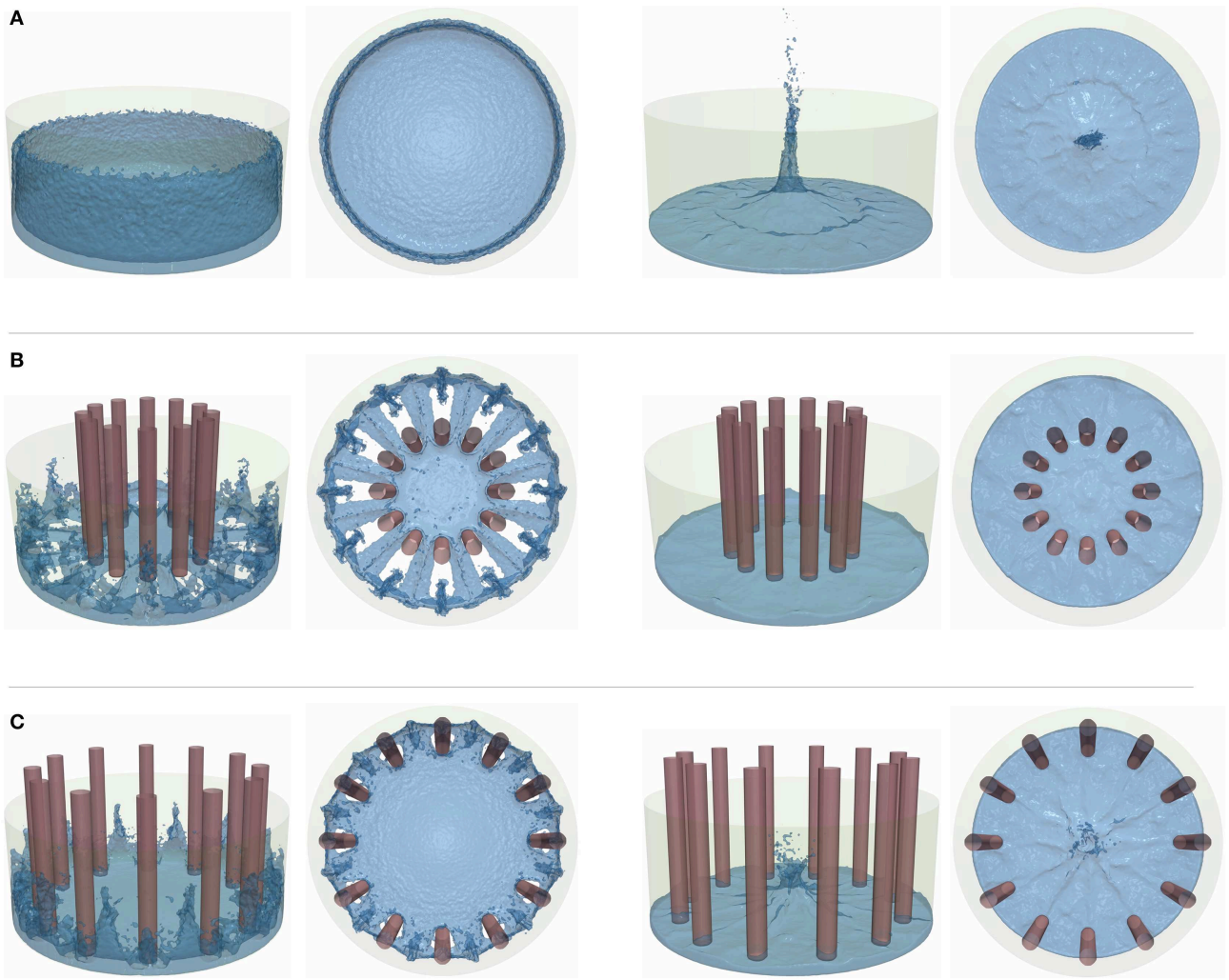

FIGURE 10 | Snapshots of surface motion of the simulation cases with rendering: **(A)** Case 1 simulation results, **(B)** Case 2 simulation results, and **(C)** Case 3 simulation results.

TABLE 4 | Comparison of SOPHIA simulation with experiments (Maschek et al., 1992b; Pigny, 2010).

	Slosh at outer container wall			Slosh at pool center	
	Arrival time (s)	**Time of max height (s)**	**Max height (cm)**	**Time of max height (s)**	**Max height (cm)**
Case 1. Central sloshing					
Experiment	0.20 ± 0.02	0.42 ± 0.02	16.0 ± 1.0	0.88 ± 0.04	40.0 ± 5.0
SIMMER-IV	0.2	0.38	18.75	–	>50
SOPHIA	0.2	0.41	17.5	0.88	38.0
Case 2. Inner vertical rods					
Experiment	0.22 ± 0.02	0.44 ± 0.02	15.0 ± 1.0	0.90 ± 0.04	3.0 ± 2.0
SOPHIA	0.21	0.43	16.0	0.88	3.5
Case 3. Outer vertical rods					
Experiment	0.20 ± 0.02	0.42 ± 0.02	15.0 ± 1.0	0.88 ± 0.04	15.0 ± 3.0
SOPHIA	0.20	0.41	17.5	0.88	12.9

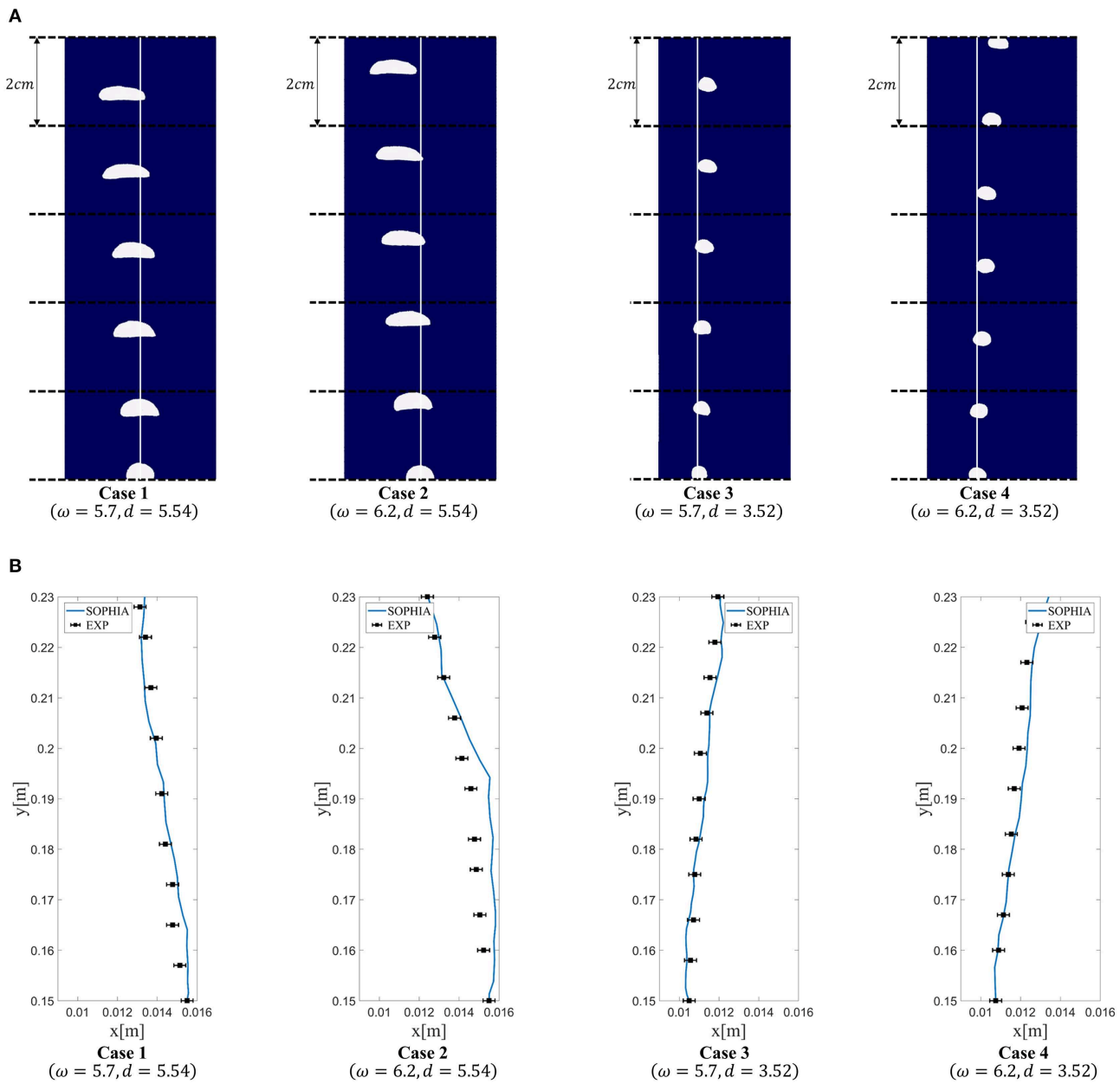

FIGURE 11 | The simulation results for bubble lift force: **(A)** bubble floating sequence with rendering and **(B)** comparison of bubble trajectories with the experimental data (Tomiyama et al., 2002).

- Case 4 has a large velocity gradient ($\omega = 6.2\ s^{-1}$) and small bubble diameter ($d = 3.52$ mm).

Figure 11 presents the simulation results of four cases and validations. **Figure 11A** shows image sequences of the simulations. The left two figures are the results for a large bubble diameter ($d = 5.54$ mm) and the right two figures for a small bubble diameter ($d = 3.52$ mm). As shown in the figure, the large bubble drifts toward the left wall as it rises up, while the small bubble drifts toward the right wall. This is because the shear-induced lift force is most dominant for the small bubbles. At the surface of the bubble, a relative velocity gradient is generated by the linear shear flow, and this gradient drags the small bubble so that it rotates toward the large drag force (high velocity). However, for large bubbles, slanted-wake-induced lift force is more dominant than shear-induced lift force. When the large bubble floats through the linear shear flow, asymmetric wakes are formed right behind the bubble, and this wake configuration perturbs the surrounding pressure field. Due to the pressure gradient, the large bubble tends to move toward the lower velocity with deformation. **Figure 11B** compares the trajectories of the bubbles in the experiment

and in the simulation. As shown in the figure, the simulation results are agreed very well with the experimental results within measurement error.

SUMMARY AND CONCLUSION

This paper summarizes the recent progress and on-going activity in the development of the Lagrangian-based CFD code (SOPHIA), with some demonstrations on nuclear applications. The SOPHIA code is based on the smoothed particle hydrodynamics (SPH), which is the most widely used full-Lagrangian method. Like other conventional CFD methods, the SOPHIA code basically solves mass, momentum, and energy conservation equations. However, unlike conventional SPH, the SOPHIA code formulates the density and the continuity equations in terms of normalized density in order to handle multi-phase, multi-fluid, and multi-component flows in a simple and effective manner. In addition, the SOPHIA code incorporates physical models, including fluid flow, heat transfer, mass transfer, multi-phase, phase change, turbulence, and diffusion, with various numerical correction schemes so that the code can be applied well to many different nuclear safety-related issues.

In spite of its great potential for nuclear thermal hydraulics and safety, the Lagrangian-based CFD still faces some technical challenges that need to be further addressed. One of the critical drawbacks of the SPH method is the high computational cost. In order to address this issue, this study implements the code using multi-GPU parallelization with various parallel computing techniques such as multi-threading, mapping, and sorting. The main algorithm consists of four steps: (1) multi-GPU allocation, (2) sub-domain division, (3) multi-GPU concurrent execution, and (4) inter-GPU communication. Especially, the multi-GPU concurrent execution step parallelizes the computation procedure into two streams to optimize calculation and memory exchange. The computational performance of the multi-GPU parallelized SOPHIA code is evaluated by both strong and weak scaling. The results indicate that SOPHIA code showed remarkable performance from small-scale to large-scale problems with an increase in the number of GPUs, and it reached 78% efficiency with a maximum six GPUs.

To demonstrate its applicability to nuclear thermal hydraulics and safety, three benchmark simulations were conducted: (1) water jet breakup of FCI, (2) LMR centralized core sloshing, and (3) bubble lift force. All of these simulations showed that the SOPHIA code can predict the key phenomena in the experiments, both qualitatively and quantitatively. According to the benchmark results and discussions, SPH methods such as the SOPHIA code seem to be well-suited to safety-related analysis (i.e., for severe accident and natural disaster), numerical experiments, and visualization of phenomena. All of these activities have a large potential to reduce the uncertainties regarding the phenomena related to decision-making.

Although the SOPHIA code has great potential in nuclear thermal hydraulics and safety analysis, technical challenges remain that require further investigations. The following lists some of the items that should be addressed in the future:

- Method for handling multi-scale problems (i.e., boiling, turbulence, etc.)
- Method for reducing large computational cost (i.e., optimization, numerical schemes)
- Method for handling various boundary conditions (i.e., symmetry, open boundary, etc.)
- Method for improving both accuracy and stability (i.e., numerical schemes)
- Method for verification and validation (i.e., benchmark experiment, visualization, etc.)

DATA AVAILABILITY STATEMENT

All datasets generated for this study are included in the article/supplementary material.

AUTHOR CONTRIBUTIONS

S-HP developed the code and performed simulations, analyzed data, and drafted or provided the revision of the paper. YJ and YA developed the code and performed simulations, analyzed data, and co-wrote the paper. HC, TC, S-SP, HY, and JK developed the code, performed simulations, and analyzed data. EK supervised the research and resolved appropriately, provided the revision of the paper, and approved of the final version to be published.

FUNDING

This research was supported by the Nuclear Energy Technology Development Program (U.S.-ROK I-NERI Program) through the National Research Foundation of Korea (NRF), funded by the Ministry of Science and ICT (2019M2A8A1000630), and the Nuclear Safety Research Program through the Korea Foundation of Nuclear Safety (KoFONS), using the financial resources granted by the Nuclear Safety and Security Commission (NSSC) of the Republic of Korea (No. 1903003).

REFERENCES

Allelein, H., Basu, S., Berthoud, G., Jacobs, H., Magallon, D., Petit, M., et al. (1999). *Technical Opinion Paper on Fuel-Coolant Interaction (No. NEA-CSNI-R—1999-24).* Organisation for Economic Co-Operation and Development-Nuclear Energy Agency.

Antuono, M., Colagrossi, A., Marrone, S., and Molteni, D. (2010). Free-surface flows solved by means of SPH schemes with numerical diffusive terms. *Comput. Phys. Commun.* 181, 532–549. doi: 10.1016/j.cpc.2009.11.002

Arnason, H., Petroff, C., and Yeh, H. (2009). Tsunami bore impingement onto a vertical column. *J. Disaster Res.* 4, 391–403. doi: 10.20965/jdr.2009.p0391

Barto, A. (2014). *Consequence Study of a Beyond-Design-Basis Earthquake Affecting the Spent Fuel Pool for a U.S. Mark I Boiling Water Reactor*. United States Nuclear Regulatory Commission, Office of Nuclear Regulatory Research.

Bauer, T. H., Wright, A. E., Robinson, W. R., Holland, J. W., and Rhodes, E. A. (1990). Behavior of modern metallic fuel in treat transient overpower tests. *Nuclear Technol.* 92, 325–352. doi: 10.13182/NT92-325

Belytschko, T., Krongauz, Y., Organ, D., Fleming, M., and Krysl, P. (1996). Meshless methods: an overview and recent developments. *Comput Methods Appl Mech. Eng.* 139, 3–47. doi: 10.1016/S0045-7825(96)01078-X

Bonet, J., and Lok, T. S. (1999). Variational and momentum preservation aspects of smooth particle hydrodynamic formulations. *Comput. Methods Appl. Mech. Eng.* 180, 97–115. doi: 10.1016/S0045-7825(99)00051-1

Bonnet, J. M., Cranga, M., Vola, D., Marchetto, C., Kissane, M., Robledo, F., et al. (2017). *State-of-the-Art Report on Molten Corium Concrete Interaction and Ex-Vessel Molten Core Coolability (No. NEA—7392).* Organisation for Economic Co-Operation and Development.

Brackbill, J. U., Kothe, D. B., and Zemach, C. (1992). A continuum method for modeling surface tension. *J. Comput. Phys.* 100, 335–354. doi: 10.1016/0021-9991(92)90240-Y

Chen, J. K., and Beraun, J. E. (2000). A generalized smoothed particle hydrodynamics method for nonlinear dynamic problems. *Comput. Methods Appl. Mech. Eng.* 190, 225–239. doi: 10.1016/S0045-7825(99)00422-3

Cleary, P. W. (1998). Modelling confined multi-material heat and mass flows using SPH. *Appl. Math. Modell.* 22, 981–993. doi: 10.1016/S0307-904X(98)10031-8

Cummins, S. J., Silvester, T. B., and Cleary, P. W. (2012). Three-dimensional wave impact on a rigid structure using smoothed particle hydrodynamics. *Int. J. Numer. Methods Fluids* 68, 1471–1496. doi: 10.1002/fld.2539

Dehnen, W., and Aly, H. (2012). Improving convergence in smoothed particle hydrodynamics simulations without pairing instability. *Monthly Notices R. Astrono. Soc.* 425, 1068–1082. doi: 10.1111/j.1365-2966.2012.21439.x

Gingold, R. A., and Monaghan, J. J. (1977). Smoothed particle hydrodynamics: theory and application to non-spherical stars. *Monthly Notices R. Astrono. Soc.* 181, 375–389. doi: 10.1093/mnras/181.3.375

Gomez-Gesteira, M., Rogers, B. D., Crespo, A. J., Dalrymple, R. A., Narayanaswamy, M., and Dominguez, J. M. (2012). SPHysics–development of a free-surface fluid solver–Part 1: theory and formulations. *Comput. Geosci.* 48, 289–299. doi: 10.1016/j.cageo.2012.02.029

Grenier, N., Antuono, M., Colagrossi, A., Le Touzé, D., and Alessandrini, B. (2009). An Hamiltonian interface SPH formulation for multi-fluid and free surface flows. *J. Comput. Phys.* 228, 8380–8393. doi: 10.1016/j.jcp.2009.08.009

Guo, X., Rogers, B. D., Lind, S., and Stansby, P. K. (2018). New massively parallel scheme for Incompressible Smoothed Particle Hydrodynamics (ISPH) for highly nonlinear and distorted flow. *Comput. Phys. Commun.* 233, 16–28. doi: 10.1016/j.cpc.2018.06.006

Harada, T., and Howes, L. (2011). Introduction to GPU Radix Sort. *Heterogeneous Computing with OpenCL* (San Francisco, CA: Morgan Kaufmann).

Hu, X. Y., and Adams, N. A. (2006). A multi-phase SPH method for macroscopic and mesoscopic flows. *J. Comput. Phys.* 213, 844–861. doi: 10.1016/j.jcp.2005.09.001

Huang, C., Lei, J. M., Liu, M. B., and Peng, X. Y. (2016). An improved KGF-SPH with a novel discrete scheme of Laplacian operator for viscous incompressible fluid flows. *Int. J. Numer. Methods Fluids* 81, 377–396. doi: 10.1002/fld.4191

Ikeda, H., Koshizuka, S., Oka, Y., Park, H. S., and Sugimoto, J. (2001). Numerical analysis of jet injection behavior for fuel-coolant interaction using particle method. *J. Nuclear Sci. Technol.* 38, 174–182. doi: 10.1080/18811248.2001.9715019

Jo, Y. B., Park, S. H., Choi, H. Y., Jung, H. W., Kim, Y. J., and Kim, E. S. (2019). SOPHIA: Development of Lagrangian-based CFD code for nuclear thermal-hydraulics and safety applications. *Ann. Nuclear Energy* 124, 132–149. doi: 10.1016/j.anucene.2018.09.005

Lind, S. J., Xu, R., Stansby, P. K., and Rogers, B. D. (2012). Incompressible smoothed particle hydrodynamics for free-surface flows: a generalised diffusion-based algorithm for stability and validations for impulsive flows and propagating waves. *J. Comput. Phys.* 231, 1499–1523. doi: 10.1016/j.jcp.2011.10.027

Liu, G. R., and Liu, M. B. (2003). *Smoothed Particle Hydrodynamics: A Meshfree Particle Method.* World Scientific. doi: 10.1142/5340

Liu, M. B., and Liu, G. R. (2006). Restoring particle consistency in smoothed particle hydrodynamics. *Appl. Numer. Math.* 56, 19–36. doi: 10.1016/j.apnum.2005.02.012

Liu, M. B., Liu, G. R., and Lam, K. Y. (2003). Constructing smoothing functions in smoothed particle hydrodynamics with applications. *J. Comput. Appl. Math.* 155, 263–284. doi: 10.1016/S0377-0427(02)00869-5

Lucy, L. B. (1977). A numerical approach to the testing of the fission hypothesis. *Astrono. J.* 82, 1013–1024. doi: 10.1086/112164

Ma, W., Yuan, Y., and Sehgal, B. R. (2016). In-vessel melt retention of pressurized water reactors: historical review and future research needs. *Engineering* 2, 103–111. doi: 10.1016/J.ENG.2016.01.019

Maschek, W., Munz, C. D., and Meyer, L. (1992a). Investigations of sloshing fluid motions in pools related to recriticalities in liquid-metal fast breeder reactor core meltdown accidents. *Nuclear Technol.* 98, 27–43. doi: 10.13182/NT92-A34648

Maschek, W., Roth, A., Kirstahler, M., and Meyer, L. (1992b). Simulation experiments for centralized liquid sloshing motions. *Kernforschungszentrum Karlsruhe, 5090* (Karlsruhe).

Molteni, D., and Colagrossi, A. (2009). A simple procedure to improve the pressure evaluation in hydrodynamic context using the SPH. *Comput. Phys. Commun.* 180, 861–872. doi: 10.1016/j.cpc.2008.12.004

Monaghan, J. J. (1992). Smoothed particle hydrodynamics. *Ann. Rev. Astrono. Astrophys.* 30, 543–574. doi: 10.1146/annurev.aa.30.090192.002551

Monaghan, J. J. (1994). Simulating free surface flows with SPH. *J. Comput. Phys.* 110, 399–406. doi: 10.1006/jcph.1994.1034

Monaghan, J. J. (2005). Smoothed particle hydrodynamics. *Rep. Progr. Phys.* 68:1703. doi: 10.1088/0034-4885/68/8/R01

Morris, J. P. (2000). Simulating surface tension with smoothed particle hydrodynamics. *Int. J. Numer. Methods Fluids* 33, 333–353. doi: 10.1002/1097-0363(20000615)33:3<333::AID-FLD11>3.0.CO;2-7

Morris, J. P., Fox, P. J., and Zhu, Y. (1997). Modeling low Reynolds number incompressible flows using SPH. *J. Comput. Phys.* 136, 214–226. doi: 10.1006/jcph.1997.5776

Nishiura, D., Furuichi, M., and Sakaguchi, H. (2015). Computational performance of a smoothed particle hydrodynamics simulation for shared-memory parallel computing. *Comput. Phys. Commun.* 194, 18–32. doi: 10.1016/j.cpc.2015.04.006

Park, S., Park, H. S., Jang, B. I., and Kim, H. J. (2016). 3-D simulation of plunging jet penetration into a denser liquid pool by the RD-MPS method. *Nuclear Eng. Des.* 299, 154–162. doi: 10.1016/j.nucengdes.2015.08.003

Park, S.H., Chae, H., Jo, Y. B., and Kim, Y. S. (2019). "SPH for general density gradient driven flow," in *Proceedings of the 14th SPHERIC International Workshop* (Exeter), 67–75.

Park, S. H., Choi, T. S., Choi, H. Y., Jo, Y. B., and Kim, E. S. (2018). Simulation of a laboratory-scale experiment for wave propagation and interaction with a structure of undersea topography near a nuclear power plant using a divergence-free SPH. *Ann. Nuclear Energy* 122, 340–351. doi: 10.1016/j.anucene.2018.08.045

Pigny, S. L. (2010). Academic validation of multi-phase flow codes. *Nucl. Eng. Design* 240, 3819–3829. doi: 10.1016/j.nucengdes.2010.08.007

Randles, P. W., and Libersky, L. D. (1996). Smoothed particle hydrodynamics: some recent improvements and applications. *Comput. Methods Appl. Mech. Eng.* 139, 375–408. doi: 10.1016/S0045-7825(96)01090-0

Rogers, B. D., and Dalrymple, R. A. (2008). "SPH modeling of tsunami waves," in *Advanced Numerical Models for Simulating Tsunami Waves and Runup*, Vol. 10, eds P. L.-F. Liu, H. Yeh, and C. Synolakis (World Scientific), 75–100. doi: 10.1142/9789812790910_0003

Sehgal, B. R., Dinh, T. N., Nourgaliev, R. R., Bui, V. A., Green, J., Kolb, G., et al. (1999). *Final Report for the'Melt-Vessel Interactions' Project.* European Union R and TD Program 4th Framework. MVI project final research report (No. SKI-R—00-53). Swedish Nuclear Power Inspectorate.

Shigorina, E., Kordilla, J., and Tartakovsky, A. M. (2017). Smoothed particle hydrodynamics study of the roughness effect on contact angle and droplet flow. *Phys. Rev. E* 96:033115. doi: 10.1103/PhysRevE.96.033115

Sun, P. N., Colagrossi, A., Marrone, S., Antuono, M., and Zhang, A. M. (2017). "Targeting viscous flows around solid body at high Reynolds numbers with the delta-plus-SPH model," in *Proceedings of 12th International SPHERIC Workshop* (Ourense).

Suzuki, T., Kamiyama, K., Yamano, H., Kubo, S., Tobita, Y., Nakai, R., et al. (2014). A scenario of core disruptive accident for Japan sodium-cooled fast

reactor to achieve in-vessel retention. *J. Nucl. Sci. Technol.* 51, 493–513. doi: 10.1080/00223131.2013.877405

Tartakovsky, A., and Meakin, P. (2005). Modeling of surface tension and contact angles with smoothed particle hydrodynamics. *Phys. Rev. E* 72:026301. doi: 10.1103/PhysRevE.72.026301

Tomiyama, A., Tamai, H., Zun, I., and Hosokawa, S. (2002). Transverse migration of single bubbles in simple shear flows. *Chem. Eng. Sci.* 57, 1849–1858. doi: 10.1016/S0009-2509(02)00085-4

Valdez-Balderas, D., Domínguez, J. M., Rogers, B. D., and Crespo, A. J. (2013). Towards accelerating smoothed particle hydrodynamics simulations for free-surface flows on multi-GPU clusters. *J. Parallel Distr. Comput.* 73, 1483–1493. doi: 10.1016/j.jpdc.2012.07.010

Violeau, D., and Issa, R. (2007). Numerical modelling of complex turbulent free-surface flows with the SPH method: an overview. *Int. J. Numer. Methods Fluids* 53, 277–304. doi: 10.1002/fld.1292

Wang, Z. B., Chen, R., Wang, H., Liao, Q., Zhu, X., and Li, S. Z. (2016). An overview of smoothed particle hydrodynamics for simulating multiphase flow. *Appl. Math. Modell.* 40, 9625–9655. doi: 10.1016/j.apm.2016.06.030

Zhang, M. Y., Zhang, H., and Zheng, L. L. (2008). Simulation of droplet spreading, splashing and solidification using smoothed particle hydrodynamics method. *Int. J. Heat Mass Transfer* 51, 3410–3419. doi: 10.1016/j.ijheatmasstransfer.2007.11.009

Zhang, N., Zheng, X., and Ma, Q. (2017). Updated smoothed particle hydrodynamics for simulating bending and compression failure progress of ice. *Water* 9:882. doi: 10.3390/w9110882

Zhao, Y., Wilson, P. R., and Stevenson, J. D. (1996). Nonlinear 3-D dynamic time history analysis in the reracking modifications for a nuclear power plant. *Nucl. Eng. Design* 165, 199–211. doi: 10.1016/0029-5493(96)01197-1

Ziegenhein, T., Tomiyama, A., and Lucas, D. (2018). A new measuring concept to determine the lift force for distorted bubbles in low Morton number system: results for air/water. *Int. J. Multiphase Flow* 108, 11–24. doi: 10.1016/j.ijmultiphaseflow.2018.06.012

Conflict of Interest: The authors declare that the research was conducted in the absence of any commercial or financial relationships that could be construed as a potential conflict of interest.

NOMENCLATURE

c_0	Speed of sound (m/s)	p	Pressure (Pa)
C_μ	Turbulent viscous coefficient	P	Turbulence production (J/kg·s)
C_ϵ	Turbulent dissipation coefficient	$\dot{q}$	Heat generation rate (J/kg·s)
C_s	SPS turbulence coefficient	$\mathbf{r}$	Position vector
D	Molecular diffusivity (m^2/s)	$\delta\mathbf{r}$	Particle adjustment vector
d	Dimension (=1, 2, 3)	$\Delta\mathbf{r}$	Initial particle spacing (m)
E_w	Efficiency factor	S	Molecular concentration (mol)
$\boldsymbol{f}_{ext}$	External body force acceleration (m/s^2)	S_0	Initial (reference) concentration
g	Gravitational acceleration (m/s^2)	S_s	Speed-up factor
h	Smoothing length (m)	$\boldsymbol{S}^{\alpha}\beta$	Strain rate tensor
h	Specific enthalpy (J/kg)	t	Time (sec)
k	Turbulence kinetic energy (J/kg)	Δt	Time step (sec)
k_{ij}	$k_i - k_j$	T	Temperature (K)
L	Kernel Gradient Correction operator	T_0	Initial (reference) temperature (K)
Δl	Length scale (m)	$\boldsymbol{u}$	Velocity vector (m/s)
m	Mass (kg)	$\boldsymbol{u}_{ij}$	$\boldsymbol{u}_i - \boldsymbol{u}_j$
m_0	Initial mass (kg)	V	Volume (m^3)
M	Molar mass (kg/mol)	V_0	Initial volume (m^3)
$\boldsymbol{n}$	Surface normal vector	W	Kernel function
$\hat{n}$	Unit surface normal vector	x	Molar fraction
Greek			
α_T	Thermal expansion coefficient (K^{-1})	μ_T	Turbulent viscosity (Pa·s)
α_S	Saline contraction coefficient (psu^{-1})	ν	Kinematic viscosity (m^2/s)
δ	Dirac delta function	Ω	Infinite volume domain
$\delta^{\alpha\beta}$	Kronecker delta	ω	Velocity gradient (s^{-1})
ϵ	Turbulent dissipation rate (J/kg·s)	ρ	Density (kg/m^3)
γ	EOS stiffness parameter	ρ_{ref}	Reference density (kg/m^3)
κ	Smoothing parameter	$\delta\rho$	Density variation
κ	Curvature	σ	Surface tension coefficient (N/m)
λ	Conductivity (W/m·K)	$\boldsymbol{\tau}^{\alpha\beta}$	SPS stress tensor
μ	Dynamic viscosity (Pa·s)	ξ	Diffusion intensity coefficient of δ-SPH
μ_v	Laminar viscosity (Pa·s)		
Superscript		**Subscript**	
$\alpha,\ \beta,\ \gamma$	Cartesian coordinate (= x, y, z)	i	Center particle
c	Corrector	j	Neighboring particle
fb	Buoyancy force	k	Neighbors of neighboring particle j
fp	Pressure force		
fv	Viscous force		
p	Predictor		
$turb$	Turbulence force		

frontiers in Energy Research

ORIGINAL RESEARCH
published: 30 June 2020
doi: 10.3389/fenrg.2020.00129

CFD Investigation of MHTGR Natural Circulation and Decay Heat Removal in P-LOFC Accident

Chengqi Wang[1], *Xiaodong Sun*[1]* *and Piyush Sabharwall*[2]

[1] Department of Nuclear Engineering and Radiological Sciences, University of Michigan, Ann Arbor, MI, United States, [2] Idaho National Laboratory, Idaho Falls, ID, United States

One of the key postulated accidents in a high-temperature gas-cooled reactor (HTGR) is the pressurized loss of forced cooling (P-LOFC) of the primary loop, which can be triggered by its primary helium circulator trip or turbine trip. If the reactor shutdown cooling system (SCS) fails during a P-LOFC accident, part of the reactor decay heat is absorbed by the reactor core materials and the rest removed by the reactor cavity cooling system (RCCS). In the extended period of P-LOFC accident, compounded with SCS failure, the core decay heat is supposed to be removed by conduction, natural circulation/convection, and radiation. Three-dimensional computational fluid dynamics (CFD) simulations were performed in this research to study the long-term heat removal mechanisms in the General Atomics' Modular High Temperature Gas-cooled Reactor (MHTGR) design during a P-LOFC accident. The reactor core temperature distribution and flow field were obtained at different decay power levels. The sensitivity of the natural circulation flow to the bypass gap width was investigated. The natural circulation flow intensity is relatively weak but very sensitive to the width of the bypass gaps.

Keywords: HTGRs, CFD, P-LOFC, natural circulation, decay heat removal, MHTGR

OPEN ACCESS

Edited by:
Wenxi Tian,
Xi'an Jiaotong University, China

Reviewed by:
Heng Xie,
Tsinghua University, China
Yixiang Liao,
Helmholtz-Gemeinschaft Deutscher Forschungszentren (HZ), Germany
Nejdet Erkan,
The University of Tokyo, Japan

***Correspondence:**
Xiaodong Sun
xdsun@umich.edu

Specialty section:
This article was submitted to Nuclear Energy, a section of the journal Frontiers in Energy Research

Received: *17 February 2020*
Accepted: *27 May 2020*
Published: *30 June 2020*

Citation:
Wang C, Sun X and Sabharwall P (2020) CFD Investigation of MHTGR Natural Circulation and Decay Heat Removal in P-LOFC Accident. Front. Energy Res. 8:129. doi: 10.3389/fenrg.2020.00129

INTRODUCTION

The high-temperature gas-cooled reactors (HTGRs) have received great attention due to their potential to provide high-temperature process heat in addition to their high thermal-to-electric power conversion efficiency and inherent safety features (Alonso et al., 2014; Fang et al., 2017; Wang et al., 2019). One of the postulated accidents in HTGRs is the pressurized loss of forced cooling (P-LOFC), which is caused by an abnormal trip of the main helium circulator or turbine in the power conversion system. During a P-LOFC accident, core decay heat will be removed by a combination of heat conduction, natural circulation/convection, and finally thermal radiation to the reactor cavity cooling system (RCCS), so the maximum fuel temperature does not exceed the design limit. To perform reactor safety analysis, validated system-level analysis codes are usually adopted to analyze reactor transients and accidents. For example, steam ingress accidents in HTGRs were investigated using a code named RETRAN-02 (Wang et al., 2014) and air-ingress accidents in Gas Turbine Modular High-temperature Reactor (GT-MHR) were studied using GAMMA (No et al., 2007), and RELAP5 (Jin et al., 2012). The P-LOFC accident in the Pebble-bed Modular High-Temperature Gas-cooled Reactor (HTR-PM) was studied using TINT and SPECTRA (Zheng et al., 2018) and their results showed that the fuel temperature design limit, 1,630°C, was not

exceeded during the accident. However, the geometries used in the system-level code analyses are usually simplified, which could lead to misleading results under certain circumstances (Oh et al., 2011a, 2012).

In General Atomics' (GA's) Modular High Temperature Gas-cooled Reactor (MHTGR) design, the reactor relies on its shutdown cooling system (SCS) to cool down after reactor scram (U.S. Department of Energy, 1986). However, if the SCS fails to start, the reactor has to remove the core decay heat via passive means. Under this circumstance the materials in the reactor core, especially the graphite, serve as temporary energy storage before passive heat removal capacity exceeds the core decay power. Limited experimental studies are available for P-LOFC accidents in the literature. A prismatic HTGR P-LOFC accident without reactor scram was performed using the High-Temperature engineering Test Reactor (HTTR) (Takamatsu et al., 2014). In addition, an experimental study was performed using a scaled-down, reduced-pressure, dual coolant channel facility and the experimental results showed that the heat transfer coefficient and Nusselt number increased with increasing helium pressure (Said et al., 2018). While the experiment provided very useful information to better understand the accident, three shortcomings were noted: the natural circulation flow velocity was not measured; the boundary conditions applied to the two channels did not necessarily represent the prototypic conditions; and the dual coolant channel experiment did not provide sufficient information to allow readers to estimate the helium velocity and temperature fields during a P-LOFC accident. On the modeling and simulation side, Tung and Johnson (2011) using computational fluid dynamics (CFD), simulated the natural circulation flow pattern in a 1/12 section of a fuel column. Nevertheless, the 1/12 fuel column model cannot reflect the scenario in the prototypic accident because the model assumed all vertical boundaries were symmetric. In reality, heat flux can cross these "symmetric" boundaries depending on the locations of the fuel columns in the core.

To obtain more accurate flow and temperature distributions in an HTGR core under a P-LOFC accident, it is desirable to include in the model all the heat transfer paths, including: the fuel columns, graphite reflectors, helium flow, and reactor pressure vessel (RPV) wall. However, a CFD simulation including all these domains with their prototypic structural features will be very computationally expensive. For example, in GA's MHTGR design, there are about 7,000 coolant channels with a diameter of 15.8 mm and a length of 7.93 m in the active core, which can require billions of mesh elements. Therefore, appropriate simplifications will have to be made to avoid generating overly fine meshes for each individual coolant channel. One strategy is to simplify the fuel columns to a homogeneous porous medium. Using this method, an air ingress accident in the GT-MHR, following a double ended guillotine break on the cross duct, was investigated by Oh et al. (2012). A similar strategy was applied to study the steam and air ingress accidents in HTR-PM and the associated graphite reaction (Ferng and Chen, 2011; Ferng and Chi, 2012a,b). In our current study, the porous medium flow model is adopted to study reactor decay heat removal during an extended period of the P-LOFC accident combined with SCS failure in GA's MHTGR.

CFD MODELING METHOD

Geometry and Mesh Generation

GA's MHTGR was chosen as the reference design in this research. The active core of MHTGR consists of 66 fuel columns (U.S. Department of Energy, 1986). These fuel columns form an annular region that is surrounded by replaceable graphite reflectors on the inner, outer, top, and bottom sides. The weight of the active core and the replaceable reflectors is loaded onto the graphite posts in the hot plenum just below the reactor core. Permanent graphite reflectors are installed in the annulus between the outer replaceable reflectors and core barrel. In the free volume between the core barrel and the RPV wall, 12 coolant risers are designed to lead the primary helium flow into the upper plenum during normal reactor operation. The MHTGR design is schematically shown in **Figure 1A** with a side cut view of the RPV and in **Figure 1B** with a cross-sectional view of the reactor core. In our current study, a 1/12 sector of the core (the highlighted section in **Figure 1B**) is simulated to take advantages of the azimuthal symmetry of the core.

Even with the 1/12 reactor core, maintaining all the detailed structures is still very expensive, if not infeasible, given the computational resources available to the group. Therefore, additional simplifications were made to accelerate the computation. First, the fuel columns and bypass flow gaps between graphite reflectors were regarded as homogeneous porous bodies. The porous body simplification will be discussed in section Porous Medium Parameters. During a P-LOFC accident global natural circulation flow through the primary loop is negligible because the primary loop will be shut off by closing the shut-off valve on the helium circulator. In addition, the lower elevation of the steam generator (SG) prevents a global natural circulation flow from forming. Therefore, it was assumed there is no helium exchange between the upper plenum and coolant risers. Accordingly, the zig-zag helium distribution system below the hot plenum was neglected since it is no longer accessible to the helium flow. Finally, one equivalent helium gap was built to replace the 12 individual coolant risers between the core barrel and RPV wall. The two symmetric planes of the simulation domain are depicted in **Figure 2A**. A cross-sectional view of the active core and the hot plenum is depicted in **Figure 2B**. There are seven fuel columns labeled as 1–7 as shown in **Figure 2B**, which will be referred to in the results section.

In the simulation domain, there are more than one hundred components. Therefore, the meshes were created separately for different domains using ANSYS Meshing or ICEM to take advantage of their abilities in capturing a specific geometric feature. The meshes were then imported to ANSYS Fluent 19.1 (ANSYS Inc., 2018), and merged using the interface tool. The realizable k-ε turbulence model with scalable wall functions was applied to accommodate different mesh sizes. To satisfy the requirements of the turbulence model, the meshes were refined in the near-wall region. The y^+ value range is about 50–150 for most regions but some local points have a y^+ value $<$10. The meshes of the fuel columns, hot plenum, and bypass gaps are depicted in **Figure 3A** with a detailed view of the

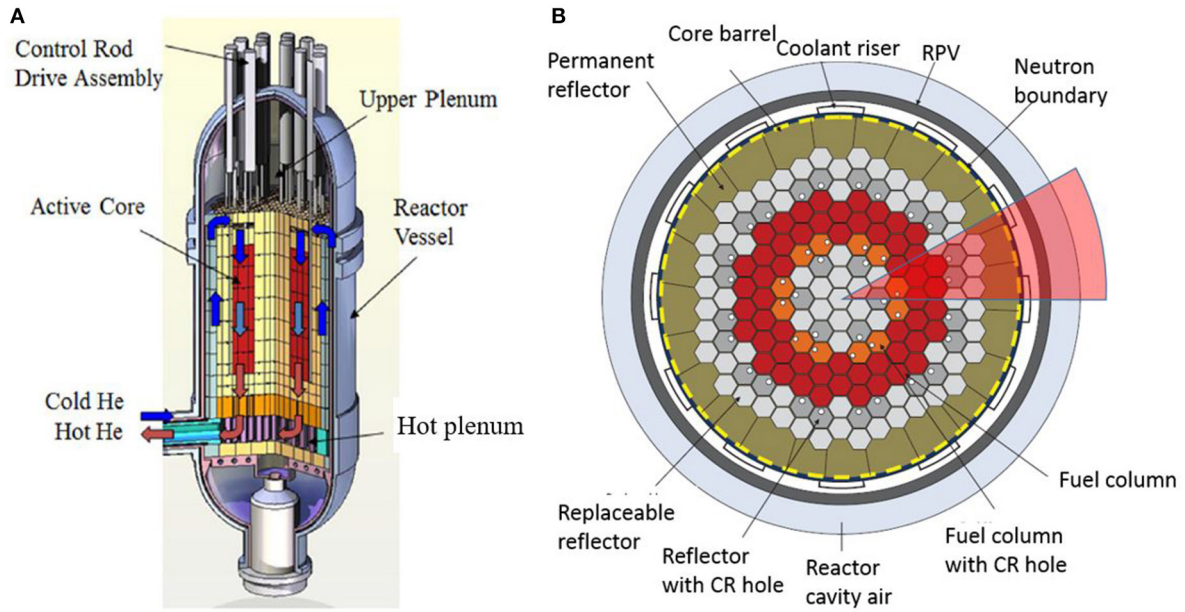

FIGURE 1 | MHTGR design: **(A)** cut away view of the RPV and **(B)** cross-sectional view of the reactor core (Nuclear Energy Agency, 2018).

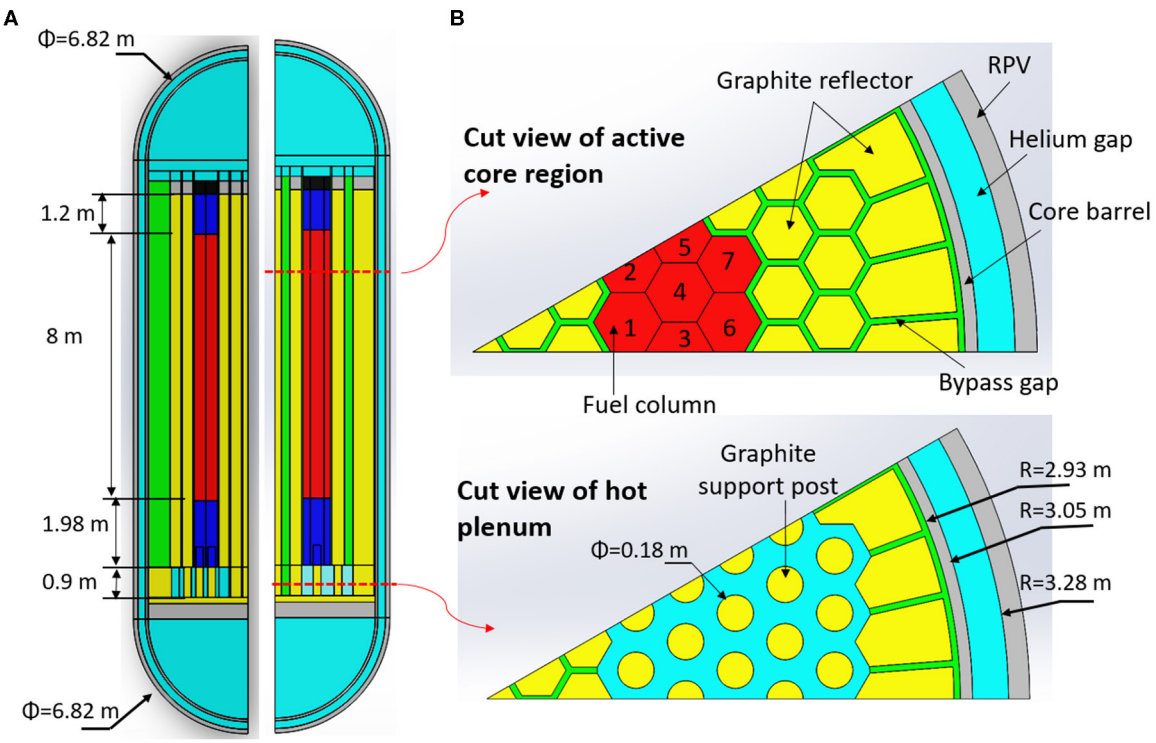

FIGURE 2 | Structure of the simulated domains: **(A)** two symmetric planes and **(B)** cross-sectional views of the active core and hot plenum.

mesh interfaces shown in **Figure 3B**. Before the simulation, a mesh independence study was performed. However, the mesh independence study was not performed on the whole integrated model. Instead, grid independence was verified for each flow region separately. For example, the natural circulation flow between the core barrel and RPV was studied using meshes

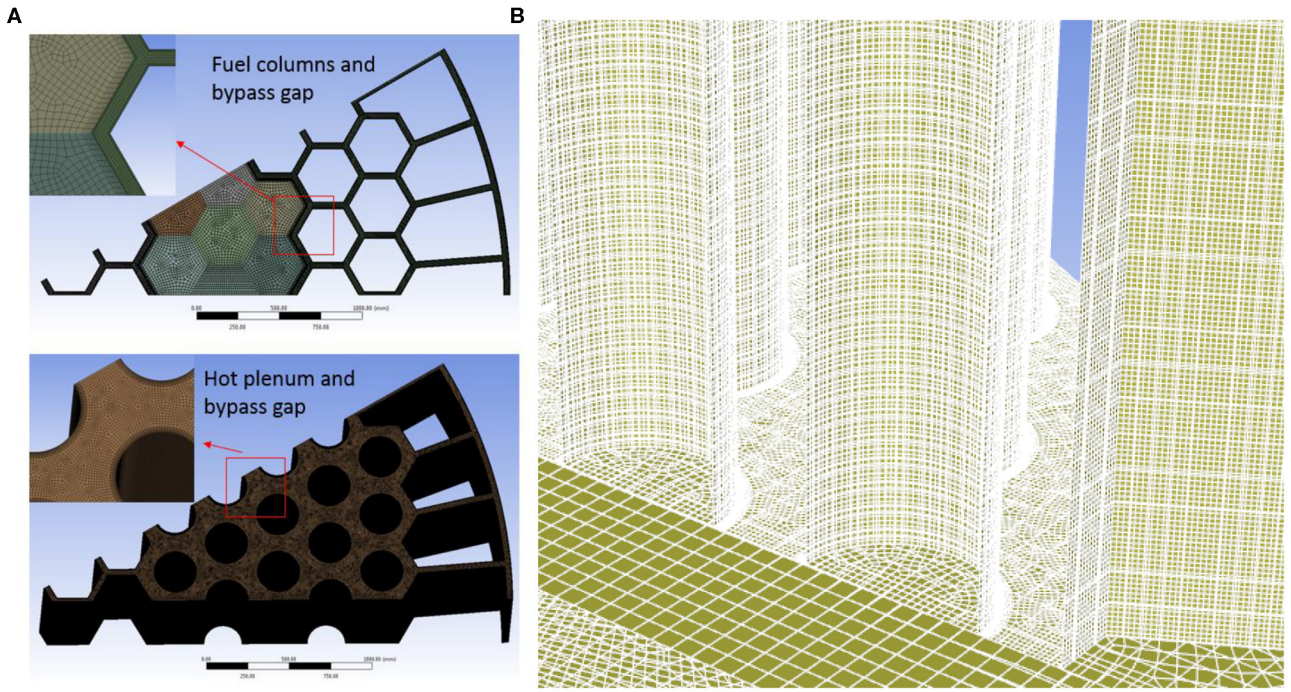

FIGURE 3 | Mesh generation for the: **(A)** fuel columns, hot plenum, bypass gaps, and **(B)** mesh interfaces.

TABLE 1 | Mesh sizes for each computation domain.

Simulated domain	Mesh size [mm]	Simulated domain	Mesh size [mm]
Bypass gaps	6 × 6 × 25	Helium gap between the core barrel and RPV	6 × 10 × 30
Hot plenum (helium)	6 × 6 × 25	Graphite reflectors	30 × 30 × 30
Fuel columns	15 × 15 × 30	Graphite support posts	10 × 10 ×25
Upper plenum	6~25*	Core barrel	10 × 10 × 30
Lower plenum	6~25*	RPV	10 × 16 × 30

**Tetrahedron mesh elements with a minimum edge length of 6 mm and a maximum edge length of 25 mm.*

with different sizes, aspect ratio, and prism layer thickness until mesh-independent results were obtained. Then, the mesh information was recorded and applied to the whole integrated model. A total of about 35.7 million mesh elements were generated with a minimum quality of 0.4. The simulated domains and their respective mesh sizes are summarized in **Table 1**.

Governing Equations and Boundary Condition

The steady-state continuity, momentum and energy equations are solved simultaneously in this model. Equations (1) and (2) are the continuity and momentum equations, respectively, and Equations (3)–(5) are the energy equations for the free flow, reactor solid structure, and porous flow, respectively:

$$\nabla \cdot \left(\rho_f \vec{u}\right) = 0, \tag{1}$$

$$\nabla \cdot \left(\rho_f \vec{u}\vec{u}\right) = -\nabla p + \nabla \cdot \bar{\bar{\tau}} + \rho_f \vec{g} + \vec{F}, \tag{2}$$

$$\nabla \cdot \left[\vec{u}\left(\rho_f E_f + p_f\right)\right] = \nabla \cdot \left(k_f \nabla T\right), \tag{3}$$

$$\nabla \cdot \left(k_s \nabla T\right) = 0, \text{ and} \tag{4}$$

$$\nabla \cdot \left[\vec{u}\left(\rho_f E_f + p_f\right)\right] = \nabla \cdot \left(k_{eff} \nabla T\right) + \dot{q}''', \tag{5}$$

where ρ, $\vec{u}$, p, $\bar{\bar{\tau}}$, $\vec{g}$, k, T, and $\dot{q}'''$ are, respectively, the density, velocity, pressure, stress tensor, gravity acceleration, thermal conductivity, temperature, and power density. The subscript f and s indicate fluid and solid, respectively. The porous flow shares the same continuity and momentum equations with the free flow except that the velocity in porous flow is superficial velocity, defined as $\vec{u}_{\text{superficial}} = \vec{u} \cdot \varepsilon$, where ε is the porosity. The momentum source $\vec{F}$ in porous flow is discussed later. The effective thermal conductivity k_{eff} in Equation (5) is defined as $k_{eff} = \varepsilon k_f + (1 - \varepsilon) k_s$.

In this study, the helium gas was treated as a compressible ideal gas when calculating its density. The Nuclear Safety Standards Commission (KTA) correlations were adopted for its other thermophysical properties (Nuclear Safety Standards

Commission, 1978):

$$c_{p\ \text{helium}} = 5195, \text{unit in J/kg/K} \quad (6)$$

$$k_{\text{helium}} = 2.682 \times 10^{-3}\left(1 + 1.123 \times 10^{-3}p\right) T^{0.71(1-2\times10^{-4}p)}, \text{unit in W/m/K} \quad (7)$$

$$\mu_{\text{helium}} = 3.674 \times 10^{-7} T^{0.7}, \text{unit in Pa·s} \quad (8)$$

It should be noted the units of temperature T and pressure p in Equations (7) and (8) are K and bar, respectively.

The thermal conductivity of un-irradiated graphite IG-110 is about 80–126 W/m-K and its value decreases with increasing temperature (Sumita et al., 2009; Oh et al., 2011b). The irradiated nuclear graphite IG-110 is less sensitive to its temperature, which varies between 30 and 52 W/m-K depending on the irradiation damage level (Sumita et al., 2009). Therefore, in this study, the graphite thermal conductivity was set as 50 W/m-K. The thermal conductivity of core barrel and RPV, in units of W/m/K, was calculated using the correlation for Alloy 800H (T in K):

$$k = 4.7857 \times 10^{-5}T^2 - 0.0768T + 51.8715 \quad (9)$$

Since this study focuses on the decay heat removal after a natural circulation flow through the reactor core has been established, the reactor core is cooled down slowly, which could be reasonably regarded as a quasi-steady state condition (Oh et al., 2012). The heat source is the decay heat from the active fuel columns and the final heat sink is the RCCS. The core axial power profile for each fuel ring was divided into three regions with a parabolic curve fit to the results by Strydom and Epiney (2012) to obtain the power profiles. The fitting correlations are expressed by Equations (10)–(12), and a comparison with Strydom and Epiney's values is depicted in **Figure 4**. It should be noted that the variable z in Equations (10)–(12) is the height measured from the bottom surface of the hot plenum in unit of meters. The correlations were then multiplied by a factor to simulate the reactor decay power. The material thermophysical properties and the power distribution were imported to ANSYS Fluent 19.1 via User Defined Functions (UDF).

$$\dot{q}'''_{\text{inner}} = \begin{cases} 0.0488z^2 + 0.316z + 2.44, & 1.983 \le z < 6.088 \\ -0.2957z^2 + 5.5407z - 16.32, & 6.088 \le z < 8.738 \\ -1.2639z^2 + 21.5887z - 82.6285, & 8.738 < z \le 10.813 \end{cases} \quad (10)$$

$$\dot{q}'''_{\text{middle}} = \begin{cases} 0.0209z^2 + 0.5352z + 1.3183, & 1.983 \le z < 6.150 \\ -0.3151z^2 + 5.4858z - 16.41, & 6.150 \le z < 8.681 \\ -1.0699z^2 + 18.1784z - 69.7261, & 8.681 < z \le 10.813 \end{cases} \quad (11)$$

$$\dot{q}'''_{\text{outer}} = \begin{cases} -0.0145z^2 + 0.9010z + 0.8160, & 1.983 \le z < 5.969 \\ -0.3334z^2 + 5.9138z - 17.7431, & 5.969 \le z < 8.623 \\ -1.42z^2 + 24.2054z - 94.6761, & 8.623 < z \le 10.813 \end{cases} \quad (12)$$

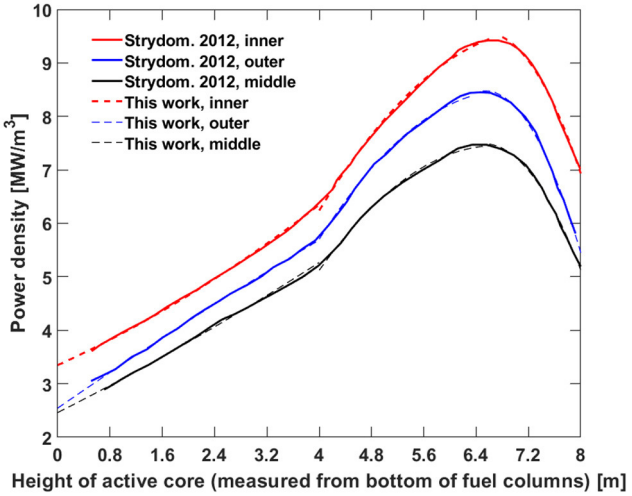

FIGURE 4 | Comparison of the reactor power density correlations with original reference values.

In addition to the helium natural convection flow in the core, thermal radiation between the outer surface of the core barrel and the inner surface of the RPV wall was computed by the surface to surface (S2S) radiation module. The cooling mechanism outside the RPV includes natural convection in the reactor cavity and thermal radiation to the RCCS. The radiation to the RCCS was simulated by assuming an emissivity value of 0.87 for the RPV outer surface with an RCCS temperature of 373 K. The natural convection flow was computed by assigning a heat transfer coefficient with an environment temperature of 423 K. In this work, the heat transfer coefficient was estimated by the following process. First, a steady-state condition is assumed so the energy balance can be written as:

$$Q = \int h(T_w - T_\infty)\mathrm{d}A + \int \sigma(T_w^4 - T_{RCCS}^4)\mathrm{d}A, \quad (13)$$

where Q, h, T_w, T_∞, T_{RCCS}, and σ are the total decay power, heat transfer coefficient, RPV wall temperature, reactor cavity air temperature, RCCS temperature, and Stefan-Boltzmann constant, respectively. However, the RPV surface temperature distribution was unknown. Therefore, we assumed an uniform RPV wall temperature distribution when estimate the heat transfer coefficient. Accordingly, Equation (13) can be simplified to:

$$Q = Ah(T_w - T_b) + A\sigma(T_w^4 - T_{RCCS}^4). \quad (14)$$

The Nusselt number for free natural convection over a vertical surface can be calculated by the Churchill correlation (Churchill and Chu, 1975):

$$Nu = \frac{hL}{k} = \left\{0.825 + 0.387Ra^{1/6}/\left[1 + (0.492/\,\mathrm{Pr})^{9/16}\right]^{8/27}\right\}^2. \quad (15)$$

TABLE 2 | Verification of the fuel block and bypass gap simplifications.

Category		Parameter	Porous hexagonal body	One single coolant channel	
Fuel block	Input	Shape	Hexagonal block	Circular tube	
		Dimension [m]	W0.208 × H2	D0.0158 × H2	
		Porosity	0.188	–	
		Inlet velocity [m/s]	0.0942	0.5	
		Inlet temperature [K]	973	973	
		Thermal power	$\dot{q}''' = 190.8$ [kW/m^3]	$\dot{q}'' = 4000$ [W/m^2]	
	Results		Simulation	Simulation	Theoretical
		Pressure drop [Pa]	5.79	6.01	5.81
		Maximum temperature [K]	1221.3	1260.7	1281.2
Bypass gap	Input	Parameter	Porous gap	Free flow gap	
		Shape	Rectangular	Rectangular	
		Dimension (W × L× H) [m]	0.04 × 0.208 × 1.0	0.002 × 0.208 × 1.0	
		Porosity	0.05	–	
		Inlet velocity [m/s]	0.05	1.0	
		Inlet temperature [K]	973	973	
		Wall heat flux [kW/m^2]	5.0	5.0	
	Results		Simulation	Simulation	Theoretical
		Pressure drop [Pa]	136.0	134.2	135.9
		Maximum wall temperature [K]	1273.1	1284.7	1286.3

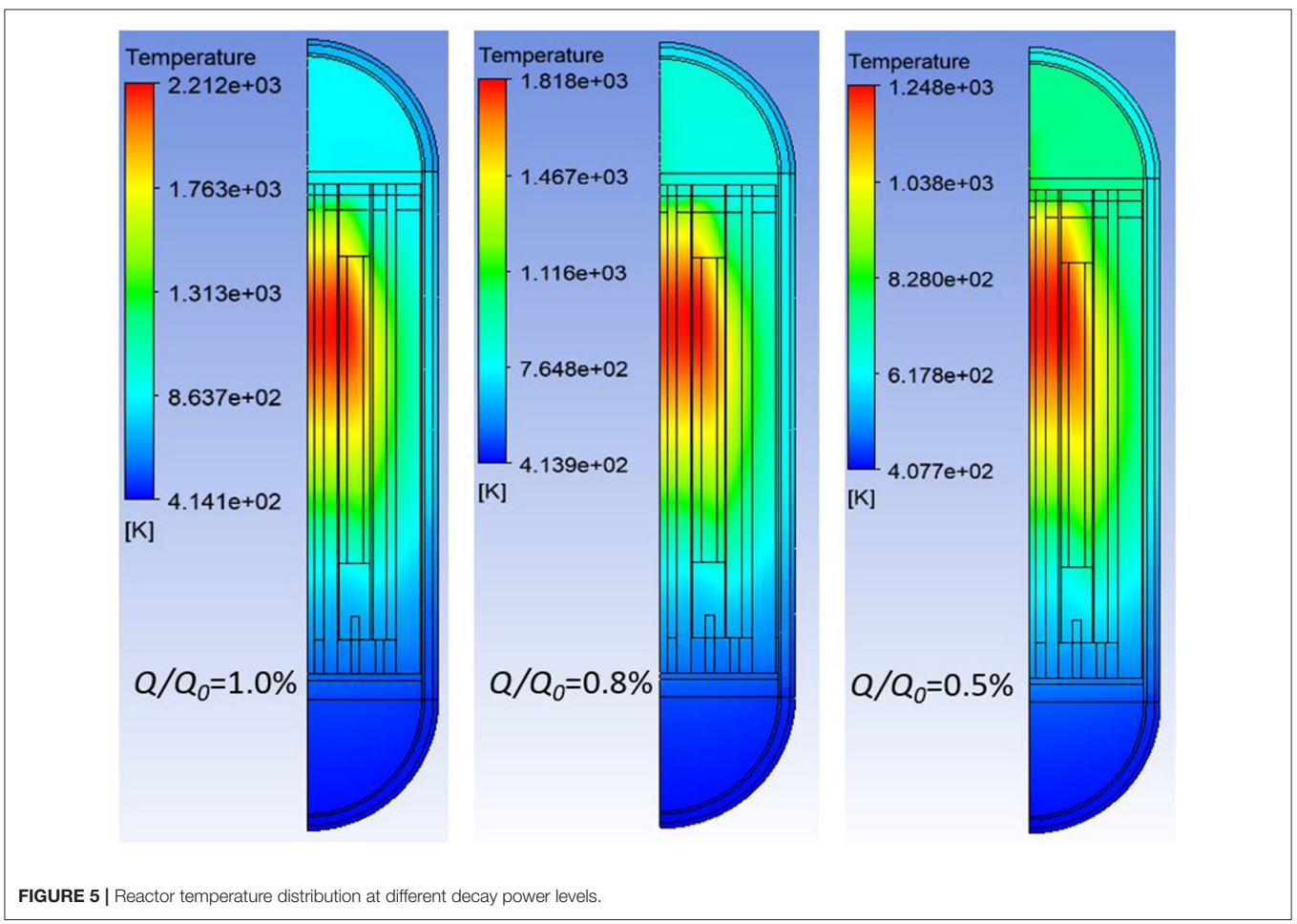

FIGURE 5 | Reactor temperature distribution at different decay power levels.

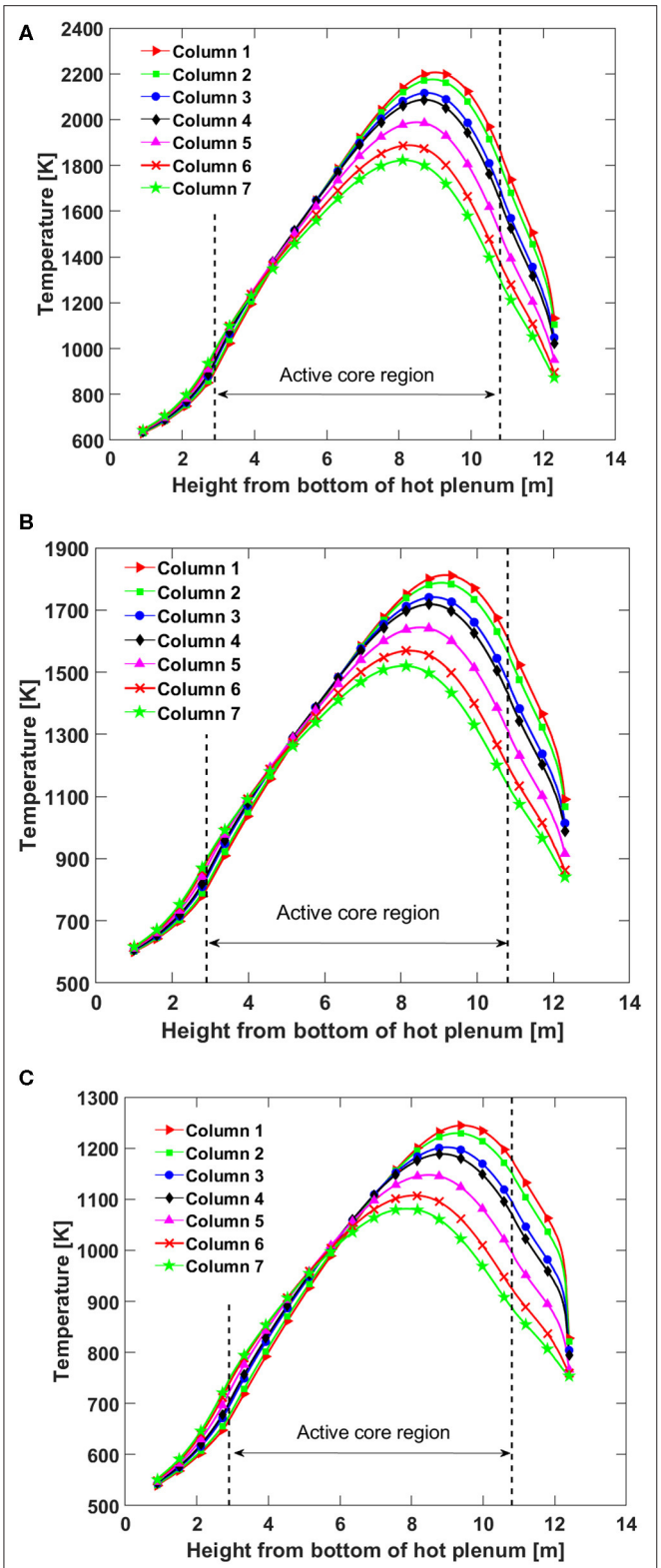

FIGURE 6 | Reactor temperature distributions for the decay power at: **(A)** 1.0%, **(B)** 0.8%, and **(C)** 0.5% of the reactor rated thermal power.

Then, the heat transfer coefficient can be obtained by solving Equations (14) and (15). In the calculation, an arbitrary RPV surface temperature was used as an initial estimate. The Rayleigh number and Prandtl number in Equation (15) are evaluated at a gas film temperature that is the mean value of the RPV wall temperature and environment temperature. Therefore, iteration can be carried out to obtain the value of T_w, and thus the value of h. In this work, the heat transfer coefficient is about 15 W/m^2-K. The boundary condition of the RPV wall used in this study is more conservative than studies performed by Zheng et al. (2018).

Porous Medium Parameters

The fuel columns were simplified into homogenous porous bodies to avoid generating tremendous extra fine meshes for each individual coolant channel. The pressure loss in these porous bodies should be maintained the same as the prototypic values given the same mass flow rate and temperature conditions. The porous flow is modeled by a momentum source in ANSYS Fluent 19.1 (ANSYS Inc., 2018). For a homogeneous porous medium equation, the momentum source is given as (ANSYS Inc., 2018):

$$S_i = -\left(\frac{\mu}{\alpha}u_i + C_2\frac{1}{2}\rho u_{mag}u_i\right), \tag{16}$$

where μ, α, u_{mag}, and C_2 are the fluid viscosity, permeability, flow velocity magnitude, and inertial resistance factor, respectively. The subscript i indicates a specified flow direction.

The porosity of the porous fuel column is defined as the ratio of the fluid volume to the total fuel column volume:

$$\varepsilon = \frac{\frac{1}{4}\pi D^2 N}{\frac{3\sqrt{3}}{2}L^2}, \tag{17}$$

where N, D, and L are the number of the coolant channels in one fuel column, the diameter of the coolant channel, and the length of the hexagon short edge, respectively. Assume the flow velocity in a prototypic coolant channel is u_1, then the flow velocity in the porous medium can be calculated by:

$$u_2 = \frac{u_1\frac{N}{4}\pi D^2}{\frac{3\sqrt{3}}{2}L^2} = u_1\varepsilon. \tag{18}$$

For the natural circulation in the extended P-LOFC accident the flow in the coolant channels falls into the laminar flow regime. Therefore, the pressure change rate in the circular coolant channel, neglecting the developing flow region, is given as:

$$\frac{\triangle p}{L} = -\frac{1}{2}\frac{64}{\mathrm{Re}}\rho u_1^2\frac{1}{D} = -\frac{32\mu u_1}{D^2}. \tag{19}$$

Equation (19) should be equal to Equation (16) if the same pressure loss is maintained at the same mass flow rate:

$$\frac{32\mu u_1}{D^2} = \frac{\mu}{\alpha}u_2 + C_2\frac{1}{2}\rho {u_2}^2. \tag{20}$$

Therefore, the porous flow parameter for the fuel columns can be obtained as: $\frac{1}{\alpha} = \frac{32}{\varepsilon D^2}$ m^{-2} and $C_2 = 0$.

In the prototypic MHTGR design, small bypass gaps with a width of 2∼3 mm were left between the graphite reflectors, and between the permanent reflectors and the core barrel, as shown in **Figure 1**. These gaps are used to accommodate the graphite manufacturing tolerance and thermal expansion during operation. However, the exact dimension of the bypass gaps is unknown because of possible misalignment during installation and graphite densification caused by neutron irradiation. A gap width of 2 mm was therefore adopted as a reference value in this research to study the natural circulation flow pattern for different core decay power levels. Two additional simulations were also carried out with different bypass gap width values, i.e., 3 and 4 mm, to study the sensitivity of the natural circulation flow rate to the bypass gap size. However, the narrow gap leads to difficulties in generating high-quality meshes within an acceptable quantity. In this research, the width of the bypass gaps were enlarged to 40 mm so the length/width ratio can be reduced to avoid high skewness of the mesh elements. To compensate the enlarged cross sectional area of the bypass gaps, a porous flow model was applied. The prototypic gap width is much smaller than the horizontal edge length of the graphite blocks, which can be regarded as infinitely parallel. Using the same method described above, the porous parameters for the bypass gaps are: $\frac{1}{\alpha} = \frac{12}{\varepsilon W^2}$ and $C_2 = 0$, where W is the prototypic gap width and $\varepsilon = \frac{W}{40\text{ mm}}$.

To verify the porous body assumption, simulations were performed for the fuel columns and bypass gaps. Comparisons of the two simplifications are shown in **Table 2**. It can be seen that both simplifications preserve the pressure loss with good accuracy for the same given mass flow rate. However, the

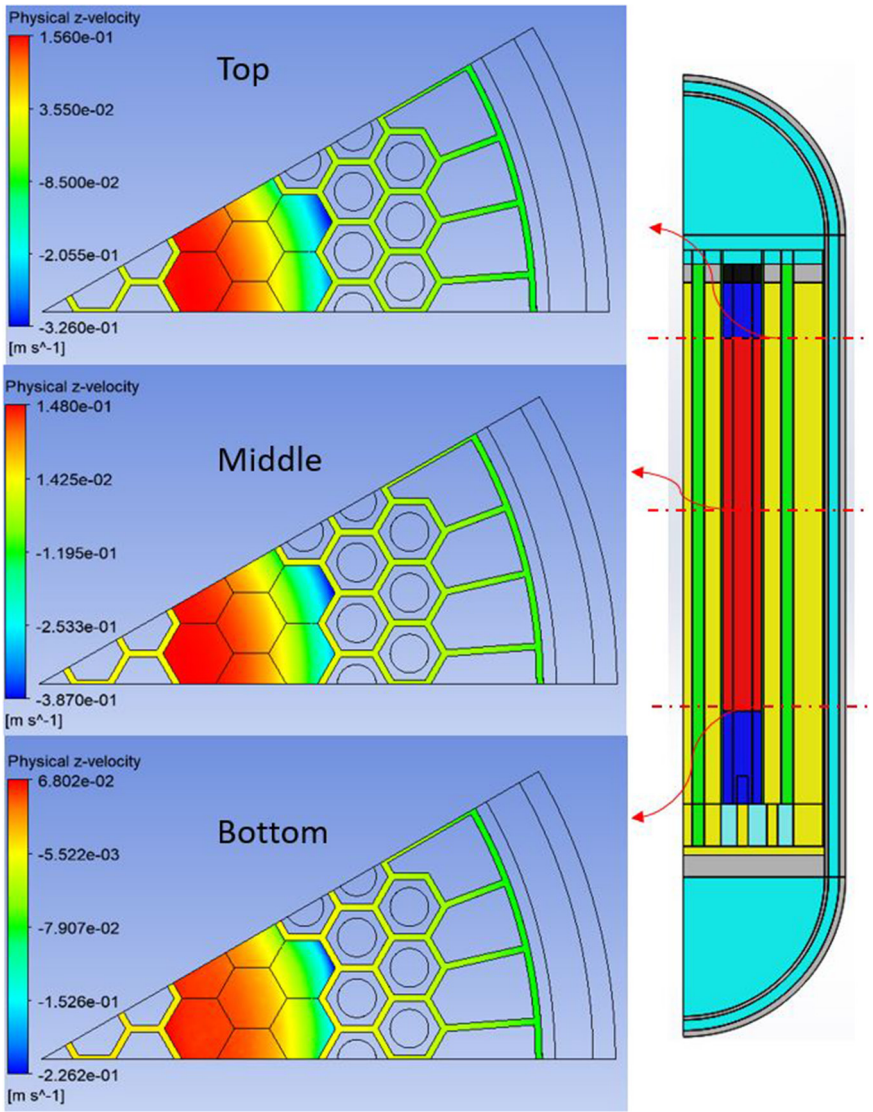

FIGURE 7 | Vertical helium velocity contour at the decay power of 1.0% of the reactor rated power.

maximum temperature of the porous flow simulation is always lower than the theoretical solution due to the thermal equilibrium assumption in the porous heat transfer model. This assumption does not calculate the heat transfer between the solid and fluid domains. Therefore, the temperature gradient near the solid-fluid interface of the prototypic structure cannot be preserved. In general, the porous flow assumption for the fuel columns and bypass gaps is acceptable.

RESULTS AND DISCUSSION

Decay Heat Removal at Different Power Levels

The reactor temperature distributions at decay power levels of 1, 0.8, and 0.5% are shown in **Figure 5**. As can be seen, the maximum temperature of the three simulated cases are 2,212, 1,818, and 1,248 K, respectively. The hot zones appear at the upper half region of the active fuel columns due to the peak power values there, as shown in **Figure 4**. The homogenized temperature distributions of the seven fuel columns in the simulation domain at the core decay power levels of 1.0, 0.8, and 0.5% of the reactor rated power are depicted in **Figure 6**. Fuel column 7 has the lowest temperature because its distance to the core barrel is the smallest. In **Figure 6**, the temperature peaks at a height about 8–9 m measured from the bottom of the hot plenum mainly due to the axial power distribution shape (Strydom and Epiney, 2012). The fuel column temperature starts to decrease

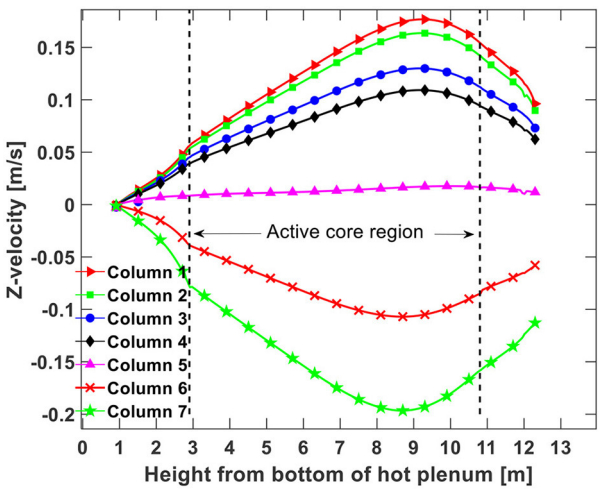

FIGURE 8 | Distributions of the helium axial velocity for a decay power of 1.0% of the reactor rated power.

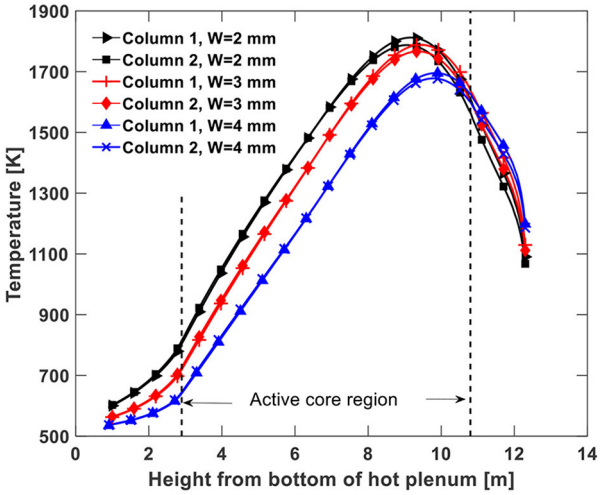

FIGURE 9 | Temperature distributions of fuel columns 1 and 2 with different gap widths.

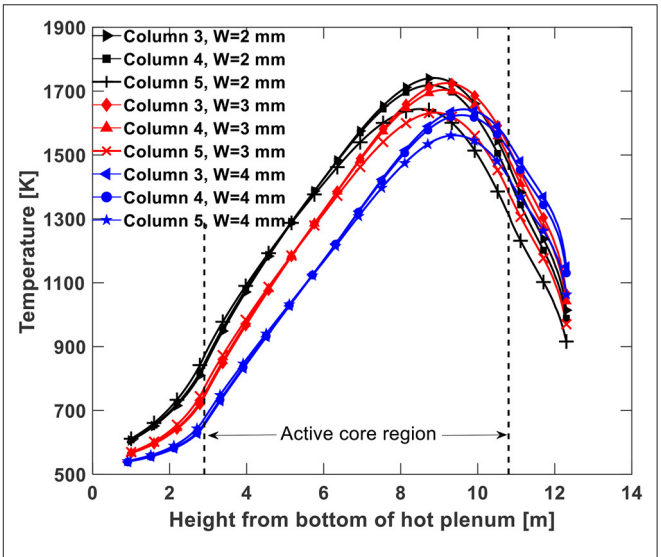

FIGURE 10 | Temperature distributions of fuel columns 3, 4, and 5 with different gap widths.

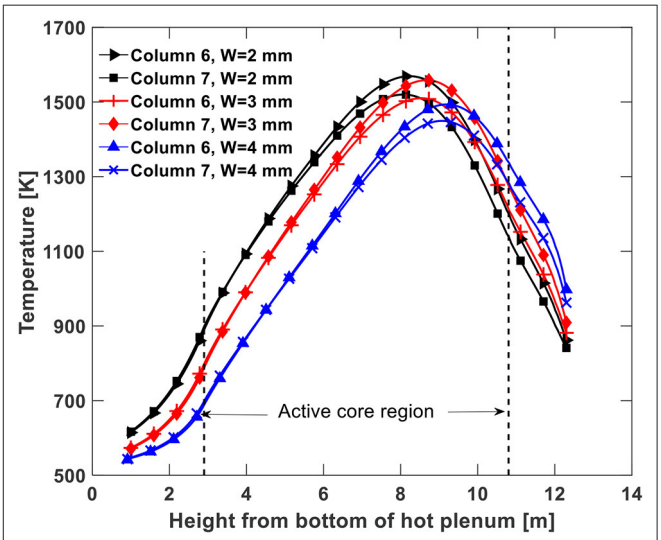

FIGURE 11 | Temperature distributions of fuel columns 6 and 7 with different gap widths.

after the peaks, which indicates that the natural circulation is not strong enough to bring the maximum fuel temperature to the top of the fuel column. Instead, the horizontal thermal conduction through graphite material plays a more dominant role in decay heat removal.

The maximum fuel temperature at the 1.0% decay power exceeds the fuel design limit of 1,873 K for the fuel. However, it does not necessarily mean that the reactor core will be overheated because it depends on the duration of the transient. The time required for the reactor shutdown heat generation rate, i.e., essentially the decay power, to drop to 1.0, 0.8, and 0.5% of the reactor rated power is about 3.48, 10.6, and 111.3 h, respectively, if a typical light water reactor decay power curve is assumed for MHTGR (Todres and Kazimi, 2012). If the decay power during the first 3.48 h heats up the reactor core materials to a temperature close to the design limit, then the design limit might be exceeded. The other possibility is that the accumulated decay energy cannot heat the reactor materials up to a value close to 1,873 K. Then under this scenario, the reactor core will slowly cool down from some time after reactor shutdown.

Therefore, a short-term P-LOFC transient simulation is required in the future to confirm whether there is any fuel overheating and whether that would result in significant fuel damage.

One concern regarding the P-LOFC accident is possible thermal jet flow that can result in overheating of or thermal striping to the upper plenum wall. However, as depicted in **Figure 7**, the maximum velocity of the upward helium flow from the active core to the upper plenum is only about 0.16 m/s. **Figure 8** presents the computed distributions of the helium axial flow velocity in the seven fuel columns for the decay power of 1.0% of the reactor rated power. The helium axial flow velocity profile for the other two cases are very similar to **Figure 8**, therefore they are not presented.

Due to the lower temperatures in fuel columns 6 and 7, the downward flow mainly occurs in those two fuel columns.

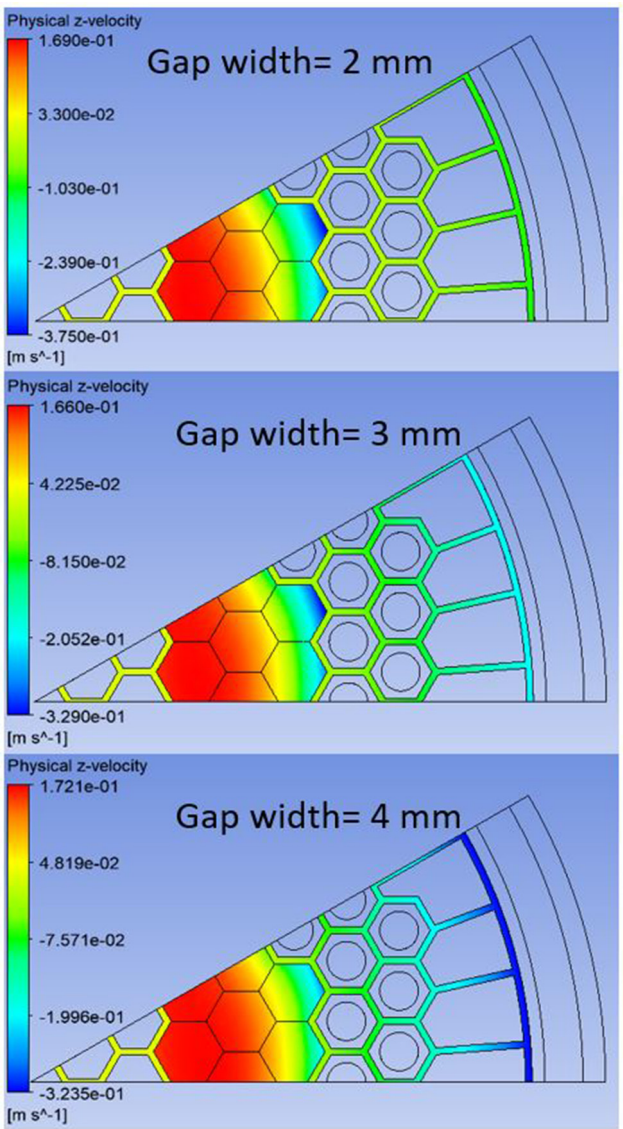

FIGURE 12 | Distributions of the helium axial velocity at the top of the active core ($z = 10.88$ m measured from the bottom surface of the hot plenum) with different bypass gap widths.

Effect of Bypass Gap Width on Decay Heat Removal

It has been assumed in the literature that the bypass gaps play a significant role in the plenum-to-plenum natural circulation during the HTGR pressurized cooling down process because the lower helium temperature there generates the largest downward flow potential. However, the width of the bypass gaps can vary due to graphite block misalignment, neutron irradiation, and thermal expansion. In this study, three width values, namely 2, 3, and 4 mm, were used in simulations at a decay power level of 0.8% of the reactor rated power to examine its effect on decay heat removal. The temperature distributions along the centerline of the seven fuel columns are given in **Figures 9–11** for the three gap width value cases. As can be found, the peak fuel column temperature drops by small values if the gap was enlarged from 2 to 3 mm. However, if the bypass gaps were further enlarged to 4 mm, the peak fuel temperatures drop considerably. The temperature drop is caused by stronger natural circulation flow brought on by the wider bypass gap. In addition, another trend observed is that the temperature peaks move to higher positions with increased bypass gap widths, which also results from the stronger natural circulation flow.

TABLE 3 | Helium mass flow rate in the fuel columns and bypass gaps for the 1/12 core sector [$\times 10^{-2}$ kg/s].

Gap width W (mm)	2	3	4
Upward flow in fuel columns	3.627	3.828	4.623
Downward flow in fuel columns	3.061	2.058	1.033
Upward flow in bypass gaps	0.055	0.054	0.071
Downward flow in bypass gaps	0.620	1.824	3.670

Figure 12 shows the helium axial flow velocity contours in the fuel columns using three different bypass gaps widths. As discussed in section Porous Medium Parameters, the flow resistance factor drops by a factor of 8 if the bypass gaps are enlarged from 2 to 4 mm with the same helium mass flow rate. Accordingly, the helium flow rate in the bypass gaps should increase with larger bypass gaps, which is confirmed by the simulation data in **Table 3**. When the bypass gap width is 2 mm the fraction of the downward helium flow in the bypass gaps is only about 16.8% of the total downward flow, which increases to 78% when the gap width is 4 mm. Depending on the location of the downward flow, the heat transfer rate of the helium natural circulation is different. The closer the downward flow is to the core barrel, the more effectively it can be cooled. This is the main reason for the decreased maximum fuel temperature with increasing bypass gaps, as depicted in **Figures 9–11**.

CONCLUSION

Three-dimensional CFD simulations were performed to investigate the development of the plenum-to-plenum natural circulation flow during an extended P-LOFC accident in the MHTGR. Potential heat transfer paths were included in the simulation while the multi-channel reactor core was regarded as a porous medium.

Helium natural circulation flow and temperature distributions in the reactor were obtained at three decay power levels, 1.0, 0.8, and 0.5% of the reactor rated power. The helium flow velocity distributions are similar in the three cases studied. Maximum fuel temperature appears in the upper half of the fuel column region due to the larger heat generation rate there. The helium natural circulation flow does not lead to significant thermal jets into the upper plenum. In general, the heat conduction through the graphite reflectors and RPV vessel to the RCCS in the horizontal direction plays a dominant role in decay heat removal. In addition, the simulation results suggest additional transient studies covering the first several hours after reactor shutdown be conducted for reactor safety analysis in the future.

Helium natural circulation flow is very sensitive to the width of the bypass gaps between graphite blocks, permanent reflectors, and the core barrel. The helium flow in the bypass gaps is only about 16.8% of the total flow when the bypass gap width is 2 mm. However, this increase to 78% in this simulation if the width is enlarged to 4 mm. In conclusion, the enlarged bypass gaps have two effects on the natural circulation pattern. First, the total helium flow rate will be increased and second, more downward flow occurs in the bypass gaps. These effects lead to lower maximum fuel temperature for larger bypass gap widths. In addition, the stronger natural circulation brings the maximum fuel temperature to a higher position. Therefore, the actual width of the bypass gaps is worth of investigation in detail.

DATA AVAILABILITY STATEMENT

The datasets generated for this study are available on request to the corresponding author.

AUTHOR CONTRIBUTIONS

CW performed this study under the supervision of XS and PS. All authors contributed to the article and approved the submitted version.

FUNDING

This research was performed using funding received from the DOE Office of Nuclear Energy's Nuclear Energy University Program (NEUP). The authors appreciate the financial support from the DOE NEUP office.

ACKNOWLEDGMENTS

The authors wish to acknowledge Prof. Annalisa Manera and Dr. Victor Petrov of the University of Michigan for their insightful suggestions to this work.

REFERENCES

Alonso, G., Ramirez, R., Valle, E., Del, and Castillo, R. (2014). Process heat cogeneration using a high temperature reactor. *Nucl. Eng. Des.* 280, 137–143. doi: 10.1016/j.nucengdes.2014.10.005

ANSYS Inc. (2018). *ANSYS Fluent User's Guide. 19.1*. Canonsburg, PA. Available online at: https://www.afs.enea.it/project/neptunius/docs/fluent/html/ug/main_pre.htm (accessed February 12, 2020).

Churchill, S. W., and Chu, H. H. S. (1975). Correlating equations for laminar and turbulent free convection from a vertical plate. *Int. J. Heat Mass Transf.* 18, 1323–1329. doi: 10.1016/0017-9310(75)90243-4

Fang, C., Morris, R., and Li, F. (2017). Safety features of high temperature gas cooled reactor. *Sci. Technol. Nucl. Install.* 2017, 3–6. doi: 10.1155/2017/9160971

Ferng, Y. M., and Chen, C. T. (2011). CFD investigating thermal-hydraulic characteristics and hydrogen generation from graphite-water reaction after SG tube rupture in HTR-10 reactor. *Appl. Therm. Eng.* 31, 2430–2438. doi: 10.1016/j.applthermaleng.2011.04.007

Ferng, Y. M., and Chi, C. W. (2012a). CFD investigating the air ingress accident for a HTGR simulation of graphite corrosion oxidation. *Nucl. Eng. Des.* 248, 55–65. doi: 10.1016/j.nucengdes.2012.03.041

Ferng, Y. M., and Chi, C. W. (2012b). CFD investigating the air ingress accident occurred in a HTGR-simulation of thermal-hydraulic characteristics. *Nucl. Eng. Des.* 245, 28–38. doi: 10.1016/j.nucengdes.2012.01.004

Jin, H. G., No, H. C., and Park, B. H. (2012). Effects of the onset time of natural circulation on safety in an air ingress accident involving a HTGR. *Nucl. Eng. Des.* 250, 626–632. doi: 10.1016/j.nucengdes.2012.06.028

No, H. C., Lim, H. S., Kim, J., Oh, C., Siefken, L., and Davis, C. (2007). Multi-component diffusion analysis and assessment of GAMMA code and improved RELAP5 code. *Nucl. Eng. Des.* 237, 997–1008. doi: 10.1016/j.nucengdes.2006.10.020

Nuclear Energy Agency (2018). *NEA Benchmark of the Modular High-Temperature Gas-Cooled Reactor-350 MW Core Design Volumes I and II*. Available online at: http://www.oecd.org/officialdocuments/publicdisplaydocumentpdf/?cote=NEA/NSC/R(2017)4&docLanguage=En (accessed February 12, 2020).

Nuclear Safety Standards Commission (1978). *Safety Standards of the Nuclear Safety Standards Commission (KTA) Part 1: Calculation of the Material Properties of Helium*.

Oh, C. H., Kang, H. S., and Kim, E. S. (2011a). Air-ingress analysis: part 2 - computational fluid dynamic models. *Nucl. Eng. Des.* 241, 213–225. doi: 10.1016/j.nucengdes.2010.05.065

Oh, C. H., Kim, E. S., and Kang, H. S. (2012). Natural circulation patterns in the VHTR air-ingress accident and related issues. *Nucl. Eng. Des.* 249, 228–236. doi: 10.1016/j.nucengdes.2011.09.031

Oh, C. H., Kim, E. S., No, H. C., and Cho, N. Z. (2011b). *Final Report on Experimental Validation of Stratified Flow Phenomena, Graphite Oxidation, and Mitigation Strategies of Air Ingress Accidents*. Idaho Falls, ID.

Said, I. A., Taha, M. M., Usman, S., and Al-Dahhan, M. H. (2018). Effect of helium pressure on natural convection heat transfer in a prismatic dual-channel circulation loop. *Int. J. Therm. Sci.* 124, 162–173. doi: 10.1016/j.ijthermalsci.2017.10.004

Strydom, G., and Epiney, A. S. (2012). "RELAP5-3D results for Phase I (exercise 2) of the OECD/NEA MHTGR-350 MW Benchmark," *in International Congress on Advances in Nuclear Power Plants (Chicago*, IL*)*, 387–395.

Sumita, J., Shibata, T., Nakagawa, S., Iyoku, T., and Sawa, K. (2009). Development of an evaluation model for the thermal annealing effect on thermal conductivity of IG-110 graphite for high-temperature gas-cooled reactors. *J. Nucl. Sci. Technol.* 46, 690–698. doi: 10.1080/18811248.2007.9711576

Takamatsu, K., Tochio, D., Nakagawa, S., Takada, S., Yan, X. L., Sawa, K., et al. (2014). Experiments and validation analyses of HTTR on loss of forced cooling under 30% reactor power. *J. Nucl. Sci. Technol.* 51, 1427–1443. doi: 10.1080/00223131.2014.967324

Todres, N. E., and Kazimi, M. S. (2012). *Nuclear Systems, Volume 1, Thermal Hydraulic Fundamentals, 2nd Edn*. Moca Raton, FL: CRC Press. doi: 10.1201/b14887

Tung, Y., and Johnson, R. W. (2011). "CFD calculations of natural circulation in a high temperature gas reactor rollowing pressurized circulator shutdown," in *Proceedings of the ASME 2011 International Mechanical Engineering Congress and Exposition* (Denver, CO), 1–9. doi: 10.1115/IMECE2011-64259

U.S. Department of Energy (1986). *Preliminary Safety Information Document for the Standard MHTGR*.

Wang, C., Sun, X., and Christensen, R. N. (2019). Multiphysics simulation of moisture-graphite oxidation in MHTGR. *Ann. Nucl. Energy* 131, 483–495. doi: 10.1016/j.anucene.2019.03.040

Wang, Y., Zheng, Y., Li, F., and Shi, L. (2014). Analysis on blow-down transient in water ingress accident of high temperature gas-cooled reactor. *Nucl. Eng. Des.* 271, 404–410. doi: 10.1016/j.nucengdes.2013.12.009

Zheng, Y., Stempniewicz, M. M., Chen, Z., and Shi, L. (2018). Study on the DLOFC and PLOFC accidents of the 200 MWe pebble-bed modular high temperature gas-cooled reactor with TINTE and SPECTRA codes. *Ann. Nucl. Energy* 120, 763–777. doi: 10.1016/j.anucene.2018.06.041

Conflict of Interest: The authors declare that the research was conducted in the absence of any commercial or financial relationships that could be construed as a potential conflict of interest.

frontiers in Energy Research

ORIGINAL RESEARCH
published: 03 July 2020
doi: 10.3389/fenrg.2020.00112

Numerical Investigation of Turbulent Heat Transfer Properties at Low Prandtl Number

Xiang Chai[1]*, *Xiaojing Liu*[1], *Jinbiao Xiong*[1] and *Xu Cheng*[2]

[1] School of Nuclear Science and Engineering, Shanghai Jiao Tong University, Shanghai, China, [2] Institute for Applied Thermofluidics, Karlsruhe Institute of Technology, Karlsruhe, Germany

The sodium-cooled fast reactor (SFR), which is one of the most promising candidates for meeting the goal declared by the Generation IV International Forum (GIF), has drawn a lot of attention. Turbulent heat transfer in liquid sodium, which is a low-Prandtl fluid, is an extremely complex phenomenon. The limitations of the commonly used eddy diffusivity approach have become more evident when considering low-Prandtl fluids. The current study focuses on the assessment and optimization of the existing modeling closure for single-phase turbulence in liquid sodium based on reference results provided by the LES method. In this study, a wall-resolved Large-Eddy Simulation was performed to simulate the flow and heat transfer properties in a turbulent channel at low Prandtl number. The simulation results were first compared with the DNS results obtained from the literature. A good agreement demonstrated the capability of the employed numerical approach to predict the turbulent and heat transfer properties in a low-Prandtl number fluid. Consequently, new reference results were obtained for the typical Prandtl number and wall heat flux of an SFR. A time-averaged process was employed to evaluate the temperature profile quantitatively as well as the turbulent heat flux. Their dependency was also evaluated based on a systematic CFD simulation that covers the typical Reynolds numbers of SFRs. Based on the reference results obtained, the coefficients employed in an algebraic turbulent heat flux model (AFM) are calibrated. The optimized coefficients provide more accurate prediction of heat transfer properties for typical flow conditions of an SFR than the existing models found in the literature.

Keywords: CFD, sodium, low Prandtl number, Large-Eddy Simulation, AFM model

OPEN ACCESS

Edited by:
Wenxi Tian,
Xi'an Jiaotong University, China

Reviewed by:
Victor Petrov,
University of Michigan, United States
Igor A. Bolotnov,
North Carolina State University, United States
Yixiang Liao,
Helmholtz-Gemeinschaft Deutscher Forschungszentren (HZ), Germany

***Correspondence:**
Xiang Chai
xiangchai@sjtu.edu.cn

Specialty section:
This article was submitted to Nuclear Energy, a section of the journal Frontiers in Energy Research

Received: *11 January 2020*
Accepted: *12 May 2020*
Published: *03 July 2020*

Citation:
Chai X, Liu X, Xiong J and Cheng X (2020) Numerical Investigation of Turbulent Heat Transfer Properties at Low Prandtl Number. Front. Energy Res. 8:112. doi: 10.3389/fenrg.2020.00112

INTRODUCTION

The sodium-cooled fast reactor (SFR), which is one of the new generation of nuclear power plant designs, has been considered to be one of the most promising candidates for meeting the goal declared by the Generation IV International Forum (GIF) (Sun, 2012). The pitch between neighboring fuel rods in the design of the fuel assembly is usually very small due to the good thermal conductivity of liquid sodium. A small change of flow area caused by corrosive products may have a significant influence on coolant temperature and threaten the integrity of the fuel assembly. Hence, the thermal hydraulics of liquid sodium have drawn a lot of attention. It is believed that turbulent heat transfer in the liquid sodium, which is a low-Prandtl fluid, is an extremely complex phenomenon. Due to a lack of detailed knowledge about the heat transfer process, turbulent modeling of low-Prandtl number fluid is still quite limited.

In the past few decades, a lot of effort has been devoted to investigating the flow and heat transfer properties of liquid sodium (Schumm et al., 2016; Da Vià and Manservisi, 2019). A lot of work, including both experimental and numerical studies, has been carried out to provide information on heat transfer in liquid sodium. In these studies, the sodium flow inside a 7-pin rod bundle with wire-wrapped spacers was experimentally measured by Lorenz and Ginberg (1977). The temperature distributions obtained can be employed for the validation calculations of numerical configuration. Moreover, Bogoslovskaya et al. (2000) investigated the integral mixing factors between neighboring sub-channels based on the measurement of the velocity distribution surrounding fuel pins in which the electrical conductivity of liquid metal was employed. Because sodium coolant is a potential fire hazard, experimental data of liquid sodium is still quite limited. More recently, experimental study of lead-bismuth eutectic, which is another low Prandtl fluid, has become much more popular (Pacio et al., 2016). However, it is almost infeasible to provide detailed profiles of flow and heat transfer properties inside the rod bundle of an SFR with standard measurement devices. Hence, accurate modeling of turbulent heat transfer in liquid sodium remains a great challenge due to the lack of information about the complex mechanism involved.

With increasing computer power, the employment of the CFD approach has gained considerable attention. If employing the commonly used eddy diffusivity approach, it is necessarily important to clearly clarify the influence from the turbulent Prandtl number. In this classical approach, a turbulent Prandtl number which is equal to unity or close to unity fails to accurately predict the heat transfer, especially for liquid sodium (Cheng and Tak, 2006a; Grotzbach, 2013). Several models that aim at solving this problem have been proposed to estimate the turbulent Prandtl number for low-Prandtl fluids over several decades (Kays, 1994; Churchill, 2002). The turbulent Prandtl number is treated as a function of the Reynolds number or Peclet number. Based on it, a strong circumferential non-uniformity of heat transfer in bare rod bundles can be found in the numerical results of liquid metal. However, it has been found that a uniform profile of the turbulent Prandtl number is not suitable to describe the profile of turbulent heat flux and fails to accurately predict the profile of turbulent heat flux, especially in the near-wall region (Duponcheel et al., 2014). The value of the turbulent Prandtl number in the near-wall region is much larger than that in the channel center. In order to circumvent the drawbacks of the eddy diffusivity approach, the transport equation of the turbulent heat flux is carefully analyzed based on the assumption of fully developed flow and local equilibrium, and the algebraic heat flux model (AFM) is obtained. This model is believed to be suitable for anisotropic and buoyant flows and adapted to liquid metal convection (Grotzbach, 2013). An additional value named temperature variance is introduced in the model, and a large number of closures appear to evaluate several coefficients used in this model (Kenjeres et al., 2005; Shams et al., 2014). These coefficients are usually calibrated based on experimental data or DNS data. As discussed above, statistical analyses of low-Prandtl fluid are not quite sufficient, and hence consideration of the modeling of turbulent heat flux, which is necessary for the analysis of heat transfer properties of liquid sodium, is still limited.

This paper assesses the turbulent heat flux of turbulent convection at extremely low Pr. The object of the current work is to propose a more accurate closure to estimate the coefficient used in an AFM model that is more suitable for low-Prandtl fluids. Constant thermo-physical properties are assumed, and buoyancy is accounted for in the momentum equation using the Boussinesq assumption. Due to a lack of DNS and experimental data for liquid sodium, new reference results were obtained by performing a wall-resolved Large-Eddy Simulation of turbulent channel flows at Pr = 0.005. The Reynolds number was varied over a wide range to consider its influence on the turbulent heat flux. Based on the proposed results of the LES model, the algebraic turbulent heat flux model is first assessed against the LES data for a channel flow. The coefficients employed in this model are then further calibrated to reproduce the turbulent properties of liquid sodium. The optimized coefficients may provide a better prediction accuracy for application to the convection flow regime in fuel assemblies of SFRs.

NUMERICAL MODELS

LES Model

In the current study, an LES model is chosen to predict the turbulence properties of the flow field. The basic equations of the LES model were first formulated by Smagorinsky (1963). With the filtering process, the incompressible Navier-Stokes equations were filtered to separate the small scales from the large scales of motion, as shown below:

$$\nabla \cdot \widetilde{U} = 0 \tag{1}$$

$$\frac{\partial \widetilde{U}}{\partial t} + \nabla \cdot (\widetilde{U}\widetilde{U}) = -\frac{1}{\rho}\nabla \widetilde{p} + \nabla \cdot [\nu(\nabla \widetilde{U} + \nabla \widetilde{U}^{T})] - \nabla \cdot \tau_{sgs} - F \tag{2}$$

$$\frac{\partial T}{\partial t} + \nabla \cdot (\widetilde{U}T) = \nabla \cdot (\alpha \nabla T) \tag{3}$$

where $\tilde{\mathbf{U}} = \left(\tilde{U}_x, \tilde{U}_y, \tilde{U}_z\right)$ is the filtered velocity field. $\tilde{p}$ and $\tilde{T}$ are the filtered pressure and temperature, respectively. F stands for the body force $F = \beta\left(\tilde{T} - T_m\right)\boldsymbol{g}$, in which β is the thermal expansion ratio and $T_m = (T_h + T_c)/2$ is the mean temperature. α stands for the thermal diffusivity. The term τ_{sgs} is known as the sub-grid scale stress (SGS), which reflects the effect from the sub-grid part of the velocity field on the resolved field through the sub-grid scale model. The components of sub-grid scale stress are evaluated as follows:

$$\tau_{ij} - \frac{1}{3}\tau_{kk}\delta_{ij} = -2\nu_{sgs}S_{ij} \tag{4}$$

In order to close the modeling, sub-grid scale eddy-viscosity ν_{sgs} is required. In the literature, a lot of research has been carried out to propose different models to evaluate its value. The WALE model (Nicoud and Ducros, 1999), which includes the effects from both the strain and the rotation rate of the smallest resolved turbulent fluctuations based on the square of the velocity gradient tensor, is employed in the current study.

The subject of interest is the fully developed turbulent flow of a low-Prandtl number flow through a heated channel with fixed heat flux at the walls. By feeding the outlet flow back to the inlet boundary, a fully developed flow field in a channel with a cyclic boundary condition is employed in the simulation. The modified variable Θ is then introduced to obtain a time-averaged profile of temperature in the simulation domain as:

$$\Theta = x\frac{dT_w}{dx} - T \tag{5}$$

where the gradient $\frac{dT_w}{dx}$ stands for the temperature increase in the periodic streamwise direction (x) due to the mean uniform heat flux q_w. Its value is calculated as:

$$\frac{dT_w}{dx} = \frac{q_w}{\rho\delta C_p \overline{U}_b} \tag{6}$$

where δ stands for the half-width of the channel, C_p is the heat capacity, and $\overline{U}_b$ is the bulk velocity.

With the introduction of Θ, the energy equation is modified as:

$$\frac{\partial\Theta}{\partial t} + \nabla\cdot(\widetilde{U}\Theta) - U_x\frac{dT_w}{dx} = \nabla\cdot(\alpha\nabla\Theta) \tag{7}$$

In the current study, all of the governing equations are integrated into the three-dimensional finite-volume CFD platform OpenFOAM, which is constituted by a large base library and offers the core capabilities of dynamic mesh, automatic parallelization, several generally physical models, etc.

A transient solver proposed by OpenFOAM, "buoyantPimpleFOAM," is employed to predict buoyant, turbulent flow of incompressible fluid for heat transfer. The PISO algorithm is used to solve Navier-Stokes equations. Limited linear differencing schemes are employed for approximating the convective terms to maintain second-order accuracy. Linear, linear corrected, backward and corrected schemes are employed for the gradient term, diffusive term, time derivation, and surface gradient term, respectively. The mean profiles of temperature and velocity were obtained based on the functions provided by OpenFOAM. The arithmetic mean is calculated by:

$$\bar{x} = \frac{1}{N}\sum_{i=0}^{N} x_i \tag{8}$$

The prime-squared mean is calculated by:

$$\overline{x'}^2 = \frac{1}{N}\sum_{i=0}^{N}(x_i - \bar{x})^2 \tag{9}$$

Algebraic Turbulent Heat Flux Model

Analogous to the analysis of Reynolds stress, if applying the Reynolds decomposition to the energy transport equation, turbulent heat flux $\overline{u_i\theta}$ appears in the time-averaged form of the energy equation. In the past few decades, different models have been proposed to estimate its value based on different assumptions, such as the Simple Gradient Diffusion Hypothesis (SGDH) model and the General Gradient Diffusion Hypothesis (GGDH) model (Xiong and Cheng, 2014). In these two models, turbulent heat flux is proportional to the turbulent viscosity or Reynolds stress without considering the influence of energy equilibrium. These models may not be applicable for flows in which buoyancy has to be considered. Hence, an AFM model is proposed to estimate turbulent heat flux with consideration of buoyancy force. The resulting algebraic expression has the following form (Kenjereš and Hanjalić, 2000):

$$\overline{u_i\theta} = -C_{t_0}\frac{k}{\varepsilon}\left(C_{t_1}\overline{u_iu_j}\frac{\partial\overline{\Theta}}{\partial x_j} + C_{t_2}\overline{u_j\theta}\frac{\partial\overline{U_i}}{\partial x_j} + C_{t_3}\eta\beta g_i\overline{\theta^2}\right) + C_{t_4}a_{ij}\overline{u_j\theta} \tag{10}$$

TABLE 1 | Model coefficients for the algebraic turbulent heat flux model.

	C_{t0}	C_{t1}	C_{t2}	C_{t3}	C_{t4}
AFM-2005 (Kenjeres et al., 2005)	0.15	0.6	0.6	0.6	1.5
AFM-2014 (Shams et al., 2014)	0.2	0.25	0.6	2.5	0.0
AFM-CS	0.15	0.5	0.1	0.6	0.0

TABLE 2 | Dimensionless numbers for validating the CFD approach employed.

Reference	Re_τ [–]	Pr [–]
Abe et al. (2004)	640	0.025

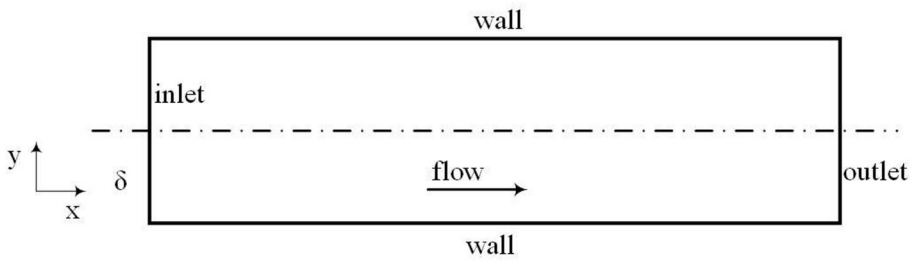

FIGURE 1 | Schematic diagram of the simulation domain.

where a_{ij} is estimated based on the Reynolds stress as: $a_{ij} = \overline{u_i u_j}/3 - 2\delta_{ij}/3$. The first three terms on the right-hand side of Equation 10 consider the influences of temperature gradient, velocity gradient, and buoyancy, respectively. It should be noted that the AFM model involves the temperature variance, which is unknown. An equation is introduced to solve its value:

$$\frac{\partial \overline{\theta}^2}{\partial t} + \frac{\partial \overline{U}_j \overline{\theta^2}}{\partial x_j} = 2P_{tt} - 2\varepsilon_{tt} + \frac{\partial}{\partial x_j}[(\frac{k}{C_p} + \frac{\nu_t}{\sigma_t})\frac{\partial \overline{\theta^2}}{\partial x_j}] \quad (11)$$

in which $P_{tt} = \overline{uu_i\theta}/\frac{d\overline{\Theta}}{dx_i}$ and $\varepsilon_{tt} = \frac{\varepsilon\theta}{2kR}$.

In the past few decades, numerous models have been proposed to evaluate the coefficients used in Equation 10. The coefficients proposed by Kenjeres et al. (2005) and Shams et al. (2014) are analyzed in the current study. Their values are summarized in **Table 1**. The optimized coefficient based on the simulation results obtained in section LES Simulations of Turbulent Channel Flow at Pr = 0.005 is also shown in **Table 1**. An algebraic turbulent heat flux model has already been implemented in OpenFOAM by the authors and validated in previous numerical studies of supercritical fluid (Xiong and Cheng, 2014). It should be mentioned that a k-ω SST model is employed to predict turbulent viscosity in the current study (Menter et al., 2003).

VALIDATION FOR PREDICTING TURBULENT CHANNEL FLOW AT RE_τ=640

Numerical Configuration

In order to assess the solver and numerical configurations employed in this study, it is essential to appropriately define target parameters to show how good the performance of simulation is. In this study, mean velocity, mean temperature, temperature variance, and turbulent heat flux are chosen to prove the accuracy of predicting turbulent properties. Hence, direct numerical simulation (DNS) results of turbulent channel flow at low-Prandtl number fluid published by Abe et al. (2004) are selected in this study for validation purposes. The data found in the literature will be compared with simulation results, and a good agreement will demonstrate the capability of the employed CFD approach.

The computational domain with a size of $L_x \times L_y \times L_z = 6.4\delta \times 2\delta \times 2\delta$ has been discretized into $N_x \times N_y \times N_z = 256 \times 256 \times 128$ grid cells based on sensitivity analysis of the grid resolution and geometry size. A schematic sketch of the simulation domain is shown in **Figure 1**. The related dimensionless numbers for the validation calculations can be found in **Table 2**. A no-slip velocity condition is imposed on the walls, and the values of turbulent properties on the walls are set to a constant, small value.

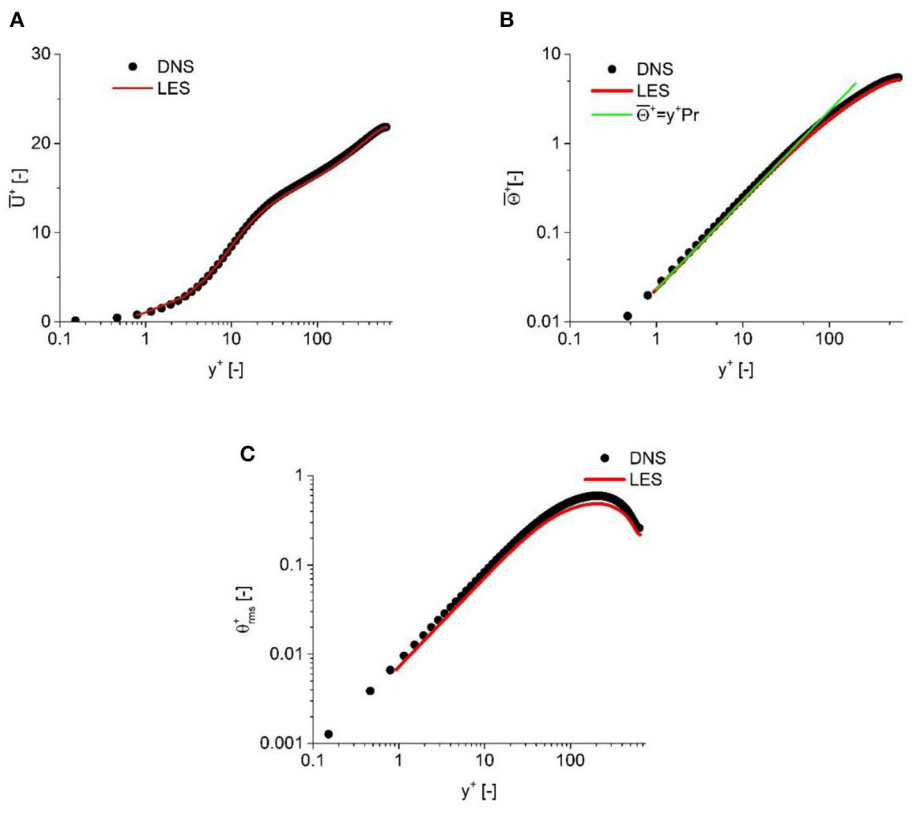

FIGURE 2 | Comparison against the results of Abe et al. (2004). **(A)** Mean velocity, **(B)** Mean temperature, and **(C)** Root mean square of temperature variance.

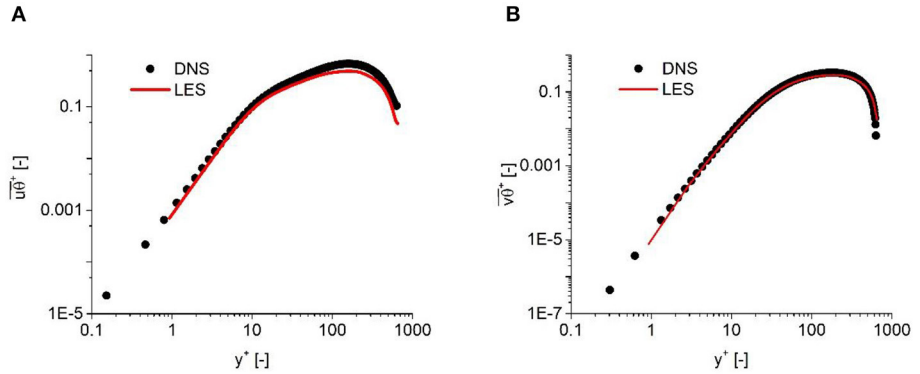

FIGURE 3 | Time-averaged turbulent heat flux compared with the results of Abe et al. (2004). **(A)** Streamwise direction and **(B)** Wall-normal direction.

TABLE 3 | Summary of averaged velocity with the corresponding dimensionless numbers.

Name	Case 1	Case 2	Case 3	Case 4
$\overline{U}_b$ [m/s]	0.613	0.767	0.920	1.073
Re [–]	20000	25000	30000	35000
Pr [–]	0.005	0.005	0.005	0.005

TABLE 4 | Mesh sensitivity analysis.

Grid number	Friction velocity [m/s]
3.5 million	0.048055
6 million	0.050577
8 million	0.050253

Validation Calculation of the CFD Approach Employed With DNS Results

The predicted results of turbulent channel flow at low Prandtl number are compared with the DNS results from Abe et al. (2004), in which the Reynolds number calculated by the friction velocity is equal to 640. The results employed include the velocity distribution in the near-wall region, temperature profile, temperature variance, and turbulent heat flux in the streamwise and transverse directions. In **Figure 2**, the simulation results of velocity and temperature distributions are plotted against DNS results. It is clearly indicated that the predicted results show a good qualitative and quantitative agreement with DNS results. The predicted velocity also shows a good agreement with the wall function, while the predicted temperature in the laminar sub-layer is consistent with the function $\Theta^+ = y^+ Pr$.

In order to further validate the simulation results for the prediction of the turbulent heat flux, the predicted temperature variance is plotted against DNS results in **Figure 2**. It can be observed that a good agreement is also achieved. For the turbulent heat flux, as shown in **Figure 3**, a good agreement demonstrates the capability of the solver and numerical configurations employed to predict the turbulent and heat transfer properties for low-Prandtl number fluid.

The comparison between the simulation results and the DNS results provided by Abe et al. (2004) demonstrates the capability of the CFD method employed to predict the flow and heat transfer properties in a low-Prandtl fluid. Hence, this numerical configuration will be employed in the following simulation to provide detailed results for turbulent heat flux under a typical flow condition of SFRs.

LES SIMULATIONS OF TURBULENT CHANNEL FLOW AT Pr = 0.005

Based on the previous study, the LES method is employed in this paper to investigate the time-averaged properties of turbulent statistics and heat flux in sodium flow. The numerical configuration is the same as the validation calculations, as described in section Algebraic Turbulent Heat Flux Model. In the design of the fuel assembly of an SFR, cylindrical fuel rods are arranged in a triangular array. The geometry of the sub-channel formed between walls of fuel rods is quite different from the rectangular channel employed in the validation calculations. In order to eliminate the influence from the geometry, a rectangular channel is still considered in the following simulation with the same range of Reynolds numbers for the SFR. Considering the typical flow rate of a China Experimental Fast Reactor (CEFR), the Reynolds numbers evaluated based on the equivalent diameters of central, side, and corner sub-channels are 25,200, 32,500, and 24,300, respectively. Hence, the Reynolds numbers considered in the current study are chosen from 20000 to 35000, which are calculated by the half-width of the channel and the mean velocity as shown in **Table 3**. Information on the geometrical size and mass flow rate of the fuel assembly can be found in Chai et al. (2020). It was also the best compromise we could provide due to a limitation of computational resources. Its influence on both turbulent statistics and heat flux will be discussed later. The typical Prandtl number of sodium is also considered in the current study.

In order to consider the influence of grid resolution, three different meshes are evaluated in which the total grid number

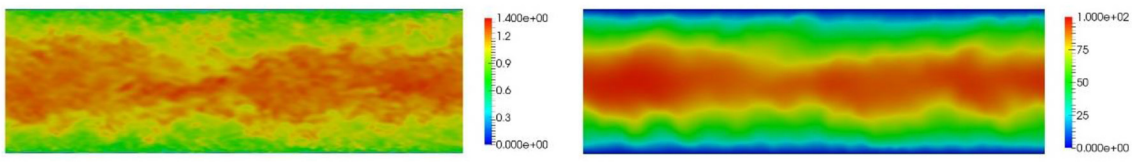

FIGURE 4 | Visualization of simulation results for Re = 35000. **(A)** Instantaneous velocity and **(B)** Instantaneous temperature.

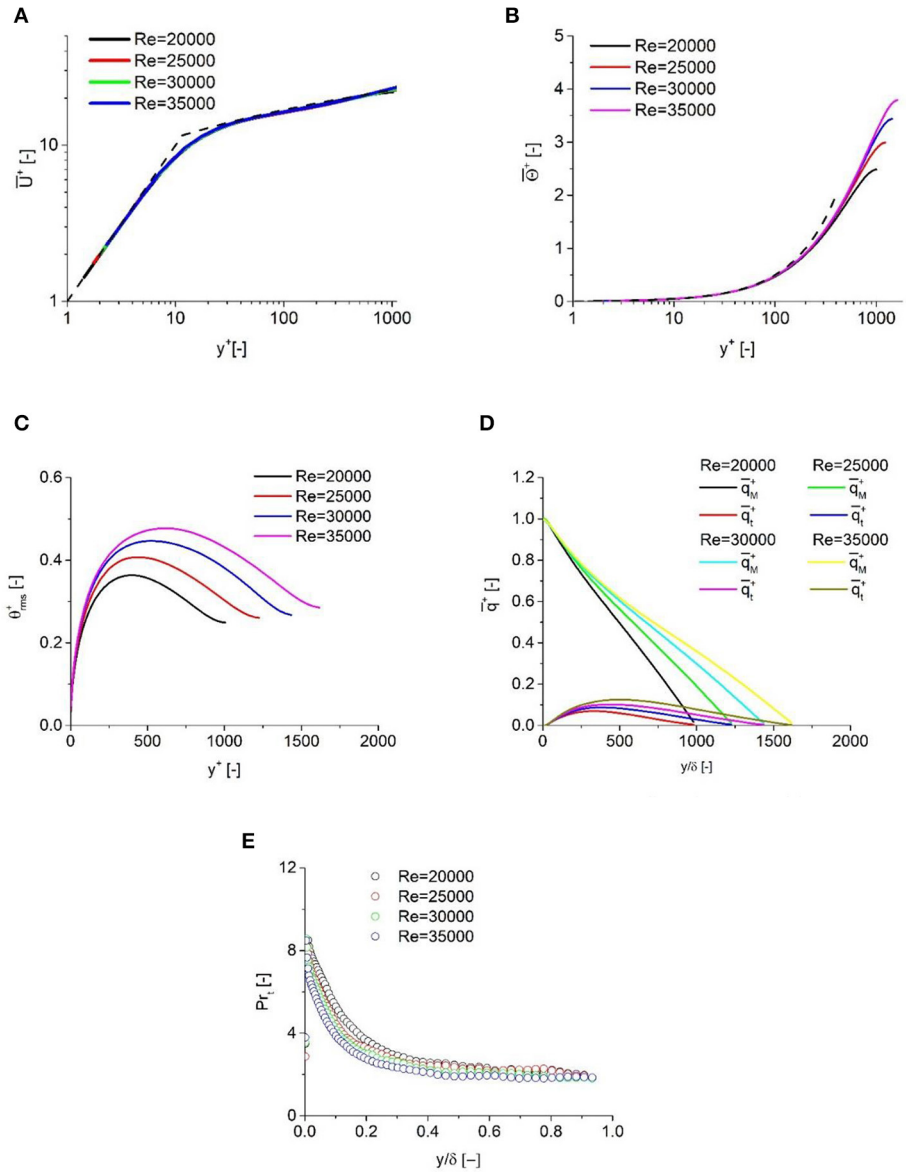

FIGURE 5 | Dependency on Reynolds number. **(A)** Mean velocity, **(B)** Mean temperature, **(C)** Temperature fluctuation, **(D)** Heat flux decomposition, and **(E)** Turbulent Prandtl number.

is varied from 3.5 to 8 million, as listed in **Table 4**. The computational domain employed in this part of the LES simulations is the same as in the previous validation calculations. The finest mesh was discretized into $N_x \times N_y \times N_z = 256 \times 256 \times 128$ grid cells, which is the same as in the previous validation calculations. The value of y+ is kept around 0.5 for all cases. It can be found that the predicted friction velocity tends to approach a constant value when the mesh number is larger than 6 million. With consideration of accuracy and computation efforts, the last mesh is chosen in the following analysis. The simulations were carried out on a Dell R730 server with the Intel Xeon E5-2697 v4 @ 2.30 GHZ (2 CPUs). Each simulation requires almost 168 h to obtain time-averaged values of turbulent properties if using the finest mesh.

The instantaneous results of velocity and temperature are shown in **Figure 4**, in which the Reynolds number is equal to 35,000. Due to a low Prandtl number, small structures can be found in the velocity field, while large structures are more obvious in the temperature field. It is also confirmed that the grids employed to capture the turbulent motions are also sufficient to predict the temperature distribution. Hence, the approximation that the sub-grid heat flux can be neglected in the simulation is justified, as shown in Equation 7.

In **Figure 5**, the simulation results of the mean velocity profile in the near-wall region are plotted. The wall function, which includes both the laminar sublayer and the logarithmic region, is also plotted in this figure. It is shown that the predicted results show a good quantitative agreement with theoretical results when the Reynolds number varies.

The temperature profiles obtained in the simulation results are shown in **Figure 5**. It is shown that the linear law, $\overline{\Theta}^+ = y^+ Pr$, is well-obeyed in the near-wall region for all cases until y^+ reaches 100. This finding is consistent with the LES results proposed by Duponcheel et al. (2014), in which Prandtl numbers are equal to 0.01. In their results, this dependency tends to vanish when y^+ reaches 60, which is much smaller than in the current study. It is confirmed that the molecular heat flux is more dominant as the Prandtl number decreases, especially in the near-wall region. Also, the variance of the Reynolds number has little effect on the temperature profile in the laminar sub-layer.

The profiles of temperature fluctuations are also shown in **Figure 5**. As the Reynolds number increases, the peak of temperature fluctuation is pushed further away from the wall, and their profiles are much flatter than the velocity fluctuation profiles. As the Reynolds number varies from 20000 to 35000, the location of peaks tends to approach the channel center from $y^+ \approx 400$ to $y^+ \approx 630$, which implies an influence of the turbulent motions on the temperature fluctuations. If considering the results of Duponcheel et al. (2014), in which the peaks of temperature fluctuation are at around $y^+ \approx 500$ for two different Prandtl numbers, dependency of temperature fluctuations on the Reynolds number can be identified based on the current study.

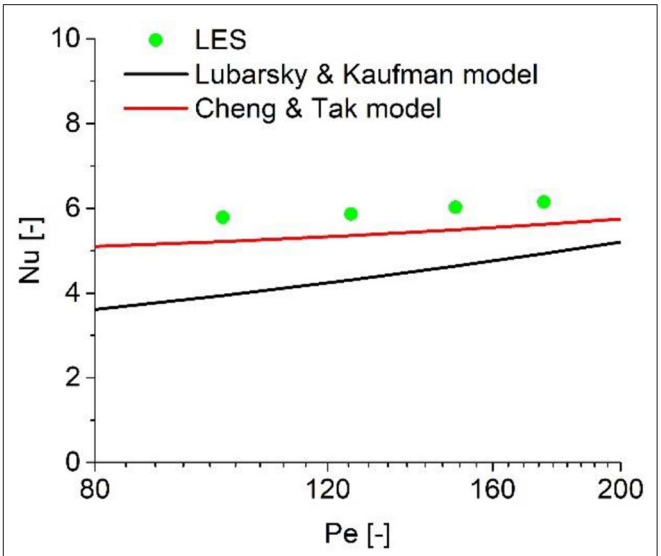

FIGURE 6 | Nusselt number as a function of Peclet number.

As shown in **Figure 5**, the molecular heat flux is more dominant than turbulent heat flux. Hence, it is necessary to decompose the total heat flux into molecular heat flux and turbulent heat flux and investigate the ratio of these two components. The molecular heat flux is estimated based on the temperature gradient as $\overline{q}_M^+ = Pr^{-1} d\overline{\Theta}^+ / dy^+$, while the turbulent heat flux is calculated by $\overline{q}_t^+ = -\overline{v\theta}^+$. As shown in **Figure 5**, the molecular heat flux is more dominant and much larger than the turbulent heat flux. As the Reynolds number increases, the peaks of the turbulent heat flux tend to approach the channel center and their values become larger. Furthermore, the results of Duponcheel et al. (2014) suggested that the turbulent heat flux is of the same order or larger than the molecular heat flux. This discrepancy confirms that, for low-Prandtl fluid like sodium, the contribution from the turbulent flux becomes less important, and more attention should be paid to the modeling of the heat transfer process in sodium.

In RANS simulation, the turbulent Prandtl number is used to estimate the ratio between turbulent viscosity and turbulent diffusivity, and its modeling is important for estimating the turbulent heat transfer process, especially for low-Prandtl fluid. The profiles of the turbulent Prandtl number Reynolds number varies are shown in **Figure 5**. Its value is calculated by turbulent diffusivity and turbulent viscosity as $Pr_t = \frac{\nu_t}{\alpha_t}$. The turbulent diffusivity and turbulent viscosity are calculated as $\alpha_t = \overline{v'\Theta'} / \frac{d\overline{\Theta}}{dy}$ and $\nu_t = \overline{u'v'} / \frac{d\overline{u}}{dy}$, respectively. From the results obtained, it is found that the peaks of the turbulent Prandtl number exist in the near-wall region, followed by a sharp decrease. When approaching the channel center, the turbulent Prandtl number shows a slight decrease. The turbulent Prandtl number profile is consistent with the results of Duponcheel et al. (2014). However, the results obtained in the current study prove that a smaller turbulent Prandtl number can be expected for sodium,

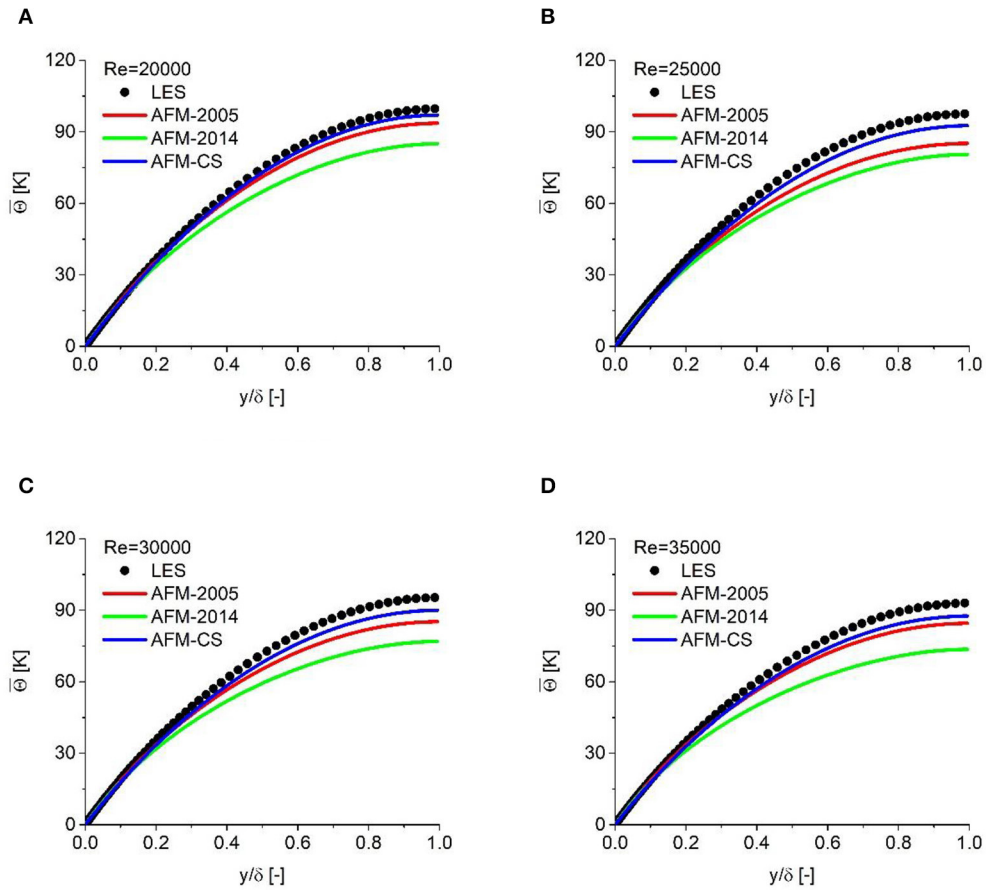

FIGURE 7 | Coolant temperature vs. vertical position for different Reynolds numbers. **(A)** Re = 20000, **(B)** Re = 25000, **(C)** Re = 30000, and **(D)** Re = 35000.

the Pr of which is extremely low. Moreover, as the Reynolds number increases, a smaller turbulent Prandtl number can be expected.

Heat transfer performance is usually characterized by the Nusselt number *Nu*, which is calculated based on the bulk temperature T_b. For liquid metal, several correlations are proposed to estimate the relationship between the Nusselt number and the Peclet number *Pe*. The Nusselt number obtained from the predicted results was plotted against the Peclet number and compared with the Lubarsky and Kaufman model (Lubarsky and Kaufman, 1955) and the Cheng and Tak model (Cheng and Tak, 2006b), and shown in **Figure 6**. It can be observed that the latter provides a better prediction accuracy when compared with the LES results, while the Lubarsky and Kaufman model obviously underestimates it.

RANS SIMULATIONS AT Pr = 0.005

Because it is numerically economical and robust, the RANS model is a very popular model for investigating the flow and heat transfer properties in a fuel assembly. In this section, the RANS method is employed to investigate the flow and heat transfer properties of turbulent channel flow. All the numerical configuration and boundary conditions are the same as in the LES simulation described in section LES Simulations of Turbulent Channel Flow at Pr = 0.005. The inlet velocity and the corresponding dimensionless numbers can be found in **Table 3**, which covers the typical range of Reynolds numbers of SFRs. The simulation results obtained in section LES Simulations of Turbulent Channel Flow at Pr = 0.005 are employed to calibrate the parameters used in the algebraic turbulent heat flux model (AFM), which is derived from the full second moment transport equation for the turbulent heat flux under the hypothesis of local equilibrium between production and dissipation (Dol et al., 1997). The optimized coefficients will show more accurate prediction of turbulent heat flux for sodium.

The RANS model is employed to predict the flow and heat transfer properties in a turbulent channel for Pr = 0.005. The range of Reynolds number is consistent with the previous LES simulation. The results provided by AFM-2005 and AFM-2014 are also included in this figure. In this part, a low-Reynolds k-ω SST model is used to evaluate the turbulent viscosity. The predicted velocity profiles show a good agreement with

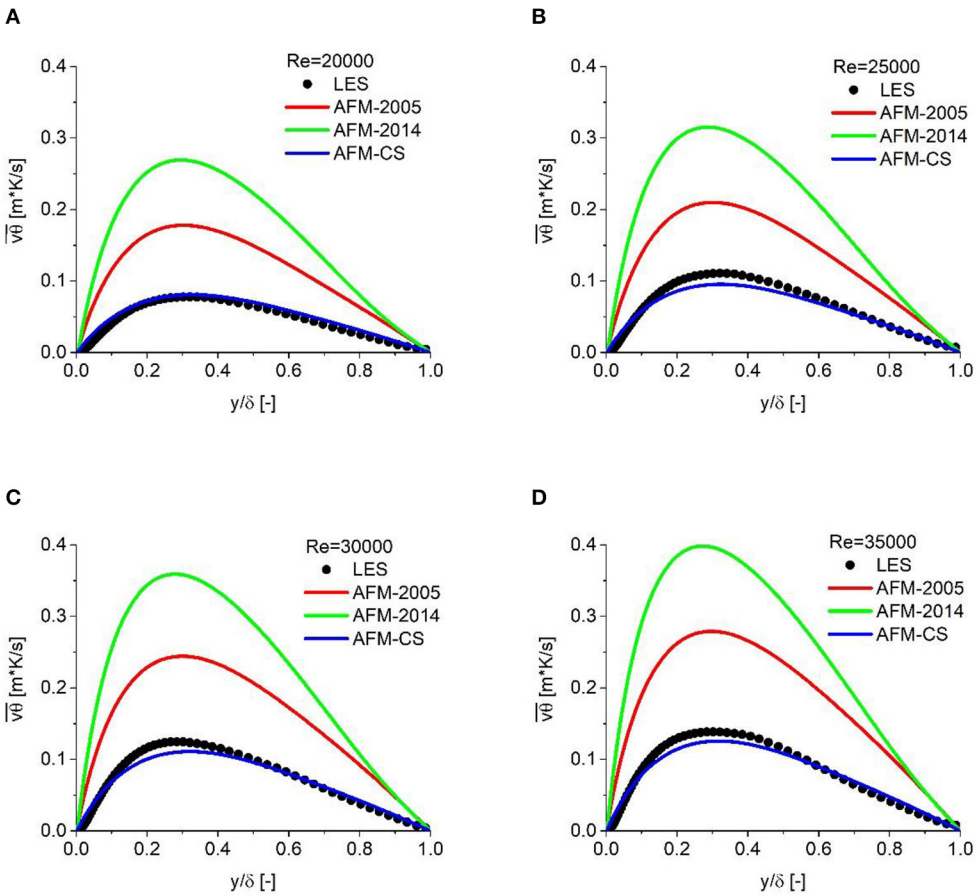

FIGURE 8 | Turbulent heat flux in the wall-normal direction for different Reynolds numbers. **(A)** Re = 20000, **(B)** Re = 25000, **(C)** Re = 30000, and **(D)** Re = 35000.

LES results, and hence they are not shown in the following analysis. The predicted temperature profiles are compared with LES results in **Figure 7**. It is clearly indicated that the existing models, especially AFM-2014, underestimate the variance of coolant temperature in the wall-normal direction. The optimized coefficients show better performance compared with the models found in the literature. This phenomenon can be attributed to the fact that the turbulent heat flux in liquid sodium is greatly reduced due to the extremely low Prandtl number, and the decreased coefficients used in the proposed model are more suitable for reproducing the distribution of turbulent flux.

In order to further assess the calibrated coefficients, the distribution of turbulent heat flux in the wall-normal direction is shown in **Figure 8**. The profile of turbulent heat flux is quite similar to the previous results for coolant temperature. In comparison with the two models found in the literature, the calibrated model also shows a better prediction accuracy. The predicted results also confirm the fact that these two existing models overestimate the turbulent heat flux, especially AFM-2014. The proposed model, in which smaller coefficients are employed, shows a significant improvement when compared with the LES results. It can be concluded that the optimized coefficients, which are smaller than those in the existing models, show a better prediction accuracy for turbulent heat flux due to the weaker turbulent heat properties caused by the extremely low Prandtl number.

CONCLUSION

In this paper, a numerical method is used to investigate the turbulent heat transfer properties in a turbulent channel flow. A systematic CFD simulation covering the typical range of Reynolds numbers for SFRs was performed at very low Prandtl number: Pr = 0.005, which corresponds to liquid sodium. Based on a wall-resolved LES method, new reference results were obtained for the typical Prandtl number and wall heat flux of an SFR. To prove the correctness of the calculated turbulent and heat transfer properties in low-Prandtl fluid, this method has been compared against DNS results. Statistics of the temperature profile were obtained based on a time-averaged process as well as turbulent heat transfer properties. Based on this configuration, the influence of the extremely low Prandtl number is identified. It is observed that for the channel flow, the peaks of the turbulent Prandtl number exist in the near-wall region, and its value shows a slight decrease while approaching the channel center.

Moreover, the results obtained in the current study indicate that, as the Reynolds number increases, a smaller turbulent Prandtl number can be expected. Based on the reference results obtained, the coefficients employed in the algebraic turbulent heat flux model are calibrated. The optimized coefficients have the potential to provide more accurate prediction of coolant temperature for sodium flow as well as turbulent heat flux.

DATA AVAILABILITY STATEMENT

The raw data supporting the conclusions of this article will be made available by the authors without undue reservation.

AUTHOR CONTRIBUTIONS

XCha carried out the CFD simulation and prepared the manuscript. XL, JX, and XChe provided their suggestion on the contents of the manuscript.

FUNDING

The work in this paper was supported by the Natural Science Foundation of Shanghai (Grant number: 17ZR1415300) and the National Natural Science Foundation of China (Grant numbers: 11922505 and 51806139).

REFERENCES

Abe, H., Kawamura, H., and Matsuo, Y. (2004). Surface heat-flux fluctuations in a turbulent channel flow up to Reτ = 1020 with Pr= 0.025 and 0.71. *Int. J. Heat Fluid Flow*. 25, 404–419. doi: 10.1016/j.ijheatfluidflow.2004.02.010

Bogoslovskaya, G. P., Zhukov, A. V., and Sorokin, A. P. (2000). *Models and Characteristics of Interchannel Exchange in Pin Bundles Cooled by Liquid Metal (No. IAEA-TECDOC–1157)*. International Atomic Energy Agency (IAEA), Vienna.

Chai, X., Zhao, L., Hu, W., Yang, Y., Liu, X., Xiong, J., et al. (2020). Numerical investigation of flow blockage accident in SFR fuel assembly. *Nucl. Eng. Design* 359:110437. doi: 10.1016/j.nucengdes.2019.110437

Cheng, X., and Tak, N.-I. (2006b). Investigation on turbulent heat transfer to lead–bismuth eutectic flows in circular tubes for nuclear applications. *Nucl. Eng. Design* 236, 385–393. doi: 10.1016/j.nucengdes.2005.09.006

Cheng, X., and Tak, N. I. (2006a). CFD analysis of thermal-hydraulic behavior of heavy liquid metals in sub-channels. *Nucl. Eng. Design* 236, 1874–1885. doi: 10.1016/j.nucengdes.2006.02.001

Churchill, S. W. (2002). A reinterpretation of the turbulent Prandtl number. *Indust. Eng. Chem. Res*. 41, 6393–6401. doi: 10.1021/ie011021k

Da Vià, R., and Manservisi, S. (2019). Numerical simulation of forced and mixed convection turbulent liquid sodium flow over a vertical backward facing step with a four parameter turbulence model. *Int. J. Heat Mass Transf.* 135, 591–603. doi: 10.1016/j.ijheatmasstransfer.2019.01.129

Dol, H., Hanjalić, K., and Kenjereš, S. (1997). A comparative assessment of the second-moment differential and algebraic models in turbulent natural convection. *Int. J. Heat Fluid flow* 18, 4–14. doi: 10.1016/S0142-727X(96)00149-X

Duponcheel, M., Bricteux, L., Manconi, M., Winckelmans, G., and Bartosiewicz, Y. (2014). Assessment of RANS and improved near-wall modeling for forced convection at low Prandtl numbers based on LES up to Reτ = 2000. *Int. J. Heat Mass Transf.* 75, 470–482. doi: 10.1016/j.ijheatmasstransfer.2014.03.080

Grotzbach, G. (2013). Challenges in low-Prandtl number heat transfer simulation and modelling. *Nucl. Eng. Design* 264, 41–55. doi: 10.1016/j.nucengdes.2012.09.039

Kays, W. M. (1994). Turbulent Prandtl number. Where are we? *ASME Transac. J. Heat Transf.* 116, 284–295. doi: 10.1115/1.2911398

Kenjeres, S., Gunarjo, S. B., and Hanjalic, K. (2005). Contribution to elliptic relaxation modelling of turbulent natural and mixed convection. *Int. J. Heat Fluid Flow* 26, 569–586. doi: 10.1016/j.ijheatfluidflow.2005.03.007

Kenjereš, S., and Hanjalić K. (2000). Convective rolls and heat transfer in finite-length Rayleigh-Bénard convection: a two-dimensional numerical study. *Phys. Rev. E* 62:7987. doi: 10.1103/PhysRevE.62.7987

Lorenz, J., and Ginberg, T. (1977). Coolant mixing and subchannel velocities in an LMFBR fuel assembly. *Nucl. Eng. Design* 40, 315–326. doi: 10.1016/0029-5493(77)90042-5

Lubarsky, B., and Kaufman, S. J. (1955). *Review of Experimental Investigations of Liquid-Metal Heat Transfer*. University of North Texas.

Menter, F. R., Kuntz, M., and Langtry, R. B. (2003). "Ten years of industrial experience with the SST turbulence model," in *4th International Symposium on Turbulence, Heat and Mass Transfer, ICHMT 4 (Antalya)*.

Nicoud, F., and Ducros, F. (1999). Subgrid-scale stress modelling based on the square of the velocity gradient tensor. *Flow Turbul. Combust*. 62, 183–200. doi: 10.1023/A:1009995426001

Pacio, J., Daubner, M., Fellmoser, F., and Wetzel, T. H. (2016). Experimental study of heavy-liquid metal (LBE) flow and heat transfer along a hexagonal 19-rod bundle with wire spacers. *Nucl. Eng. Design* 301, 111–127. doi: 10.1016/j.nucengdes.2016.03.003

Schumm, T., Frohnapfel, B., and Marocco, L. (2016). Numerical simulation of the turbulent convective buoyant flow of sodium over a backward-facing step. *J. Phys. Conf. Ser.* 745:032051. doi: 10.1088/1742-6596/745/3/032051

Shams, A., Roelofs, F., Baglietto, E., Lardeau, S., and Kenjeres, S. (2014). Assessment and calibration of an algebraic turbulent heat flux model for low-Prandtl fluids. *Int. J. Heat Mass Transf.* 79, 589–601. doi: 10.1016/j.ijheatmasstransfer.2014.08.018

Smagorinsky, J. (1963). General circulation experiments with the primitive equations: I. The basic experiment. *Monthly Weather Rev*. 91, 99–164.

Sun, K. (2012). *Analysis of Advanced Sodium-Cooled Fast Reactor Core Designs With Improved Safety Characteristics*. Lausanne: École Polytechnique.

Xiong, J., and Cheng, X. (2014). Turbulence modelling for supercritical pressure heat transfer in upward tube flow. *Nucl. Eng. Design* 270, 249–258. doi: 10.1016/j.nucengdes.2014.01.014

Conflict of Interest: The authors declare that the research was conducted in the absence of any commercial or financial relationships that could be construed as a potential conflict of interest.

NOMENCLATURE

English alphabets

$\tilde{\mathbf{U}}$	Filtered velocity field
C_p	Heat capacity
F	Buoyancy force
k	Turbulent kinetic energy
$\tilde{p}$	Filtered pressure
q_w	Heat flux
$\overline{q}_M^+$	Dimensionless molecular heat flux
$\overline{q}_t^+$	Dimensionless turbulent heat flux
T_m	Mean temperature
$\tilde{T}$	Filtered temperature
U^+	Dimensionless velocity
$\overline{U}_b$	Bulk velocity
$\overline{u_i u_j}$	Reynolds stress
y^+	Dimensionless distance to wall

Greek symbols

α	Thermal diffusivity
α_t	Turbulent heat diffusivity
β	Thermal expansion ratio
τ_{sgs}	Sub-grid scale stress
ν_{sgs}	Sub-grid scale eddy-viscosity
δ	Half-width of channel
Θ	Modified temperature
$\overline{u_i}\theta$	Turbulent heat flux
$\overline{\theta^2}$	Temperature variance
ε	Temperature dissipation rate
ν_t	Turbulent viscosity
Θ^+	Dimensionless temperature

Acronyms

AFM	Algebraic turbulent heat flux model
CFD	Computational fluid dynamics
DNS	Direct numerical simulation
GGDH	General Gradient Diffusion Hypothesis
Re_τ	Reynolds number based on friction velocity
SFR	Sodium-cooled fast reactor
SGDH	Simple Gradient Diffusion Hypothesis
SGS	Sub-grid scale stress

frontiers in Energy Research

ORIGINAL RESEARCH
published: 11 August 2020
doi: 10.3389/fenrg.2020.00184

Numerical Investigation of Helium Bubble Rising Behavior in Cross-Type Channel

Chunjie Zeng[1,2], Baoxin Yuan[3], Zhaoming Meng[1]*, Xin Zhang[4], Herui Jiang[1], Defang Mu[2] and Ruihao Yan[1]*

[1] College of Nuclear Science and Technology, Harbin Engineering University, Harbin, China, [2] School of Nuclear Science and Technology, Xi'an Jiaotong University, Xi'an, China, [3] China Academy of Engineering Physics, Mianyang, China, [4] Institute of Nuclear and New Energy Technology, Tsinghua University, Beijing, China

In a certain nuclear reactor, the coolant channel is a cross-type channel. There is little research about bubble rising behavior in this kind of channel, but the neutron detection would be affected by the bubbles. Through comparing with previous experiment, proper numerical model has been determined, and the cross-type channel under different helium flow rates is studied with CFD software Fluent. Research shows that the bubble distribution exhibits some similarities under different helium flow rates, and the bubbles tend to rise near the tube wall; In the axial direction of the flow channel, the bubble coalescence can be observed, which leads the void fraction in the axial direction to increase first and then to be stable; The void fraction increases with increasing helium flow rates.

Keywords: CFD, fluent, bubble, cross-type channel, void fraction

OPEN ACCESS

Edited by:
Mingjun Wang,
Xi'an Jiaotong University, China

Reviewed by:
Yixiang Liao,
Helmholtz-Zentrum Dresden-Rossendorf, Helmholtz-Gemeinschaft Deutscher Forschungszentren (HZ), Germany
Ivo Kljenak,
Institut "Jožef Stefan" (IJS), Slovenia

****Correspondence:***
Chunjie Zeng
870678383@qq.com
Zhaoming Meng
mengzhaoming@hrbeu.edu.cn

Specialty section:
This article was submitted to Nuclear Energy, a section of the journal Frontiers in Energy Research

Received: *25 May 2020*
Accepted: *13 July 2020*
Published: *11 August 2020*

Citation:
Zeng C, Yuan B, Meng Z, Zhang X, Jiang H, Mu D and Yan R (2020) Numerical Investigation of Helium Bubble Rising Behavior in Cross-Type Channel. Front. Energy Res. 8:184. doi: 10.3389/fenrg.2020.00184

INTRODUCTION

The cross-section of the coolant channel is cross-shape in a certain nuclear reactor, and in some cases there are hydrogen bubbles in it. Under the effect of various forces such as buoyancy, resistance, pressure, etc., the bubbles are unstable (the trajectory of the rising bubbles is not a line, but more like the "Z," and also the shape of bubbles changes a lot) during the rising process, which leads to significant deformation and coalescence. The existence of these bubbles in the channel will cause errors in neutron detection in the nuclear reactor, furthermore it will affect the safety of the reactor. so it is of great necessity to do some research about the bubble rising behavior in cross-type channel, which can help other researchers know where to put the neutron detector is better (less influence by bubbles).

There are two types of research about submerged bubbles rising: submerged jet upward and submerged jet downward as shown in **Figure 1**. These researches are mainly carried out in a large water tank or conventional pipe, through submerging a small diameter pipe with gas to generate bubbles to study the laws of bubble formation, detachment, rising behavior, etc. In the submerged jet upward, the effects of surface tension, nozzle diameter, gas flow rates, liquid density, liquid viscosity, rolling conditions, etc. have been extensively studied (Gerlach et al., 2006; Buwa et al., 2007; Guang, 2010; Haijing, 2010; Chen et al., 2019; Khan et al., 2020). There exists bubble coalescence during the rising process of multiple bubbles. Related researches have been performed by Haijing (2010) and Ying (2014); In the submerged jet downward, the influencing factors of bubble formation and detachment are also related to the immersion depth of the nozzle, nozzle shape, the inner and outer

diameter, etc. (Tsuge et al., 2005; Wei, 2016; Xuan and Jingjing, 2016; Xuan and Songyang, 2019). In these researches, the focus is on the study of bubbles formation and detachment, but less attention is paid to the distribution of bubbles during the rising process. On the other hand, considering the effect of wall on the rising bubbles, the study about rising bubble in a narrow rectangular channel has been carried out (Jin et al., 2014; Hashida et al., 2019). However, these studies about narrow rectangular channel also can't reflect the situation in the cross-type flow channel. The width of the cross-type flow channel is wider than a narrow rectangular one, and the cross-type flow channel is not a conventional channel which causes bubble motion more complex. On the other hand, the previous researches did not pay much attention to the void fraction in the axial direction of the flow channel, but void fraction can exactly reflect the influence of the bubbles on neutron detection in the reactor. In summary, existing researches, neither bubble rising behavior in large-sized flow channels nor narrow rectangular channels can well reflect the situation in cross-type flow channel.

The most advantage of numerical simulation is cheap, and it can get more detailed parameters than experiments. So the purpose of the present study is to investigate the rising behavior of helium bubbles (considering that the helium is often used instead of hydrogen for research in the laboratory) in cross-type channel through CFD numerical simulations, which can provide a basis for the improvement of neutron detector in the nuclear reactor.

NUMERICAL SIMULATIONS

Numerical Model

The VOF model (Jiapeng, 2014) is built on the premise that two or more fluids (or phases) do not mix with each other, which is used to track the moving interface. The basic principle is to use the volume fraction of each phase in each grid cell and the corresponding function to determine the interface of each phase, so as to indirectly determine the changes of the fluids, rather than track the movement of the particles on the interface. When dealing with the volume fraction of different phases passing through the region, the VOF model assumes that there is a clear interface between the different phases, and there is no interpenetration between each other. This makes the

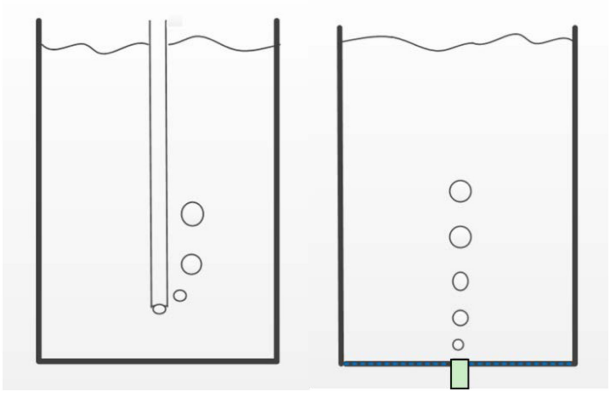

FIGURE 1 | Submerged jet downward (left) and Submerged jet upward (right).

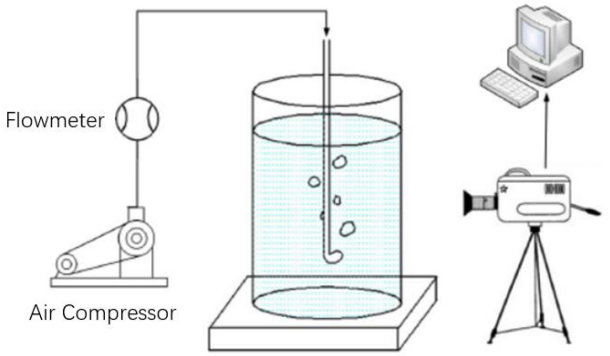

FIGURE 2 | Schematic diagram of experimental apparatus (Wei, 2016).

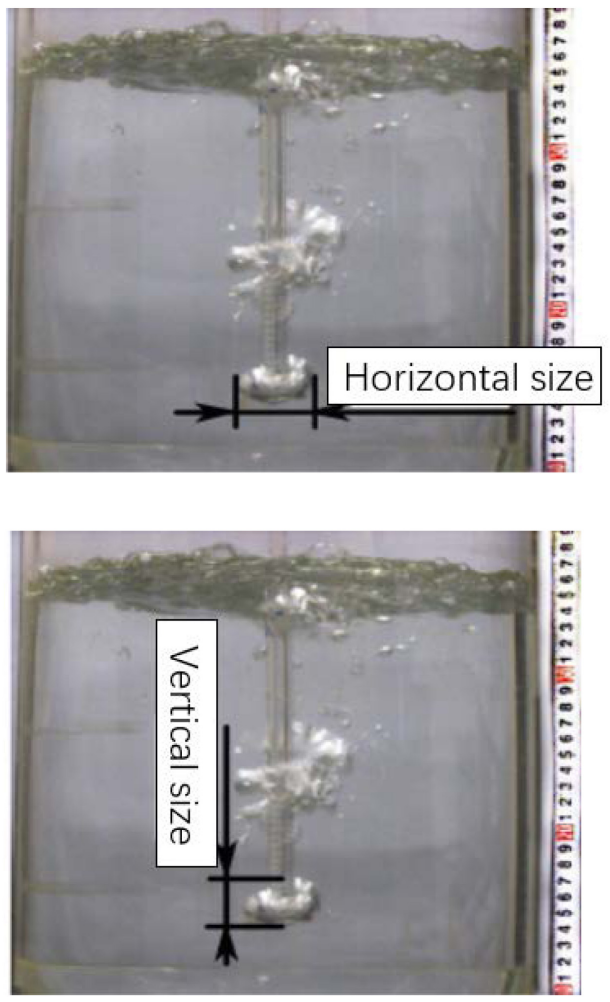

FIGURE 3 | Selection criteria of bubble size (Wei, 2016).

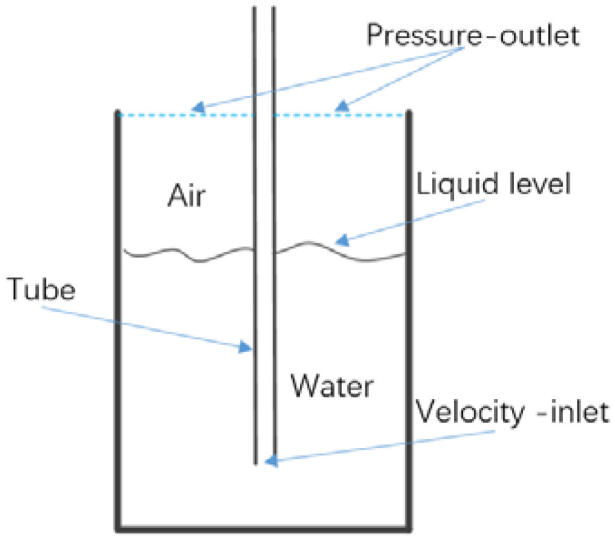

FIGURE 4 | Schematic diagram of numerical simulation.

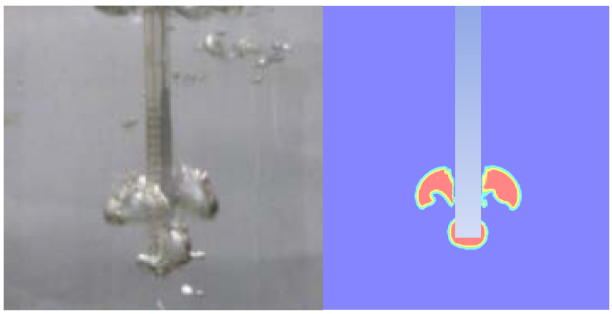

FIGURE 5 | The comparison of Wei (2016)'s experiment results and simulation results.

volume fraction of each phase independent of each other, which means when a phase is added, a corresponding volume fraction equation is introduced, combining with each corresponding separate momentum equation, the simulation of the motion of two or more fluids can be realized. In each control unit, the sum of the volume fractions of all phases is 1. When calculating each unit, the properties and volume fractions of each phase are used to obtain a volume average value of the physical parameters in the unit. The obtained average value is shared by every phase in the unit, so that the properties in the grid unit may be a certain phase or a mixture of multiple phases, which depending on the volume fraction. In other words, in the unit, if the volume fraction of the nth phase fluid is α_n, there are three kinds of situations:

1. $\alpha_n = 0$: There is no nth phase in the unit;
2. $\alpha_n = 1$: Filled with nth phase in the unit;
3. $0 < \alpha_n < 1$: There exists interface between nth phase and another phase (or other phases).

The SST (shear stress transport) k-ω model (Ansys Fluent 17.2 Theory Guide, 2016) was developed from the Baseline k-ω model. The SST k-ω model combined the stability of standard k-ω model near the wall and the independence of the k-ε model outside the boundary layer. Also the propagation of turbulent shear stress affected by the turbulent viscosity was considered. The SST k-ω model has higher accuracy and credibility in the simulation of various complex flow conditions than the standard k-ω and k-ε model.

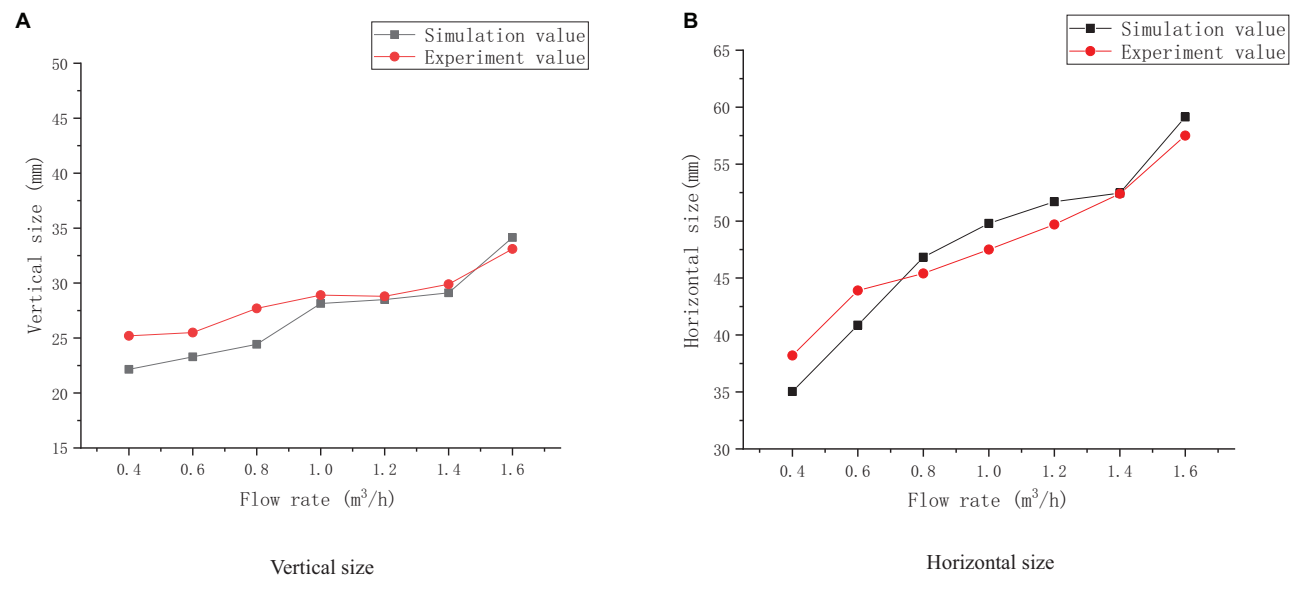

FIGURE 6 | Bubble size comparison. **(A)** Vertical size. **(B)** Horizontal size.

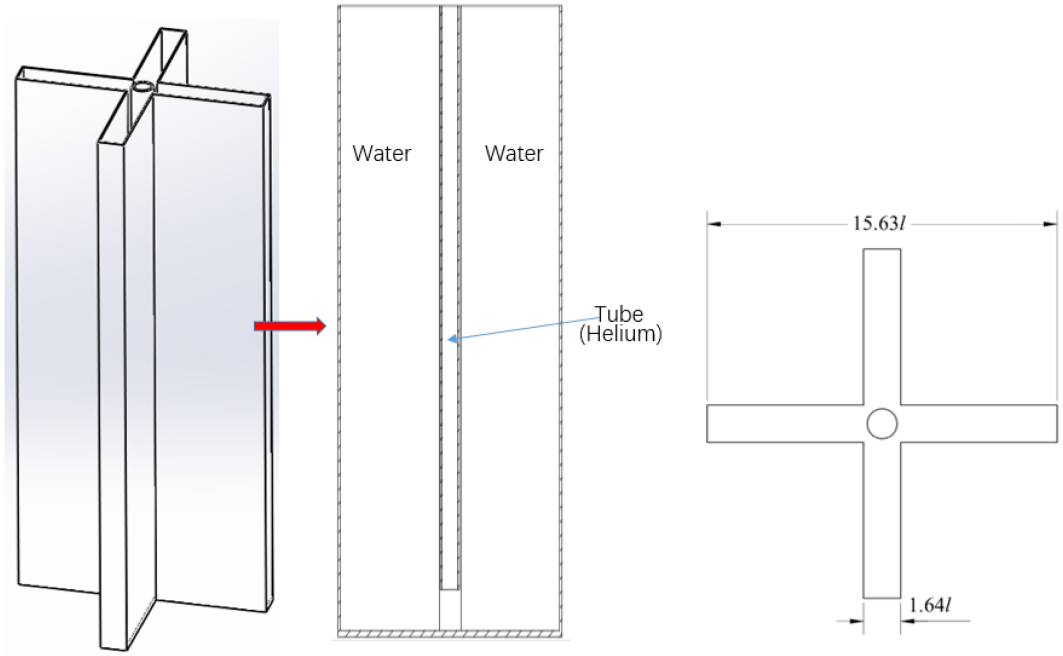

FIGURE 7 | Cross-type channel model and radial size.

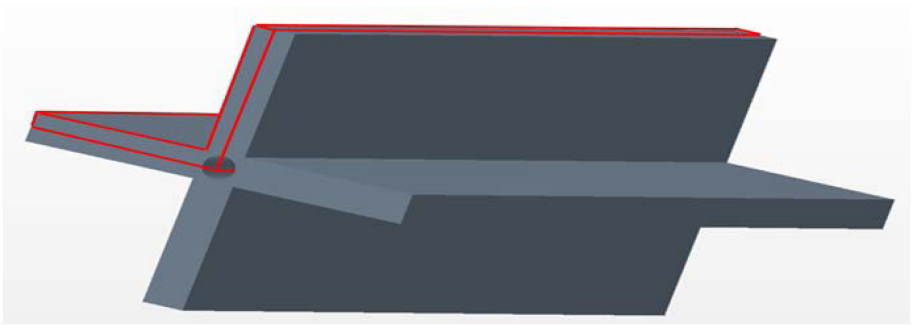

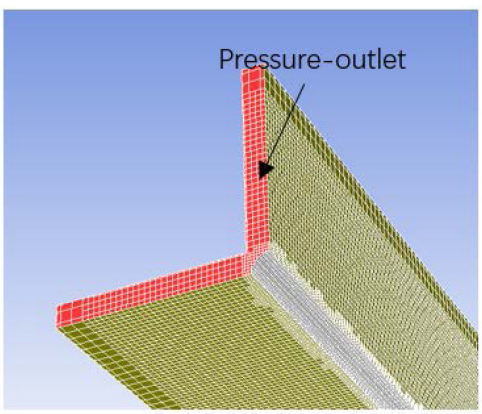

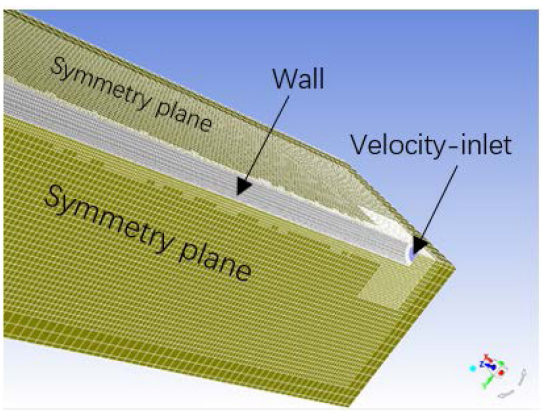

FIGURE 8 | Computational domain, mesh and boundary conditions.

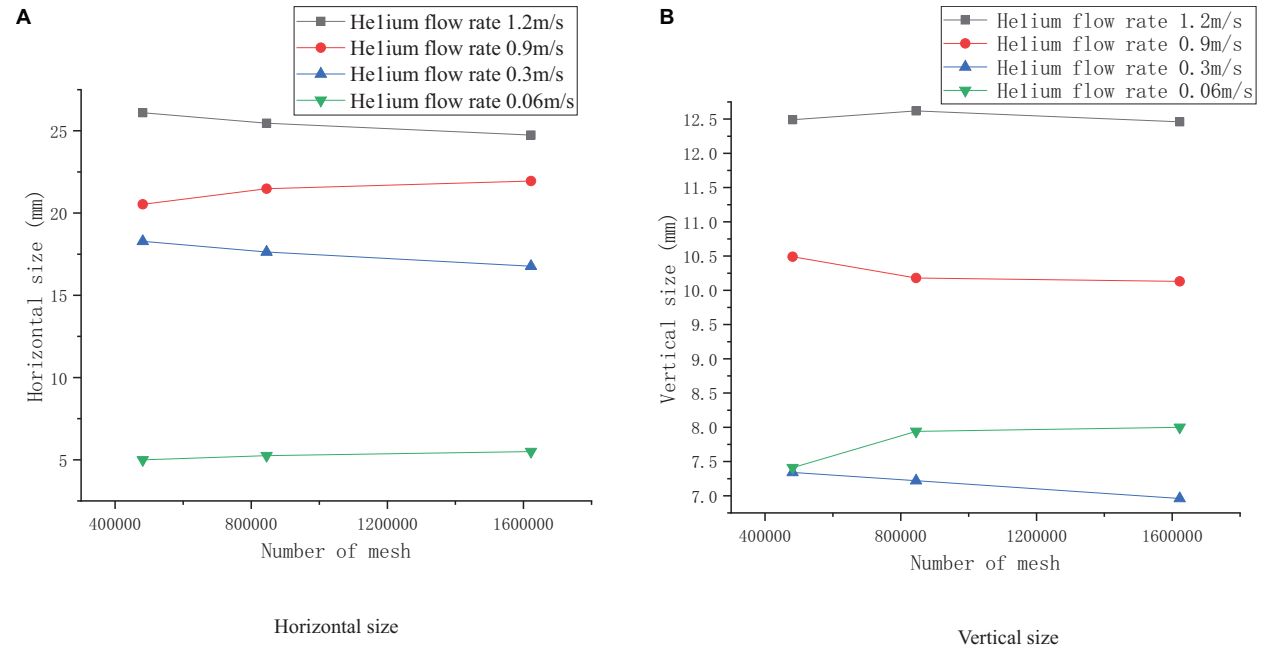

FIGURE 9 | Bubble size comparison. **(A)** Horizontal size. **(B)** Vertical size.

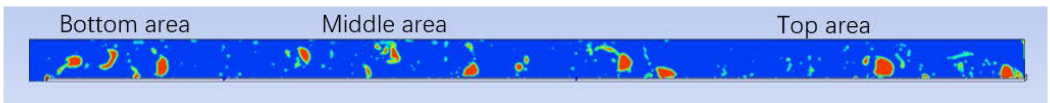

FIGURE 10 | Flow channel division.

Validation

For researching the law of bubble formation in the process of gas-liquid stirring during the industrial production, an experiment of submerged jet directed upward has been done by Wei (2016), as shown in **Figure 2**. And the data like bubble size under several flow rates has been achieved.

In this experiment, the bubble that has just left the nozzle is selected as the research object, at this time, the bottom of the bubble just rises to be aligned with the bottom end of the nozzle. In the horizontal direction, the size of the bubble is obtained directly by the ruler; in the vertical direction, the distance between the top and bottom of the bubble is measured, which is the vertical size of the bubble. **Figure 3** shows the selection criteria.

In order to validate the rationality of the adopted numerical method, a corresponding numerical simulation model according to Wei (2016)'s experiment has been established. **Figure 4** shows the schematic diagram.

The similarity in **Figure 5** preliminarily illustrates the rationality of the simulation method. Furthermore, the bubble size of experimental results and numerical results have been compared as shown in **Figure 6**. The maximum error between the numerical results and the experimental results does not exceed 12.2%, and the trend of the increase of the bubble size with the increase of the helium rates is also coincident. Considering that the numerical simulation itself is under the ideal conditions, so the error is acceptable, which verifies the correctness of this numerical method.

Simulation of Cross-Type Channel

Figure 7 shows the cross-type channel model, the axial length of the channel is 185.25 *l*, the outer diameter of the tube is 1.33 *l* (the inner diameter is *l*, *l* = 6.1 mm) in size, and the tube reaches 3.28 *l* from the bottom of the flow channel. **Figure 7** also shows the radial size of flow channel.

Considering that the cross-type channel is a symmetric structure, a quarter symmetry is adopted to improve the calculation efficiency. The calculation domain is shown in of **Figure 8** (the region inside the red frame), and there are two symmetric boundaries, the velocity inlet is used at the bottom of the pipe. The top of the cross-type channel is the pressure outlet, and the rest are the walls. We used hexahedral grids, and the wall surface and the inlet part are densified. Because it is a transient problem, the PISO algorithm is adopted. For the convergence condition, the Fluent default values are used.

Aiming to the number of cells of 481181, 845306, and 1622105, the validation of mesh independence has been established. Four different inlet helium flow rates from 0.06 to 1.2 m/s were selected

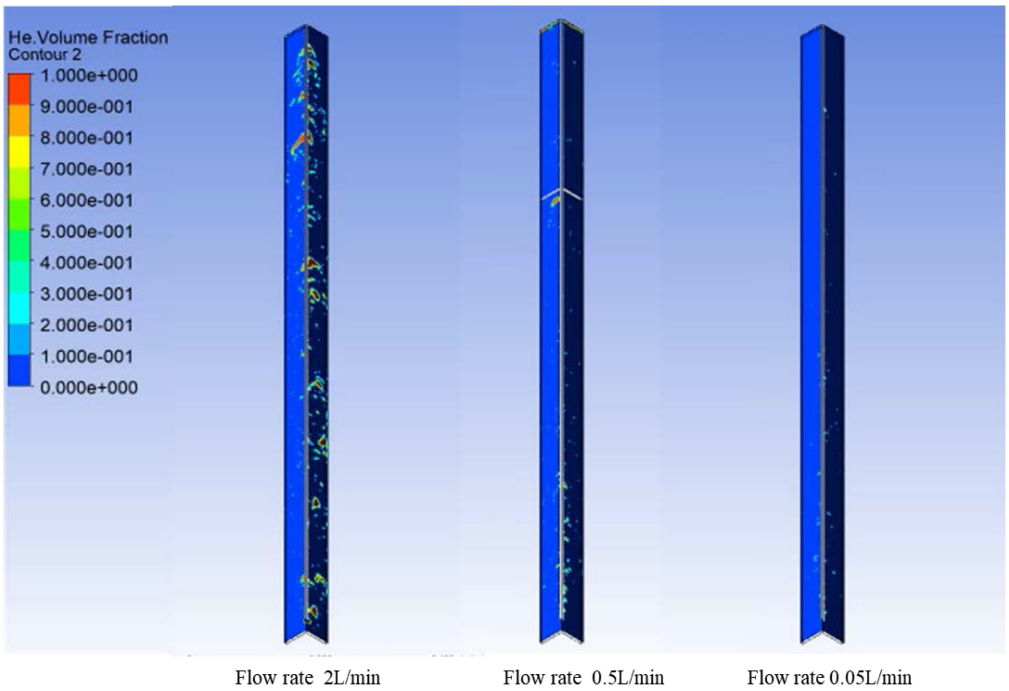

FIGURE 11 | Axial helium distribution under different flow rates.

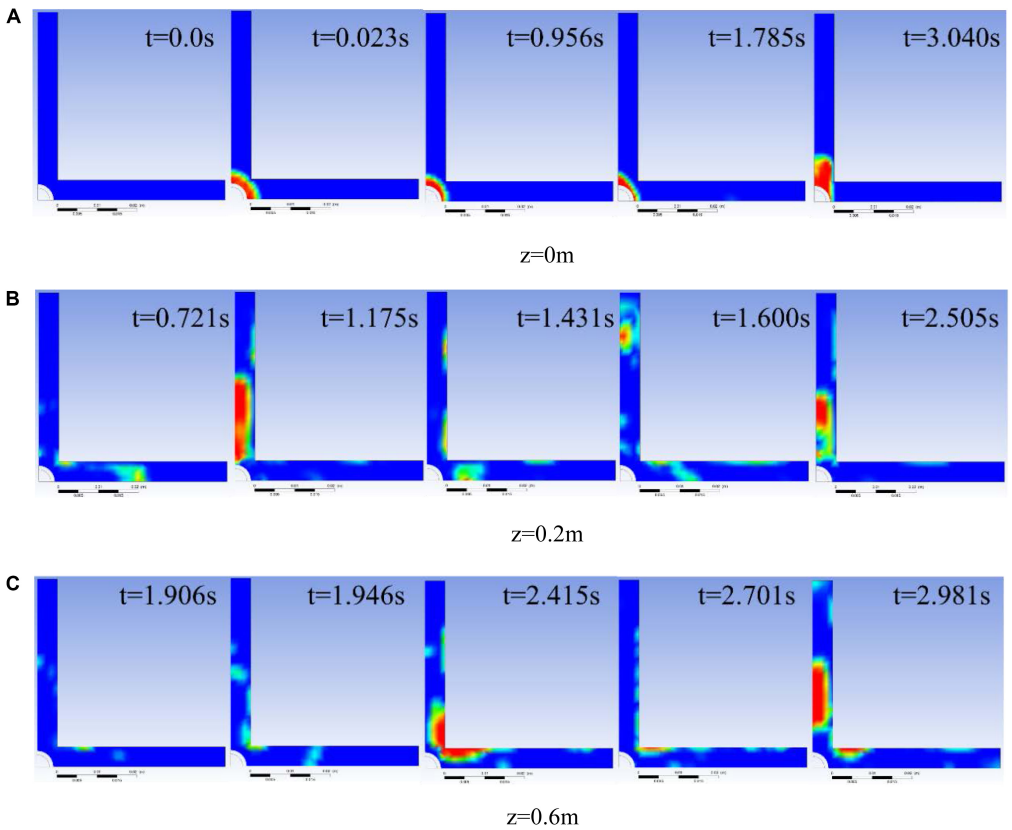

FIGURE 12 | Contours of helium distribution for helium flow rates is 2 L/min. **(A)**= z 0 m. **(B)** z = 0.2 m. **(C)** z = 0.6 m.

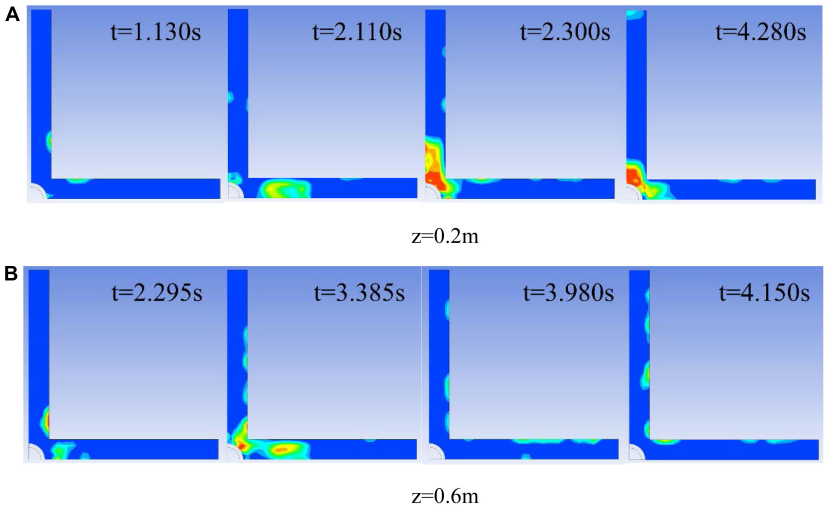

FIGURE 13 | Contours of helium distribution for helium flow rates is 0.5 L/min. **(A)** z = 0.2 m. **(B)** z = 0.6 m.

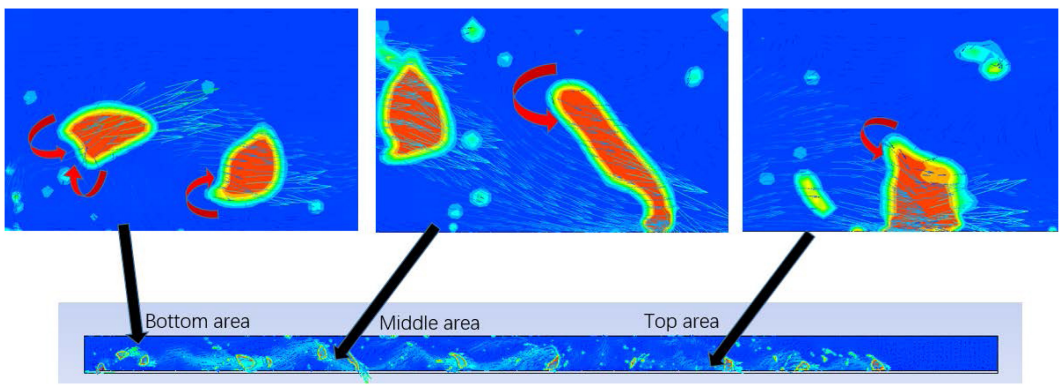

FIGURE 14 | Velocity vector distribution in the flow channel for helium flow rates is 2 L/min.

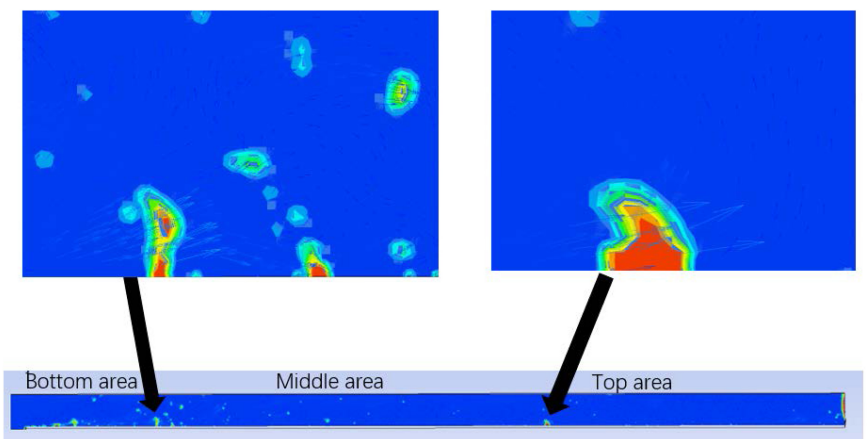

FIGURE 15 | Velocity vector distribution in the flow channel for helium flow rates is 0.5 L/min.

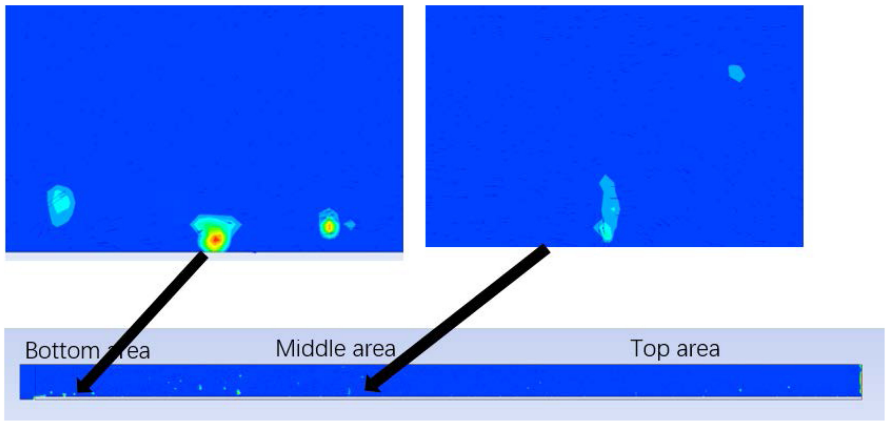

FIGURE 16 | Velocity vector distribution in the flow channel for helium flow rates is 0.05 L/min.

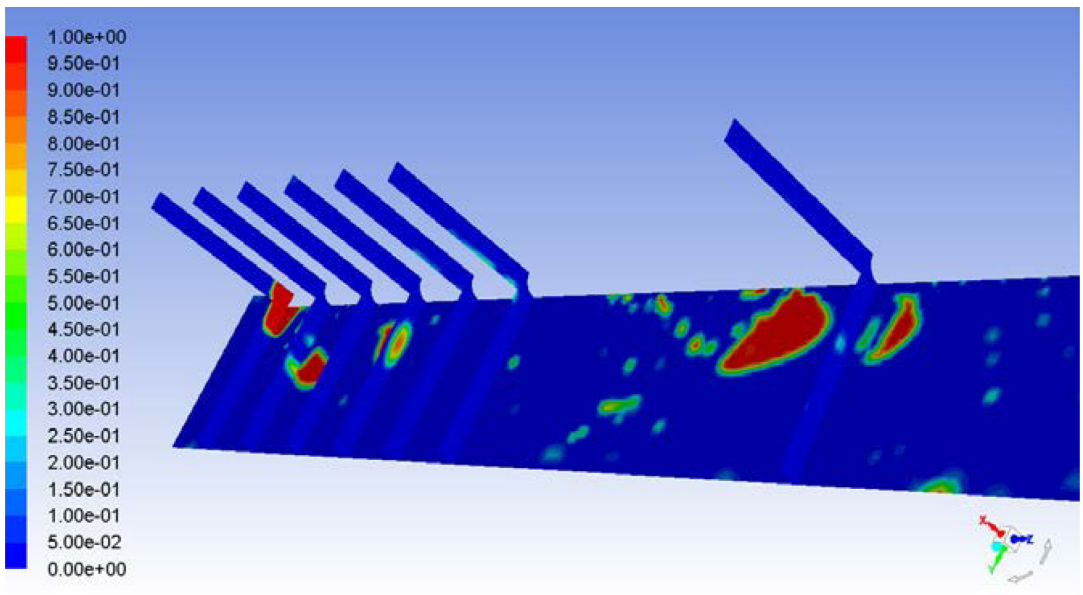

FIGURE 17 | Part of selected planes.

as the comparison conditions under different number of cells. As shown in **Figure 9**, the bubble sizes (the bubbles measured at the exit of the nozzle as described above) are almost the same (order of 0.1 mm) with these under the number of cells of 845306 and 1622105, even the gap between 481181 grids and 1622105 grids is small. So in this research a meshing method between 481181 and 845306 grids is adopted.

RESULTS AND DISCUSSION

In this study, a numerical simulation of helium flow rates from 0.01 to 2 L/min was carried out. The study found that some characteristics of bubbles have obvious regularity under different flow rates of helium. Due to space limitations, the following will select some representative working conditions for detailed discussion.

For the sake of analysis, the channel has been divided into three parts, the inlet is $z = 0$ m, the region of $z < 0.2$ m is called bottom area, 0.2 m $< z <$ 0.6 m is middle area, $z >$ 0.6 m is top area as shown in **Figure 10**.

Research on Bubble Distribution Characteristics

Through the contours of phases and animation in the axial direction of the cross-type channel, we found that the bubble size increased with the increase of helium flow rates, manifesting the area occupied by the helium (red one) became larger and larger in the axial section, as shown in **Figure 11**; Combining the animation of the contours of phases in the axial and radial

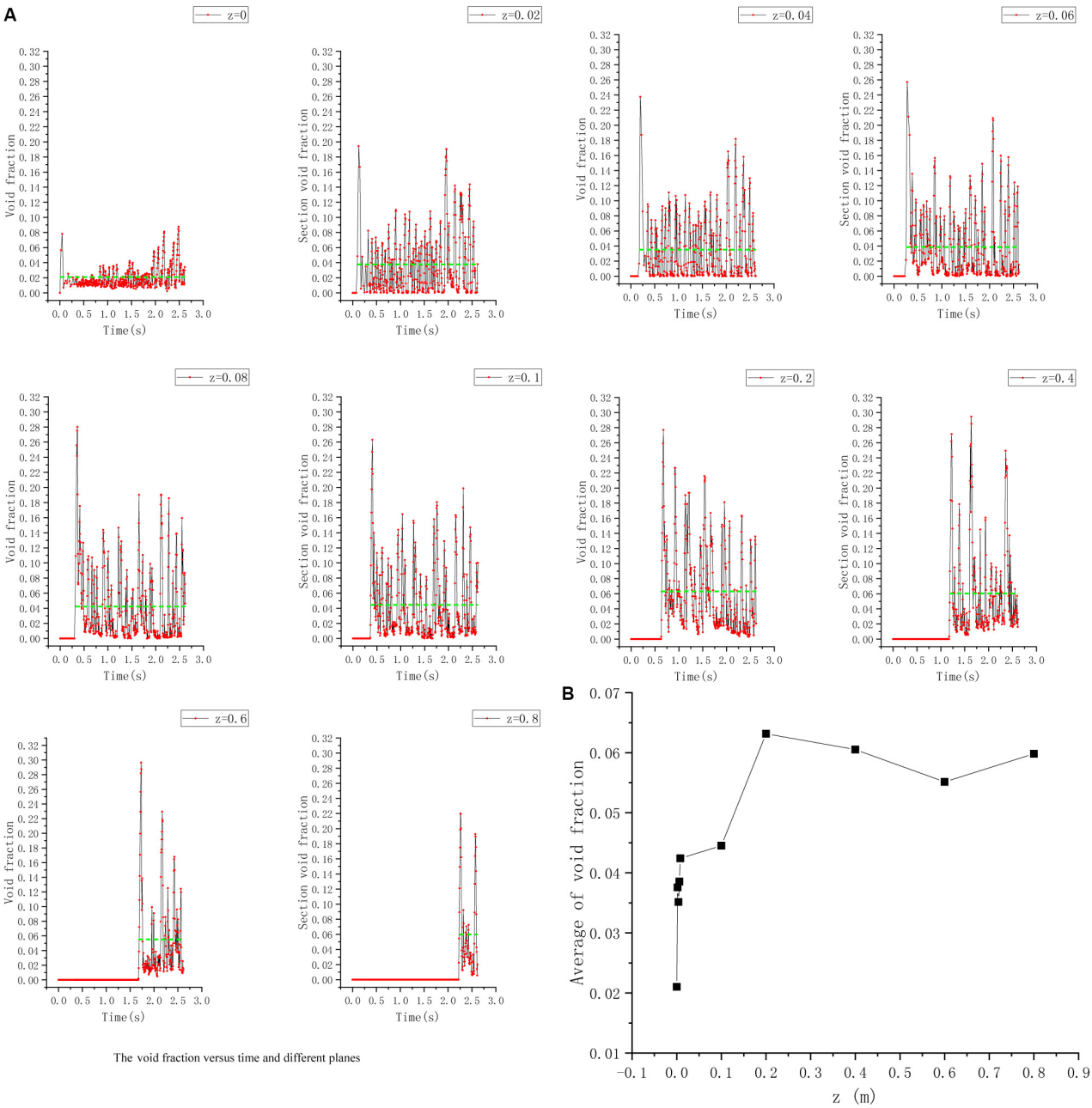

FIGURE 18 | Curve of void fraction, 2 L/min helium flow rates. **(A)** The void fraction vs. time and different planes. **(B)** The average of the void fraction.

sections, it can be seen that most bubbles tended to rise near the tube wall (the smaller the flow rates are, the more obvious it will be). There were also a few smaller bubbles distributed far away from the tube wall (some can reach one of the four corners of the cross-type channel), and move downward during the process of bubble rising.

In the radial section, take the helium flow rate of 2 L/min for instance. As shown in **Figure 12**, at z = 0 m, the distribution of helium was concentrated at the nozzle. Initially, the shape of the bubble was relatively regular, and the helium distribution at the cross-section was approximately circular (quarter symmetry), but then the bubble gradually became irregular, as shown in **Figure 12A** t = 3.040 s, the helium distribution on the cross-section was biased to one side. The reason is that the rising bubbles detached from the nozzle cause the flow disturbance which makes the bubbles near nozzle under complex stress. **Figure 13** shows the radial helium distribution at helium flow rate of 0.5 L/min. It is similar to other working conditions, just the proportion of helium in the cross-section of the flow channel decreasing with reduction of helium flow rates.

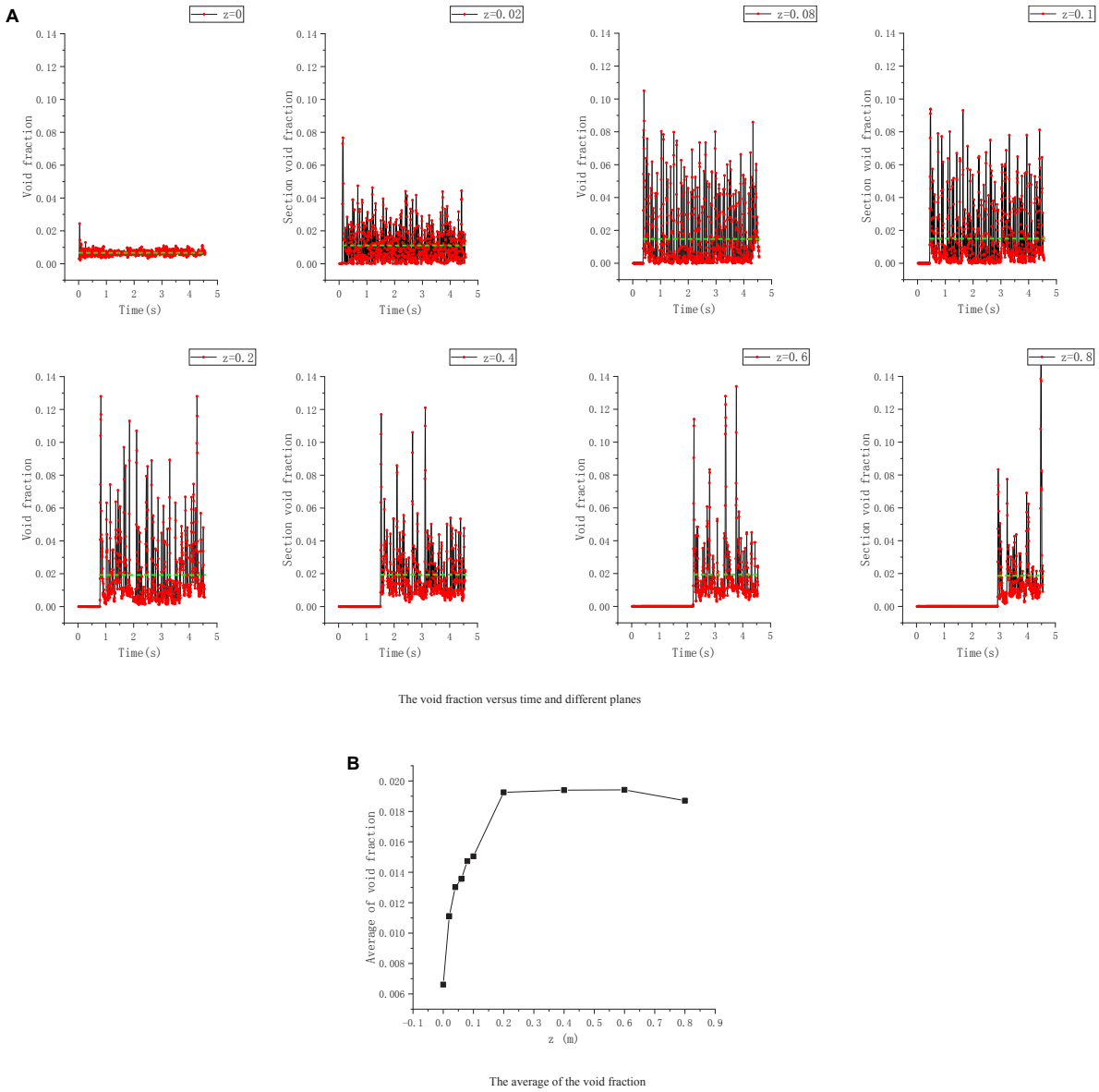

FIGURE 19 | Curve of void fraction, 0.5 L/min helium flow rates. **(A)** The void fraction vs. time and different planes. **(B)** The average of the void fraction.

Overall, at high flow rates (above 1 L/min), the movement of bubbles in the flow channel is similar to the slug flow in a vertical pipe. At low flow rates (below 0.1 L/min), the form is similar to the bubbly flow in a vertical pipe.

Research on the Characteristics of Bubble Coalescence

Through flow animation under different flow rates, it can be found that in the middle area and top area of the flow channel, large bubbles were distributed at a certain interval in the axial direction, and among the large bubbles were small bubbles (not obvious when helium flow rates is lower than 0.1 L/min) as shown in **Figure 14**.

During the process of bubble rising, the motion of fluid around the bubble will affect the subsequent bubbles. Taking the velocity vector distribution at the flow rate of 2 L/min for instance as shown in **Figure 14**, the direction of the fluid vector on the side of the rising bubble was opposite. This is why some small bubbles move downward within a certain range. Also, the direction of the fluid vector at the tail of the rising bubble was the same, which accelerated the subsequent bubbles to catch up with the previous one, then bubble coalescence happened. In the axial direction, the bubbles were getting larger and larger due to the bubble coalescence, which leads to an upward trend in void fraction at the bottom area of the flow channel along the axial direction. In the area after the middle area of flow channel, as the bubbles were accelerated by buoyancy,

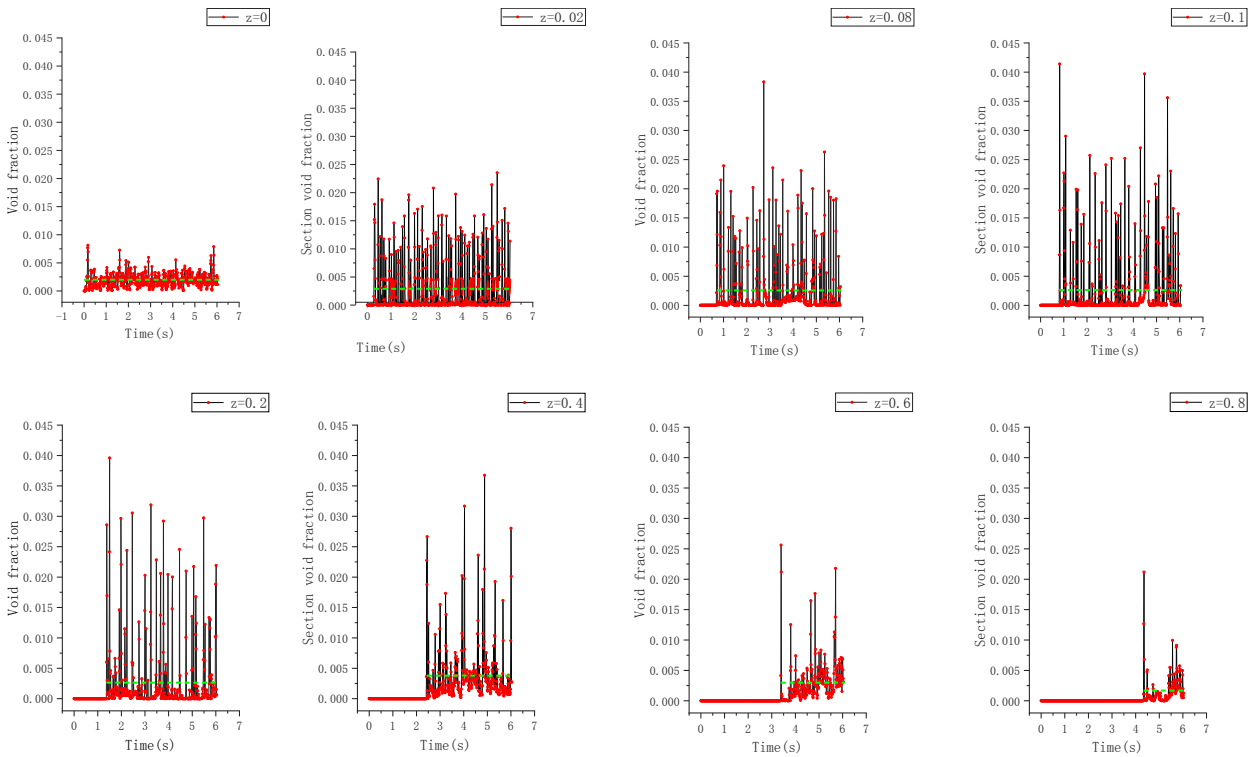

FIGURE 20 | Curve of void fraction, 0.05 L/min helium flow rates.

the distance among bubbles became large, which weakened the influence of surrounding fluid on bubbles. Finally, large bubbles were distributed at a certain interval, and some small bubbles were separated among the large bubbles.

Figure 15 shows the velocity vector distribution of helium flow rates 0.5 L/min. Compared with the condition of 2 L/min, the rising bubbles had less disturbance on the flow field, but the bubble coalescence still exited, especially at the bottom area of the channel. It was just not as frequent as the helium flow rates of 2 L/min. **Figure 16** shows the condition of helium flow rates 0.50 L/min. As the flow rates of helium gas was further decreased, the bubble volume became smaller and smaller, and the flow channel space occupied also became smaller, so that the disturbance caused by the rising bubble became smaller, as a result, the frequency of the bubble coalescence is reduced.

Research on the Influence of Flow Rate on the Void Fraction

Analyzing 10 planes in the axial direction of the flow channel, they are planes of $z = 0$, $z = 0.02$, $z = 0.04$, $z = 0.06$, $z = 0.08$, $z = 0.1$, $z = 0.2$, $z = 0.4$, $z = 0.6$, $z = 0.8$ m respectively, as shown in **Figure 17**.

The void fraction of a plane can be obtained through calculating the proportion of the helium share in the selected plane. The graph of the void fraction of each plane with time is shown as followed (The green dotted line is the average of the void fraction).

Figure 18 shows the curve of void fraction vs. time and the average of the void fraction.

The figures above show that, during a period of time, the larger value of the transient void fraction occurs less frequently (the maximum transient void fraction can reach 0.3), which leads to a lower average void fraction (the maximum average void fraction can only reach 0.063); In the bottom area of the flow channel, the average value of the void fraction increases rapidly with increasing axial position. In the middle area and the top area of the flow channel, the average value of the void fraction does not change much.

The reason for the above phenomenon is the bubble coalescence, as analyzed in Section "Research on the Characteristics of Bubble Coalescence." Within a certain distance, the latter bubble is accelerated by the disturbance of flow field and will catch up with the previous bubble, which leads to bubble coalescence. As a result, causing an upward trend in void fraction of the bottom area of the flow channel in the axial direction, and in the middle area and top area of the flow channel, due to the accelerated rising bubbles by the buoyancy, the distance among bubbles in the axial direction becomes larger, resulting in the decrease of bubble coalescence frequency. Eventually, large bubbles are distributed at a certain interval, and some small bubbles are separated by large bubbles, this is why the maximum value of the void fraction of a certain cross-section is much larger than the average value.

When the flow rates of helium are 0.5 L/min, the variation law of the void fraction in the axial direction of the flow channel is similar to the situation of 2 L/min helium flow rates: the maximum transient void fraction of a plane of the flow channel is much larger than its average value (maximum transient void fraction can reach 0.14, and maximum average void fraction is only 0.019); in the bottom area of the flow channel, the average void fraction increases rapidly, while in the middle area and top area of the flow channel does not change much and tends to be stable. **Figure 19** shows the curve of void fraction vs. time and the average of the void fraction.

Figure 20 shows the curve of void fraction vs. time and 0.05 L/min helium flow rates. It can be found that the void fraction of each plane is generally very low under 0.05 L/min helium flow rates. The maximum transient void fraction is only about 0.042, and the maximum average void fraction is even lower than 0.005. So, it is not rather meaningful to further analyze the void fraction.

SUMMARY AND CONCLUSION

In this study, taking the influence of bubbles on neutron detection as the background, a numerical simulation for the rising rules of helium bubbles in the cross-type flow channel has been carried out with CFD software. The major conclusions are as the following:

1. Because of flow disturbance caused by rising bubbles, the bubble coalescence exists widely in the middle area and bottom area of the flow channel ($z < 0.6$ m). The larger the helium flow rates are, the more frequent the coalescence will be. In the top area of the flow channel, due to the larger distance among the bubbles, the disturbance effect is small, so the coalescence is hard to happen. In the bottom area of the flow channel, the coalescence is most frequent, because of short distance;
2. During the process of bubble rising, the larger bubbles tend to move near to the tube wall, and some smaller bubbles tend to be far away from the tube wall (some can reach the one of the four corners of the cross-type channel), moving downward, due to the disturbance of the larger bubbles on the flow field;
3. When the helium flow rate is greater than 0.1 L/min, the average value of the void fraction increases rapidly along the axial direction, and then tends to stabilize in the middle area and top area of the flow channel ($z > 0.2$ m), and the greater the helium flow rate, the greater the void fraction.

DATA AVAILABILITY STATEMENT

All datasets generated for this study are included in the article/supplementary material.

AUTHOR CONTRIBUTIONS

ZM as the tutor guided the whole process of the simulation. RY and DM performed the selection and validation of the numerical method. HJ carried out the validation of mesh independence. CZ planned and carried out the simulation of cross-type channel. XZ finished the data processing. CZ and XZ wrote the manuscript with input from all authors. All authors provided critical feedback and helped shape the research, analysis, and manuscript.

REFERENCES

Ansys Fluent 17. 2 Theory Guide (2016). *ANSYS Fluent 17.2 Theory Guide*. Canonsburg, PA: ANSYS, Inc.

Buwa, V. V., Gerlach, D., Durst, F., and Schlücker, E. (2007). Numerical simulations of bubble formation on submerged orifices: period-1 and period-2 bubbling regimes. *Chem. Eng. Sci.* 62, 7119–7132. doi: 10.1016/j.ces.2007.08.061

Chen, C., Wang, M., Zhao, X., Ju, H., Wang, X., Tian, W., et al. (2019). Numerical study on the single bubble rising behaviors under rolling conditions. *Nuclear Eng. Design* 349, 183–192. doi: 10.1016/j.nucengdes.2019.04.039

Gerlach, D., Alleborn, N., Buwa, V., and Durst, F. (2006). Numerical simulation of periodic bubble formation at a submerged orifice with constant gas flow rate. *Chem. Eng. Sci.* 62, 2109–2125. doi: 10.1016/j.ces.2006.12.061

Guang, L. (2010). *Two-Phase Flow Dynamical Simulations and Modelling of Bubble Column Reactors*. Shanghai: East China University of Science and Technology.

Haijing, Y. (2010). *Numerical Simulation of Bubble Formation and Movement*, Ph. D thesis, Tianjin University, Wuhan.

Hashida, M., Hayashi, K., and Tomiyama, A. (2019). Rise velocities of single bubbles in a narrow channel between parallel flat plates. *Intern. J. Multiphase Flow* 111, 285–293. doi: 10.1016/j.ijmultiphaseflow.2018.09.015

Jiapeng, T. (2014). *Fluent 14.0 Super Learning Manual*, Master thesis, Post & Telecom Press, Beijing.

Jin, G., Yan, C., Sun, L., Xing, D., and Zhou, B. (2014). Void fraction of dispersed bubbly flow in a narrow rectangular channel under rolling conditions. *Prog. Nuclear Energy* 70, 256–265. doi: 10.1016/j.pnucene.2013.10.012

Khan, I., Wang, M., Zhang, Y., Tian, W., Su, G., and Qiu, S. (2020). Two-phase bubbly flow simulation using CFD method: a review of models for interfacial forces. *Prog. Nuclear Energy* 125, 1–17.

Tsuge, H., Tezuka, Y., and Mitsudani, M. (2005). Bubble formation mechanism from downward nozzle—Effect of nozzle shape and operating parameters. *Chem. Eng. Sci.* 61, 3290–3298. doi: 10.1016/j.ces.2005.12.002

Wei, L. (2016). *Experimental and Numerical Simulation Research on the Gas-Liquid Stirring Characteristics of Immersion Top-Blown from Single Orifice*. Wuhan: Wuhan University of Science and Technology.

Xuan, W., and Jingjing, J. (2016). Expansion and detachment characteristics of bubble at downward nozzle of vertical flat pipe. *CIESC J.* 67, 1869–1877.

Xuan, W., and Songyang, L. (2019). Numerical simulation on bubble behavior at nozzle of vertical flat pipe. *J. Yangtze River Sci. Res. Instit.* 36, 68–73.

Ying, H. (2014). *Numerical Study of Bubble Behavior in Vertical Rectangular Narrow Channel*. Harbin: Harbin Engineering University.

Conflict of Interest: The authors declare that the research was conducted in the absence of any commercial or financial relationships that could be construed as a potential conflict of interest.

frontiers in Energy Research

ORIGINAL RESEARCH
published: 07 December 2020
doi: 10.3389/fenrg.2020.548065

Numerical Study on the Thermal Hydraulic Characteristics in a Wire-Wrapped Assembly of LFRs

Jun Li[1], Di Fang[1], Chao Guo[2], Mingjun Wang[1], Jian Deng[2]*, Wenxi Tian[1], Suizheng Qiu[1] and G. H. Su[1]*

[1]School of Nuclear Science and Technology, Shaanxi Key Laboratory of Advanced Nuclear Energy and Technology, State Key Laboratory of Multiphase Flow in Power Engineering, Xi'an Jiaotong University, Xi'an, China, [2]Science and Technology on Reactor System Design Technology Laboratory, Nuclear Power Institute of China, Chengdu, China

The concept of wire-wrapped assembly has been widely adopted in liquid metal-cooled reactors to enhance the capability of flow and heat transfer. The detailed 3D thermal hydraulic behaviors of liquid metal in the wire-wrapped assembly directly affect the safety of the reactor. In the present work, a numerical study on a 19-pin wire-wrapped assembly cooled by a lead-bismuth eutectic was carried out using the CFD method. The geometrical model is referred to in the test section in KIT's 19-pin experiments, which is a scaled test assembly based on the MYRRHA reactor. The established CFD model was validated against experimental data and results showed that the SST k-ω model accompanied with the modified Pr_t was appropriate for the current problem. Then the numerical models were extensively used in the modeling of the blocked assembly flow with a cylindrical blockage. Also, the influences of blockage longitude, position, and porosity on the thermal hydraulic characteristics in the assembly were evaluated in detail. This work is meaningful for the deep understanding of safety features under the condition of assembly blockage operation in LFRs.

Keywords: CFD, sub-channel blockage, fuel assembly, lead-bismuth eutectic, wire-wrapped assembly

OPEN ACCESS

Edited by:
Muhammad Zubair,
University of Sharjah,
United Arab Emirates

Reviewed by:
Mariano Tarantino,
Italian National Agency for New Technologies, Energy and Sustainable Economic Development (ENEA), Italy
Ivo Kljenak,
Institut Jožef Stefan (IJS), Slovenia

****Correspondence:***
Mingjun Wang
wangmingjun@mail.xjtu.edu.cn
Jian Deng
dengjian_npic@163.com

Specialty section:
This article was submitted to Nuclear Energy, a section of the journal Frontiers in Energy Research

Received: *01 April 2020*
Accepted: *09 November 2020*
Published: *07 December 2020*

Citation:
Li J, Fang D, Guo C, Wang M, Deng J, Tian W, Qiu S and Su GH (2020) Numerical Study on the Thermal Hydraulic Characteristics in a Wire-Wrapped Assembly of LFRs. Front. Energy Res. 8:548065. doi: 10.3389/fenrg.2020.548065

1. INTRODUCTION

For the sake of decreasing the emission of greenhouse gases and improving the intrinsic safety of nuclear reactors, the concept of liquid metal reactors has garnered more interest in recent years. Fast reactors have been incorporated into the GEN-IV nuclear energy system. Among various kinds of fast reactors, the lead or lead-bismuth eutectic (LBE)-cooled reactor is regarded as one of the most promising next-generation nuclear energy systems and has already been put onto the schedule for practical usage. Consequently, a variety of designs have sprung up around the world, like SVBR (Zrodnikov et al., 2011), MYRRHA (Abderrahim et al., 2001; Biarrotte et al., 2010), CLEAR (Wu, 2016a; Wu, 2016b), ALFRED (Damiani et al., 2014; Frogheri et al., 2013; Frignani et al., 2019a; Frignani et al., 2019b), etc.,

The thermal-hydraulic phenomenon in liquid metal fast reactors has recently attracted attention. Particularly, the numerical method has been widely adopted due to its higher efficiency and cost-effectiveness compared with the experimental method. Yu et al. (Yu et al., 2015) proposed a two-region porous-medium model for predicting the temperature profile on the duct wall, with the existence of inter-wrapper flow (IWF). Similarly, Wang et al. (Wang et al., 2019b) put forward a modified model with coarse mesh for a three-assembly system with IWF, based on the 61-pin

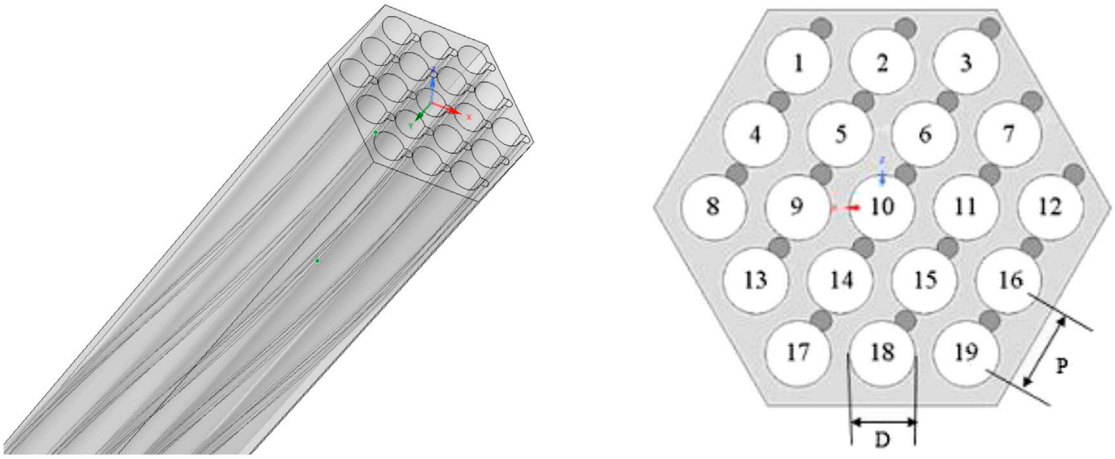

FIGURE 1 | The three dimensional model of the computational domain.

assembly in Chinese experimental fast reactors. Vanderhaegen et al. (Qin et al., 2019) modeled the core and hot pool of MYRRHA, and the fuel bundles, heat exchangers, and pumps were simplified with the porous-medium model. Similarly, Wang et al. (Wang et al., 2020) contributed a full-scale numerical model based on the porous-medium model for the Monju reactor (SFR). Steady-state and transient analyses on the thermal-stratification phenomenon in the upper plenum were performed.

Coarse-mesh methodology is no longer sufficient in calculation at the subassembly level, and various methods for solving the N-S equations (DNS, LES, and RANS) can be found in open literature. The validation and calculations for benchmarks are widely implemented in different kinds of assemblies. The objects of experiments and simulations include a wire-wrapped annulus (Qin et al., 2019), 7- (Merzari et al., 2016), 19- (Pacio et al., 2016; Piazza et al., 2016; Pacio et al., 2017), 61- (Nguyen et al., 2017; Chen et al., 2018; Goth et al., 2018a; Goth et al., 2018b; Nguyen et al., 2018), and 127-pin assemblies (Kennedy et al., 2015), and for detailed outcomes, readers can refer to the paper by Roelof (Roelofs et al., 2019b) which makes key conclusions on these numeric practices. Among these studies, a variety of numerical results have confirmed the feasibility of the RANS models in simulating the turbulent heat transfer of liquid-metal coolants. Although RANS models cannot predict the local characteristics in the flow field (especially in the vicinity of the wire) to a satisfactory accuracy, as Merzari et al. (Merzari et al., 2016) pointed out, so far the RANS is still sufficient and effective in calculation at the assembly level.

During the design and safety analyses of liquid metal fast reactors, a series of issues at the assembly level still need to be addressed (Roelofs et al., 2019a; Zhang et al., 2020), and it is a fact that most of the current numerical studies focus on the normally operated subassemblies. However, the off-normal conditions also deserve great attention. One of the typical off-normal conditions is a blockage accident, which can be caused by the accumulation of corrosive products in the fuel assembly (Zhang et al., 2020). Blockage accidents in LFRs may threaten the safety of reactors, leading to fuel assembly damage or melt. Therefore, the thermal-hydraulic characteristics in LFRs under off-normal conditions (partially or completely blocked fuel assembly) should be paid more attention to. Pacio et al. (Pacio et al., 2018) focused on the local heat transfer of internal blockages in fuel assemblies with wire spacers in the European MAXSIMA project. Rasu et al. (Rasu et al., 2014) investigated the effects of porous blockages with a 19-pin bundle cooled by sodium. More factors of the blockage are taken into consideration, such as the porosity, size, and radial location. In addition to correctly modeling the geometry of wire-wrapped subassemblies, Sakar et al. (Sarkar et al., 2019; Sarkar et al., 2020) developed the porous-medium simplification method based on the non-Darcy theory for saving computational cost efficiently. In the simulations, both the natural convection under an instantaneous blockage and the forced convection with sub-channels partially blocked were modeled. Piazza et al. (Piazza et al., 2014) modeled a partial blockage in a lead-cooled bundle under different blockage ratios with URANS, and the results show that a higher cladding temperature is induced by a larger area of blockage under the same boundary conditions. Chai et al. (Chai et al., 2019) investigated the internal blockages in a subassembly with wire spacers numerically under the conditions with different positions and longitudes.

TABLE 1 | Some detailed parameters of the subassembly in the present study (Pacio et al., 2016).

Parameters	Symbol	Value	Unit
Number of rods	—	19	—
Distance between two centroids of rods	*p*	10.49	Mm
Outer diameter of rods	D	8.2	Mm
Pitch-to-diameter ratio	P/D	1.279	—
Length of heated rods	L	870	Mm
Wire pitch	H	328	Mm
Flow area of subassembly	$A_{hexchannel}$	1,012.74	mm^2

TABLE 2 | Details of the five grids adopted in the sensitivity study.

Case	Case 1 (base)	Case 2 (coarse)	Case 3 (coarser)	Case 4 (fine)	Case 5 (finer)
Base cell size (mm)	1	2	2.7	0.7	0.5
Quantity of cells (million)	30.0	14.9	7.7	42.1	72.9

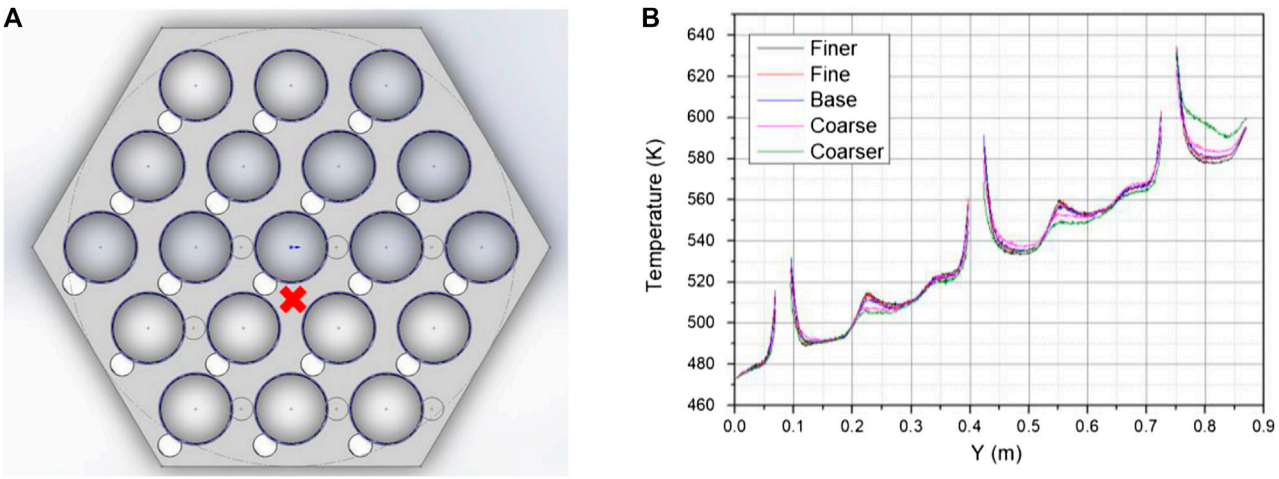

FIGURE 2 | (A) The schematic position of the characteristic line; **(B)** the temperature profile along the characteristic line at the central sub-channel.

TABLE 3 | GCI evaluated on the highest fluid temperature at the chosen line and *Nu* on ML2.

Index	Grids adopted in case	The highest temperature estimated at the characteristic line (K)	GCI_t	Local *Nu* at ML2	GCI_{Nu}
#1	Fine	635	$GCI_{t,12}$ = 0.0380%	8.69	$GCI_{Nu,12}$ = 2.55%
#2	Base	634	$GCI_{t,23}$ = 0.418%	8.61	$GCI_{Nu,23}$ = 3.70%
#3	Coarse	623	—	8.32	—

In summary, the thermal hydraulic characteristics in fuel assemblies with wire spacers cooled by LBE under the non-normal conditions should be paid more attention to. In the present study, the flow and heat transfer features in a 19-pin wire-wrapped fuel assembly are numerically studied with a RANS model. The geometric and mesh models for the 19-pin bundle are described, and the numerical methods and algorithms adopted are introduced. Then the validation between simulation and experiments is performed. Finally, the accidental scenario of partial blockage at the inlet is outlined and investigated.

2. GEOMETRIC AND MESH MODELS

2.1. The Geometric Model

A series of experiments related to the LBE flow and heat transfer study have been conducted by the KALLA Laboratory (Karlsruhe Institute of Technology, Germany). The experiments performed by Pacio et al. cover the assemblies with different spacer types, including the grid spacer (Pacio et al., 2014) and the wire-wrapped spacer (Pacio et al., 2016; Pacio et al., 2017). As for the geometric model in the current study, it fully refers to the wire-wrapped test section, which is a scaled model from the real MYRRHA subassembly. Specifically, the tested assembly contains 19 rods fixed in a triangle arrangement, and it is divided into three parts: the developing region upstream of the inlet with a length of 824 mm, the heated zone representing the active region in the real core with a length of 870 mm, and the outlet region with a length of 535 mm (Pacio et al., 2016). More details about the geometric scales of assembly are presented in **Figure 1** and **Table 1**. Additionally, in the current simulation, the geometric model is simplified to save computational cost with necessary accuracy. A shorter developing region (328 mm, one wire

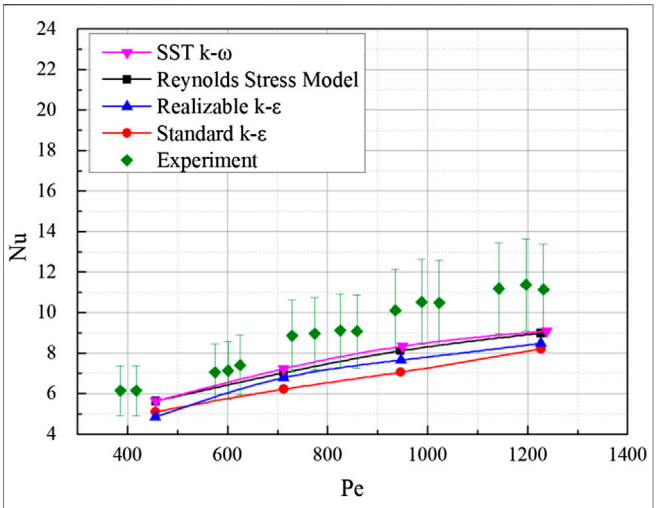

FIGURE 3 | The local *Nu* at ML3 estimated by different turbulence models against the experiment.

pitch) is adopted, and the outlet region is not considered in the final domain. Moreover, wires are prepared and embedded in the rods and smoothed, and a gap of 0.1 mm (Merzari et al., 2010; Ranjan et al., 2010) is kept between the wire-pin assembly and the other rods, to avoid direct contact. Finally, a geometric model of the assembly with a total length of 1,198 mm is established.

2.2. Grid Models

As for the grid model, polyhedral cells are adopted to fill up the final fluid domain. A polyhedral cell has more connective cells than a hexahedral or tetrahedral cell, meaning that high-resolution of the complex geometry and better convergence can be achieved (Wang et al., 2018; Wang et al., 2019a). Hence comprehensively making a balance between the grid quality and the cell quantity, the polyhedral type is a better choice to guarantee the high-quality mesh model with a relatively smaller cell quantity due to the complex wire spacers and narrow proximity between the wire and the fuel rod. More specifically, there are five wall-resolved models that adopt different cell quantities (minimum 7.7 million, maximum 72.9 million, as summarized in **Table 2**) in this simulation to obtain the mesh-independence solution. In addition, the y^+ value of the first cell layer near the wall is controlled within the range of 1 to 10.

2.3. Mesh Independence Analysis

In the reference case, the inlet temperature and the mass flow rate of the LBE are 473 K and 19.18 kg/s, respectively. Besides, the heated rod surface is specified with a uniform heat flux of 463,000 w/m^2. Firstly, the effect of the mesh refinement is analyzed qualitatively. The temperature profile at one central sub-channel (the position is shown in **Figure 2A**) is assessed in five different cases. **Figure 2B** illustrates that the profiles estimated by the "coarse", "base", and "fine" models are closed, while the results estimated by the two other models are more divergent. Consequently, considering these five profiles and the computational cost, the final grid is chosen from the three "coarse", "base", and "fine" models.

Secondly, quantitative analyses about the grids are supplemented. In this part, a grid convergence index (Roache, 1994; Roache, 1997) (GCI) is adopted and the evaluation is performed in the three grids mentioned above. Besides, the desired parameters in the GCI calculation are chosen as the local Nusselt number at the plane ML2 and the maximum temperature along the characteristic line (ML2 shown in **Figure 4**, the characteristic line shown in **Figure 2A**). In the

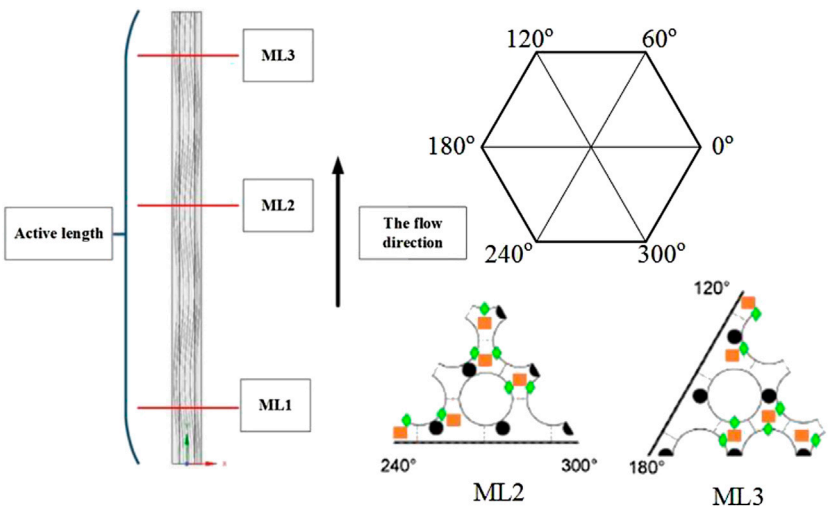

FIGURE 4 | The schematic positions of temperature measuring points in the sub-channels at ML2 and ML3 (Pacio et al., 2016) (Z: the distance downstream of the entrance of the active length).

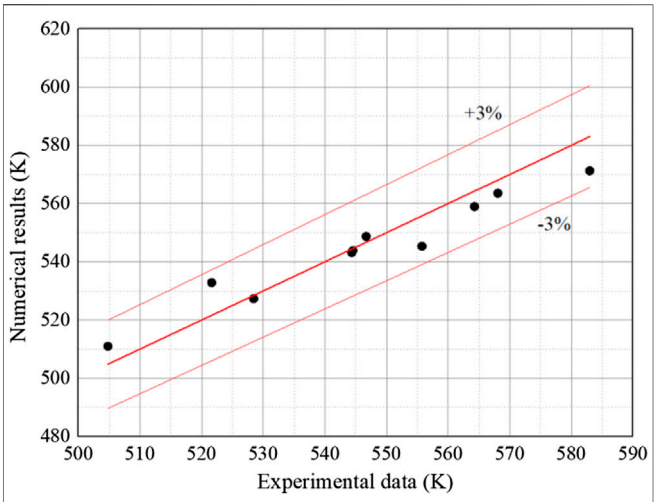

FIGURE 5 | The variations of numerical simulation errors.

GCI methodology, for the current grid models, the refinement ratio is defined as:

$$r = \left(N_{f+1}/N_f\right)^{1/D} \tag{1}$$

where N_{f+1} denotes the cell quantity of the grid after refinement, N_f is the quantity before refinement. What is more, for the current three-dimensional case, D is equal to three in **Eq. 1**, representing the dimensionality of the problem. Subsequently, we can derive the convergence index for the desired parameters using **Eq. 2**, which can be written as:

$$GCI = \frac{F_S|e|}{r^p - 1} \tag{2}$$

where F_s denotes a safety factor, and it is suggested as 1.25 (Roache, 1997). $|e|$ is the absolute value of relative error between the two solutions estimated by the two grids. And p is the order of convergence. The grids in this part are not refined uniformly, i.e., the refinement ratio is not constant, and the evaluation of p needs an iterative process (Roache, 1997). Specifically, iterative equations are presented as:

$$\beta = \frac{\left(r_{12}^{p_{li}} - 1\right)}{\left(r_{23}^{p_{li}} - 1\right)} \frac{e_{23}}{e_{12}} \tag{3a}$$

$$p = \omega p_{li} + (1 - \omega)\frac{\ln(\beta)}{\ln(r_{12})} \tag{3b}$$

where p_{li} is the value of p in the last iteration, ω is a relaxation factor and determined as 0.5, and r_{12} and r_{23} are the refinement ratios of the finest grid to the intermediate grid, and the intermedium to the coarse grid, respectively. So in this case, the index 1, 2, and 3 represent the "fine" grid, the "base" grid, and the "coarse" grid, respectively.

Results of GCI analyses on the two concerned parameters are shown in **Table 3**. The highest temperature along the characteristic line decreases gradually with the grid refining. Moreover, the GCI analysis for the highest temperature suggests that the "fine" model in #1 would be optimum for the current study, with a very low GCI ($GCI_{t,12}$) value at 0.0380%. Besides, the same analysis for local Nu at ML2 presents a similar conclusion. Specifically, after refinement, the GCI value of Nu at ML2 decrease to 2.55%, a relatively low value with the "fine" grid in #1.

TABLE 4 | The case matrix of blockage analysis.

Case number	Blockage type	Porosity	Blockage length
Case 1	Normal	—	—
Case 2	Central	0	1/6H
Case 3	Corner	0	1/6H
Case 4	Edge	0	1/6H
Case 5	Central	0	1/3H
Case 6	Central	0	1/2H
Case 7	Central	0.4	1/6H
Case 8	Central	0.6	1/6H
Case 9	Central	0.8	1/6H

2.4. Blockage Modeling

The "mesh-marking" method, which is performed using user-defined memories in ANSYS-FLUENT (FLUENT 19.2, 2019) to distinguish the cells of the blockage region from the fluid domain, is adopted to set up the mesh model under a blockage condition. After the method is implemented, the marked blockage region is specified as porous, and stainless steel is chosen as the solid material. The properties of the solid material are shown as the following equations (Chai et al., 2019):

$$\rho_{steel} = 8084 - 0.4209T - 3.894 \times 10^{-5}T^2 \tag{4}$$

$$\lambda_{steel} = 9.248 + 0.01571T \tag{5}$$

$$Cp_{steel} = 462 + 0.134T \tag{6}$$

The source term induced by the porous region is:

$$S_i = -\left(\frac{\mu}{\alpha}v_i + C_2\frac{1}{2}\rho|v|v_i\right) \tag{7}$$

where S_i denotes the source term added in the momentum equation, α represents the permeability of the porous region, which is the ability of the medium to allow fluid to pass through, and C_2 is the inertial resistance factor. Besides, the steady-state energy equation inside the porous region can be written as:

$$\nabla \cdot \left[v\left(\rho_f E_f + P\right)\right] = \nabla \cdot \left[k_{\text{eff}}\nabla T - \left(\sum_i h_i J_i\right)\right] \tag{8a}$$

$$k_{eff} = \gamma k_f + (1 - \gamma)k_s \tag{8b}$$

where E_f is the total energy of fluid, k_{eff} represents the effective thermal conductivity, and can be derived as **Eq. 8b**, where k_f and k_s are the thermal conductivities of fluid and solid, respectively, and γ denotes the porosity of the material. In the current problem, the viscous and inertial loss coefficients are derived using the Ergun equation (FLUENT 19.2, 2019):

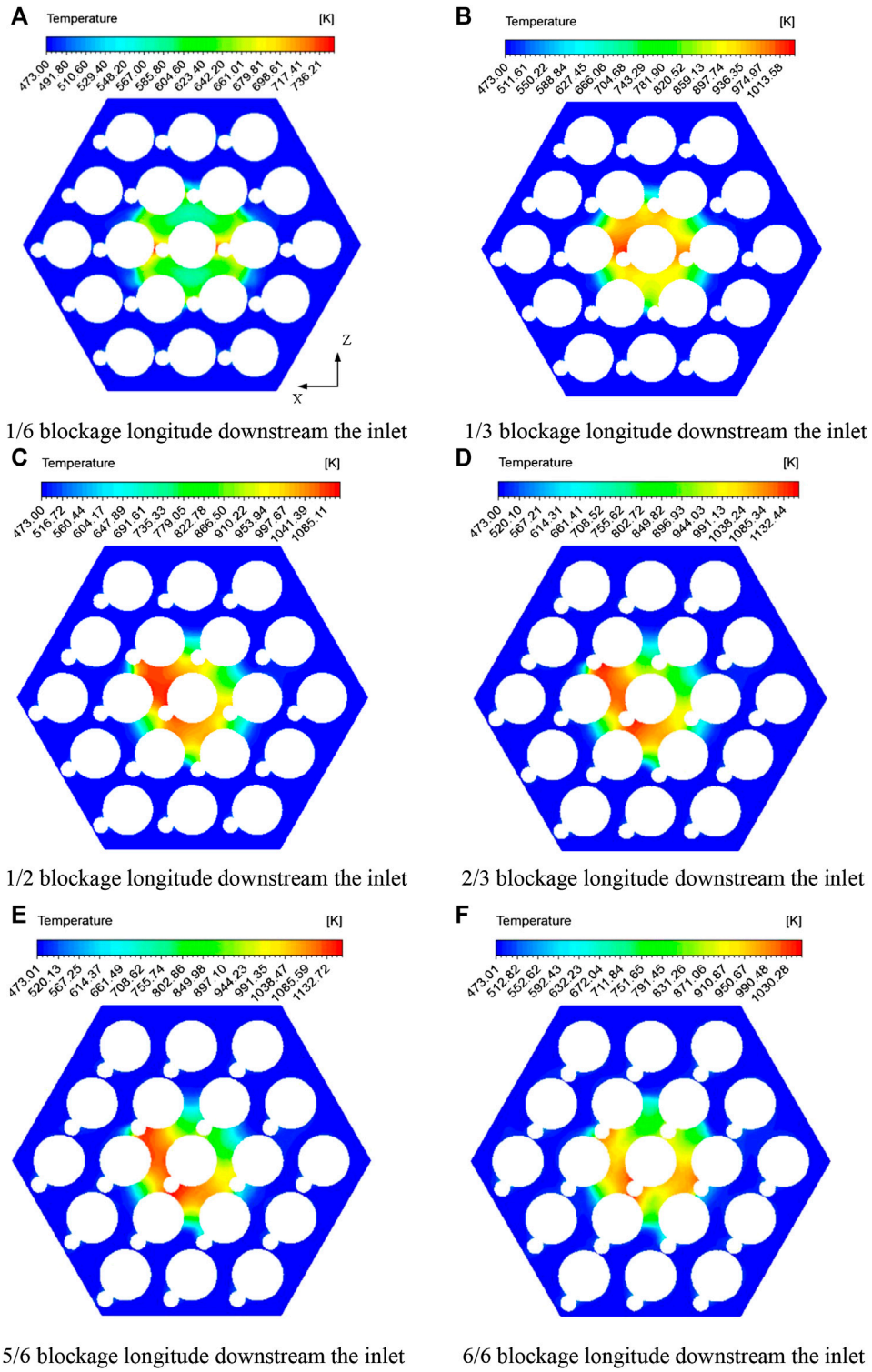

FIGURE 6 | The temperature distributions at six sectional planes in the blocked region. **(A)** 1/6 blockage longitude downstream of the inlet. **(B)** 1/3 blockage longitude downstream of the inlet. **(C)** 1/2 blockage longitude downstream of the inlet. **(D)** 2/3 blockage longitude downstream of the inlet. **(E)** 5/6 blockage longitude downstream of the inlet. **(F)** 6/6 blockage longitude downstream of the inlet.

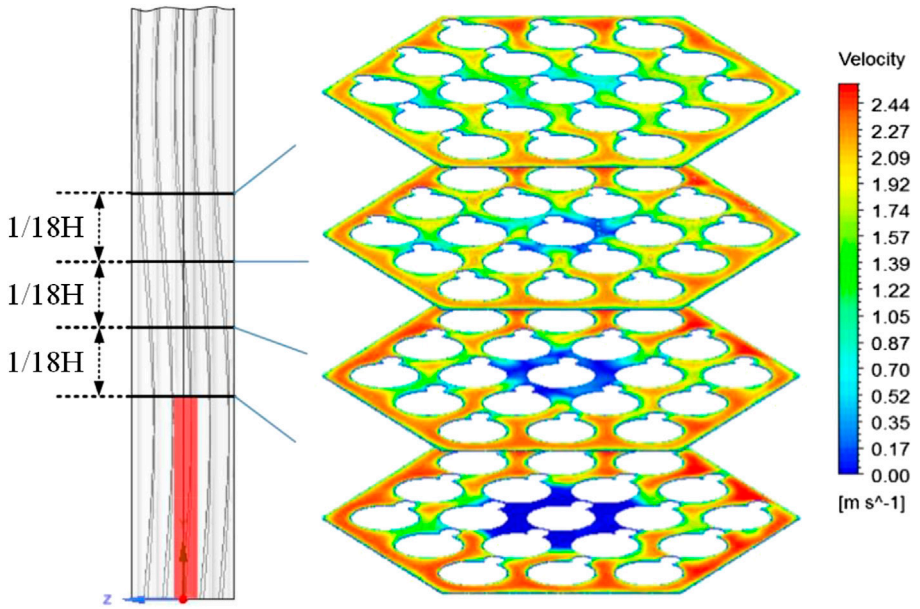

FIGURE 7 | The velocity contours downstream of the blockage.

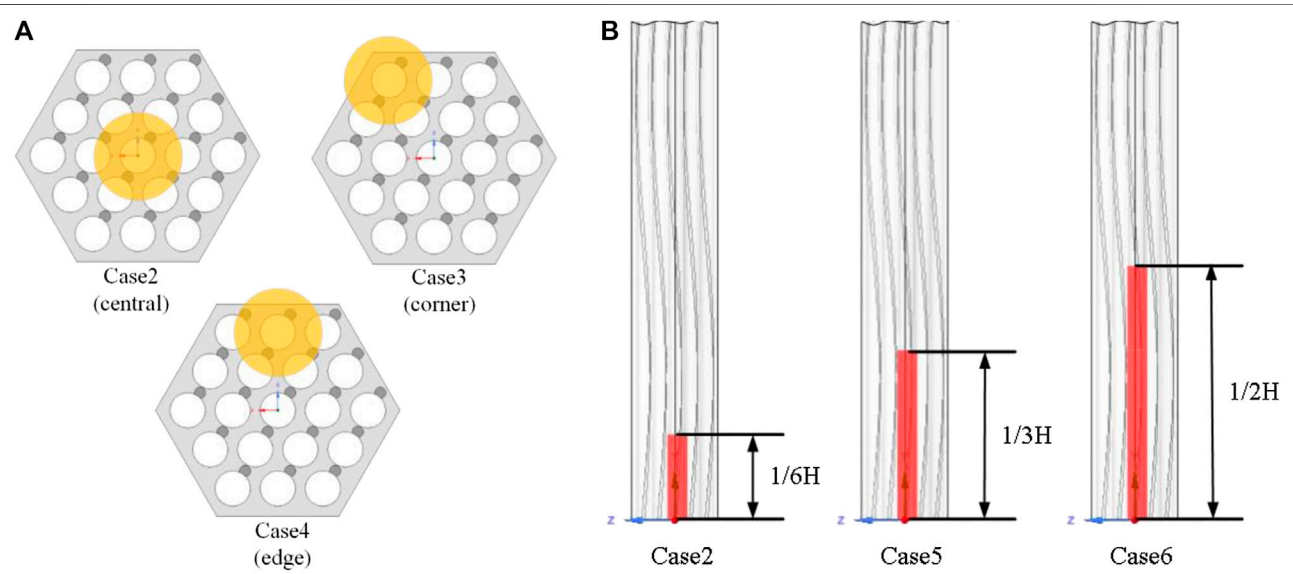

FIGURE 8 | The schematic positions and layouts of the blockages in the six cases. **(A)** Blockages positions in cases 2, 3, and 4. **(B)** Blockage positions in cases 2, 5, and 6.

$$\frac{|\Delta p|}{L} = \frac{150\mu}{D_p^2}\frac{(1-\gamma)^2}{\gamma^3}u_s + \frac{1}{2}\rho\frac{3.5}{D_p}\frac{(1-\gamma)}{\gamma^3}u_s^2 \tag{9}$$

where D_p represents the particle diameter, and u_s is the superficial velocity of fluid. During the calculation, the different flow state in the region can be conveniently established by changing the porosity and the resistance factors.

3. CALCULATION IMPLEMENTATION

3.1. Numeric Methods

In the present study, the steady-state governing equations, including continuum, momentum, and energy equations, are solved in a FLUENT pressure-based solver. In the solver, gradient terms are discretized in the "least square cell based"

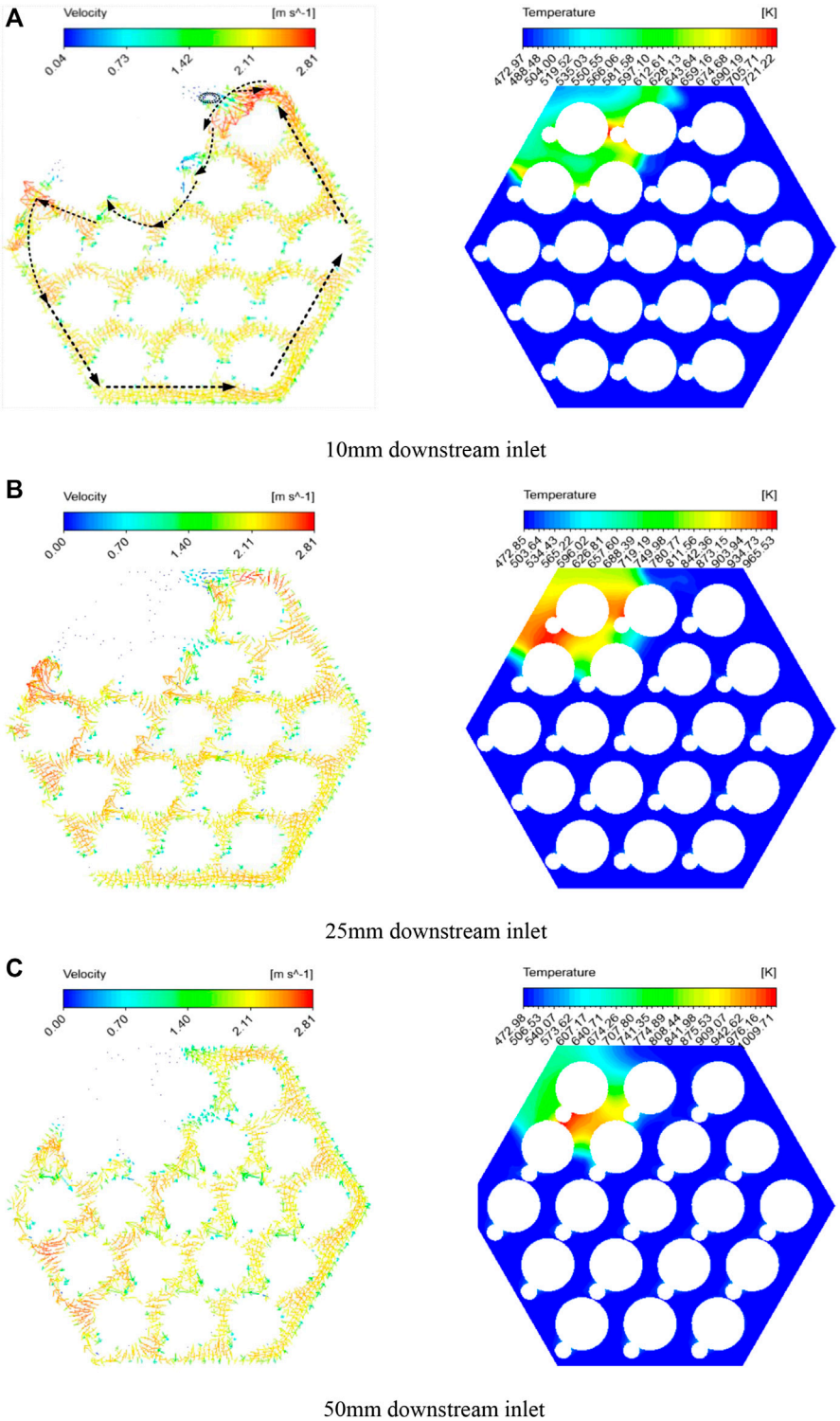

FIGURE 9 | The vector and temperature contours in case 3. **(A)** 10 mm downstream of the inlet. **(B)** 25 mm downstream of the inlet. **(C)** 50 mm downstream of the inlet. **(D)** 25 mm downstream of the blockage. **(E)** 50 mm downstream of the blockage. **(F)** 75 mm downstream of the blockage.

scheme, while convection terms are addressed with a second order upwind scheme. During the calculation, the coupling between the velocity field and the pressure field is achieved by the SIMPLEC algorithm. Simultaneously, when the residuals during the iterative process of solving the equations decays to 10^{-4}, the iteration process is judged to be convergent.

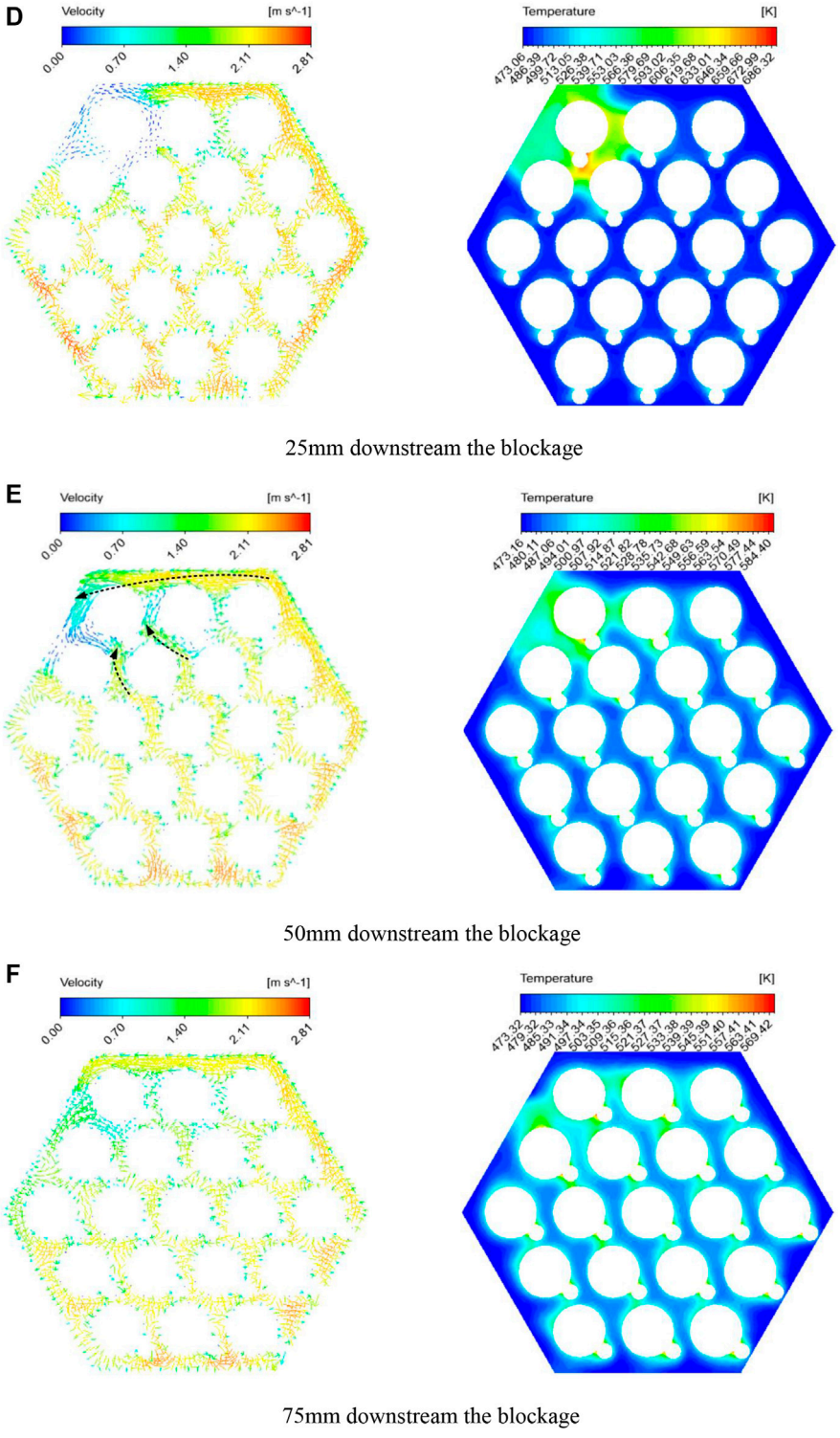

FIGURE 9 | (Continued).

3.2. Properties of LBE

The physical properties of LBE may change significantly in the process of flow and heat transfer. So in the present work, temperature-dependent properties are adopted. They can be presented as the following equations (Kutateladze, 1959; Hultgren, 1973; Lida and Guthrie, 1988; Su et al., 2013):

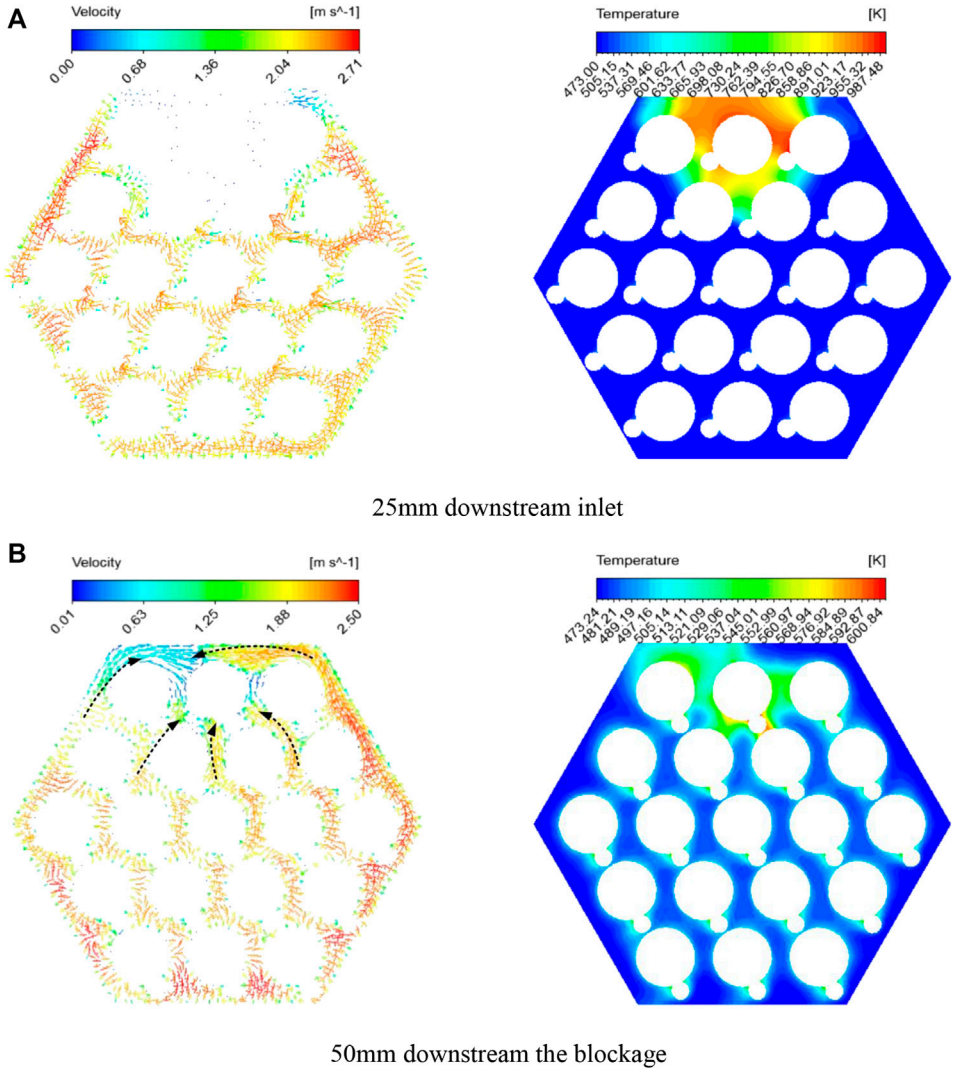

FIGURE 10 | The vector and temperature contours in case 4. **(A)** 25 mm downstream of inlet. **(B)** 50 mm downstream the of blockage.

Density ρ:

$$\rho = 11096 - 1.3236T \tag{10}$$

Thermal capacity Cp:

$$Cp = 159 - 2.72 \times 10^{-2}T + 7.12 \times 10^{-6}T^2 \tag{11}$$

Thermal conductivity λ:

$$\lambda = 3.61 + 1.517 \times 10^{-2}T - 1.741 \times 10^{-6}T^2 \tag{12}$$

Viscosity μ:

$$\mu = 4.94 \times 10^{-4} \exp\left(\frac{754.1}{T}\right) \tag{13}$$

3.3. The Turbulent Heat Transfer Model

The Pr_t of LBE in the energy equation should be treated carefully in this study. The Pr_t of liquid metal is far less than 1.0, which means that the velocity boundary layer is not similar to the thermal boundary layer, so the Reynolds analogy is no longer feasible for liquid metal. For solving this problem, many modifications have been proposed. The Cheng-Tak (Cheng and Tak, 2006) model has a better estimation capacity for the heat transfer characteristics of LBE flow, which are presented as:

$$\mathrm{Pr}_t = \begin{cases} 4.12, & Pe \le 1000 \\ \dfrac{0.01Pe}{[0.08Pe^{0.8} - (7.0 - A)]^{1.25}}, & 1000 < Pe \le 6000 \end{cases} \tag{14}$$

$$A = \begin{cases} 5.4 - 9.0 \times 10^{-4}Pe, & 1000 < Pe \le 2000 \\ 3.6, & 2000 < Pe \le 6000 \end{cases}$$

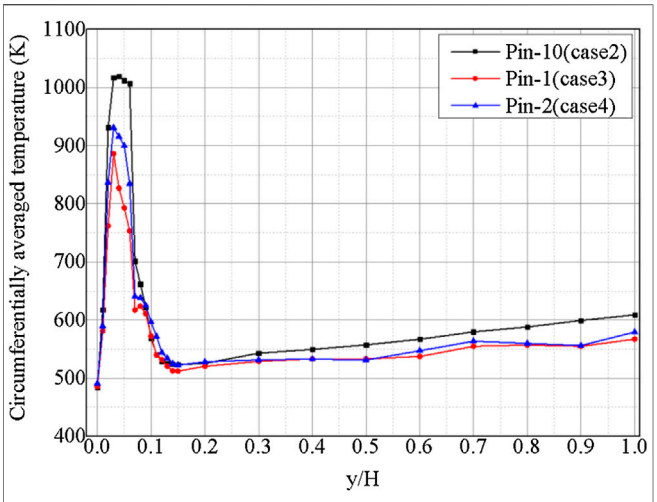

FIGURE 11 | Variation of the circumferentially averaged temperature on pin 1, 2, and 10 along the axial position.

4. VALIDATION

In the present work, the numerical results are validated against the experimental data under the normal operation conditions from experiments conducted by Pacio et al. (Pacio et al., 2016) The validation simulation aims to confirm that the numerical model is correct and can be extensively used in non-normal condition simulations.

Firstly, the local *Nu* at ML3 (Pacio et al., 2016) is evaluated to assess the suitable turbulence models. In the experiment, the variation of *Nu* with the *Pe* ranging from 400 to approximately 1,300 is presented. Comparing with the numerical results estimated by different models, the SST k-ω model predicts the local thermal field much closer to the experimental data. As shown in **Figure 3**, both SST and the Reynolds stress model (RSM) have a relatively high precision prediction of the *Nu*, but with the *Pe* increasing, the RSM is found to underestimate the *Nu* by over 20% (green error bars present the ±20% deviation).

For further validation, the specific coolant temperatures in the sub-channels at ML2 and ML3 (positions are depicted in **Figure 4**) are compared between CFD results and experimental data. As shown in **Figure 5**, the present CFD model can predict the temperature profile in the sub-channels with satisfactory precision, and the errors are less than 3%.

5. RESULTS AND DISCUSSION

In the simulation, various blockage conditions are tested and analyzed, including the influences of blockage longitude, position, and porosity. All the calculated cases are summarized in **Table 4**.

TABLE 5 | The local peak cladding temperature and maximum temperature at the outlet.

Case number	The maximum cladding temperature (K)	The maximum cladding temperature at the outlet (K)
Case 2 (center)	1,174.13	677.525
Case 3 (corner)	1,044.06	672.544
Case 4 (edge)	1,030.24	670.744

5.1. The Flow and Thermal Fields After Inlets Are Partially Blocked

In this section, the flow and heat transfer characteristics under the assembly blockage in the central sub-channels are discussed. After the stainless steel blockage propagates along the axis direction, the thermal hydraulic features inside the assembly change significantly. The coolant is forced to bypass the surrounding channels, so a cylindrical region with high temperature and a wake region downstream of the blockage can be observed. **Figure 6** shows the temperature distribution in the six sectional planes along different axis positions with a 1/6, 1/3, 1/2, 2/3, 5/6, and 6/6 blockage length from the inlet. At the 1/6 blockage length plane (depicted as **Figure 6A**), the temperature is observed to be symmetrical. Because the helical spacer wires contribute to different heat transfer efficiency at different positions of the blockage, a large-scale hot spot appears and extends gradually in the anti-clockwize direction with the flow developing downstream. Specifically, the circumferential velocity of the coolant is induced in the anti-clockwize direction on the depicted plane. Hence at the upwind surface, the coolant floods and cools down the hot rods to a certain extent.

After passing the blockage, the bypassed coolant begins to re-fill the downstream region of the blocked sub-channels. The velocity contours on the four planes downstream of the blockage are shown in **Figure 7**. As the contours illustrate, in a short distance downstream of the blockage, the sub-channels above the blocked region are still in a state of coolant loss, while at position 1/18H (18.2 mm) downstream of the blockage, the re-flood LBE begins to cool down the central pin surrounded by the cylindrical region. Besides, the wake region is filled up circumferentially, and it is nearly fully cooled from plane 1/6H (54.7 mm) downstream of the blockage. Nevertheless, because of the difference in filling velocity from different circumferential bearings, pin 10 (the position shown in **Figure 1**) is still partially exposed to the hot coolant.

5.2. The Influence of the Blockage Position

The effects of a solid blockage (porosity at 0) at different radial positions are studied in this section. A schematic of blockage positions of cases 3 and 4 are shown in **Figure 8A**. More specifically, in case 3, pin 1 (as depicted in **Figure 1**) is surrounded by a solid blockage that has the same length as

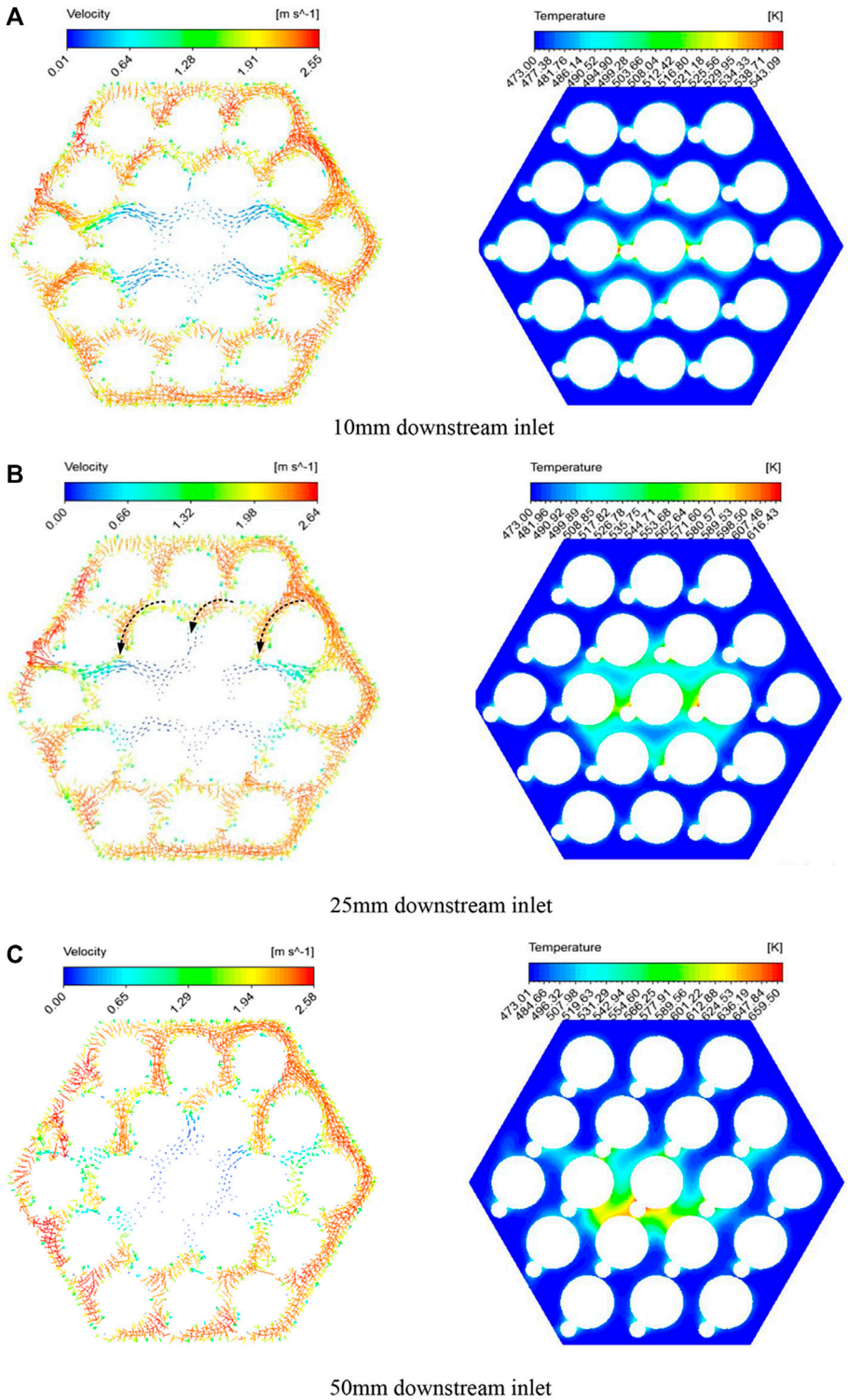

FIGURE 12 | The vector and temperature distributions in case 7. **(A)** 10 mm downstream of the inlet **(B)** 25 mm downstream of the inlet. **(C)** 50 mm downstream of the inlet. **(D)** 25 mm downstream of the blockage. **(E)** 50 mm downstream of the blockage. **(F)** 75 mm downstream of the blockage.

case 2, and the corner channels are blocked. In case 4, the edge channels are blocked and pin two is in the central blockage region.

Considering the blockages at different radial positions, six sectional planes were chosen to depict velocity vectors and temperature distribution. In case 3, after the blocked corner is

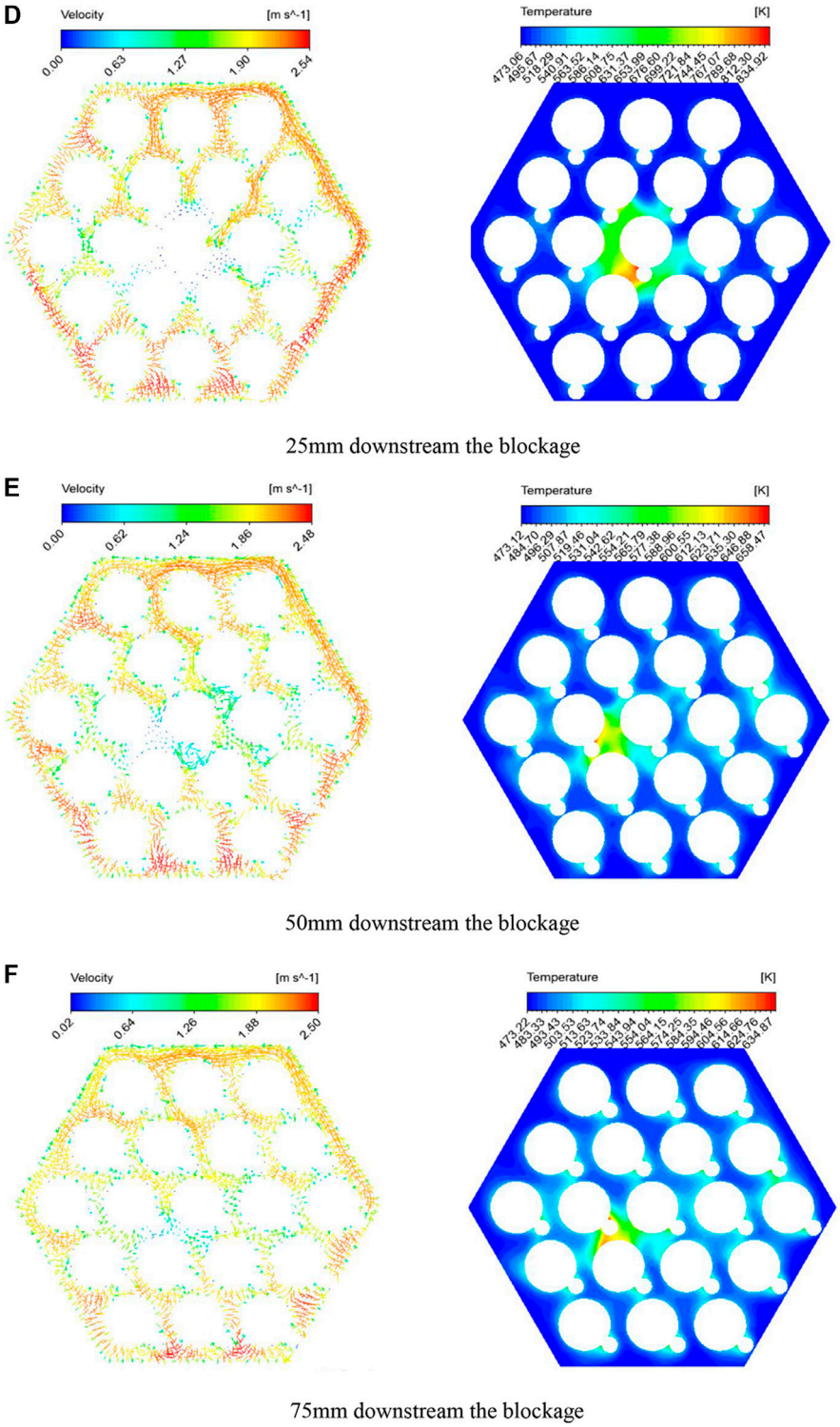

FIGURE 12 | (Continued).

generated, the circumferential flow in the peripheral sub-channels close to the hexagonal wrapper is revealed. The original anti-clockwize flow along the hexagonal wrapper is forced back by impacting the blockage material, and a small scale vortex is formed, shown as the dotted arrow line in **Figure 9A**. Although the blockage region obstructs the

anti-clockwize peripheral flow significantly, the LBE will flow into the nearby channels, and simultaneously, the outer wall of the blockage is flooded and cooled down by the counter-clockwize flowing coolant. Downstream of the blockage, the coolant rapidly fills up the wake region from two different directions. As shown in **Figure 9E**, the coolant from the peripheral channel and central channel flood toward pin 1, which is the centroid of the cylindrical blockage. In addition, unlike the conditions in the central blockage, the hot spot in case 3 seems to be stationary. Because of the assembly wrapper, the coolant is only able to cool down one side of the circular area in an anti-clockwize fashion, hence the hot spot remains in the vicinity of pin 1, as shown in **Figures 9B–E**. Similar flow and temperature fields can also be observed in case 4 with a circular blockage located at the edge (pin two is surrounded fully and some edge sub-channels are covered). As can be seen in **Figure 10B**, the filling flow floods toward the center rod quickly. Because the flooding velocity from the right side is much higher than the other side, asymmetrical cooling is obvious. That is to say, pin two suffers a high temperature difference on the surface of the rod.

From a macroscopic view, blockages in different radial positions have evidential effects on the cladding temperature. The evolution of circumferentially averaged temperature in an individual rod that is surrounded by a blockage (pin one in case 3 and pin two in case 4) varies with the axial position as shown in **Figure 11**. It illustrates that the evolution laws of averaged temperature on different rod surfaces are similar. The average temperatures almost peak at the same height (26.1 mm downstream of the inlet) in all three cases. What is different is the peak temperature value, and in the case with a central blockage, the peak temperature is the largest at approximately 1020 K. Subsequently, the rapid decrease of circumferentially averaged temperature is witnessed. Simultaneously, the average temperatures at the outlet also show discrepancies, and the largest is approximately 610 K in case 2, which is 31 K higher than the value estimated in case 4 (579 K) and 43 K larger than that in case 3 (567 K).

In addition, as summarized in **Table 5**, the effect of a blockage on the local and global cladding temperature is quantitatively analyzed. Firstly, the deviations can be found when considering the local maximum cladding temperature. Specifically, the highest peak temperature of the cladding in the bundle in case 2 is 1,174.13 K due to the peripheral flow. In the central part of the assembly, most of the coolant flows downstream, while the circumferential velocity is relatively low, so the coolant cannot effectively cool down the outer blockage and fulfill the wake region downstream. But when the blockage occupies near the hexagonal wrapper, the peripheral flow dominates. From the view of safety, central blockages can be more dangerous than the other two conditions.

5.3. The Influence of Porosity

Under normal operation conditions, a porous blockage may propagate to occupy sub-channels as the debris accumulates and the coolant can still flow inside the porous region. But the flow and heat transfer characteristics may change considerably. Hence, a central blockage at an inlet with three different porosities were calculated (case 7 with porosity at 0.4, case 8 with porosity at 0.6, and case 9 with porosity at 0.8), as summarized in **Table 4**.

Figure 12 presents the velocity and temperature fields at six sectional planes in case 7. As can be seen in **Figures 12A–C**, although the sub-channels are blocked, a small amount of LBE is still able to contribute to rod cooling. So the temperature distribution at the beginning of the blockage is homogeneous, and the temperature increase in the porous region is less significant than that in the solid cases. In a short distance, at the plane 25 mm downstream of the inlet (nearly half of the whole blockage height), the coolant rapidly floods into the blocked area with an anti-clockwize direction. And downstream of the blockage, the coolant cools the wake region in the same pattern. In addition, the development of the temperature field can be asymmetric, which is similar with the solid case. When the flow develops to the position of 75 mm downstream of the blockage, the wake region is fully cooled by the coolant, and the temperature distribution is observed to be homogeneous, though hot spots are found in the sub-channel among the pins 9, 10, and 14.

The evolution of circumferentially averaged temperature on pin 10 surrounded by materials with different porosities is shown in **Figure 13A**. As the porosity increases, the peak temperature decreases. The peak temperature position moves closer to the outlet when the porosity decreases. Nevertheless, the evolution of the average temperature on the rod surface downstream of the blockage is similar among all four of the different cases. Additionally, the maximum cladding temperatures in the four cases are shown as the line graph in **Figure 13B**. The line graph illustrates that the porosity has an evidential effect on the maximum temperature of the cladding, and the cladding temperature may exceed 1000 K when the porosity is smaller than 0.4. But the influence becomes weaker as the porosity increases.

5.4. The Influence of Blockage Length

In addition to the porosity and blockage position, the blockage longitude also has a significant effect on the thermal-hydraulic behaviors of the LBE inside the blocked assembly. In this part, two more cases (cases 5 and 6) were supplemented and analyzed to summarize the influence of blockages at different longitudes. The blockages in the two cases propagate downstream from the inlet of the heated region to 1/3H and 1/2H, of which the size in the y direction are two and three times as long as that in case 2, respectively. The blockage layout and the scales are shown in **Figure 8B**.

It can be confirmed that prolonging the solid blockage contributes to a longer region with weaker heat transfer between the rods and coolant. **Figure 14** shows variations of circumferentially averaged temperature. In case 2, the circumferentially average temperature of pin 10 increases sharply from 473 K to approximately 1000 K in a short distance (~0.02 L) because of coolant loss. Then the average temperature peaks at approximately 1020 K at 0.04 L

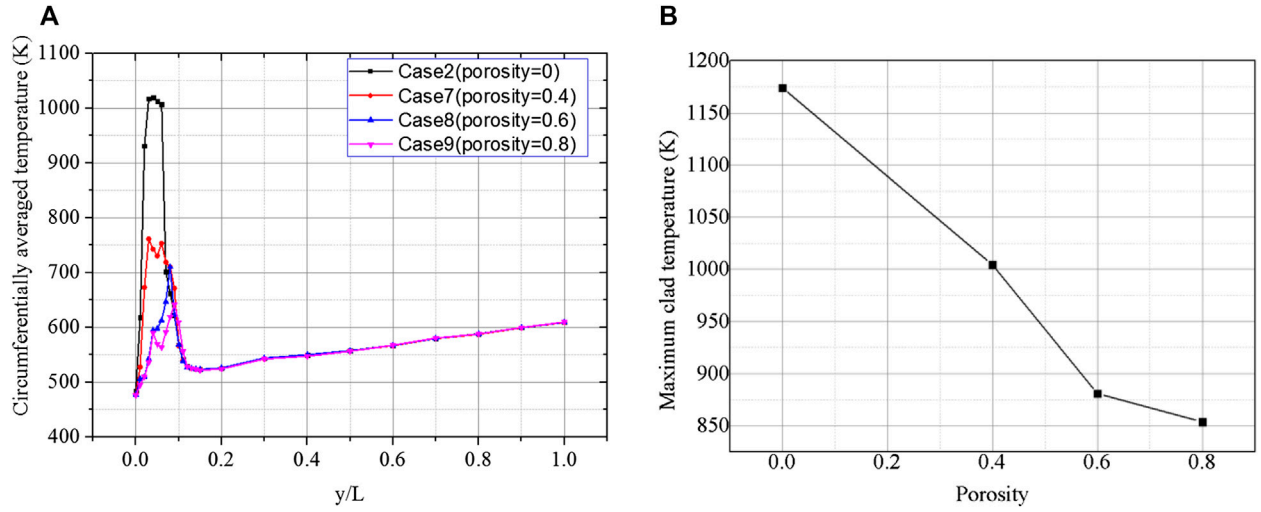

FIGURE 13 | The characteristics of the temperature evolution under a porous blockage with different porosities. **(A)** Circumferentially averaged temperature. **(B)** The maximum cladding temperature.

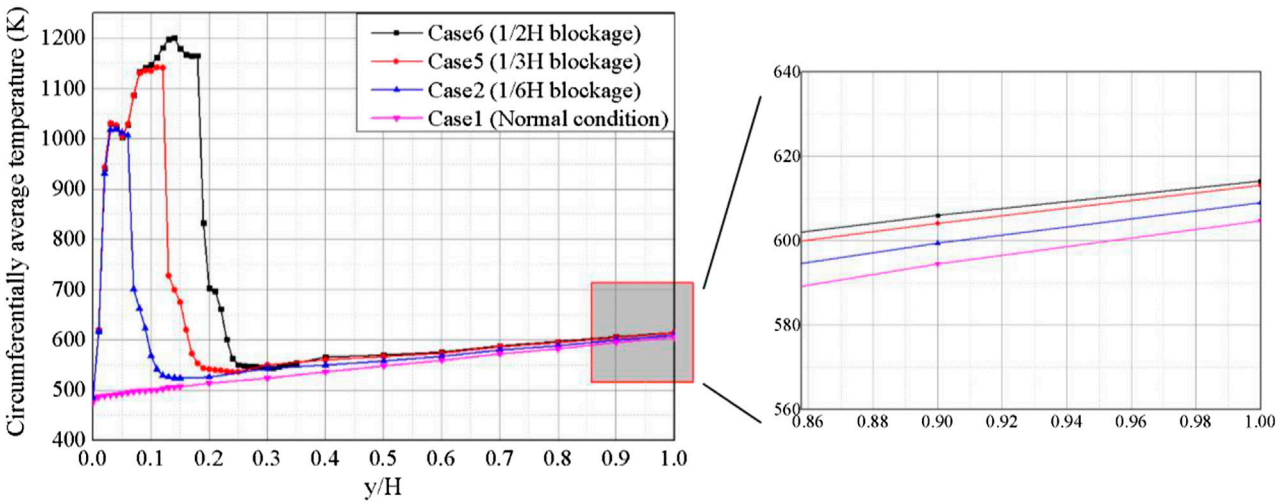

FIGURE 14 | Variations of the circumferentially averaged temperature on pin 10 along the axis direction.

(34.8 mm) downstream of the inlet inside the blocked area. Downstream of the blockage region, the average temperature rapidly decreases due to the reflooding of rod 1. In cases 5 and 6, the blockage length is prolonged by two and three times, respectively. Although the blockage length is different, the variation laws are the same in all three cases, i.e., the wake regions are the same length.

Similarly, the local and global effects of the blockage were also determined. As summarized in **Table 6**, two kinds of maximum cladding temperature are confirmed. With the increase of blockage length, the maximum temperature of cladding is found when the blockage is prolonged three times, and the maximum is 1,351.68 K in case 6. The maximum temperature at the outlet of case 6 is also the highest among the three cases. What is worth mentioning here is that, although the longitude has evidently influenced the local maximum, the influence on the global effect becomes weaker when the blockage is prolonged.

TABLE 6 | The local peak cladding temperature and the maximum temperature at the outlet.

Case number	The maximum local cladding temperature (K)	The maximum cladding temperature at the outlet (K)
Case 2	1,174.13	677.525
Case 5	1,297.78	682.679
Case 6	1,351.68	683.564

6. CONCLUSIONS

In the present work, a CFD model for a 19-pin assembly that is cooled by LBE was established and validated against the experimental data. In the simulation, the Pr_t was modified and various RANS models were assessed for the selection of a proper liquid-metal coolant turbulent heat transfer model. Then the validated numerical models were adopted to investigate the blocked flow inside the assembly. The simulation results suggested that the Cheng-Tak Pr_t model cooperating with the SST k-ω turbulence model were appropriate, and the relative error between the simulation results and experimental data of the *Nu* and coolant temperatures in the sub-channels were less than 20% and 3%, respectively. Then the thermal hydraulic features of the 19-pin assembly under blocked conditions were studied. Some detailed conclusions could be drawn:

(1) Although a wake region downstream of the blockage was observed, the direction effect by wire spacers contributed to rapid re-flooding.
(2) The average cladding temperature exhibited a nearly monotonic variation with the axial position. The effect of a porous blockage was strongly influenced by porosity, and the peak cladding temperature was proportional to the porosity.
(3) From the view of safety, the most dangerous case was when a partially porous blockage was located near the outlet of an active section. What is more, a rapid temperature increase appeared with a decrease in porosity.

DATA AVAILABILITY STATEMENT

The raw data supporting the conclusions of this article will be made available by the authors, without undue reservation.

AUTHOR CONTRIBUTIONS

JL has written and organized the structure of the article, and has performed some of the calculations presented in the article. DF and CG have performed some of the calculations in the article. MW, JD, WT, SQ, and GS give some advice about the article.

FUNDING

This research has been supported by the National Natural Science Foundation of China (Grant No. 11705139) and the National Key Research and Development Program of China (No. 2019YFB1901300).

REFERENCES

Abderrahim, H. A., Kupschus, P., Malambu, E., Benoit, P., Van Tichelen, K., Arien, B., et al. (2001). MYRRHA: a multipurpose accelerator driven system for research & development. *Nucl. Instrum. Methods Phys. Res.* 463 (3), 487–494. doi:10.1016/s0168-9002(01)00164-4

Biarrotte, J. L., Mueller, A. C., Klein, H., Pierini, P., and Vandeplassche, D. (2010). "Accelerator reference design for the MYRRHA European ADS demonstrator," in Proceedings of linear accelerator conference LINAC2010, Tsukuba, Japan, September 12–17, 2010, 440-443. Available at: https://accelconf.web.cern.ch/LINAC2010/papers/tup020.pdf.

Chai, X., Liu, X. J., Xiong, J. B., and Cheng, X. (2019). CFD analysis of flow blockage phenomena in a LBE-cooled 19-pin wire-wrapped rod bundle. *Nucl. Eng. Des.* 344, 107–121. doi:10.1016/j.nucengdes.2019.01.019

Chen, J., Zhang, D. L., Song, P., Wang, X., Wang, S., Liang, Y., et al. (2018). CFD investigation on thermal-hydraulic behaviors of a wire-wrapped fuel subassembly for sodium-cooled fast reactor. *Ann. Nucl. Energy* 113, 256–269. doi:10.1016/j.anucene.2017.11.023

Cheng, X., and Tak, N. (2006). Investigation on turbulent heat transfer to lead–bismuth eutectic flows in circular tubes for nuclear applications. *Nucl. Eng. Des.* 236 (4), 385–393. doi:10.1016/j.nucengdes.2005.09.006

Damiani, L., Prato, A. P., and Revetria, R. (2014). Innovative steam generation system for the secondary loop of 'ALFRED' lead-cooled fast reactor demonstrator. *Appl. Energy* 121, 207–218. doi:10.1016/j.apenergy.2014.02.014

FLUENT 19.2 (2019). FLUENT 19.2 documentation, user's guide manual. Available from: https://www.twirpx.com/file/3179054/.

Frignani, M., Alemberti, A., and Tarantino, M. (2019a). ALFRED: A revised concept to improve pool related thermal-hydraulics. *Nucl. Eng. Des.* 355, 110359. doi:10.1016/j.nucengdes.2019.110359

Frignani, M., Alemberti, A., Tarantino, M., and Grasso, G. (2019b). "ALFRED staged approach," in International congress on advances in nuclear power plants (ICAPP 2019), Juan-les-pins, France, May 12–15, 2019.

Frogheri, M., Alemberti, A., and Mansani, L. (2013). "The lead fast reactor: demonstrator (ALFRED) and ELFR design," in International conference on fast reactors and related fuel cycles: safe technologies and sustainable scenarios, Paris, France, March 4–7, 2013. (International Atomic Energy Agency). Available at: https://www-pub.iaea.org/MTCD/Publications/PDF/Pub1665Vol1Web-68441300.pdf.

Goth, N., Jones, P., Nguyen, D. T., Vaghetto, R., Hassan, Y., Salpeter, N., et al. (2018a). Comparison of experimental and simulation results on interior subchannels of a 61-pin wire-wrapped hexagonal fuel bundle. *Nucl. Eng. Des.* 338, 130–136. doi:10.1016/j.ijheatfluidflow.2018.03.021

Goth, N., Jones, P., Nguyen, T. D., Vaghetto, R., Hassan, Y. A., Obabko, A., et al. (2018b). PTV/PIV measurements of turbulent flows in interior subchannels of a 61-pin wire-wrapped hexagonal fuel bundle. *Int. J. Heat Fluid Flow* 71, 295–304. doi:10.1016/j.nucengdes.2018.08.002

Hultgren, R. R. (1973). *Selected values of the thermodynamic properties of binary alloys*. Metals Park, OH: American Society for Metals. 1435.

Kennedy, G., Tichelen, K., and Doolaard, H. (2015). "Experimental investigation of the pressure loss characteristics of the full-scale MYRRHA fuel bundle in the COMPLOT LBE facility," in NURETH16, Chicago, IL, August 30–September 4, 2015. Available at: http://glc.ans.org/nureth-16/data/papers/13119.pdf.

Kutateladze, S. S. (1959). *Liquid-metal heat transfer media*. New York, NY: Springer. 149.

Lida, T., and Guthrie, R. I. L. (1988). *The physical properties of liquid metals*. Ann Arbor, MI: Oxford University Press.

Merzari, E., Fischer, P., Yuan, H., Van Tichelen, K., Keijers, S., De Ridder, J., et al. (2016). Benchmark exercise for fluid flow simulations in a liquid metal fast reactor fuel assembly. *Nucl. Eng. Des.* 298, 218–228. doi:10.1016/j.nucengdes.2015.11.002

Merzari, E., Pointer, W. D., and Smith, J. G. (2010). "Numerical simulation of the flow in wire-wrapped pin bundles: effect of pin wire contact modeling," in Computational fluid dynamics (CFD) for nuclear reactor safety applications - workshop proceedings, CFD4NRS-3 - experimental validation and application of cfd and cmfd codes to nuclear reactor safety issues. Nuclear Energy Agency of the OECD. 1231. Nuclear Engineering and Design, 2012, 253 (1-4), 374–386.

Nguyen, T., Goth, N., Jones, P., Lee, S., Vaghetto, R., and Hassan, Y. (2017). PIV measurements of turbulent flows in a 61-pin wire-wrapped hexagonal

fuel bundle. *Int. J. Heat Fluid Flow* 65, 47–59. doi:10.1016/j.ijheatfluidflow.2017.03.007

Nguyen, T., Goth, N., Jones, P., Vaghetto, R., and Hassan, Y. (2018). Stereoscopic PIV measurements of near-wall flow in a tightly packed rod bundle with wire spacers. *Exp. Therm. Fluid Sci.* 92, 420–435. doi:10.1016/j.expthermflusci.2017.11.009

Pacio, J., Daubner, M., Fellmoser, F., Litfin, K., Marocco, L., Stieglitz, R., et al. (2014). Heavy-liquid metal heat transfer experiment in a 19-rod bundle with grid spacers. *Nucl. Eng. Des.* 273, 33–46. doi:10.1016/j.nucengdes.2014.02.020

Pacio, J., Daubner, M., Fellmoser, F., Litfin, K., and Wetzel, T. (2016). Experimental study of heavy-liquid metal (LBE) flow and heat transfer along a hexagonal 19-rod bundle with wire spacers. *Nucl. Eng. Des.* 301, 111–127. doi:10.1016/j.nucengdes.2016.03.003

Pacio, J., Daubner, M., Fellmoser, F., Litfin, K., and Wetzel, T. (2018). Heat transfer experiment in a partially (internally) blocked 19-rod bundle with wire spacers cooled by LBE. *Nucl. Eng. Des.* 330, 225–240. doi:10.1016/j.nucengdes.2018.01.034

Pacio, J., Wetzel, T., Doolaard, H., Roelofs, F., and Van Tichelen, K. (2017). Thermal-hydraulic study of the LBE-cooled fuel assembly in the MYRRHA reactor: experiments and simulations. *Nucl. Eng. Des.* 312, 327–337. doi:10.1016/j.nucengdes.2016.08.023

Piazza, I. D., Angelucci, M., Marinari, R., Tarantino, M., and Forgione, N. (2016). Heat transfer on HLM cooled wire-spaced fuel pin bundle simulator in the NACIE-UP facility. *Nucl. Eng. Des.* 300, 256–267. doi:10.1016/j.nucengdes.2016.02.008

Piazza, I. D., Magugliani, F., Tarantino, M., and Alemberti, A. (2014). A CFD analysis of flow blockage phenomena in ALFRED LFR demo fuel assembly. *Nucl. Eng. Des.* 276, 202–215. doi:10.1016/j.nucengdes.2014.05.033

Qin, H., Wang, C., Wang, M., Zhang, D., Tian, W., Su, G. H., et al. (2019). Numerical investigation on thermal-hydraulic characteristics of NaK in a helical wire wrapped annulus. *Int. J. Heat Mass Tran.* 145, 118689. doi:10.1016/j.ijheatmasstransfer.2019.118689

Ranjan, R., Pantano, C., and Fischer, P. (2010). Direct simulation of turbulent swept flow over a wire in a channel. *J. Fluid Mech.* 651, 165. doi:10.1017/s0022112009993958

Rasu, N. G., Velusamy, K., Sundararajan, T., and Chellapandi, P. (2014). Thermal hydraulic effect of porous blockage in fuel subassembly of sodium cooled fast reactor. *Ann. Nucl. Energy* 70, 64–81. doi:10.1016/j.anucene.2014.01.045

Roache, P. J. (1994). Perspective: a method for uniform reporting of grid refinement studies. *J. Fluid Eng.* 116, 405–413. doi:10.1115/1.2910291

Roache, P. J. (1997). Quantification of uncertainty in computational fluid dynamics. *Annu. Rev. Fluid Mech.* 29, 123–160. doi:10.1146/annurev.fluid.29.1.123

Roelofs, F., Gerschenfeld, A., and Tarantino, M. (2019a). *Thermal-hydraulic aspects of liquid-metal-cooled reactors*. Cambridge, MA: Elsevier Science. 462.

Roelofs, F., Uitslag-Doolaard, H., Dovizio, D., Mikuz, B., Shams, A., Bertocchi, F., et al. (2019b). Towards validated prediction with RANS CFD of flow and heat transport in a wire-wrap fuel assembly. *Nucl. Eng. Des.* 353, 110273. doi:10.1016/j.nucengdes.2019.110273

Sarkar, M., Velusamy, K., Munshi, P., and Singh, O. P. (2019). Thermal hydraulic investigation of heat transfer from a completely blocked fuel subassembly of SFR. *Ann. Nucl. Energy* 130, 131–141. doi:10.1016/j.anucene.2019.02.030

Sarkar, M., Velusamy, K., Munshi, P., and Singh, O. P. (2020). Analysis of flow and heat transfer through a partially blocked fuel subassembly of fast breeder reactor. *Prog. Nucl. Energy* 118, 103142. doi:10.1016/j.pnucene.2019.103142

Su, Z. W., Zhou, T., and Liu, M. Y. (2013). Thermophysical properties of liquid lead-bismuth eutectic. *Nucl. Technol.* 36 (9): 90205–91806.

Wang, M. J., Chen, J., Zhang, D. L., Zhang, J., Tian, W., Su, G. H., et al. (2020). Numerical study on the thermal stratification characteristics in the upper plenum of sodium-cooled fast reactor (SFR). *Ann. Nucl. Energy* 138, 107222. doi:10.1016/j.anucene.2019.107222

Wang, M. J., Manera, A., Petrov, V., Qiu, S., Tian, W., and Su, G. H. (2018). Numerical study of integral inherently safe light water reactor in case of inadvertent DHR operation based on the multiscale method. *Nucl. Technol.* 203 (2), 194–204. doi:10.1080/00295450.2018.1446656

Wang, M. J., Manera, A., Petrov, V., Memmott, M. J., Qiu, S., and Su, G. H. (2019a). Passive decay heat removal system design for the integral inherent safety light water reactor (I2S-LWR). *Ann. Nucl. Energy* 145, 106987. doi:10.1016/j.anucene.2019.106987

Wang, X. A., Zhang, D. L., Wang, M. J., Song, P., Wang, S., Liang, Y., et al. (2019b). Hybrid medium model for conjugate heat transfer modeling in the core of sodium-cooled fast reactor. *Nucl. Eng. Tech.* 52, 708–720. doi:10.1016/j.net.2019.09.009

Wu, Y. C. (2016a). CLEAR-S: an integrated non-nuclear test facility for China lead-based research reactor. *Int. J. Energy Res.* 40 (14), 1951–1956. doi:10.1002/er.3569

Wu, Y. C. (2016b). Design and R&D progress of China lead-based reactor for ADS research facility. *Engineering* 2 (1), 124–131. doi:10.1016/j.eng.2016.01.023

Yu, Y., Merzari, E., Obabko, A., and Thomas, J. (2015). A porous medium model for predicting the duct wall temperature of sodium fast reactor fuel assembly. *Nucl. Eng. Des.* 295, 48–58. doi:10.1016/j.nucengdes.2015.09.020

Zhang, Y., Wang, C. L., Lan, Z. K., Wei, S., Chen, R., Tian, W., et al. (2020). Review of thermal-hydraulic issues and studies of lead-based fast reactors. *Renew. Sustain. Energy Rev.* 120, 109625. doi:10.1016/j.rser.2019.109625

Zrodnikov, A. V., Toshinsky, G. I., Komlev, O. G., Stepanov, V. S., and Klimov, N. N. (2011). SVBR-100 module-type fast reactor of the IV generation for regional power industry. *J. Nucl. Mater.* 415 (3), 237–244. doi:10.1016/j.jnucmat.2011.04.038

Conflict of Interest: The authors declare that the research was conducted in the absence of any commercial or financial relationships that could be construed as a potential conflict of interest.

GLOSSARY

CFD Computational fluid dynamics

Cp Thermal capacity of LBE

Cpsteel Thermal capacity of stainless steel

FA Fuel assembly

GEN-IV Generation IV

GCI Grid convergence index

IWF Inter-wrapper flow

LBE Lead-bismuth eutectic

LFR Lead-cooled fast reactor

LMFR Liquid metal fast reactor

RANS Reynolds averaged Navier-Stokes equations

RSM Reynolds stress model

SFR Sodium-cooled fast reactor

Si Source term in momentum equation

T-H Thermal hydraulic

TIB Total instantaneous blockage

U′ Component of fluctuating velocity

vi Component of velocity

|v| Velocity magnitude

ρ Density of LBE

λ Thermal conductivity of LBE

μ Viscosity of LBE (Pas)

ρsteel Density of stainless steel

λ Thermal conductivity of stainless steel

frontiers in Energy Research

ORIGINAL RESEARCH
published: 22 January 2021
doi: 10.3389/fenrg.2020.526035

Interface Tracking Simulation for Subcooled Flow Boiling Using VOSET Method

Kong Ling[1,2]*, *Shuai Zhang*[1,2], *Wenxing Liu*[3], *Xiaowei Sui*[4] *and Wenquan Tao*[1]

[1]Key Laboratory of Thermo-Fluid Science and Engineering of MOE, Xi'an Jiaotong University, Xi'an, China, [2]Xi'an ShuFeng Technological Information, Ltd., Xi'an, China, [3]CNNC Key Laboratory on Nuclear Reactor Thermal Hydraulics Technology, Nuclear Power Institute of China, Chengdu, China, [4]National Institute Corporation of Additive Manufacturing, Xi'an, China

This article presents a numerical simulation on subcooled flow boiling at a high-pressure condition. An interface tracking method, VOSET, was used to handle the moving interface, and conjugate heat transfer between the wall and the fluid was included in the numerical model. In order to consider the evaporation on the microlayer below a growing bubble, a depletable micorlayer model was employed. Our simulation illustrated typical processes of subcooled boiling flow including bubble sliding, coalescence, detachment and annihilation, and revealed many mechanisms in increasing the heat transfer coefficient. A transition in flow regime from isolated bubbly flow to elongated bubbly flow was reproduced by our simulations. The void fraction obtained by time-averaging the volume fraction of the vapor phase under various flow conditions was analyzed.

Keywords: subcooled boiling flow, wall heat flux, void fraction, interface tracking, volume of fluid and level set

OPEN ACCESS

Edited by:
Nejdet Erkan,
The University of Tokyo, Japan

Reviewed by:
Ivo Kljenak,
Institut Jožef Stefan (IJS), Slovenia
Deqi Chen,
Chongqing University, China
Yohei Sato,
Paul Scherrer Institut (PSI), Switzerland

***Correspondence:**
Ling Kong
lingkongcs@mail.xjtu.edu.cn

Specialty section:
This article was submitted to Nuclear Energy, a section of the journal Frontiers in Energy Research

Received: *11 January 2020*
Accepted: *28 October 2020*
Published: *22 January 2021*

Citation:
Ling K, Zhang S, Liu W, Sui X and Tao W (2021) Interface Tracking Simulation for Subcooled Flow Boiling Using VOSET Method. Front. Energy Res. 8:526035. doi: 10.3389/fenrg.2020.526035

INTRODUCTION

Subcooled flow boiling has been known as an effective way of heat transfer between coolant and heating wall. It is a kind of complex process with evaporation and condensation occurring simultaneously. At a specific system pressure, the coolant flows at a temperature lower than the corresponding saturation point. The heat flux imposed on the wall produces a thermal layer around it in which bubbles may nucleate and grow. However, condensation occurs as a bubble migrates into the bulk liquid region with temperature under saturation point. Subcooled flow boiling can produce much higher heat transfer coefficient than single phase flows, which makes it playing an important role in the heat transfer process in the core of pressurized water reactor.

A considerable number of experiments have been conducted on subcooled flow boiling. Pradanovic et al. (2002) carried out a study on the size and lifetime of bubbles in subcooled flow boiling and analyzed the influences by the applied heat flux, the degree of subcooling, the mass flow rate and the system pressure. It was found by Okawa et al. (2018) that bubbles were accelerated to enter the bulk region after departing from the wall. Yuan et al. (2018) carried out a visualization experiment on subcooled flow boiling under various system pressures and found that, sliding bubbles on the heating surface grew faster than stationary ones. A flow boiling experiment in rectangular channel was performed by Kim et al. (2018), who suggested, as the wall heat flux increases, the flow regime transforms progressively from isolated bubbly flow to elongating bubbly flow. Recently, Lee Y. G. et al., 2019) carried out an experimental investigation to measure the local bubble parameters for subcooled boiling flow in a vertical tube at low pressure. By using optical fiber probes, Park et al. (2020) then measured the local distribution of void fraction and demonstrated its influences by flow conditions.

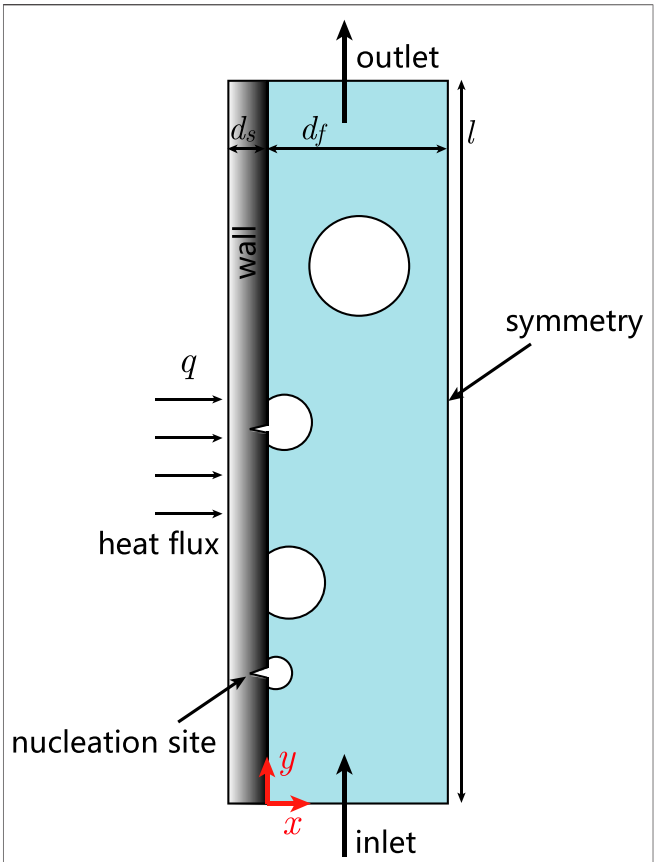

FIGURE 1 | The subcooled flow boiling problem and applied boundary conditions.

Taking advantage from the fast development of computers' performance, computational fluid dynamics (CFD) has become an effective way for the study on multiphase flows. Various numerical methods have been developed for liquid-gas two phase flows. Among those methods, interface tracing method (ITM) such as volume of fluid (VOF) and level set (LS) is one class describing the interface between liquid and gas phases and tracking its movement with the fluid flow. Therefore, ITM method gives results with higher fidelity than other methods such as mixture model and two-fluid model, and can therefore provide more details for studying the mechanism of boiling flows.

Lal et al. (2015) simulated the growth and departure of a single bubble in a subcooled boiling flow. Using VOF method, Lee J. et al. (2019) simulated subcooled boiling flow of FC-72 and numerically predicted the heat transfer coefficient under different heat fluxes and mass flow rates. Yi et al. (2019) numerically studied the growth of a single bubble in subcooled liquid under microgravity, in which phase field method was used for handling the phase boundary. Their results show that, under specific conditions, evaporation and condensation in the bubble can reach balance.

In the present study, VOSET (Sun and Tao, 2010), a new ITM method, was adopted to study a subcooled flow boiling process, and the conjugation with heat conduction in the solid wall was taken into consideration. To fully describe the processes of bubble nucleation and its growth on the wall, models were introduced for bubble nucleation and microlayer evaporation.

The rest of this article is organized as follows. *Problem Description* introduces the subcooled flow boiling problem studied. *Numerical Methods* describes the governing equations and numerical methods. The numerical results are displayed and discussed in *Results and Discussion*; and finally some conclusions are summarized in *Discussion*. The purpose of the present study is to reveal more details in the process of subcooled flow boiling at high-pressure conditions by means of high fidelity numerical simulations.

PROBLEM DESCRIPTION

Figure 1 describes the problem considered in the present study. The computational domain is composed of solid and fluid regions, in which heat conduction in solid and boiling heat transfer were considered simultaneously. The monocrystal silicon and water at 1.0 MPa were respectively considered as the materials of the solid and the fluid. Physical properties including density, viscosity, thermal conductivity and heat capacity are summarized in **Table 1**. At the considered system pressure, saturation temperature is 453 K, and the latent heat is 2.02×10^6 J/kg. The liquid-vapor surface tension was specified as 0.042 N/m. The channel has a width of $d_f = 5$ mm and a length of $l = 50$ mm in the flow direction; a thickness of $d_s = 0.5$ mm was specified for the solid wall. Liquid water having a subcooling of 20 K flows in from the bottom boundary with a velocity of 0.1 m/s (corresponding to a mass flow rate of 88.81 kg/m^{2}s). The selected channel has no significant difference with the one in real rod buddle in terms of hydraulic diameter. Since pressurized water reactor usually works at pressure about 7–8 MPa, simulation should be done at some high pressure. And the pressure of 1 MPa is adopted here. It is our understanding that the interface tracking algorithms, such as VOF, Level set and VOSET, suffer from poor stability at large density difference between the liquid and the vapor phases. Hence if our method can get converged solution at 1 MPa, then it is easier to handle boiling simulations at higher pressure, except for the need of finer mesh for smaller departure diameter (Sakashita, 2011). That is why we select 1 MPa as the simulation condition. (Corresponding to Comment 1 by Reviewer #4); A wall heat flux was specified on the left boundary of the solid wall; symmetry condition was given on the right boundary of the fluid region. Uniform grids of 10×500 and 50×500 were respectively used for the domain discretizations of the solid and the fluid regions. In the present

TABLE 1 | Physical properties of the solid wall and the working fluid.

	Solid wall	Liquid	Vapor
Density (kg·m^{-3})	2,330	888.1	5.14
Viscosity (Pa·s)	—	1.51×10^{-4}	1.5×10^{-5}
Thermal conductivity (W·m^{-1}·K^{-1})	148	0.674	0.036
Heat capacity (J·kg^{-1}·K^{-1})	766	4,400	2,712

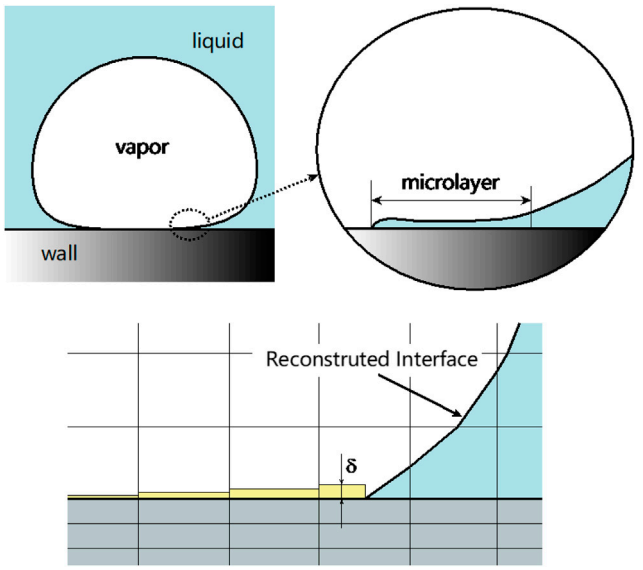

FIGURE 2 | A depletable microlayer model used.

study, numerical investigation for the boiling flow was investigated on wall heat fluxes ranging from 100 kW/m^2 to 500 kW/m^2.

NUMERICAL METHODS

Governing equations

In the solid region, heat conduction is considered only, therefore, the temperature field satisfies

$$\frac{\partial\left(\rho c_{p,s}T\right)}{\partial t} = \nabla\cdot\left(\lambda_s\nabla T\right) \tag{1}$$

In the fluid region, the governing equation for temperature can be expressed as:

$$\frac{\partial\left(\rho c_p T\right)}{\partial t} + \nabla\cdot\left(\rho c_p \boldsymbol{u} T\right) = \nabla\cdot\left(\lambda\nabla T\right) \tag{2}$$

Considering the movement of the liquid-vapor phase boundary and the evaporation occurring on it, the equation for the vapor volume fraction, the continuity equation and the momentum equation can be respectively expressed as:

$$\frac{\partial c}{\partial t} + \nabla\cdot\left(\boldsymbol{u}c\right) = \frac{1}{\rho_v}\dot{m} \tag{3}$$

$$\nabla\cdot\boldsymbol{u} = \left(\frac{1}{\rho_v} - \frac{1}{\rho_l}\right)\dot{m} \tag{4}$$

$$\frac{\partial\left(\rho\boldsymbol{u}\right)}{\partial t} + \nabla\cdot\left(\rho\boldsymbol{u}\boldsymbol{u}\right) = -\nabla p + \nabla\cdot\left(\eta\nabla\boldsymbol{u} + \eta\nabla\boldsymbol{u}^T\right) + \boldsymbol{f}_{\mathrm{st}} + \rho\boldsymbol{g} \tag{5}$$

In **Eqs 3–5**, c is the volume fraction of the vapor phase, and $\boldsymbol{f}_{\mathrm{st}}$ denotes the surface tension. $\dot{m}$ represents the rate of phase change. Considering a control volume, denoted by V, and the liquid-vapor interface inside it, denoted by Γ, it satisfies:

$$\int_V \dot{m}\mathrm{d}V = \frac{1}{h_{lv}}\int_\Gamma \dot{q}\mathrm{d}A \tag{6}$$

in which $\dot{q} = \dot{q}_{\mathrm{macro}} + \dot{q}_{\mathrm{micro}}$ is the heat flux on the phase boundary. $\dot{q}_{\mathrm{macro}}$ was calculated from the temperature gradients on the two sides of the phase boundary, and the detailed calculation approach is described in Ling et al. (2015b). $\dot{q}_{\mathrm{micro}}$ is the heat flux contributed by microlayer evaporation which was calculated by the adopted microlayer model.

Microlayer Model

The existence of microlayer has been confirmed in many previous studies (Cooper and Lloyd, 1969; Koffman and Plesset, 1983; Utaka et al., 2013). As shown in **Figure 2**, beneath a growing bubble on the heating wall, there exists a thin liquid film usually having only several microns. The large temperature gradient in the microlayer can produce great amount of evaporation rate, which takes an important portion of the overall mass transfer rate. Since the film thickness is much smaller than the grid size used in the present study, it was solved by a depletable model form microlayer proposed by Sato and Niceno (2015). As **Figure 2** shows, in the present study, we considered the microlayer evaporation in the fluid-region cells near the wall. As receding occurred at the contact line, an initial thickness was given for the microlayer.

The heat flux through the microlayer was calculated as:

$$\dot{q}_{\mathrm{micro}} = \lambda_l\frac{T_w - T_{lv}}{\delta} \tag{7}$$

The microlayer thickness decreases due to the evaporation, and therefore,

$$\frac{d\delta}{dt} = -\frac{\dot{q}_{\mathrm{micro}}}{\rho_l h_{lv}} \tag{8}$$

As the microlayer thickness was reduced down to a threshold ($\delta < \delta_{\min} = 10^{-10}$ m), the computational cell was then marked to be dry out, and microlayer is no longer considered there.

The initial thickness of the microlayer plays an important role in microlayer evaporation, However, there remains great uncertainty in experimental measurements. Recent experimental studies (Jung and Kim, 2014; Chen et al., 2020) suggests, the microlayer thickness of water varies from around 1–4 μm at low-pressure conditions under various heat fluxes. Urbano et al. (2018) performed a direct numerical simulation, where a small enough grid size, 0.5 μm, was used to capture the formation of the microlayer. The numerically obtained microlayer thickness varies between 2 and 3 μm, which is consistent with the experiments. Unfortunately, at the best knowledge of the authors, no experimental result is reported for microlayer thickness at high pressures such as 1 MPa. The parametric study by Urbano et al. (2018) suggests that the formation of microlayer results form a balance between the bubble growth rate, the capillary actions and liquid viscous

TABLE 2 | Locations of nucleation sites and required superheat.

No.	Location	Required superheat (K)
1	y = 5 mm	5.00
2	y = 7 mm	11.18
3	y = 15 mm	17.32
4	y = 17 mm	20.00
5	y = 20 mm	13.23
6	y = 22 mm	7.07
7	y = 25 mm	14.14
8	y = 27 mm	15.00
9	y = 30 mm	18.03
10	y = 32 mm	10.00
11	y = 35 mm	15.81
12	y = 37 mm	8.66
13	y = 40 mm	19.36
14	y = 42 mm	12.25
15	y = 45 mm	16.58

dissipation. Owing to the large difference in vapor density, the bubble growth rate at high-pressure conditions may differ greatly from that at atmosphere pressure. Therefore, the microlayer thickness as well as whether or not the microlayer can form are unclear for system pressure and wall heat fluxes studied at present paper. As a first attempt using microlayer model for subcooled boiling flow at high-pressure conditions, we followed the existing experimental measurements at atmosphere pressure, and specified the initial microlayer thickness as $\delta_{initial}$ = 2 μm in the present study. The influence by the parameters in the microlayer model is left as one of our future work.

(Corresponding to Comment **2** by Reviewer #4)

Bubble Nucleation Model

Bubble nucleation usually occurs at on the cavity on the solid surface, and the conditions required for the nucleation depends on the microstructure of the solid surface (Hibiki and Ishii, 2003). Since the CFD method used in the present study is based on continuum assumption, it cannot model the process of the bubble nucleation which may need to be considered from the perspective of molecular dynamics. To simulate the process of bubble growth using ITM, therefore, bubble seeds need to be given in prior. In this regard, we followed the nucleation model used by Sato and Niceno (2017). They randomly set a number of nucleation sites on the solid wall, and each of them has a certain nucleation activation temperature. In the present study, we specified 15 nucleation sites on the wall in the range y = 5–45 mm, and each of them corresponds to a specific nucleation superheat ranging from 5 to 20 K. In this model, a bubble seed can be generated only at the preset nucleation site, and it requires the liquid temperature exceeds the preset superheat. The locations and the required nucleation superheats are summarized in **Table 2**. It should to be noted that, since the microstructure of the solid surface cannot be fully considered in the present CFD study, the nucleation model is simply a description for the solid surface in terms of bubble nucleation. A different wall roughness usually requires another set of nucleation sites as well as another range of activation temperature.

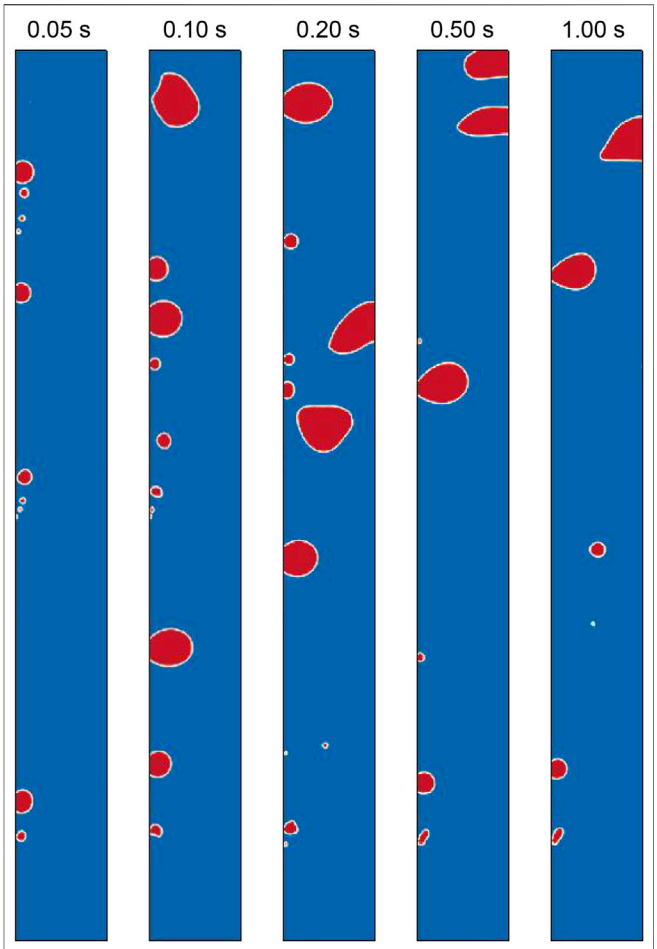

FIGURE 3 | Evolution of phase distribution at low heat flux (q = 100 W/m^2).

RESULTS AND DISCUSSION

Subcooled Flow Boiling at Low Heat Flux

We first considered the subcooled flow boiling with the lowest wall heat flux of 100 kW/m^2 and simulated the boiling process within 1.0 s. **Figure 3** illustrates the evolution of phase distribution. From the figure at t = 0.05 one can see that bubbles continuously formed, grew and moved upwards at nucleation sites #1, #6 and #12, which indicates those sites were activated. It lies in that the preset nucleation superheats at those three sites were lower than the initial wall superheat (ΔT = 9 K). With the further progress of boiling heat transfer, the wall temperature was decreases, and bubbles nucleation occurred only at site #1. The numerical result suggested several ways of bubble departure from the heating wall. As a sliding bubble grew to a certain size, it departed from the wall and moved into the bulk region. Simultaneously, some smaller bubbles could depart due to the oscillation induced by coalescences. Overall, at the wall heat flux of 100 kW/m^2, the subcooled boiling flow is located in a typical flow regime of isolated bubbly flow.

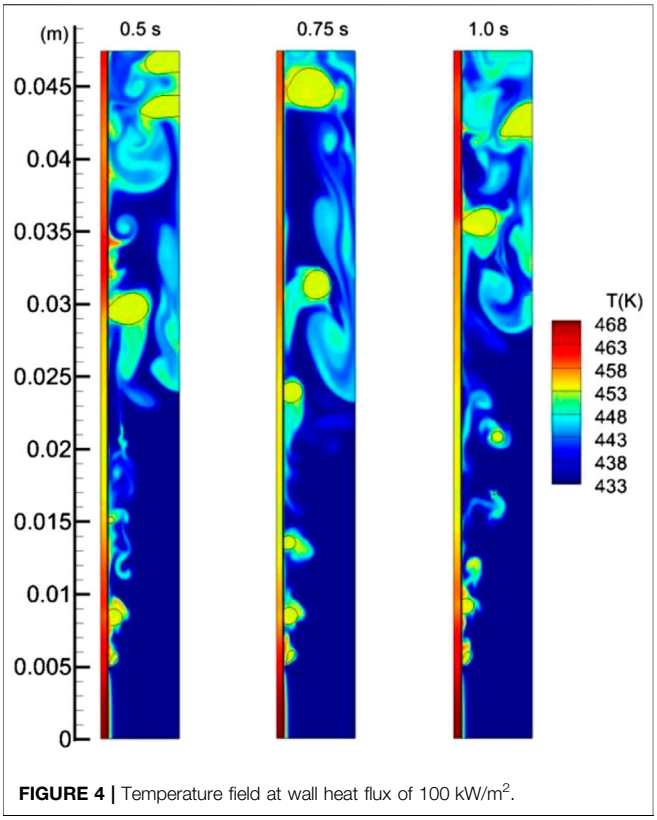

FIGURE 4 | Temperature field at wall heat flux of 100 kW/m^2.

Figure 4 shows the temperature fields at some instances between 0.5 and 1.0 s, in which the boundary between the solid and the fluid regions is marked as a solid black line. We can clearly see the influences of the bubbles to the heat transfer process. The bubble induced turbulence greatly enhanced the fluid mixing between the near wall region and the subcooled bulk region. As a result, the solid temperature in boiling region (y > 5 mm) is evidently lower than that in single-phase region (y < 5 mm).

Yuan et al. (2018) pointed out important influences by sliding bubbles in subcooled flow boiling. **Figure 5** shows a bubble sliding on the wall, where the velocity and temperature fields around it are displayed. From the velocity field inside the bubble we can see the effect of the microlayer located at around 12 mm < y < 12.4 mm. Some vapor was produced by the microlayer evaporation, which contributed to the bubble growth. The wall temperature was plotted as **Figure 5C**, from which we can see the lowest temperature was located at the microlayer (around y = 12.2 mm). Furthermore, the wall temperature downstream the bubble was remarkably lower than that upstream. In summary, we can find the important influence of a sliding bubble. In the process of a single bubble along the wall, a bubble can continuously reduce the temperature of the solid, and absorb heat from the wall to support its growth.

Figure 6 tracks a small bubble (marked by an arrow) after its departure from the wall. In spite of the boiling process around the heating wall, the liquid in the bulk region remained subcooled. As the bubble entered the bulk region, the condensation rate began to be greater than the evaporation rate, which made bubble reduced in size until eliminated.

Subcooled Flow Boiling at Higher Heat Fluxes

The results for higher heat fluxes are presented in this subsection. **Figures 7**, **8** respectively show the evolutions of phase distribution at wall heat fluxes of 300 and 500 kW/m^2. Compared with **Figure 3**, we can find some features of increased wall heat flux. Owing to the increased wall temperature, more nucleation sites were activated, and the bubble growth rate was increased. Interaction between vapor bubbles became more intensive. Some rising bubbles could absorb smaller bubbles to get larger. Under the wall heat flux of 300 kW/m^2, the bubble size at the bulk region got remarkably larger, but the flow regime seems remained in the isolated bubbly flow (**Figure 6**). At wall heat flux of q = 500 kW/m^2, due to the more frequent coalescences of vapor bubbles, the two-phase flow

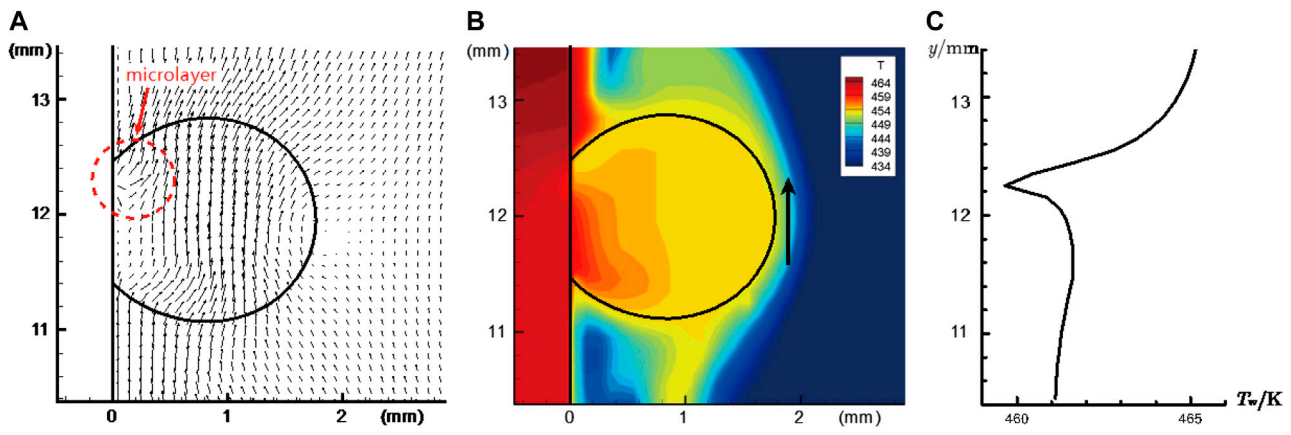

FIGURE 5 | A bubble sliding on the heating wall: **(A)** local velocity vector; **(B)** local temperature field; **(C)** local wall temperature.

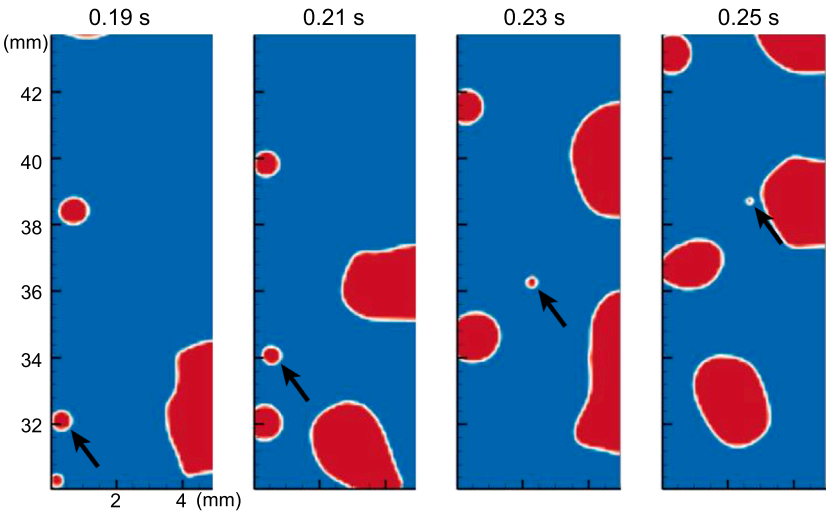

FIGURE 6 | Condensation of a small bubble in the bulk region.

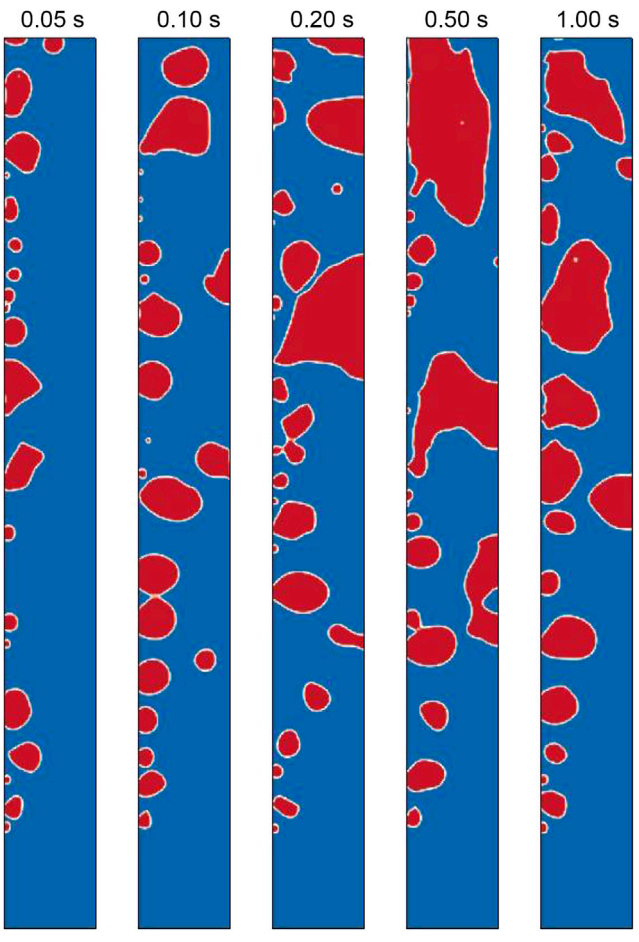

FIGURE 7 | Evolution of phase distribution at wall heat flux of 300 kW/m^2.

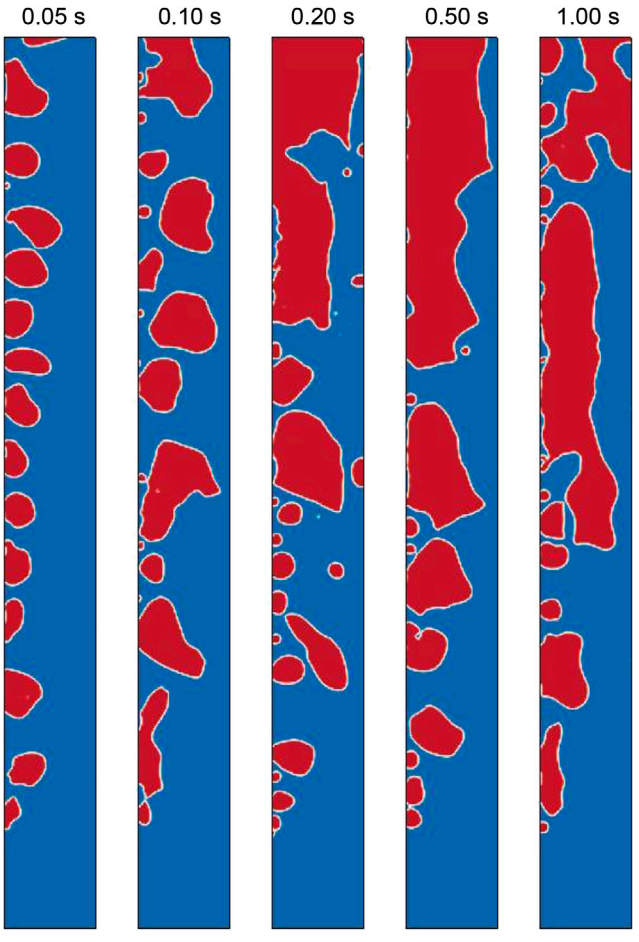

FIGURE 8 | Evolution of phase distribution at wall heat flux of 500 kW/m^2.

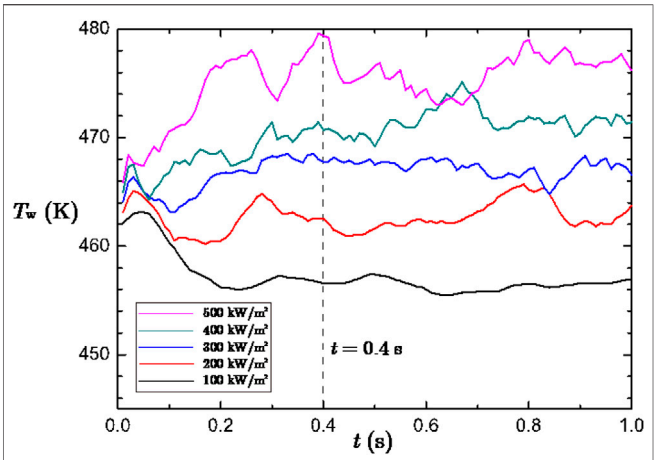

FIGURE 9 | Spatial average wall temperature under various wall heat fluxes.

developed into a flow pattern of elongated bubbly flow. Also, we can see the formation of a liquid film between the elongated bubble and the heating wall. The transformation from dispersed bubbly flow to elongated bubbly flow has been reported by Kim et al. (2018), and it was successfully reproduced by the present numerical simulations.

Average Wall Superheat

From the results discussed in *Subcooled Flow Boiling at Low Heat Flux* and *Subcooled Flow Boiling at Higher Heat Fluxes*, we can see many important influences of bubbles to the heat transfer process. The bubble growth, sliding and departure and condensation can continuously transfer heat from the heating wall to the bulk fluid region. In order to quantitatively analyze the heat transfer efficiency of subcooled flow boiling, we calculated a spatial average wall temperature for each case:

$$\overline{T}_w = \frac{\int_{y_1}^{y_2} T_w(y)dy}{y_2 - y_1} \tag{9}$$

in which y_1 = 5 mm and y_2 = 45 mm.

Figure 9 plots the spatial average wall temperature calculated by **Eq. 9** under the five cases with the wall heat flux ranging from 100 to 500 kW/m^2. It can be seen that, for each of the five cases, the influence of initially given temperature had been eliminated at t = 0.4 s, after which the average wall temperature almost kept floating up and down around a constant value. We therefore consider quasi-steady states were reach at 0.4 s for all the five cases.

In order to evaluate the overall heat transfer coefficient, we then calculated the time average of the spatial average wall temperature, to obtain a time-space average wall temperature:

$$\langle \overline{T}_w \rangle = \frac{\int_{t_1}^{t_2} \overline{T}_w dt}{t_2 - t_1} \tag{10}$$

in which t_1 = 0.4 s and t_2 = 1.0 s.

Heat Transfer Coefficient

A considerable number of heat transfer correlations were previously reported for subcooled flow boiling, and the correlations by Shah (1977), Liu and Winterton (1991), and by Kandlikar (1998) are most widely used ones among them. Based on a database containing 500 data points from 18 independent experimental studies, Shah (1977) proposed a correlation for heat transfer coefficient of subcooled flow boiling. The two-phase heat transfer coefficient was expressed as a correction on that of single-phase forced convection:

$$q = h_{tp}\Delta T_{sat} = \psi h_{sp}\Delta T_{sat} \tag{11}$$

Where ΔT_{sat} is wall superheat defined as

$$\Delta T_{sat} = T_w - T_{sat} \tag{12}$$

In **Eq. 11**, ψ is the correction factor determined by:

$$\psi = \psi_0 + \Delta T_{sub}/\Delta T_{sat} \tag{13}$$

$$\psi_0 = \begin{cases} 230Bo^{0.5} for\ Bo > 0.3 \times 10^{-4} \\ 1 + 46Bo^{0.5} for\ Bo < 0.3 \times 10^{-4} \end{cases} \tag{14}$$

where the boiling number Bo and the subcooling ΔT_{sub} are defined as:

$$Bo = \frac{q}{Gh_l^{\nu}} \tag{15}$$

$$\Delta T_{sub} = T_{sat} - T_b \tag{16}$$

The single-phase heat transfer coefficient was calculated with the Dittus-Boelter correlation:

$$h_{sp} = 0.023Re^{0.8}Pr^{0.4}\frac{\lambda_l}{D} \tag{17}$$

Liu and Winterton (1991) expressed the relationship between the heat flux and the wall superheat in a power form, which can be written as follows for subcooled water at the inlet.

$$q^2 = \left[h_{sp}(\Delta T_{sat} + \Delta T_{sub})\right]^2 + [Sh_{nb}\Delta T_{sat}]^2 \tag{18}$$

where h_{sp} is the single-phase heat transfer coefficient determined by **Eq. 17**, and h_{nb} refers to the heat transfer coefficient for nucleate boiling calculated by Cooper correlation (Cooper, 1984; Ji et al., 2015), S is a factor considering the suppression factor given by:

$$S = \frac{1}{1 + 0.055Re^{0.16}} \tag{19}$$

Considering the effects of mass flow rate and the latent heat, Kandlikar proposed a correlation for fully developed subcooled boiling which can be expressed as follows for water.

$$\Delta T_{sat} = \frac{q^{0.3}}{1058(Gh_{lv})^{-0.7}h_{sp}} \tag{20}$$

in which h_{sp} denotes convective heat transfer coefficient predicted by Gnielinski equation (Gnielinski, 1976).

For the validation purpose, the equations presented above were used for predicting the wall superheat of the problem

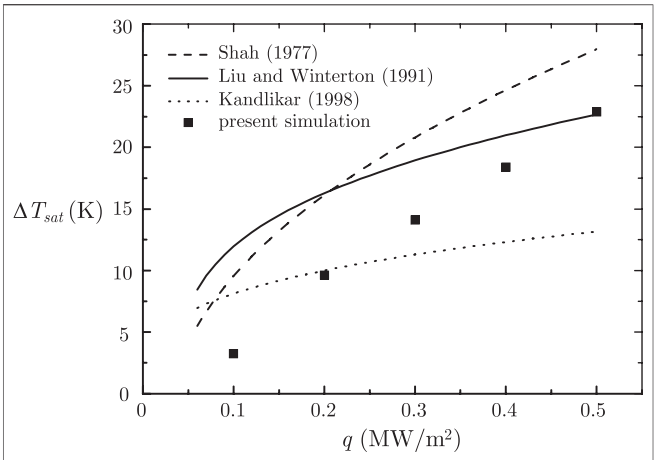

FIGURE 10 | Comparison of wall superheats predicted by our simulation and by some reported correlations.

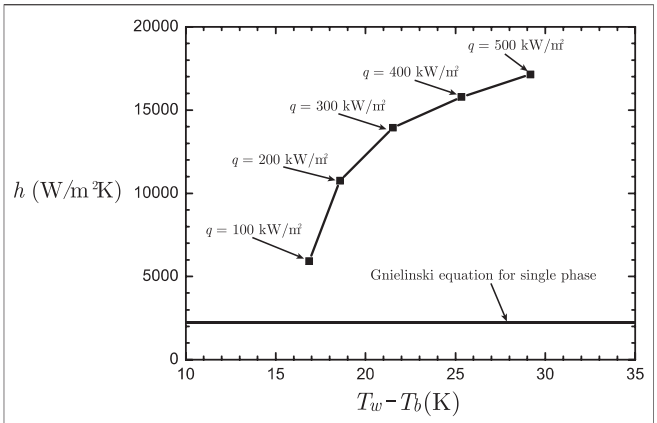

FIGURE 11 | Heat transfer coefficient under various heat fluxes.

studied here, in which the characteristic length (D) appearing in **Eq. 17** was calculated as the hydraulic diameter, namely, $D = 4d_f = 0.02$ m. The wall superheats obtained by our simulations were evaluated by the time-space wall temperature (**Eq. 10**). The wall superheats are plotted in **Figure 10**. From the plotted results we can see, first, our simulation gives the same variation trend of wall superheat with heat flux. However, the predictions by the three correlations show large differences in predicting the wall superheat, even though they are selected owing to their superior accuracy (Chen et al., 2021). Compared with the correlation by Shah (1977), the present simulation gives under prediction of around 30% in wall superheat. This discrepancy seems a bit large. However, it is well-known in heat transfer textbook (Cengel, 2007; Bergman et al., 2011) that the Rohsenow equation for pool boiling heat transfer can be in error by 30% for a wall superheat by given a heat flux. Thus our prediction discrepancy is acceptable.

In subcooling boiling the bulk of fluid temperature is below saturated temperature. The disturbance of the generated bubbles enhances the fluid mixing, hence enhances heat transfer. In order to reveal this enhancement the definition of single phase convective heat transfer coefficients adopted here:

$$h = \frac{q}{T_w - T_b} \tag{21}$$

where T_w is the time-space average wall calculated by **Eq. 10**, and T_b refers to the time-space average liquid temperature calculated by:

$$\left\langle \overline{T}_b \right\rangle = \frac{1}{t_2 - t_1} \frac{\int_{t_1}^{t_2} \int_{\Omega} T(1-c) dV dt}{\int_{\Omega} T(1-c) dV} \tag{22}$$

To be consistent with the average wall temperature, Ω in **Eq. 22**, where the liquid temperature averaged was averaged, refers to the computational domain in the range 5 mm < y < 45 mm. **Figure 11** plots the heat transfer coefficients calculate by **Eq. 21**. In the figure the single phase convective heat transfer coefficient predicted by Gnielinski equation (Gnielinski, 1976) at the same conditions is also presented. It can be seen that subcooled boiling has an appreciable effect on enhancing heat transfer. In addition we can clearly see greater heat transfer coefficient at higher wall heat flux, but the growth rate is decreasing. The result indicates that, for the cases studied, the boiling is in the stage of nucleate boiling where the increase of wall heat flux leads to enhancement of heat transfer.

Void Fraction

The distribution of void fraction plays as a key role in heat transfer performance of flow boiling. We therefore evaluated the void faction by time-averaging the vapor volume fraction in the period when quasi-steady states were reached. Concretely, the void fraction was calculated by:

$$\langle c \rangle = \frac{\int_{t_1}^{t_2} c dt}{t_2 - t_1} \tag{23}$$

in which t_1 = 0.4 s and t_2 = 1.0 s.

The void fraction obtained under the five wall heat fluxes are displayed in **Figure 12**, and the average void fraction on the cross section of the tube is plotted in **Figure 13**. From the two figures one can clearly see the development of the void fraction along the flow direction. Obviously, higher wall heat flux resulted in faster generation of vapor, hence increased the void fraction. Under the highest wall heat flux (0.5 MW/m^2), an average void fraction of around 0.8 was reached at the tube outlet. The void fraction distributed rather unevenly on the cross section. From **Figure 12** we can see, even in higher wall heat flux where elongating bubbly flow was formed, there remains a thin liquid film around the heating wall, which avoids the occurring of critical heat flux. The existence of the thin liquid film is an important mechanism to prevent the heat transfer regime from film boiling. The distribution of void fraction further enhances our understanding the mechanism of flow boiling heat transfer.

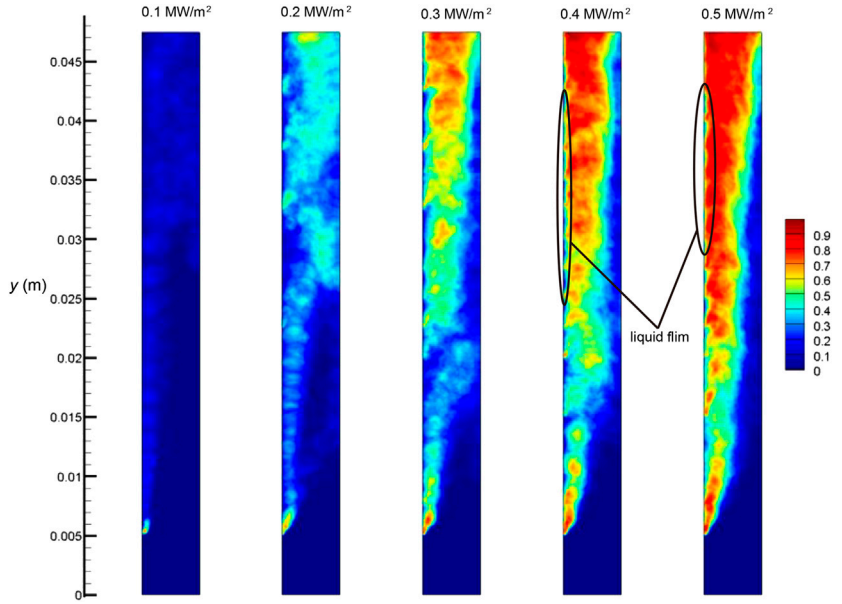

FIGURE 12 | Void fraction obtained by time averaging the vapor volume fraction.

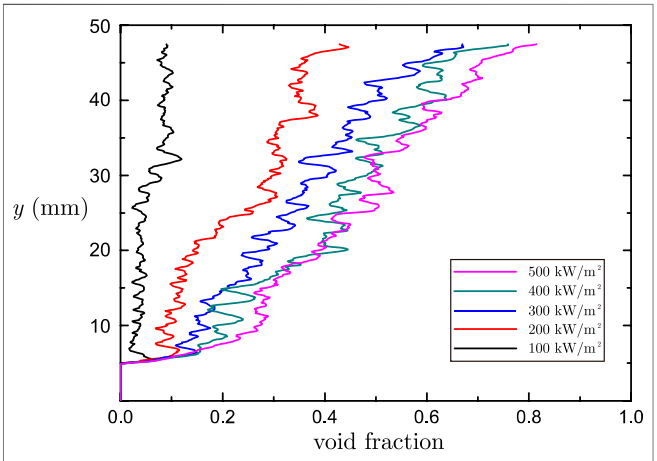

FIGURE 13 | Average void fraction along the flow direction.

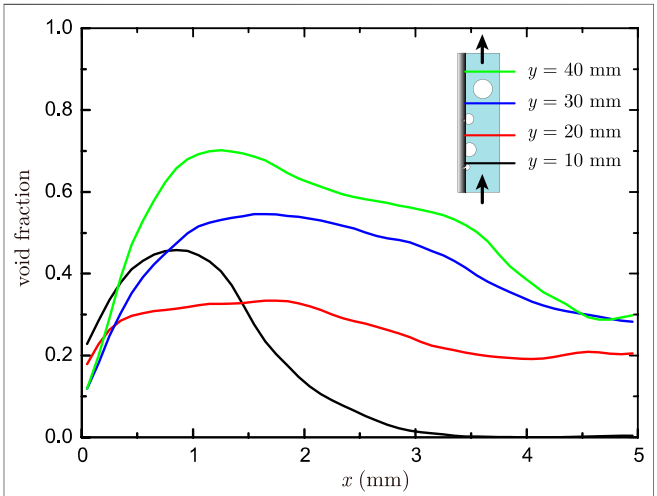

FIGURE 14 | Local void fraction along the radial direction (q = 300 kW/m^2).

The experimental results reported by Park et al. (2020) show that, along the radial direction (from the wall to bulk region), the local void fraction first increases and then decreases, and the maximum value appears at a certain distance from the wall. **Figure 14** plots the local profiles of the void fraction in the radial direction at y = 10, 20, 30, and 40 mm for wall heat flux of 300 kW/m^2. Those curves show the same feature of the local distribution of the void fraction except for the one at y = 20 mm, where the local void fraction almost kept a constant value from x = 0.5 mm to x = 2 mm.

Through some parametric studies, Park et al. (2020) demonstrated how the local void fraction is influenced by the flow conditions. In general, the void fraction at a specific cross section increases when the heat flux increase, the mass flux decreases and the inlet subcooling decreases. Simultaneously, the peak of its local profile along the radial direction is shifted toward the bulk region with the decrease of the inlet subcooling.

In the present study, we changed the mass flow rate and subcooling at the inlet on the basis of the case where q = 300 kW/m^2 to study their effect on the void fraction. In terms of the mass flow rate, we carried out simulations with a smaller inlet velocity (0.05 m/s) and a greater one (0.15 m/s), and the obtained radial distributions of the void fraction at y = 30 mm are plotted in **Figure 15**. As a whole, we can find smaller mass flux resulted in greater average void fraction at the same cross section. Simulations on two more cases

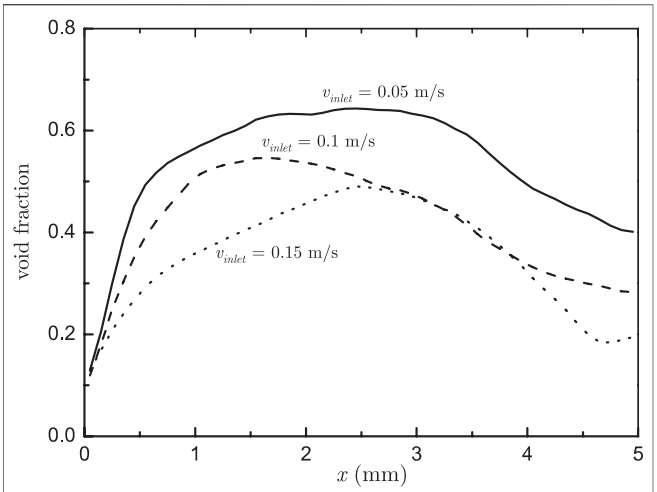

FIGURE 15 | Local profile of void fraction at y = 30 mm under various inlet velocities.

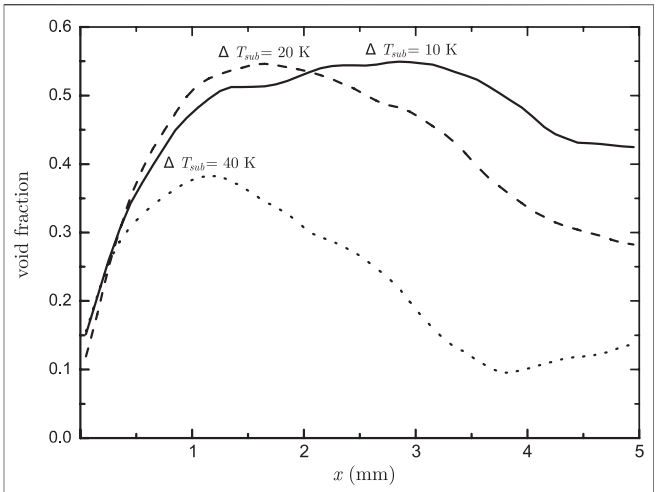

FIGURE 16 | Local profile of void fraction at y = 30 mm under various inlet subcoolings.

with a greater inlet subcooling (40 K) and a smaller one (10 K) was then conducted, and the obtained local void fractions at y = 30 mm are compared in **Figure 16**. It shows that, the void fraction in average was increased at lower inlet subcooling. Moreover, the peak of the local void fraction was shifted away from the wall. The peak values appear at around x = 1.2 mm, x = 1.8 mm, and x = 3 mm at subcoolings of 40, 20, and 10 K, respectively. As a whole, our interface-tracking simulations successfully reproduced the new findings of subcooled boiling flow in terms of the local distribution of the void fraction as well as its influences by the mass flow rate and the inlet subcooling.

DISCUSSION

Subcooled boiling flow is the physical process occurring at various scales, and the influences of small-scale processes are not negligible compared with large-scale ones. Such multi-scale feature makes subcooled boiling being one of the most challenging problems in nuclear engineering. From the perspective of numerical simulation, the present study can only resolve the processes under the grid resolution, while the small-scale problems are left behind to be modeled. Concretely, the present study used models for bubble nucleation and microlayer evaporation for a smaller scale, and illustrated some features at larger scale such as the distribution of the void fraction. Indeed, the accurate simulation requires the influences by small-scale processes being accurately modeled. Due to the lake of small-scale data, especially at high-pressure conditions, there remain many uncertainties in the present simulations. From the validation we can see large discrepancy between the numerical simulation and existing correlations, which may lie in the 2D model used in our simulation, and various uncertainties such as wall roughness and the thickness of the microlayer. For this, the authors believe the following studies are of great help in providing more reliable micro-scale models for interface-tracking simulations for subcooled boiling flows: 1) measurement of microlayer thickness at various system pressures; 2) measurement of nucleation site density at various system pressures; 3) direct simulation for bubble nucleating using molecular dynamics simulation. Moreover, 3D simulations are necessary to make interface-tracking simulations approaching to what is occurring in real subcooled boiling flow, and it will be conducted by the authors in near future using 3D VOSET (Ling et al., 2015a).

CONCLUSION

In the present study, VOSET method was used as the interface tracking method for the simulation of subcooled flow boiling at high-pressure condition, and the conjugation with heat conduction in the solid wall was considered in the model. By means of numerical simulations at various flow conditions, many features of flow boiling were presented.

Results at the lowest wall heat flux demonstrated some mechanisms how bubbles enhance the heat transfer efficiency. Firstly, the bubble motions can greatly intensify fluid mixing between near wall region and bulk region. Owing to the microlayer, bubbles sliding on the wall can greatly increase the evaporation rate and reduce the local solid temperature.

In the range of wall heat flux investigated here, we found the flow pattern in the channel transforms from isolated bubbly flow to elongated bubbly flow with the increase of the heat flux. The heat transfer coefficient kept increasing. In the cases studied, there remains a thin liquid film around the heating wall, even in

the flow regime of elongated bubbly flow, which prevented the occurring of critical heat flux.

The present study successfully replicated the features of the cross-sectional local void fraction in subcooled flow boiling. It first increase and then decrease from the near-wall region to the bulk fluid region. With the increase of the mass flow rate, the peak location was shifted away from the heating wall.

DATA AVAILABILITY STATEMENT

All datasets generated for this study are included in the article/supplementary files.

AUTHOR CONTRIBUTIONS

KL wrote the code needed for simulation and wrote the article submitted; WL designed the problem studied; SZ and XS conducted numerical simulations; WT supervised the analysis of the results.

FUNDING

The present work is supported by Project for Young Talents of China National Nuclear Corporation, the Key Project of National Natural Science Foundation of China (51836005), the Foundation for Innovative Research Groups of the National Natural Science Foundation of China (51721004) and 111 Project (B16038).

REFERENCES

Bergman, T. L., Lavine, A. S., Incropera, F. P., and DeWitt, D. P. (2011). *Introduction to heat transfer*. 6th Edn. New York, NY: John Wiley & Sons Inc., 628.

Cengel, Y. A. (2007). Heat and mass transfer, *A practical approach*. 3rd Edn. Boston, MA: McGraw-Hill, 569.

Chen, Z., Hu, X., Hu, K., Utaka, Y., and Mori, S. (2020). Measurement of microlayer characteristics in the whole range of nucleate boiling for water by laser interferometry. *Int. J. Heat Mass Tran.* 146, 118856. doi:10.1016/j.ijheatmasstransfer.2019.118856

Chen, Z., Li, W., Li, J., Zhou, K., and Feng, Z. (2021). A new correlation for subcooled flow boiling heat transfer in a vertical narrow microchannel. *ASME Journal of Electronic Packaging* 143, 014501. doi:10.1115/1.4046755

Cooper, M. G., and Lloyd, A. J. P. (1969). The microlayer in nucleate pool boiling. *Int. J. Heat Mass Tran.* 12, 895–913. doi:10.1016/0017-9310(69)90154-9

Cooper, M. G. (1984). Saturation nucleate pool boiling, a simple correlation. *Int. Chem. Eng. Symp. Ser.* 16, 157–239. doi:10.1016/s0065-2717(08)70205-3

Gnielinski, V. (1976). New equations for heat mass transfer in turbulent pipe and channel flows. *Int. Chem. Eng.* 8 (1), 359–368.

Hibiki, T., and Ishii, M. (2003). Active nucleation site density in boiling systems. *Int. J. Heat Mass Tran.* 46, 2587–2601. doi:10.1016/s0017-9310(03)00031-0

Ji, W., Zhao, C., He, Y., and Tao, W. (2015). Experimental validation of Cooper correlation at higher heat flux. *Int. J. Heat Mass Tran.* 90, 1241–1243. doi:10.1016/j.ijheatmasstransfer.2015.05.107

Jung, S., and Kim, H. (2014). An experimental method to simultaneously measure the dynamics and heat transfer associated with a single bubble during nucleate boiling on a horizontal surface. *Int. J. Heat Mass Tran.* 73, 365–375. doi:10.1016/j.ijheatmasstransfer.2014.02.014

Kandlikar, S. G. (1998). Heat transfer characteristics in partial boiling, fully developed boiling, and significant void flow regions of subcooled flow boiling. *J. Heat Transfer* 120, 395–401. doi:10.1115/1.2824263

Kim, S. H., Chu, I. C., Choi, M. H., and Euh, D. J. (2018). Mechanism study of departure of nucleate boiling on forced convective channel flow boiling. *Int. J. Heat Mass Tran.* 126, 1049–1058. doi:10.1016/j.ijheatmasstransfer.2018.05.105

Koffman, L. D., and Plesset, M. S. (1983). Experimental observations of the microlayer in vapor bubble growth on a heated solid, *Int. J. Heat Mass Tran.* 105, 625–632. doi:10.1115/1.3245631

Lal, S., Sato, Y., and Niceno, B. (2015). Direct numerical simulation of bubble dynamics in subcooled and near-saturated convective nucleate boiling. *Int. J. Heat Fluid Flow* 51, 16–28. doi:10.1016/j.ijheatfluidflow.2014.10.018

Lee, J., O'Neill, L. E., Lee, S., and Mudawar, I. (2019). Experimental and computational investigation on two-phase flow and heat transfer of highly subcooled flow boiling in vertical upflow. *Int. J. Heat Mass Tran.* 136, 1199–1216. doi:10.1016/j.ijheatmasstransfer.2019.03.046

Lee, Y. G., Park, I. W., Yoo, J. W., and Kim, S. (2019). Measurement of multi-dimensional distribution of local bubble parameters in a vertical annulus under subcooled boiling conditions. *Int. J. Heat Mass Tran.* 140, 992–1005. doi:10.1016/j.ijheatmasstransfer.2019.05.106

Ling, K., Li, Z., Sun, D., He, Y., and Tao, W. (2015a). A three-dimensional volume of fluid & level set (VOSET) method for incompressible two-phase flow. *Comput. Fluids* 118, 293–304. doi:10.1016/j.compfluid.2015.06.018

Ling, K., Son, G., Sun, D., and Tao, W. (2015b). Three dimensional numerical simulation on bubble growth and merger in microchannel boiling flow. *Int. J. Therm. Sci.* 98, 135–147. doi:10.1016/j.ijthermalsci.2015.06.019

Liu, Z., and Winterton, R. H. S. (1991). A general correlation for saturated and subcooled flow boiling in tubes and annuli based on a nucleate pool boiling equation. *Int. J. Heat Mass Tran.* 34, 2759–2766. doi:10.1016/0017-9310(91)90234-6

Okawa, T., Kaiho, K., Sakamoto, S., and Enoki, K. (2018). Observation and modeling of bubble dynamics in isolated bubble regime in subcooled flow boiling. *Nucl. Eng. Des.* 335, 400–408. doi:10.1016/j.nucengdes.2018.06.009

Park, I. W., Kim, S., and Lee, Y. G. (2020). The profiles of the local void fraction close to the heated wall in the subcooled flow boiling. *Int. J. Heat Mass Tran.* 151, 119438. doi:10.1016/j.ijheatmasstransfer.2020.119438

Prodanovic, V., Fraser, D., and Salcudean, M. (2002). Bubble behavior in subcooled flow boiling of water at low pressure and low flow rates. *Int. J. Multiphas. Flow* 28, 1–19. doi:10.1016/s0301-9322(01)00058-1

Sakashita, H. (2011). Bubble growth rates and nucleation site densities in saturated pool boiling of water at high pressures. *J. Nucl. Sci. Technol.* 48, 734–743. doi:10.1080/18811248.2011.9711756

Sato, Y., and Niceno, B. (2015). A depletable micro-layer model for nucleate pool boiling. *J. Comput. Phys.* 300, 20–52. doi:10.1016/j.jcp.2015.07.046

Sato, Y., and Niceno, B. (2017). Nucleate pool boiling simulations using the interface tracking method: boiling regime from discrete bubble to vapor mushroom region. *Int. J. Heat Mass Tran.* 105, 505–524. doi:10.1016/j.ijheatmasstransfer.2016.10.018

Shah, M. (1977). A general correlation for heat transfer during subcooled boiling in pipes and annuli. *ASHRAE Trans.* 81, 205–217.

Sun, D., and Tao, W. (2010). A coupled volume-of-fluid and level set (VOSET) method for computing incompressible two-phase flows. *Int. J. Heat Mass Tran.* 53, 645–655. doi:10.1016/j.ijheatmasstransfer.2009.10.030

Urbano, A., Tanguy, S., Huber, G., and Colin, C. (2018). Direct numerical simulation of nucleate boiling in micro-layer regime. *Int. J. Heat Mass Tran.* 123, 1128–1137. doi:10.1016/j.ijheatmasstransfer.2018.02.104

Utaka, Y., Kashiwabara, Y., and Ozaki, M. (2013). Microlayer structure in nucleate boiling of water and ethanol at atmospheric pressure. *Int. J. Heat Mass Tran.* 57, 222–230. doi:10.1016/j.ijheatmasstransfer.2012.10.031

Yi, T., Lei, Z., and Zhao, J. (2019). Numerical investigation of bubble dynamics and heat transfer in subcooling pool boiling under low gravity. *Int. J. Heat Mass Tran.* 132, 1176–1186. doi:10.1016/j.ijheatmasstransfer.2018.12.096

Yuan, D., Chen, D., Yan, X., Xu, J., Lu, Q., and Huang, Y. (2018). Bubble behavior and its contribution to heat transfer of subcooled flow boiling in a vertical rectangular channel. *Ann. Nucl. Energy* 119, 191–202. doi:10.1016/j.anucene.2018.05.010

Conflict of Interest: Authors Kong Ling and Shuai Zhang were employed by Xi'an ShuFeng Technological Information, Ltd. Author Xiaowei Sui was employed by National Institute Corporation of Additive Manufacturing. The remaining authors declare that the research was conducted in the absence of any commercial or financial relationships that could be constructed as a potential conflict of interest

frontiers in Energy Research

ORIGINAL RESEARCH
published: 16 March 2022
doi: 10.3389/fenrg.2022.847458

Numerical Investigations of Liquid Film Offtake by Transverse Gas Flow in a Downcomer Annulus Geometry

*Chi-Jin Choi and Hyoung Kyu Cho**

Department of Nuclear Engineering, Seoul National University, Seoul, South Korea

Advances in computational power have enabled the application of computational fluid dynamics (CFD) to nuclear reactor safety analyses, which require accurate predictability for two-phase flow in complex geometries. This study is aimed at validating CFD simulation of liquid film off-take in a 1/10-scale downcomer of a reactor pressure vessel under emergency core coolant (ECC) bypass conditions. Even though different flow regimes can exist simultaneously in real flow, the traditional two-phase flow models used in CFD have a disadvantage with respect to regime dependency. In this study, VOF–slip, which is a hybrid model that combines volume-of-fluid (VOF) and mixture models and is offered in STAR-CCM+ 15.04, was used to simulate the film off-take phenomenon. The key parameters in the simulation were found to be the droplet diameter and interface turbulence damping coefficient. A parametric study was performed to determine the value of the parameters that yield a reasonable liquid film thickness and ECC bypass fraction which were measured at the Seoul National University (SNU) experiment facility. For the conditions of the SNU experiment, the droplet diameter was found to be 150 μm, and the interface turbulence damping coefficient was found to be in the range of 0–30. The validation results confirmed that the VOF–slip model can describe the behavior of the liquid film and the unresolved droplet appropriately. This resulted in an improvement in predicting the ECC bypass fraction in comparison to the results using the conventional VOF model.

Keywords: volume-of-fluid-slip model, multi-regime, droplet diameter, interface turbulence damping, emergency core coolant bypass

OPEN ACCESS

Edited by:
Victor Petrov,
University of Michigan, United States

Reviewed by:
Mingjun Wang,
Xi'an Jiaotong University, China
Andrey Minakov,
Siberian Federal University, Russia
Lukas Robers,
ETH Zürich, Switzerland

****Correspondence:***
Hyoung Kyu Cho
chohk@snu.ac.kr

Specialty section:
This article was submitted to Nuclear Energy, a section of the journal Frontiers in Energy Research

Received: *02 January 2022*
Accepted: *28 February 2022*
Published: *16 March 2022*

Citation:
Choi C-J and Cho HK (2022) Numerical Investigations of Liquid Film Offtake by Transverse Gas Flow in a Downcomer Annulus Geometry. Front. Energy Res. 10:847458. doi: 10.3389/fenrg.2022.847458

INTRODUCTION

Two-phase liquid film flow occurs in various industrial fields, such as chemical and mechanical engineering. In a nuclear power plant, liquid film can appear in several areas, including the reactor core, reactor downcomer, and heat exchanger surface. Liquid films influence heat and mass transfer in two-phase flows. Therefore, investigating the thermal–hydraulic phenomena related to liquid film is an important aspect of nuclear reactor safety analysis.

The field of computational fluid dynamics (CFD) has come to occupy an important position in nuclear reactor safety analyses, which require accurate prediction of the three-dimensional geometric effects of two-phase flow. Many researchers have been conducting the CFD simulation for the fluid flow and heat transfer in fuel assembly, lower plenum, heat exchanger, pressurizer surge line, etc. (Conner et al., 2010; Feng et al., 2019; Khan et al., 2020, 2021; Wang et al., 2021). Small-scale flow processes that are not seen by the reactor system codes can be accessed using CFD, which results in better estimation of safety margins. CFD is therefore an appropriate approach to investigating the

FIGURE 1 | ECC bypass phenomenon in RV downcomer (Cho et al., 2005).

liquid film behavior at a reactor vessel (RV) upper downcomer (**Figure 1**) If a loss-of-coolant accident occurs with a break in a primary coolant system of the pressurized water reactor, the emergency core coolant (ECC) is injected into the RV downcomer through the direct vessel injection (DVI) nozzle. The ECC water impinges on the core barrel wall and flows downward in the form of a liquid film. At the same time, the steam generated in the reactor core by the decay heat flows out through the broken cold leg, and some of the ECC water bypasses out because of the steam flow. In the process of the film off-take, three different forms of the liquid phase can be observed: a liquid film, wisps, and droplets. The more the ECC water bypasses out, the less it contributes to the emergency core cooling. If the liquid flow is insufficient to remove the decay heat, the nuclear fuel rods might be overheated. Therefore, several experimental and analytical studies have been carried out to better understand the ECC bypass mechanism and predict it more accurately (Murao et al., 1982; Bae et al., 2000; Kwon et al., 2003a; Cho et al., 2005; Yang et al., 2017).

Prediction of the ECC bypass phenomenon using a CFD code was first attempted by (Kwon et al., 2003b). The objective of their study was to verify the similarity of the velocity profile in the RV downcomer, which was scaled down based on the modified linear scaling method (Yun et al., 2004). A commercial CFD code, FLUENT ver. 5.5, was used to analyze gas flow characteristics in a full-scale RV downcomer for the APR1400 and at 1/5 scale for the MIDAS test facility. In addition, the spreading phenomenon of the ECC film on the inner wall of the downcomer was simulated using the volume-of-fluid (VOF) model, and it was validated based on experimental results. As a follow-up study, Kwon et al. (2007) showed that CFD analysis could be extended to the two-phase film off-take phenomenon. Using the two-fluid model in the CFX code, the direct vessel injection visualization analysis (DIVA) test (Yun et al., 2000) was simulated and the effect of the azimuthal angle of the DVI nozzle on the ECC bypass was quantified. The predicted ECC bypass fraction was in good agreement with the experimental data for the current DVI azimuthal angle (15°) of APR1400, but it was overestimated for a shifted angle (52°). Yoon et al. (2015) numerically investigated the effects of air-water cross-flow on the advanced DVI (DVI+) system for the new advanced power reactor plus (APR+) design. The performance of the emergency core barrel duct (ECBD) was assessed by predicting the bypass fraction. A homogenous model considering the surface tension and volume fraction at each phase was used to examine the air–water two-phase flow. The CFD analysis results were used to determine the fraction of the ECC water outside the ECBD and form loss factor at the opening of the ECBD for one-dimensional two-phase system code.

As described above, several attempts have been made to investigate the ECC bypass phenomenon using CFD. However, this type of investigation remains challenging for the following reasons. First, in most previous CFD studies, the overall capability of CFD codes to predict the ECC bypass phenomenon was assessed only by comparing the calculation results for global parameters, such as the bypass fraction, with experimental data. This was because of the lack of local measurements of two-phase flow parameters, which prevented the CFD code from being validated sufficiently and limited model improvement. In a previous experimental study of the ECC bypass phenomenon, a DIVA test was carried out by the Korea Atomic Energy Research Institute (KAERI). The test sections at the DIVA facility were 1/7- and 1/5-scale APR1400 RV downcomers, and the two-phase air–water flow near the broken cold leg was investigated. A MIDAS (multi-dimensional investigation in the downcomer annulus simulation) test (Yun et al., 2002) was also conducted by KAERI. This test was similar to the DIVA test, except steam was used as the working fluid rather than air. In both experiments, the film off-take behavior was investigated by the visual observation and by measuring the ECC bypass rate, but the local flow parameters were not obtained. Another test performed at KAERI and Seoul National University (SNU) was a two-dimensional (2-D) air–water film flow experiment (Yang et al., 2015). The experiment was conducted in a 1/10-scale plane channel-type downcomer and focused on the 2-D behavior of the liquid film without considering the film off-take to the broken cold leg. Pitot tubes, a depth-averaged particle image velocimetry method, and an ultrasonic gauge were used to obtain the local air velocity, film velocity, and film thickness, respectively. Although the local parameters were known for the 2-D air–water film flow experiment, they could not be used for the CFD validation because the film off-take by the gas flow was not described in the experiment. The limitations of these previous studies have motivated our previous studies, conducted in the SNU experimental facility (Choi and Cho, 2019), in which the film off-take behavior was investigated using local measurements obtained using the 1/10-scale RV downcomer. An electrical conductance sensor was developed to measure the thickness of the liquid film, and it was fabricated on a flexible printed circuit board, which enabled the sensor to be installed at the curved test section. The developed sensor is an array-type, and is used to measure the field data and adopted the three-electrode method to widen the

measurable film thickness range. During the experiment, the local liquid film thickness and ECC bypass fraction were measured, and the values obtained can be utilized for validation of the CFD model.

In addition to the lack of validation data, there has been an issue with two-phase CFD models. Traditional two-phase flow models, such as VOF and the two-fluid model are known for providing relatively reliable outcomes for only either the segregated (VOF) or dispersed (two-fluid model) flow, which is not sufficient for simulating the ECC bypass phenomenon. The STAR-CCM + *v*13.02 commercial CFD code (Siemens, 2018) introduced VOF–slip as a hybrid model that combines VOF and mixture models and can be applied to large- and small-scale interfaces simultaneously. Because the VOF–slip model has only relatively recently become available in a commercial CFD code, few studies using this model have been reported in literature.

Another challenge in CFD simulation is modeling the turbulence at a large-scale interface. Insufficiently sophisticated modeling of interface turbulence results in unrealistic descriptions of the physical behavior of turbulence near such an interface. For example, according to experimental studies (Fabre et al., 1987; Rashidi and Banerjee, 1990) and direct numerical simulations (Fulgosi et al., 2003), the gas–liquid interface in stratified and annular flows behaves similarly to a solid wall in single-phase flows. To reproduce this wall-like behavior, researchers have made various attempts to dampen the turbulence near the interface so that the turbulence is modeled more realistically at the interface.

The objective of this study was to validate the CFD simulation of the air–water film off-take in the 1/10-scale RV downcomer at the SNU experimental facility. A CFD model implemented in STAR-CCM + *v*15.04 was used for this purpose. A parametric study was conducted to identify the key parameters for the simulation. As the key parameters, the interface turbulence damping coefficient and droplet diameter were chosen because both are found to be the factors that greatly affect the simulation results, even though they were uncertain values. The effects of the interface turbulence damping coefficient and droplet diameter were investigated in detail. The simulation results were validated using SNU experimental data, including the local liquid film thickness and the ECC bypass fraction. The validation was also conducted to demonstrate best practices for accurate simulation of the liquid film off-take phenomenon.

CFD MODELING

VOF-Slip Model

The VOF model proposed by Hirt and Nichols (1981) is one of the most widely used two-phase CFD models for capturing the interface. In the VOF model, two-phase flows are recognized as homogeneous mixtures consisting of immiscible fluids. The continuous and dispersed phases can be lumped into a single continuum in which they share the same pressure and velocity fields. Therefore, the VOF model is not capable of describing dispersed phase flow in which the interface length is smaller than the mesh size.

The mixture model is applicable to interpenetrated phases which are treated as a mixture in a cell. The mixture model is similar to the VOF model in that it solves a single set of transport equations. However, the model cannot be expected to resolve a sharp interface even on a fine grid, as the VOF does. In addition, the phase slip velocity is considered in the mixture model; hence, the behavior of the dispersed phase, which cannot be captured with a coarse grid, can be properly simulated.

A commercial CFD code, STAR-CCM + *v*13.02, introduced the VOF–slip model as a hybrid model combining the VOF and the mixture models. This hybrid model can treat a large-scale interface and small-scale interface simultaneously. In the VOF–slip model, the volume fraction transport equation and momentum equation can be expressed as follows:

$$\frac{\partial \alpha_i}{\partial t} + \nabla \cdot (\alpha_i \mathbf{v}) = -\frac{1}{\rho_i} \nabla \cdot \left(\alpha_i \rho_i \mathbf{v}_{d,i}\right) \tag{1}$$

$$\frac{\partial (\rho \mathbf{v})}{\partial t} + \nabla \cdot (\rho \mathbf{v}\mathbf{v}) = -\nabla p + \rho \mathbf{g} + \nabla \cdot \mathbf{T} + \boldsymbol{f}_{\mathbf{s}} + \nabla \cdot \Sigma \alpha_i \rho_i \mathbf{v}_{d,i} \mathbf{v}_{d,i} \tag{2}$$

where α_i is the volume fraction of phase i, ρ_i is the density of phase i, $\mathbf{v}$ is the mixture velocity, $v_{d,i}$ is the diffusion velocity, p is the pressure, T is the stress tensor, and f_s is the surface tension force. The above two equations are the same as those that result from adding a diffusion velocity term to the existing transport equations in VOF. The diffusion velocity is the difference between the phase velocity and the mixture velocity, and it is defined as follows:

$$\mathbf{v}_{d,i} = \mathbf{v}_i - \mathbf{v} \tag{3}$$

The diffusion velocity and slip velocity, v_{ps} are related as follows:

$$\mathbf{v}_{d,p} = \left(\frac{\alpha_p \rho_p}{\rho} - 1\right) \mathbf{v}_{ps} \tag{4}$$

$$\mathbf{v}_{ps} = \mathbf{v}_s - \mathbf{v}_p \tag{5}$$

where p and s denote the primary and secondary phase, respectively. Here, the slip velocity that determines the diffusion velocity can be modeled with a drag coefficient C_D and specific body force b, as shown below.

$$\mathbf{v}_{ps} = C_D \mathbf{b} \tag{6}$$

$$\mathbf{b} = \mathbf{g} - (\mathbf{v} \cdot \nabla)\mathbf{v} - \frac{\partial \mathbf{v}}{\partial t} \tag{7}$$

In STAR-CCM+, the Schiller–Naumann drag model (Schiller and Naumann, 1935) can be used to obtain C_D, which assumes that the primary phase (referred to as the gas phase in this paper) is continuous and that the secondary phase (referred to as the liquid phase in this paper) is dispersed. The drag coefficient is modeled as follows:

$$C_D = C_D^{ps} = \frac{\tau_s}{f_{drag}^{ps}} \frac{(\rho_s - \rho)}{\rho_s} \tag{8}$$

$$\tau_s = \frac{\rho_s d_s^2}{18 \mu_p} \tag{9}$$

$$f_{drag}^{ps} = \begin{cases} 1 + 0.15Re_{ps}^{0.687} & if\ Re_{ps} \le 1000 \\ 0.0183Re_{ps} & if\ Re_{ps} > 1000 \end{cases}, Re_{ps} = \frac{\rho_p |\mathbf{v}_{ps}| d_s}{\mu_p} \quad (10)$$

where d_s is the droplet diameter and μ_p is the viscosity of the primary phase. **Equations 8–10** show that the drag coefficient increases as the droplet diameter increases, which means that the slip velocity increases.

The wettability of the wall is reflected as a contact angle that is required in VOF-slip model. Because the liquid film is formed at the acrylic test section and the film sensor which surface is made of the polyimide film and gold layer, it was difficult to determine the value of the contact angle. Besides, there are anisotropic surface irregularities due to the electrode arrangement in the sensor, which makes the distortion of the wall friction inevitable. For this reason, in the case of no air injection, the contact angle that can yield a reasonable film spreading width was found to be 0°. However, when the air velocity became large enough to cause an entrainment, it was confirmed that the effect of the contact angle became minor and the gravitational force and the interfacial friction force had a dominant influence on the simulation results.

Activation of Diffusion Velocity Term in VOF-Slip

The diffusion velocity terms in the transport equations of the VOF–slip model (**Eqs 1**, **2**) should not be activated in the gas–liquid interface region, and they should only work effectively in the unresolved dispersed phase. Therefore, a different value of the droplet diameter was used, based on the γ term defined as follows:

$$\gamma = |\nabla \alpha| \, dx \quad (11)$$

$$d_s = \begin{cases} d_s^* & if\ \gamma \le 0.33 \\ \frac{-d_s^*}{0.17}(\gamma - 0.5) & if\ 0.33 < \gamma < 0.5 \\ 1 \times 10^{-7} & if\ \gamma \ge 0.5 \end{cases} \quad (12)$$

where dx is the cell size and d_s^* is the input droplet diameter.

The variable γ plays a role in determining whether the regime in the cell is a free-surface or unresolved dispersed phase. If its value is greater than 0.5, the corresponding region is interpreted as an interface. For this case, a very small droplet diameter of 0.1 μm is utilized in the slip velocity estimation so that the VOF approach can be applied, i.e., without phase slip. If γ is less than 0.5, it is interpreted as a dispersed-phase region. In this case, the droplet diameter set by the user is utilized in the slip velocity estimation for the interpolation region.

Another required condition is that the droplet diameter should be used only when the liquid volume fraction is reasonably large. This condition can be expressed as follows:

$$d_s = \begin{cases} d_s^* & if\ \sqrt[3]{\frac{6\alpha_l V_{grid}}{\pi}} \ge d_s^* \\ 1 \times 10^{-7} & if\ \sqrt[3]{\frac{6\alpha_l V_{grid}}{\pi}} < d_s^* \end{cases} \quad (13)$$

where α_l is the liquid volume fraction and V_{grid} is the volume of the grid.

Interface Turbulence Damping

The $k-\omega$ SST (shear-stress transport) model (Menter, 1994) was used as the turbulence model in the present study. This model, which combines the best characteristics of the $k-\omega$ and $k-\varepsilon$ turbulence models, behaves like a $k-\omega$ -type model near the wall, otherwise it behaves as $k-\varepsilon$ -type model, which avoids strong freestream sensitivity.

The simulation of the liquid film off-take near the broken cold leg should consider the interface turbulence damping so that the estimated interfacial friction between the gas and liquid phases leads to reasonable predictions of the liquid film behavior and bypass phenomenon. One of the most widely used ways of damping the interface turbulence is to apply the Egorov model (Egorov et al., 2004). The Egorov model is only available with the $k-\omega$ model, however, other models such as the $k-\varepsilon$ model may also benefit from an Egorov-like turbulence damping term near large-scale interface (Frederix et al., 2018). In this model, a source term is added to the ω equation of the $k-\omega$ model, which enhances the specific turbulence dissipation rate as follows:

$$S_i = \alpha A_i \cdot \Delta n \beta \rho_i (\omega_i)^2 = \alpha A_i \cdot \frac{36 B^2 \mu_i^2}{\beta \rho_i \Delta n^3} \quad (14)$$

$$\omega_i = B \frac{6\mu_i}{\beta \rho_i \Delta n^2} \quad (15)$$

where B is a damping coefficient and Δn is the cell height across the interface. This source term is only activated in the interfacial region by introducing an indicator A_i which is the interfacial area density. As the value of the damping coefficient B increases, the specific dissipation rate increases, which makes the eddy viscosity decrease.

Thus, determining an appropriate value for B is crucial to predicting how the free surface behavior is affected by the interfacial friction. However, there has been no general guideline provided for the selection of B in previous studies. In most cases, B has been tuned to match the experimental results well (Hohne et al., 2002; Egorov et al., 2004; Lo and Tomasello, 2010; Gada et al., 2017; Fan et al., 2019). Therefore, in the present study, a sensitivity analysis was performed to investigate the effect of B on the simulation results, and the value of B that yielded reasonable results for each simulation case was determined.

Because the effect of interface turbulence damping is also dependent on the cell height, as shown in **Eq. 15**, Frederix et al. (2018) introduced a mesh-independent length scale δ, which was incorporated into the Egorov approach to obtain consistent results regardless of the grid cell size, as shown below:

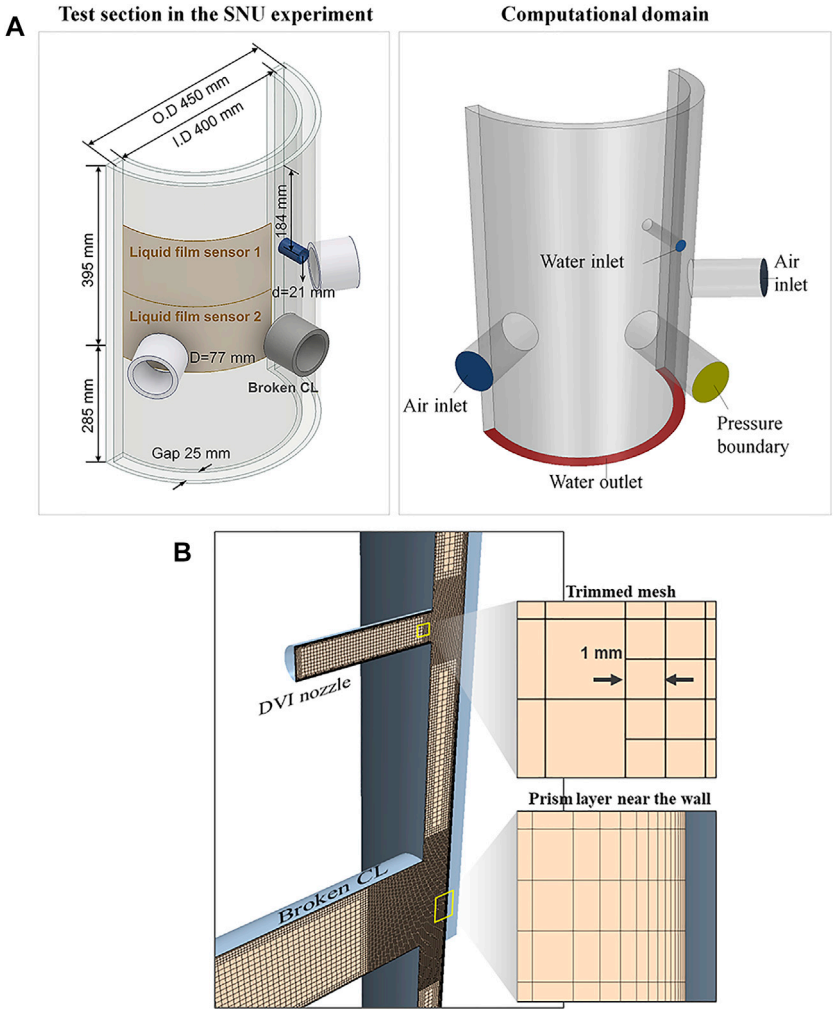

FIGURE 2 | (A) Computational domain for CFD simulation. **(B)** Meshing configuration.

$$\delta^2 = \frac{\Delta n^2}{6B} \tag{16}$$

then the ω_i term in **Eq. 15** can be expressed independent of the cell size by adopting δ as follows:

$$\omega_i = \frac{\mu_i}{\beta \rho_i \delta^2} \tag{17}$$

Using this approach, Frederix simulated a co-current stratified flow in a parametric study of δ, and found that the maximum value of δ was 10^{-4} m. In the present study, the effect of interface turbulence damping was first investigated in terms of B. Then, an appropriate value of B that yielded reasonable results was converted to δ following the approach used by Frederix.

Computational Domain and Meshing

The test section in the SNU experiment (Choi and Cho, 2019) was modeled as shown in **Figure 2A**. In the experiment, the test section describes 1/10th scale of APR1400 reactor vessel downcomer. There were two intact cold legs for air intake and a broken cold leg for air–water outtake. The DVI nozzle was placed above the broken cold leg, and water was injected through this nozzle. The liquid film sensor installed at the inner wall of

TABLE 1 | Simulation conditions.

Water inlet velocity	Re_f	**j_f [m/s]**
	2.32×10^4	**0.63**
	3.28×10^4	**0.89**
Air outlet velocity	$Re_{g,o}$	$j_{g,o}$ [m/s]
Low	1.00×10^5	20
	1.10×10^5	22
High	1.20×10^5	24
	1.30×10^5	26
	1.40×10^5	28

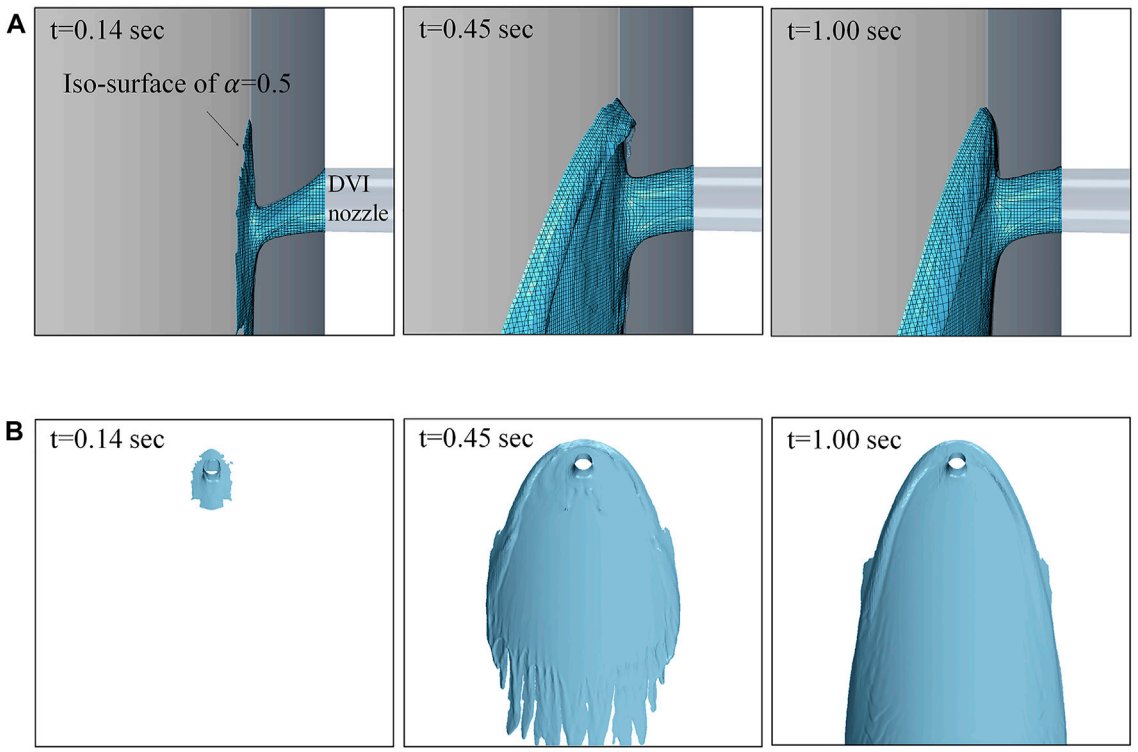

FIGURE 3 | Transient simulation under no-airflow condition (W089A00). **(A)** Water impingement (side view). **(B)** Liquid film flow (front view).

annular test section measured the film thickness in the region between the DVI nozzle and the cold legs. To reduce the computational cost, the lengths of the cold legs and the DVI nozzle were reduced, and the velocity profiles obtained from the fully developed flow were used as inlet boundary conditions. The bottom of the domain was set as a water outlet that controlled the water out flow rate to keep the water level constant.

Figure 2B shows the meshing configuration. Trimmed meshes were used, and 13 prism layers were generated near the wall. Considering the requirements of the turbulence model used, the $k-\omega$ SST model, wall y + values were maintained at approximately 1. The total number of cells was 6,223,381. Mesh convergence tests were conducted by changing the number of near-wall meshes. The results are presented in *Simulation Under No-Airflow Conditions* Section, along with the liquid film thickness prediction results.

The flow conditions for the simulations are summarized in **Table 1**.

RESULTS AND DISCUSSION

Simulation Under no-Airflow Conditions

For the case of no airflow, a transient simulation with a time step of 0.2 ms was conducted, as shown in **Figure 3** (W089A00). The time step was determined based on the local Courant number, which should be less than 1.0 for applying the High-Resolution Interface Capturing (HRIC) scheme suited for tracking sharp interfaces. The film interface was expressed by the iso-surface of the void fraction at 0.5. In the simulation, the injected water from the DVI nozzle impinged on the wall and spread in the form of a liquid film. Because the size of a computational cell in CFD is about 70 times smaller than that of a measurement area on the liquid film sensor, it was necessary to spatially average the simulation results for quantitative comparison with the experimental results. Therefore, the calculated film thickness in the areas corresponding to the measurement point on the sensor was extracted and spatially averaged. Then, the averaged thickness was compared with the experimental result and used to validate the CFD simulation.

The front view of the averaged film thickness is compared with the experiment results in **Figure 4**. It was found that the CFD predicted the position of the thick film boundary and the film distribution reasonably. A quantitative comparison of the liquid film thicknesses is shown in **Figure 5A**. The film thicknesses were comparable overall, but there were some points at which the liquid film thickness was greatly underestimated (see the area marked in gray). The points at which significant errors occurred are shown in **Figure 5B**. In the figure, x = 0 corresponds to the center of the broken cold leg, and the peak of the graph appears on the film boundary region. Large discrepancies in film thickness could be seen at positions where the change in the film thickness was large in the film boundary region. Nevertheless, the CFD model predicted the peak value of the film thickness and the position at which the value appears well, which is important for the prediction of the ECC bypass induced by entrainment.

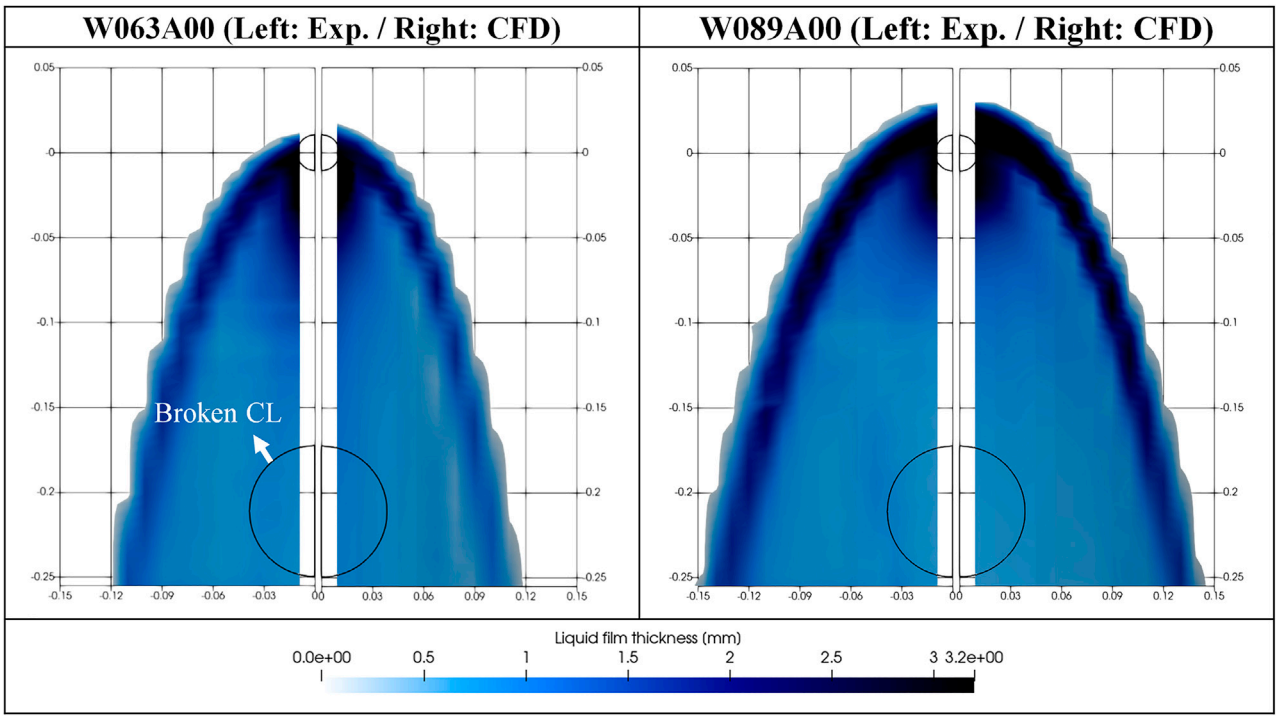

FIGURE 4 | Comparison of liquid film distributions.

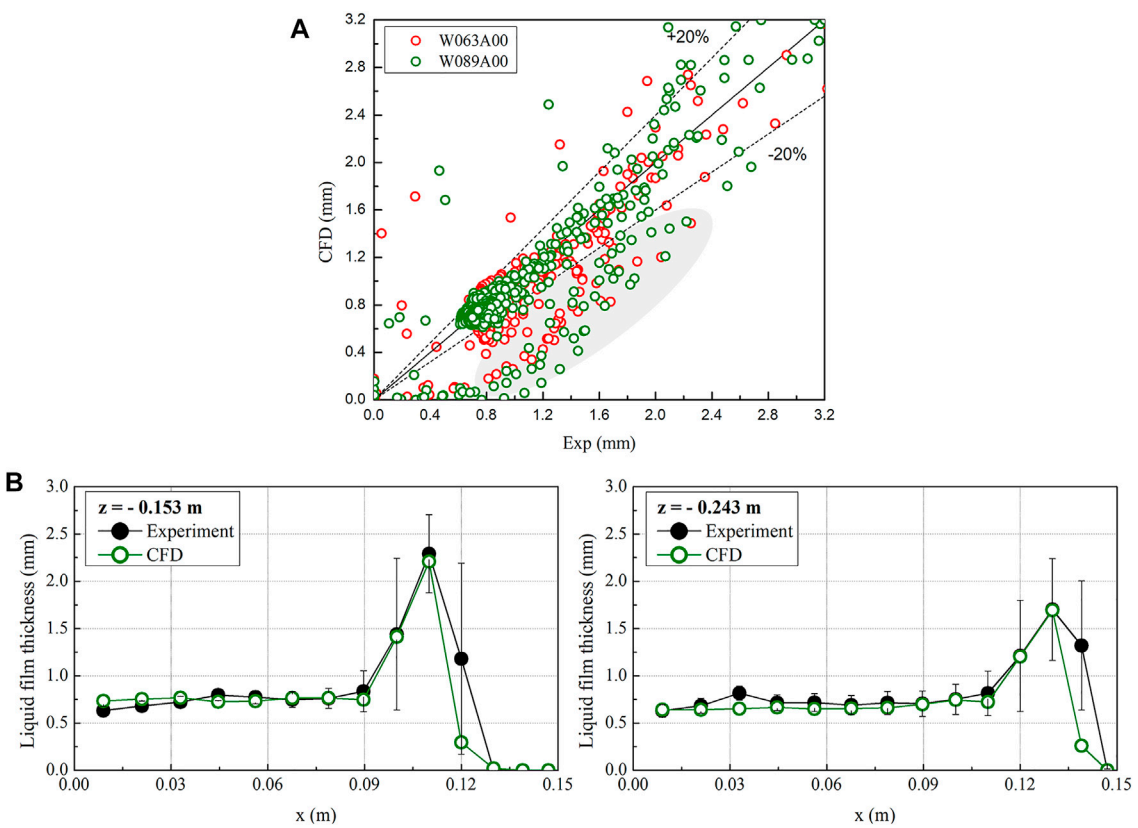

FIGURE 5 | (A) Quantitative comparison of liquid film thickness. **(B)**. Large discrepancies in film thicknesses near the film boundary (W089A00).

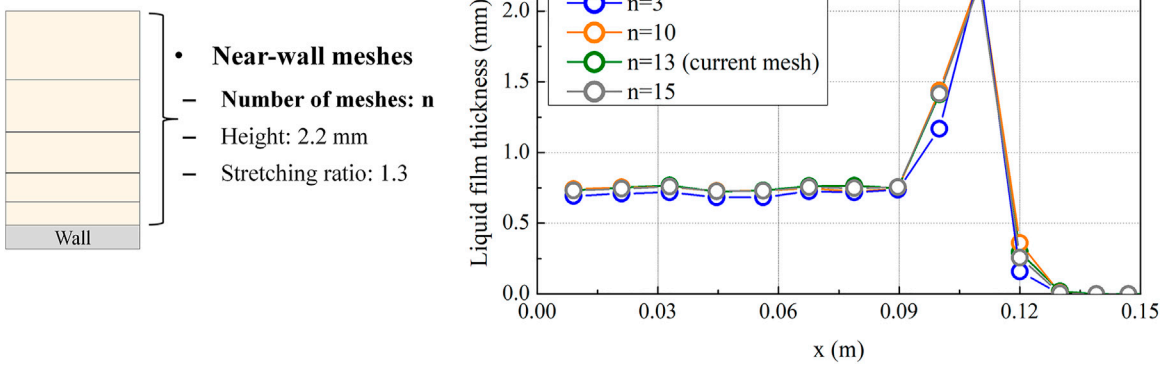

FIGURE 6 | Sensitivity test for near-wall meshes.

To confirm the validity of using the current mesh configuration near the wall where the liquid film is formed, the effect of the mesh size on the film thickness prediction was investigated as shown in **Figure 6**. In the case of a coarse mesh (n = 3), the film thickness was predicted to be thinner than in other cases. When the number of near-wall meshes was greater than 10, the film thickness converged to a specific value. Consequently, taking into consideration the computational cost, the current mesh configuration (n = 13) was judged to be adequate for describing the film behavior.

Simulation Under Airflow Conditions

To simulate the film off-take phenomenon with airflow, the boundary conditions for the two intact cold legs were set as the velocity inlets. **Figure 7** shows the streamline of the airflow in the computational domain. The injected air first impinges against the inner wall of the downcomer, and radial airflow is formed near each intact cold leg. Then, the air flows to the broken cold

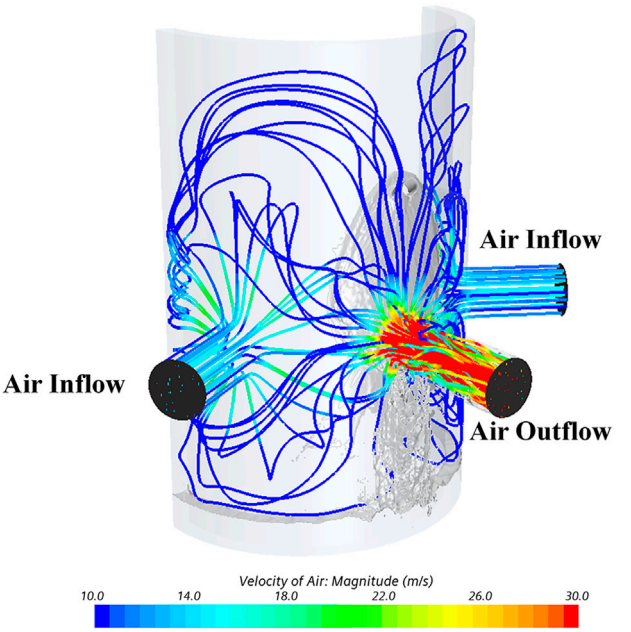

FIGURE 7 | Streamline of airflow (W063A26).

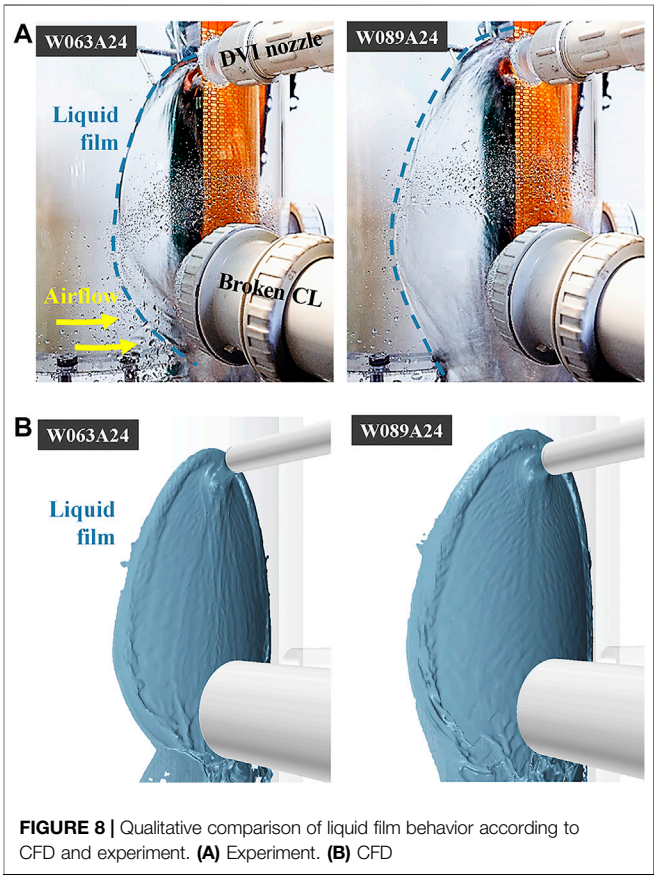

FIGURE 8 | Qualitative comparison of liquid film behavior according to CFD and experiment. **(A)** Experiment. **(B)** CFD

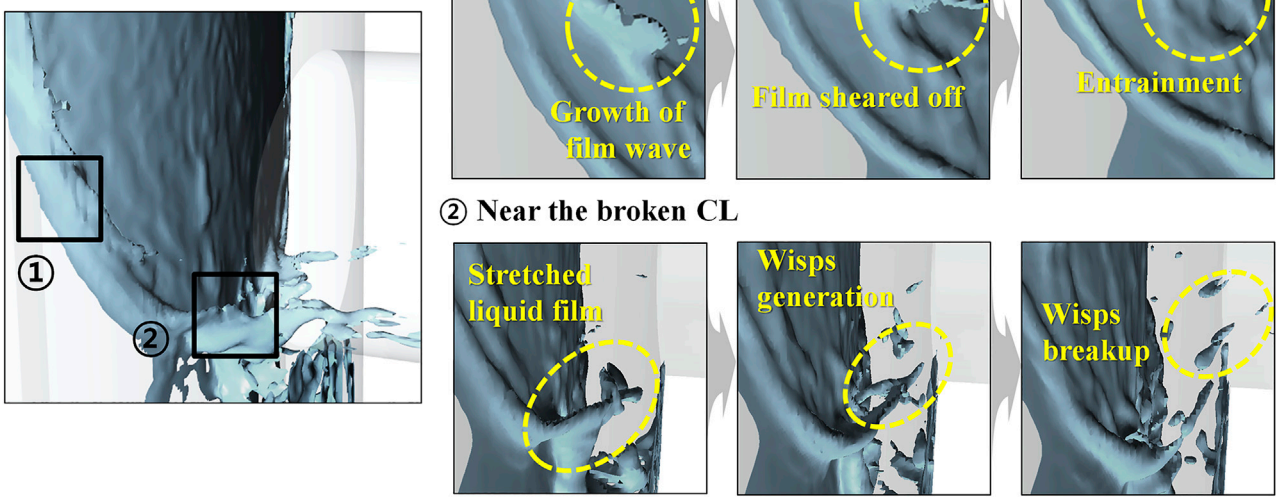

FIGURE 9 | Principal mechanisms of ECC bypass phenomenon (W063A24).

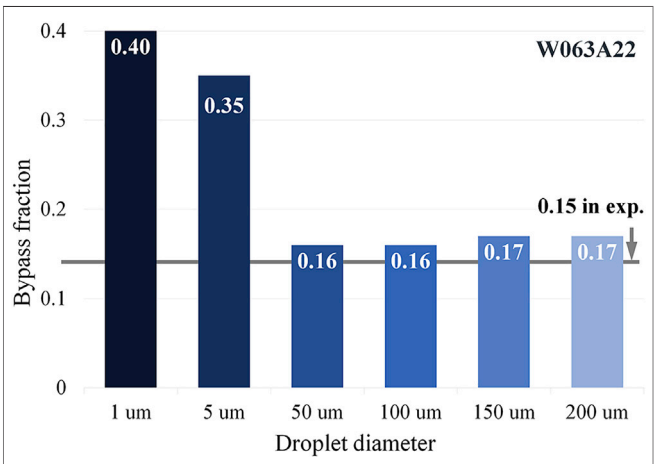

FIGURE 10 | Bypass fraction versus droplet diameter (W063A22).

leg, which narrows the spreading width of the liquid film and leads to film off-take.

The results obtained for the shape of the liquid film were compared with visual observations from the SNU experiment as shown in **Figure 8**. The visual observations (**Figure 8A**) show that the flow rate of the liquid film affects how much the film boundary is dragged for a given air flow rate. When the film flow rate is higher, the film boundary is dragged less by the airflow because of the greater momentum of the film flow. As shown in **Figure 8B**, the CFD simulation also successfully reproduced this film behavior.

Based on the simulation results, two mechanisms were found to contribute to ECC bypass, as shown in **Figure 9**. The first mechanism is the entrainment phenomenon that occurred at the thick film boundary. This mechanism involved the roll wave formed at the thick film being sheared off by the airflow and droplets then being generated from the roll wave. These generated droplets flowed into the broken cold leg with the airflow. If the liquid film boundary spreads farther from the broken cold leg, the bypass rate could be inferred to decrease because the position of the film boundary is related to the distance the droplets must travel toward the break. The second mechanism is the film off-take phenomenon that occurred near the broken cold leg. Under conditions of high airflow, the thick film region appeared near the broken cold leg as the gravitational and interfacial friction forces were balanced, creating a hanging liquid film. This thick film could easily be stretched by the airflow, and wisps in the form of large liquid lumps were generated. Then, the wisps that flowed to the broken cold leg retained their shape or broke up into droplets. These principal mechanisms of ECC bypass detected in the CFD simulation results were also confirmed in a previous experimental study (Choi and Cho, 2002). Thus, it was qualitatively demonstrated that the proposed CFD model can accurately predict the film off-take phenomenon, including the entrainment at the thick film boundary.

As described above, the prediction accuracy of the ECC bypass rate is determined by the behavior of the liquid film and the detached liquid (wisps and droplets). Therefore, further investigations of the parameters that affect the liquid phase behavior by means of quantitative assessment of simulation results are needed.

Determination of Droplet Diameter

When airflow toward the broken cold leg occurred, the spreading width of the liquid film became narrower, and entrainment

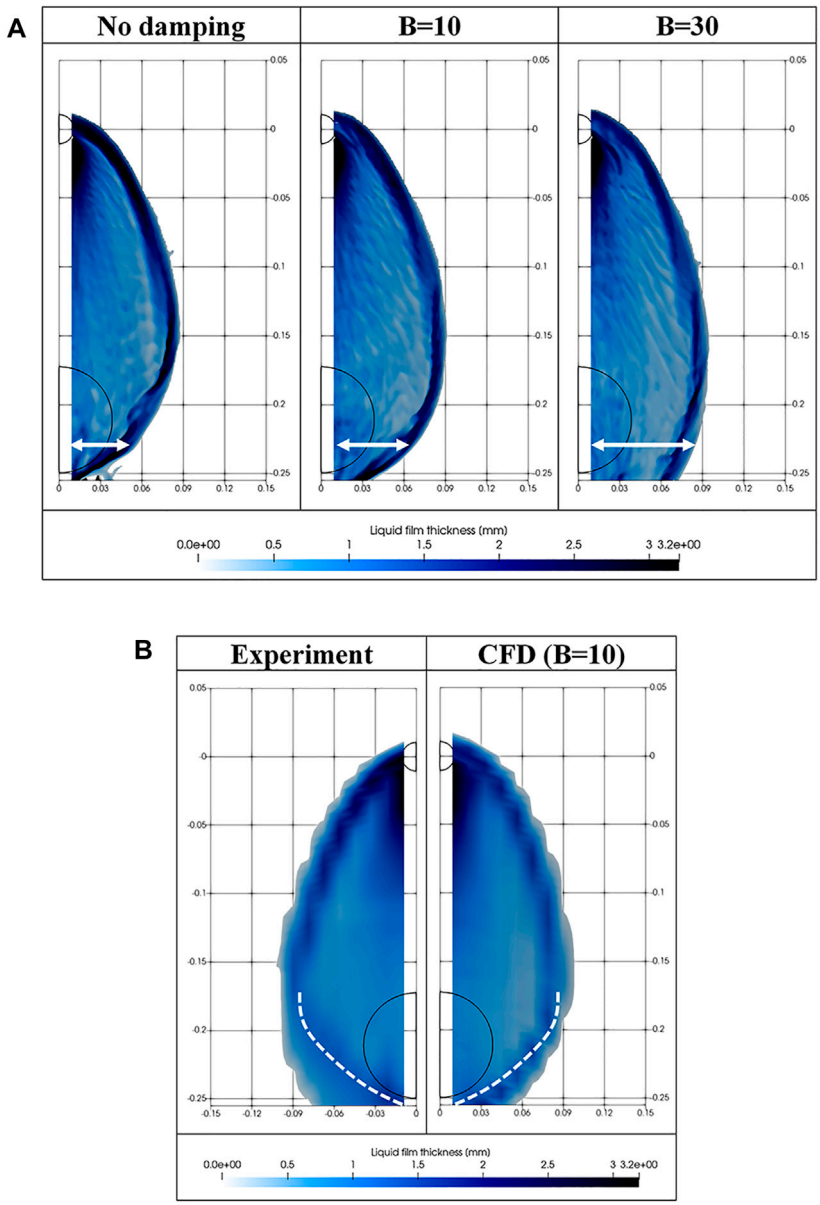

FIGURE 11 | (A) Effect of B on spreading width of liquid film (W063A24). **(B)**. Comparison of film boundary position for ***B*** = 10 (W063A24).

occurred from the liquid film boundary. Under the flow conditions for the simulation, the entrainment started to occur when $j_{g,o}$ reached 20 m/s regardless two different liquid flow rates, which was also confirmed in the experiment. This indicates that the sensitivity of the gas inertia related to the interfacial shear stress is dominant for determining the onset of entrainment. The generated droplets flowed to the broken cold leg with the airflow and contributed to the ECC bypass. Among these droplets, those that the mesh could not resolve because of their small size were treated with the mixture approach. To determine the slip velocity for the unresolved droplets, the droplet diameter had to be known, but it was not measured in the SNU experiment. It can however be estimated that the mean droplet diameter would be in the range of approximately 100–200 μm, based on existing empirical correlations (Tatterson et al., 1977; Kataoka et al., 1983) and the results of experiments (Zaidi et al., 1998; Hurlburt and Hanratty, 2002; Westende, 2008) in which the droplet diameter was measured under conditions similar to those of the SNU experiment. Therefore, in this study, simulations were performed for droplet diameters in the range of 100–200 μm, and a reasonable diameter was determined based on the calculated ECC bypass fraction. The simulations for determining the droplet diameter were carried out under relatively low airflow conditions ($j_{g,o} \leq 22\ m/s$) to minimize the effect of wisps generated by strong airflow on the bypass fraction, so that the droplet size effect could be independently confirmed.

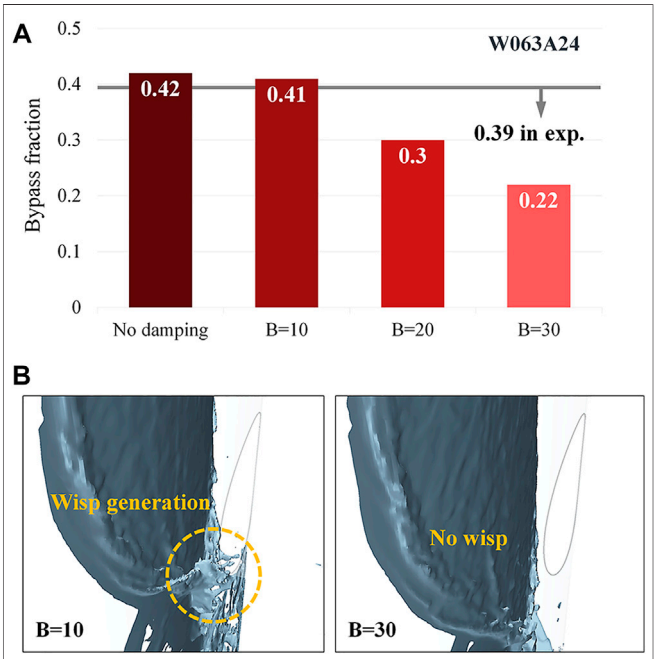

FIGURE 12 | (A) Effect of B on bypass fraction (W063A24). **(B)** Different film off-take phenomena depending on B value (W063A24).

Figure 10 shows the variation in the ECC bypass fraction with the droplet diameter. The bypass fraction was obtained from the water injection rate and the water flow rate to the broken cold leg, as follows.

$$(\text{Bypass fraction}) = \frac{\dot{m}_{f,break}}{\dot{m}_{f,in}} \tag{18}$$

As the droplet diameter increased, the drag coefficient and the phase slip velocity increased according to **Eqs 6–10**. The increase in the slip velocity indicates the decrease in the velocity of the unresolved droplets. Accordingly, the ECC bypass fraction decreased as the droplet diameter increased. It was confirmed that the bypass fraction was nearly saturated with at droplet diameter of 50 μm. When the VOF model was applied, the bypass fraction was overestimated by more than two times because phase slip was not considered for the dispersed phase flow. Based on fact that a 150 μm droplet diameter in the VOF–slip model yielded reasonable bypass fraction prediction results for this condition, a droplet diameter of 150 μm was used for all simulation cases.

Effect of Interface Turbulence Damping

Under high-airflow conditions ($j_{g,o} > 22\,m/s$), the spreading width of the liquid film became much narrower, and a thick film was formed near the broken cold leg. A strong airflow toward the broken cold leg made the thickened film stretch, generating wisps. This implies that not only the unresolved droplet behavior but also the liquid film and wisp behavior are major factors that affect the ECC bypass fraction under high-airflow conditions. This free-surface behavior is closely related to interfacial friction, which may have to be reduced using the Egorov damping model. Therefore, the effect of the damping coefficient B on the simulation results was investigated.

Figure 11A shows snapshots of the film spreading width for different values of B (W063A24). As B increases, the spreading width of the liquid film near the broken cold leg increases because of reduced interfacial friction. As shown in **Figure 11B**, the CFD model was able to predict the film boundary most comparable to the experiment results for $B = 10$. In the figure, the dotted white lines indicate the peak position of the film boundary confirmed in the SNU experiment.

The effect of B on the bypass fraction is shown in **Figure 12A**. When the turbulence was not damped at the film interface, the overestimated interfacial friction made the spreading width of liquid film excessively narrow, which caused a large error in predicting the bypass fraction. It should be noted that the calculated bypass fraction for $B = 10$ was the most comparable to the experiment results. This means that accurate simulation of the free-surface behavior achieved by adopting a suitable B value led to reliable

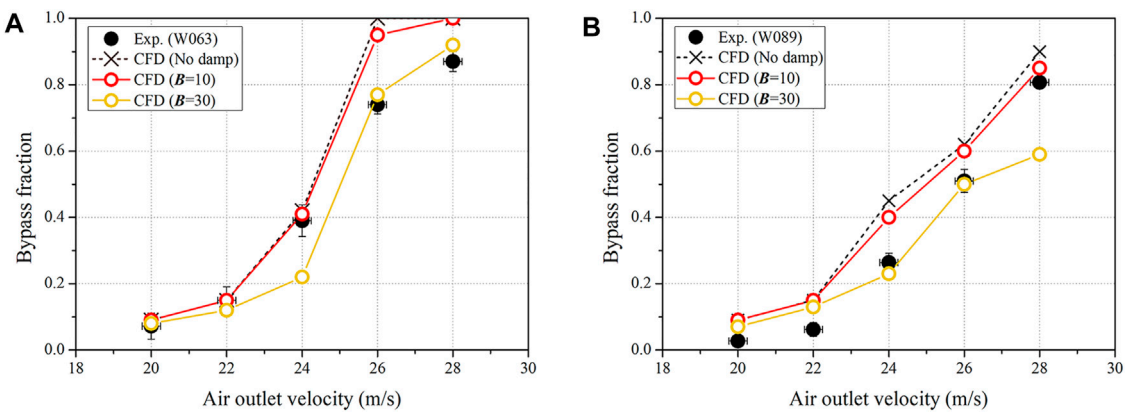

FIGURE 13 | (A) vf = 0.63 m/s, **(B)** vf = 0.89 m/s. Change in bypass fraction with ***B***.

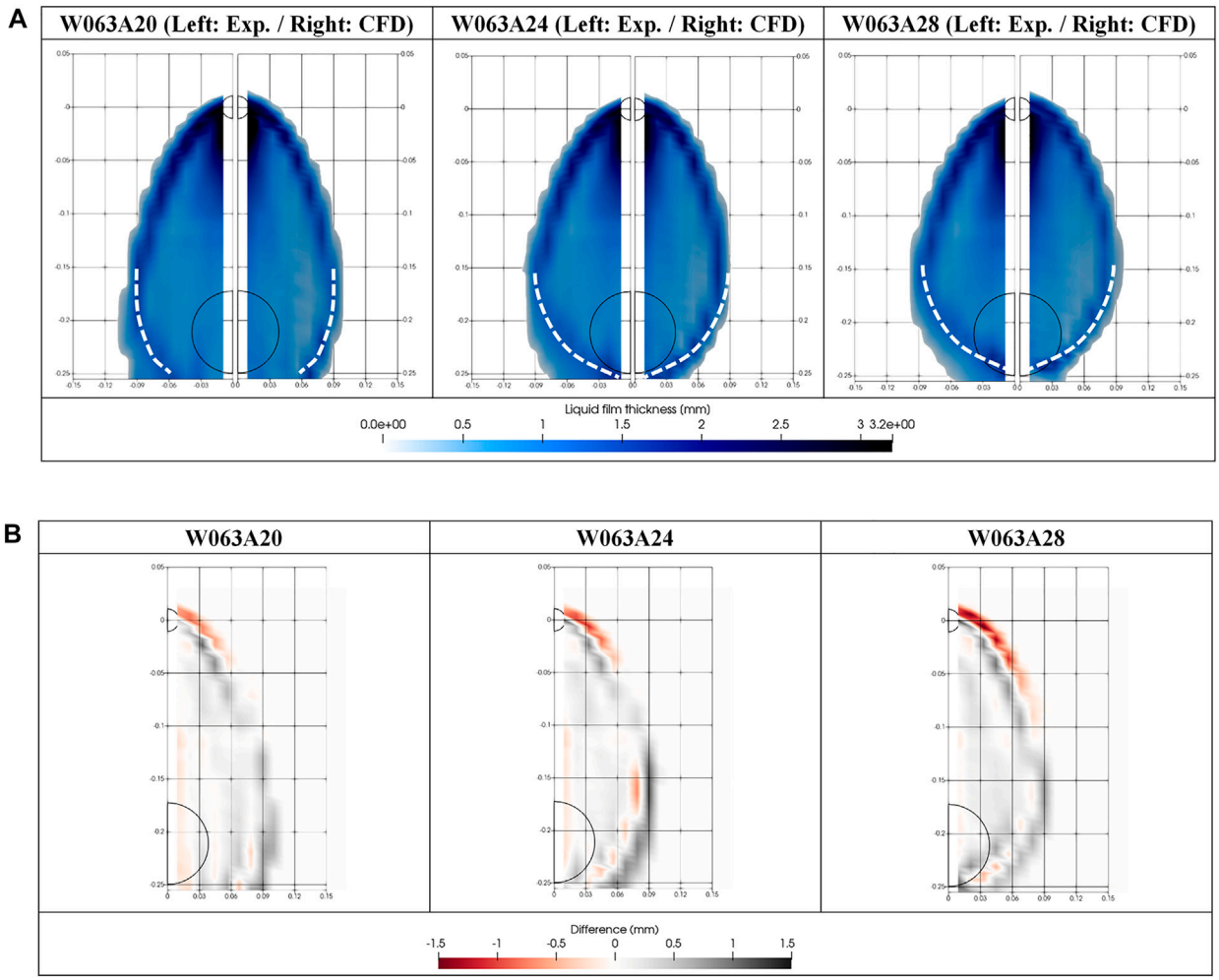

FIGURE 14 | (A) Comparison of liquid film thicknesses. **(B)** Liquid film thickness differences between the experiment and CFD.

prediction of the bypass fraction as well. The prediction of the film spreading width is directly related to the position at which droplets are generated, as well as the formation of wisp flow around the broken cold leg, as shown in **Figure 12B**. If an excessive damping effect occurs at B = 30, wisp flow is not generated around the broken cold leg because of the excessively wide liquid film width, and as a result, the bypass rate is reduced.

Figure 13 illustrates the calculated bypass fraction for B values of 0, 10, and 30 for each simulation case. The figure shows that the appropriate value of B depends on the flow conditions, which is consistent with the results of previous studies described in *Interface Turbulence Damping* Section . Under low-airflow conditions, for which the $j_{g,o}$ is less than 22 m/s, B has little effect on the bypass fraction, which can be predicted well even without the damping model. This means that there is no need to dampen the interface turbulence when the velocity difference between the phases at the interface is small, which can no longer be regarded as wall-like behavior. When $j_{g,o}$ exceeds 22 m/s, the appropriate value of the interface turbulence damping coefficient ranges from 10 to 30 in terms of B and from 2.7×10^{-5} m to 5.4×10^{-5} m in terms of δ. It is worth noting that the range of δ identified in the present study is consistent with the results reported by Frederix et al. (2018) (in which the maximum value of δ was 10^{-4} m). However, finding an appropriate value for B or δ for each flow condition by means of multiple simulations is a very time-consuming process; hence, modeling of interface turbulence damping for various flow conditions is required in future research.

The predicted liquid film width and thickness obtained using a suitable value of B was compared with the experiment results, as shown in **Figure 14**. Although the spreading width of the liquid film was under-predicted in the CFD simulation, the peak position of the film boundary was comparable. Because entrainment mostly occurs at the thick film, it can be deduced that the accurate prediction of these peak positions results in reliable prediction of the ECC bypass phenomenon by the CFD simulation.

CONCLUSION

The air–water film flow at an RV upper downcomer (SNU experiment) was simulated using the STAR-CCM + code. Using the VOF–slip model, both the free surface flow and dispersed flow could be properly modeled. The key parameters in the simulation were found to be the droplet diameter and the interface turbulence damping coefficient. A parametric study was performed to determine the value of the parameters that would yield a reasonable liquid film thickness and ECC bypass fraction, consistent with that measured in the SNU experiment. The suitable droplet diameter was determined to be 150 μm, and the suitable range for the interface turbulence damping coefficient was found to be from 0 to 30, for the conditions of the SNU experiment. However, because determining B by means of several time-consuming simulations is not ideal, physical modelling of B for various flow conditions is required in future research. The validation results confirm that the VOF–slip model can describe the behavior of the liquid film and unresolved droplets appropriately. This results in an improvement in the accuracy of the prediction of the ECC bypass fraction in comparison to the results obtained using the conventional VOF model. The validation procedures and simulation results in this study demonstrate the applicability of the VOF–slip CFD model to two-phase nuclear reactor safety problems. The local parameters obtained from the CFD simulation can be used to develop physical models for macroscopic tools.

DATA AVAILABILITY STATEMENT

The original contributions presented in the study are included in the article/Supplementary Material, further inquiries can be directed to the corresponding author.

AUTHOR CONTRIBUTIONS

C-JC and HC contributed to conception and design of the study. C-JC carried out the CFD simulation. C-JC and HC contributed to the interpretation of the simulation results. C-JC wrote the first draft of the manuscript. C-JC and HC contributed to manuscript revision, read, and approved the submitted version.

FUNDING

This work was supported by the Nuclear Safety Research Program through the Korea Foundation of Nuclear Safety (KoFONS) with the financial resources granted by the Nuclear Safety and Security Commission (NSSC) of the Republic of Korea (No. 2003005).

REFERENCES

Bae, K. H., Kwon, T. S., Chung, Y. J., Lee, W. J., Kim, H. C., and Bae, Y. Y. (2000). "Pre-test Analysis for the KNGR LBLOCA DVI Performance Test Using a Best Estimate Code MARS," in *NTHAS2: Second Japan-Korea Symposium on Nuclear Thermal Hydraulics and Safety, Fukuoka, Japan. Oct. 15-18.*

Cho, H. K., Yun, B. J., Song, C.-H., and Park, G. C. (2005). Experimental Study for Multidimensional ECC Behaviors in Downcomer Ann with Direct Vessel Injection Mode during the LBLOCA Reflood Phase. *J. Nucl. Sci. Technol.* 42 (6), 549–558. doi:10.1080/18811248.2004.9726421

Choi, C.-J., and Cho, H. K. (2019). Investigation on Emergency Core Coolant Bypass with Local Measurement of Liquid Film Thickness Using Electrical Conductance Sensor Fabricated on Flexible Printed Circuit Board Fiexible Printed Circuit Board. *Int. J. Heat Mass Transfer* 139, 130–143. doi:10.1016/j.ijheatmasstransfer.2019.05.019

Choi, C. J., and Cho, H. K. (2020). Efiect of Asymmetric Airfiow on Liquid Film Behavior and Emergency Core Coolant Bypass in the Downcomer Geometry of a Nuclear Reactor Pressure Vessel. *Int. Commun. Heat Mass Transfer* 117, 104765. doi:10.1016/j.icheatmasstransfer.2020.104765

Conner, M., Baglietto, E., and Elmahdi, A. (2010). CFD Methodology and Validation for Single-phase Flow in PWR Fuel Assemblies. *Nucl. Eng. Des.* 240, 31. doi:10.1016/j.nucengdes.2009.11.031

Egorov, Y., Boucker, M., Martin, A., Pigny, S., Scheuerer, M., and Willemsen, S. (2004). *Validation of CFD Codes with PTS-Relevant Test Cases*. 5th Euratom Framework Programme ECORA Project, 91–116.

Fabre, J., Suzanne, C., and Masbernat, L. (1987). Experimental Data Set No. 7: Stratified Flow, Part I: Local Structure. *MultScienTechn* 3 285–301. doi:10.1615/multscientechn.v3.i1-4.120

Fan, W., Li, H., and Anglart, H. (2019). Numerical Investigation of Spatial and Temporal Structure of Annular Flow with Disturbance Waves. *Int. J. Multiphase Flow* 110, 256–272. doi:10.1016/j.ijmultiphaseflow.2018.10.003

Feng, T., Wang, M., Song, P., Liu, L., Tian, W., Su, G. H., et al. (2019). Numerical Research on thermal Mixing Characteristics in a 45-degree T-junction for Two-phase Stratified Flow during the Emergency Core Cooling Safety Injection. *Prog. Nucl. Energ.* 114, 91–104. doi:10.1016/j.pnucene.2019.03.009

Frederix, E. M. A., Mathur, A., Dovizio, D., Geurts, B., and Komen, E. M. J. (2018). Reynolds-averaged Modeling of Turbulence Damping Near a Large-Scale Interface in Two-phase Flow. *Nucl. Eng. Des.* 333, 122130. doi:10.1016/j.nucengdes.2018.04.010

Fulgosi, M., Lakehal, D., Banerjee, S., and De Angelis, V. (2003). Direct Numerical Simulation of Turbulence in a Sheared Airwater Flow with a Deformable Interface. *J. Fluid Mech.* 482, 319–345. doi:10.1017/s0022112003004154

Gada, V. H., Tandon, M. P., Elias, J., Vikulov, R., and Lo, S. (2017). A Large Scale Interface Multi-Fluid Model for Simulating Multiphase Flows. *Appl. Math. Model.* 44, 189–204. doi:10.1016/j.apm.2017.02.030

Hirt, C. W., and Nichols, B. D. (1981). Volume of Fluid (VOF) Method for the Dynamics of Free Boundaries. *J. Comput. Phys.* 39 (1), 201–225. doi:10.1016/0021-9991(81)90145-5

Hohne, T., Porombka, P., and Moya Saez, S. (2002). Validation of AIAD Sub-models for Advanced Numerical Modelling of Horizontal Two-phase Flows. *Fluids* 5, 102. doi:10.3390/fluids5030102

Hurlburt, E., and Hanratty, T. (2002). Measurement of Drop Size in Horizontal Annular Flow with the Immersion Method. *Exp. Fluids* 32, 692–699. doi:10.1007/s00348-002-0425-8

Kataoka, I., Ishii, M., and Mishima, K. (1983). Generation and Size Distribution of Droplet in Annular Two-phase Flow. *J. Fluids Eng.* 105 (2), 230–238. doi:10.1115/1.3240969

Khan, I., Wang, M., Abdul Basit, M., Tian, W., Su, G., and Qiu, S. (2021). CFD Modeling of Liquid Entrainment through Vertical T-junction of Fourth Stage Automatic Depressurization System (ADS-4). *Ann. Nucl. Energ.* 159, 108317. doi:10.1016/j.anucene.2021.108317

Khan, I., Wang, M., Zhang, Y., Tian, W., Su, G., and Qiu, S. (2020). Two-phase Bubbly Flow Simulation Using CFD Method: A Review of Models for Interfacial Forces. *Prog. Nucl. Energ.* 125, 103360. doi:10.1016/j.pnucene.2020.103360

Kwon, T.-S., Choi, C.-R., and Song, C.-H. (2003a). Three-dimensional Analysis of Flow Characteristics on the Reactor Vessel Downcomer during the Late Reflood Phase of a Postulated LBLOCA. *Nucl. Eng. Des.* 226, 255–265. doi:10.1016/s0029-5493(03)00181-x

Kwon, T.-S., Yun, B.-J., Euh, D.-J., Chu, I.-C., and Song, C.-H. (2003b). Multidimensional Mixing Behavior of Steam-Water Flow in a Downcomer Annulus during LBLOCA Reflood Phase with a Direct Vessel Injection Mode. *Nucl. Technol.* 143 (1), 57–64. doi:10.13182/nt03-a3397

Kwon, T. S., Choi, N. H., and Song, C. H. (2007). *A Feasibility of a CFD Simulation for an ECC Bypass*. PyeongChang, Korea: Transactions of the Korean Nuclear Society Autumn Meeting.

Lo, S., and Tomasello, A. (20102010). *Recent Progress in CFD Modelling of Multiphase Flow in Horizontal and Near-Horizontal Pipes*. Banff: Canada. Paper presented at the 7th North American Conference on Multiphase Technology.

Menter, F. R. (1994). Two-equation Eddy-Viscosity Turbulence Models for Engineering Applications. *AIAA J.* 32 (8), 1598–1605. doi:10.2514/3.12149

Murao, Y., Akimoto, H., Sudoh, T., and Okubo, T. (1982). Experimental Study of System Behavior during Reflood Phase of PWR-LOCA Using CCTF. *J. Nucl. Sci. Technol.* 19 (9), 705–719. doi:10.1080/18811248.1982.9734205

Rashidi, M., and Banerjee, S. (1990). The Effect of Boundary Conditions and Shear Rate on Streak Formation and Breakdown in Turbulent Channel Flows. *Phys. Fluids A: Fluid Dyn.* 2, 1827–1838. doi:10.1063/1.857656

Schiller, L., and Naumann, Z. (1935). A Drag Coefficient Correlation. *Zeit Ver. Deutsch. Ing.* 77, 318–320.

Siemens (2018). *STAR-CCM+ User Guide*. Version 13.02. TX Plano: Siemens PLM Software

Tatterson, D. F., Dallman, J. C., and Hanratty, T. J. (1977). Drop Sizes in Annular Gas-Liquid Flows. *Aiche J.* 23, 68–76. doi:10.1002/aic.690230112

Wang, M., Wang, Y., Tian, W., Qiu, S., and Su, G. H. (2021). Recent Progress of CFD Applications in PWR thermal Hydraulics Study and Future Directions. *Ann. Nucl. Energ.* 150, 107836. doi:10.1016/j.anucene.2020.107836

Westende, J. M. C. (2008). *Droplets in Annular-Dispersed Gas-Liquid Pipe-Flows, PhD Thesis*. The Netherlands: Delft University of Technology TUDelft.

Yang, J.-H., Cho, H.-K., Kim, S., Euh, D.-J., and Park, G.-C. (2015). Experimental Study on Two-Dimensional Film Flow with Local Measurement Methods. *Nucl. Eng. Des.* 294, 137–151. doi:10.1016/j.nucengdes.2015.07.073

Yang, J.-H., Choi, C.-J., Cho, H.-K., Euh, D.-J., and Park, G.-C. (2017). Assessment of wall Friction Model in Multi-Dimensional Component of MARS with Air-Water Cross Flow experiment. *Nucl. Eng. Des.* 312, 106–120. doi:10.1016/j.nucengdes.2016.06.018

Yoon, D.-H., Bang, Y. S., and Cheong, A.-J. (2015). CFD Analysis of Effects of Cross Flow on Water Injection of DVI+. *Ann. Nucl. Energ.* 80, 172–177. doi:10.1016/j.anucene.2015.02.009

Yun, B. J., Cho, H. K., Euh, D. J., Song, C.-H., and Park, G. C. (2004). Scaling for the ECC Bypass Phenomena during the LBLOCA Reflood Phase. *Nucl. Eng. Des.* 231, 315–325. doi:10.1016/j.nucengdes.2004.04.005

Yun, B. J., Kwon, T. S., Euh, D. J., Chu, I. C., Park, W. M., Song, C. H., et al. (2002). Direct ECC Bypass Phenomena in the MIDAS Test Facility during LBLOCA Reflood Phase. *J. Korean Nucl. Soc.* 34, 421–432. doi:10.1115/icone10-22224

Yun, B. J., Kwon, T. S., Song, C. H., Euh, D. J., Park, J. K., Cho, H. K., et al. (2000). *Air/Water Test on Direct ECC Bypass during LBLOCA Reflood Phase of KNGR, 2000 KNS Autumn Meeting*. Daejeon, Korea: Korea Nuclear Society.

Zaidi, S. H., Altunbas, A., and Azzopardi, B. J. (1998). A Comparative Study of Phase Doppler and Laser Diffraction Techniques to Investigate Drop Sizes in Annular Two-phase Flow. *Chem. Eng. J.* 71, 135–143. doi:10.1016/s1385-8947(98)00125-9

Conflict of Interest: The authors declare that the research was conducted in the absence of any commercial or financial relationships that could be construed as a potential conflict of interest.

NOMENCLATURE

Δn Cell size across the interface [m]

ρ Density [kg/m^3]

$v_{d,i}$ Diffusion velocity [m/s]

C_D Drag coefficient [s]

d_s Droplet diameter [m]

g Gravitational acceleration [m/s^2]

A_i Interfacial area density [/m]

B Interface turbulence damping coefficient

$\dot{m}$ Mass flow rate [kg/s]

v Mixture velocity [m/s]

τ_s Particle relaxation time [s]

Re Reynolds number

$v_{p,s}$ Slip velocity [m/s]

b Specific body force [m/s^2]

j Superficial velocity [m/s]

σ Surface tension [N/m]

μ Viscosity [kg/m-s]

α Void fraction

V_{grid} Volume of grid [m^3]

Subscript

f Liquid phase

g Gas phase

o Outlet

p Primary phase

s Secondary phase

frontiers | Frontiers in Energy Research

METHODS
published: 12 May 2022
doi: 10.3389/fenrg.2022.891074

Modeling and Simulation Analysis on Mixing Characteristics of Two-Phase Flow Around Spacer Grid

Y. Xiao[1], T. C. Duan[1], Quan-Yao Ren[2]*, Xiao-Yu Zheng[3], Meiyin Zheng[2] and Rui He[2]*

[1]School of Flight Technology, Civil Aviation Flight University of China, Guanghan, China, [2]Science and Technology on Reactor System Design Technology Laboratory, Nuclear Power Institute of China, Chengdu, China, [3]Department of ATM, Civil Aviation Flight University of China, Guanghan, China

The spacer grid has a significant impact on the thermal-hydraulic characteristics of the rod bundle channel, which directly determines the possibility of a boiling crisis. The multi-phase flow model coupling boiling model is proposed to acquire the secondary flow and void fraction for subcooled flow boiling in the fuel assembly. Compared with the experimental data, the RNG k–ε turbulence model is selected in the current research. In addition, the thermal-hydraulic parameters of subcooled boiling flow in the 5 × 5 rod bundle with a spacer grid are studied focusing on the influence of different arrangements of mixing vanes. It is found that the distribution of the vapor phase is greatly influenced by the intensity and flow direction of secondary flow. In addition, the thermal–hydraulic characteristics in the sub-channels and around the fuel rods are investigated, which demonstrates that uniform crossflow makes vapor harder to accumulate around the fuel rods. Furthermore, the mixing characteristics of different types of spacer grids are also discussed in detail.

Keywords: spacer grid, boiling two-phase flow, void fraction, sub-channels, CFD

OPEN ACCESS

Edited by:
Mingjun Wang,
Xi'an Jiaotong University, China

Reviewed by:
Luteng Zhang,
Chongqing University, China
Yixiang Liao,
Helmholtz Association of German Research Centres (HZ), Germany

****Correspondence:***
Y. Xiao
xiaoyi_cafuc@foxmail.com
Quan-Yao Ren
renquanyao@foxmail.com

Specialty section:
This article was submitted to Nuclear Energy, a section of the journal Frontiers in Energy Research

Received: *07 March 2022*
Accepted: *06 April 2022*
Published: *12 May 2022*

Citation:
Xiao Y, Duan TC, Ren Q-Y, Zheng X-Y, Zheng M and He R (2022) Modeling and Simulation Analysis on Mixing Characteristics of Two-Phase Flow Around Spacer Grid. Front. Energy Res. 10:891074. doi: 10.3389/fenrg.2022.891074

HIGHLIGHTS

- The multiphase flow model coupling boiling model has been applied in the fuel assembly.
- The distribution of secondary flow, secondary flow intensity, axial velocity, and void fraction has been discussed.
- The thermal-hydraulic characteristics of sub-channels and fuel rod surfaces have been analyzed.
- The numerical results of secondary flow intensity are proven to be in good agreement with experimental data.

1 INTRODUCTION

The main purpose of thermal-hydraulic research in the nuclear reactor is to improve the heat transfer and its uniformity so that to keep more heat away from the fuel rod surface and increase the critical heat flux. As a component existing in the heating section of the fuel rod, the spacer grid directly affects the flow and heat transfer characteristics in the fuel assembly. The swirl flow in a rod bundle with a spacer grid includes natural convection and forced convection. Natural convection occurs in the rod bundle sub-channel, while forced convection is produced due to the strong disturbance of the fluid caused by the leaf springs, dimples, and mixing vanes in the spacer grid. The 17 × 17 rod bundles are used in the nuclear reactor. However, considering the experimental conditions, the number of

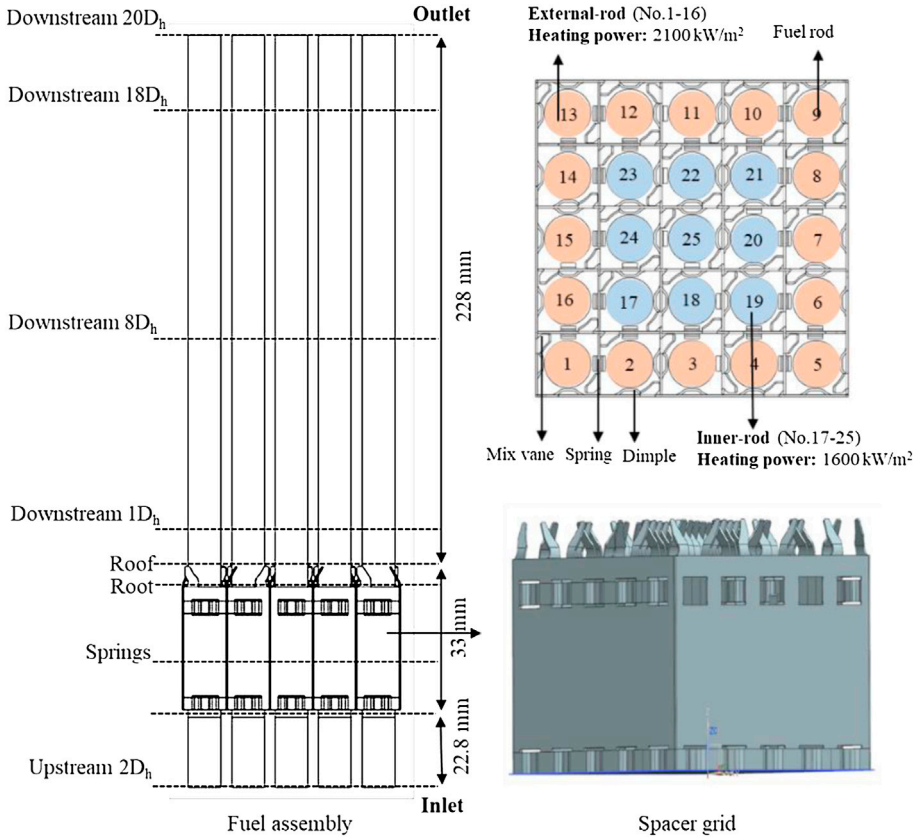

FIGURE 1 | Structure of the rod bundle with spacer grid and arrangement of the rods.

TABLE 1 | Distance of different cross sections.

Cross section	Distance (mm)
Upstream of spacer grid 2D_h	0
Upstream of spacer grid 1D_h	11.4
Upstream of spacer grid 0D_h	22.8
Middle of springs	41.8
Roof of mixing vanes	65
Downstream of spacer grid 0D_h	66.8
Downstream of spacer grid 1D_h	78.2
Downstream of spacer grid 2D_h	89.6
Downstream of spacer grid 3D_h	101
Downstream of spacer grid 4D_h	112.4
Downstream of spacer grid 5D_h	123.8
Downstream of spacer grid 6D_h	135.2
Downstream of spacer grid 7D_h	146.6
Downstream of spacer grid 8D_h	158
Downstream of spacer grid 9D_h	169.4
Downstream of spacer grid 10D_h	180.8
Downstream of spacer grid 11D_h	192.2
Downstream of spacer grid 12D_h	203.6
Downstream of spacer grid 13D_h	215
Downstream of spacer grid 14D_h	226.4
Downstream of spacer grid 15D_h	237.8
Downstream of spacer grid 16D_h	249.2
Downstream of spacer grid 17D_h	260.6
Downstream of spacer grid 18D_h	272
Downstream of spacer grid 19D_h	283.4

TABLE 2 | Operating conditions in two-phase flow.

Boundary condition	Value
Material	Steam–water
Outlet pressure (MPa)	12.5
Inlet mass velocity (kg/m^2·s)	1,990
Inlet temperature (K)	601
Inlet void fraction (steam)	0.39
Inner-rod power (kW/m^2)	1,600
External-rod power (kW/m^2)	2,100
Axial power distribution	Uniform

fuel rods is reduced for research. Among so many studies, the rod bundle size used by the researchers is not consistent, and 5 × 5 rod bundles have been relatively more studied.

For the experimental study of the thermal-hydraulic characteristics in fuel assemblies, there are some differences in the obtained parameters due to different measurement methods. Rehme (1987; 1989) studied the effect of velocity boundary layer reconstruction downstream of the spacer grid on heat transfer and analyzed the fluid pulsation between channels through the measured interleaving coefficient. It is shown that the exchange of heat is mainly caused by the hydrodynamic interaction between channels. Wu and Trupp (1993) measured the axial velocity of the

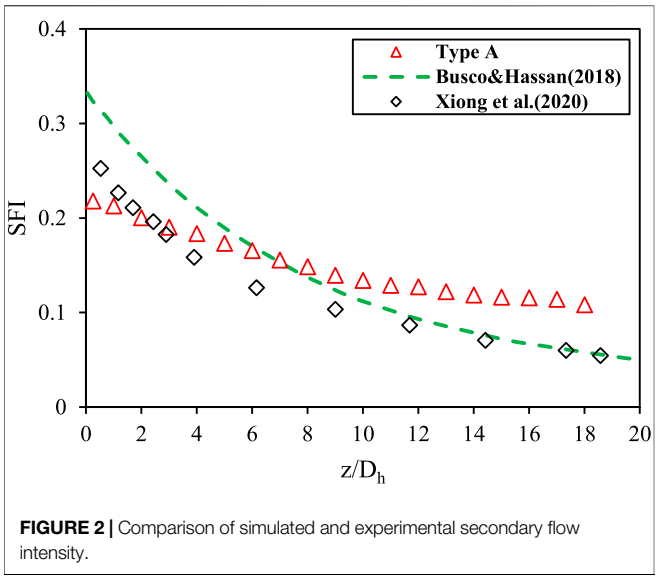

FIGURE 2 | Comparison of simulated and experimental secondary flow intensity.

coolant between the rod bundles and the distribution of turbulent kinetic energy by a hotline instrument. The experimental results showed that the axial turbulent kinetic energy of the sub-channels between the rod bundle and the near-wall surface was higher than that of the channels between the rod bundles, and there were differences in the flow patterns as well. McClusky et al. (2002) determined that sub-channel heat transfer is mainly influenced by mixed and interlaced flows. Although the experimental measurements were unsatisfactory due to the shortcomings of the experiment itself, the study still has an important academic value. In the current experimental research, laser Doppler velocimetry (LDV) and particle image velocimetry (PIV) measurements were heavily used because of the high accuracy of measuring the flow field parameters in the fuel assembly. Based on the 4 × 4 rod bundle geometry model with the spacer grid (mixing wing only) in the rectangular frame, Shen et al. (1991) used LDV to measure the crossflow downstream of the spacer grid in the center of the sub-channel and the transverse flow in the gap between fuel rods. This study shows that the turbulence intensity downstream of the spacer grid decays to almost zero at $21D_h$, and the greater the angle of the mixing vane, the stronger the crossflow is formed. By using 1-D LDV measurement, Yang and Chung (1996) and Yang and Chung (1998) characterized the variation trend of axial velocity upstream and downstream of fuel assembly with the 5 × 5 rod bundle and the turbulent flow between rod bundles and then explained the turbulent kinetic energy caused by the spacer grid and the physical phenomenon of gradual attenuation of turbulent intensity along the downstream of the spacer grid. The results show that turbulent swirl flow and forced swirl flow occur at $10D_h$ and $20D_h$ downstream of the grid, respectively, and the swirl factor reaches the maximum near the spacer grid. Through the flow field downstream of the grid measured by the LDA system, Han et al. (2009) studied the traditional split vane and the new series arranged mixing vane. It shows that the vortex generated by the split mixing vane usually reaches the maximum at $4–5D_h$ and then decays rapidly, and the strong swirl flow generated by the new mixing vane can last up to $20D_h$. The flow field distribution in the rod bundle channel upstream and downstream of the spacer grid was, respectively, measured with PIV by Dominguez-Ontiveros et al. (2009), Dominguez-Ontiveros et al. (2012), Conner et al. (2013), and Dominguez-Ontiveros and Hassan (2014). The research team has carried out a lot of research work on different rod bundle channels with spacer grids in recent years. They used DPIV and MIR methods to capture the distribution of the flow field in the rod bundle. They deeply analyzed the changes of the flow field before and after the spacer grid and also measured the changes of velocity in the 5 × 5 rod bundle channel and the changes of the turbulent flow pattern and mainstream velocity in the 3 × 3 rod bundle channel. The results show that the vortex decreases gradually downstream of the spacer grid due to interaction between the vortex, which can be used for the validation of the computational fluid dynamics (CFD) calculation. In recent years, with the development of experimental technology, many researchers began to pay attention to the two-phase flow characteristics of the coolant in fuel assemblies. Pham et al. (2014; 2015) used a high-speed camera to study the cross-sectional characteristics of the swirl flow in a 3 × 3 rod bundle channel, which revealed the whole change process of the swirl flow. Arai et al. (2012) studied the cavitation behavior and the two-phase flow behavior of the sub-channel in a 10 × 10 rod bundle channel, measured the void fraction and bubble velocity with the advanced cavitation detection system, and established the dynamic behavior of two-phase flow along the flow direction. Cho et al. (2011) studied the change of droplets in the 6 × 6 rod bundle channel when passing through the spacer grid as well as clarified the process of breaking into smaller droplets after droplet entrainment. By observing the characteristics of two-phase flow in a single channel, Liu et al. (2021) studied the effect of the spacer grid on the bubble behavior and the critical heat flux (CHF). Ren et al. (2018a), Ren et al. (2018b), and Ren et al. (2021) carried out the air–water two-phase flow experiment and determined the distribution characteristic of the two phases in the rod bundle channel by using a miniaturized four-sensor conductivity probe (MFSCP).

Since the experimental method has many limitations in the research of the spacer grid, most of the research is still based on numerical methods. Navarro and Santos (2011) studied the hydraulic performance of the 5 × 5 fuel assembly with a split vane spacer grid. The results showed that the numerical results were in good agreement with the experimental values, which confirmed the feasibility of using the numerical method to study the fuel assembly. Cinosi et al. (2014) used STAR-CCM + software to compare the velocity values measured in the experiment with the results calculated by the four turbulence models. It was considered that the standard k–epsilon, k–omega, and Reynolds tress turbulence models could predict the distribution of average velocity, and the difference between the simulation results of the standard k–ε model and the experimental values was the smallest. Also using STAR-CCM + software, Podila and Rao (2016) used the realizable k–ε, k–ω SST, and Reynolds stress models to simulate 5 × 5 rod bundles with a split spacer grid. The results showed that the axial velocities

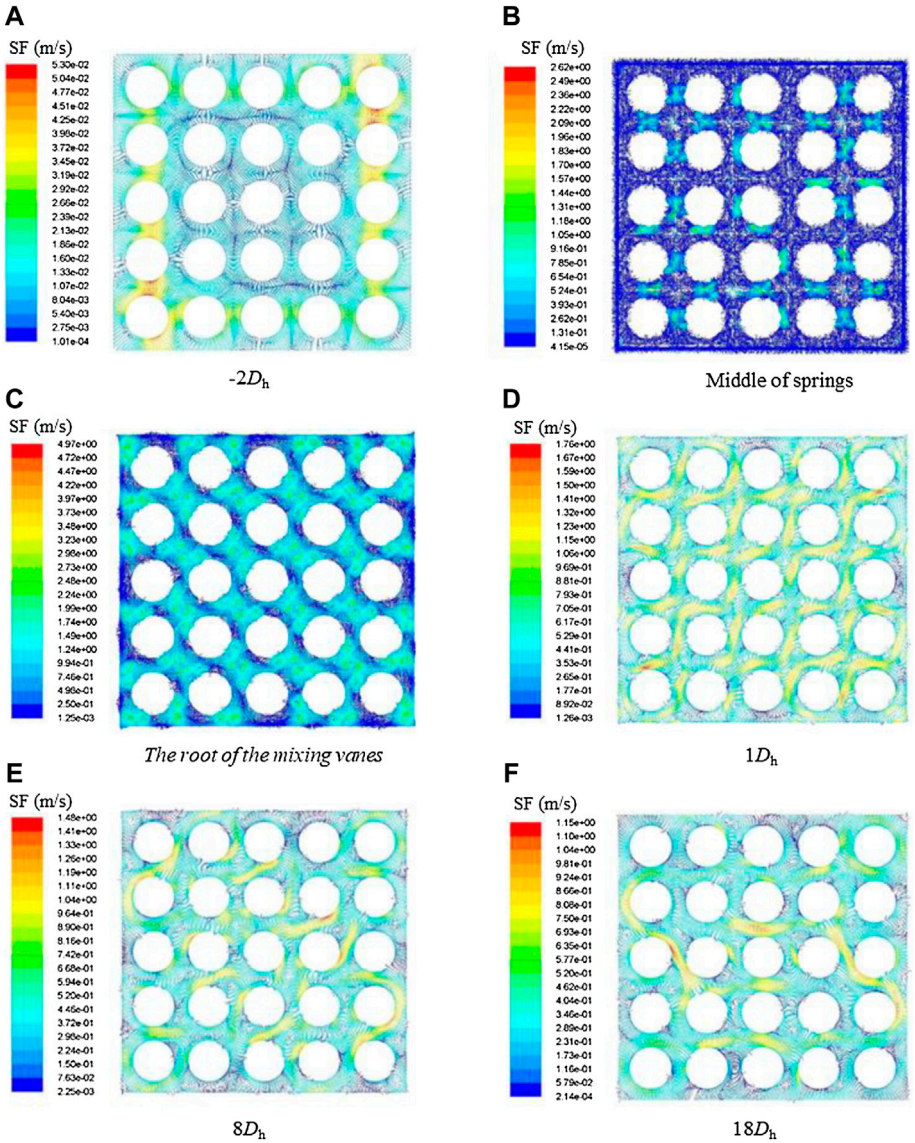

FIGURE 3 | Cross-sectional profile of secondary flow along axial direction.

calculated by the three turbulence models were close to the experimental results, but the turbulence intensity obtained by the realizable k–ε model is the closest to the experimental measurement value. Caraghiaur et al. (2009) studied the turbulent flow behavior in the rod bundle with a spacer grid. The result shows that the turbulence intensity downstream of the spacer grid in the sub-channel gradually decreases to less than the one upstream of the grid, then continues to increase until the distance between the two grids is the largest, and then decreases again. However, there is no such sudden increase in the turbulence intensity in the side channel and corner channel, and there is only a little increase when flowing after the mixing vanes. Liu and Ishiwatari (2013) studied the single-phase flow behavior of the sub-channel center under unsteady conditions. The results show that the geometric structure of the sub-channel center, the gap width between fuel rods, and the size of fuel rods have a great influence on the flow. Agbodemegbe et al. (2015; 2016) studied the influence of mixing vanes on crossflow according to the velocity changes of fluid along the deflection direction of vanes as well as in the transverse and axial directions. By comparing with the experimental data, the authors believed that the realizable k–ε model could not accurately predict the velocity fluctuation and established a model to calculate the crossflow resistance coefficient. Liu and Ferng (2010), Chen et al. (2014), and Lin et al. (2014) carried out in-depth research on the thermal-hydraulic characteristics of the spacer grid using the CFD method and studied the single-phase flow and heat transfer of the spacer grid with single-channel and the 5 × 5 rod bundle channel with spacer grid, respectively. The study of heat transfer characteristics in a single channel shows that the

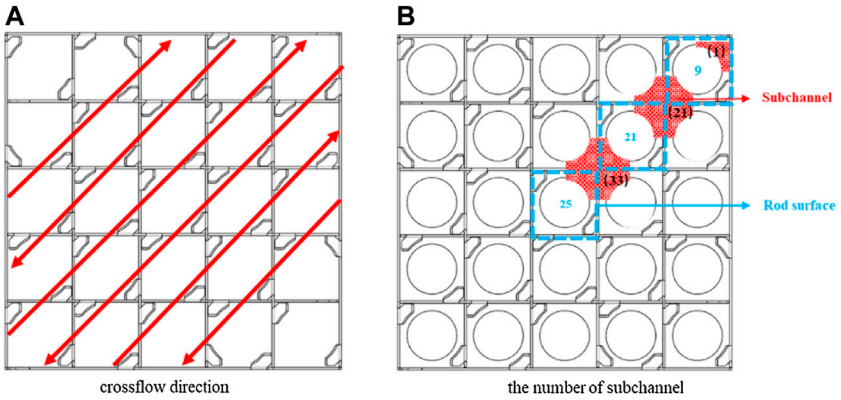

FIGURE 4 | Flow direction diagram of secondary flow and sub-channel number.

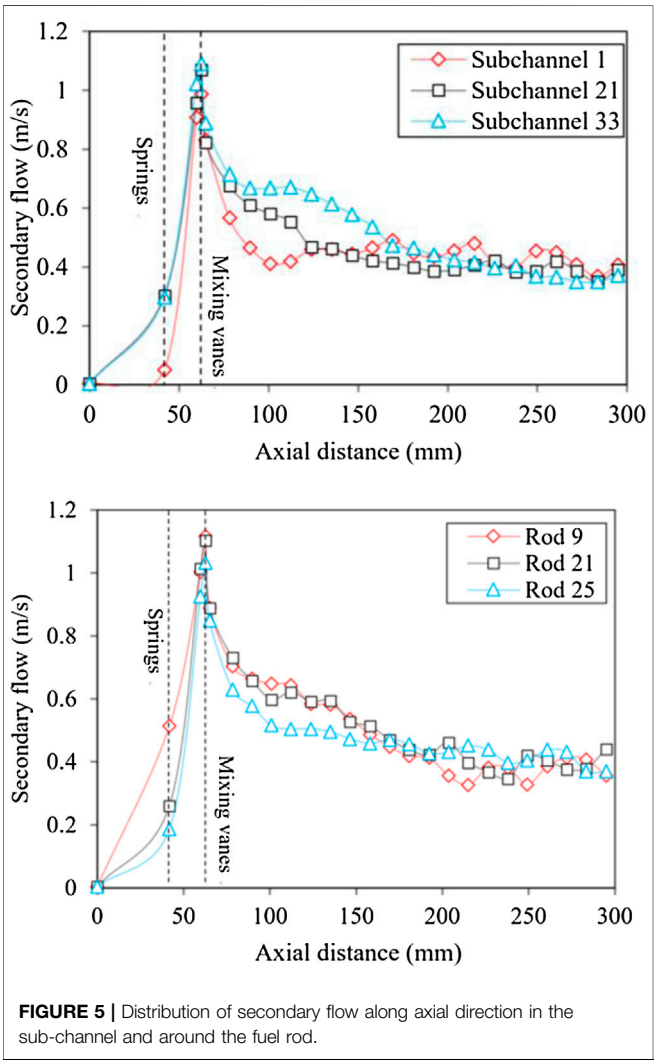

FIGURE 5 | Distribution of secondary flow along axial direction in the sub-channel and around the fuel rod.

grid with mixing vanes has a great influence on flow and heat transfer. The comparison between the calculated Nusselt number and the experimental value shows that the numerical method can be used to study the thermal-hydraulic characteristics in fuel assemblies. At the same time, the study also analyzed the thermal-hydraulic characteristics of the rod bundle channel under the condition of non-uniform heating. The results show that there is no obvious difference between the steady-state calculation and the unsteady-state calculation of the 5 × 5 rod bundle channel, and the SST k–ω turbulence model is suitable for the geometric structure. Based on the comparison results of the Nu number downstream of the grid and in the circumferential direction of the fuel rod, it is found that the flow characteristics are the main factors that determine the law of heat transfer. Bakosi et al. (2013) used large eddy simulation (LES) to study the turbulence and mechanical behavior in a single channel. The study shows that LES is suitable for studying the wear between fuel rods and grids. Anglart and Nylund (1996) and Anglart et al. (1997) studied the axial and transverse void distribution in the sub-channel and predicted the variation trend of vapor and liquid flow fields in two-phase flow. Considering the influence of buoyancy drift in the rod bundle channel, Carlucci et al. (2004) explained the relationship between swirl flow in turbulence under the single-phase and two-phase conditions. Yang et al. (2021) proposed a multiphase flow model based on the Euler equation, studied the axial distribution of thermal-hydraulic parameters of subcooled boiling in the 3 × 3 rod bundle channel, and obtained the conclusion that the heat transfer characteristics of the coolant will be significantly reduced when the deflection angle of mixing vanes is greater than 30°. Wang et al. (2020), Khan et al. (2020), and Zhang et al. (2022) have also developed and applied the high fidelity thermal-hydraulic models using the CFD method to analyze flow and heat transfer characteristics of the rod bundles.

Currently, most of the CFD research work is based on the single-phase condition for the thermal-hydraulic characteristics of the rod bundle with the spacer grid. Considering the two-phase flow, especially the two-phase flow under boiling conditions, the two-phase calculation model and the boiling phase transition model needs to be further improved. The CFD calculation results of the single-phase flow in the complex fuel assembly with the grid have limited guidance for the design of the fuel assembly. In addition, the calculation results of single-phase flow cannot

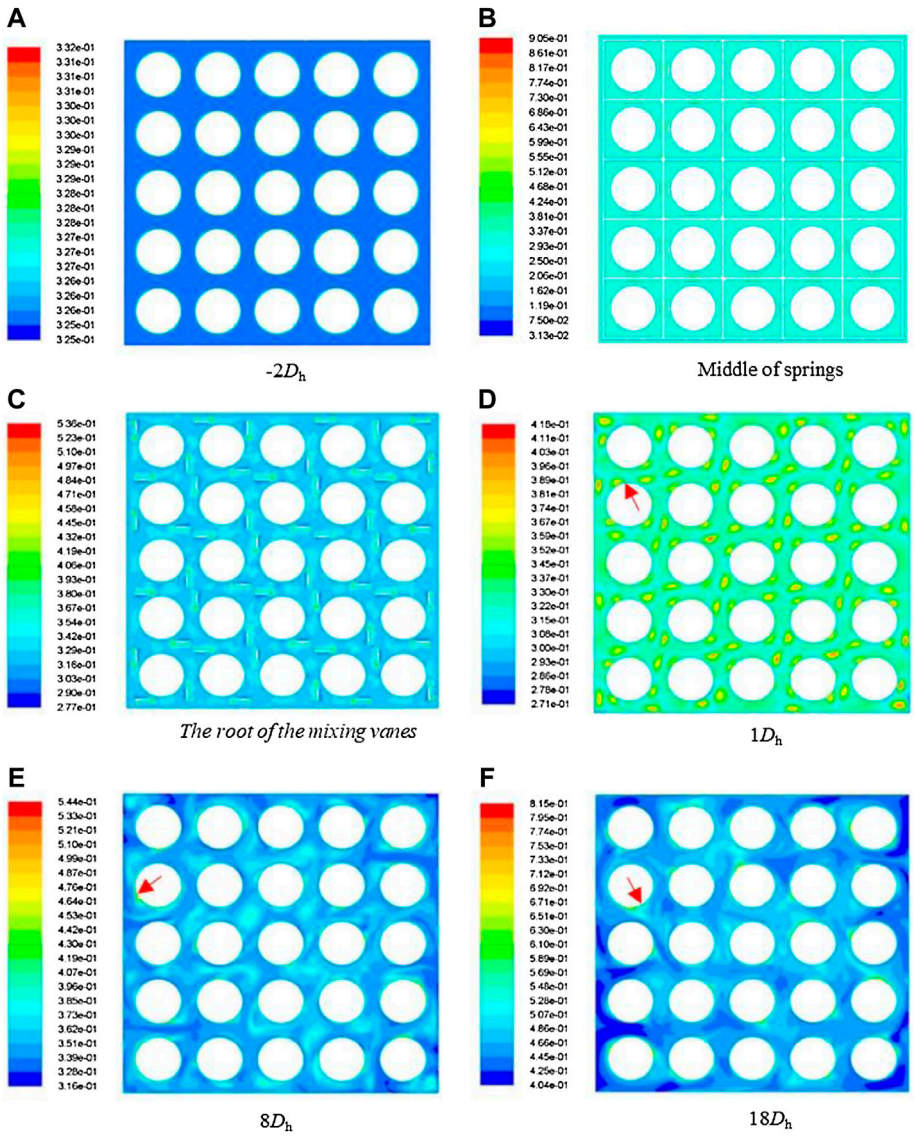

FIGURE 6 | Variations of vapor-phase distribution along axial direction.

reflect the real two-phase flow, especially the distribution characteristics of the void fraction in the fuel assembly and the influence of void fraction distribution characteristics on the critical heat flux. Therefore, it is of great significance to study the two-phase flow in the fuel assembly based on the CFD method (Wang et al., 2021).

In this article, the two-phase flow model and the boiling phase transition model for the complex fuel assembly are first established. Second, based on the CFD method to calculate the two-phase flow in the fuel assembly, the two-phase flow behavior characteristics, including the mixing characteristic of the spacer grid, the secondary flow evolution, the sub-channel characteristics as well as the void fraction distribution characteristics, and their influence on the CHF are studied. The quantitative analysis of the flow parameters will provide theoretical support for the thermal design of the fuel assembly.

2 GEOMETRIC MODEL AND NUMERICAL METHOD

2.1 Geometric Model and Boundary Conditions

The geometric configuration used in this article is a 5 × 5 rod bundle channel with a spacer grid as shown in **Figure 1**, and the fuel assembly is placed in a 65 mm × 65 mm rectangular frame. The total length of the fuel assembly is 283.8 mm, including the length of the spacer grid downstream and upstream as 228 and 22.8 mm, respectively, and the spacer grid of height 33 mm. A

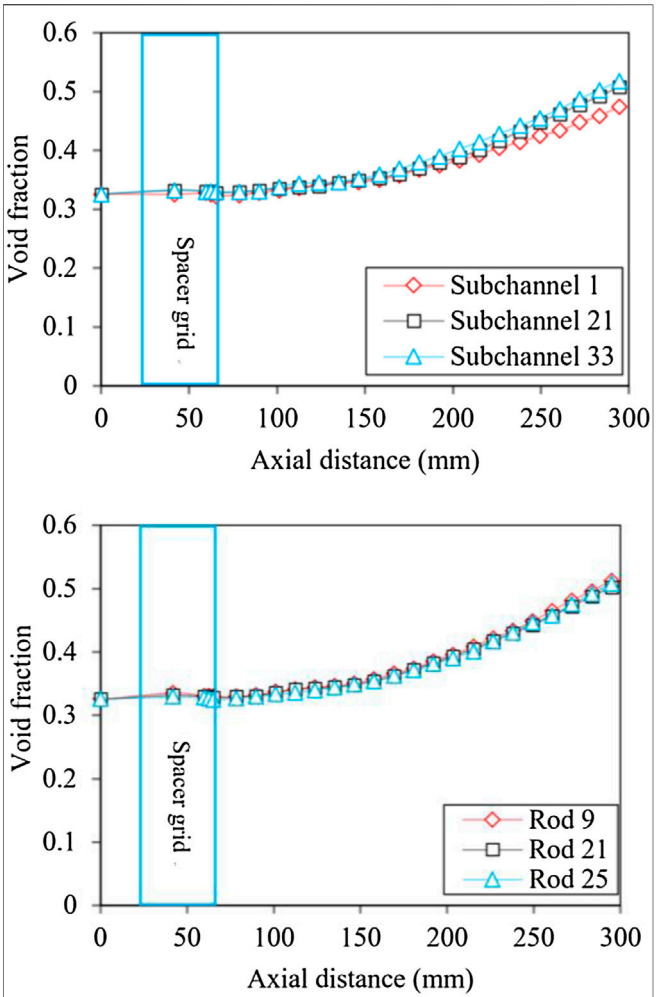

FIGURE 7 | Average void fraction along axial direction in the sub-channel and around the fuel rod.

total of 25 fuel rods were used in the fuel assembly with an outer diameter of 9.5 mm, and the rod bundle hydraulic diameter (D_h) is 11.4 mm. The rod bundle with spacer grid is divided into different sections along the flow direction, for which the distance is shown in **Table 1.** The geometry structure of the spacer grid is very complex, which consisted of dimples, springs, and mixing vanes. On the one hand, the springs and dimples can clamp fuel rods to prevent sloshing. On the other hand, these structural components will produce a very strong secondary flow. Furthermore, the mixing vanes can induce secondary flow intensity, which affects the phase distribution characteristics of the two-phase flow downstream of the spacer grid in the fuel assembly.

The iterative method of pressure coupling velocity field is performed in this study. The boundary conditions involved are shown in **Table 2**. A uniform velocity inlet with a mass flow rate of 1990 kg/m^2 s is considered, a pressure (12.5 MPa) outlet boundary condition is used for the outlet, the inlet temperature and inlet average void fraction are set to 601 K and 0.39, respectively, and the wall boundary is a no-slip boundary condition. Due to the power distribution of the fuel rods in a nuclear reactor are not uniform, the different heating power of fuel rods is imposed as shown in **Figure 1**, in which the heating power is 2,100 kW/m^2 for the 16 fuel rods (No. 1–16) outside the fuel assembly and 1,600 kW/m^2 for the 9 fuel rods (No. 17–25) inside.

2.2 Mathematical Model

2.2.1 Turbulence Model

For most research on flow and heat transfer characteristics in fuel assemblies, the turbulence model generally uses the Reynolds-averaged Navier–Stokes equations due to the complexity of the geometric model. By comparing the experimental measurements with the numerical results, the standard k–ε model can predict the mean velocity better (Cinosi et al., 2014), while the realizable k–ε model calculates the turbulence intensity closer to the experimental measurements (Podila and Rao, 2016). The author of this article concluded that the RNG k–ε model is more suitable for the current calculation conditions through a comparative analysis between the sub-channel temperature obtained by experimental measurements and the results calculated by different turbulence models in previous studies (Chen et al., 2016). In addition, the flow and heat transfer characteristics downstream of the spacer grid under single-phase conditions have been investigated. This article is a further discussion of the thermal-hydraulic characteristic of the downstream of spacer grid under two-phase conditions based on the previous study; therefore, the turbulence model, mesh analysis, near-wall treatment, and numerical solution involved in this study are the same as in the article (Chen et al., 2016) and no longer described in this article. Thus, the RNG k–ε model is used for the flow field and temperature distribution inside the rod bundle. In the present study, Fluent software is adopted to solve nonlinear equations.

2.2.2 Mixture Model

Considering that the void fraction in fuel assembly exceeds 10% and the vapor–liquid interface is not required to be tracked, the mixture model is selected to solve the mass, momentum, and energy conservation equations of vapor–liquid two-phase flow in rod bundles. Although the Eulerian model considers the flow of the vapor phase and the liquid phase, it requires huge computational resources and is more difficult to converge. Therefore, the mixture model is applied to calculate the two-phase flow of fuel assemblies with a spacer grid in this article.

Mixture model continuity equation:

$$\frac{\partial}{\partial t}(\rho m) + \nabla \cdot \left(\rho_m \vec{v}_m\right) = 0 \tag{1}$$

$$\vec{v}_m = \frac{\sum_{k=1}^{n} \alpha_k \rho_k \vec{v}_k}{\rho_m} \tag{2}$$

$$\rho_m = \sum_{k=1}^{n} \alpha_k \rho_k \tag{3}$$

where $\vec{v}_m$ and ρ_m are average mass velocity and mixture density, respectively, and α_k is the volume fraction of the k phase.

Mixture model momentum equation:

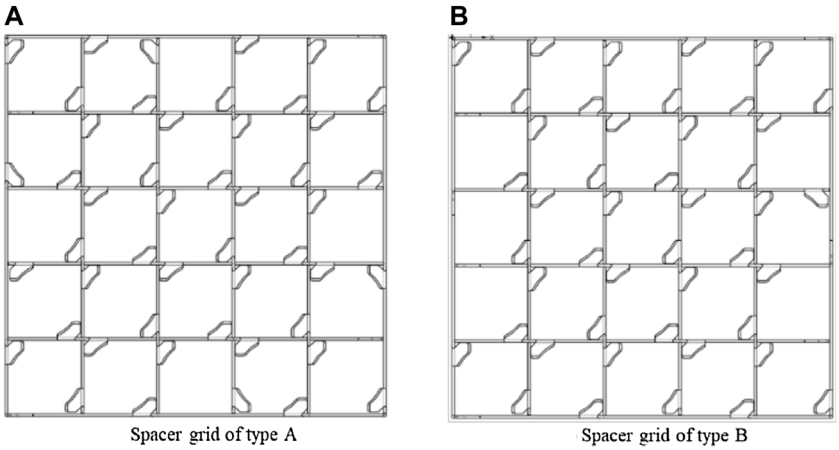

FIGURE 8 | Structure of the spacer grids **(A)** and **(B)**.

$$\frac{\partial}{\partial}\left(\rho_m\vec{v}_m\right)+\nabla\cdot\left(\rho_m\vec{v}_m\vec{v}_m\right)=-\nabla p+\nabla\cdot\left[\mu_m\left(\nabla\vec{v}_m+\nabla\vec{v}_m^T\right)\right]+\rho_m\vec{g}+\nabla\cdot\left(\sum_{k=1}^{n}\alpha_k\rho_k\vec{v}_{dr,k}\vec{v}_{dr,k}\right) \tag{4}$$

$$\vec{v}_{dr,k}=\vec{v}_k-\vec{v}_m \tag{5}$$

$$\mu_m=\sum_{k=1}^{n}\alpha_k\mu_k \tag{6}$$

where $\vec{v}_{dr,k}$ is the drift velocity of the k phase and μ_m is the mixture viscosity.

Mixture model energy equation:

$$\frac{\partial}{\partial t}\sum_{k=1}^{n}\left(\alpha_k\rho_kE_k\right)+\nabla\cdot\sum_{k=1}^{n}\left(\alpha_k\vec{v}_k\left(\rho_kE_k+p\right)\right)=\nabla\cdot\left(k_{eff}\nabla T\right) \tag{7}$$

$$k_{eff}=k+k_t \tag{8}$$

where k_{eff} is the effective thermal conductivity and k_t is the turbulent heat conduction. For incompressible phase: $E_k=h_k$.

Volume fraction equation for the secondary phases:

$$\frac{\partial}{\partial t}\left(\alpha_p\rho_p\right)+\nabla\cdot\left(\alpha_p\rho_p\vec{v}_m\right)=-\nabla\cdot\left(\alpha_p\rho_p\vec{v}dr,p\right)+\sum_{q=1}^{n}\left(\dot{m}_{qp}-\dot{m}_{pq}\right) \tag{9}$$

2.2.3 Boling Model

As the heating power increases, fine vapor bubbles start to form on the fuel rod surface and gradually grow into big bubbles on the rod bundle surface. The continuous big bubble separates the heated wall surface from the liquid phase, making a liquid film appear between the big bubble and the heated wall surface. The heated wall delivers energy to the bubble by heat transfer through the micro-layer liquid film, while the vapor–liquid interface transfers energy through convective heat transfer. For the mass transfer process, the vapor generation rate due to the phase change will be calculated based on the energy balance. Therefore, in this article, the process of mass and energy transfer of the phase transition is implanted into the CFD codes through user-defined function (UDF) by considering the heat and mass transfer at the bubble contact area and the phase interface to realize the numerical analysis of the two-phase flow and obtain the phase distribution characteristics in the fuel assembly. The mathematical equations for the mass and energy transfer between phase interfaces during the phase transition are described as follows:

The mass source by phase transition $\Delta\dot{m}$ is defined as

$$\Delta\dot{m}=\dot{m}_{w,n}+\dot{m}_{v,m} \tag{10}$$

where the vapor generation rate on the heated wall $\dot{m}_{w,n}$ and the vapor generation rate on the liquid–vapor interface $\dot{m}_{v,m}$ are defined separately for

$$\dot{m}_{v,m}=\frac{\rho_lc_{p,l}\Delta T_{sub,m}\Delta V_l}{h_{fg}\tau_m} \tag{11}$$

$$\dot{m}_{w,n}=\frac{q_{w,n}A_{w,n}}{h_{fg}} \tag{12}$$

where ρ_l is the density of the liquid phase, $c_{p,l}$ is the specific heat capacity of the liquid phase, $\Delta T_{sub,m}$ is the superheat of the vapor–liquid interface grid, ΔV_l is the liquid phase volume of cell volume, τ_m is bubble relaxation times, $q_{w,n}$ is the heat transfer of cell by the heating wall, $A_{w,n}$ is an area of wall grid, and h_{fg} is the latent heat of vaporization.

3 SIMULATION RESULTS AND DISCUSSION

When the coolant flows through the fuel assembly with the spacer grid, it is affected by the spacer grid belts, springs, dimples, and mixing vanes, which will result in a very strong swirl flow in the lateral direction. Due to the guidance of the design, the mixing of the coolant by the mixing vanes will lead to regular secondary flow

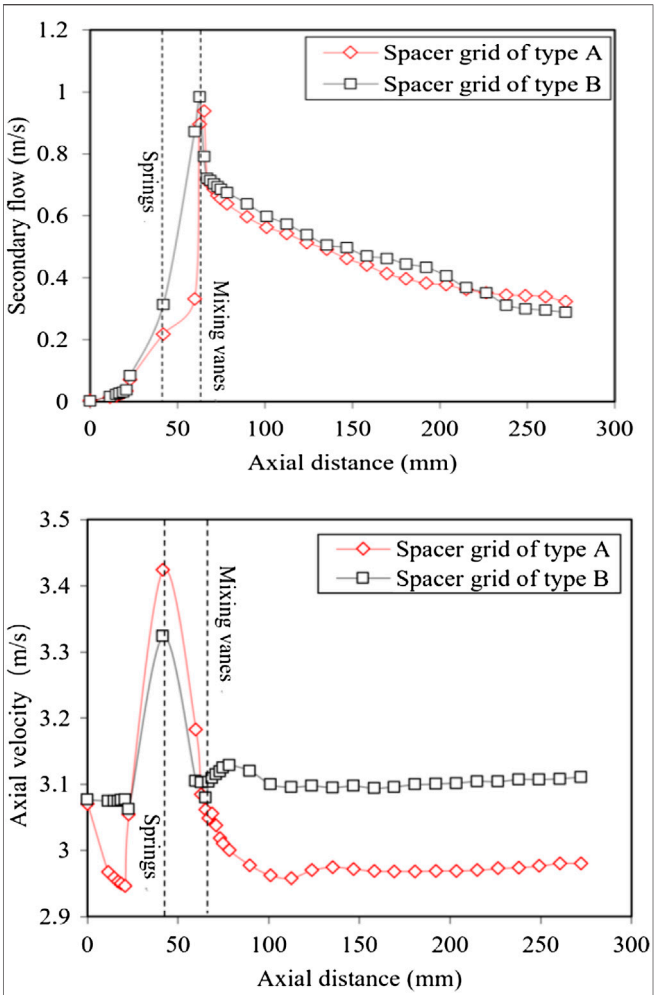

FIGURE 9 | Distribution of velocity along axial direction for different types of the spacer grid.

($SF = \sqrt{V_x^2 + V_y^2}$) downstream of the spacer grid. The strength and the attenuation rates of the secondary flow at the downstream of the spacer grid play an important role in the cooling of fuel assemblies and have a great impact on the accumulation of vapor on the surface of fuel rods. In addition, the secondary flow intensity is also defined (Busco and Hassan, 2018) as **Eq. 13**. As shown in **Figure 2**, the simulation values of secondary flow intensity are compared with the experimental data measured by Xiong et al. (2020) and Busco and Hassan (2018). It is observed in the figure that the variation trends of CFD simulation and experimental data are similar for secondary flow intensity. However, the downstream secondary flow intensity decreases more slowly in this study, and it is about 0.1 in the type A spacer grid at $18D_h$, while the secondary flow intensity already falls to approximately 0.05 in the study of Xiong et al. (2020)and Busco and Hassan (2018).

$$SFI = \frac{1}{A}\sum_i \frac{A_i\sqrt{V_x^2 + V_y^2}}{\overline{V_z}} \tag{13}$$

In this article, the effect of spacer grids on the mixing characteristics of two-phase flows in fuel assemblies, especially the evolution of secondary flow between channels after passing through the spacer grid is investigated. Then, the trends of secondary flow and void fraction in different sub-channels under boiling conditions as well as at the downstream of two different spacer grids are compared. Consequently, the swirl capacity of the mixing vane is quantitatively evaluated.

3.1 The Mixing Characteristics of Spacer Grid With Boiling

3.1.1 The Secondary Flow Distribution Characteristics

Based on the secondary flow distribution under boiling conditions shown in **Figure 3**, it can be found that a strong secondary flow begins to appear at the root of the mixing vane and is located in the inclined direction of the mixing vanes. On the contrary, there is no strong secondary flow in the opposite direction. The phenomenon shows that the secondary flow is mainly caused by the mixing vanes, and the direction of the mixing vanes will directly determine the location of the strong vortex. Comparing the secondary flow on the cross sections at $1D_h$, $8D_h$, and $18D_h$, once the coolant flows through the grid region, the fluid mixing and pulsation between different sub-channels makes a non-uniform distribution of the secondary flow intensity downstream of the spacer grid as shown in **Figure 4**, and different sub-channels will be affected by the energy and mass exchange as well as the wall effects. Because the wall effects of the side sub-channel and corner sub-channel are more obvious than those of the middle sub-channel, the secondary flow of the side sub-channel and middle sub-channel will be smaller. In addition, because of the flow resistance of fuel rods and no further excitation of mixing vanes, the secondary flow continues to weaken at the downstream of the whole spacer grid. As shown in **Figure 3**, the maximum secondary flows of $1D_h$ and $18D_h$ downstream of the grid are 1.7 m/s and 1.1 m/s, respectively. According to the aforementioned analysis, the lateral flow of the flow field downstream of the grid is mainly caused by the mixing vanes, while the structure and arrangement of the mixing vanes have a significant influence on the distribution and intensity of the secondary flow downstream of the grid. However, the influence disappears in a certain distance, and the secondary flow distribution downstream of the grid presents an asymmetric morphology.

In the analysis of the thermal-hydraulic characteristics in the rod bundle channel, the flow field on the cross section along the flow direction cannot fully express the local characteristics, but the changing trend of the flow pattern in the sub-channel can truly reflect the heat transfer characteristics of the internal flow. Meanwhile, the flow field on the surface of the fuel rod is also selected to study its importance on the critical heat flux. In this article, the average secondary flow evolution in adjacent sub-channels and on the fuel rod surfaces is analyzed, and the selected sub-channels and fuel rods are shown in **Figure 4**. Since the sub-channel data cannot be extracted by the original calculation software, they are obtained by UDF.

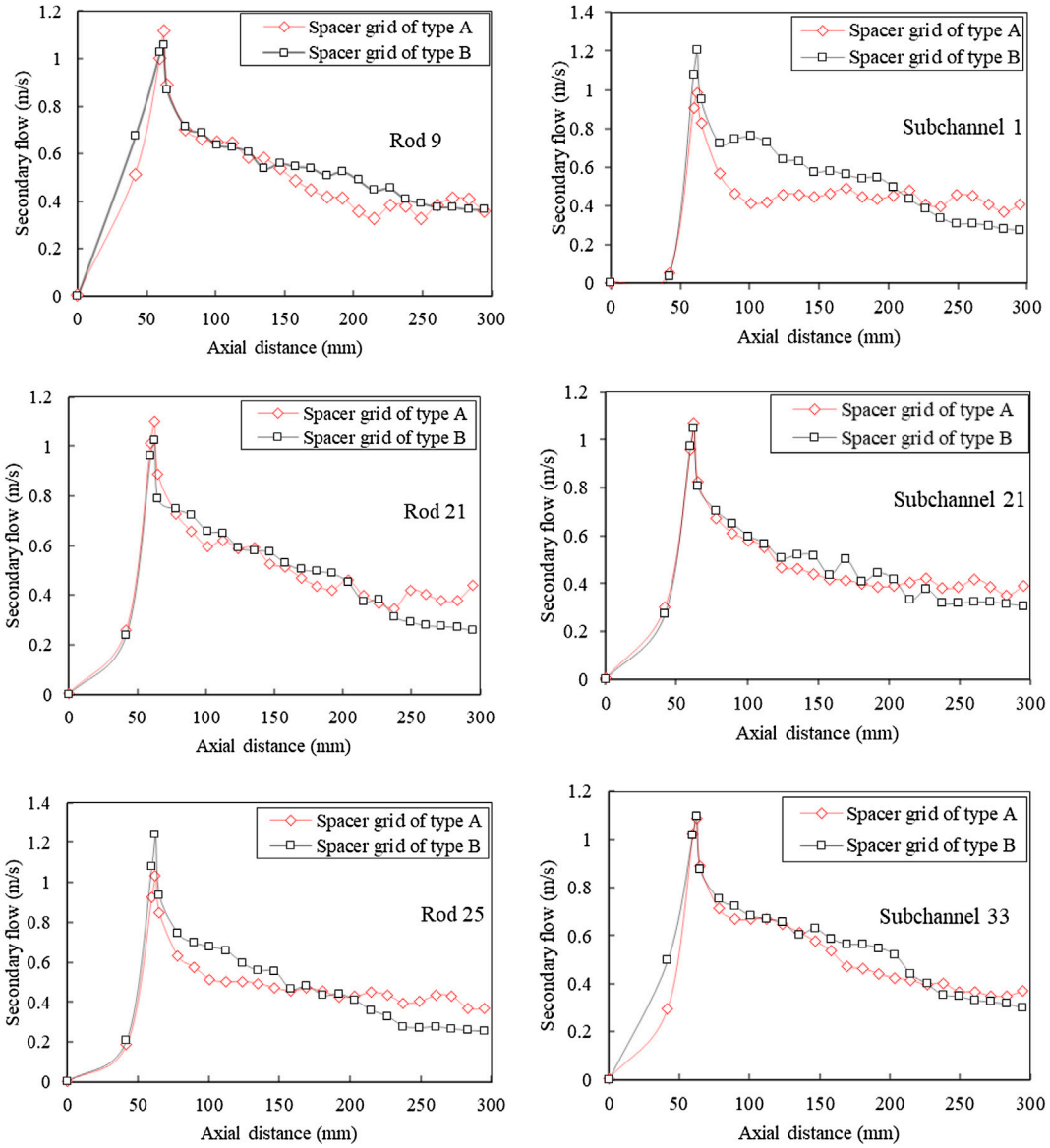

FIGURE 10 | Distribution of secondary flow along axial direction in the sub-channel and around the fuel rod.

According to the arrangement of mixing vanes of the current spacer grid, three sub-channels, including two middle sub-channels (21 and 33) and one corner sub-channel (1), and the surfaces of three corresponding fuel rods (9, 21, and 25) are selected as the research objects. The secondary flow curves along the axial direction in the three sub-channels and on fuel rod surfaces are shown in **Figure 5**. As one can see, the secondary flow along the axial direction shows a similar trend for both the sub-channel and the fuel rod surface roughly. The largest secondary flow all appears at the top of the mixing vanes and then gradually attenuates along the downstream of the grid, while the secondary flow at the root of the mixing wing is about 1 m/s, which indicates that the springs and dimples in the spacer grid will also cause the transverse mixing of the coolant. For different sub-channels, the secondary flow of the corner channel is only caused by a single vane and limited by the casing tube, while in the middle channels it is affected by a pair of mixing vanes. The secondary flow in the corner channel at the upstream and downstream of the spacer grid is smaller than that in the other two middle channels. The secondary flow in the corner channel does not decay and fluctuates after $6D_h$. This phenomenon mainly lies in the fact that the corner channel is influenced by the wall channel downstream of the grid. For the middle channel, sub-channel 33 is more obviously affected by the transverse pulsation of the surrounding sub-channel flow field than sub-channel 21, so the secondary flow of the former is a little larger than that of the latter

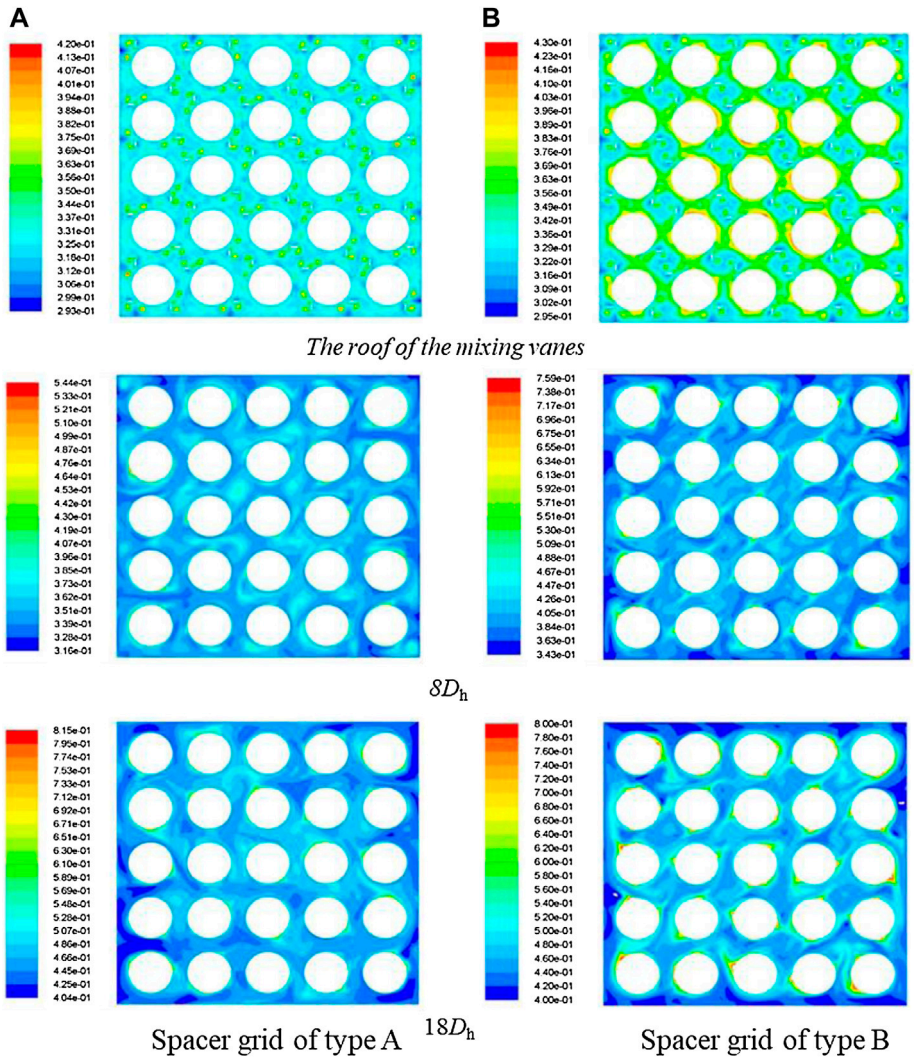

FIGURE 11 | Variations of vapor-phase distribution at different axial cross sections.

before $12D_h$. Since the arrangement of the mixing vanes around fuel rod 9 is different from that of fuel rod 21 and fuel rod 25, the secondary flow velocity at the upstream and downstream of the mixing vanes on the surface of fuel rod 9 is greater than that of the other two, and its attenuation rate is also greater. The data analysis shows that the secondary flow in the fuel assembly is mainly caused by the mixing vanes in the spacer grid and attenuates gradually after passing through the grid, but there are differences in the changing trend between different sub-channels.

3.1.2 The Vapor-Phase Distribution Characteristics

The boiling crisis is usually under a low void fraction in a pressurized water reactor. In this case, the accumulation of the vapor phase on the surface of the fuel rod and the formation of a vapor film are the key influencing factors for DNB. The phase distribution characteristics of boiling two-phase flow are revealed at the downstream of spacer grid with mixing vanes, and the accumulation degree of vapor on the surface of different fuel rods after passing through the spacer grid is quantitatively studied. **Figure 6** shows the vapor phase distribution clouds at the root of the mixing vane, $1D_h$, $8D_h$, and $18D_h$. The vortex at the root of the mixing vane makes the vapor phase involved in the vortex center, resulting in more obvious vapor accumulation around the mixing vanes. With the increase of vortex intensity and bubble growth along the axial direction, more vapor phase is brought into the vortex center along the flow direction, making the vapor phase gather in the center of the sub-channel. However, after $1D_h$ downstream of the grid, the decrement of vortex intensity and the development of secondary flow lead to non-uniform distribution of vapor phase distribution. Taking fuel rod 14 as an example, the local extreme value of the void fraction on the fuel rod surface is continuously changed along the axial direction due to the influence of secondary flow, and the changing direction

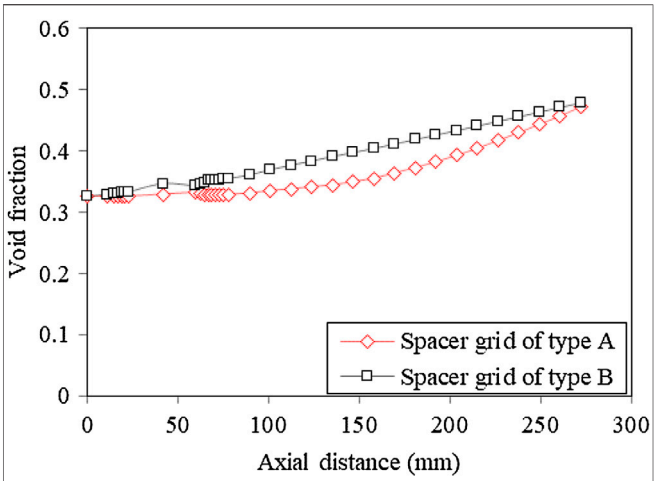

FIGURE 12 | Average void fraction of cross sections along axial direction.

of the void fraction is the same as that of secondary flow. Combined with the secondary flow distribution diagram shown in **Figure 4**, it can be seen that the more uniform distribution of secondary flow around the fuel rod corresponds to a more uniform distribution of the vapor phase because the uniform transverse flow field around the fuel rod will not make the vapor phase stay in this region. As shown in **Figure 7**, the variation trend of the void fraction increases gradually along the axial flow direction. However, since the secondary flow in the corner channel is larger than that in the middle channel after $12D_h$, its void fraction becomes smaller. At the downstream of the spacer grid with mixing vanes, a part of the vapor phase is taken away from the center of the sub-channel and the rest accumulates on the surface of the fuel rod, when it is mixed by the transverse flow. As the transverse mixing capacity decreases gradually along the flow direction, the vapor phase accumulation phenomenon is more obvious in the area far from the downstream of the grid.

3.2 Comparison of Mixing Characteristics of Different Types of Spacer Grids

3.2.1 The Secondary Flow Distribution Characteristics

The geometric structure of the spacer grid, especially the arrangement and guidance of its mixing vanes, has a very important influence on the mixing characteristics of the spacer grid. To fully verify the mixing characteristics caused by the spacer grid, it is necessary to analyze the influence of the mixing vane arrangement of the spacer grid on the secondary flow and phase distribution. In this article, two different types of spacer grids are taken as the research objects, and their structures are shown in **Figure 8**. The type-A grid and the type-B grid have different arrangements of mixing vanes around external fuel rods.

From the curves of secondary flow and axial velocities for the cross section along the axial direction in **Figure 9**, one can see that they increase and then decrease along the flow direction, the maximum value of secondary flow appears at the top of the mixing vanes, and the maximum value of axial velocities appears at the bottom of the spring. The difference in axial velocity between the two types of grids is greater than that in secondary flow. Due to the differences in the arrangement and guidance of the mixing vanes in the two spacer grids, a stronger disturbance occurs in the type-B grid. The larger secondary flow after the grid strengthens the interaction between the lateral flow fields, resulting in a greater decay rate of the mixing flow caused by the mixing vanes of the type-B grid than that of the type-A grid, especially the secondary flow is smaller than that of the type-A after $12D_h$ downstream of the grid. Because of different mixing capacities and different secondary flows, the axial velocity of the type-B grid is smaller than that of the type-A grid while downstream is reversed. By comparing the secondary flow and axial velocities of the two-type grids in the flow direction, it can be seen that the type-B grid results in a stronger mixing rate than the type-A grid.

As shown in **Figure 10**, for the type-A grid, the trends of the secondary flow in the two middle sub-channels are the same, and both of them have smaller secondary flow before $12D_h$ downstream of the grid than that of the type-B grid, while it is larger in the latter half downstream of the grid than in the type-B grid. Such a trend is consistent with that of the cross-sectional secondary flow. Although the decay rate of the type-A grid is greater in the middle section downstream of the grid in the corner channel, the secondary flow is still greater in the latter half of the downstream section of the grid than in the type-B grid. The same trend can be seen in the secondary flow variation near the fuel rods, where the trend of the type-A grid is larger than that of the type-B grid in all the latter half of the downstream parts of the grid. Based on the analysis of the changing trend of the secondary flow on the surface of fuel rod 21 and fuel rod 25, the difference of the secondary flow after $12D_h$ is strong due to the different guidance of the mixing vanes. Therefore, the influence distance of the type-A grid downstream of the grid is farther than that of the type-B grid, which might be associated with the direction of the induced secondary flow and the effect of the casing tube. In summary, the mixing vane leads to strong secondary flow. The arrangement and guidance of different mixing vanes have a great impact on the secondary flow downstream of the grid. The patterns of secondary flow between the same sub-channels are different, but the change trends are consistent with the cross-sectional average one. The secondary flow can maintain larger values at locations further from the grid, but the distance of influence is limited, which will have an important impact on the suppression of boiling crisis occurrence.

3.2.2 The Vapor-Phase Distribution Characteristics

The variation of the secondary flow directly affects the degree of vapor phase accumulation on the fuel rod surfaces. Since the secondary flow has a large effect on the vapor phase distribution and a limited effect on the average void fraction at the cross-section, the difference in the average void fraction distribution between the two types of grids is small upstream of the spacer grid and inside the grid. However, for different fuel rod surfaces, the degree of vapor accumulation is different due to the influence of different secondary flows around the fuel

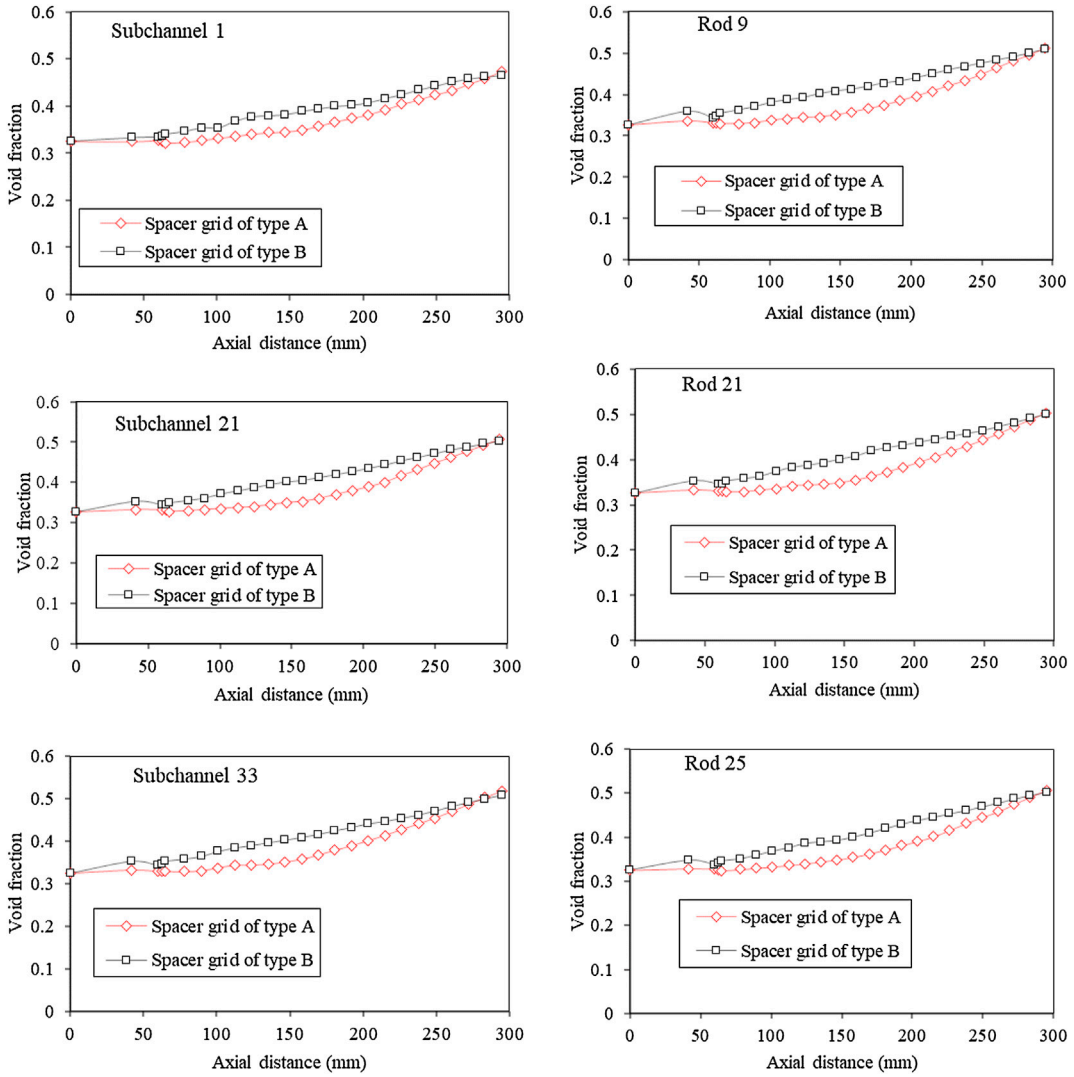

FIGURE 13 | Average void fraction of cross sections in the sub-channel and around the fuel rod along axial direction for different spacer grids.

rods. As shown in **Figures 11**, **12**, the void fraction distribution of the two types of the grid shows different changes, especially at the top of the mixing vane. The vapor phase of the type-A grid is more concentrated in the center of the channel, while the vapor phase of the type-B grid is concentrated on the surface of the fuel rod and the vapor phase accumulation is more pronounced at $18D_h$. In contrast, the secondary flow of the type-A grid does not decay significantly after $12D_h$, so the vapor phase distribution on the fuel rod surface is more uniform at the $18D_h$ position. To deeply analyze the vapor phase distribution characteristics downstream of the two grids, the void fraction of different fuel rods and sub-channels of the two types of grids were compared and analyzed. It can be seen from **Figure 13** that the void fraction increases gradually in the flow direction, both in the sub-channels and around the fuel rods. However, since the secondary flow of the type-B grid is smaller than that of the type-A grid, its void fraction is overall larger than that of the type-A grid, and such a trend is consistent with the variation of the average void fraction of the cross section along the flow direction. Through the analysis of the void fraction of different sub-channels, it can be seen that whether the sub-channel or the fuel rod surface is selected as the analysis object, and there is no difference in the variation trend of the void fraction.

4 CONCLUSION

In this article, a multiphase flow model coupling boiling model based on thermal equilibrium was applied to investigate the two-phase flow characteristics in a 5 × 5 rod bundle with a spacer grid. The analysis of secondary flow and vapor phase

distribution at different axial positions was carried out, including sub-channels, fuel rod surface, and cross sections. The main conclusions are listed as follows:

- The secondary flow is mainly caused by mixing vanes; the springs and dimples can induce a secondary flow of about 0.25 m/s, and the difference of secondary flow before and after the grid is about 0.64 m/s. The intensity and flow direction of secondary flow lead to the different distribution of the vapor phase on the fuel rod surface. Furthermore, the uniformity of secondary flow also has a great influence on the vapor accumulation of the fuel rod surface.
- Comparing two different types of spacer grids, the secondary flow of the type A spacer grid is greater after $12D_h$ than that of the type B spacer grid both in the sub-channel and around the fuel rod. The vapor phase of the type B spacer grid is easier to accumulate on the surface of fuel rods, and the average void fraction of the type A spacer grid is generally less than that of the type B spacer grid.

DATA AVAILABILITY STATEMENT

The original contributions presented in the study are included in the article/Supplementary Material, further inquiries can be directed to the corresponding authors.

AUTHOR CONTRIBUTIONS

YX: numerical simulation and writing. TD: numerical simulation, data processing, and writing—draft manuscript. Q-YR: writing—reviewing and supervision. XY-Z: data processing and writing—editing. MZ: manuscript editing. RH: data processing.

FUNDING

The authors are grateful for the support of the Natural Science Foundation of China (Grant No. 12105273) and the Fundamental Research Funds for the Central Universities (Nos Q2020-011, J2020-001 and ZJ 2021-08).

REFERENCES

Agbodemegbe, V. Y., Cheng, X., Akaho, E. H. K., and Allotey, F. K. A. (2016). An Investigation of the Effect of Split-type Mixing Vane on Extent of Crossflow between Subchannels through the Fuel Rod Gaps. *Ann. Nucl. Energ.* 88, 174–185. doi:10.1016/j.anucene.2015.10.036

Agbodemegbe, V. Y., Cheng, X., Akaho, E. H. K., and Allotey, F. K. A. (2015). Correlation for Cross-Flow Resistance Coefficient Using STAR-CCM+ Simulation Data for Flow of Water through Rod Bundle Supported by Spacer Grid with Split-type Mixing Vane. *Nucl. Eng. Des.* 285, 134–149. doi:10.1016/j.nucengdes.2015.01.003

Anglart, H., and Nylund, O. (1996). CFD Application to Prediction of Void Distribution in Two-phase Bubbly Flows in Rod Bundles. *Nucl. Eng. Des.* 163 (1-2), 81–98. doi:10.1016/0029-5493(95)01160-9

Anglart, H., Nylund, O., Kurul, N., and Podowski, M. (1997). CFD Prediction of Flow and Phase Distribution in Fuel Assemblies with Spacers. *Nucl. Eng. Des.* 177 (1-3), 215–228. doi:10.1016/s0029-5493(97)00195-7

Arai, T., Furuya, M., Kanai, T., and Shirakawa, K. (2012). Development of a Subchannel Void Sensor and Two-phase Flow Measurement in 10×10 Rod Bundle. *Int. J. multiphase flow* 47, 183–192. doi:10.1016/j.ijmultiphaseflow.2012.07.012

Bakosi, J., Christon, M. A., Lowrie, R. B., Pritchett-Sheats, L. A., and Nourgaliev, R. R. (2013). Large-eddy Simulations of Turbulent Flow for Grid-To-Rod Fretting in Nuclear Reactors. *Nucl. Eng. Des.* 262, 544–561. doi:10.1016/j.nucengdes.2013.06.007

Busco, G., and Hassan, Y. A. (2018). Space and Energy-Based Turbulent Scale-Resolving Simulations of Flow in a 5 × 5 Nuclear Reactor Core Fuel Assembly with a Spacer Grid. *Int. J. Heat Fluid Flow* 71 (JUN), 420–441. doi:10.1016/j.ijheatfluidflow.2018.04.003

Caraghiaur, D., Anglart, H., and Frid, W. (2009). Experimental Investigation of Turbulent Flow through Spacer Grids in Fuel Rod Bundles. *Nucl. Eng. Des.* 239 (10), 2013–2021. doi:10.1016/j.nucengdes.2009.05.029

Carlucci, L. N., Hammouda, N., and Rowe, D. S. (2004). Two-phase Turbulent Mixing and Buoyancy Drift in Rod Bundles. *Nucl. Eng. Des.* 227 (1), 65–84. doi:10.1016/j.nucengdes.2003.08.003

Chen, D., Xiao, Y., Xie, S., Yuan, D., Lang, X., Yang, Z., et al. (2016). Thermal-hydraulic Performance of a 5 × 5 Rod Bundle with Spacer Grid in a Nuclear Reactor. *Appl. Therm. Eng.* 103, 1416–1426. doi:10.1016/j.applthermaleng.2016.05.028

Chen, S. R., Lin, W. C., Ferng, Y. M., Chieng, C. C., and Pei, B. S. (2014). CFD Simulating the Transient thermal-hydraulic Characteristics in a 17 × 17 Bundle for a Spent Fuel Pool under the Loss of External Cooling System Accident. *Ann. Nucl. Energ.* 73, 241–249. doi:10.1016/j.anucene.2014.06.054

Cho, H. K., Choi, K. Y., Cho, S., and Song, C.-H. (2011). Experimental Observation of the Droplet Size Change across a Wet Grid Spacer in a 6×6 Rod Bundle. *Nucl. Eng. Des.* 241 (12), 4649–4656. doi:10.1016/j.nucengdes.2011.03.042

Cinosi, N., Walker, S. P., Bluck, M. J., and Issa, R. (2014). CFD Simulation of Turbulent Flow in a Rod Bundle with Spacer Grids (MATIS-H) Using STAR-CCM+. *Nucl. Eng. Des.* 279, 37–49. doi:10.1016/j.nucengdes.2014.06.019

Conner, M. E., Hassan, Y. A., and Dominguez-Ontiveros, E. E. (2013). Hydraulic Benchmark Data for PWR Mixing Vane Grid. *Nucl. Eng. Des.* 264, 97–102. doi:10.1016/j.nucengdes.2012.12.001

Dominguez-Ontiveros, E. E., Hassan, Y. A., Conner, M. E., and Karoutas, Z. (2012). Experimental Benchmark Data for PWR Rod Bundle with Spacer-Grids. *Nucl. Eng. Des.* 253, 396–405. doi:10.1016/j.nucengdes.2012.09.003

Dominguez-Ontiveros, E., Estrada-Perez, C., and Hassan, Y. (2009). "Non-intrusive Experimental Investigation of Flow Behavior inside a 5x5 Rod Bundle with Spacer Grids Using PIV and MIR,"International Conference On Nuclear Engineering, 351–360.

Dominguez-Ontiveros, E., and Hassan, Y. A. (2014). Experimental Study of a Simplified 3×3 Rod Bundle Using DPTV. *Nucl. Eng. Des.* 279, 50–59. doi:10.1016/j.nucengdes.2014.04.037

Fen Shen, Y., Dong Cao, Z., and Gang Lu, Q. (1991). An Investigation of Crossflow Mixing Effect Caused by Grid Spacer with Mixing Blades in a Rod Bundle. *Nucl. Eng. Des.* 125 (2), 111–119. doi:10.1016/0029-5493(91)90071-o

Han, S. Y., Seo, J. S., Park, M. S., and Choi, Y. D. (2009). Measurements of the Flow Characteristics of the Lateral Flow in the 6×6 Rod Bundles with Tandem Arrangement Vanes. *Nucl. Eng. Des.* 239 (12), 2728–2736. doi:10.1016/j.nucengdes.2009.09.026

Khan, I., Wang, M., Zhang, Y., Tian, W., Su, G., and Qiu, S. (2020). Two-phase Bubbly Flow Simulation Using CFD Method: A Review of Models for Interfacial Forces. *Prog. Nucl. Energ.* 125, 103360. doi:10.1016/j.pnucene.2020.103360

Lin, C.-H., Yen, C.-H., and Ferng, Y.-M. (2014). CFD Investigating the Flow Characteristics in a Triangular-Pitch Rod Bundle Using Reynolds Stress Turbulence Model. *Ann. Nucl. Energ.* 65, 357–364. doi:10.1016/j.anucene.2013.11.023

Liu, C. C., and Ferng, Y. M. (2010). Numerically Simulating the thermal-hydraulic Characteristics within the Fuel Rod Bundle Using CFD Methodology. *Nucl. Eng. Des.* 240 (10), 3078–3086. doi:10.1016/j.nucengdes.2010.05.021

Liu, M., and Ishiwatari, Y. (2013). Unsteady Numerical Simulations of Single-phase Turbulent Mixing in Tight Lattice Geometries. *Nucl. Eng. Des.* 256, 28–37. doi:10.1016/j.nucengdes.2012.11.008

Liu, W., Liu, Y., Peng, S., Jiang, G., Liu, Y., Li, J., et al. (2021). Visualization of Spacer Grid Effect on Bubble Behavior and CHF in a Single-Rod Channel. *Nucl. Eng. Des.* 382, 111376. doi:10.1016/j.nucengdes.2021.111376

McClusky, H. L., Holloway, M. V., Beasley, D. E., and Conner, M. E. (2002). Development of Swirling Flow in a Rod Bundle Subchannel. *J. Fluids Eng.* 124 (3), 747–755. doi:10.1115/1.1478066

Navarro, M. A., and Santos, A. A. C. (2011). Evaluation of a Numeric Procedure for Flow Simulation of a 5 × 5 PWR Rod Bundle with a Mixing Vane Spacer. *Prog. Nucl. Energ.* 53 (8), 1190–1196. doi:10.1016/j.pnucene.2011.08.002

Pham, S. H., Kawara, Z., Yokomine, T., and Kunugi, T. (2014). Detailed Observations of Wavy Interface Behaviors of Annular Two-phase Flow on Rod Bundle Geometry. *Int. J. multiphase flow* 59, 135–144. doi:10.1016/j.ijmultiphaseflow.2013.11.004

Pham, S. H., Kawara, Z., Yokomine, T., and Kunugi, T. (2015). Measurements of Liquid Film and Droplets of Annular Two-phase Flow on a Rod-Bundle Geometry with Spacer. *Int. J. Multiphase Flow* 70, 35–57. doi:10.1016/j.ijmultiphaseflow.2014.11.010

Podila, K., and Rao, Y. (2016). CFD Modelling of Turbulent Flows through 5 × 5 Fuel Rod Bundles with Spacer-Grids. *Ann. Nucl. Energ.* 97, 86–95. doi:10.1016/j.anucene.2016.07.003

Rehme, K. (1989). Experimental Observations of Turbulent Flow through Subchannels of Rod Bundles. *Exp. Therm. Fluid Sci.* 2 (3), 341–349. doi:10.1016/0894-1777(89)90023-x

Rehme, K. (1987). The Structure of Turbulent Flow through Rod Bundles. *Nucl. Eng. Des.* 99, 141–154. doi:10.1016/0029-5493(87)90116-6

Ren, Q.-Y., Pan, L.-M., Pu, Z., Zhu, F., and He, H. (2021). Two-group Phase Distribution Characteristics for Air-Water Flow in 5 × 5 Vertical Rod Bundle Channel with Mixing Vane Spacer Grids. *Int. J. Heat Mass Transfer* 176, 121444. doi:10.1016/j.ijheatmasstransfer.2021.121444

Ren, Q., Pan, L., Zhou, W., Ye, T., and Li, S. (2018b). Comparison of Drift-Flux Models for Void Fraction Prediction in Sub-channel of Vertical Rod Bundles. 26th International Conference On Nuclear Engineering. doi:10.1115/icone26-81435

Ren, Q-y., Zhou, W-x., Si-jia, D., Zhong-chun, Li., and Pan, L-m. (2018a). Sub-channel Flow Regime Maps in Vertical Rod Bundles with Spacer Grids. *INTERNATIONAL JOURNAL HEAT. MASS TRANSFER* 122, 1138–1152. doi:10.1016/j.ijheatmasstransfer.2018.01.133

Wang, M., Wang, Y., Tian, W., Qiu, S., and Su, G. H. (2021). Recent Progress of CFD Applications in PWR thermal Hydraulics Study and Future Directions. *Ann. Nucl. Energ.* 150, 107836. doi:10.1016/j.anucene.2020.107836

Wang, Y., Wang, M., Ju, H., Zhao, M., Zhang, D., Tian, W., et al. (2020). CFD Simulation of Flow and Heat Transfer Characteristics in a 5×5 Fuel Rod Bundles with Spacer Grids of Advanced PWR. *Nucl. Eng. Technol.* 52 (7), 1386–1395. doi:10.1016/j.net.2019.12.012

Wu, X., and Trupp, A. C. (1993). Experimental Study on the Unusual Turbulence Intensity Distributions in Rod-To-wall gap Regions. *Exp. Therm. Fluid Sci.* 6 (4), 360–370. doi:10.1016/0894-1777(93)90014-a

Xiong, J., Qu, W., Zhang, T., Chai, X., Liu, X., and Yang, Y. (2020). Experimental Investigation on Split-Mixing-Vane Forced Mixing in Pressurized Water Reactor Fuel Assembly. *Ann. Nucl. Energ.* 143, 107450. doi:10.1016/j.anucene.2020.107450

Yang, P., Zhang, T., Hu, L., Liu, L., and Liu, Y. (2021). Numerical Investigation of the Effect of Mixing Vanes on Subcooled Boiling in a 3 × 3 Rod Bundle Channel with Spacer Grid. *Energy* 236, 121454. doi:10.1016/j.energy.2021.121454

Yang, S.-K., and Chung, M.-K. (1996). Spacer Grid Effects on Turbulent Flow in Rod Bundles. *Nucl. Eng. Technol.* 28 (1), 56–71.

Yang, S. K., and Chung, M. K. (1998). Turbulent Flow through Spacer Grids in Rod Bundles, *J. Fluids Eng.* 120, 786–791. 10.1115/1.2820739.

Zhang, J., Wang, M., Chen, C., Tian, W., Qiu, S., and Su, G. H. (2022). CFD Investigation of the Cold wall Effect on CHF in a 5 × 5 Rod Bundle for PWRs. *Nucl. Eng. Des.* 387, 111589. doi:10.1016/j.nucengdes.2021.111589

Conflict of Interest: The authors declare that the research was conducted in the absence of any commercial or financial relationships that could be construed as a potential conflict of interest.

Publisher's Note: All claims expressed in this article are solely those of the authors and do not necessarily represent those of their affiliated organizations, or those of the publisher, the editors, and the reviewers. Any product that may be evaluated in this article, or claim that may be made by its manufacturer, is not guaranteed or endorsed by the publisher.

NOMENCLATURE

$A_{w,n}$ area of wall grid, m^2

$c_{p,l}$ specific heat capacity of the liquid phase, J/(kg·°C)

D_h hydraulic diameter, mm

$\vec{g}$ gravity acceleration, m/s^2

h_{fg} latent heat of vaporization, kJ/kg

k_{eff} effective thermal conductivity

$\dot{m}_{w,n}$ vapor generation rate on the heated wall

$\dot{m}_{v,m}$ vapor generation rate on the liquid–vapor interface

$\Delta T_{sub,m}$ superheat of the vapor–liquid interface grid, °C

μ_m mixture viscosity, kg/m·s

ΔV_l liquid phase volume of cell volume, m^3

V_{SF} velocity of secondary flow, m/s

$\vec{v}_m$ turbulence kinetic energy, m/s

$\vec{v}_k$ velocity of the k-phase, m/s

α_k volume fraction of the k-phase

ρ_m mixture densities, kg/m^3

ρ_k density of the k-phase, kg/m^3

ρ_l density of the liquid phase, kg/m^3

τ_m bubble relaxation times

frontiers | Frontiers in Energy Research

TYPE Original Research
PUBLISHED 22 July 2022
DOI 10.3389/fenrg.2022.939499

OPEN ACCESS

EDITED BY
Zhaoming Meng,
Harbin Engineering University, China

REVIEWED BY
Haozhi Bian,
Harbin Engineering University, China
Shuiqing Zhan,
Jiangsu University, China

*CORRESPONDENCE
Liu Liu,
l.liu@csu.edu.cn

SPECIALTY SECTION
This article was submitted to Nuclear Energy,
a section of the journal
Frontiers in Energy Research

RECEIVED 09 May 2022
ACCEPTED 27 June 2022
PUBLISHED 22 July 2022

CITATION
Yan H, Zhang H, Höhne T, Liao Y, Lucas D and Liu L (2022), Numerical modeling of horizontal stratified two-phase flows using the AIAD model. *Front. Energy Res.* 10:939499. doi: 10.3389/fenrg.2022.939499

Numerical modeling of horizontal stratified two-phase flows using the AIAD model

Hongjie Yan[1], Huimin Zhang[1], Thomas Höhne[2], Yixiang Liao[2], Dirk Lucas[2] and Liu Liu[1]*

[1]School of Energy Science and Engineering, Central South University, Changsha, China, [2]Institute of Fluid Dynamics, Helmholtz-Zentrum Dresden-Rossendorf, Dresden, Germany

In nuclear reactor safety research, the countercurrent gas-liquid two-phase flow in the hot leg of a pressurized water reactor (PWR) has attracted considerable attention. Previous work has proven that the algebraic interfacial area density (AIAD) model implemented in ANSYS CFX can effectively capture the gas-liquid interface and avoid the loss of information regarding the interfacial structure, which occurs after phase averaging in the Euler–Euler two-fluid approach. To verify the accuracy of the AIAD module implementation in ANSYS Fluent, the model based on the experimental data from the WENKA facility is validated in this work. The effects of the subgrid wave turbulence model, turbulence damping model, and droplet entrainment model are simultaneously investigated, which have been shown to be important in the previous work with CFX. The results show that the simulations are considerably and significantly deviate from the experiments when the turbulence damping is not considered. The free surface modeling of two-phase flow can be optimized by using the droplet entrainment model. The consistency between the simulation and experimental results is not enhanced after the subgrid wave turbulence model is adopted. Further investigations regarding the implementation of the subgrid wave turbulence model are necessary.

KEYWORDS

thermal hydraulics, two-phase flow, AIAD, CFD, subgrid wave turbulence, droplet entrainment, turbulence damping

1 Introduction

Multiphase flows are widely encountered in natural and industrial applications. In the nuclear reactor safety domain, the countercurrent gas-liquid two-phase flow in the hot leg of a pressurized water reactor (PWR) has been the focus of the research community for several decades. The behavior of countercurrent two-phase flows, which can be accurately predicted through three-dimensional (3D) computational fluid dynamics (CFD) codes, has critical implications for the safety and efficiency of the associated processes. CFD is widely used in many fields, such as evaluation of steam condensation heat transfer effects (Bian et al., 2018; Bian et al., 2019) and aerodynamic design of aircraft (Yang and Yang, 2012), etc., ANSYS Fluent is a commercial CFD software application that is highly

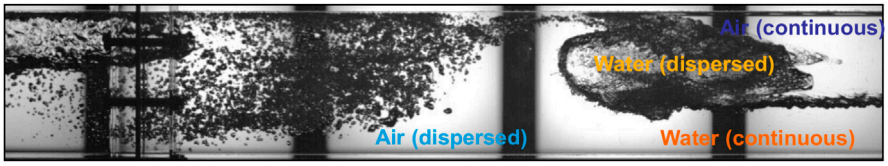

FIGURE 1
Different morphologies (Höhne and Mehlhoop, 2014).

universal and contains a variety of optimized physical models. In ANSYS Fluent, a broad range of mathematical models for multiphase phenomena is available, and the software can model complex geometries that are being increasingly used in both engineering practice and academic research (ANSYS Fluent, 2019). In horizontal gas-liquid two-phase flows, the key flow regimes pertain to smooth stratified flow, wavy flow, slug flow, and elongated bubbly flow. The different morphologies that occur under slug flow conditions are shown in Figure 1. Mandhane et al. (1974) and Taitel and Dukler (1976) introduced flow maps that can predict the transition between horizontal flow regimes in pipelines.

With respect to turbulence three types of numerical simulation methods can be used to model free surface two-phase flows (Lakehal, 2002; Bestion, 2012): direct numerical simulation (DNS), large eddy simulation (LES), and the Reynolds average method (RANS). The Navier–Stokes equation can be solved directly using the DNS, the results of which involve all the spatial and temporal scales in turbulent two-phase flows. However, the computational cost of this method is extremely high, which limits its use in industrial applications. The computational costs associated with the LES are smaller; however, considerable resources may be consumed for large-scale and two-phase flows. The theoretical basis of the RANS technique is the Reynolds averaging concept, which represents a relatively effective and feasible solution to engineering problems. The principle of the Euler–Euler two-fluid method is to treat the phases as continuous media that penetrate each other (Porombka and Höhne, 2015). Due to the loss of information regarding the interfacial structure after phase averaging, the influence of the nonresolved small-scale structures of the interface on the mass, momentum, and heat transfer is ignored. Consequently, additional interphase forces must be introduced in the form of source terms to restore the gas-liquid interaction law in the Euler–Euler model.

To increase the accuracy of interfacial momentum transfer modelling under the Euler–Euler framework, it is necessary to select adequate force models, therein interphase drag is dominant. Several empirical correlations have been proposed for the estimation of drag coefficient, and their predictability is affected by various factors such as bubble size, aspect ratio, material properties as well contaminants. A generic model is still missing, especially in the case of complex flow conditions encountered in technical applications, where a hybrid model is often necessary (Tas-Koehler, et al., 2021). Researchers have proposed several techniques to ensure the applicability of their correlations under various hydrodynamics (Lockhart and Martinelli, 1949; Kim et al., 1985), for example, by including the particle Reynolds number, Eotvös number and Morton number as parameters (Ohnuki et al., 1988; Tomiyama et al., 1998). The parameter method based on empiricism is often limited by the form of the flow region, that is, a certain drag coefficient correlation is only suitable for a specific type of flow (Porombka, 2015). To overcome this limitation, Yao et al. (2005) and Coste (2013) proposed a local drag model to calculate the interfacial friction in two-phase flows involving large interfaces by estimating the position of the interface and applying a wall function on it. Moreover, Höhne and Vallée (2009), Höhne and Vallée (2010) presented the algebraic interfacial area density (AIAD) model, which enables the use of different models to calculate the drag force coefficient and interfacial area density for different flow patterns. In this method, an interfacial drag coefficient is directly calculated from the shear stress distribution at the stratified gas-liquid interface. The AIAD method has been successfully applied to simulating the countercurrent flow in the hot leg of a PWR (Höhne et al., 2011; Höhne et al., 2020).

Within the RANS Euler–Euler framework, the influence of turbulence must be modeled using a specific closure law. In terms of the introduction of two-equation turbulence models to the governing equation, Porombka and Höhne (2015) verified that the k–ω turbulence model was less sensitive to grid refinement and significantly enhanced the agreement with the experimental liquid levels. Moreover, the authors validated that near interface turbulence damping is indispensable for simulating the horizontal stratified flow. Another improvement is to consider the turbulent influence exerted by subgrid waves created by Kelvin–Helmholtz instabilities, which are smaller than the grid size. Höhne and Mehlhoop (2014) confirmed that the subgrid wave turbulence (SWT) model can enhance the processing capacity of the AIAD model for the physical process of the two-phase flow. In addition, Höhne and Hänsch (2015) previously proposed a new droplet entrainment model inside the AIAD framework to describe

the droplet formation process. The simulation with the droplet entrainment model can reproduce the slug formation and propagation behavior observed in the experiment, and the model can be directly applied for industrial cases. The above developments have been implemented and tested in ANSYS CFX, while in the past years they were transferred to ANSYS Fluent. A comparative study of the model against experimental data and previous CFX studies is necessary for checking the implementation. This study focuses on modelling horizontally stratified two-phase flows in the hot leg of a PWR with the AIAD model in ANSYS Fluent.

This paper aims to provide additional levels of simulation support for the use of the AIAD method. The simulation results and experimental data for validation are derived from Porombka and Höhne (2015) and Höhne and Porombka (2018), whose studies were based on ANSYS and Stäbler et al. (2006) and Stäbler (2007), who conducted experiments at the WENKA facility, respectively.

2 Mathematical formulation

2.1 Basic equations

The CFD simulation of free surface flows can be performed using the multi-fluid Euler–Euler modeling approach available in ANSYS Fluent. A detailed derivation of the governing equations can be found in Ishii and Mishima (1984). The continuity and momentum equations have the following form.

$$\frac{\partial(\alpha_i\rho_i)}{\partial t} + \nabla\cdot(\alpha_i\rho_i\mathbf{u}_i) = 0 \tag{1}$$

$$\frac{\partial}{\partial t}(\alpha_i\rho_i\mathbf{u}_i) + \nabla\cdot(\alpha_i\rho_i\mathbf{u}_i\otimes\mathbf{u}_i) = -\alpha_i\nabla p + \nabla\cdot\left[\alpha_i\mu_i^{eff}\left(\nabla\mathbf{u}_i + (\nabla\mathbf{u}_i)^T\right)\right] + \alpha_i\rho_i\mathbf{g} + \mathbf{F} \tag{2}$$

where α is the gas void fraction, ρ the density, $\mathbf{u}$ the velocity vector. The subscript $i = G$ denotes the gas phase and $i = L$ the liquid phase. The terms on the right-hand side of Eq. 2 represents the pressure gradient, the viscous stress, the gravity force, and the interfacial forces. For interfacial forces, here only the drag force $\mathbf{F}_D$ is considered. In the viscous stress term, μ_i^{eff} is the effective viscosity of phase i, which is the summation of the molecular viscosity and turbulent viscosity.

To obtain a closed equation system, a turbulence model must be supplemented for the determination of fluctuations. In this paper, the shear stress transport (SST) k–ω model is adopted to predict the turbulence parameters in a countercurrent free surface flow, which is less sensitive to grid refinement than the other two-equation turbulence models. Details regarding the model can be found in the work of Menter (1994).

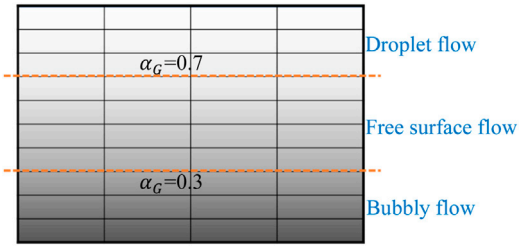

FIGURE 2
Morphology recognition of the AIAD model.

2.2 AIAD model

The AIAD model has been depicted by previous researchers, so a brief description is given here. According to the flow condition, three regime forms—namely, bubbly flow, droplet flow, and free surface flow can be present in the domain. The AIAD approach identifies the local flow form firstly and selects suitable models to calculate the drag coefficient and the interfacial area density. Blending functions based on the volume fraction for droplets, bubbles, and free surface morphologies (f_D, f_B, and f_{FS}) are used to realize the switch between the models. They are defined as

$$f_D = \left[1 + e^{a_D(\alpha_L - \alpha_{D,\text{limit}})}\right]^{-1} \tag{3}$$

$$f_B = \left[1 + e^{a_B(\alpha_G - \alpha_{B,\text{limit}})}\right]^{-1} \tag{4}$$

$$f_{FS} = 1 - f_D - f_B \tag{5}$$

where α_L and α_G are the volume fractions of the liquid and gas phases, α_D and α_B are the blending coefficients for droplets and bubbles, respectively. In addition, $\alpha_{D,\text{limit}}$ and $\alpha_{B,\text{limit}}$ are the volume fraction limiters of the droplet flow and bubble flow. The default values of $\alpha_D = \alpha_B = 50$ and $\alpha_{D,\text{limit}} = \alpha_{B,\text{limit}} = 0.3$ are used in this study. When the gas phase volume fractions are $\alpha_G < 0.3$ and $\alpha_G > 0.7$, the flow is a bubbly flow and droplet flow, respectively. Otherwise, the flow is free surface flow, as shown in Figure 2.

2.2.1 Drag force and interfacial area density

The drag force $\mathbf{F}_D$ is the shear force generated at the phase interface due to the relative velocity between the gas and liquid, which is affected by the contact area, fluid density, and other factors. In this paper, the classical AIAD model is used to model the drag force of a gas-liquid two-phase flow:

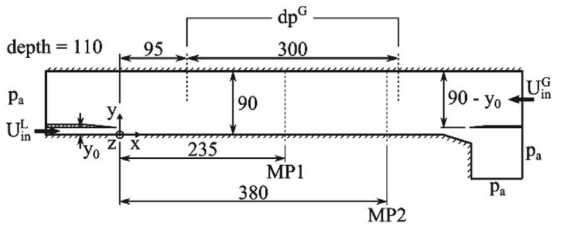

FIGURE 3
Cross-section of the WENKA test section, from Porombka and Höhne (2015).

TABLE 1 Relevant parameters at the inlet and outlet.

$U_{in}^{L}[m/s]$	$U_{in}^{G}[m/s]$	$y_0[mm]$	Re_d^L	Re_d^G	Fr_0
0.7	4.44	9	1.2×10^4	2.7×10^4	2.36

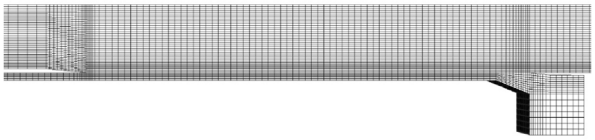

FIGURE 4
The sectional view of the computational grid.

$$\mathbf{F}_D = \frac{1}{2} A \rho_{LG} C_D |\mathbf{U}| \mathbf{U} \tag{6}$$

where A is the interfacial area density, C_D is the drag force coefficient, and $\mathbf{U}$ is the relative velocity of the two phases. When the local flow field is a droplet flow or a bubble flow, ρ_{LG} is the density of the liquid or gas phase (continuous phase). In addition, ρ_{LG} is the average of the gas density ρ_G and liquid density ρ_L in the case of free interfacial flow:

$$\rho_{LG} = \rho_G \alpha_G + \rho_L \alpha_L \tag{7}$$

The bubbles and droplets in the AIAD approach are regarded as regular spheres with a constant diameter, represented as d_B and d_D, respectively. The interfacial area density A_D for the droplet flow is calculated as

$$A_D = \frac{6\alpha_L}{d_D} \tag{8}$$

where α_L is the liquid volume fraction. The same method is used to address the bubbly flow:

$$A_B = \frac{6\alpha_G}{d_B} \tag{9}$$

where A_B is the interfacial area density of the bubbly flow.

$$A_{FS} = |\nabla \alpha_L| = \frac{\partial \alpha_L}{\partial \mathbf{n}} \tag{10}$$

$$\mathbf{n} = -\frac{\nabla \alpha_G}{|\nabla \alpha_G|} \tag{11}$$

The interfacial area density of the free interfacial flow, A_{FS}, is defined as the magnitude of the volume fraction gradient of the liquid phase, and $\mathbf{n}$ is the normal vector of the free surface.

$$A = f_{FS} A_{FS} + f_B A_B + f_D A_D \tag{12}$$

The local interfacial area density A is calculated as the sum of A_{FS}, A_B, and A_D, weighted by the blending functions f_{FS}, f_B, and f_D.

In the Euler multiphase flow framework, the velocity and turbulence for each phase are described by separate sets of equations. A velocity difference exists between the different phases in the fluids. And the drag force coefficient C_D is calculated as

$$C_D = f_{FS} C_{D,FS} + f_B C_{D,B} + f_D C_{D,D} \tag{13}$$

In the range of medium and high Reynolds numbers, the interfacial drag force coefficient of the droplet flow and bubbly flow $C_{D,D/B}$ can be approximated with a constant value of 0.44. For free surface flow, Höhne and Mehlhoop (2014) assumed that the effect of the drag force on both sides of the phase interface was similar to the wall shear force and served to reduce the countercurrent velocity difference between the gas-liquid two phases. In AIAD model, the following formula is used:

$$C_{D,FS} = \frac{2\left(\alpha_L \left|\boldsymbol{\tau}_{W,L}\right| + \alpha_G \left|\boldsymbol{\tau}_{W,G}\right|\right)}{\rho |\mathbf{U}|^2} \tag{14}$$

where $\tau_{W,L}$ and $\tau_{W,G}$ are the interfacial friction on the liquid and gas sides, respectively, which are functions of the viscosity of the liquid and gas phases, boundary area, and velocity gradient in the x- and y-directions. $\mathbf{U}$ is the relative velocity of the two phases. For more details, the reader is referred to the study of Porombka and Höhne (2015).

2.2.2 Sub-grid wave turbulence model (SWT model)

The small wave created by Kelvin–Helmholtz instabilities that are smaller than the grid size is neglected in traditional two-phase flow CFD simulations; however, the influence of these waves on the turbulence kinetic energy of the liquid side in free surface flow can be significantly large. The interfacial stability of two-phase flow is the result of the interaction of gravity and surface tension. Brocchini and Peregrine, (2001) described a wide range of free surface behavior when turbulence occurs at the interface. The surface behavior depends on two dimensionless

TABLE 2 Overview of the performed simulations.

Case	Droplet entrainment model	Turbulence damping model	Subgrid wave turbulence model
Run 1	Yes	Yes	Yes
Run 2	No	Yes	Yes
Run 3	Yes	No	Yes
Run 4	Yes	Yes	No

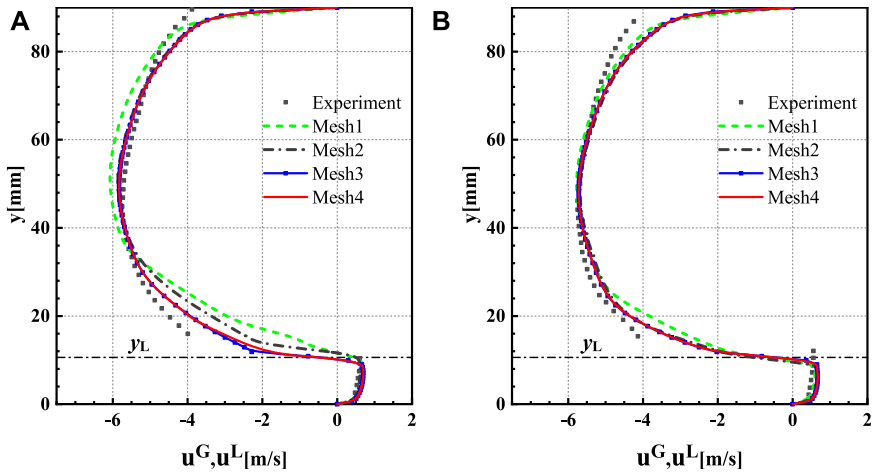

FIGURE 5
Comparison of the *x*-velocity at MP1 and MP2 for the four meshes, **(A)** the distribution of the *x*-velocity at MP1, **(B)** the distribution of the *x*-velocity at MP2.

numbers, namely, the Weber number ($We = q^2L/2\sigma$) and turbulent Froude number ($Fr = (q/2gL)^{1/2}$, where q is the turbulent velocity. And g, L, and σ represent the gravity, the length scale, and the surface tension coefficient. To clarify the effect of subgrid waves, AIAD considers these dimensionless numbers by delineating a critical region of the parameter space between smooth surfaces and surfaces that are completely disintegrated. The corresponding source term for the SWT was formulated by Höhne and Hänsch (2015) as

$$P_{k,SWT} = f_{FS}\frac{2}{3}\frac{\partial U_i}{\partial x_i}\rho_L k_{sw} \tag{15}$$

where $\partial U_i/\partial x_i$ is the gradient of the local liquid velocities, and k_{sw} is the turbulent kinetic energy created by the unresolved subgrid waves, which can be defined as

$$k_{sw} = 0.5\left(q_u^2 - q_l^2\right) \tag{16}$$

where q_u and q_l represent the lower and upper bounds of a surface that is no longer smooth and finally disintegrates due to turbulence. They are defined as

$$q_l^2 \approx \left(\frac{5}{3} - \frac{\pi}{2}\right)\frac{g_n L}{125} + \frac{(\pi-2)\sigma}{5L} \tag{17}$$

$$q_u^2 \approx \left(\frac{\pi}{24}\right)g_n L + \frac{\pi\sigma}{2L} \tag{18}$$

where L is a typical length scale of the dominant interface features and g_n is the scalar product of the interface normal and gravity. Finally, the source term $P_{k,SWT}$ is added to the turbulent kinetic energy equations, which are blended only in the vicinity of the free surface by using the blending function.

2.2.3 Droplet entrainment model

In a horizontal two-phase flow, where droplets, bubbles and free surface co-exist (see Figure 1), the entrainment rate is a key parameter that changes the flow characteristics. Under the high gas velocity conditions, the shear stress leads to the deformation of the interface. The interfacial waves generated by the Kelvin–Helmholtz instability are converted into dispersed droplets carried by the gas phase, and the number of droplets increases with the motion of the disturbance waves. Consequently, a portion of the wave disintegrates into several droplets. The breakage

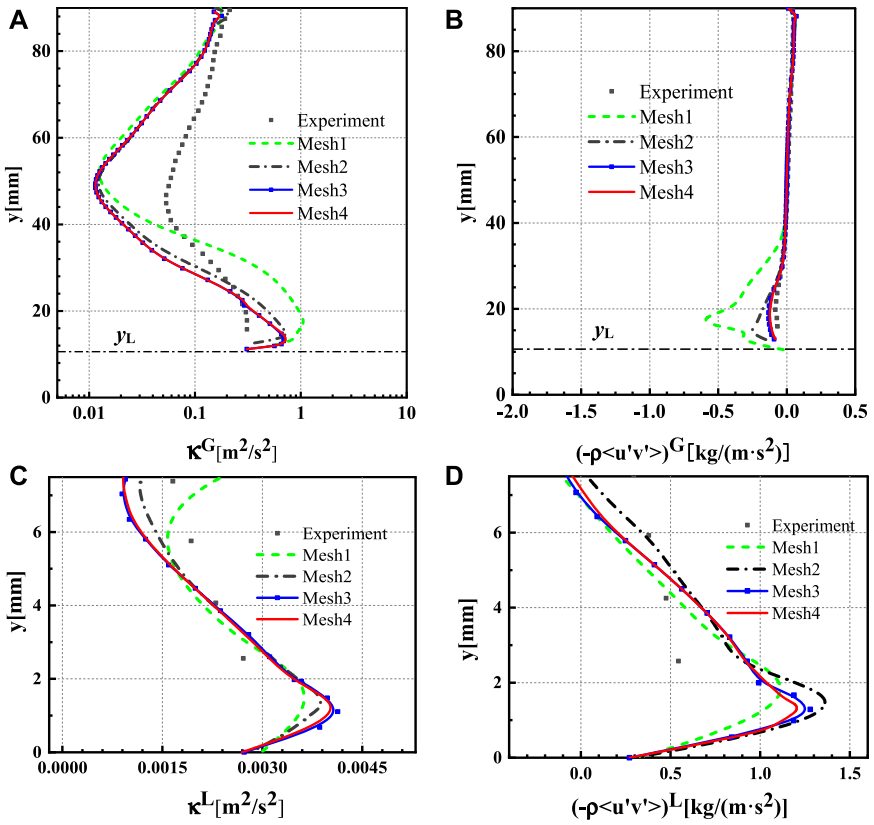

FIGURE 6
Turbulent kinetic energy (**κ**) and Reynolds stress component (**-ρ<u'v'>**) for four meshes at MP1, **(A)** turbulent kinetic energy distribution of the gas phase, **(B)** Reynolds stress component distribution of the gas phase, **(C)** turbulent kinetic energy distribution of the liquid phase, **(D)** Reynolds stress component distribution of the liquid phase.

depends on the surrounding flow pattern and shape of the interface. Höhne and Hänsch (2015) constructed a droplet entrainment model (DEM) for horizontal segregated flows in the AIAD framework. The new droplet phase has the material properties of the liquid phase, the velocity of which is generally consistent with the gas phase. Considering the DEM, the free surface modeling of the two-phase flow can be optimized.

2.2.4 Turbulence damping model

In free surface flows, a high-velocity gradient exists at the interface between two fluids, which generates high turbulence in both phases. Turbulence damping is needed to be considered for correct modelling of such flows. Thompson and Sawko (2012) investigated the influence of the additional turbulence damping in the interfacial region. Egorov et al. (2004) proposed an asymmetric dampening function within the Euler–Euler framework, in which an extra source term S_D was added to the right-hand side of the ω-equation in both liquid and gas phases:

$$S_D = A_{FS}\Delta y\beta\frac{1}{\rho}\left(B\cdot\frac{6\mu}{\beta\Delta n^2}\right)^2 \quad (19)$$

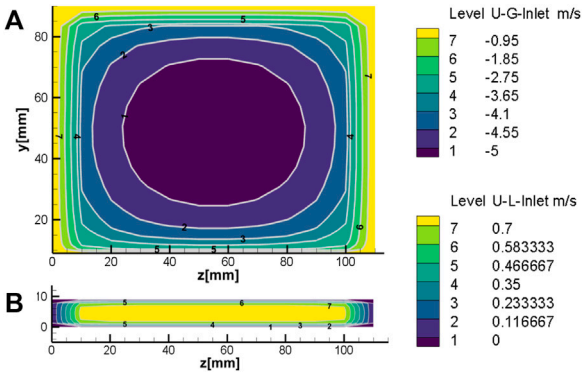

FIGURE 7
Inlet conditions for velocity u, **(A)** gas inlet, **(B)** liquid inlet.

where Δy is the vertical grid width to the phase boundary. And β is a constant, set to 0.075. Δn is the characteristic size of a grid cell at the phase boundary, and a model coefficient $B = 100$ is selected according to Egorov et al. (2004). In addition, the interfacial area

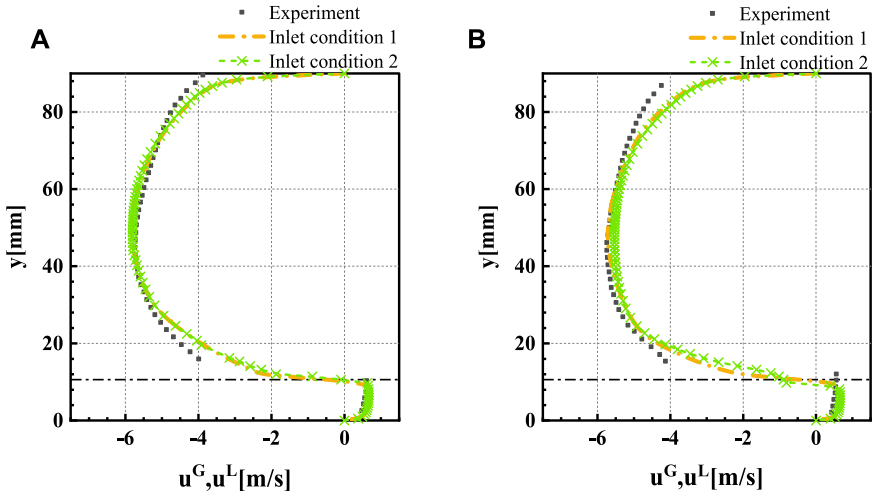

FIGURE 8
Comparison of the *x*-velocity at MP1 and MP2 for four meshes.

density A_{FS} in this equation ensures that only the flow in the region near a free surface is affected by turbulence damping.

3 Simulation setup

The experimental data of the horizontally stratified two-phase flow for validation of the models are obtained from the WENKA facility, as reported by Stäbler et al. (2006), Stäbler (2007). The data correspond to a simplified model of hot leg injection in a PWR, as shown in Figure 3. Water enters from the left side of the rectangular pipe, while air enters from the right side of the pipe, and a splitter plate exists to adjust the liquid level height at the left entrance.

ANSYS Fluent 2019R3 is used to perform the two-phase flow simulation, and the AIAD model is implemented for the first time in the form of a beta function. The flow parameters in the experiment are as specified in Table 1, and two measurement positions MP1 and MP2 are considered.

The inlet boundary conditions are assumed to be a fully developed turbulent channel flow at the air inlet, and a turbulent plane channel flow is assumed at the liquid inlet. The profile that is rescaled and normalized at the gas inlet is derived from the work of Melling and Whitelaw (1976), and a 1/7 power law profile is implemented at the liquid inlet, as indicated by Wilcox (1995). Furthermore, the supercritical flow condition is adopted considering the dimensionless number $Fr_0 = U_{in}^L/\sqrt{gy_0} > 1$ at the water inlet. Therefore, the downstream liquid level rises in this case, and the liquid level at MP2 is higher than that at MP1.

In addition, both the gas and liquid outlets are connected to the external environment involving a constant atmospheric pressure of 0.101,325 MPa. The wall and plates are treated as no-slip boundaries, which indicates that the velocity of the fluid at the wall (or relative velocity) is zero. The meshing of the 3D computational domain is performed using the commercial grid generation software ICEM CFD, which consists of $4.56 \cdot 10^5$ block-structured hexahedral cells, as shown in Figure 4. The computational domain includes part of the air inlet and outlet channel to avoid possible backflow at the outlet. In the range $y < y_0$ and near the sharp edges of the water inlet and outlet, the grid is additionally refined by a factor of two.

The pseudo transient solver is adopted in Fluent in the context of the AIAD; this method adjusts the implicit "under relaxation" of the stationary flow through a physical pseudo time step. The achievement of steady-state flow is determined not only by the residuals but also by the balance of the mass flows at the inlets and outlets. The acceptable difference is 1–3% of the inlet mass flow. This criterion is reached after 250,000 iterations in all runs. The other parameters and numerical discretization methods used in Fluent are shown in Supplementary Appendix Tables SA1,SA2 in the appendix.

4 Numerical results

Within the scope of the work, four numerical runs are compared based on the experimental data, which consider fully or partly the effects of droplet entrainment, turbulence damping and subgrid wave turbulence discussed above. An overview of the four run configurations is given in Table 2.

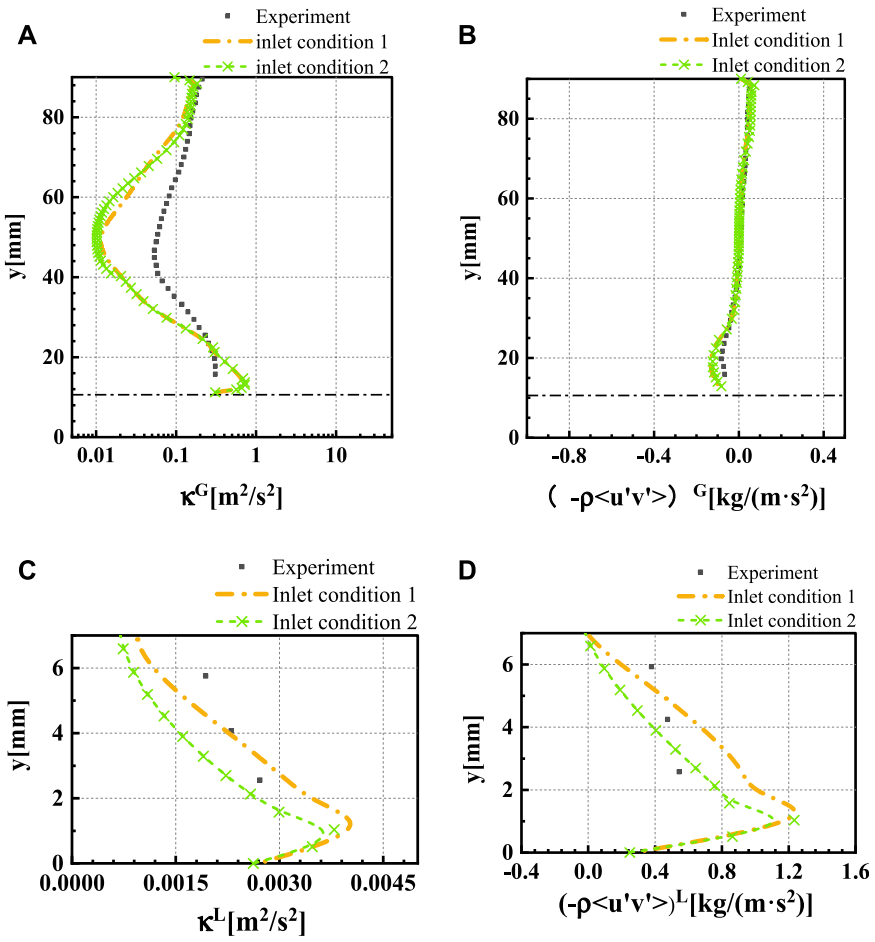

FIGURE 9
Turbulent kinetic energy (**κ**) and Reynolds stress component (**-ρ<u'v'>**) at MP1 under different inlet conditions, **(A)** turbulent kinetic energy distribution of the gas phase, **(B)** Reynolds stress component distribution of the gas phase, **(C)** turbulent kinetic energy distribution of the liquid phase, **(D)** Reynolds stress component distribution of the liquid phase.

4.1 Mesh sensitivity analysis

Meshing is an integral part of CFD simulations, which directly influences the simulation results. To avoid the influence of the mesh on the results, four mesh resolutions are compared for Run 4. The four meshes are labeled "Mesh 1," "Mesh 2," "Mesh 3," and "Mesh 4," and the associated parameters are shown in Supplementary Appendix Table SA3 (see the appendix). The sensitivity of the grid is verified by comparing the following variables: the measured mean wave amplitude y_d at MP1 and MP2, velocities u, turbulence kinetic energy k, and Reynolds stress components $\tau_{T,x,y}$ of the liquid and gas at MP1.

Figure 5 shows that phase velocities obtained with the coarse meshes, i.e. Mesh 1 and Mesh 2, deviate slightly from those with Mesh 3 and Mesh 4. The deviation decreases from MP1 to MP2. Additional information on the liquid levels is provided in Supplementary Appendix Table SA4 (see the appendix), which shows little deviation under the four investigated grid resolutions.

The main differences pertain to the turbulent kinetic energy and Reynolds stress component. As can be seen from Figure 6, due to high gradients the region close to the gas-liquid interface is sensitive to mesh refinement. On the gas-phase side, both the turbulent kinetic energy and Reynolds stress are apt to be over-estimated by the coarse mesh. While on the liquid-phase side the turbulent kinetic energy increases with mesh resolution, no consistent trend is observed for the Reynolds stress component. Overall, the result of Mesh 3 is in agreement with that of Mesh 4. Considering the accuracy of the simulation results and finiteness of the computing resources, Mesh 3 is selected to perform the subsequent calculations.

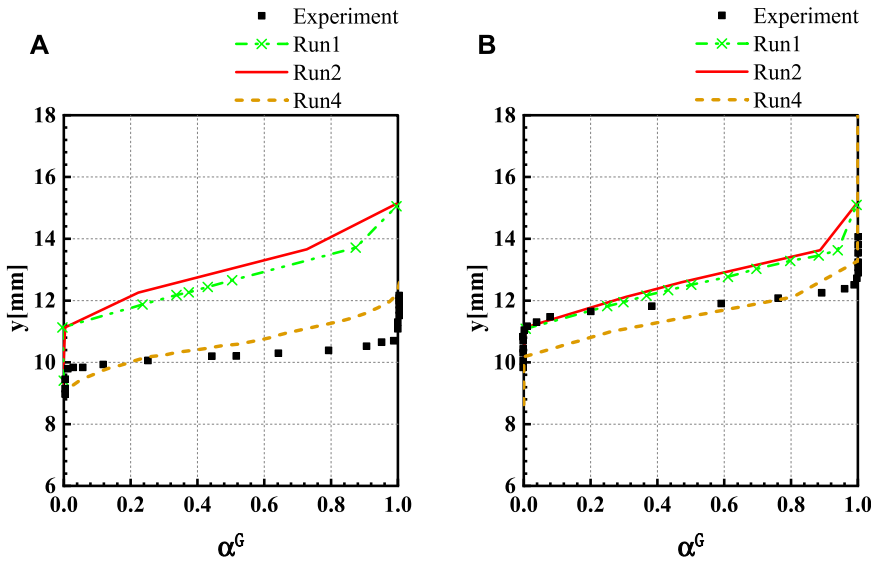

FIGURE 10
Gas volume fraction, **(A)** gas volume fraction distribution at MP1 and **(B)** gas volume fraction distribution at MP2.

4.2 Influence of the inlet conditions

In the experiment, only bulk quantities were specified at the inlets. Therefore, the velocity profiles were assumed according to previous studies. Porombka and Höhne (2015) considered a fully developed turbulent channel flow as a reasonable assumption for the gas inlet and plane turbulent channel flow for the liquid inlet. This condition is referred to as "inlet condition 1". In this work, another inlet condition referred to as "inlet condition 2" is applied to investigate the influence of inlet boundary conditions in the AIAD model. This condition contains the velocity and turbulence profile obtained by extending the gas and liquid inlet piping in a precursor simulation. The gas and liquid inlets extend by 3,000 and 500 mm, respectively, and the velocity profiles obtained in this way are shown in Figure 7.

No significant difference exists between the two conditions in terms of the velocity profile and gas-phase turbulence parameters, see Figure 8, Figures 9A,B. However, in terms of the turbulence parameter profile on the liquid side, the results under inlet condition 1 are closer to the experimental value, see Figures 9C,D. Therefore, to the best of our knowledge, the assumption of the entry conditions introduced by Porombka and Höhne (2015) is reasonable. Nonetheless, regardless of the two inlet conditions, the simulation results show no complete approximation of the experimental results. Further validation for more suitable entry conditions must be performed in future work.

4.3 Influence of the AIAD Submodels

To investigate the effect of the DEM, SWT model, and turbulence damping model, four runs, as shown in Table 2, are compared. The profiles of gas volume fraction at MP1 and MP2 are shown in Figure 10. The gas-liquid interface is identified at $\alpha_G = 0.5$. One can see that at MP1 the result is significantly over-estimated in Run1 and Run 2. The over-prediction in Run 3 is even large, which is not included here. In contrast, Run 4, which accounts for both the droplet entrainment and turbulence damping but not the subgrid wave turbulence, conforms to the data. Consequently, as shown in Supplementary Appendix Table SA5 (see the appendix), the liquid levels in Run 3 are grossly overestimated compared to the experimental values, in which turbulence damping is not considered. Moreover, this run does not reflect the characteristics of the liquid level rising in supercritical flow. The predictions of Run 1 and Run 2 are close to each other, indicating that the droplet entrainment phenomenon is not significant in the investigated case. The finding that Run 4, in which the SWT model is not considered, shows the highest agreement with

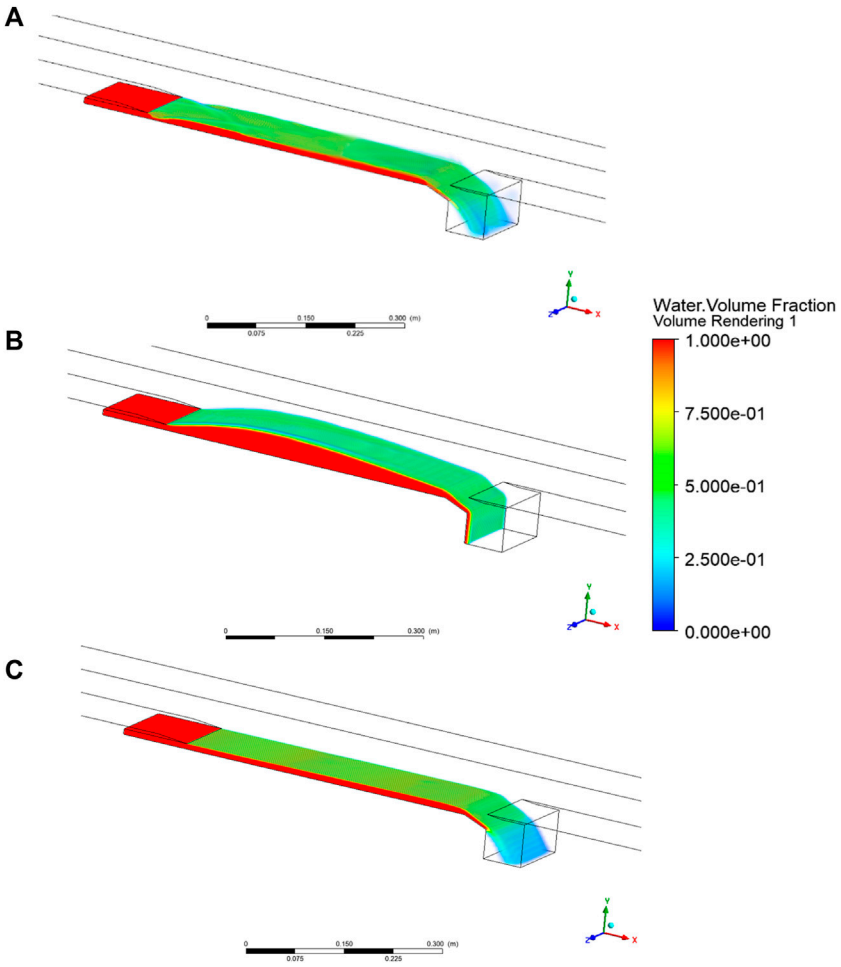

FIGURE 11
The contour of the phase fraction α_G, **(A)** Run 2, **(B)** Run 3 and **(C)** Run 4.

the experimental measurements in terms of the liquid levels leads to a conclusion that further investigation on the model and its implementation in the ANSYS Fluent is necessary.

The significance of the turbulence damping in modelling the horizontal two-phase stratified flow simulation has been verified and validated by Porombka and Höhne (2015). The authors found that the water level is larger than that in the experiment and decreases in the mean flow direction when the turbulence dampening term is neglected. These findings are confirmed by the simulation results of Run 3 based on Fluent in this work. The deactivation of the turbulence damping leads to a partial reversal of the flow and fluctuation of the liquid level, as depicted in Figure 11B). In addition to yielding a qualitatively different velocity profile, the turbulence kinetic energy and Reynolds stress are overpredicted in Run 3 compared with the measured values. Excessive turbulence is produced in the gas-liquid interface region due to the increase in the interfacial shear when the turbulence damping model is not applied. The gas volume fraction, turbulence kinetic energy, and Reynolds stress in the liquid phase predicted in Run 3 are not shown as they are considerably greater than the measured values. This aspect highlights the importance of the turbulence damping model in the AIAD framework.

The flow regimes change from a wavy flow to a lamellar flow when the SWT model is not considered in Run 4, as depicted in Figure 11C). Generally, the deviation between the simulation results and measured profile decreases when

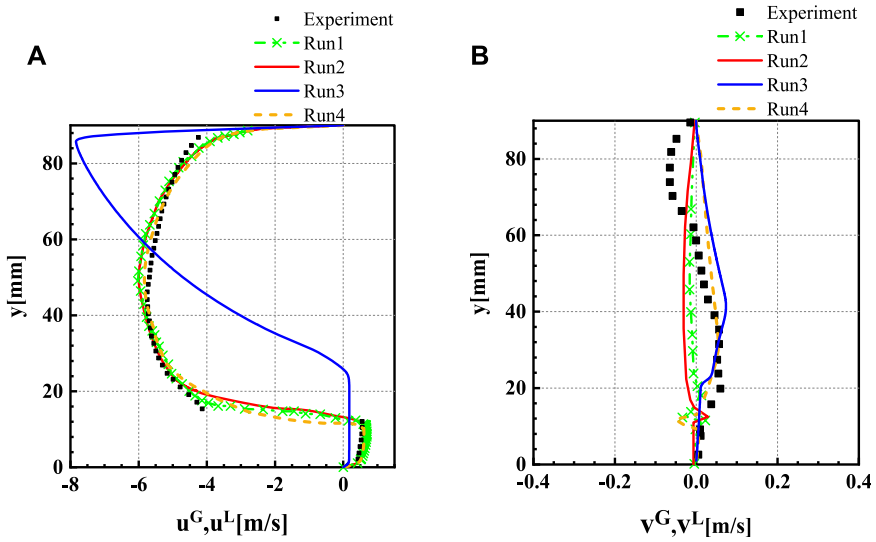

FIGURE 12
Velocity component at MP1, **(A)** the distribution of *x*-velocity, **(B)** the distribution of *y*-velocity.

the SWT model is not applied. Run 4 exhibits the highest agreement with the experimental liquid levels. This finding contradicts the CFX simulation results obtained by Höhne and Porombka (2018), who noted that introducing additional liquid-side turbulence production due to the SWT mechanism does not significantly influence the liquid levels.

The horizontal and vertical velocity profiles of the gas and liquid phases are depicted in Figure 12 along with the measured profiles. The velocity profile in Run 2 is nearly identical to that in Run 1, indicating that the DEM does not considerably influence the velocity in the horizontal stratified flow model. Run 4 yields an x-velocity profile that is qualitatively similar to the experimentally obtained one. When the SWT model is not applied, the y-velocity profile matches the experimental values. In addition, compared to the turbulence damping model, the effect of the SWT model is less notable when modeling a two-phase stratified flow. The SWT source term is added to the *k* transport equation of the liquid phase. The SWT model, directly and indirectly affects the turbulence parameters on the liquid and gas sides. In the center of the upper airflow zone of the square pipe, the curves of the turbulent kinetic energy are nearly identical, although the values are underestimated compared to the measured values, as shown in Figure 13A). When the SWT source term is neglected, the overprediction of the turbulent kinetic energy in the interface region is reduced. Moreover, the SWT model exhibits a notable effect, which can be observed in terms of the Reynolds stress components at MP1, see Figure 13B) and Figure 13D). While increasing both gas and liquid turbulent kinetic energy at the interface, including SWT decreases and increases the Reynolds stress on the gas and liquid side, respectively. Since no further configuration options exist for the SWT model in Fluent, the correctness of the model implementation requires further verification.

Additionally, except for the turbulent kinetic energy at the gas-liquid interface, other quantities are qualitatively indistinguishable whether the DEM is considered or not. When the entrainment of the droplets at the gas-liquid interface is ignored, the turbulent kinetic energy at the interface increases sharply, and the deviation from the experiment results increases for the gas phase. In summary, the free surface modeling of two-phase flow can be optimized using the DEM. Due to the small amount of droplet entrainment in this case, the absence of this model does not considerably influence the results. Further validation is desirable for the cases where droplet entrainment plays an important role.

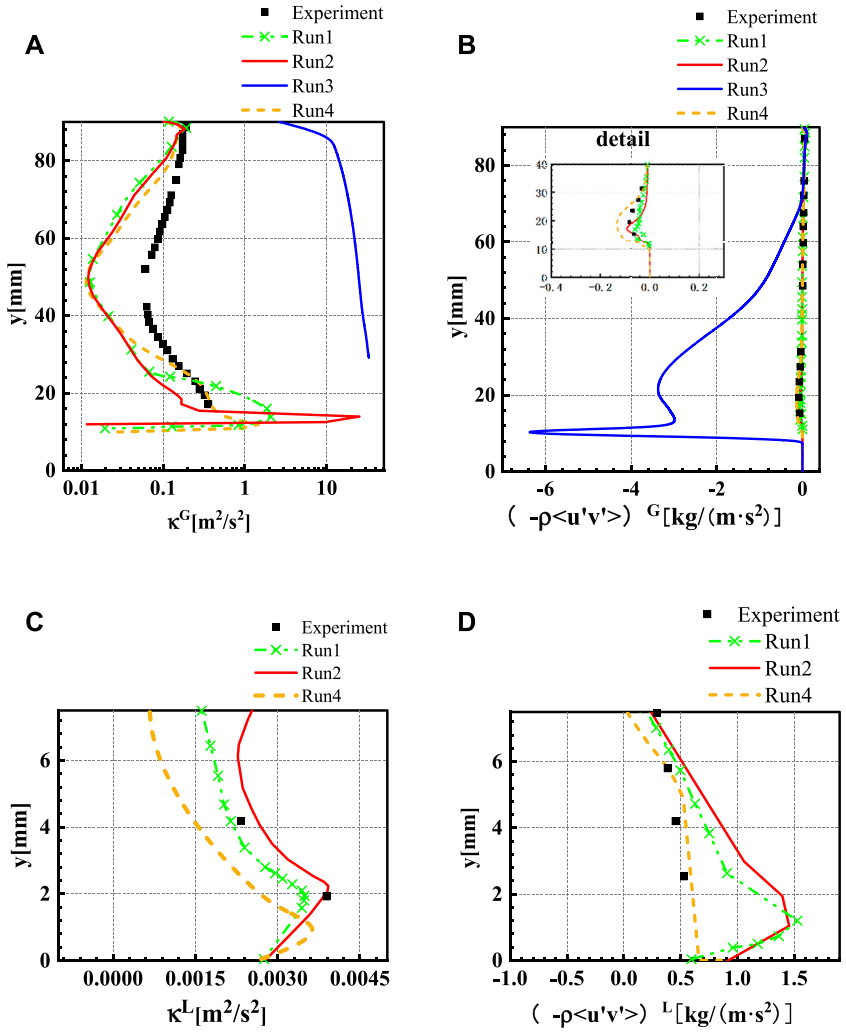

FIGURE 13
Turbulent kinetic energy (κ) and Reynolds stress component (-ρ<u'v'>) at MP1, **(A)** turbulent kinetic energy distribution of the gas phase, **(B)** Reynolds stress component distribution of the gas phase, **(C)** turbulent kinetic energy distribution of the liquid phase, **(D)** Reynolds stress component distribution of the liquid phase.

5 Summary and conclusion

The accuracy of the AIAD module implementation in ANSYS Fluent is investigated based on the experimental data from the WENKA facility, and the following conclusions are obtained:

1) The existing inlet assumptions regarding the fully developed and plane turbulent channel flows were verified to be reasonable and appropriate for the simulation.
2) The simulation results are critically distorted and deviate significantly from the experimental results when the effect of turbulence damping is not considered. The absence of turbulence damping results in the instability of the simulation.
3) The accuracy of the AIAD model at the phase interface is enhanced after the entrained phase is considered. However, the enhancement effect of the DEM for depicting the interface is not significant since only a few droplets are entrained in the WENKA two-phase flow experiment.
4) The effect of the SWT generated by Kelvin–Helmholtz instabilities is not yet clear. The consistency between the simulation results obtained using Fluent and experimental results is not enhanced after the SWT model is adopted.

Further validation in terms of the SWT of higher *We* and *Fr* regimes should be performed in future work. Furthermore, the conclusion regarding the effect of the SWT model is inconsistent with that found in the previous studies with ANSYS CFX.

Data availability statement

The raw data supporting the conclusion of this article will be made available by the authors, without undue reservation.

Author contributions

HY and LL contributed to the conception and design of the study. HZ performed the numerical simulation. LL and HZ wrote the first draft of the manuscript. YL wrote sections of the manuscript. All authors contributed to manuscript revision, read, and approved the submitted version.

Funding

This work was supported by the National Natural Science Foundation of China (Grant No. 51906262) and Natural Science Foundation of Hunan Province, China (Grant No. 2020JJ5735).

Acknowledgments

The computational resource at the High-Performance Computing Center of Central South University is also gratefully acknowledged.

Conflict of interest

The authors declare that the research was conducted in the absence of any commercial or financial relationships that could be construed as a potential conflict of interest.

Publisher's note

All claims expressed in this article are solely those of the authors and do not necessarily represent those of their affiliated organizations, or those of the publisher, the editors and the reviewers. Any product that may be evaluated in this article, or claim that may be made by its manufacturer, is not guaranteed or endorsed by the publisher.

Supplementary material

The Supplementary Material for this article can be found online at: https://www.frontiersin.org/articles/10.3389/fenrg.2022.939499/full#supplementary-material

References

ANSYS Fluent (2019). *ANSYS fluent theory guide*. Canonsburg: Ansys Inc.

Bestion, D. (2012). Applicability of two-phase CFD to nuclear reactor thermalhydraulics and elaboration of Best Practice Guidelines. *Nucl. Eng. Des.* 253, 311–321. doi:10.1016/j.nucengdes.2011.08.068

Bian, H., Sun, Z., Cheng, X., Zhang, N., Meng, Z., Ding, M., et al. (2018). CFD evaluations on bundle effects for steam condensation in the presence of air under natural convection conditions. *Int. Commun. Heat Mass Transf.* 98, 200–208. doi:10.1016/j.icheatmasstransfer.2018.09.003

Bian, H., Sun, Z., Zhang, N., Meng, Z., and Ding, M. (2019). A new modified diffusion boundary layer steam condensation model in the presence of air under natural convection conditions. *Int. J. Therm. Sci.* 145, 105948. doi:10.1016/j.ijthermalsci.2019.05.004

Brocchini, M., and Peregrine, D. (2001). The dynamics of strong turbulence at free surfaces. Part 1. Description. *J. Fluid Mech.* 449, 225–254. doi:10.1017/S0022112001006012

Coste, P. (2013). A large interface model for two-phase CFD. *Nucl. Eng. Des.* 255, 38–50. doi:10.1016/j.nucengdes.2012.10.008

Egorov, Y., Boucker, M., Martin, A., Pigny, S., Scheuerer, M., and Willemsen, S. (2004). Validation of CFD codes with PTS-relevant test cases. *5th Euratom Framework Programme ECORA Project*, 91–116.

Höhne, T.Deendarlianto, and Lucas, D. (2011). Numerical simulations of counter-current two-phase flow experiments in a PWR hot leg model using an interfacial area density model. *Int. J. Heat Fluid Flow* 32 (5), 1047–1056. doi:10.1016/j.ijheatfluidflow.2011.05.007

Höhne, T., and Hänsch, S. (2015). A droplet entrainment model for horizontal segregated flows. *Nucl. Eng. Des.* 286, 18–26. doi:10.1016/j.nucengdes.2015.01.013

Höhne, T., and Mehlhoop, J.-P. (2014). Validation of closure models for interfacial drag and turbulence in numerical simulations of horizontal stratified gas–liquid flows. *Int. J. Multiph. Flow* 62, 1–16. doi:10.1016/j.ijmultiphaseflow.2014.01.012

Höhne, T., and Porombka, P. (2018). Modelling horizontal two-phase flows using generalized models. *Ann. Nucl. Energy* 111, 311–316. doi:10.1016/j.anucene.2017.09.018

Höhne, T., Porombka, P., and Moya, S. (2020). Validation of AIAD sub-models for advanced numerical modelling of horizontal two-phase flows. *Fluids* 5, 102. doi:10.3390/fluids5030102

Höhne, T., and Vallée, C. (2010). Experiments and numerical simulations of horizontal two-phase flow regimes using an interfacial area density model. *J. Comput. Multiph. Flows* 2, 131–143. doi:10.1260/1757-482X.2.3.131

Höhne, T., and Vallée, C. (2009). Modelling of stratified two phase flows using an interfacial area density model. *WIT Trans. Eng. Sci.* 63, 123–133. doi:10.2495/MPF090111

Ishii, M., and Mishima, K. (1984). Two-fluid model and hydrodynamic constitutive relations. *Nucl. Eng. Des.* 82 (2), 107–126. doi:10.1016/0029-5493(84)90207-3

Kim, H. J., Lee, S. C., and Bankoff, S. G. (1985). Heat transfer and interfacial drag in countercurrent steam-water stratified flow. *Int. J. Multiph. Flow* 11 (5), 593–606. doi:10.1016/0301-9322(85)90081-3

Lakehal, D. (2002). On the modelling of multiphase turbulent flows for environmental and hydrodynamic applications. *Int. J. Multiph. Flow* 28 (5), 823–863. doi:10.1016/S0301-9322(01)00086-6

Lockhart, R. W., and Martinelli, R. C. (1949). Proposed correlation of data for isothermal two-phase, two-component flow in pipes. *Chem. Eng. Prog.* 45 (1), 39–48.

Mandhane, J. M., Gregory, G. A., and Aziz, K. (1974). A flow pattern map for gas—Liquid flow in horizontal pipes. *Int. J. Multiph. Flow* 1 (4), 537–553. doi:10.1016/0301-9322(74)90006-8

Melling, A., and Whitelaw, J. H. (1976). Turbulent flow in a rectangular duct. *J. Fluid Mech.* 78 (2), 289–315. doi:10.1017/S0022112076002450

Menter, F. R. (1994). Menter, F.: Two-equation eddy-viscosity transport turbulence model for engineering applications. *AIAA J.* 3232 (88), 1598–1605. doi:10.2514/3.12149

Ohnuki, A., Adachi, H., and Murao, Y. (1988). Scale effects on countercurrent gas-liquid flow in a horizontal tube connected to an inclined riser. *Nucl. Eng. Des.* 107 (3), 283–294. doi:10.1016/0029-5493(88)90036-2

Porombka, P., and Höhne, T. (2015). Drag and turbulence modelling for free surface flows within the two-fluid Euler–Euler framework. *Chem. Eng. Sci.* 134, 348–359. doi:10.1016/j.ces.2015.05.029

Porombka, P. (2015). "Modelling of free surface flow within the two-fluid Euler-Euler Framework," in ASME/JSME/KSME 2015 Joint Fluids Engineering Conference. Seoul, South Korea: American Society of Mechanical Engineers.doi:10.1115/AJKFluids2015-05133

Stäbler, T. (2007). *Experimentelle Untersuchung und physikalische Beschreibung der Schichtenströmung in horizontalen Kanälen*. Stuttgart, Germany: Universität Stuttgart. (PhD Thesis). doi:10.5445/IR/200068452

Stäbler, T., Meyer, L., Schulenberg, T., and Laurien, E. (2006). "Turbulence structures in horizontal two-phase flows under counter-current conditions," in *Fluids engineering summer meeting* (Berlin, Germany: Stuttgart), 61–66. doi:10.1115/FEDSM2006-98211

Taitel, Y., and Dukler, A. E. (1976). A model for predicting flow regime transitions in horizontal and near horizontal gas-liquid flow. *AIChE J.* 22 (1), 47–55. doi:10.1002/aic.690220105

Tas-Koehler, S., Liao, Y., and Hampel, U. (2021). A critical analysis of drag force modelling for disperse gas-liquid flow in a pipe with an obstacle. *Chem. Eng. Sci.* 246, 117007. doi:10.1016/j.ces.2021.117007

Thompson, C. P., and Sawko, R. (2012). "Interface turbulence treatments in RANS model of stratified gas/liquid flows," in *Proceedings of the ASME 2012 international mechanical engineering congress and exposition*. Houston, Texas, United States: ASME, 621–626. doi:10.1115/IMECE2012-89421

Tomiyama, A., Kataoka, I., Zun, I., and Sakaguchi, T. (1998). Drag coefficients of single bubbles under normal and micro gravity conditions. *JSME Int. J. Ser. B Fluids. Therm. Eng.* 41 (2), 472–479. doi:10.1299/jsmeb.41.472

Wilcox, D. C. (1995). Turbulence modeling for CFD. *DCW Ind.* 289, 406–407. doi:10.1017/S0022112095211388

Yang, W., and Yang, Z. (2012). Aerodynamic investigation on tiltable endplate for WIG craft. *Aircr. Eng. Aerosp. Technol.* 84, 4–12. doi:10.1108/00022661211194933

Yao, W., Bestion, D., Coste, P., and Boucker, M. (2005). A three-dimensional two-fluid modeling of stratified flow with condensation for pressurized thermal shock investigations. *Nucl. Technol.* 152, 129–142. doi:10.13182/NT05-A3665

Nomenclature

Latin symbols

f blending function in AIAD model (–)
S_D dampening term [kg/(m^3 s^2)]
$\mathbf{F}_D$ drag force (kg m/s^2)
C_D drag force coefficient (–)
u liquid velocity (m/s)
U relative velocity (m/s)
k turbulence kinetic energy (m^2/s^2)
q turbulent velocity (m^2/s^2)
$\boldsymbol{A}$ interfacial area density (1/m)
$\boldsymbol{d}$ diameter (m)
$\boldsymbol{g}$ gravitational acceleration (m/s^2)
$\boldsymbol{L}$ length (m)liquid
$\mathbf{n}$ unity normal vector
$\boldsymbol{p}$ production term [kg/(m s^3)]
$\boldsymbol{t}$ time (s)
$\boldsymbol{u,v,w}$ Cartesian velocity components (m/s)
$\boldsymbol{x,y,z}$ Cartesian coordinates (m)
$\boldsymbol{y_0}$ liquid level at inlet (m)
$\boldsymbol{y_L}$ liquid level (m)

Dimensionless numbers

Fr Froude number (–)
Re Reynolds number (–)
We Weber number (–)

Greek symbols

δ_{ij} Kronecker symbol (–)
ω rate of dissipation of k (1/s)
$\boldsymbol{\tau}$ stress tensor (kg m/s^2)
μ Viscosity (Pa s)
α void fraction
$\boldsymbol{\tau}_W$ wall-like shear stress (kg m/s^2)
$\boldsymbol{\rho}$ density (kg/m^3)
$\boldsymbol{\sigma}$ surface tension (N/m)

Subscripts and superscripts

B bubble
D droplet
FS free surface
G gas
i,j,k tensor indices
k phase index
L length (m)liquid
sw subgrid waves
SWT subgrid wave turbulence
T turbulent quantity

Advantages of publishing in Frontiers

OPEN ACCESS
Articles are free to read for greatest visibility and readership

FAST PUBLICATION
Around 90 days from submission to decision

HIGH QUALITY PEER-REVIEW
Rigorous, collaborative, and constructive peer-review

TRANSPARENT PEER-REVIEW
Editors and reviewers acknowledged by name on published articles

Frontiers
Avenue du Tribunal-Fédéral 34
1005 Lausanne | Switzerland

Visit us: www.frontiersin.org
Contact us: frontiersin.org/about/contact

REPRODUCIBILITY OF RESEARCH
Support open data and methods to enhance research reproducibility

DIGITAL PUBLISHING
Articles designed for optimal readership across devices

FOLLOW US
@frontiersin

IMPACT METRICS
Advanced article metrics track visibility across digital media

EXTENSIVE PROMOTION
Marketing and promotion of impactful research

LOOP RESEARCH NETWORK
Our network increases your article's readership